The FAA's Center of Excellence for UAS Research

ASSURE

Alliance for System Safety of UAS through Research Excellence

WICHITA STATE
UNIVERSITY
NATIONAL INSTITUTE
FOR AVIATION RESEARCH

Determine the Collision Severity of small Unmanned Aircraft Systems (sUAS) in Flight Critical Zones of Manned Helicopters (A11L.UAS.115)

August 2024

NOTICE

LEGAL DISCLAIMER

The information provided herein may include content supplied by third parties. Although the data and information contained herein has been produced or processed from sources believed to be reliable, the Federal Aviation Administration makes no warranty, expressed or implied, regarding the accuracy, adequacy, completeness, legality, reliability or usefulness of any information, conclusions or recommendations provided herein. Distribution of the information contained herein does not constitute an endorsement or warranty of the data or information provided herein by the Federal Aviation Administration or the U.S. Department of Transportation. Neither the Federal Aviation Administration nor the U.S. Department of Transportation shall be held liable for any improper or incorrect use of the information contained herein and assumes no responsibility for anyone's use of the information. The Federal Aviation Administration and U.S. Department of Transportation shall not be liable for any claim for any loss, harm, or other damages arising from access to or use of data or information, including without limitation any direct, indirect, incidental, exemplary, special or consequential damages, even if advised of the possibility of such damages. The Federal Aviation Administration shall not be liable to anyone for any decision made or action taken, or not taken, in reliance on the information contained herein.

TECHNICAL REPORT DOCUMENTATION PAGE

1. Report No. A11L.UAS.115_A67	2. Government Accession No.	3. Recipient's Catalog No.
4. Title and Subtitle **Determine the Collision Severity of small Unmanned Aircraft Systems (sUAS) in Flight Critical Zones of Manned Helicopter (A11L.UAS.115)**		5. Report Date **August 2024**
		6. Performing Organization Code
7. Author(s) **Gerardo Olivares, Armando De Abreu, Luis Castillo, Akhil Bhasin, Ankit Gupta, Deepak Singh, Luis Gomez**		8. Performing Organization Report No.
9. Performing Organization Name and Address **National Institute for Aviation Research** **Wichita State University** **1845 Fairmount** **Wichita, KS 67260-0093**		10. Work Unit No. (TRAIS)
		11. Contract or Grant No.
12. Sponsoring Agency Name and Address **U.S. Department of Transportation** **Federal Aviation Administration** **Office of Aviation Research** **Washington, DC 20591**		13. Type of Report and Period Covered
		14. Sponsoring Agency Code **5401**

15. Supplementary Notes

16. Abstract

The use of unmanned aerial systems (UASs) has increased dramatically in recent years. As the number of UASs sold continues to increase, proper integration of UAVs into the airspace is a major safety concern due to the potential for a UAV-airplane collision. Recreational users are the highest safety concern since they may be unaware or unconcerned with regulations and rules concerned with restricted operation of their devices in certain airspaces. This research evaluates the collision severity levels resulting from mid-air collisions between small UASs (from 2.7 lbs to 55 lbs) and Part 27 Rotorcraft. Details regarding the different sUAS models used for this study and their development and validation efforts are shown. In addition, this report provides an overview of the reverse engineering process for the Part 27 rotorcraft chosen for this program, as well as the development of the detailed Finite Element Model of the same. Finally, a summary of the mid-air collision results and their severity with respect to the safety flight of the Part 27 rotorcraft are presented and discussed.

17. Key Words **Crashworthiness, Airborne Collision, UAS, National Institute for Aviation Research, NIAR**	18. Distribution Statement This document is available to the U.S. public through the National Technical Information Service (NTIS), Springfield, Virginia, 22161. This document is also available from the Federal Aviation Administration William J. Hughes Technical Center at actlibrary.tc.faa.gov.		
19. Security Classif. (of this report) Unclassified	20. Security Classif. (of this page) Unclassified	21. No. of Pages	22. Price

Form DOT F 1700.7 (8-72)   Reproduction of completed page authorized

REVISION HISTORY

Revision	Description of Modifications	Release Date
-	Final Report – FAA Internal - Initial release	06/28/2024
A	Fixed typos and added an additional paragraph in Section 4.1 (page 99) and Section 5.5.5 (Page 184)	08/22/2024

ACKNOWLEDGEMENTS

TABLE OF CONTENTS

LIST OF FIGURES

xvii

LIST OF TABLES

LIST OF ACRONYMS

ARC	Aviation Rulemaking Committee
CAD	Computer-Aided Design
CTOL	Conventional Takeoff and Landing
CFR	Code of Federal Regulations
CG	Center of Gravity
COVID-19	Coronavirus Disease 2019
DIC	Digital Image Correlation
ELoS	Equivalent Level of Safety
FAA	Federal Aviation Administration
FE	Finite Element
LiPo	Lithium-ion Polymer (battery)
MTOW	Maximum Takeoff Weight
NAS	National Airspace System
NRB	Nodal Ridge Body
NTSB	National Transportation Safety Board
OML	Outer Mold Line
QS	Quasi-Static
sUAS	Small Uncrewed Aircraft System
UAS	Uncrewed Aircraft System
UAV	Uncrewed Aircraft Vehicle
VTOL	Vertical Takeoff and Landing

EXECUTIVE SUMMARY

According to the latest industry forecast studies, the Uncrewed Aircraft System (UAS) market volume is expected to reach 2.78 million units by 2027 [1]. Nonetheless, safety, regulatory, social, and technical challenges must be addressed before the sight of an uncrewed aircraft in the sky becomes as common and accepted by the public as its crewed counterpart. The primary goal of regulating UAS operations in the National Airspace System (NAS) is to ensure an appropriate level of safety. The effect of an airborne collision between a UAS and a crewed aircraft is a concern to the public and government officials at all levels. Research is needed to define airborne hazard severity thresholds for collisions between uncrewed and crewed aircraft or collisions with people on the ground.

This report analyzes airborne collision scenarios between a range of UAS (2.7 lbs. to 55 lbs. quadcopters and fixed-wing) with a 14 Code of Federal Regulations (CFR) Part 27 rotorcraft. Detailed Finite Element Models of the UAS and the rotorcraft validated through NIAR's building block approach have been used to reduce the time and costs associated with physical testing at the full-scale level. The following critical areas for the rotorcraft were identified for analysis: the front cowling, horizontal stabilizer, rear servo, windshield, and main rotor blade. The severity evaluation criterion follows the guidelines of the ASSURE Airborne Collision Phase I program [2] and an updated Blade Damage criterion originally defined in the UAS Airborne Collision Severity Evaluation of Part 29 Rotorcraft program [3]. The criteria define four levels for damage assessment, as shown in Table 1.

Table 1. Damage severity evaluation criteria.

Severity	Airframe Damage Description	Blade Damage Description
Level 1	The airframe is undamaged. Small deformations.	Blade undamaged. Scratches or small dents on a rotor blade. No crack initiation.
Level 2	Extensive permanent deformation on external surfaces. Some deformation in internal structure. No Skin Failure.	Dents on a rotor blade leading edge. Minor crack initiation. No debonding.
Level 3	Skin fracture. Penetration of at least one component into the airframe.	Any debonding. Skin buckling. Major crack initiation.
Level 4	Penetration of UAS into airframe and failure of the primary structure.	Any material loss leading to a blade imbalance. Heavy blade twist and deflection leading to an imbalance on a single-blade.

Overall, the small size and type of construction utilized in the Part 27 rotorcraft results in severe damage when there is a mid-air collision with larger sUAS (25 and 55 lbs.). Conversely, impacts with sUAS less than 10 lbs. are less severe, even at higher speeds (149 knots). The findings from this research may be used to conservatively define airborne hazard severity thresholds for collisions between sUAS of several sizes and weights and a Part 27 [4] rotorcraft.

1   INTRODUCTION

Uncrewed Aircraft Systems (UASs) are the fastest-growing sector of the aviation industry today; according to The Association for Uncrewed Vehicles International, the largest trade group around UASs, estimated (as of 2013) that by 2025 more than 100,000 jobs will be created in the US with an economic impact of more than $82 billion [5]. In addition, the UAS market volume is expected to reach 2.78 million units by 2027 [1]. Nonetheless, safety, regulatory, social, and technical challenges must be addressed before the sight of an uncrewed aircraft in the sky becomes as common and accepted by the public as its crewed counterparts.

The effect of an airborne collision between a UAS and a crewed aircraft is a concern to the public and government officials at all levels. The primary goal of regulating UAS operations in the National Airspace System (NAS) is to ensure an appropriate level of safety. While the effects of bird impacts on airplanes are well documented, little is known about the effects of more rigid and higher mass UASs on aircraft structures and propulsion systems. This research evaluates the severity of small UAS (sUAS) (under 55 lbs., as defined in the Small Uncrewed Aircraft Rule (*Part 107*)) collisions on rotorcraft.

Previous research efforts on the A16 Task of ASSURE [3, 6] focused on analyzing airborne collisions between sUAS and general aviation airplanes *14 CFR Part 23* [7], as well as rotorcraft airframes certified under part *14 CFR Part 29* [8]. The research in this document extends to larger sUAS (up to 55 lbs). It will focus on the impacts to medium-sized Part 27 helicopters, which cover the larger majority of helicopters operating in the NAS. Currently, 94% of the total number of helicopters in the NAS fall under 14 CFR Part 27 [4, 9]. The impact cases under this research examine the following five locations:

1.   Horizontal Stabilizer
2.   Vertical Stabilizer
3.   Main Rotor Blade Support (Mast)
4.   Blades
5.   Windshield
6.   Nose

Three different collision speed scenarios will be considered:

1.   Forward flight at a collision speed of 94 kts. (Medium).
2.   Cruise flight at a collision speed of 149 kts. (Max).
3.   Hover condition with a speed of collision of 39 kts. In this condition, the severity of a lateral impact on the tail cone and the tail rotor needs to be considered.

To accelerate results, the lessons learned and the sUAS Finite Element Models (FEM) developed in previous ASSURE Tasks A3, A14, A16, A17, and Large sUAS Impact collision studies were used for analysis where possible.

1.1 BACKGROUND

1.1.1 Uncrewed Aircraft Systems Categories

A UAS is an Uncrewed Aircraft Vehicle (UAV) and the equipment necessary for that aircraft's safe and efficient operation. A UAV is a component of a UAS. It is defined by statute as an aircraft that is operated without the possibility of direct human intervention from within or on the aircraft [10]. It can either fly autonomously or be piloted remotely.

Currently, there is no standard for the classification of UASs. Defense agencies have their standard, and civilian agencies worldwide have their ever-evolving categories and definitions for UASs. Currently, the Federal Aviation Administration (FAA) classifies UASs into the following categories:

- **Small Uncrewed Aircraft Rule (*Part 107*) [11]:** The rule does not cover the full spectrum of UAS types or weights. The FAA acknowledges that rulemaking is an incremental stage of adding UASs into the NAS. The small non-hobby or non-recreational UASs must be operated under the following limitations:
    - Uncrewed aircraft must weigh less than 55 lbs. (25 kg).
    - It cannot be flown faster than a ground speed of 87 knots (100 mph).
    - It cannot be flown higher than 400 ft. (≈122 m) above ground level unless flown within a 400 ft. radius of a structure and does not fly higher than 400 ft. above the structure's immediate uppermost limit.
    - Minimum visibility, as observed from the location of the control station, may not be less than three statute miles (sm).
    - The minimum distance from clouds is 500 ft (≈152 m) below a cloud and no less than 2,000 ft. (≈610 m) horizontally from the cloud.
- **Micro-UAS:** The Aviation Rulemaking Committee (ARC) was focused on the flight over people and, in furtherance of that goal, identified four sUAS categories, defined primarily by the level of risk of injury posed for operations over people. For each category, the ARC recommends a risk threshold that correlates to either a weight or impact energy equivalent and, to the extent necessary to minimize the risks associated with that category, additional performance standards and operational restrictions. The following is a summary of the category recommendations [12]:
    - For Category 1, an sUAS may operate over people if the mass (including accessories/payload, *e.g.*, cameras) is 250 g or less.
    - Under Categories 2, 3, and 4, an sUAS may operate over people if it does not exceed the impact energy threshold specified for each category, as certified by the manufacturer using industry consensus test methods, and if its operator complies with operational restrictions specified for each category.

1.1.2 Uncrewed Aircraft Systems Market Size

The UAS market is divided into two groups: Hobbyist and Commercial. Table 2 presents the registration forecast for sUAS until 2027 [1].

Table 2. Registration forecast (base) summary (million sUAS units) [1].

	2023	2024	2025	2026	2027
Hobbyist (model aircraft)	1.750	1.785	1.804	1.815	1.823
Commercial (non-model aircraft)	0.805	0.862	0.904	0.933	0.955
TOTAL UASs	2.555	2.647	2.708	2.748	2.778

1.1.2.1 Hobbyist UAS Forecast

To operate in the NAS, the FAA must ensure that aircraft operators are aware of the system they are operating and that the agency also has the means to identify owners. One way to accomplish this is through aircraft registration and marking. On December 14, 2015, the FAA issued a rule requiring all UASs weighing more than 0.55 lbs. (250 g) and less than 55 lbs. (24.9 kg) to be registered using a new online system (UASs weighing more than 55 lbs. must be registered using the existing Aircraft Registration Process). This registration rule aids in investigations and allows the FAA to gather data about UAS use.

The FAA forecasts the market each year according to the sales and registration records. This yearly update identifies the UAS market growth, predicts the following years, and determines an accurate count of the actual active vehicles. Figure 1 presents the most recent record on recreational UAS registration [1] since the rule was instated in 2015. Registrations reached 1.44 million UAS by the end of 2022, which is lower than what the FAA expected in its previous annual prediction. One of the factors affecting the slower registration rate has been the COVID-19 pandemic, which has changed the market's inertia.
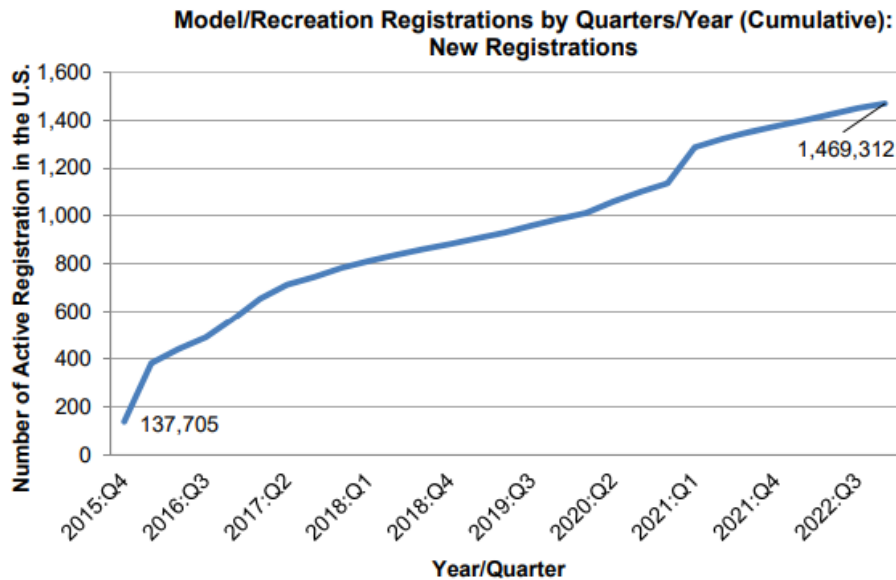
Figure 1. Recreational UAS registrations - December 2020 update [1].

3

1.1.2.2   Commercial UAS Forecast

In 2015, in support of the sUAS registration rule, a sales forecast for commercial sUASs was developed to derive the potential demand for the new online registration system. That forecast predicted that the potential sales of commercial sUAS requiring registration would grow to 2.7 million by 2020 [5]. The actual market did not evolve at the speed those predictions indicated, but it is constantly growing, as indicated in Figure 2. In addition, the FAA noted in its latest annual revision [1] that the regulatory clarity provided by Part 107 [11] in the recent update on Operation over People increases the opportunities for further integration of sUAS into the NAS.
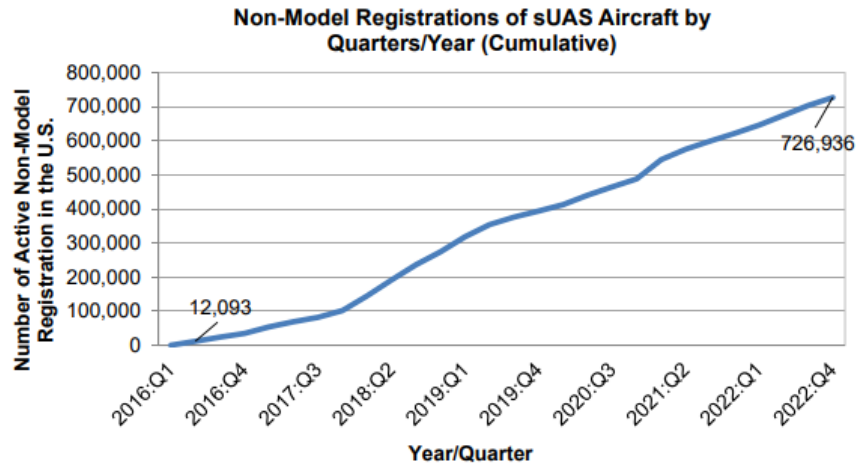
Figure 2. Commercial UAS registrations - December 2020 update [1].

The fast-growing UAS market demands waivers to operate beyond the existing Part 107 [11] regulations. Figure 3 shows the FAA's five most common waiver requests until December 2020. Waivers to operate commercial sUAS at night are the most repeated waiver requests.
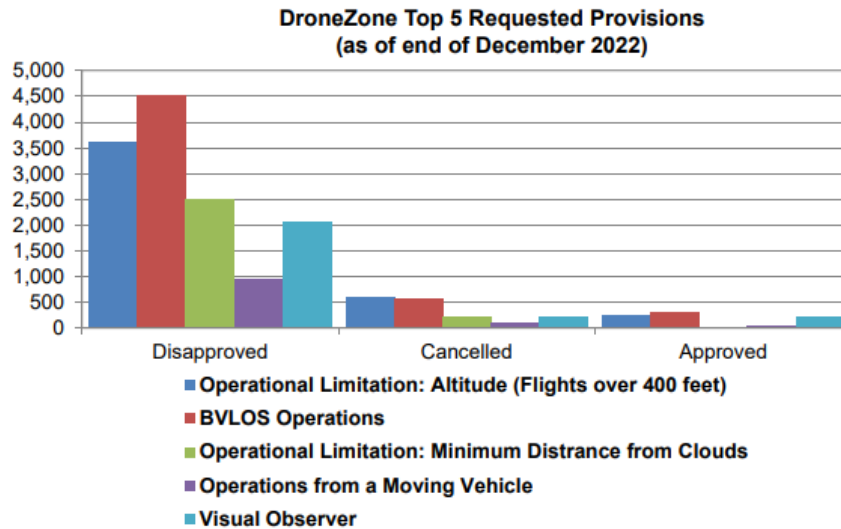
Figure 3. Five most common waiver requests to operate commercial UAS [1].

4

1.1.3   Uncrewed Aircraft Systems Impact Severity Classification

Conventional *Title 14 (14 CFR)* safety analyses [4, 7, 8, 13] include hazards to flight crew and occupants that may not be applicable to uncrewed aircraft. However, UAS operations may pose unique hazards to other aircraft and people on the ground. Therefore, it is necessary to determine hazard severity thresholds for UASs using safety characteristic factors that affect the potential severity of UASs in collisions with other aircraft on the ground or in airborne encounters and collisions with people on the ground. The factors that determine the outcome of an airborne collision are numerous and complex and highly dependent on the structural design and materials used to construct the UAS.

1.1.3.1   Uncrewed Aircraft Systems Mid-Air Collisions Equivalent Level of Safety

The primary goal of regulating UAS operations in the NAS is to assure an appropriate level of safety. National aviation agencies quantify this goal as an "Equivalent Level of Safety" (ELoS) with crewed aviation. However, there are major key differences between crewed and uncrewed aviation that lie not only in the separation of the pilot from the cockpit and the level of automation introduced but also in the variety of architectures and materials used for the construction of UASs. These differences could introduce new failure modes and, as a result, increase the perceived risk that needs to be evaluated [14].

To have an ELoS, according to the definition of the Range Commanders Council in its guidance on UAS operations, any UAS operation or test must show a level of risk to human life no greater than that for an operation or test of a piloted aircraft [15].

Although current crewed aviation regulations do not impose limits on fatality rates, a statistical analysis of historical data can provide valuable insight into crewed aviation's collision and fatality rates. It could be used to define the basis for the ELoS of UAS.

For an ELoS to be derived, accident statistics involving mid-air collisions are required. The National Transportation Safety Board (NTSB) has defined two categories of relevant collision accident scenarios: *(i)* in-flight collisions with obstacles such as birds, trees, power lines; and *(ii)* mid-air collisions with other aircraft. The latter could be used to define the UAS requirements. Data pertaining to this approach is presented in reference [14] to NTSB data compiled between 1983 and 2006. If this approach is used in the future as a reference metric to define the ELoS, it is recommended to conduct further studies that include updated NTSB data available.

Once the ELoS is defined based on historical data from crewed aviation, the next step is to develop a method to estimate the probability of mid-air collisions between UASs and crewed aircraft. Several authors have published methodologies on how to evaluate the risk of mid-air collisions between crewed aircraft and UASs [15, 16]; some of the midair collision models are based on a theory originally developed to predict the collision frequency of gas molecules [15]. This theory was similarly applied to air traffic [17, 18]. The collision frequency between a single UAS and transient air traffic is a product of the transient aircraft density, the combined frontal areas, and the relative closing velocity between the colliding crewed and uncrewed aircraft [16].

The aforementioned metrics provide statistical probabilities of UAS mid-air collisions according to specific parameters defined for the evaluation. It should be noted that not all collisions could lead to catastrophic accidents. The large variability of UAS sizes and the fact that not all aircraft

systems are critical for remaining airborne means that the aircraft involved may survive certain collisions.

The risk assessment to develop an Airborne Collision UASs Impact Severity Classification can be divided into three elements:

- **Estimation of the probability of mid-air collision** between UASs and crewed aircraft. This will be a function of the operating airspace, aircraft operating within the airspace, and the UAS configurations operating within the shared airspace. Methods to estimate the probability of impact are presented in references [15, 16].
- **Evaluation of damage potential for typical UASs** classes based on weight, architecture, operational characteristics [altitude, velocity] mid-air collision scenarios per crewed aircraft class (commercial, general aviation, rotorcraft, etc.) to assess the damage severity to crewed aircraft. Several groups advocate using simplified ballistic penetration models [19], similarity principles to existing bird strike requirements, or kinetic energy thresholds [20, 21]. This project aims to evaluate the severity of a typical quadcopter and fixed-wing UAS airborne collision with detailed FEM of the UASs and the target aircraft. These results will be compared with the proposed penetration mechanics and energy-based criteria.
- Once the probability of an airborne collision is determined, **the damage models obtained through the research presented in this study can be combined with the probabilistic collision models to define appropriate ELoS criteria.**

1.2   PROJECT SCOPE

sUAS generally operates at lower altitudes, often sharing airspace with patrol aircraft, agricultural operators, and emergency medical rotorcraft. Impact scenarios of UAS with rotorcrafts differ considerably from those scenarios involving commercial transport or business jets (Task A3). Expanding on the rotorcraft work in Task A16, an analysis of probable scenarios of a mid-air collision between sUAS from 2.7 to 55 lbs. and Part 27 helicopter components will be performed in this research. The Robinson R44 helicopter was reverse-engineered into a detailed Computer-Aided Design (CAD) and Finite Element (FE) model as a representative Part 27 helicopter for these new scenarios. Finally, impact simulations that focus on providing airframe severity evaluations after impact were completed. To accelerate results, lessons learned and the UAS FEMs developed in previous ASSURE projects were used for analysis where possible.

The main research questions being answered through this research are:

- What are the hazard severity criteria for an UAS collision (mass, kinetic energy, etc.)?
- What is the severity of an UAS collision with a Part 27 rotorcraft in mid-air?
- Can the severity of an UAS mid-air collision with a Part 27 rotorcraft be characterized into categories based on the UAS? What would those categories look like?
- Can an UAS impact be classified as similar to a bird strike?
- What are the characteristics of a UAS where it will not be a risk to an aircraft?
- How is the severity of a collision with Part 27 rotorcraft compared with Part 29 rotorcraft for relatively smaller UAS (2.7 and 4.0 lbs.)?

6

It is important to emphasize that the intent of this research was not to conduct an assessment of already certified products (*e.g., 14 CFR Part 23/25/27/29/33*) but to analyze the characteristics of small UAS that contribute to damage of the airframe of manned rotorcraft as a resulting from an airborne collision.

The collision severity evaluation criterion follows the ASSURE Airborne Collision Phase I program guidelines for the airframe [2] and the Blade Damage criterion defined in the UAS Airborne Collision Severity Evaluation of Part 29 Rotorcraft program [3]. The criteria define four levels for damage assessment: level 1 as the lowest (no damage) and level 4 as the highest (primary structure compromised/rotor blade complete failure/separation).

2 UAS PROJECTILE DEFINITION

In Task A3 [22], NIAR developed a 2.7 lbs. quadcopter, which was a representative DJI Phantom 3 Standard shown in Figure 4. The quadcopter was validated through component-level testing and full-assembly impacts. In a later effort, under Task A14 [23], NIAR updated a 4.4 lbs. fixed-wing UAS FEM developed by Mississippi State University in Task A3 [24] to develop a 4 lbs. scaled-down version of the Fixed-Wing. The fixed-wing model is based on a Precision Hawk Lancaster Hawkeye Mark III, shown in Figure 5. The updates involved coupon and impact testing carried out at NIAR facilities to validate and verify the crash behavior of the model.

In a different program that collaborated with an industry partner [25], NIAR developed larger quadcopter and fixed-wing UAS models (NIAR-UAS), as shown in Figure 6. These models were adjusted to represent a 25 lbs. and 55 lbs. configuration in the large UAS collision report [26].

This chapter presents the UAS models selected for current work. Those models are:

- UAS 2.7 lbs. Quadcopter.
- UAS 4 lbs. Fixed-Wing.
- UAS 10 lbs. Quadcopter: scaled-up model of the Task A3 [22] 2.67 lbs. Quadcopter.
- UAS 12lbs. Fixed-Wing: scaled-up model of the Task A14 [23] 4.4 lbs. Fixed-wing.
- UAS 25 lbs. Quadcopter: scaled version of UAS developed by NIAR [26].
- UAS 25 lbs. Fixed-Wing: scaled version of UAS developed by NIAR [26].
- UAS 55 lbs. Quadcopter: scaled-up version of the 25 lbs. UAS model.
- UAS 55 lbs. Fixed-Wing: scaled-up version of the 25 lbs. UAS model.

Figure 4. DJI Phantom 3.
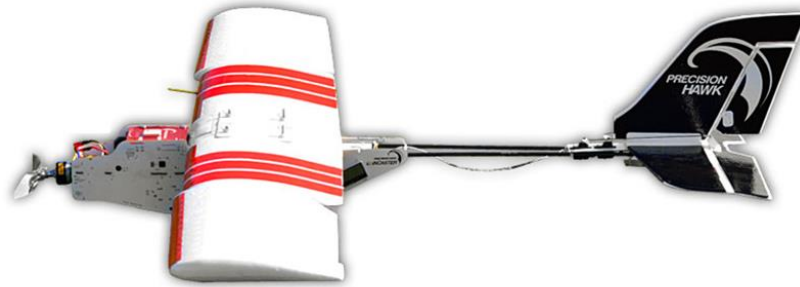
Figure 5. Precision Hawk Lancaster Hawkeye Mark III.
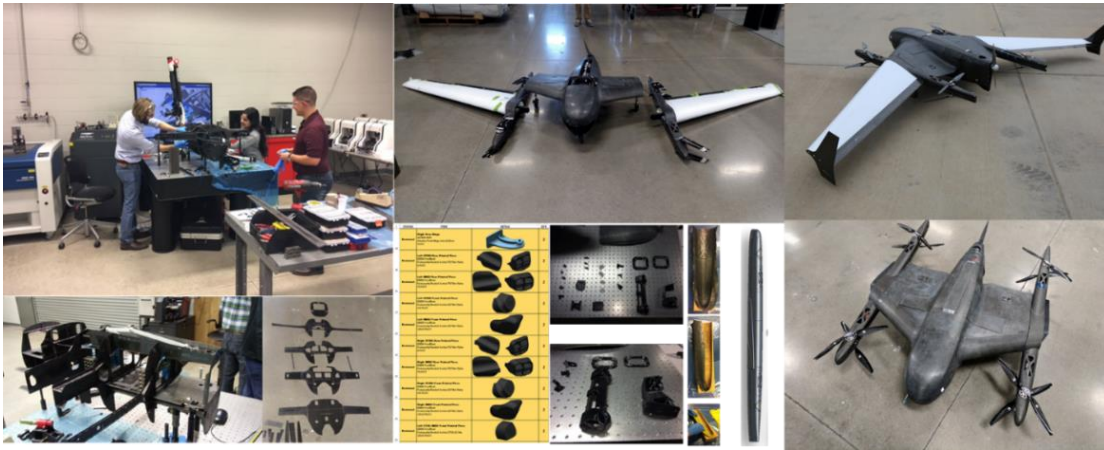
Figure 6. NIAR-UAS hybrid VTOL/CTOL configuration prototype.

Figure 7 illustrates the process followed to reverse-engineer the UAS models during the Task A3 program [22, 24]. The process consisted of scanning the physical article to generate cloud point data of the geometry, creating the CAD model, and discretizing the geometry.
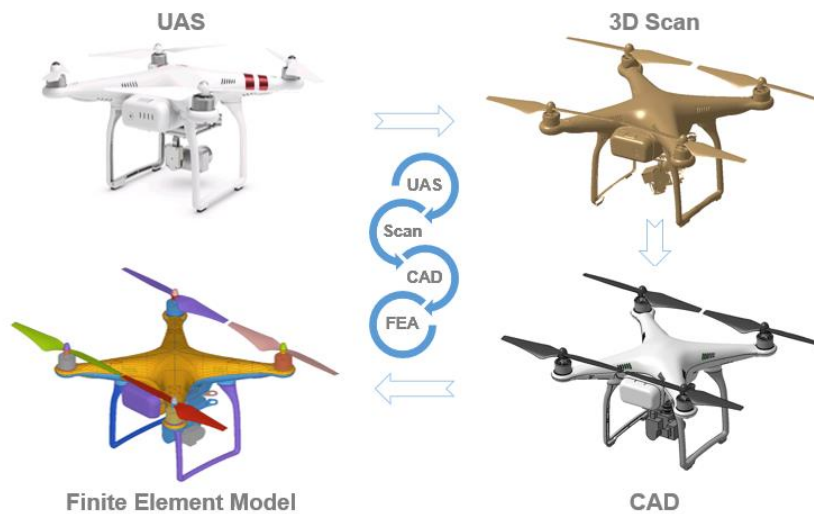
Figure 7. UAS FEM process.

2.1 CAD DEFINITION

This section provides an overview of the CAD model development process for the representative UAS geometries, including a detailed description of the models found in Task A3 final report Volumes II [22] and III [24]. Additionally, it discusses the CAD datasets used to define the UAS numerical models' variants of the 2.7 lbs. quadcopter (scaled to 10 lbs.) and the 4 lbs. fixed-wing (scaled to 12 lbs.) models used in previous ASSURE programs. Further details are available in Volume II [22] and Volume III [24] reports. Sections 2.2.3 and 2.2.4 present the scaling methodology for the Q10 and F12 models. Furthermore, this section introduces the NIAR-UAS models, ranging from 25 to 55 lbs., configured from a modular sUAS system, as shown in Figure 5. This model facilitates Vertical Takeoff and Landing (VTOL) operations, Conventional Takeoff and Landing (CTOL) modes, as well as a hybrid takeoff and landing configuration, allowing both VTOL and CTOL capabilities.
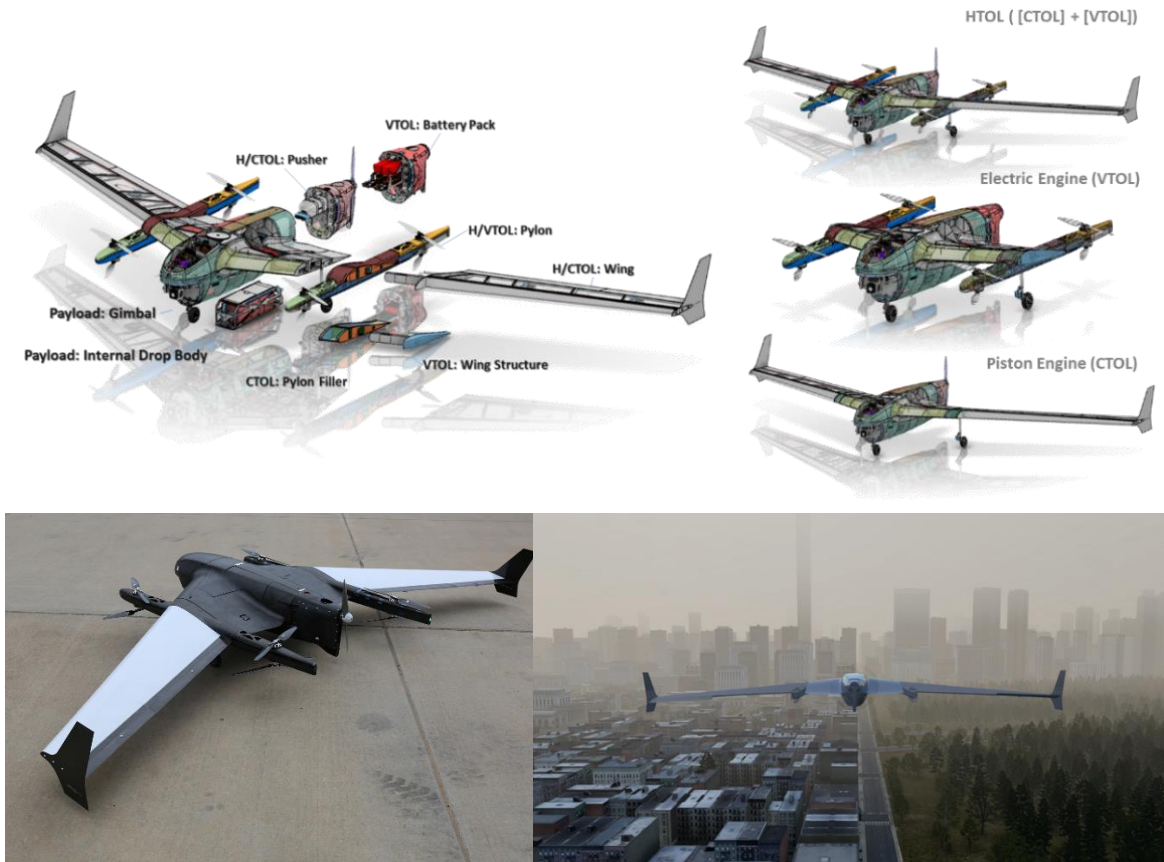
Figure 8. NIAR-UAS modular system CAD representation, hardware, and VR demo.

2.1.1 UAS 2.7 lbs. Quadcopter

The DJI Phantom 3 was identified as the most common quadcopter in the sUAS market during Task A3 [2]. As a result, a physical Phantom 3 UAS was disassembled, scanned, and reverse-engineered to create the CAD geometry of the virtual model. Figure 9 illustrates the envelopes of the quadcopter at each stage leading to the CAD creation: cloud point contour, polygonal mesh, and CAD geometry.

10

Figure 9. UAS 2.7 lbs. quadcopter CAD model development steps.

Figure 10 shows an overall and exploded view of the quadcopter that highlights the main sub-assemblies of the model.
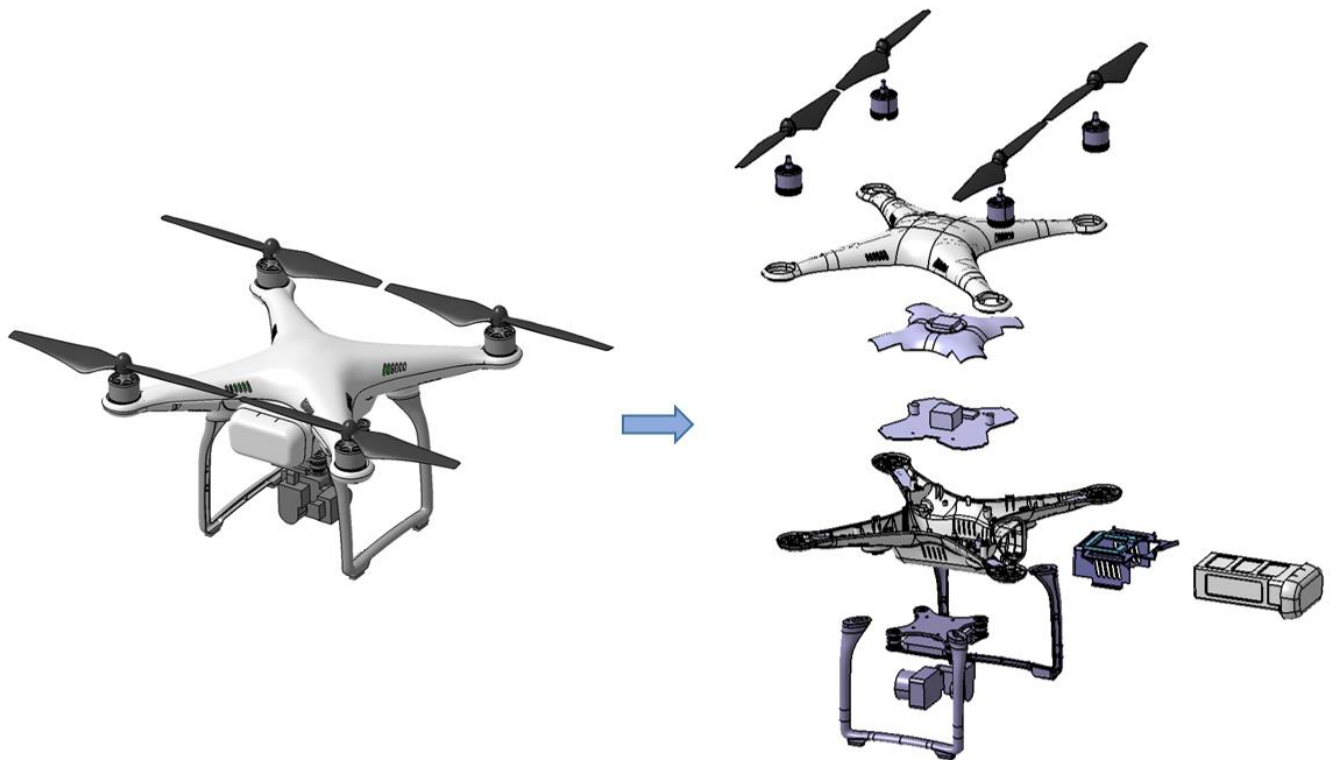
Figure 10. UAS 2.7 lbs. quadcopter geometry model.

Table 3 gathers the most relevant specifications of the DJI Phantom 3 Standard [22]. This data was considered during the CAD creation and the FEM development processes.

Table 3. Relevant specifications of the DJI Phantom 3 Standard [22].

Mass	1,216 g	2.68 lbs.
Diagonal	350 mm	13.8 in.
Max. Horizontal Speed	16 m/s	31 knots
Max. Service Ceiling	6,000 m	19,685 ft.
Electronic limit above ground	120 m	394 ft.
Max. Motor Speed	1,240 rad/s	11,840 rpm
Motors	4x brushless DC motors; mass: 54 g	
Battery	4x LiPo cells; capacity: 4480 mAh; mass: 363 g	

2.1.2   UAS 4.0 lbs. Fixed-Wing

The Precision Hawk Lancaster Mark-III was selected as a representative fixed-wing sUAS in the A3 program [24]. A physical article was disassembled and reverse-engineered to generate the CAD geometry. Figure 11 shows the CAD of the 4.0 lbs. fixed-wing UAS.

Figure 12 shows the CAD geometry of the fixed wing's sub-assemblies: motor and propeller, main body, tail, battery, wing, and camera. Table 4 gathers the most relevant specifications of the Precision Hawk Lancaster Mark III [24]. These specifications were considered for the CAD creation and FEM development processes. Note that the original fixed wing's Maximum Takeoff Weight (MTOW) (5.5 lbs.) is higher than Task A3's UAS (4.0 lbs.) [24]. This is due to the requirement in Task A3 [24] to develop a scaled-down version of the UAS to facilitate comparing a UAS airborne collision and a 4 lbs. bird strike.

(A)

(B)

(C)
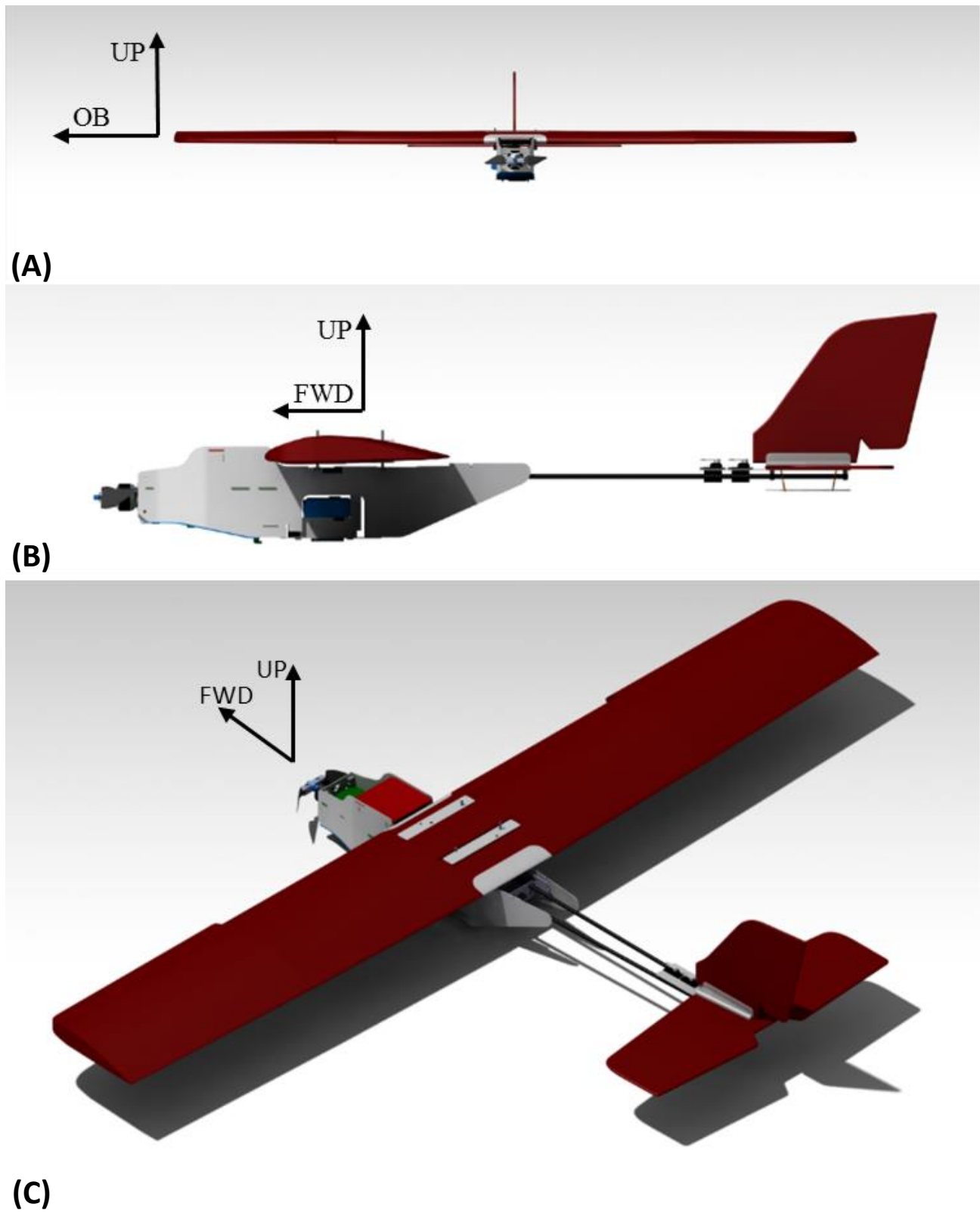
Figure 11. Fixed-wing CAD model: (A) front view, (B) side view, and (C) isometric view.
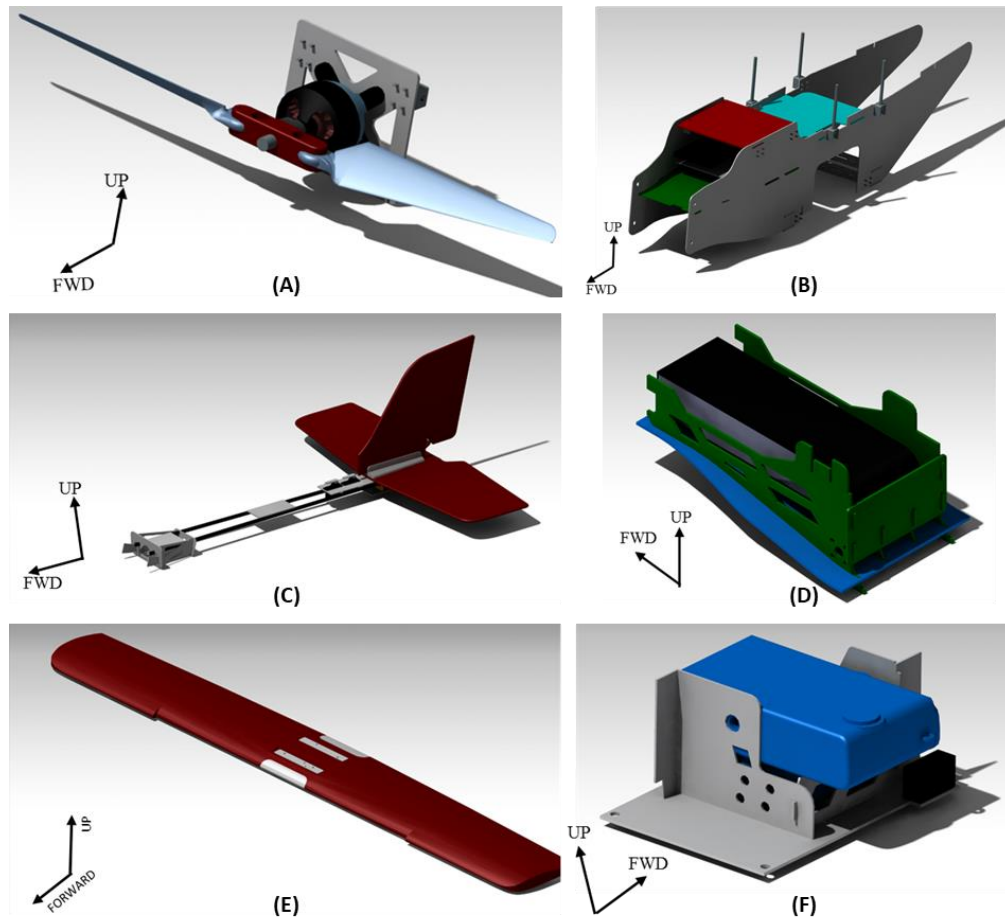
Figure 12. Fixed-wing UAS sub-assemblies: (A) motor & propeller, (B) main body, (C) tail, (D) battery, (E) wing, and (F) camera.

Table 4. Relevant specifications of the Precision Hawk Lancaster Hawkeye Mark III [24].

Mass (MTOW)	2,495 g	5.5 lbs.
Wingspan	1,500 mm	4 ft. 11 in.
Length	800 mm	2 ft. 7.5 in.
Max. Horizontal Speed	19.5 m/s	38 knots
Max. Service Ceiling	4,000 m	13,120 ft.

2.1.3 UAS 25 & 55 lbs. Quadcopter

The geometric and performance specifications of the 25lbs. and 55lbs. versions of the NIAR-UAS Quadcopter are summarized in Figure 13 and Table 5. The original design, analysis, and prototype manufacturing efforts were conducted under a technology demonstration project in 2016-2017

14

[25]. Based around the central body, the modular UAS architecture allows multiple mission profiles to be addressed via interchangeable systems and structures. The modular UAS design makes producing a Quadcopter style configuration possible, utilizing four pairs of counter-rotating VTOL-oriented motors mounted to longitudinal boom Pylons. VTOL endurance is supported by the VTOL Aft Fuselage module battery pack, housing additional batteries for extended flight time. Due to the modular architecture of the UAS, the equipment, components, and modules that are included in a given configuration can be selected based on the mission profile. Therefore, components such as the search and rescue payload are not always present in the flight configuration. The UAS has an internal payload bay, which can carry up to 5 lbs. of various objects, supplies, or alternate flight equipment. For the purpose of this research, the payload was not defined, and the weight allowance was used to incorporate conventional aircraft components such as retractable landing gear and the gimbal assembly.

25 lbs. & 55 lbs. Quadcopter
Geometry

Figure 13. NIAR UAS quadcopter configuration CAD representation.

Table 5. Relevant specifications of the NIAR UAS quadcopter configuration.

UAS Configuration	Q25 (metric)	Q25 (US)	Q55 (metric)	Q55 (US)
Mass	11.34 kg	25 lbs.	24,95 kg	55 lbs.
Length	969.4 mm	38.2 in	1261.5 mm	49.7 in
Width	875.4 mm	34.5 in	1138.9 mm	44.84 in
Height	247.6 mm	9.75 in	322 mm	12.7 in

2.1.4 UAS 25 & 55 lbs. Fixed-Wing

The 25 lbs. and 55 lbs. iterations of the NIAR UAS Fixed-Wing configuration have the geometric properties and performance specifications shown in Figure 14 and Table 6. As with the Quadcopter configuration, the original design, analysis, and prototype manufacturing efforts were conducted under a technology demonstration project in 2016-2017 [25]. The modular UAS design makes producing a Fixed-Wing style configuration possible, utilizing modular Wings, Pylon Filler Wing sections, and a CTOL Aft Fuselage Module that houses a gas motor, fuel, and exhaust systems. Due to the modular architecture of the UAS, the equipment, components, and modules that are included in a given configuration can be selected based on the mission profile. Therefore, components such as the search and rescue payload are not always present in the flight configuration. The UAS has an internal payload bay, which could carry up to 5 lbs. of various objects, supplies, or alternate flight equipment. For the purpose of this research, the payload was not defined, and the weight allowance was used to incorporate conventional aircraft components such as retractable landing gear and the gimbal assembly.

25 lbs. & 55 lbs. Fixed-Wing
Geometry

Figure 14. NIAR UAS fixed-wing configuration CAD representation.

Table 6. Relevant specifications of the NIAR UAS fixed-wing configuration.

UAS Configuration	F25 (metric)	F25 (US)	F55 (metric)	F55 (US)
Mass	11.34 kg	25.0 lbs.	25.0 kg	55.0 lbs.
Length	1388.1 mm	54.7 in	1867.1 mm	73.5 in
Wingspan	3119.6 mm	122.81 in	4200 mm	165.3 in
Height	406.0 mm	16.0 in	546.2 mm	21.5 in

2.2 FINITE ELEMENT MODEL

This chapter summarizes the UAS FEM developed in Task A3 [22, 24], Task A14 [23], Task A30 [26], and through other research efforts for 25 lbs. and 55 lbs. UAS [25]. This chapter also briefly summarizes the validation updates applied to the small UAS FEMs (specifically the 2.7 lbs. Quadcopter and 4 lbs. Fixed-Wing) based on the additional component-level testing performed in Task A16 [3].

2.2.1 *UAS 2.7 lbs. Quadcopter*

The 2.7 lbs. quadcopter geometry was discretized following NIAR's mesh quality criteria, which allowed it to capture most of the geometry features and keep a time step below 0.1 microseconds. Table 7 summarizes the mesh criteria followed for this FEM.

Table 7. Quadcopter mesh quality criteria.

Quality Parameter	Allowable Min.	Allowable Max.
Element Size	0.8 mm	5 mm
Aspect Ratio	-	5
Quad Angle	45°	140°
Tria Angle	30°	120°
Warp Angle	-	15°
Jacobian	0.7 (2D Element) 0.5 (3D Element)	-
Time-step	1E-7 s	-

Figure 15 compares the quadcopter components' geometry and mesh, providing an example of the level of detail maintained during the discretization.

Material definition and calibration were carried out in Task A3 [22] through coupon level and other test experiments at the component level. The current quadcopter FEM preserves the same materials' specifications. Figure 16 presents a color-coded exploded view indicating the materials applied in the 2.7 lbs. quadcopter FEM.
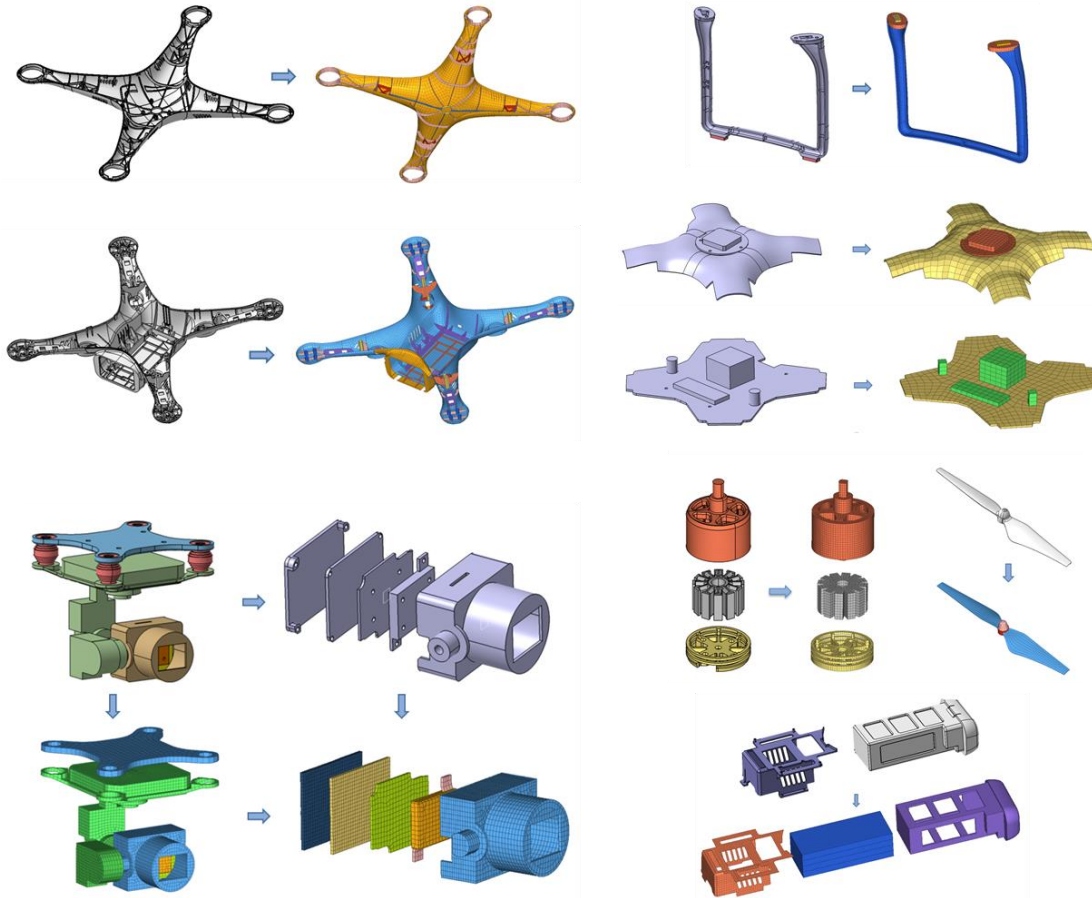
Figure 15. UAS 2.7 lbs. quadcopter sub-assembly's CAD geometry and FE mesh.

Code	Material
	Polycarbonate
	Nylon
	Cast Aluminum 520-F
	Steel 4030
	G-10 Fiberglass (PCB)
	Li-Po Battery Cell
	Aluminum Film 1145-O

Figure 16. UAS 2.7 lbs. quadcopter materials.

The definitions of connections and contacts were determined and validated in previous research [22]. Figure 17 illustrates the overall review of the 2.7 lbs. quadcopter FEM connections.
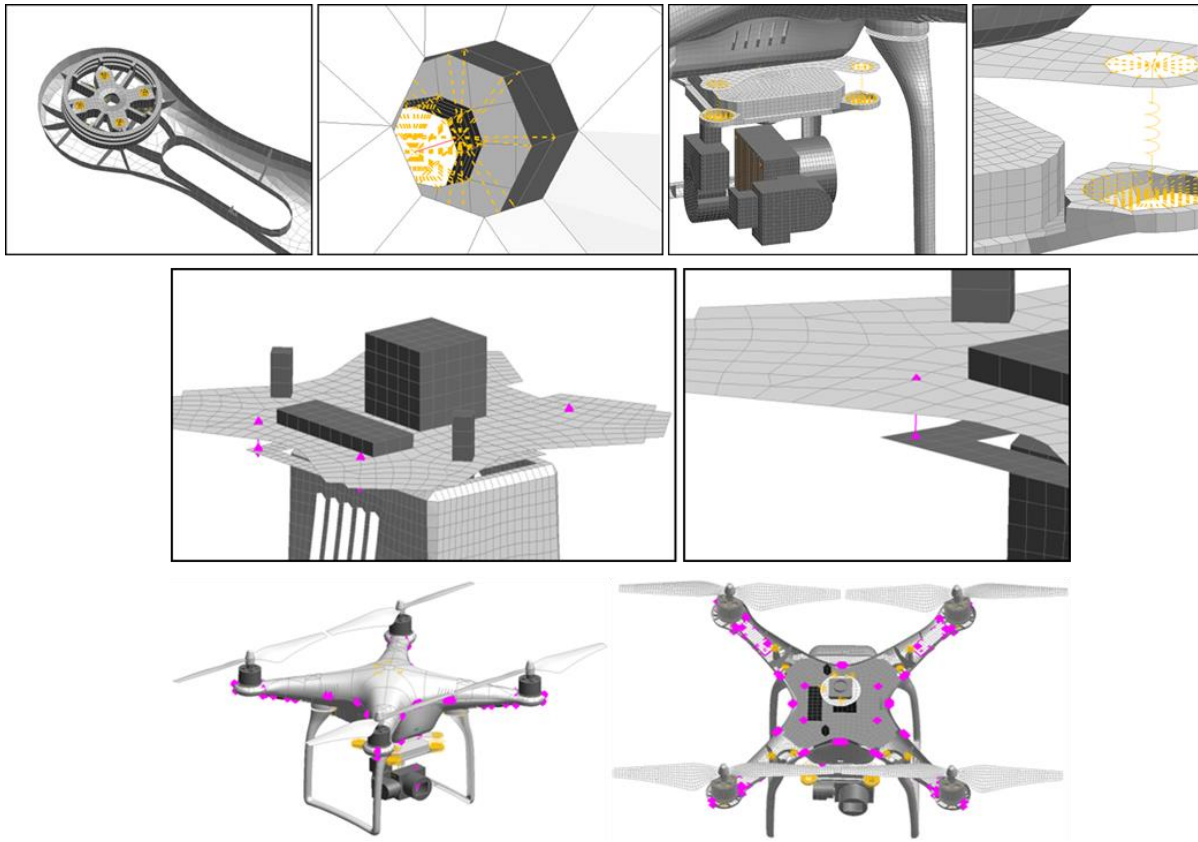
Figure 17. UAS 2.7 lbs. quadcopter connections.

A final mass check was performed to confirm that the UAS mass distribution represents the 2.7 lbs. quadcopter physical model. Figure 18 shows the 2.7 lbs. quadcopter FEM and the location of its center of gravity.
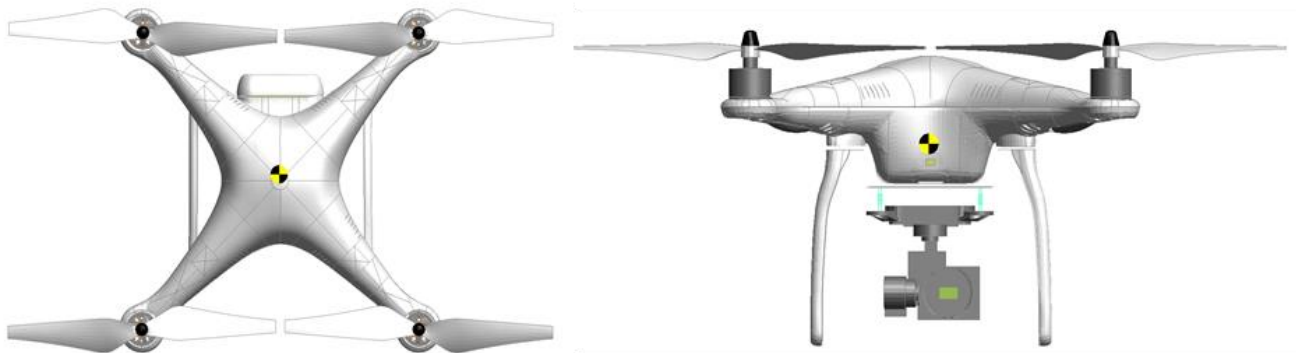
Figure 18. UAS 2.7 lbs. quadcopter FEM center of gravity.

2.2.2 UAS 4.0 lbs. Fixed-Wing

The CAD geometry was generated in a previous research program [24]. After disassembling and scanning the fixed-wing UAS components, the geometry was discretized with 2D and 3D elements. Table 8 presents the quality criteria considered to mesh the 4.0 lbs. fixed-wing model.

Table 8. Fixed-wing mesh quality criteria.

Quality Parameter	Allowable	
	Shell Elements	Solid Elements
Min. Side Length	1 mm	1 mm
Max. Aspect Ratio	5	
Min. Quad Angle	45°	-
Max. Quad Angle	140°	-
Min. Tria Angle	30°	-
Max. Tria Angle	120°	-
Max. Warp Angle	15°	
Min. Jacobian	0.7	0.5

Figure 19 separates the model components based on the type of elements used for the discretization: 2D and 3D elements.
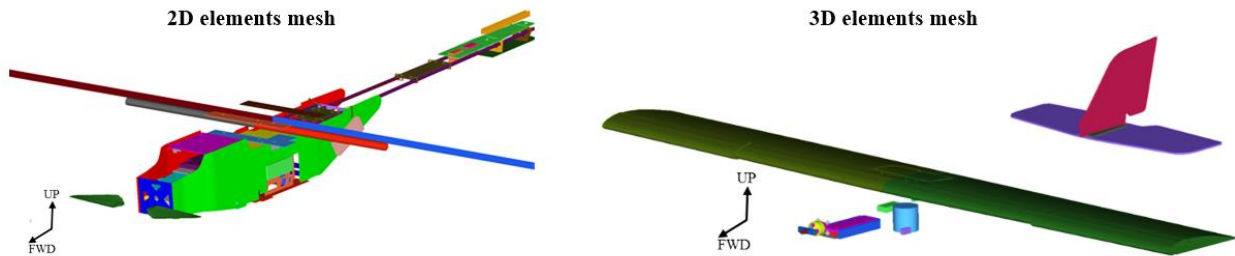
Figure 19. UAS 4.0 lbs. fixed-wing parts modeled with 2D and 3D elements.

The definitions of materials, connections, and contacts are discussed in detail in Task A3's final report [24]. The same properties and specifications were kept for this research. In addition, all the component masses were documented during the reverse-engineering process to capture an accurate mass distribution in the virtual model. Figure 20 illustrates the 4.0 lbs. fixed-wing FEM and the location of its center of gravity.
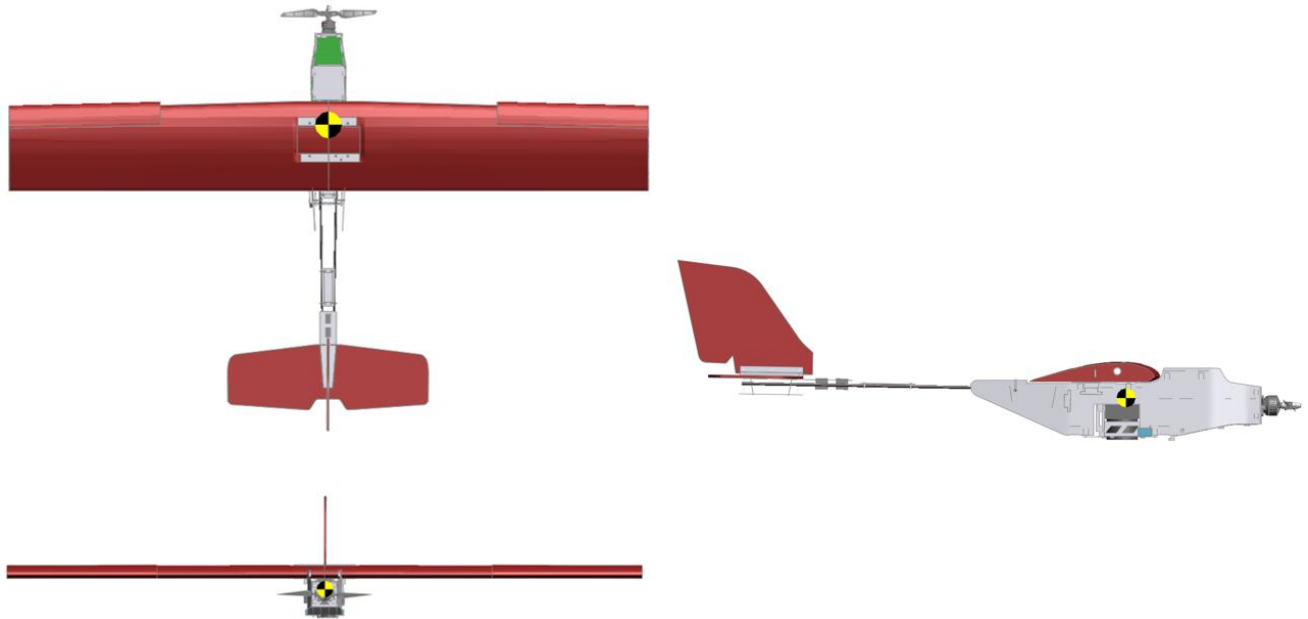
Figure 20. UAS 4.0 lbs. fixed-wing FEM center of gravity.

2.2.3   UAS 10 lbs. Quadcopter

In Task A30 [26], NIAR performed the scaling of the 2.7 lbs. quadcopter to a 10 lbs. quadcopter using the same process described in Task A3 [24]. The model scaling methodology assumes that all components of a scaled UAS would increase its mass linearly, independently of its construction and design. Consequently, if materials are not varied, the density remains constant. Therefore, a quadratic relationship between linear dimensions can be established (so volume is proportional to mass).

$$Scale\ Factor = \sqrt[3]{Mass\ Scaled\ UAS/Mass\ Baseline\ UAS}$$

For instance, to scale up the quadcopter to 10 lbs., the mesh of the FEM was increased linearly along all directions by a factor of 1.632. When re-sizing two-dimensional elements, the thickness was multiplied by the same factor to complete the element scale-up process. Non-structural mass was scaled up accordingly. Additionally, NIAR removed all the intersections/penetrations introduced during the scaling process from the scaled UAS model to avoid any contact issues within the FEM. The scaled-up 10 lbs. quadcopter follows the same mesh criteria presented in Table 7. Figure 21 shows the comparison between the original model and the 10 lbs. UAS.

2.67 lb. – Top View
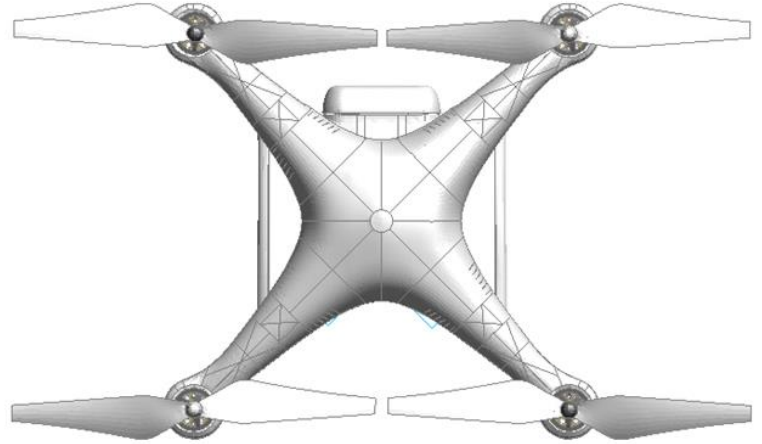
10 lb. – Top View

2.67 lb. – Front View

10 lb. – Front View

Figure 21. Comparison of A3 model vs. scaled-UAS 10 lbs. quadcopter.

Figure 22 shows the mass calculation of the 10 lbs. quadcopter FEM. The mass unit used in LS-DYNA is the metric ton. Therefore, the output value circled in Figure 22 is in terms of this mass unit. Performing unit conversion, 4.531 E-03 tons is equivalent to 10 lbs., confirming the mass of the scaled model. Overall dimensions and specifications for the assembly are shown in Figure 23.
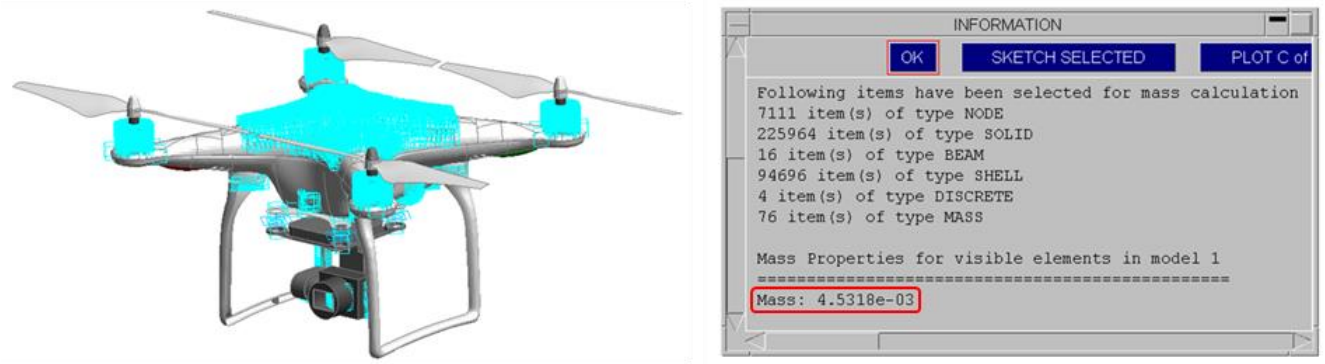
Figure 22. UAS 10 lbs. quadcopter mass check.

- MTOW: 10.0lbs (4.54kg)
- Height: 13in. (330mm)
- Length: 25in. (636mm)
- Width: 25in. (636mm)
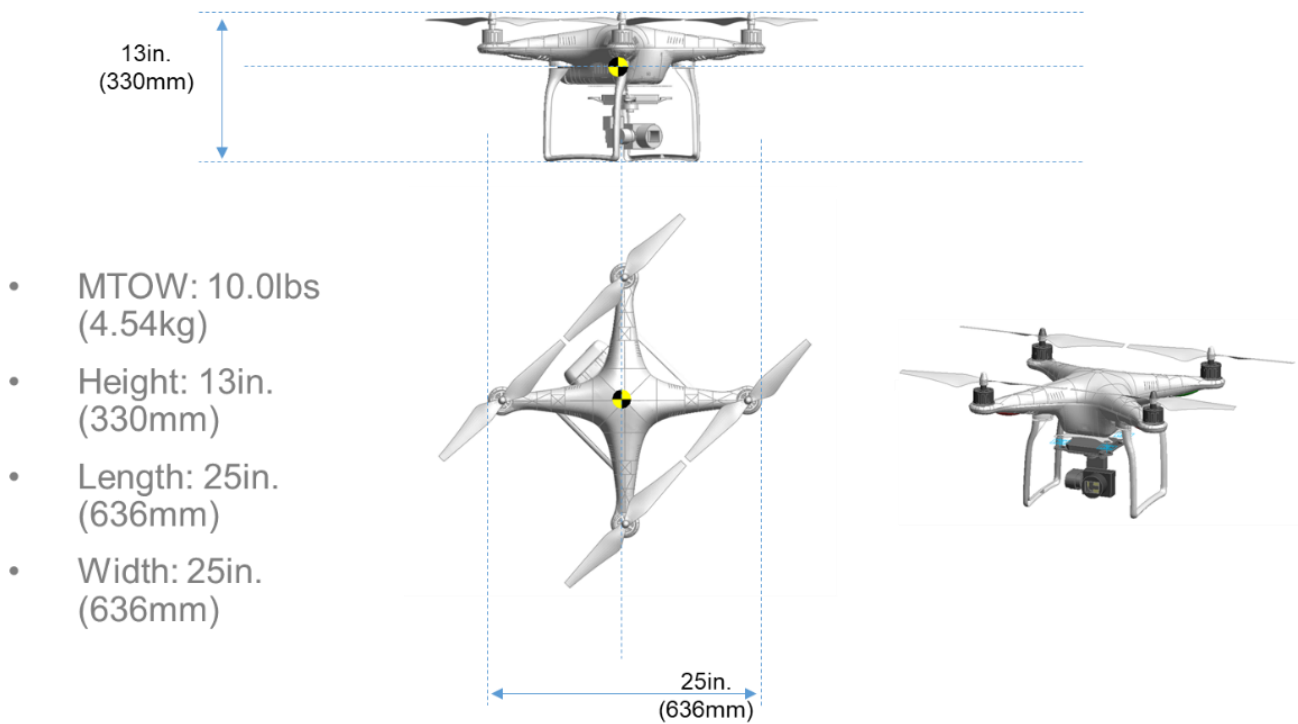
Figure 23. NIAR-UAS 10 lbs. quadcopter overall dimensions, MTOW, and c.g. location.

2.2.4   UAS 12 lbs. Fixed-Wing

Similar to the process followed for the 10 lbs. Quadcopter, NIAR also scaled the 4.4 lbs. Fixed-Wing model to 12 lbs. in Task A30 [26]. The penetrations/intersections introduced during the scaling process were removed from the scaled UAS model to avoid any contact issues. The scaled-up model follows the same mesh criterion presented in Table 8. Figure 24 compares the original 4.4 lbs. and the 12 lbs. fixed-wing models.

4.4 lbs. – Top View

12 lbs. – Top View

4.4 lbs. – Front View

12 lbs. – Front View
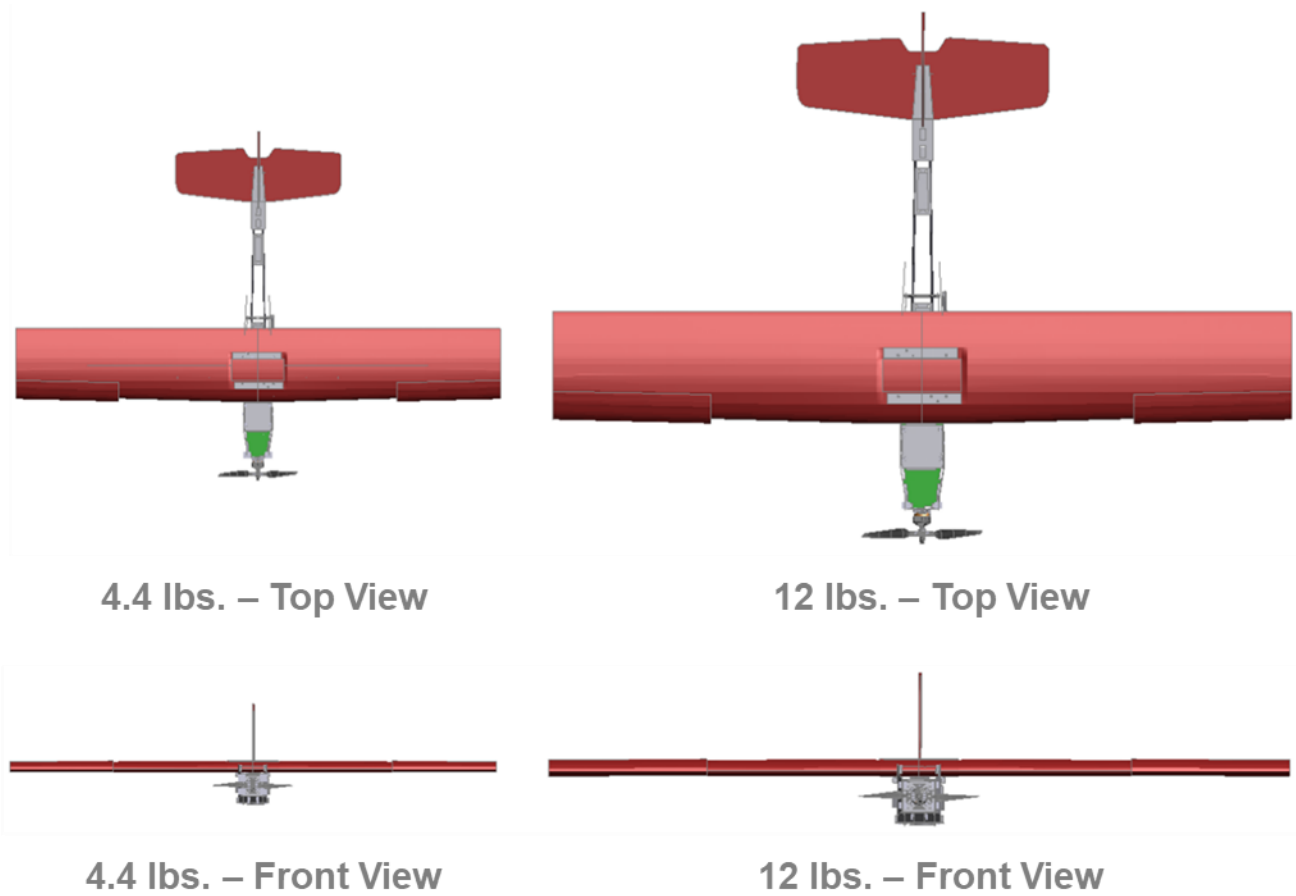
Figure 24. Comparison of A14 model vs. scaled-UAS 12 lbs. fixed-wing.

Figure 25 shows the mass calculation of the fixed-wing FEM. Performing unit conversion to the output value circled in Figure 25, 5.443 E-03 tons is equivalent to 12 lbs., confirming the mass of the scaled model. Overall dimensions and specifications for the assembly are shown in Figure 26.
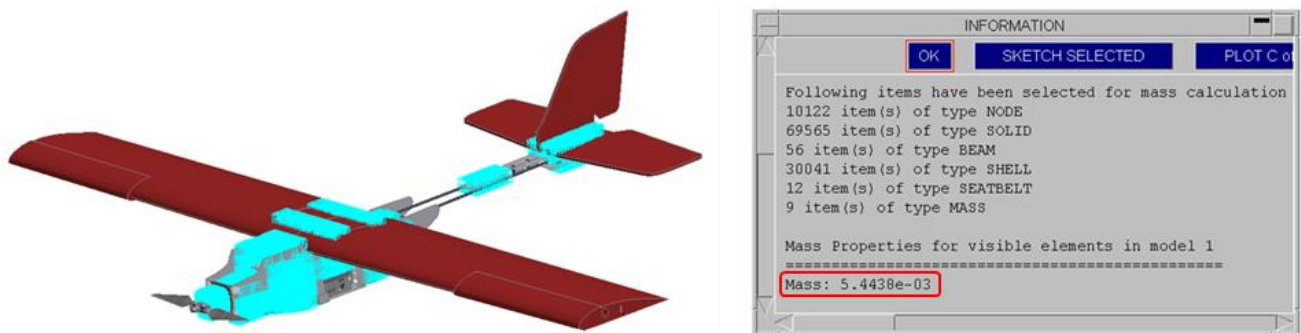
Figure 25. UAS 12 lbs. fixed-wing mass check.

- MTOW: 12lbs (5.44kg)
- Height: 18.62in. (473mm)
- Length: 64.92in. (1649mm)
- Wingspan: 90in. (2286mm)

18.62in. (473mm)

90in. (2286mm)

64.92in. (1649mm)
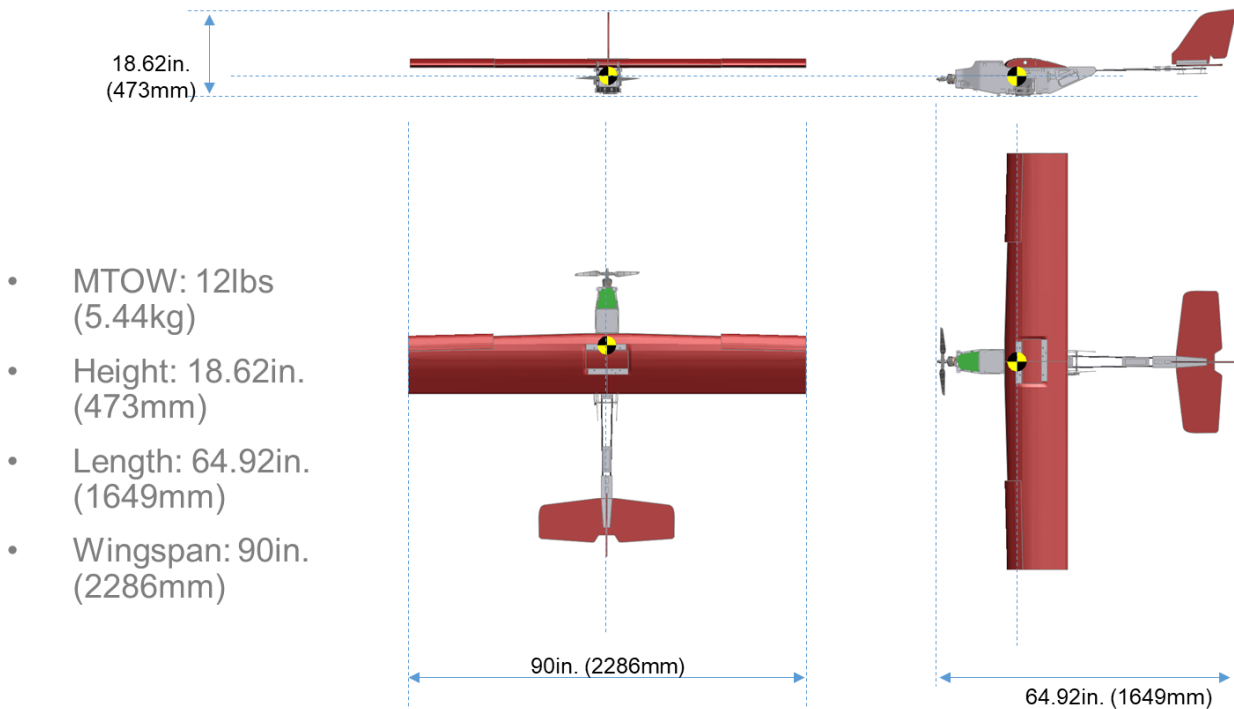
Figure 26. Scaled UAS 12 lbs. fixed wing overall dimensions, MTOW, and c.g. location.

2.2.5   UAS 25 lbs. Quadcopter

The 25lbs. Quadcopter configuration (Q25) is a scaled-version of NIAR's in-house designed modular search and rescue drone. This configuration utilizes interchangeable pylons and rear fuselage components that allow for quadcopter-style VTOL operations. All geometric details, internal structural components, design assumptions/simplifications, and their material specifications and calibrations are described in detail in Task A30 [26]. The overall dimensions and specifications for the assembly are shown in Figure 27.

The 25 lbs. Quadcopter follows the same mesh criteria presented in Table 7; however, an exception was made when establishing the minimum element size for this FEM. To facilitate the geometry discretization task, and with no penalty to the computational efficiency required to perform the analysis, the 25 lbs. quadcopter FEM minimum element size was set to 0.7 mm. The Task A30 report [26] provides details about the element types used, connections' specifications, and contact definition for the 25 lbs. quadcopter FEM. Figure 28 and Figure 29 show some details about the 25 lbs. quadcopter FEM.

- MTOW: 11.34kg
  (25.0lbs)

- Height: 247.6mm
  (9.75in.)

- Length: 969.4mm
  (38.17in.)

- Width: 875.4mm
  (34.46in.)
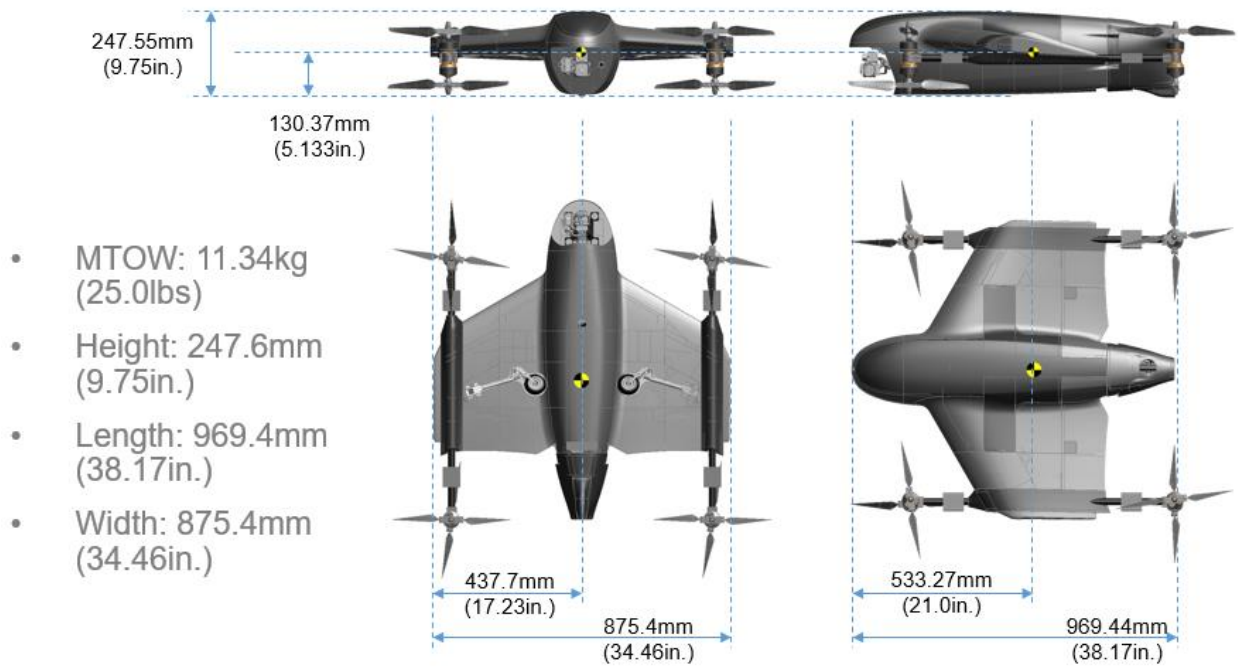
Figure 27. NIAR-UAS 25 lbs. quadcopter overall dimensions, MTOW, and c.g. location.
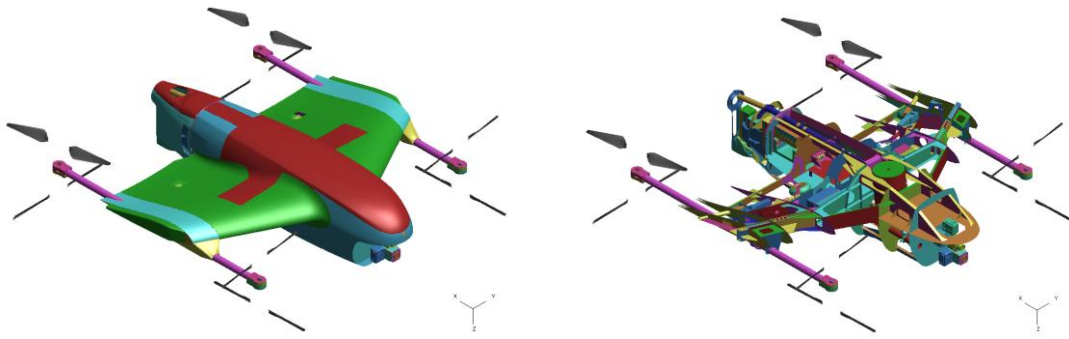
Figure 28. Quadcopter FEM – 2D element distribution exterior and interior views.
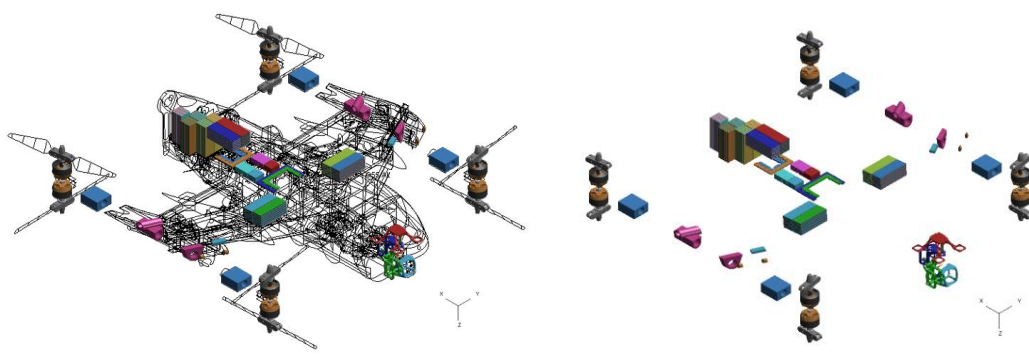
Figure 29. Quadcopter FEM – 3D element distribution on wireframe and isolated views.

2.2.6 UAS 25 lbs. Fixed-Wing

The 25 lbs. Fixed-wing configuration (F25) is a scaled-version of NIAR's modular search and rescue drone. This configuration utilizes interchangeable wings and rear fuselage components that allow for conventional aircraft operations. Comprehensive information about the model geometry, assumptions, and simplification, along with the material specifications and calibrations, are presented in the Task A30 report [26]. The overall dimensions and specifications for the assembly are shown in Figure 30.
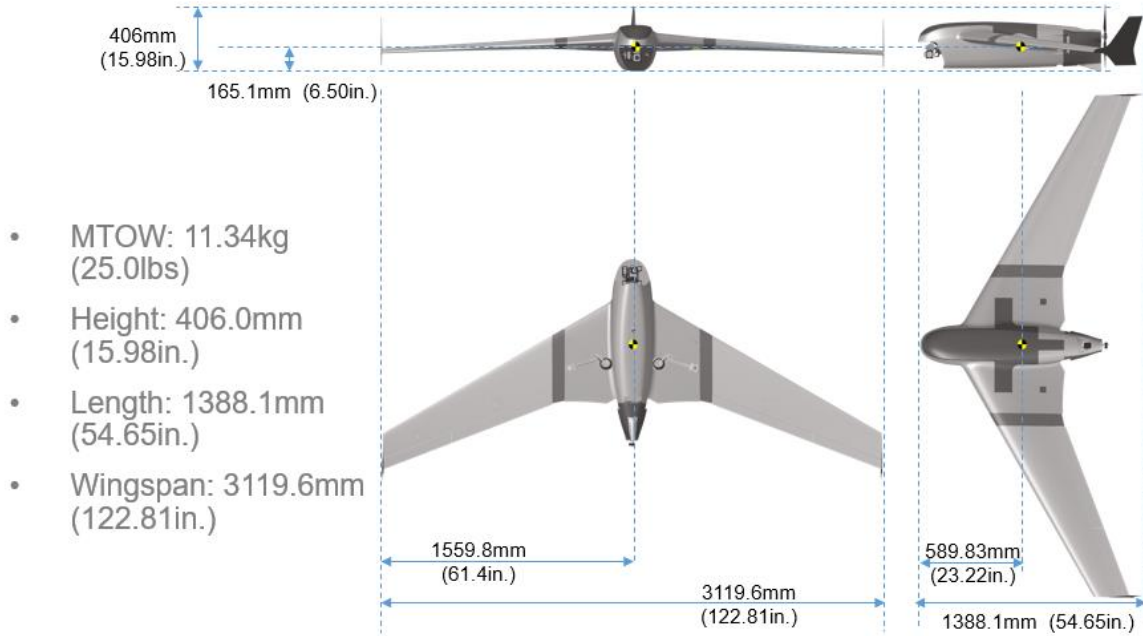
Figure 30. Fixed-wing overall dimensions, MTOW, and c.g. location.

The 25 lbs. fixed-wing FEM follows the mesh criterion presented in Table 7. Similar to the 25 lbs. quadcopter model, an exception was made when establishing the minimum element size for this FEM, setting the lower boundary element size to 0.7 mm. Figure 31 and Figure 32 show some details of the 25 lbs. fixed-wing FEM.
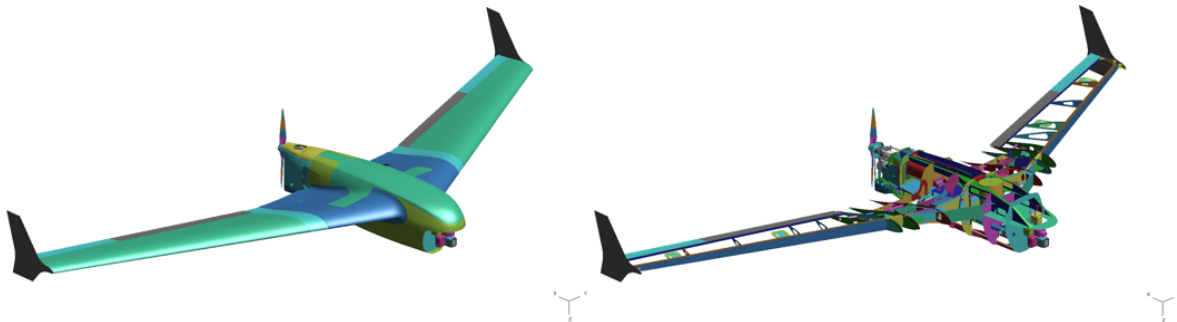
Figure 31. Fixed-wing FEM – 2D element distribution exterior and interior views.
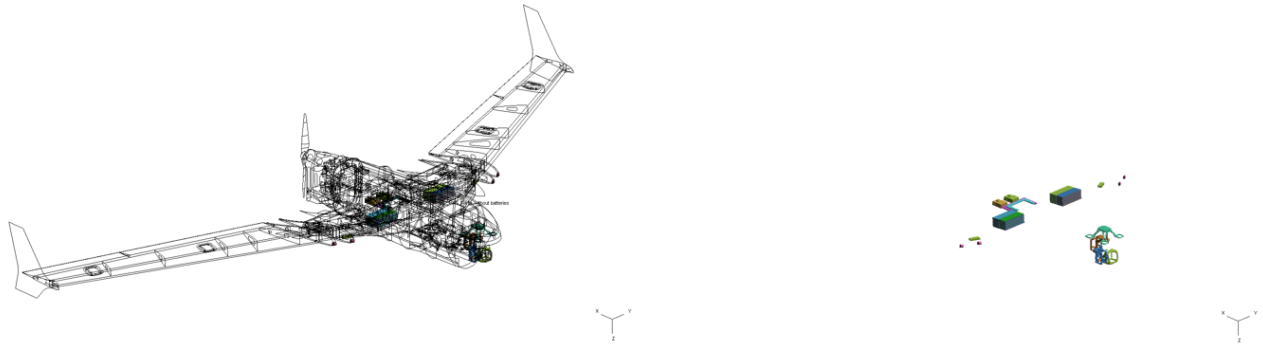
Figure 32. Fixed-wing FEM – 3D element distribution on wireframe and isolated views.

2.2.7   UAS 55 lbs. Quadcopter

The 55 lbs. quadcopter configuration (Q55) is a scaled-version of NIAR's in-house designed and analyzed modular search and rescue drone. It is identical to the Q25 model in terms of the FE representations; only the geometry and weight have been scaled. Overall dimensions and specifications for the assembly are shown in Figure 33.

- MTOW: 24.95kg (55.0lbs)
- Height: 322mm (12.68in.)
- Length: 1261.5mm (49.65in.)
- Width: 1138.9mm (44.84in.)

322mm (12.68in.)
159.3mm (6.27in.)
569.45mm (22.42in.)
1138.9mm (44.84in.)
693.8mm (27.31in.)
1261.5mm (49.65in.)
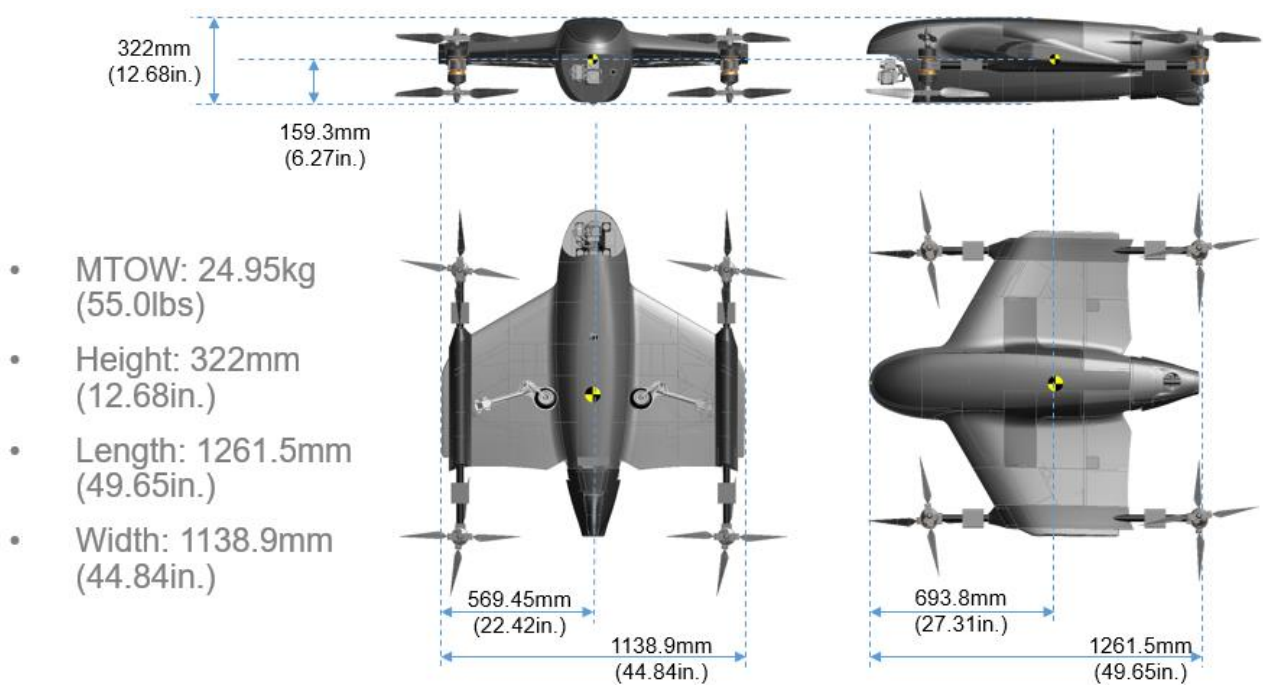
Figure 33. NIAR-UAS 55 lbs. quadcopter overall dimensions, MTOW, and c.g. location.

The 55 lbs. quadcopter FEM follows the mesh criterion summarized in Table 7. Figure 34 and Figure 35 highlight the material information of the 25 lbs. and 55 lbs. quadcopter FEM.

MAT001	(red)
MAT015	(purple)
MAT024	(yellow)
MAT054	(cyan)
MAT058	(green)
MAT063	(orange)
MAT224	(light blue)

Figure 34. Q25 & Q55 UAS material models for LS-DYNA solver.

(green)	CFRP
(blue)	Ultem 9085
(purple)	Polycarbonate
(orange)	Copper Berillium 17200
(gray)	2024-T351
(bright green)	Nylon
(tan)	Aluminum 520-F
(brown)	Steel 4030
(dark brown)	Steel 4340
(magenta)	Polyurethane
(cyan)	G-10 Fiberglass (PCB)
(red)	Li-Po Battery Cell
(light blue)	Aluminum Film 1145-O
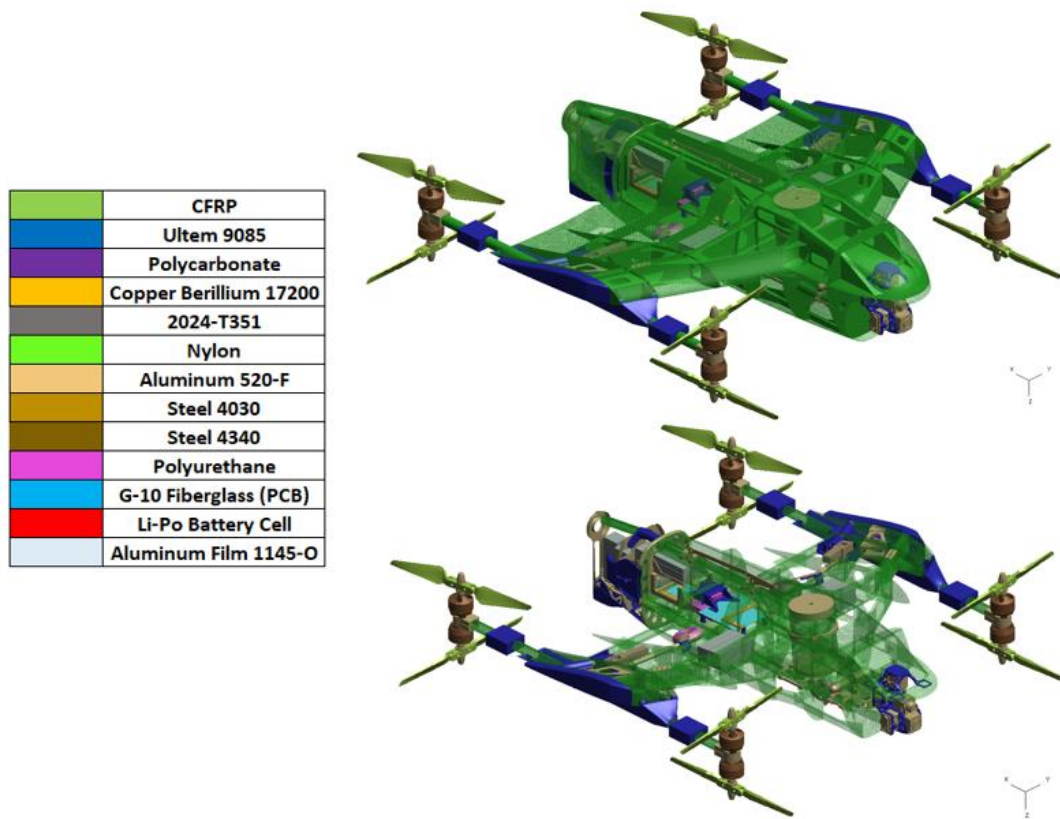
Figure 35. Q25 & Q55 UAS materials.

2.2.8 UAS 55 lbs. Fixed-Wing

The 55 lbs. fixed-wing configuration (F55) is a scaled-version of NIAR's in-house designed and analyzed modular search and rescue drone. It is identical to the F25 model in terms of the FE representations; only the geometry and weight have been scaled. This configuration utilizes interchangeable wings and rear fuselage components that allow for conventional aircraft operations. Overall dimensions and specifications for the assembly are shown in Figure 36.
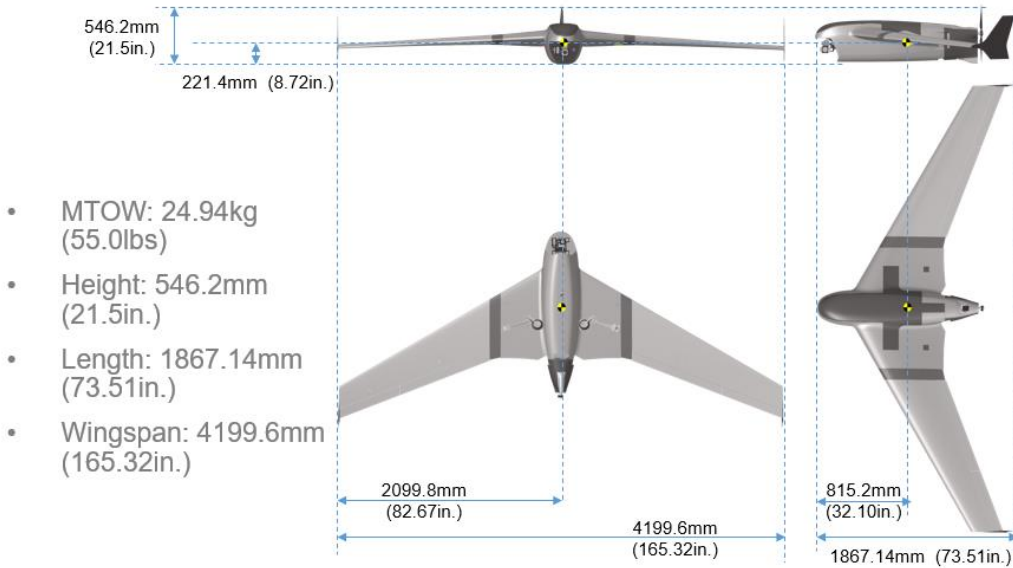
Figure 36. Fixed-wing overall dimensions, MTOW, and c.g. location.

The 55 lbs. fixed-wing FEM follows the mesh criterion summarized in Table 7. Figure 37 and Figure 38 highlight the material information for the 25 lbs. and 55 lbs. fixed-wing FEM.

Figure 37. F25 & F55 UAS material models for LS-DYNA solver.

30

	CFRP
	Ultem 9085
	Polycarbonate
	Copper Berillium 17200
	2024-T351
	Nylon
	Aluminum 520-F
	Steel 4030
	Steel 4340
	Polyurethane
	G-10 Fiberglass (PCB)
	Li-Po Battery Cell
	Aluminum Film 1145-O
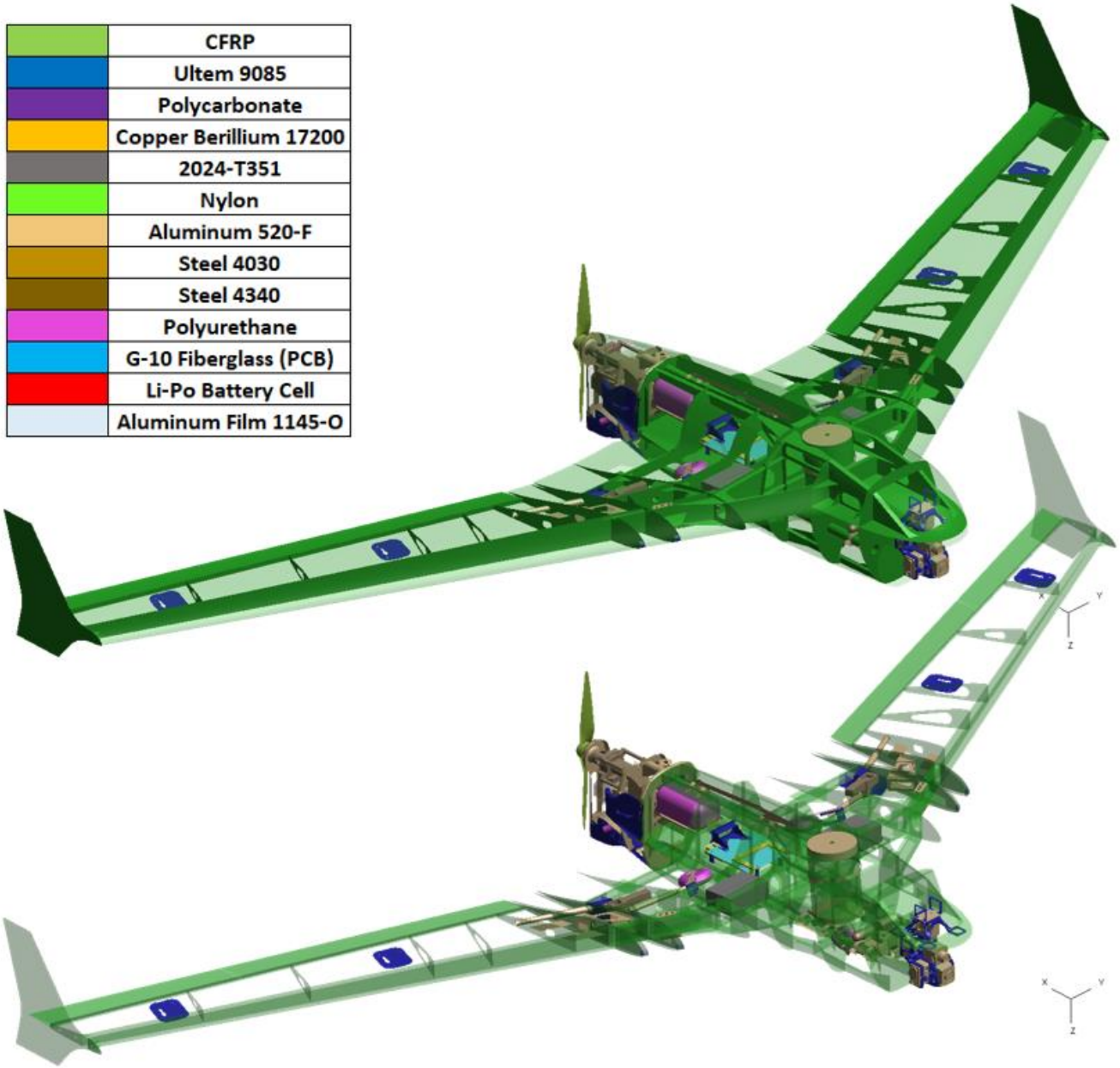
Figure 38. F25 & F55 UAS materials.

31

2.3   COMPONENT LEVEL TESTS

In Task A3 [2], The main UAS components (camera, motor, and battery) for the 2.7 lbs. quadcopter and the 4 lbs. fixed-wing were validated for impact velocities up to 250 knots. Additionally, in Task A16 [3], there were further validation efforts for the same components at impact velocities between 50 to 500 knots. These tests were conducted at the University of Alabama in Huntsville.

Task A16 report [3] provides comprehensive details about the selection of components for ballistic tests, the test conditions, test setup, test equipment, and instrumentation used, and the component level test results, validations, and summary for the main UAS components. The components evaluated during the testing include the battery, motor, and camera. These components were impacted against two different thickness aluminum panels: 1.6 mm (0.063 in.) and 6.35 mm (0.25 in.). These thicknesses are representative of the lower and upper thresholds for aluminum aerospace structures such as skins, spars, ribs, etc. Furthermore, the battery was impacted against an aluminum sharp-edge target that simulated the leading-edge shape of a rotorcraft blade.

The 10 lbs. quadcopter and 12 lbs. fixed-wing models were developed from the 2.7 lbs. quadcopter and 4.4 lbs. fixed-wing, respectively. Therefore, the component level validation efforts for impact velocities in the range of 50 to 500 knots are applicable for these models since the modeling methodology and material models remain unchanged.

The large UAS models (25 lbs. and 55 lbs.) used in the present study were modeled following the building block approach. The composite material models were validated through coupon and component level tests, and the properties of the metallic components were extracted from the metallic materials properties development and standardization handbook [27]. The composite fiber reinforced plastic coupon and component level testing performed for the 25 lbs. and 55 lbs. models in Task A30 [26] indicates that the material model is capable of characterizing the onset of laminate damage and representing the energy absorption capabilities.

2.3.1   *Example Component Level Test*

This section presents one of the component-level tests performed in Task A16 to highlight the validation efforts of the UAS components. The 2.7 lbs. quadcopter's motor was impacted with the 6.35 mm (0.25″) flat aluminum panel at a nominal velocity of 257.2 m/s (500 knots). Twenty-three (23) component-level tests were performed in this test campaign. Table 9 and Table 10 summarize the component level matrix of the quadcopter and fixed-wing component level tests, respectively. Each one of these component-level tests is documented in detail in Appendix A of Task A16 report [3]. The following data was compared between testing and simulation results:

    a. Test video kinematics
    b. Load cells' time history
    c. Strain gages time history
    d. Digital Image Correlation (DIC) in-plane strain contour.
    e. Panel maximum displacement
    f. Target damage
    g. Projectile damage

Table 9. Quadcopter component-level test matrix summary.

Test Number	Iteration	Panel Type	Projectile Type	Projectile Weight [g]	Impact Velocity [knots]	Impact Velocity [m/s]	Deviation from nominal velocity	Impact Energy [J]	Panel Penetration (Y/N)	Peak Load [N]	Permanent Deformation (H x V) [mm x mm]	Max. Panel Displacement [mm]
01	1	Sharp Edge	Battery A	350.80	510.7	262.73	2.14 %	12,107.0	NA	17,778.3	NA	NA
	2			350.80	516.6	265.76	3.32 %	12,388.4	NA	18,964.3	NA	NA
02	1	0.063" Al. Panel		344.20	503.6	259.07	0.72 %	11,551.2	Y	2,564.7	NA	6.75
	2			343.40	500.6	257.53	0.12 %	11,387.5	Y	2,297.1	211.5 x 76.29	5.58
03	1	0.25" Al. Panel		342.90	NA	NA	NA	NA	N	NA	NA	NA
	2			343.40	500.6	257.53	0.12 %	11,387.5	N	45,803.9	154.19 x 137.72	41.29
04	1	0.063" Al. Panel	Motor A	51.40	513	263.91	2.60 %	1,790.0	Y	609.3	72.46 x 81.05	N/A
	2			51.10	507	260.82	1.40 %	1,738.1	Y	809.2	62.24 x 85.06	3.35
05	1	0.25" Al. Panel		51.00	520	267.51	4.00 %	1,824.8	N	10,871.5	60.98 x 44.89	13.70
	2			50.60	NA	NA	N/A	NA	N	9,724.9	57.59 x 68.75	NA
06	1	0.063" Al. Panel	Camera	51.90	508	261.34	1.60 %	1,772.3	Y	1,986.6	160.59 x128.03	7.00
	2			52.90	518	266.48	3.60 %	1,878.3	Y	3,260.9	110.59 x 110.66	4.56
07	1	0.25" Al. Panel		52.40	522	268.54	4.40 %	1,889.4	N	17,787.4	45.72 x 57.74	12.84
	2			53.10	521	268.03	4.20 %	1,907.3	N	18,556.7	59.96 x 38.15	12.75
08	1	0.063" Al. Panel	Battery A	343.20	52	26.75	4.00 %	122.8	N	9,630.4	69.33 x 57.79	15.54
	2			343.70	51.5	26.49	3.00 %	120.6	N	8,502.4	57.96 x 60.61	15.51
09	1	0.063" Al. Panel		342.60	120.87	62.18	0.73 %	662.3	N	7,211.4	69.94 x 77.57	23.60
	2			343.10	118.5	60.96	-1.25 %	637.5	N	7,589.8	64.65 x 73.38	24.33
10	1	0.25" Al. Panel		343.80	116	59.68	-3.33 %	612.2	N	12,369.0	34.95 x 31.77	10.64
	2			334.50	122	62.76	1.67 %	658.8	N	13,567.0	48.44 x 44.93	12.05
11	1	0.063" Al. Panel	Motor A	50.80	124	63.79	3.33 %	103.4	N	1,415.2	33.01 x 40.96	9.97
	2			51.80	120	61.73	0.00 %	98.7	N	1,408.8	35.29 x 40.88	9.83
12	1	0.063" Al. Panel		51.30	57	29.32	14.00 %	22.1	N	1,739.4	22.86 x 23.92	5.90
	2			50.80	57	29.32	14.00 %	21.8	N	1,208.4	24.12 x 18.31	6.09
13	1	0.063" Al. Panel	Camera	51.30	121	62.25	0.83 %	99.4	N	1,122.8	40.63 x 37.05	8.92
	2			52.30	123	63.28	2.50 %	104.7	N	1,839.0	38.11 x 38.28	9.67
14	1	0.063" Al. Panel		52.30	53	27.27	6.00 %	19.4	N	1,692.0	20.36 x 19.87	5.67
	2			52.20	48.6	25.00	-2.80 %	16.3	N	1,525.7	26.65 x 20.91	5.59

Table 10. Fixed-wing component-level test matrix summary.

Test Number	Iteration	Panel Type	Projectile Type	Projectile Weight [g]	Impact Velocity [knots]	Impact Velocity [m/s]	Deviation from nominal velocity	Impact Energy [J]	Panel Penetration (Y/N)	Peak Load [N]	Permanent Deformation (H x V) [mm x mm]	Max. Panel Displacement [mm]
15	1	Sharp Edge	Battery B	NA	509.5	262.11	1.90 %	NA	NA	23,069.6	NA	NA
15	2	Sharp Edge	Battery B	259.60	498.87	256.64	-0.23 %	8,549.2	NA	23,202.2	NA	NA
16	1	0.063" Al. Panel	Battery B	264.80	509.5	262.11	1.90 %	9,096.0	Y	1,828.9	160.32 x 138.17	4.35
16	2	0.063" Al. Panel	Battery B	259.60	499.46	256.94	-0.11 %	8,569.4	Y	1,341.3	210.29 x 143.31	4.33
17	1	0.25" Al. Panel	Battery B	263.90	499.46	256.94	-0.11 %	8,711.4	N	45,298.8	140.50 x 91.62	28.32
17	2	0.25" Al. Panel	Battery B	264.00	501.2	257.84	0.24 %	8,775.5	N	44,350.8	138.82 x 90.06	28.18
18	1	0.063" Al. Panel	Motor B	75.90	527	271.11	5.40 %	2,789.4	Y	718.2	68.35 x 116.81	2.61
18	2	0.063" Al. Panel	Motor B	76.00	525	270.08	5.00 %	2,771.9	Y	770.2	67.69 x 137.63	2.44
19	1	0.25" Al. Panel	Motor B	76.10	527	271.11	5.40 %	2,796.7	N	NA	74.90 x 65.86	18.14
19	2	0.25" Al. Panel	Motor B	76.50	522.5	268.80	4.50 %	2,763.6	N	17,969.4	73.14 x 60.25	18.15
20	1	0.063" Al. Panel	Battery B	264.40	52	26.75	4.00 %	94.6	N	4,469.5	26.23 x 19.20	12.54
20	2	0.063" Al. Panel	Battery B	264.40	52	26.75	4.00 %	94.6	N	3,133.0	30.50 x 33.08	12.24
21	1	0.063" Al. Panel	Battery B	264.00	119.68	61.57	-0.27 %	500.4	N	11,839.6	48.27 x 45.28	19.32
21	2	0.063" Al. Panel	Battery B	265.10	120.87	62.18	0.73 %	512.5	N	11,652.7	52.35 x 45.28	19.35
22	1	0.063" Al. Panel	Motor B	76.20	49	25.21	-2.00 %	24.2	N	1,844.3	17.83 x 25.02	7.20
22	2	0.063" Al. Panel	Motor B	76.60	52	26.75	4.00 %	27.4	N	2,087.3	19.01 x 24.83	7.05
23	1	0.063" Al. Panel	Motor B	76.70	123	63.28	2.50 %	153.6	Y	3,763.6	54.66 x 36.75	6.27
23	2	0.063" Al. Panel	Motor B	76.80	123	63.28	2.50 %	153.8	Y	3,409.9	58.45 x 35.51	6.62

2.3.1.1   A.6 Test 05 – Motor at 500 Knots – 6.35 mm AL Panel

Test 05 consists of the impact of motor A on the 6.35 mm (0.25″) aluminum panel at a nominal velocity of 257.2 m/s. Two iterations were carried out to evaluate data repeatability. For iteration 2, a triggering error compromised the data recording. Hence, NIAR has selected iteration 1 for the FEM validation.

An initial velocity of 267.51 m/s (520 knots) was applied to the motor A FEM, corresponding to the velocity recorded for repetition 1 in the test documentation.

Figure 39 through Figure 42 show the comparison of the kinematics between the test and simulation at four different instances of the impact event.
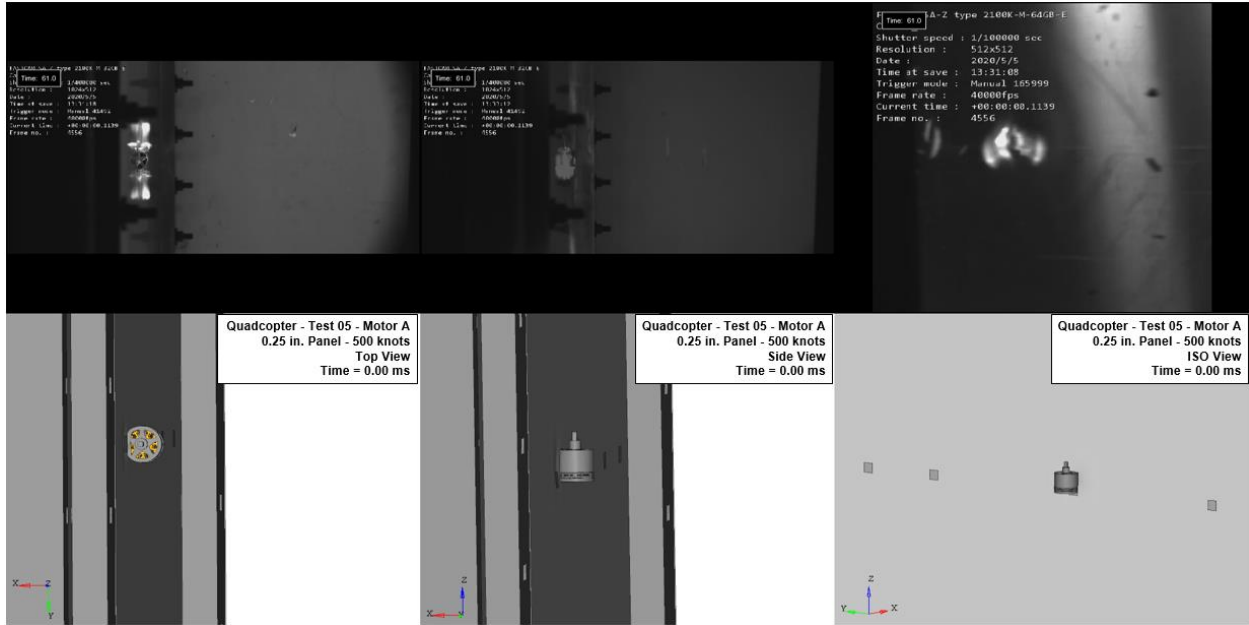
Figure 39. Comparison for motor A impact on 0.25" aluminum panel at 267.51 m/s (520 knots) at t = 0.00 ms (beginning of contact).
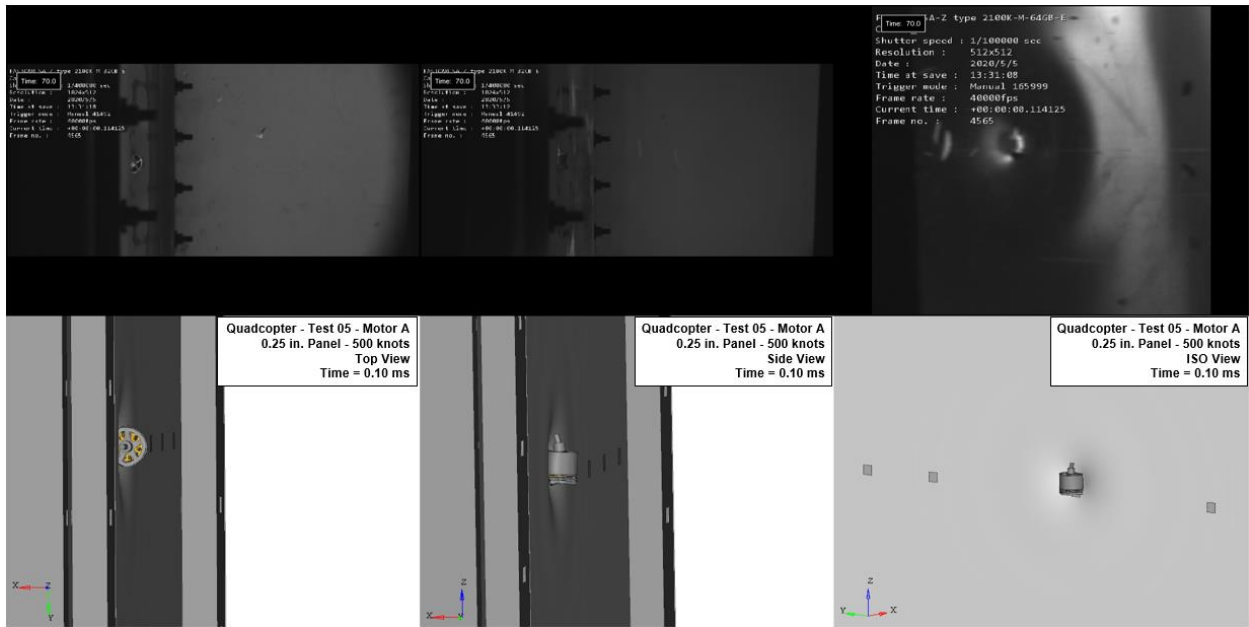
Figure 40. Comparison for motor A impact on 0.25" aluminum panel at 267.51 m/s (520 knots) at t = 0.10 ms.
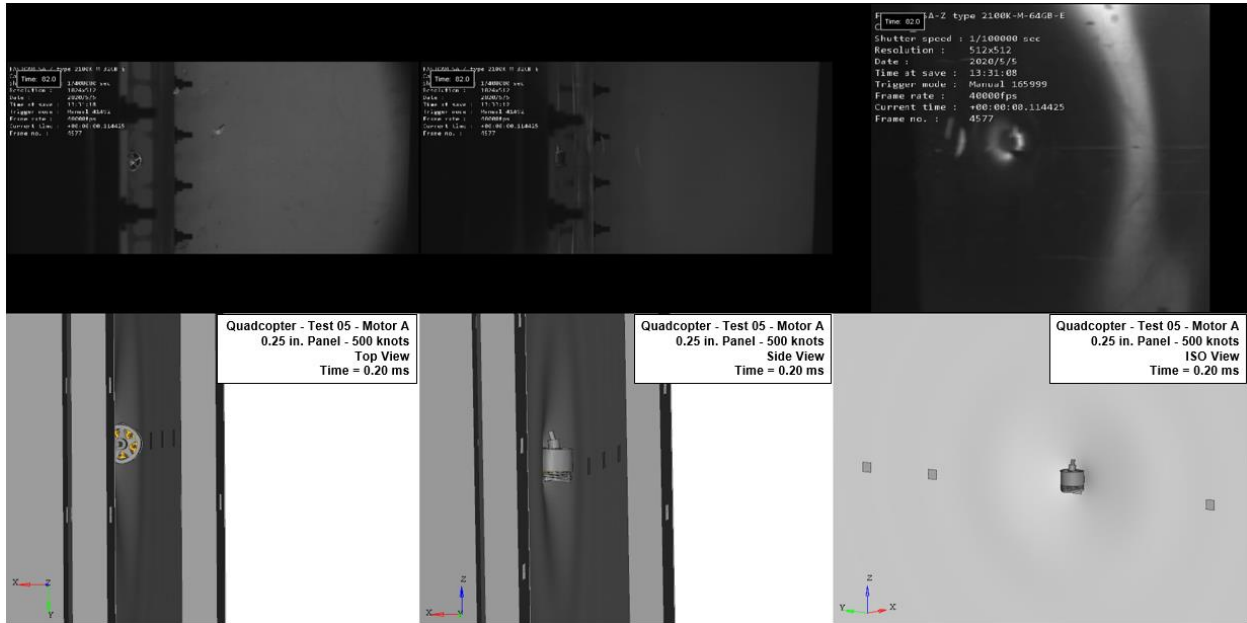
Figure 41. Comparison for motor A impact on 0.25" aluminum panel at 267.51 m/s (520 knots) at t = 0.20 ms.
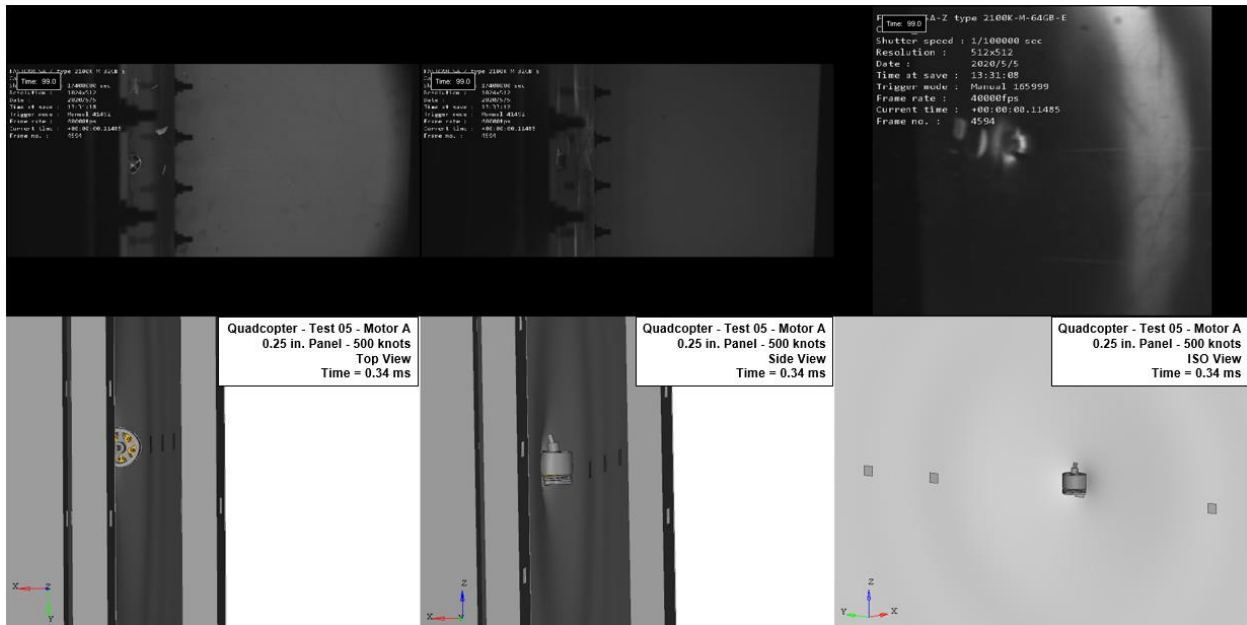
Figure 42. Comparison for motor A impact on 0.25" aluminum panel at 267.51 m/s (520 knots) at t = 0.34 ms (end of contact).

Figure 43 compares the simulation and test Y (horizontal) and Z (vertical) direction in-plane deformations and the out-of-plane displacements with a maximum displacement of the aluminum panel.
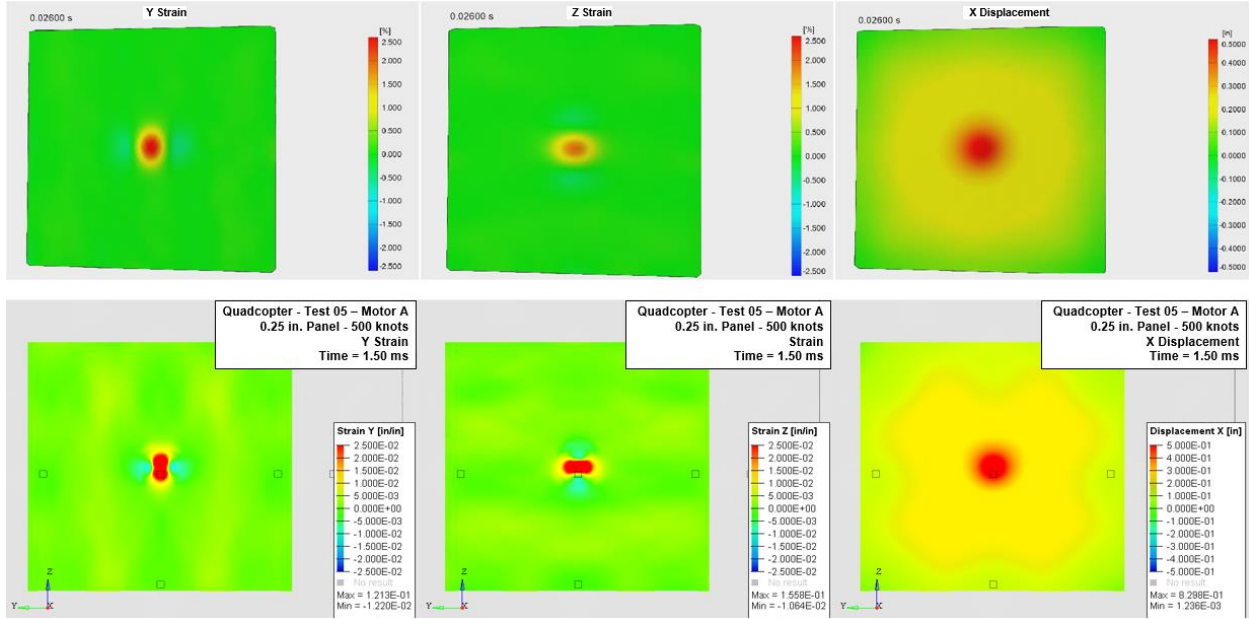
Figure 43. Comparison of test and simulation strains and displacements for motor A impact on 0.25" aluminum panel at 267.51 m/s (520 knots) at t = 1.50 ms (maximum displacement).

Figure 44 shows the out-of-plane displacement of the panel during the impact event obtained from the DIC data and the simulation tracked displacements. The values on the vertical axis are not shown for confidential reasons.
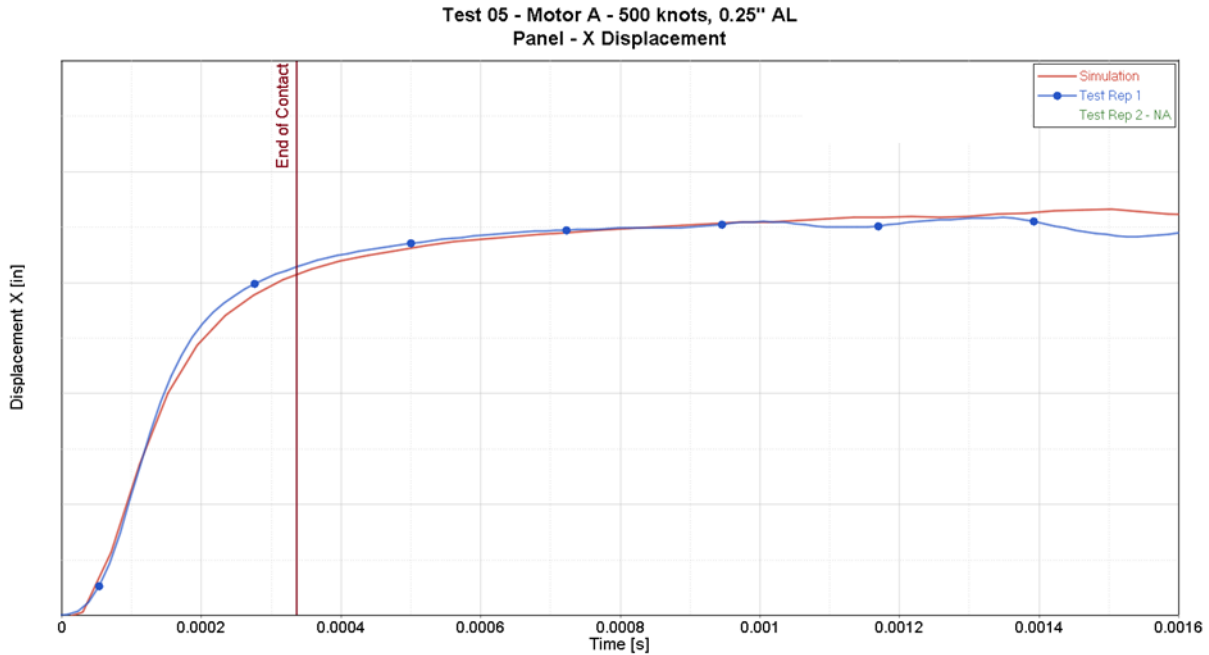
Figure 44. Comparison of the test and simulation out-of-plane displacements for motor A impact on 0.25" aluminum panel at 267.51 m/s (520 knots).

The physical panel was scanned after the test to compare the dimensions of the damaged area. Figure 45 compares the panel's damaged area dimensions for the test and simulation. Again, there is good agreement between the physical test and the predicted panel's damaged area.
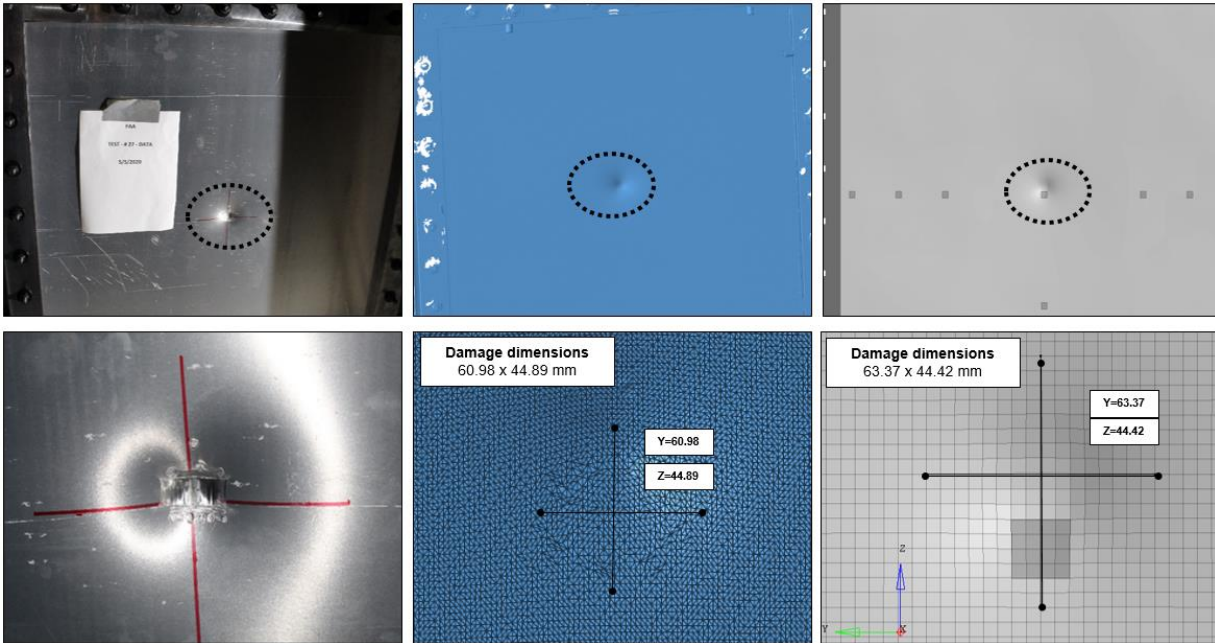
Figure 45. Comparison of the final damage of the panel for the test (left), scan (middle), and simulation (right) of the motor A impact on 0.25" aluminum panel at 267.51 m/s (520 knots).

Figure 46 compares the physical and simulation projectile damage. The motor did not penetrate the panel for both the physical test and simulation but was crushed due to the impact.

Figure 46. Comparison of the test (left) and simulation (right) projectile damage for motor A impact on 0.25" aluminum panel at 267.51 m/s (520 knots).

Figure 47 compares the load-time history of both test repetitions and the simulation load output. All the curves were filtered with a low-pass filter of 15,000 Hz. The load data shows good repeatability for test and simulation and confirms the good correlation up to the end of the contact,

marked with an asymptote. However, the post-impact oscillations of the panel deviate from those of the physical test. Figure 48 compares the strain data collected at both test iterations to the simulation strains. The values on the vertical axis are not shown for confidential reasons.
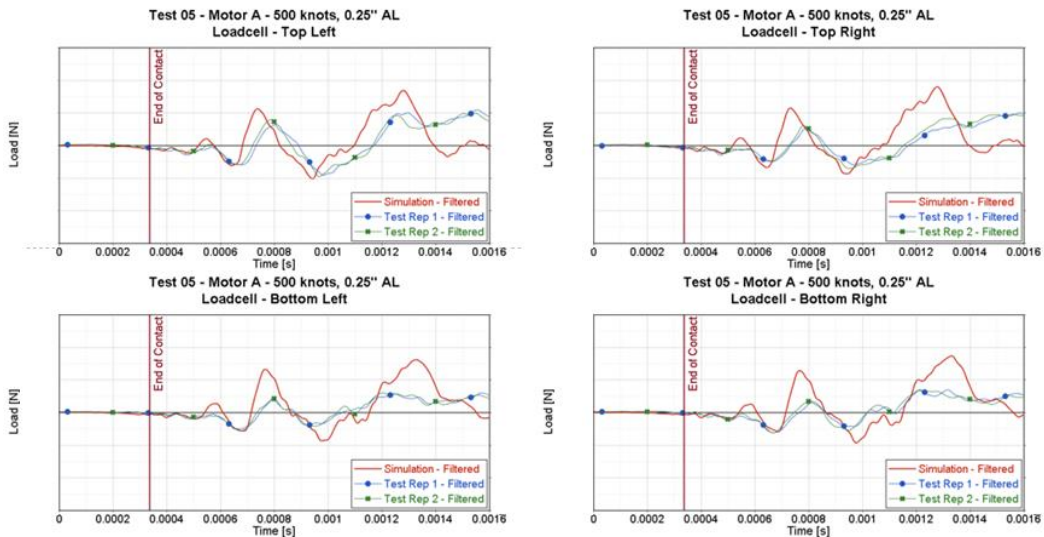
Figure 47. Load cell history data validation for motor A impact on 0.25" aluminum panel at 267.51 m/s (520 knots).
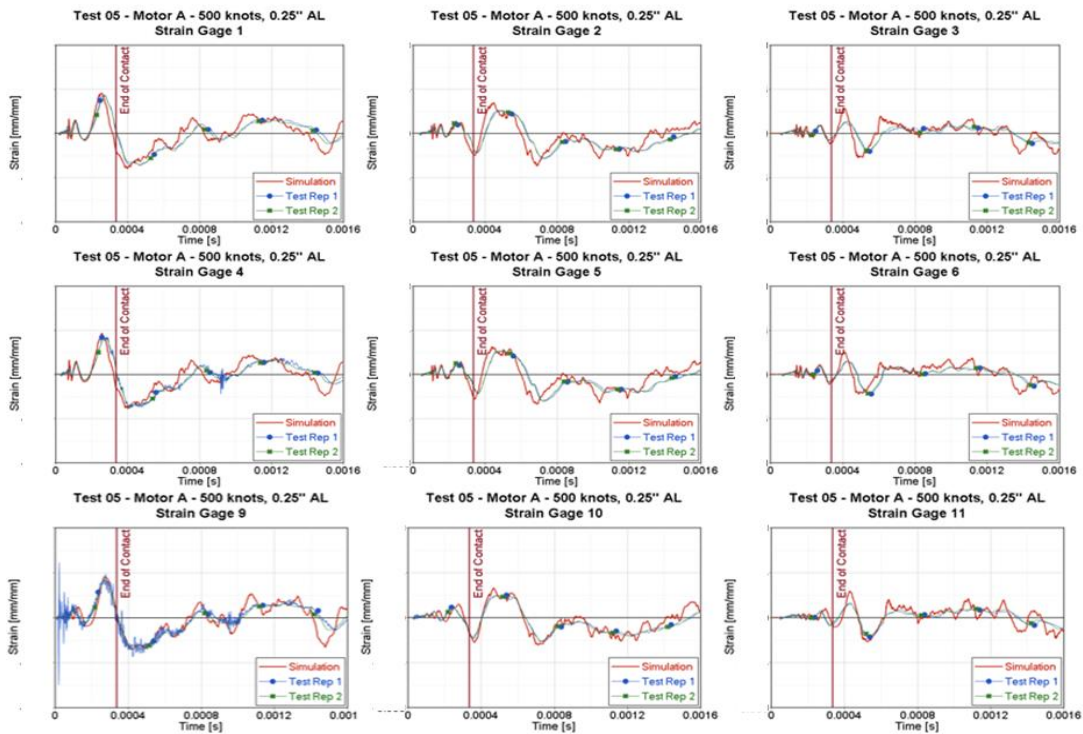
Figure 48. Strain comparison of strain gages 1-6 and 9-11 for motor A impact on 0.25" aluminum panel at 267.51 m/s (520 knots).

2.4   UAS FINITE ELEMENT MODEL VALIDATION

The UAS models introduced in previous chapters were developed following the Building Block Approach. This exercise was initiated during the Task A3 program when the 1.2 kg (2.7 lbs.) quadcopter and the 1.81 kg (4.0 lbs.) fixed-wing UAS were initially reverse-engineered. A similar approach was followed to develop 25 lbs. and 55 lbs. large UAS FEM. In summary, the UAS FEMs used in this research are supported and validated by the following testing and validation data:

- Coupon level data for material characterization from Task A3 [2] and A30 [26].
- Sub-component tests were carried out to verify the UAS case polycarbonate material (drop tower test) from Task A3 [22].
- Ballistic component-level test of the battery, motor, and camera from Task A3 [22, 24](the validation impact velocity range was 250 knots for this program).
- Full-scale test through a free drop test of the UAS from Task A3 [22].
- The full scale at low velocity from the Ground Collision Task A14 program [23].
- National Research Council of Canada full-scale level test with DJI Phantom 3 [28] up to 250 knots.
- Task A16 ballistic component-level test for impact velocity up to 500 knots [3].
- Task A16 full-scale level test against rotorcraft targets [3].
- Task A17 Engine Ingestion component and full-scale level testing against representative engine fan blades for impact velocities up to 700 knots [29].

These UAS models are intended to assess impact severity levels for mid-air collisions between UAS and aircraft structures. Due to the previous extensive validation efforts, no additional validation tests were performed for the research presented in this report.

3   TARGET DEFINITION – R44 ROTORCRAFT

This chapter covers modeling the aircraft target areas subjected to UAS impacts. For this study, a Part 27 rotorcraft was modeled. The part 27 rotorcraft selected for reverse engineering was a 1996 R44 Astro Robinson. R44 has been the world's best-selling rotorcraft in the general aviation market [30]. The R44 is a four-seater light helicopter that has been in production since 1993 [31]. As of 2009, more than 5000 R44 helicopters have been delivered, surpassing the R22, which held the position earlier for the best-selling rotorcraft of the Robinson company [31].

To build the Part 27 rotorcraft FEM discussed in this work, NIAR followed a physics-based modeling approach, which takes advantage of advances in computational power, the latest computational tools, years of research in understanding the fundamental physics of the crashworthiness event, generated test-to-test variability data, and verified & validated modeling methodologies. This approach uses the building block approach, as illustrated in Figure 49. The building block approach is the incremental development of analysis and supporting tests, where typically, there is an increase in the size and complexity of the test article and a decrease in the number of supporting tests. To develop this method, it is necessary to understand the underlying physics and corresponding test variability from the coupon to the system level. System-level test results do not drive the definition of the numerical model. Instead, it is driven by a predefined, verified, and validated building block modeling methodology. Following this approach, simulations predict the system-level test results within an acceptable scatter band. An objective validation criterion based on understanding the test-to-test variability is used to evaluate the numerical models.

The rotorcraft CAD model was created first using a 3D scan of an R44 Robinson, measurement data, and technical manuals. The CAD model was then converted into a detailed FEM for impact analysis in LS-DYNA. Detailed information for the CAD and FEMs of the Part 27 rotorcraft is documented in this chapter.
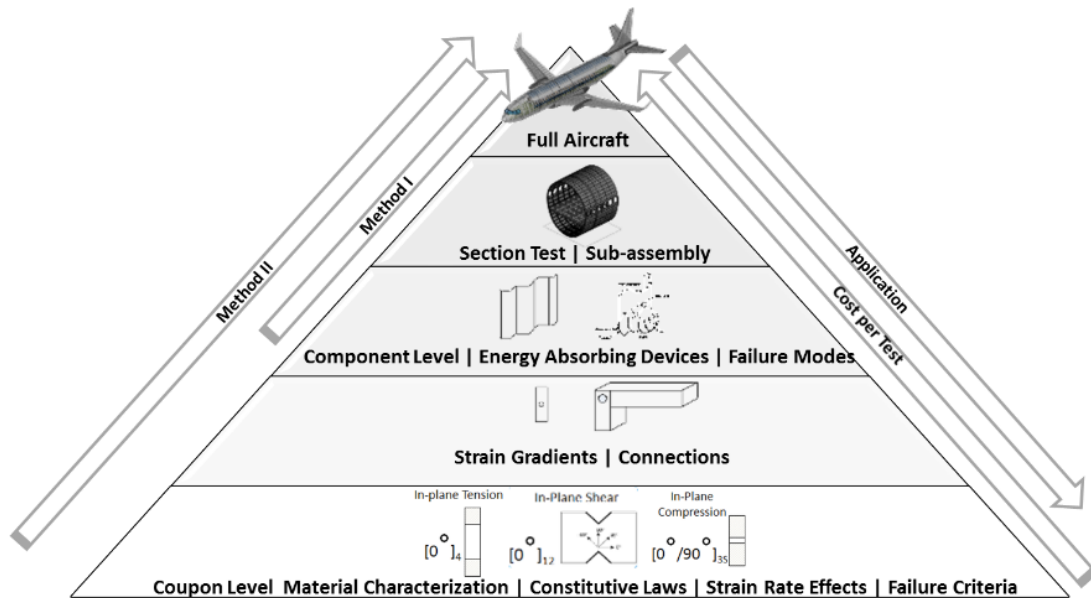
Figure 49. Building block approach for the NIAR narrow-body aircraft model.

3.1 CAD Reverse Engineering

A representative CAD model of an R44 Astro Robinson rotorcraft was generated by NIAR to be used as a target for UAS impact studies. Since actual rotorcraft drawings were unavailable, the CAD model was reverse-engineered based on 3D scan data and measurements of a physical R44 Robinson rotorcraft and available information in technical manuals [32]. In addition, input from design engineers helped refine the model and verify the structure's fidelity.

The following assumptions were made for the CAD modeling process due to the limited information found in the literature:

- Avionics and wires were not modeled.
- Internal structures such as seats and insulations were not modeled.
- Sheet metal features such as beadings and stamps were not captured on the flanges of frames and ribs.
- Holes less than 5 mm were not captured in the geometry.

The model assumptions maintain a conservative approach, which reduces the computational time necessary for FE Analysis and preserves the representative nature of the model. Figure 50 shows isometric, front, top, and side views of a representative CAD model of a Part 27 rotorcraft developed by NIAR.

Figure 51 illustrates the overall dimensions of the rotorcraft.
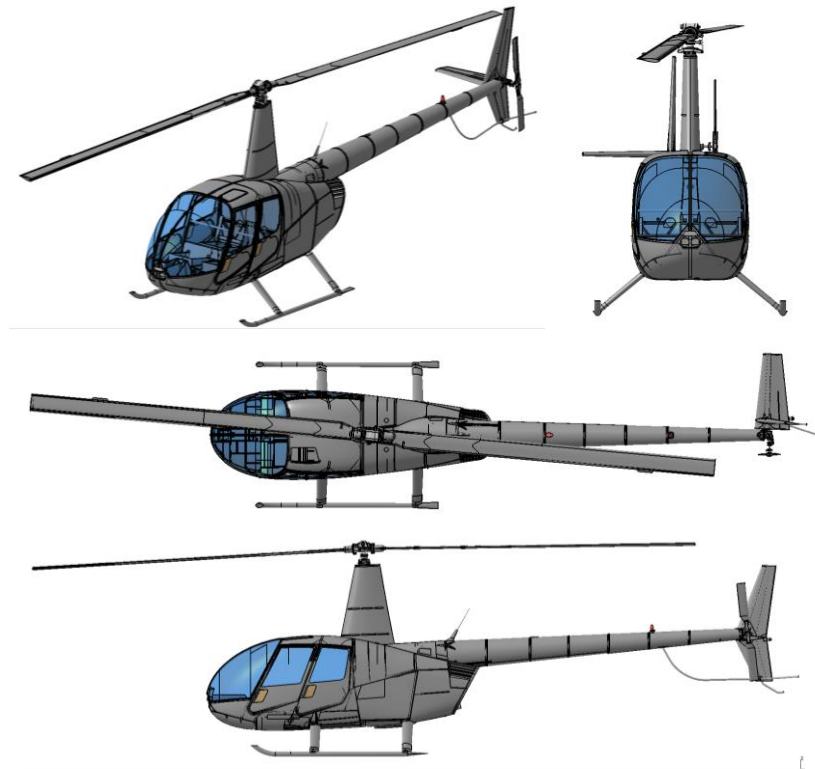
Figure 50. Representative R44 rotorcraft CAD model developed by NIAR.
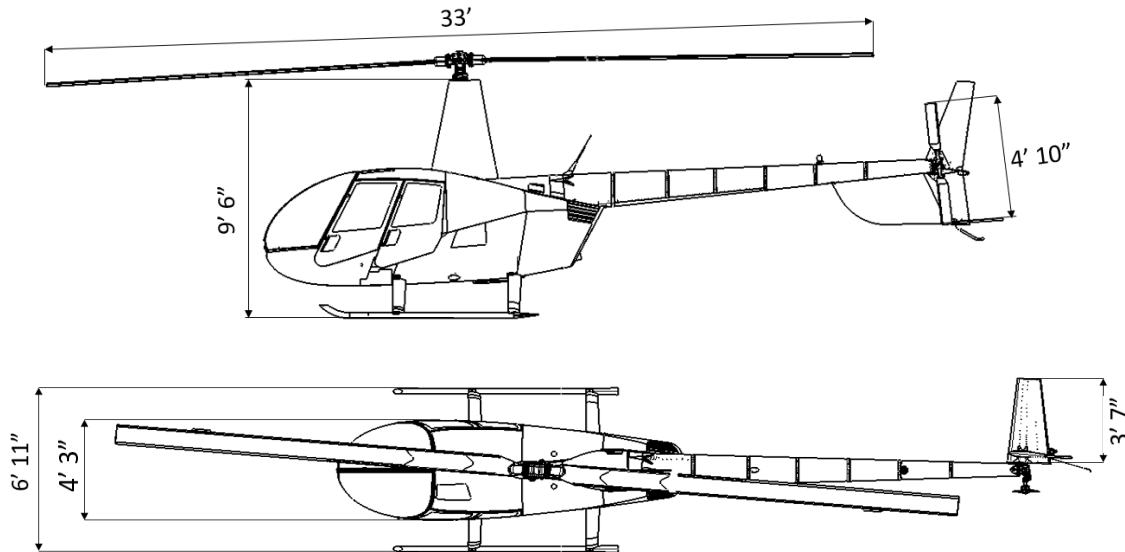
Figure 51. Part 27 Rotorcraft overall dimensions.

3.1.1 Disassembly & Scanning

NIAR acquired a 1996 R44 Astro Robinson rotorcraft, which, although fully intact, was deemed not airworthy. An outer scan was conducted in its undamaged state to obtain an Outer Mold Line (OML), which was extensively utilized for CAD generation. The OML scan is produced using point cloud data from the rotorcraft and cannot be directly used for modeling. Therefore, an equivalent OML surface was generated from the scan for CAD modeling purposes. Figure 52 shows the physical test article coated white for OML scanning.

Figure 53 shows the equivalent OML surface generated from the OML scan. The rotorcraft was then disassembled into various subsections for shipping and continued scanning of internal geometry at the NIAR facility, as shown in Figure 54:

1. Fuselage
2. Tail Cone Assembly
3. Stabilizers
4. Main Rotor Blade Assembly
5. Tail rotor blade Assembly
6. Engine Mast Assembly

Figure 52. Part 27 Rotorcraft coated for OML Scan.

OML scan

OML surface

OML scan and surface overlap
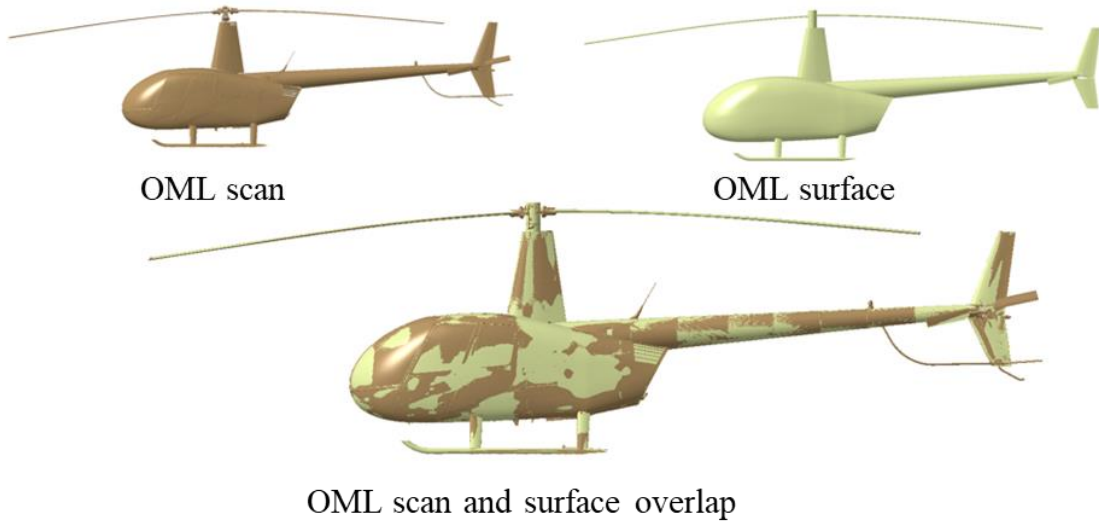
Figure 53. Part 27 Rotorcraft OML scan overlapping OML surface.
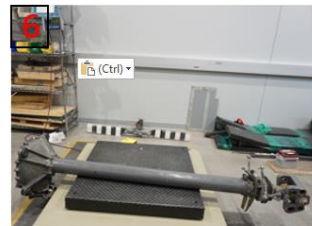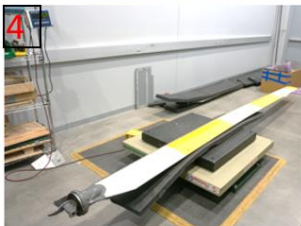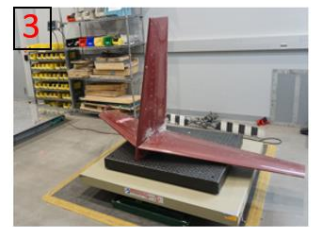
Figure 54. Part 27 rotorcraft sub-assemblies at NIAR.

Figure 55 compares the isometric view of the part 27 rotorcraft representative CAD model against the 3D scan cloud points, which is the main data source for the CAD reverse-engineering process. The 3D scan data included details and accuracy, such as small holes or cutouts. The left side of the physical test article was stripped to allow accessibility for scanning. The rotorcraft's small sections and internal structures were scanned individually to increase accuracy and facilitate the reverse-engineering process. The CAD model includes all the primary structural members. In addition, most of the secondary structures, such as support angles, clips, and doublers, were captured in the scan of the physical article. The reverse engineering of the engine was simplified to include only the major components and attachments. Hand measurements and pictures were also taken from the physical rotorcraft, especially in locations where the scan had no access to generate cloud points. The subsequent sections present detailed CAD information for each target area. Note that some assemblies, such as doors, are hidden in Figure 55 to show the internal geometry captured in the scan and CAD.

Figure 55. Part 27 rotorcraft 3D scan data vs. CAD model.

45

3.1.2 Horizontal Stabilizer

Figure 56 shows a top view of the horizontal stabilizer CAD model and its overall dimensions. As observed in Figure 50, the horizontal stabilizer is only on the right-hand side. It is a fixed horizontal stabilizer that does not include an elevator or a trim tab. The horizontal stabilizer is sandwiched between the upper and lower vertical stabilizer. Efforts were made to capture all the structural members in the CAD model. Figure 57 and Figure 58 show the stabilizer with cutouts in the skin to allow scanning of main structural members to help in CAD development. It also details the internal structure in the horizontal stabilizer CAD model. The geometry did not capture wires, actuators for the horizontal tail elevators, or any other non-metallic parts.
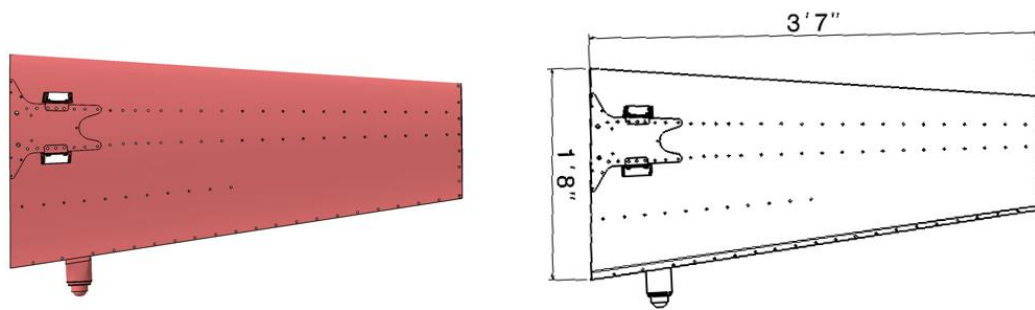
Figure 56. Part 27 Rotorcraft horizontal stabilizer CAD model overall dimensions.
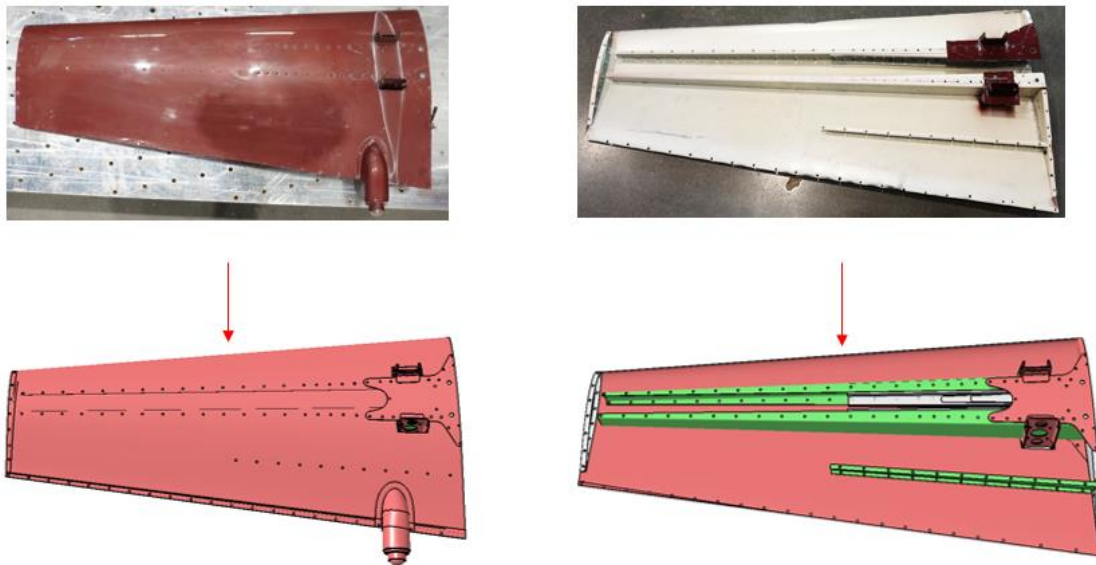
Figure 57. Part 27 Rotorcraft horizontal stabilizer CAD vs. physical test article.
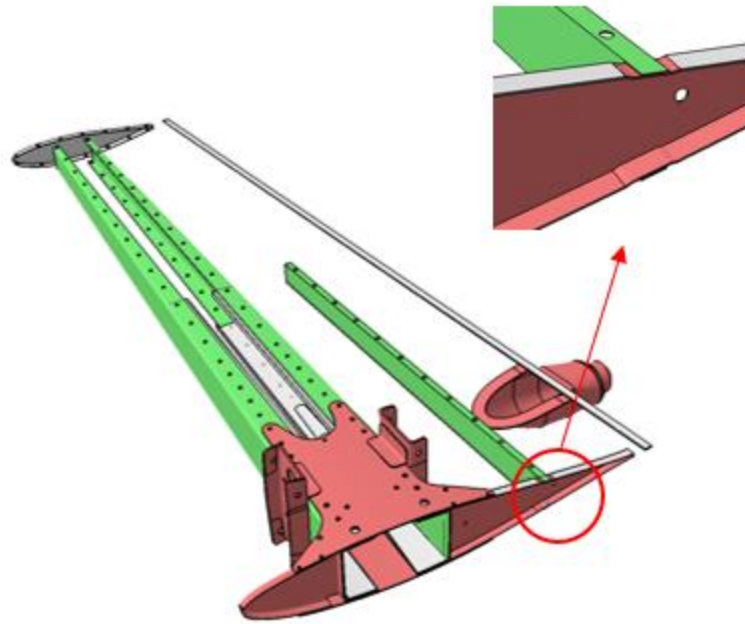
Figure 58. Part 27 Rotorcraft horizontal stabilizer CAD internal structure vs. physical test article.

3.1.3   *Vertical Stabilizer*

Figure 59 shows a side view of the vertical stabilizer CAD model and its overall dimensions. The vertical stabilizer consists of two sections: Upper Vertical Stabilizer and Lower Vertical Stabilizer. The vertical stabilizer connects to the horizontal stabilizer, which connects to the tail cone assembly to connect the stabilizer assembly to the rotorcraft airframe. The vertical stabilizer CAD geometry includes all the primary and secondary load-carrying members. Figure 60 and Figure 61 present the internal structure detailed views of the vertical stabilizer. It also shows the stabilizers with cutouts in the skin to allow scanning of main structural members to help in CAD development. The CAD geometry did not capture the wires, lights, vertical stabilizer actuators, and non-metallic parts.
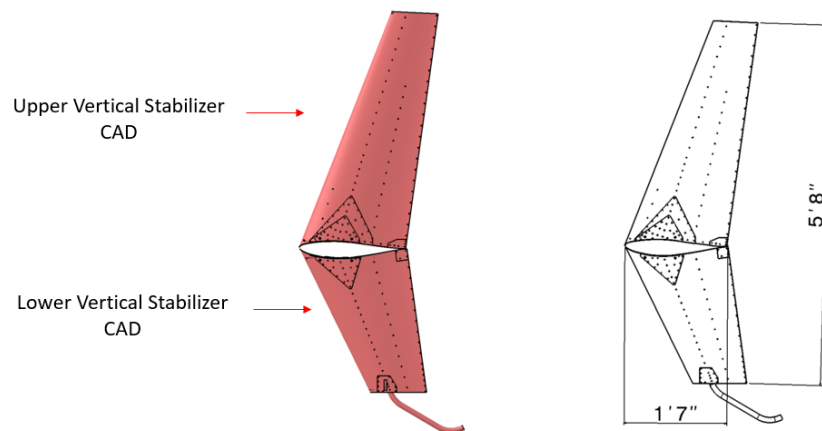
Figure 59. Part 27 Rotorcraft vertical stabilizer CAD overall dimensions.

47
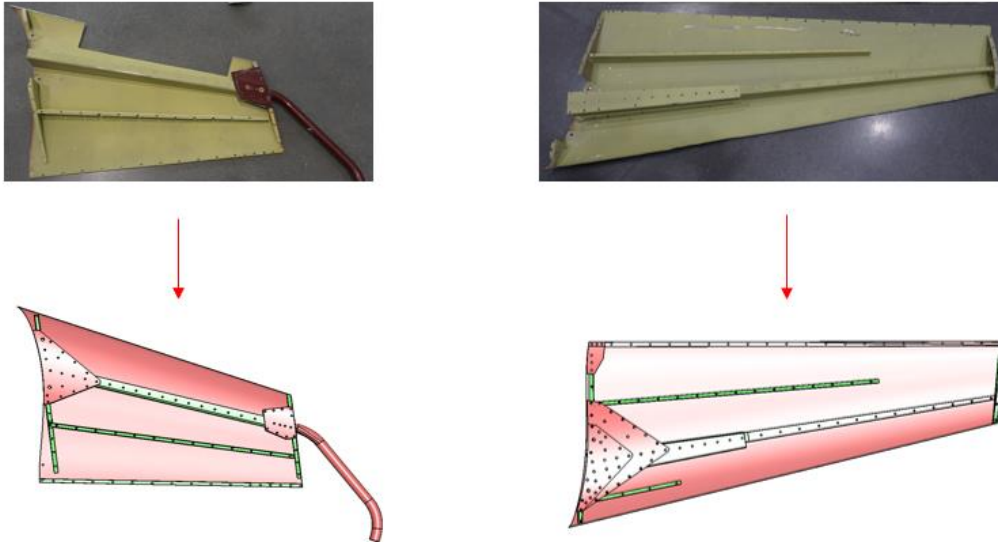
Figure 60. Part 27 Rotorcraft vertical stabilizer CAD vs. physical test article.
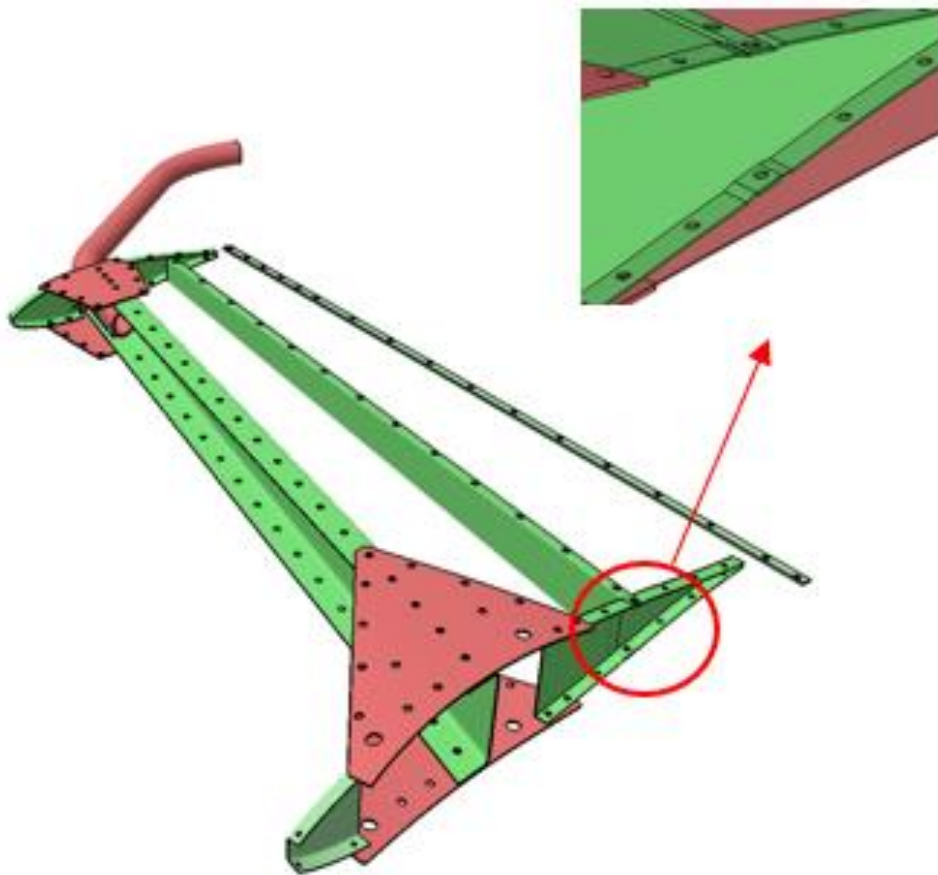
Figure 61. Part 27 Rotorcraft vertical stabilizer CAD internal structure vs. physical test article.

3.1.4 Tail Cone Assembly

Figure 62 shows the CAD geometry for the complete tail cone assembly and its overall dimensions. The CAD model captures the primary structure, such as frames and stringers, to give the structure integrity. This assembly connects the empennage and tail rotor assembly to the main fuselage body. The physical test article was dissected at the frame stations to allow detailed scanning of these frames to aid in CAD modeling. Moreover, secondary structure members, such as doublers, clips, and retainers, were also captured during the scanning process and added to the CAD geometry. Figure 63 compares the details seen in the skeletal model of the physical test article vs. the details captured in the NIAR CAD model.
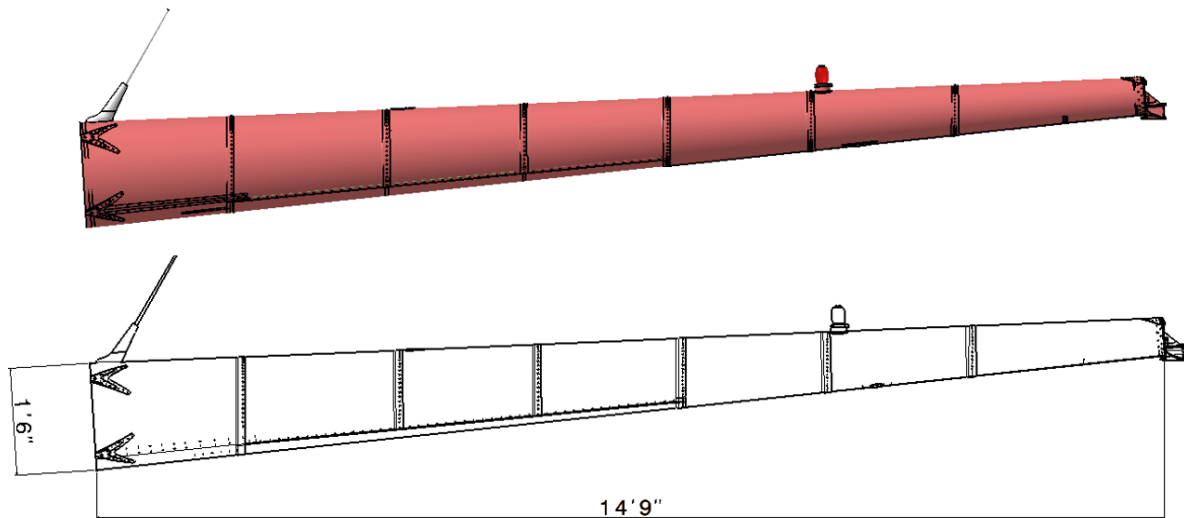
Figure 62. Part 27 Rotorcraft tail cone assembly overall dimensions.
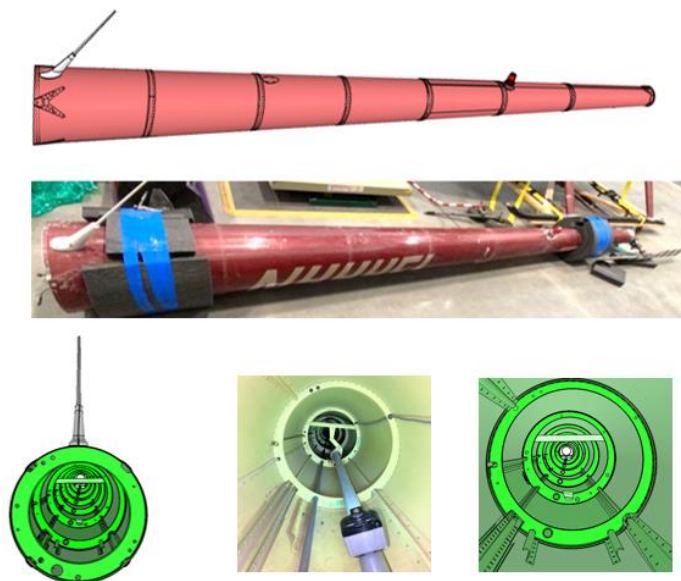
Figure 63. Part 27 Rotorcraft CAD showing the internal structure vs. physical test article.

Figure 64 compares the frames that were dissected for scanning with the CAD generation. This was essential as the tail cone is a critical section of the rotorcraft that connects various assemblies to each other.
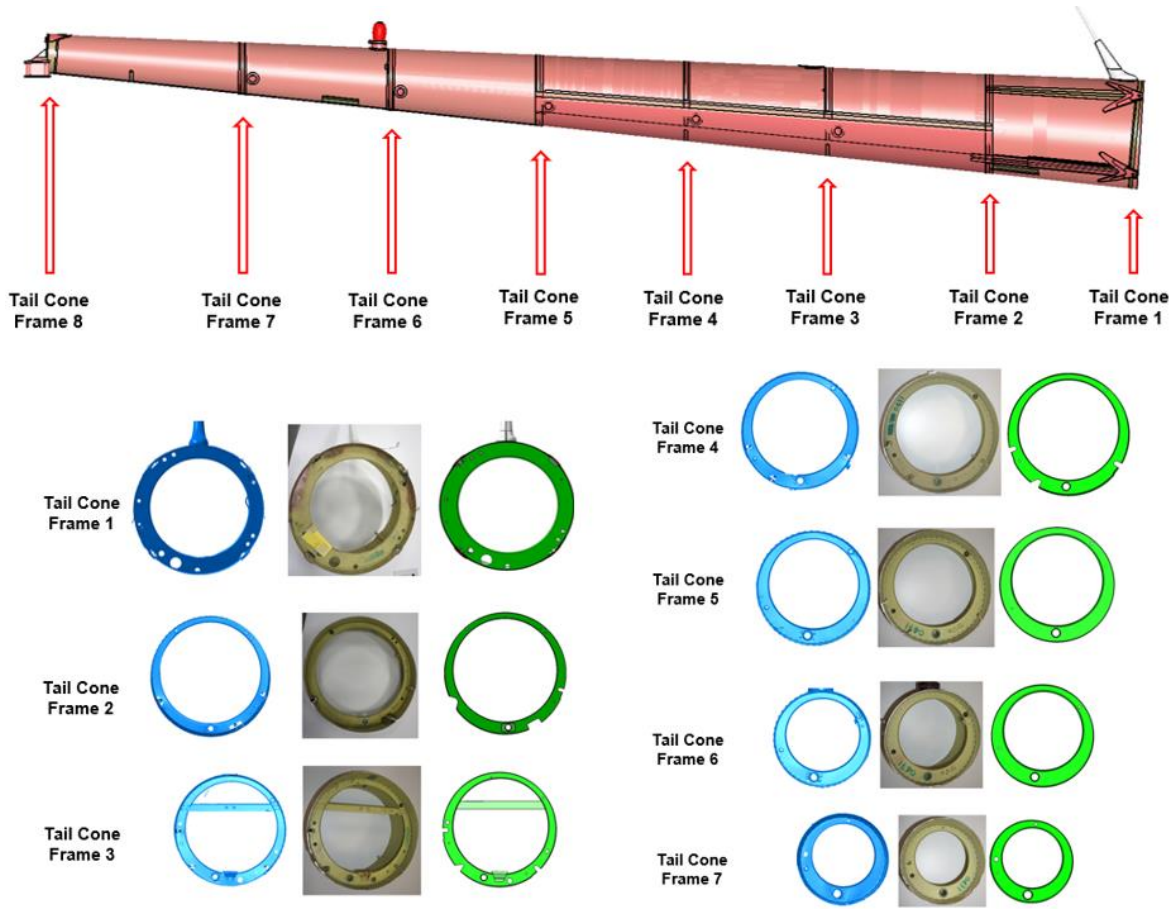
Figure 64. Part 27 Rotorcraft tail cone frames – Scan vs. physical test article vs. CAD.

3.1.5   Tail Rotor Assembly

Figure 65 shows an isometric view of the tail rotor CAD model and the 3D scan data used in the reverse-engineering process. All major components of the tail rotor assembly, such as the hub, spinner, spinner bulkheads, supports, and motor, were modeled.
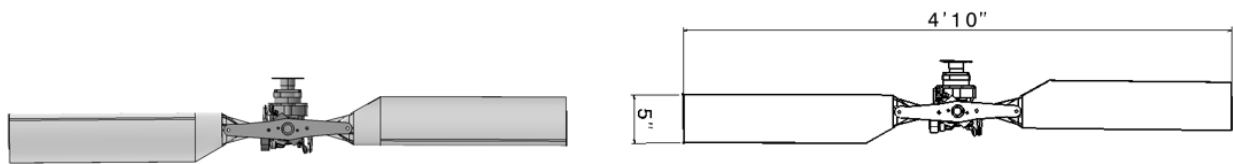
Figure 65. Part 27 Rotorcraft tail rotor CAD model overall dimensions.

The CAD geometry for these components was captured based on scan data and disassembly of the physical test article (see Figure 66). Some assumptions were made to determine the dimensions of a few propeller internal components following available manuals and dissected data.
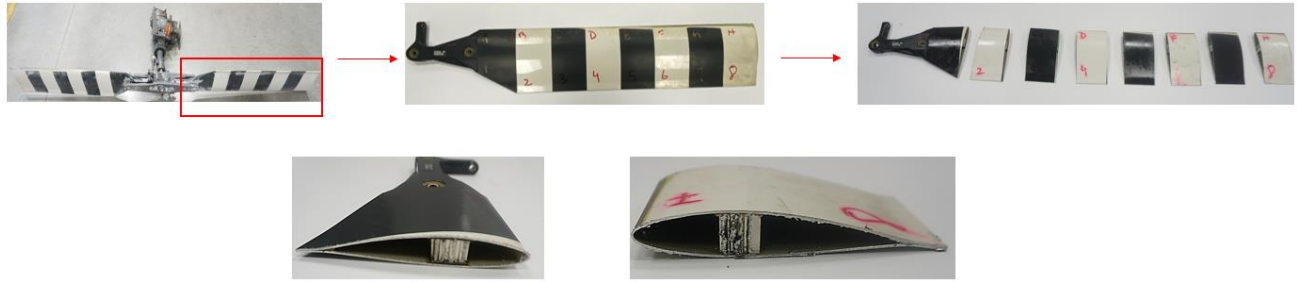
Figure 66. Part 27 Rotorcraft tail rotor blade dissections.

The motor assembly, blade honeycomb structure, yoke, caps, input cartridge, pitch assembly, etc., were also modeled in detail to ensure the structural integrity of the tail rotor region to the main fuselage. Figure 67 compares the CAD overlapped with the scan to show the degree of representation with the physical test article.
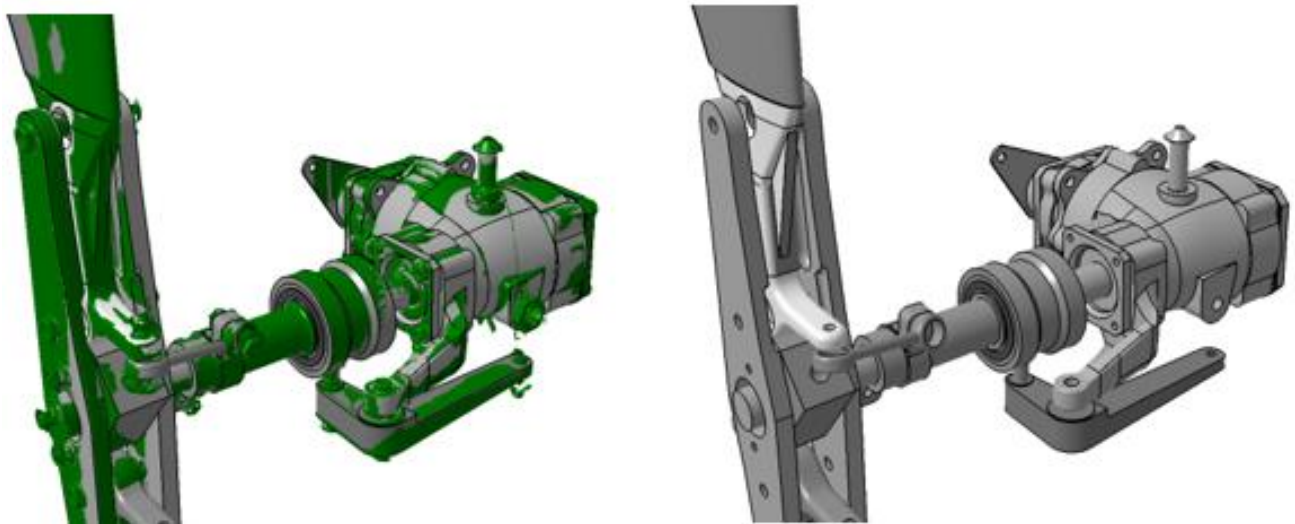
Figure 67. Part 27 Rotorcraft tail rotor assembly CAD with overlaid scan.

Fasteners and connections of the rotorcraft tail rotor assembly were defined using the scan data and visual inspection of the structure. The tail rotor assembly connects to the tail cone fuselage assembly with a machined frame through 4 bolts. Figure 68 compares the CAD with the frame's scan and physical test article.

Figure 68. Part 27 Rotorcraft tail cone machined frame.

This frame also joins the stabilizer assembly to the airframe. Hence, it was modeled with all the required details as necessary. Figure 69 presents the stabilizers and tail rotor assembly connected to the tail cone by this machined frame.
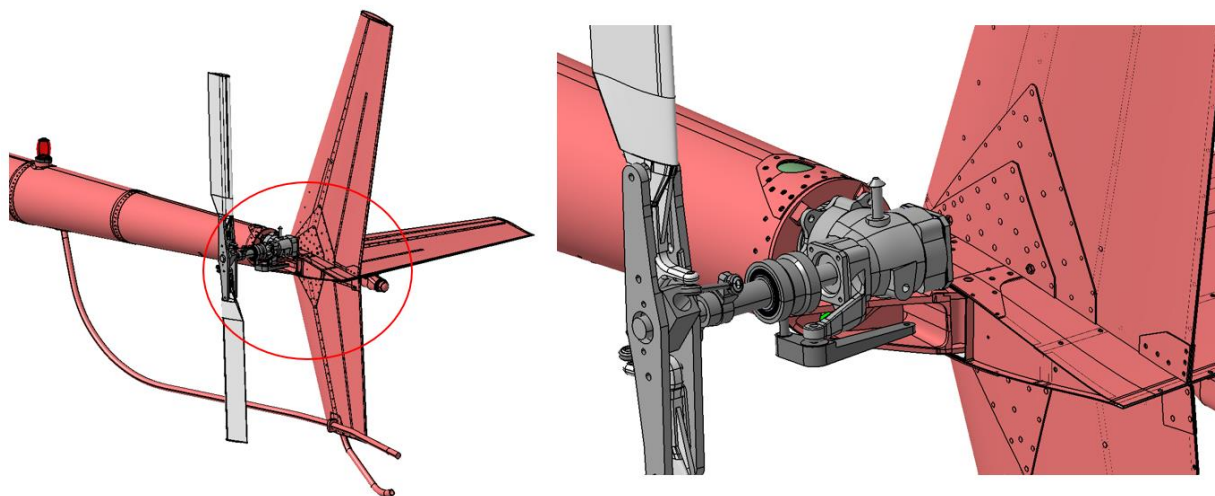
Figure 69. Part 27 Rotorcraft empennage region.

3.1.6   Fuselage

Figure 70 compares a cross-section of the scan model and the CAD geometry for the complete rotorcraft model. The fuselage body captures the primary structure, such as frames and stringers, which define the primary load paths of the airframe. Moreover, secondary structure members, such as doublers, clips, and retainers, were captured during the scanning process and added to the CAD geometry. Figure 71 compares the details seen in the skeletal model of the physical test article vs. the details captured in the NIAR CAD model.
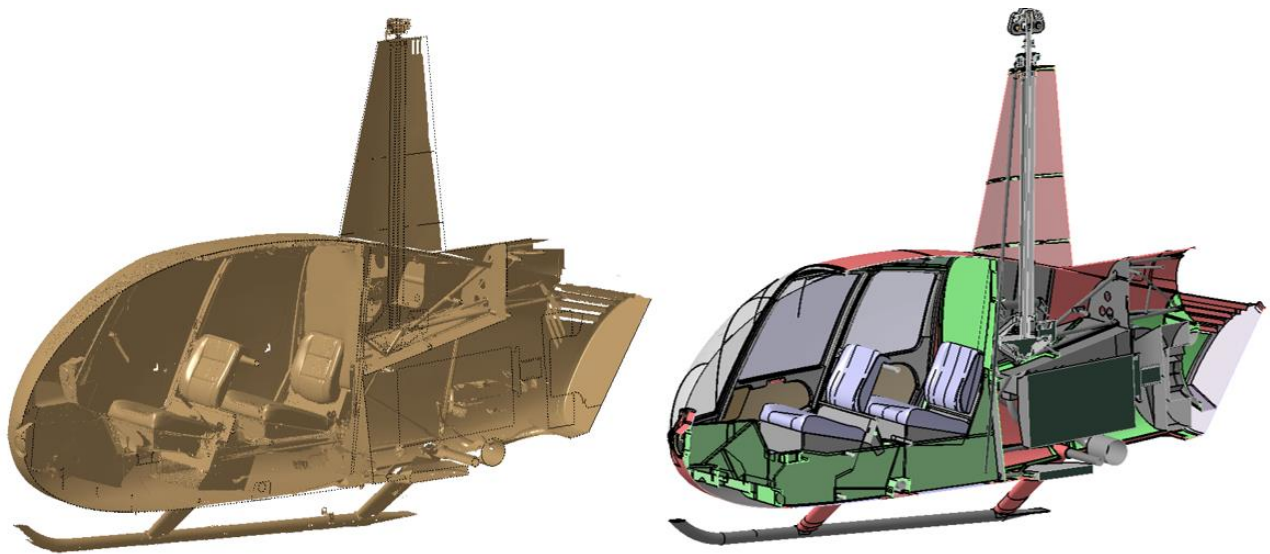
Figure 70. Part 27 Rotorcraft fuselage 3D scan (left) vs. NIAR CAD model (right).
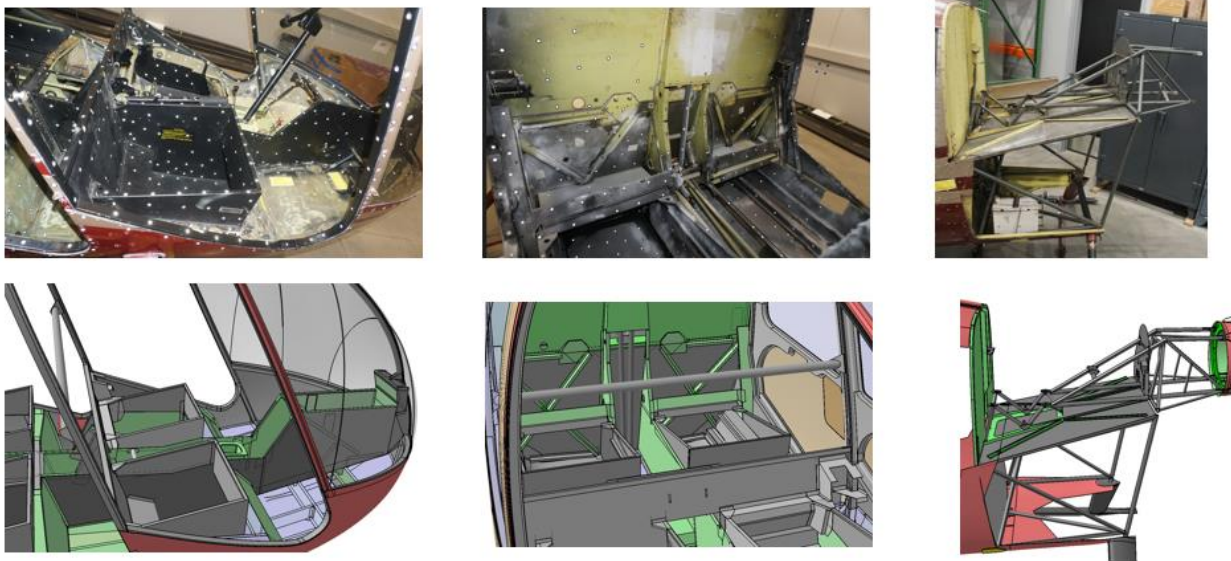
Figure 71. Part 27 Rotorcraft fuselage details – Physical test article (top) vs. NIAR CAD model (bottom).

Furthermore, the fuselage also houses the engine, fuel tanks, main rotor mast, and gearbox assembly. NIAR made detailed efforts to capture these details in the fuselage structural model since these mass items and their supporting structure contribute to this small-size airframe's overall weight and strength. Figure 72 shows the engine, engine mast assemblies, and their representation in the NIAR Part 27 rotorcraft CAD model.
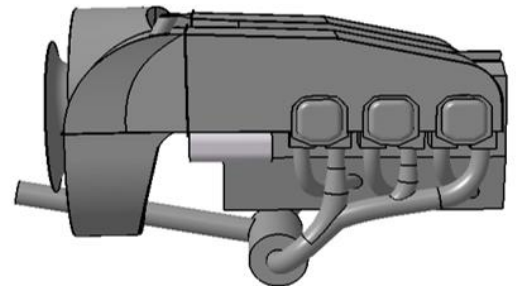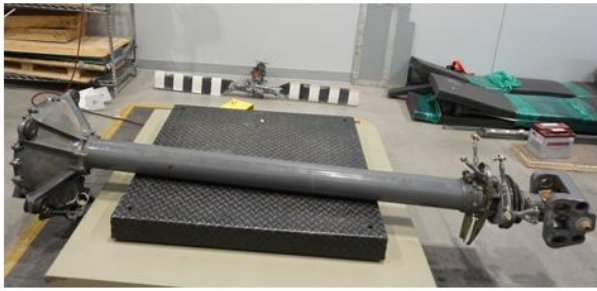
Figure 72. Part 27 Rotorcraft engine mast and engine – Physical test article (top) vs. NIAR CAD model (bottom).

3.1.7 *Windshield*

Figure 73 presents a top view of the windshield CAD and its overall dimensions. The windshield is a single-layer acrylic piece that connects to the fuselage through retainers and extrusions riveted to the skins and the front door frames. The windshield thickness was determined to be 0.118 inches. Figure 74 shows frontal and rear isolated views of the windshield and its surrounding structure.
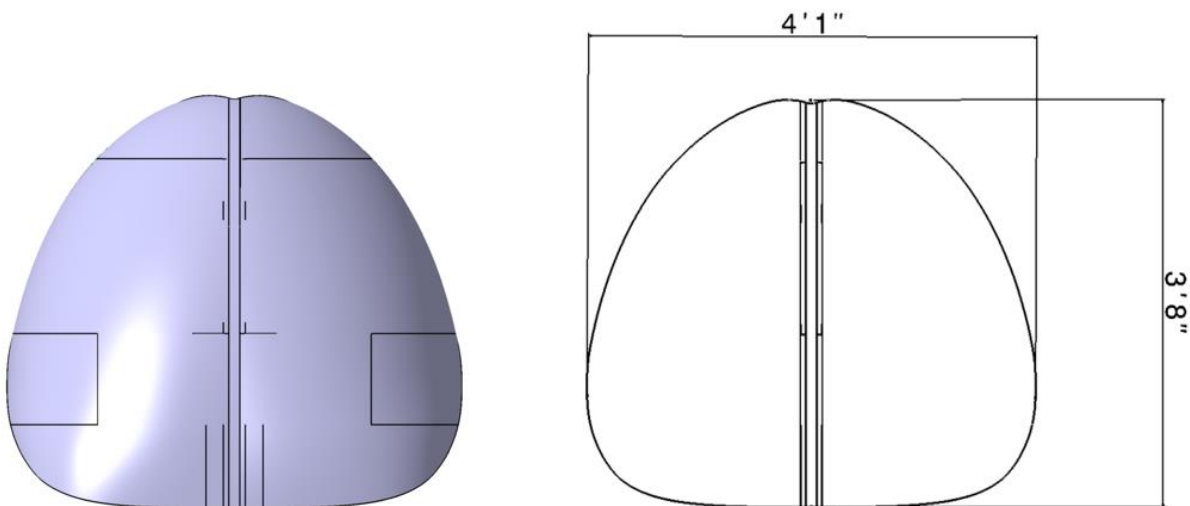
Figure 73. Part 27 Rotorcraft windshield CAD overall dimensions.

54
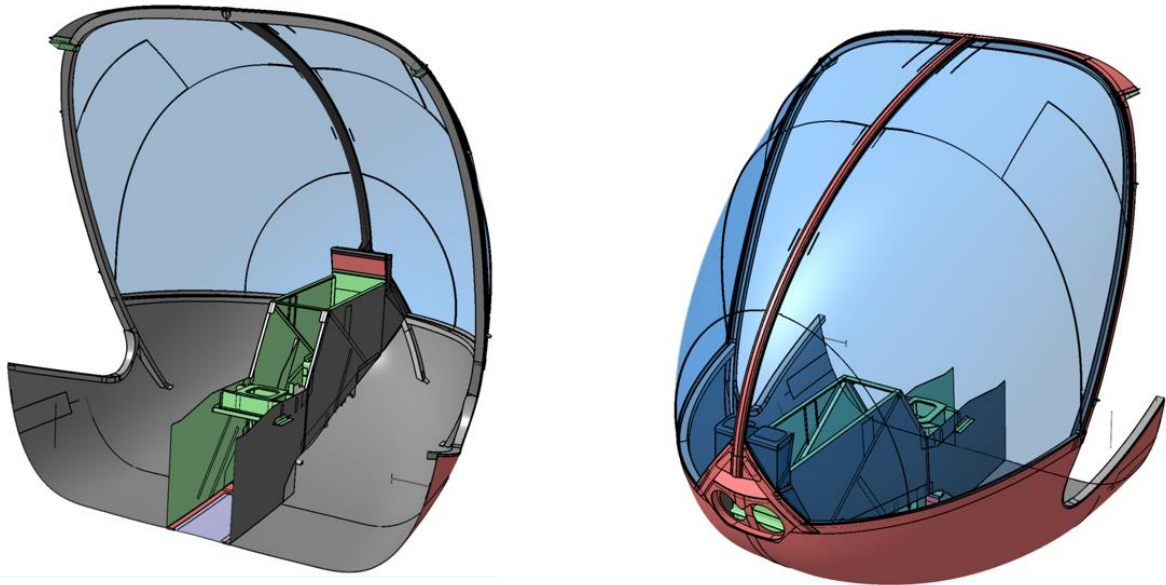
Figure 74. Part 27 Rotorcraft windshield CAD Internal structure.

3.1.8 Main Rotor Blade

Figure 75 shows the CAD geometry for the complete main rotor blade assembly and its overall dimensions for a single blade. The R44 Robinson rotorcraft is equipped with two main rotor blades for a total span of 33 feet.
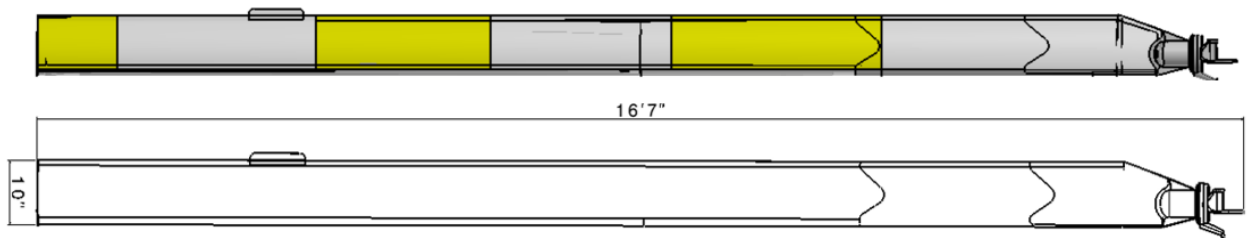
Figure 75. Part 27 Rotorcraft main rotor blade overall dimensions.

To model the geometry, the first step was to scan the entire blade. NIAR then dissected a single blade into five sections based on a literature review from available manuals [32]. As shown in Figure 76, these sections were then carefully studied to document:

- Aluminum Skin thickness/Layers
- Composite layups (if any)
- Metallic parts
- Leading edge & Trailing edge cross-sections
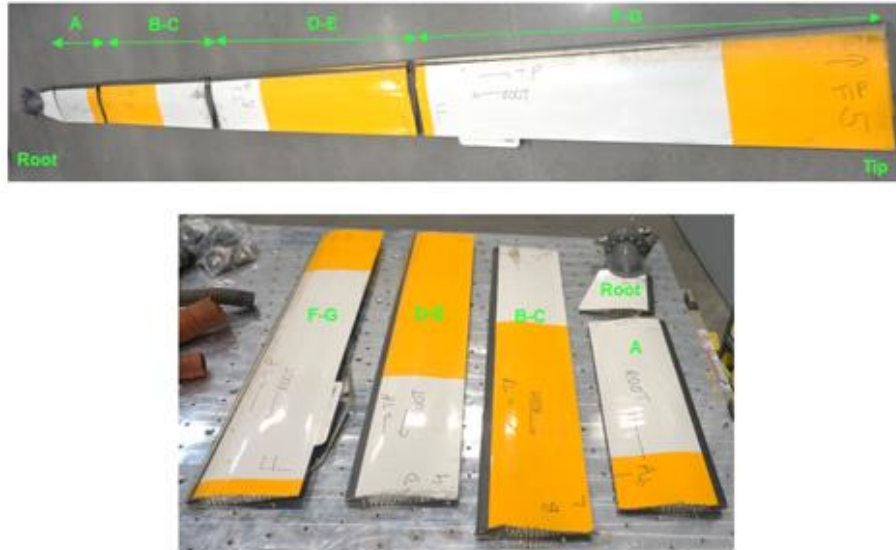
Figure 76. Part 27 Rotorcraft main rotor blade dissections.

Additionally, the root region had to be further disassembled and dissected, as per the literature review [32] in Figure 77, to ensure all major structural members were measured correctly and accounted for.
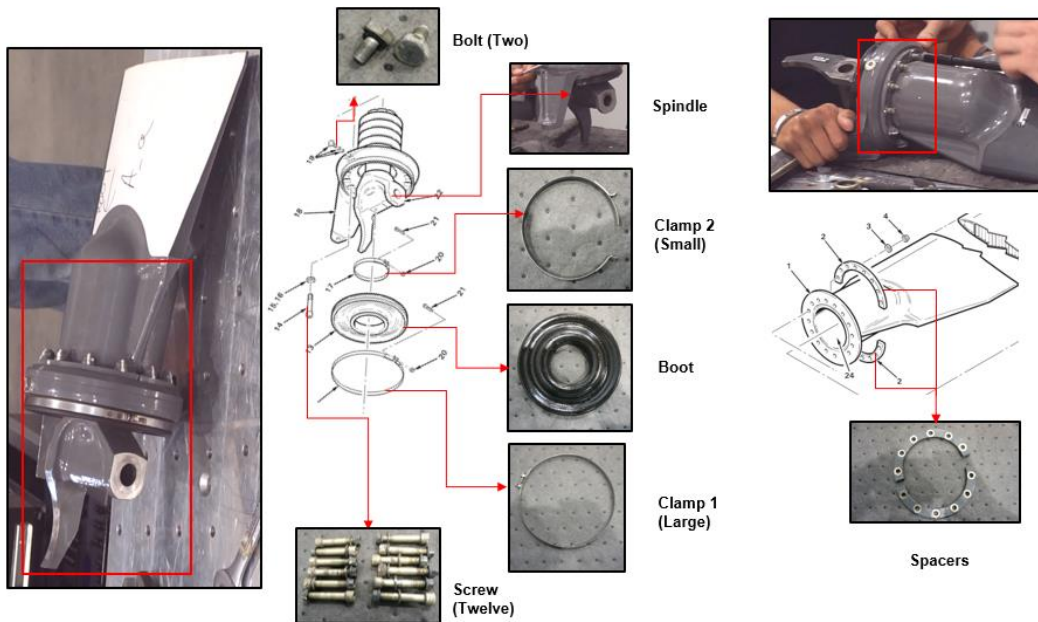
Figure 77. Part 27 Rotorcraft main rotor blade root region disassembly (Drawings from [32]).

Figure 79 through Figure 81 compare the main rotor blade CAD details with the physical test article. Some simplifications were made in the CAD:

- The honeycomb core was modeled as a solid.
- Nutplates or bolts (diameter < 5mm) were not modeled.
- Ball bearings (found in the root region) were not modeled.

56
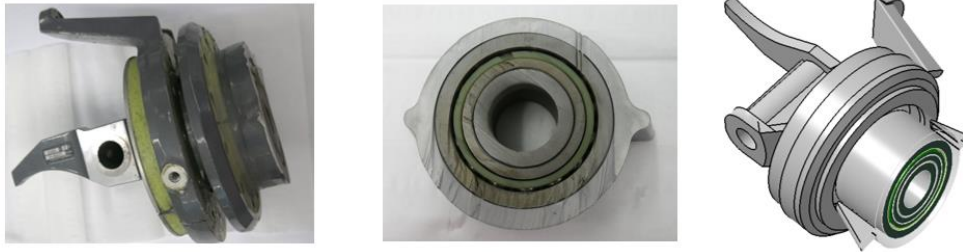
Figure 78. Part 27 Rotorcraft main rotor blade root region – Physical test article vs. CAD.
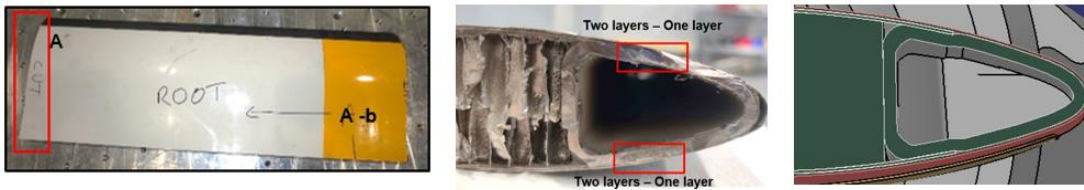
Figure 79. Part 27 Rotorcraft main rotor blade leading edge profiles/skin layers variations.

Furthermore, Figure 81 highlights how the main rotor blades are connected to the rotorcraft airframe via one bolt through the engine mast assembly.
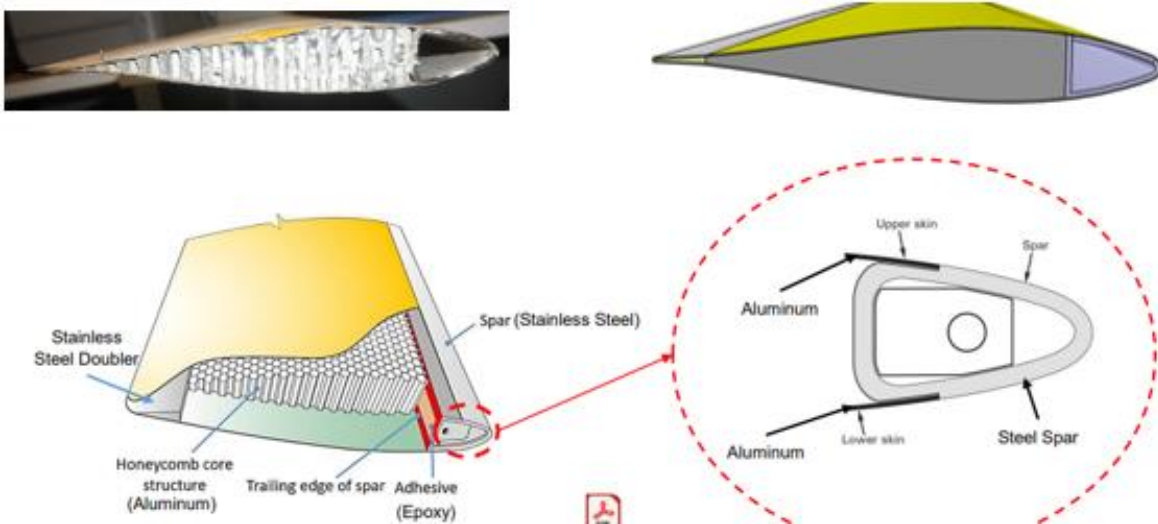
Figure 80. Part 27 Rotorcraft main rotor blade cross section LE – Physical test article vs. reference manuals vs. CAD. Image adapted from [33].
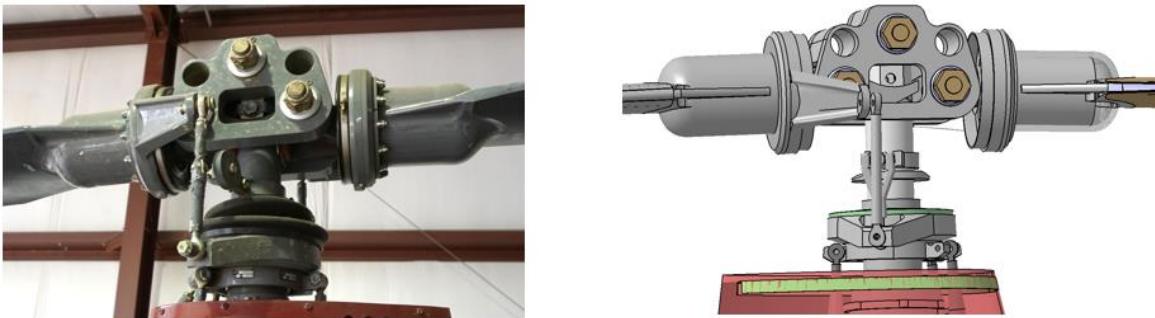
Figure 81. Part 27 Rotorcraft main rotor blade connection to the engine mast assembly.

3.2 MATERIAL TESTING

Accurate material definitions are paramount in high-fidelity impact simulations. They directly influence the accuracy and reliability of the simulation results. Without precise material properties, the simulations may yield misleading or inaccurate predictions. Moreover, typical Bills of Materials are not always available or sufficient to fully define the material models required for analysis. This complicates the simulation process, given the lack of information on materials.

Therefore, the development of proper material cards is essential for material reverse engineering tasks. Identifying the materials of areas playing a structural role in the system is crucial to ensuring the reverse-engineered materials' mechanical properties are captured. AVET's extensive experience developing numerical models for the aerospace and transportation industry has proved that accurate and traceable material modeling techniques are essential for numerical model acceptance beyond preliminary design or design optimization phases. This involves identifying critical components of the part to be modeled, extracting an appropriate amount of test coupons, and testing and extracting information from the raw data.

Producing an accurate material card, which contains all the necessary material properties for simulation, is crucial in modeling –as realistically as possible– the behavior and response of the targeted part. A comprehensive material card provides the basic mechanical properties that accurately describe the behavior of materials under various loading conditions.

3.2.1 Material Reverse Engineering Process

This chapter summarizes the material reverse engineering process followed for the R44 rotorcraft under consideration. This process involves identifying and labeling important parts of the rotorcraft, extracting the coupons, testing, analyzing raw data, extracting mechanical properties from the curves, and validating the material cards against the experimental curves.

There are three main scenarios to reverse engineer the material of a part:

- Access to the part with the possibility of conducting destructive testing.
- Access to the part without the possibility to conduct destructive testing.
- No access to the parts.

For this program, the first option is the preferred route and the focus of the current document. Testing the actual material makes it possible to ensure the use of the correct material properties for the numerical simulation. The main steps to conduct the material reverse engineering process are as follows:

- **Parts' identification**: Sectioning parts to identify the heterogeneous sections. From parts' history, structural purpose, critical use, quality of cut, and internal experience to list potential matching materials.
- **Initial assessment**: Detailed visual inspection and magnetic/electric reactions will provide information regarding the composition and nature of materials. This is essential for cases where physical testing is not possible.

- **Literature review**: Conduct a literature review of a given material in the part's domain of application. Further documented parameters provide additional knowledge and background to set physical test expectations.
- **Materials database match-up**: Matching materials are determined from expected mechanical properties and internal material database. Physical test expectations are further narrowed down.
- **Testing:** Destructive and non-destructive testing provide the basic properties required to define a metallic material. Depending upon the criticality of specific parts, additional tests may be conducted to assess the material response under complex loading.
- **Coupon level validations**: Coupon level simulation is used to verify the numerical accuracy of the basic mechanical properties and compare them to the experimental curves from testing. This verifies the numerical material response lies within the expected scatter band of the physical tests.
- **Component level validations**: Simulation of additional, more complex loading cases to calibrate non-physical numerical parameters based on physical testing and to validate the overall response, performance, and limitations of the selected material model.

3.2.2   Rotorcraft Material Construction

A general classification of the rotorcraft's parts was used for disassembling purposes, as shown in Figure 82 and Table 11. Engineering judgment was implemented to classify different parts for destructive and non-destructive testing during the disassembling process. This will be discussed later in this chapter.
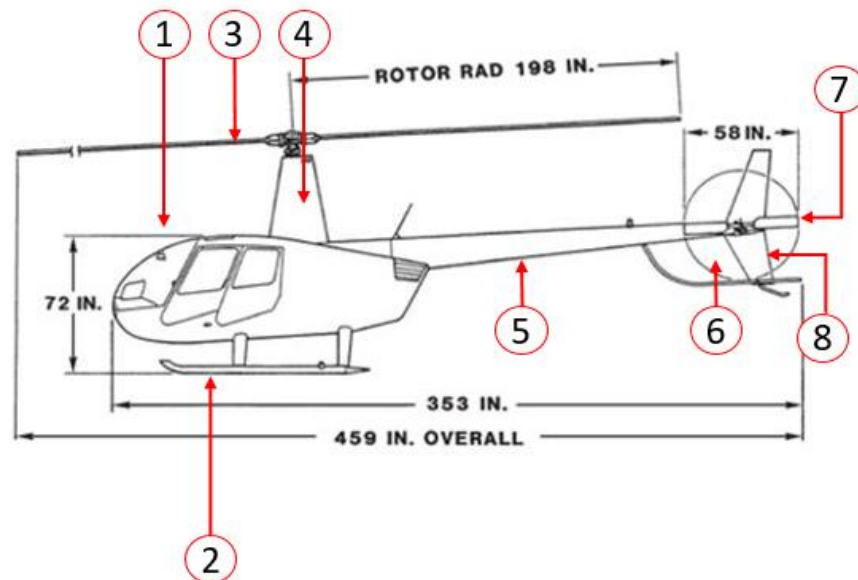
Figure 82. Rotorcraft sections identification.

Table 11. List of parts of the rotorcraft.

Number	Part
1	Cockpit
2	Landing Skid
3	Rotor Blade
4	Cowling and Engine
5	Tail Cone
6	Tail Rotor
7	Horizontal Stabilizer
8	Vertical Stabilizer

After the disassembling process, a material identification scheme was implemented to track each part to its original location within the rotorcraft.

The scheme used was: RC-MRE-Pjj-Y-XX

- RC – Internal project code.
- MRE – Project task: Material Reverse Engineering.
- Pjj – Panel number, follows the order in which each panel was extracted.
- Y – Test type: T for Tensile, C for Compressive, S for Shear, and NDT for Non-Destructive Test.
- XX – Specimen number.

Example: RC-MRE-P04-T-02

- Rotorcraft.
- Material Reverse Engineering.
- Panel 04 means that the 4th panel was extracted.
- T means tensile test.
- 02 is specimen #2 of that panel.

A single material will be presented in the following subsections. The complete list of materials is documented in Appendix A.

3.2.3   Extractions for Destructive Test

This section presents the components and the corresponding extractions made in compliance with the ASTM E8/E8M sheet-type specimen. The test specimen geometry and dimensions are shown in Figure 83 and Table 12, respectively. The components were selected based on engineering judgment and the general objective of this program. The dimensions and the accessibility of the components made the extraction of sheet-type specimens possible.
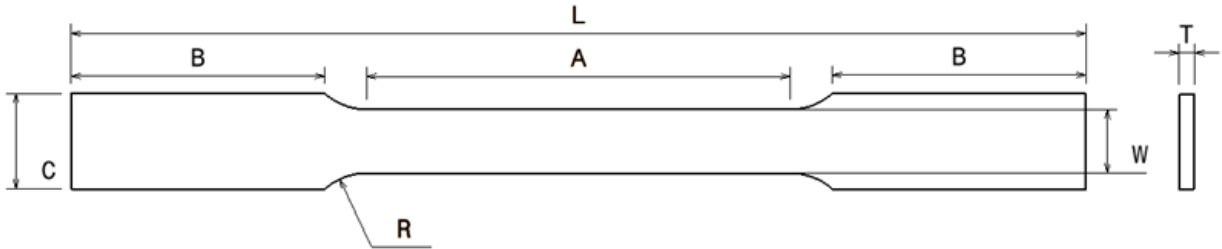
Figure 83. Geometry of sheet-type specimen.
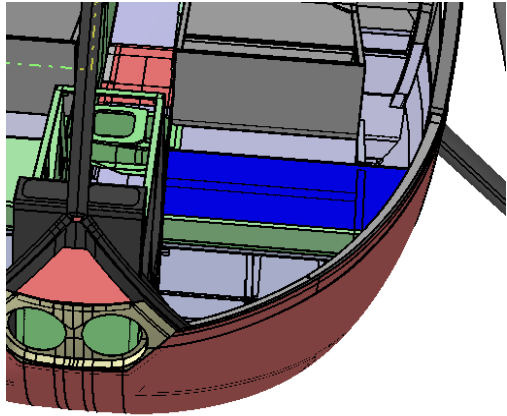
Table 12. Dimensions of a sub-size sheet-type specimen.

Dimension Description	Sub-size Sheet Type [in]
Gauge width, W	0.25
Thickness, T	t (varies per component)
Radius of fillet, R	0.25
Overall length, L	4.00
Length of reduced parallel section, A	1.25
Length of grip section, B	1.25
Width of grip section (approximate) C	0.375

3.2.3.1   Metallic Materials

A vast number of metallic components were selected for mechanical characterization. One material is presented in the main body of the report, and the rest are in Appendix A. Table 13 contains the reference location for a Floor Panel with its test identification.
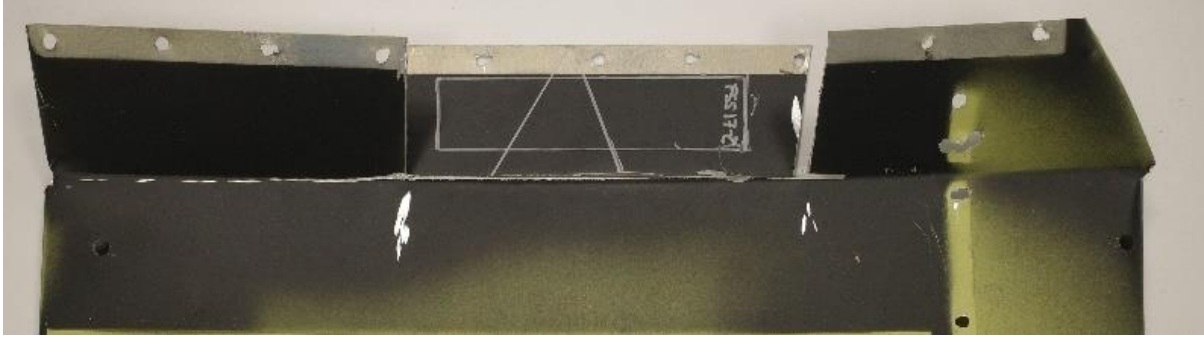
Table 13. Reference location of metallic extraction for destructive testing.

Test ID	Part Description	Reference Part Image
RC-MRE-P06-T-0X	Floor Panel 2	

3.2.3.1.1   Material Extraction

Visual evidence of the test specimen extraction is shown in Table 14. All selected metallic parts allowed the extraction of at least one sheet-type tensile test specimen per ASTM E8/E8M [34]. Appendix A contains the photographs of the extraction of the rest of the metallic components.
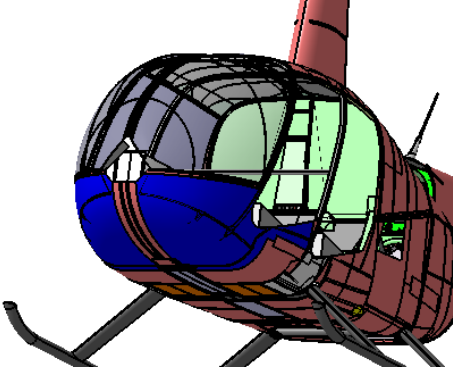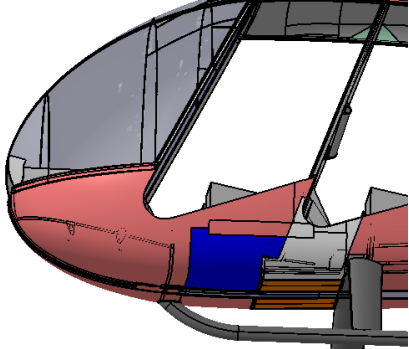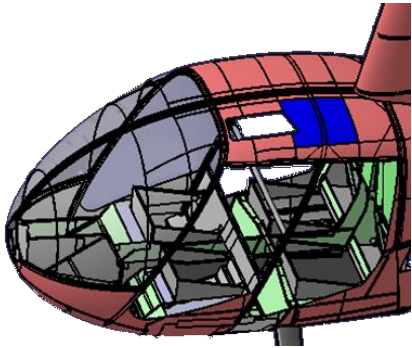
Table 14. Photographs of the extraction front of the floor panel 2 – RC-MRE-P06-T-0X.

Extracted Part
Machined Specimens

3.2.3.2   Non-Metallic Materials

The components extracted in the lower front skin, lower belly skin, and upper skin were assumed to be the same material after a detailed inspection and comparison between the thickness and density of each component. Table 15 shows the reference location of these rotorcraft parts.

Table 15. Reference location of non-metallic extraction for destructive testing.

Test ID	Part Description	Reference Part Image
RC-MRE-P03-C-0X	Lower front skin	
RC-MRE-P01-C-0X RC-MRE-P03-C-0X	Lower belly skin	
RC-MRE-P03-S-0X	Upper skin	

3.2.3.2.1   Material Extraction

The following extractions were made in accordance with ASTM D3039/D3039M [35], as shown in Table 16, ASTM D6641/D6641M [36], as shown in Table 17, and ASTM D7078/7078M [37], as shown in Table 18. Multiple specimen types were required to capture the necessary properties of the material and achieve a high-fidelity numerical model of the composite materials. The test results of extractions in Table 16, Table 17, and Table 18 were treated as a single material. They were applied to a single material model in the overall numerical model of the rotorcraft.

Table 16. Photographs of the extraction from the lower front skin – RC-MRE-P03-T-0X.

Extracted Part
Machined Specimens
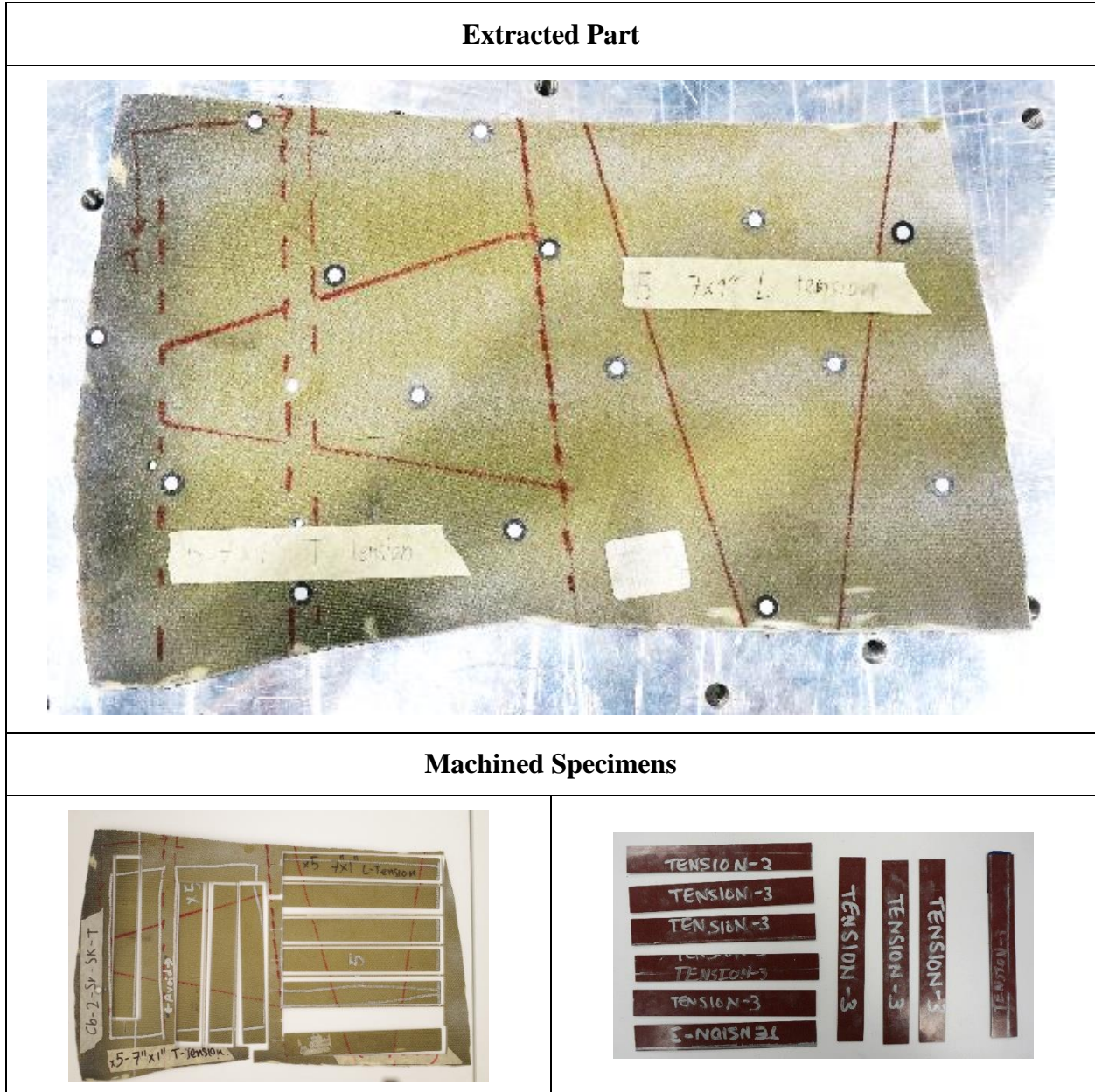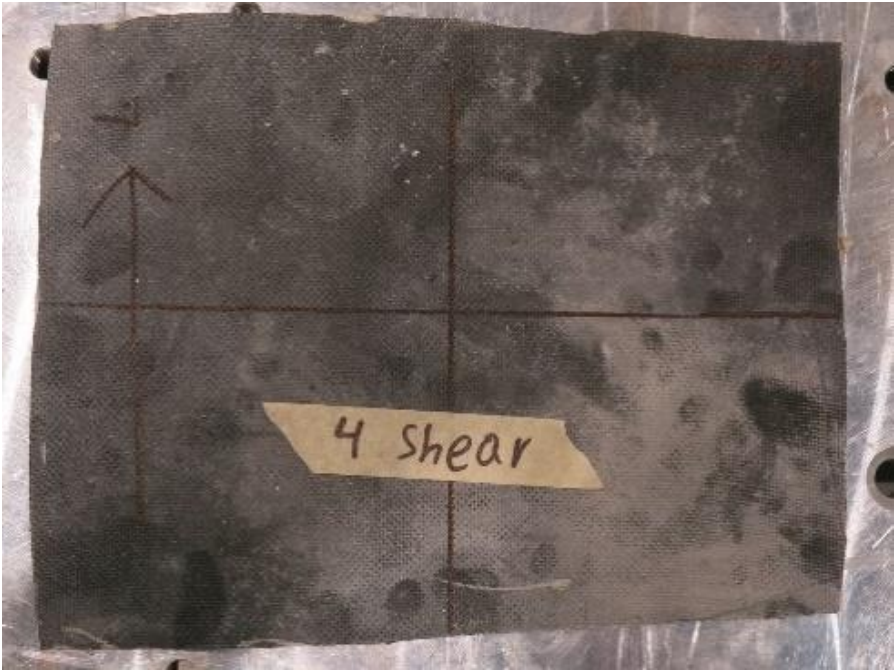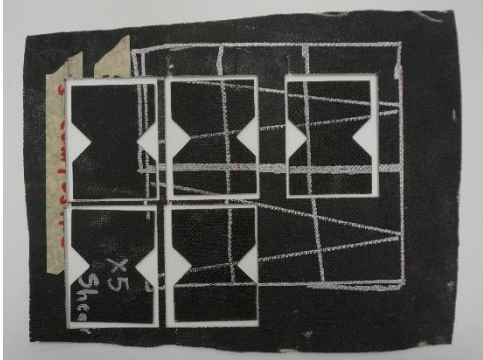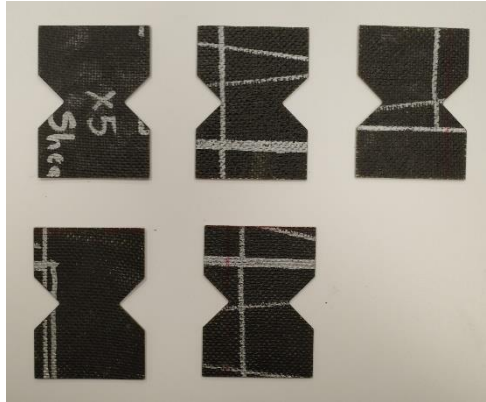
Table 17. Photographs of the extraction from the lower belly skin – RC-MRE-P01-C-0X and RC-MRE-P03-C-0X.

Extracted Part
Machined Specimens
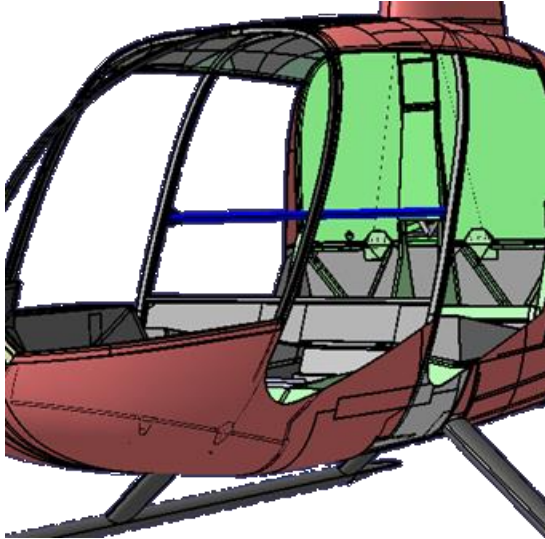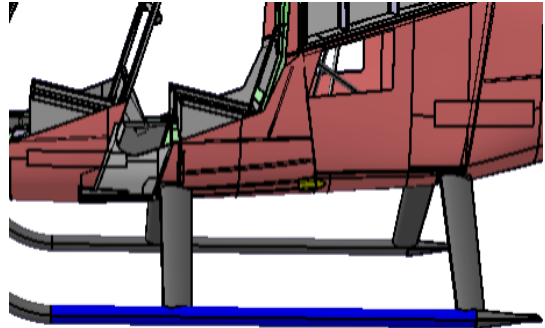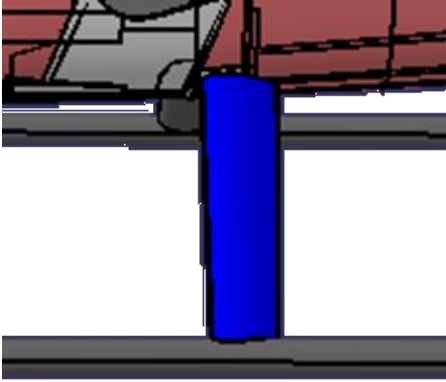
Table 18. Photographs of the extraction from the upper skin – RC-MRE-P03-S-0X.

Extracted Part
Machined Specimens

3.2.4 Extractions for Non-Destructive Tests

It was determined that extractions from some relevant components would not meet the size or geometry required to manufacture standard test specimens. For these parts, extractions were made for non-destructive testing only. The parts in Table 19 were deemed structurally necessary; hence, their material model was needed to achieve a high-fidelity numerical simulation. Non-destructive testing will be discussed in the following subsections in this chapter.

Table 19. Reference location of metallic extraction for non-destructive testing.

Test ID	Part Description	Reference Part Image
RC-MRE-P18-NDT-0X	Frame Cross Tube	
RC-MRE-P30-NDT-0X	Landing Skid	
RC-MRE-P31-NDT-0X	Landing Skid Beam	

3.2.4.1 Material Extraction

Visual evidence of the test subjects extracted for non-destructive testing is shown in Table 20, Table 21, and Table 22.

Table 20. Photographs of the extraction from the frame cross tube – RC-MRE-P18-NDT-0X.
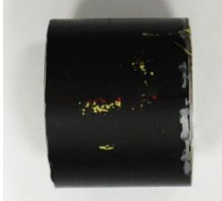
Extracted Part
Machined Specimens

Table 21. Photographs of the extraction from the landing skid – RC-MRE-P30-NDT-0X.

Extracted Part
Machined Specimens

Table 22. Photographs of the extraction from the landing skid beam – RC-MRE-P31-NDT-0X.

Extracted Part
Machined Specimens

3.2.5   Destructive Testing

3.2.5.1   Test Equipment and Instrumentation

A servo-hydraulic MTS 35-kip load frame equipped with hydraulic and mechanical grips was used for the destructive tests. An ARAMIS 6M stereo camera system was used to perform DIC measurements. The load frame and DIC equipment are shown in Figure 84. Figure 85 illustrates the test setup used for tensile testing.
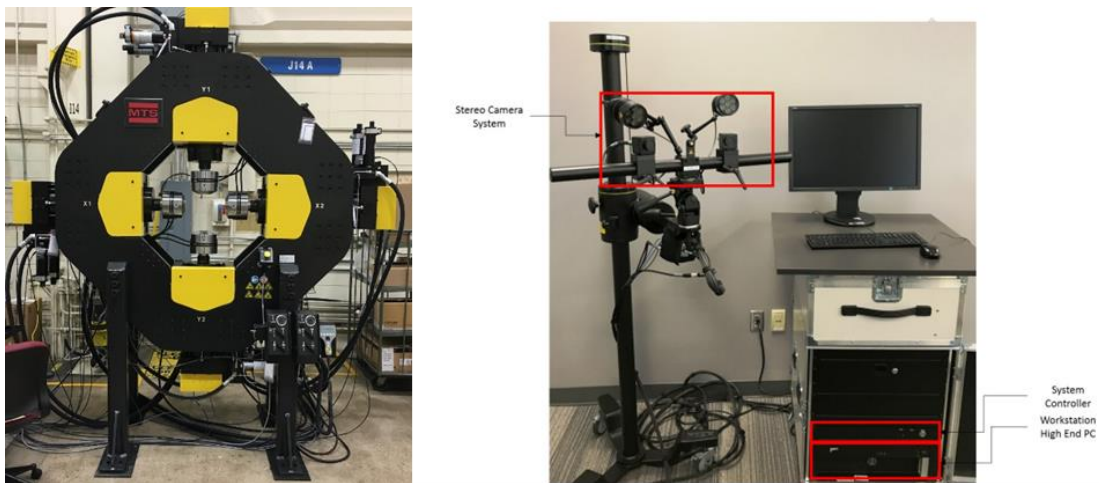
Figure 84. MTS 35-kip test frame and DIC equipment.

Figure 85. Tensile testing setup.

3.2.5.2　Metallic Materials

Test setup and post-test photographs for test RC—MRE-P06-T-0X are contained in Table 23. Similarly, Table 24 includes a test setup photograph of the honeycomb sandwich specimen extracted from the main rotorcraft blade.

Table 23. Test setup and post-test photographs for RC-MRE-P06-T-0X.

Specimen Type	Sheet type-Subsize
Test Setup	
Post Test Picture	

Table 24. Test setup photographs for the honeycomb.

Specimen Type	Sheet type-Subsize
Test Setup	

3.2.5.3 Non-Metallic Materials

The mechanical characterization of the composite material included three different test conditions. The tensile tests were conducted per ASTM D3039/D3039M-17 [35], the compressive tests complied with D6641/D6641M-16 [36], and the shear properties tests were done per ASTM D7078-7078M-12 [37].

Table 25. Test setup and post-test photographs of the tension test.
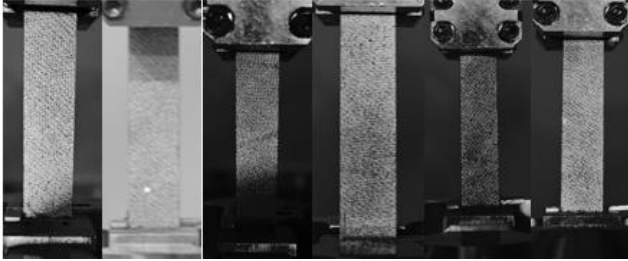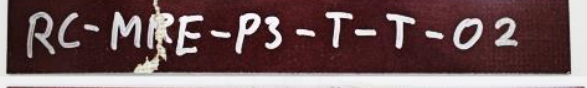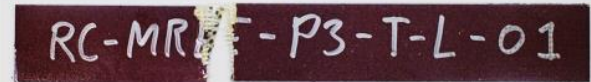
Test Setup
Post-Test Picture

Table 26. Setup and post-test photographs for the compression test.
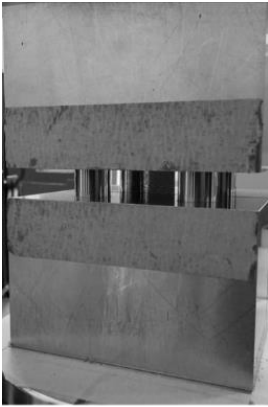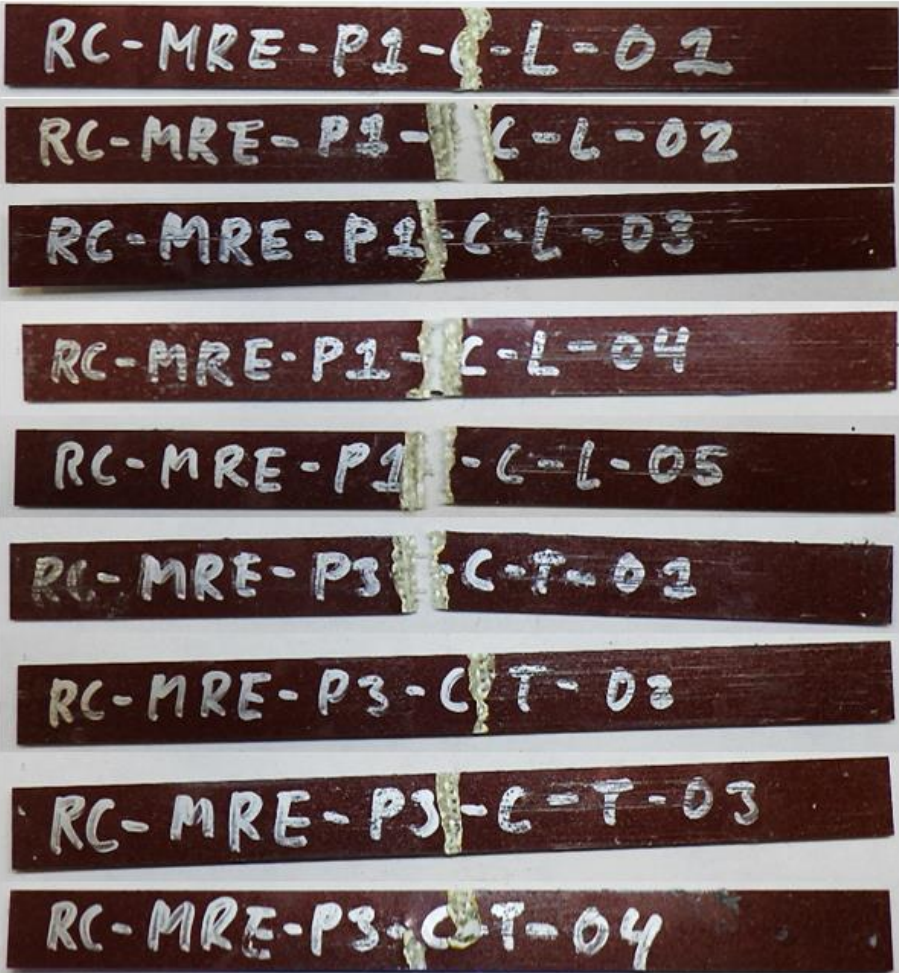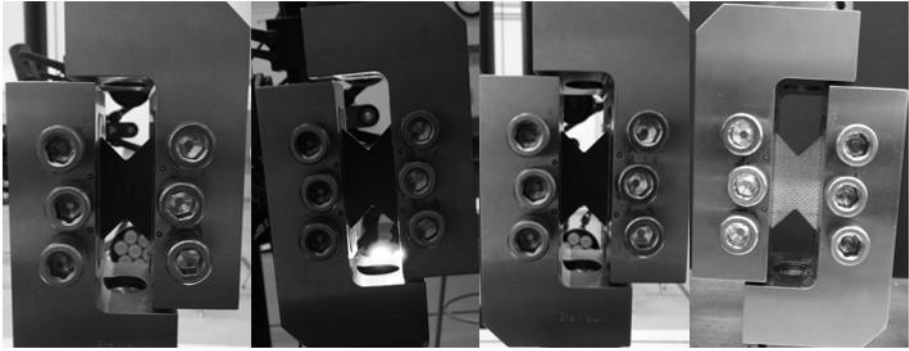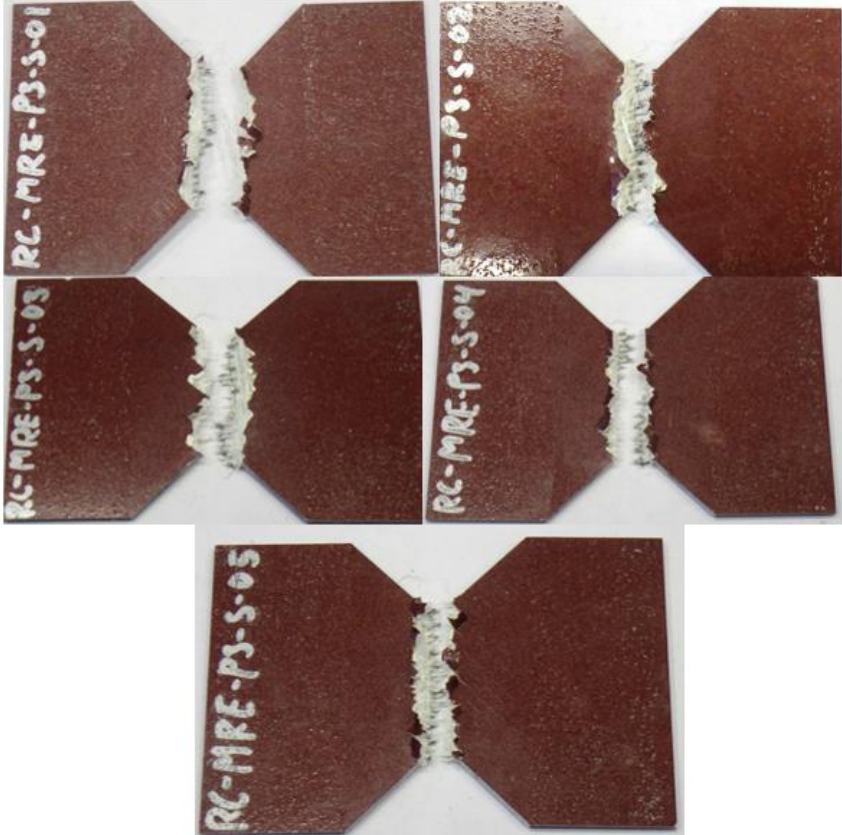
Test Setup
Post-Test Picture

Table 27. Setup and post-test photographs for the shear test.

Test Setup
Post-Test Picture

3.2.6   Non-destructive testing

Non-destructive testing consisted of direct mass density measurements and, in some cases, determination of magnetic properties. Upon determination of mass density, the obtained values were compared against typical density values of advanced materials used in the aerospace industry.

This allows the determination of the general alloy class for the extracted parts. The measurements of the specimens are presented in Table 28.

Table 28. Density measurement for non-destructive testing.

Specimen	Weight [g]	Volume [mm^3]	Density [tonne/mm^3]
RC-MRE-P18-NDT-01	8.67	3491	2.48E-09
RC-MRE-P30-NDT-01	4.52	1797	2.52E-09
RC-MRE-P30-NDT-02	4.52	1812	2.50E-09
RC-MRE-P31-NDT-01	13.11	1861	7.06E-09
RC-MRE-P31-NDT-02	13.54	1932	7.01E-09

3.2.7   *Material Card Validations*

3.2.7.1   Metallic Materials

The test data was processed to develop the corresponding LS-DYNA Mat_024 material card for each tested component. The results of the material card validation for RC-MRE-P06-T-0X are contained in Table 29 as an example. The results of the material card validations of all metallic specimens are documented in Appendix A.
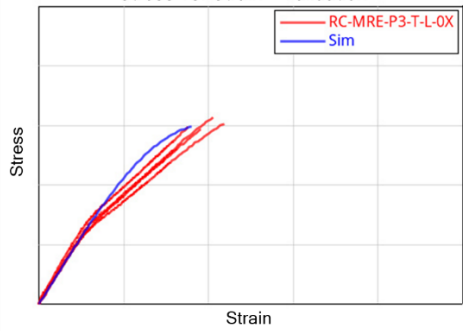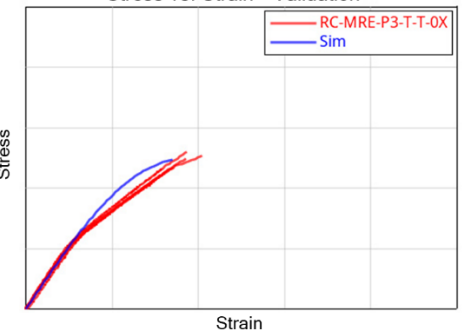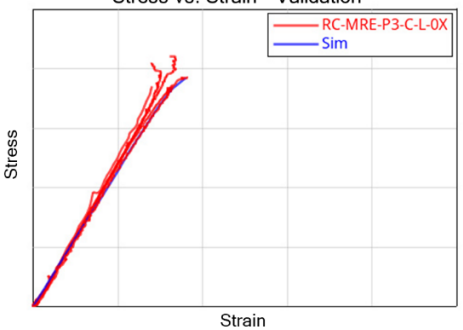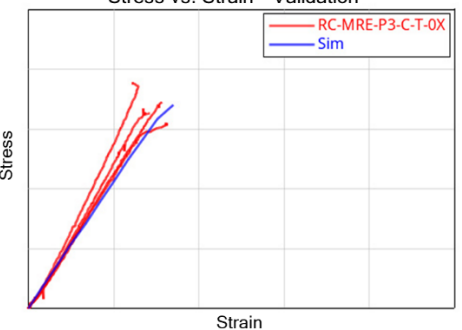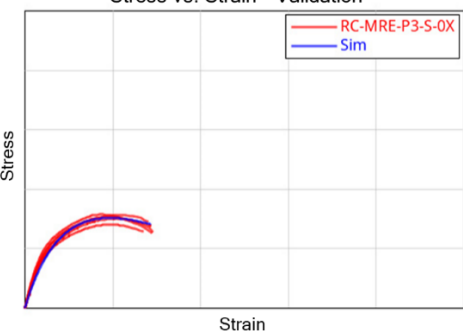
Table 29. Material card validation - RC-MRE-P06-T-0X.
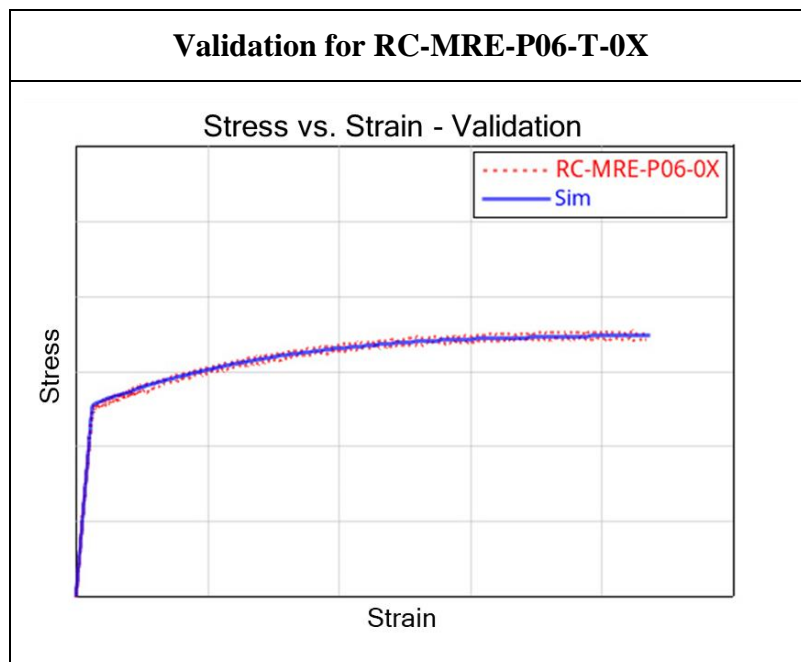
3.2.7.2 Non-Metallic Materials

The test data was processed to develop the corresponding LS-DYNA Mat_058 material card for each tested non-metallic component. The results of the material card validation for all non-metallic materials are contained in Table 30.

Table 30. Material card validation for non-metallic materials.

Validation for RC-MRE-P03-T-L-0X	**Validation for RC-MRE-P03-T-T-0X**
Validation for RC-MRE-P03-C-L-0X	**Validation for RC-MRE-P03-C-T-0X**
Validation for RC-MRE-P03-S-0X	

75

3.2.8 *Windshield Characterization and Validation*

This chapter discusses the tests and simulations conducted to generate a material model that captures the deformation and failure of the R44 helicopter windshield. The material model selected is LS-DYNA MAT_187 (Semi-Analytical Model for Polymers). Coupon-level tests were conducted under tension, compression, and shear state of stress to populate this material card. Additionally, the MAT_187 material card permits the inclusion of strain rate-dependent data under tension. Thus, tests at elevated stroke rates were also conducted, as summarized in Table 31.

Table 31. Coupon level test matrix for windshield.

Loading Condition	Test Standard	Stroke Rate			
		QS	0.1 in/s	1 in/s	10 in/s
Tension	ASTM D638 [38]	x3	x3	x3	x3
Compression	ASTM D695[39]	x3	-	-	-
Shear	ASTM D7078[37]	x3	-	-	-

Tension tests were conducted at four speeds: Quasi-Static (QS), 0.1in/s, 1in/s, and 10 in/s following ASTM D638 [38]. The test setup for quasi-static and dynamic rates is shown in Figure 86. QS tests were conducted using an electromechanical test frame, and tests at elevated stroke rates were conducted using a high-speed servo-hydraulic test frame. DIC was used to measure the longitudinal and transverse strains. The stress-strain behavior for all the stroke rate tests is shown in Figure 87. It was observed that the yield stress and tensile strength increase with the increase in stroke rate, whereas the strain at failure decreases at elevated stroke rates.

Compression tests were conducted at QS stroke rate following the test standard ASTM D695 [39]. The tests were conducted using an electromechanical test frame, and the test setup is shown in Figure 88. DIC was used to obtain longitudinal strains from the specimen.
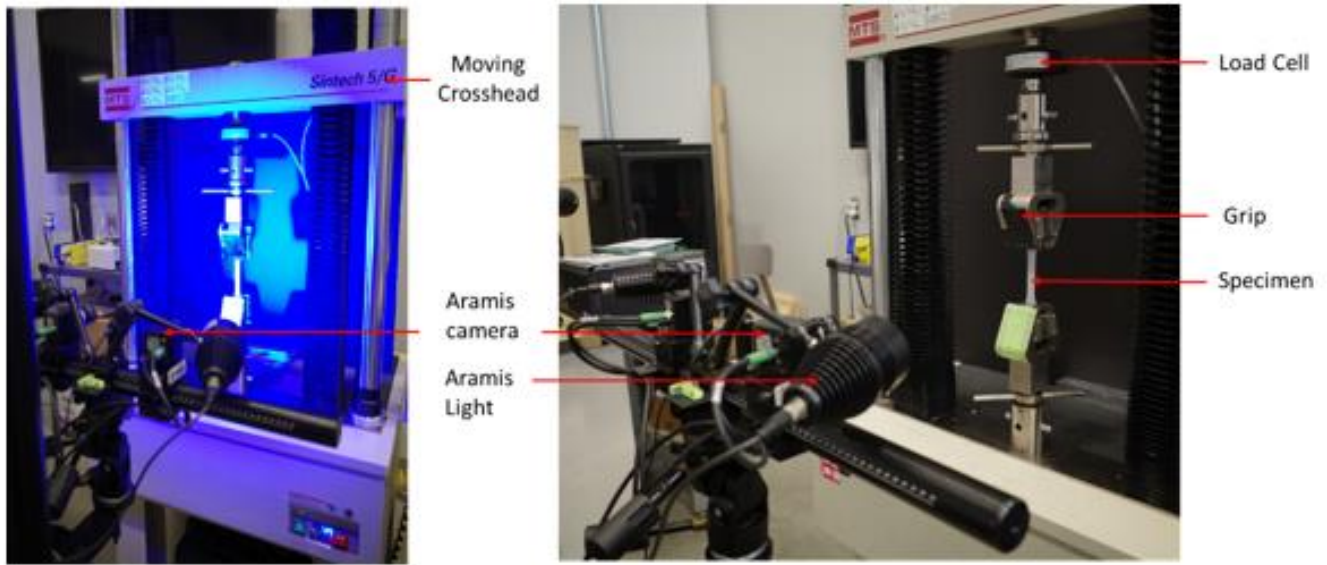
(a) Quasi-static test setup for tension
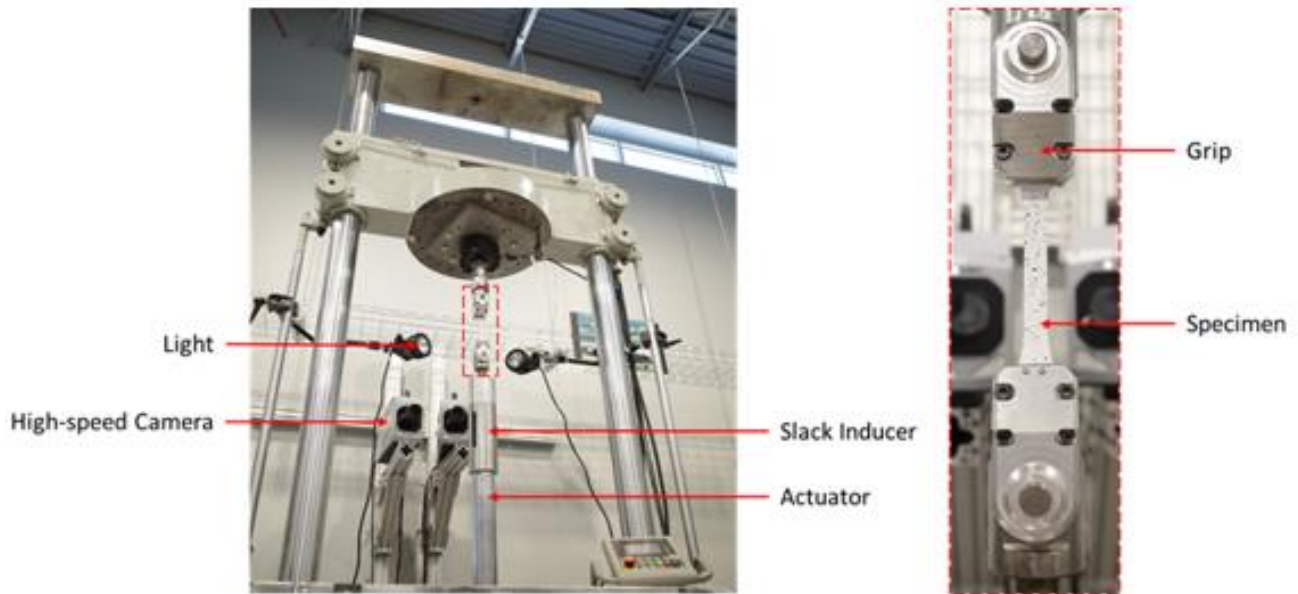
(b) Dynamic test setup for tension
Figure 86. Tension test setup for windshield characterization.

(a) QS

(b) 0.01 in/s

(c) 1 in/s

(d) 10 in/s
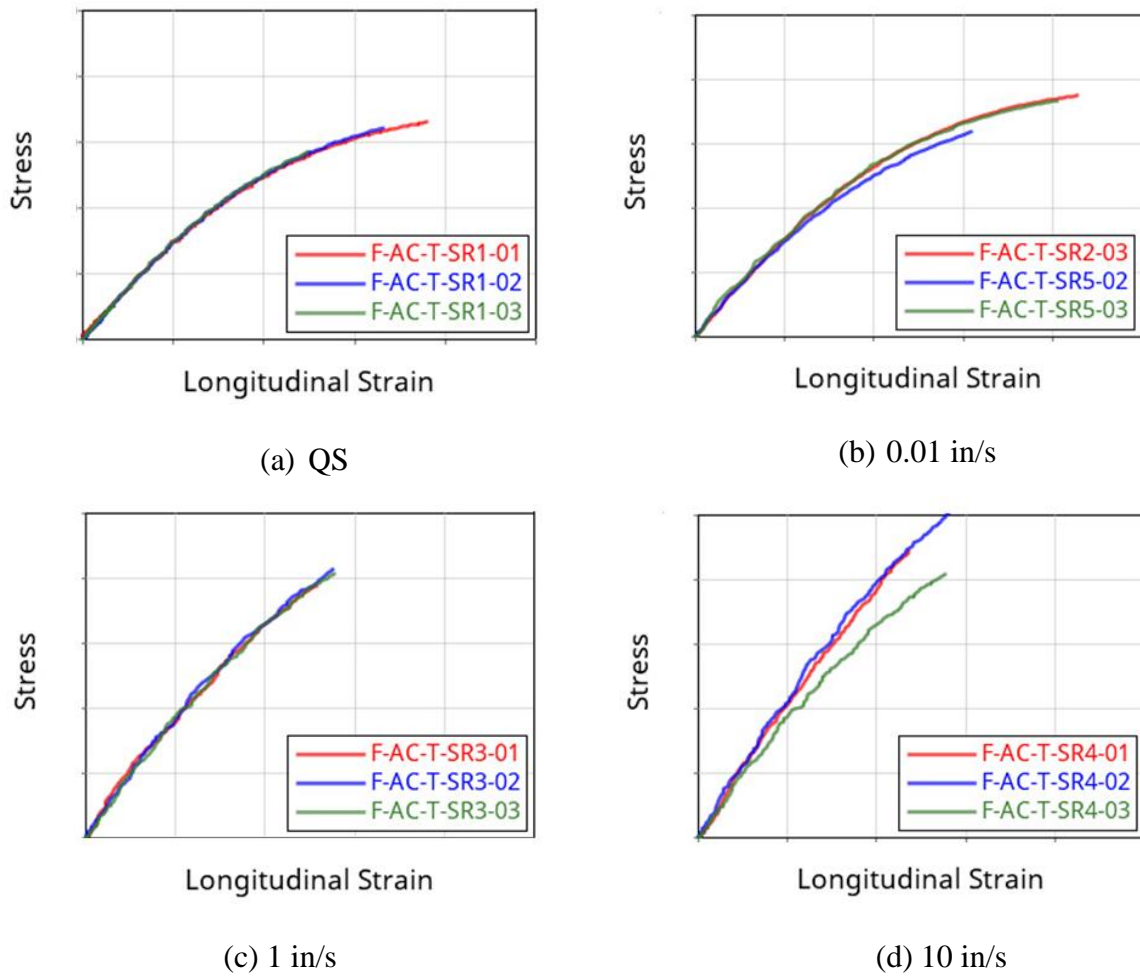
Figure 87. Tension test results for windshield.
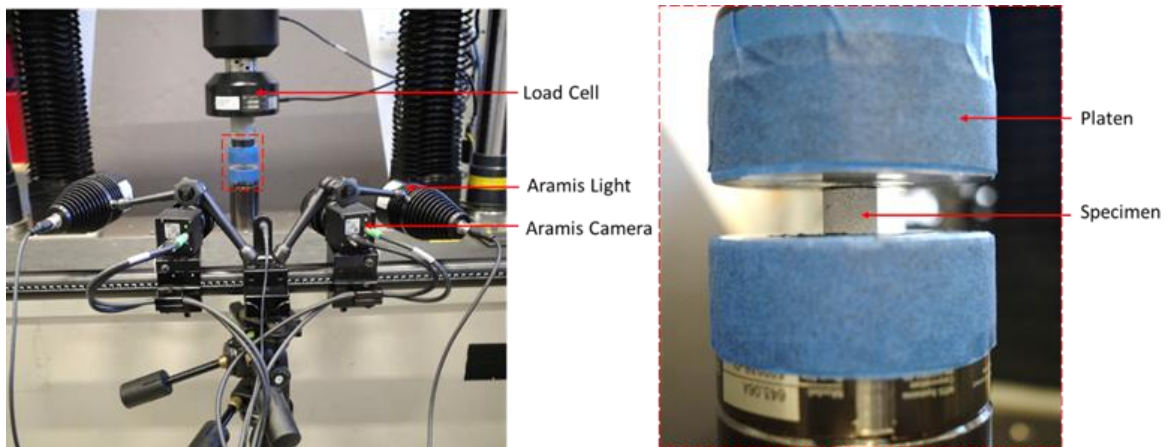
Figure 88. Compression test setup for windshield.

Three specimens were tested under compression, and the stress-strain behavior of the tests is shown in Figure 89.
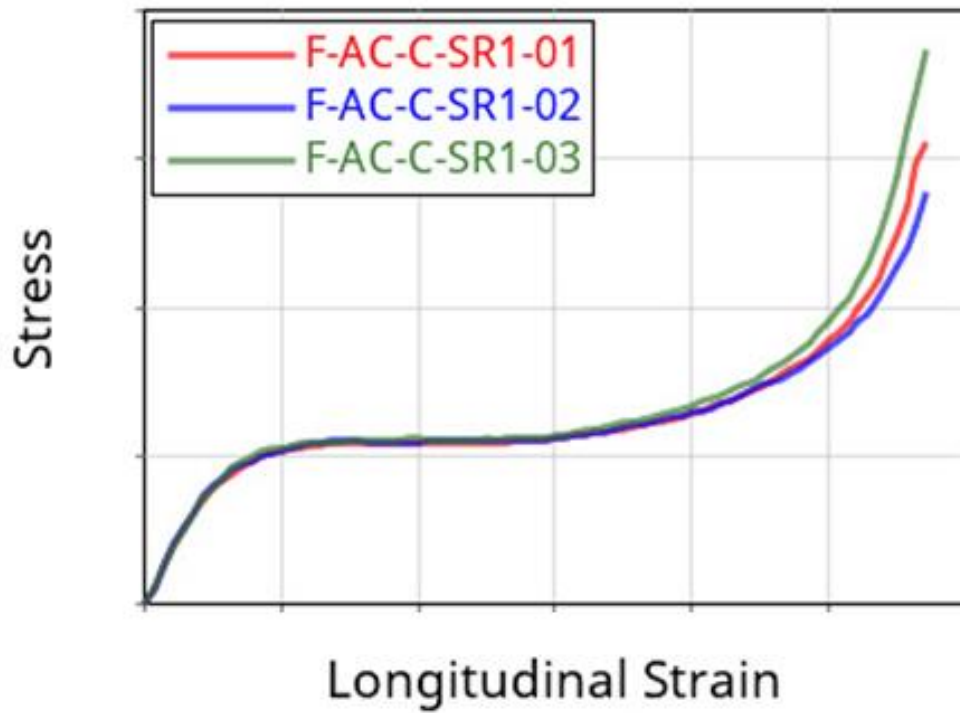
Figure 89. Compression test results for windshield.

Shear tests were conducted at QS stroke rate following the test standard ASTM D7078 [37]. The tests were conducted using an electromechanical test frame, and the test setup is shown in Figure 90. DIC was used to obtain shear strains from the specimens.
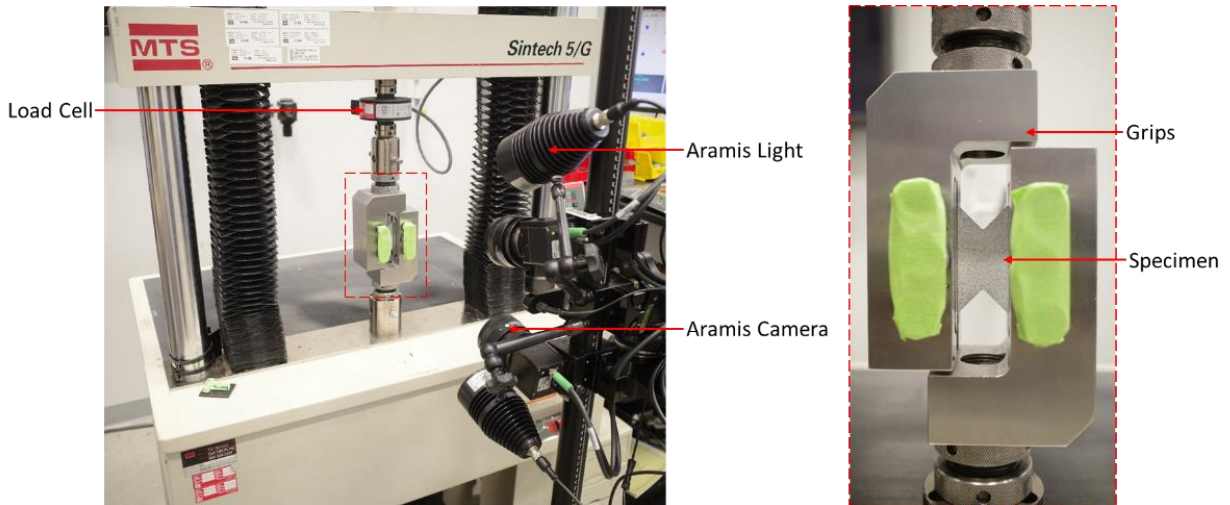
Figure 90. Shear test setup for windshield.

Three specimens were tested under shear. The stress-strain behavior for the shear tests is shown in Figure 91.
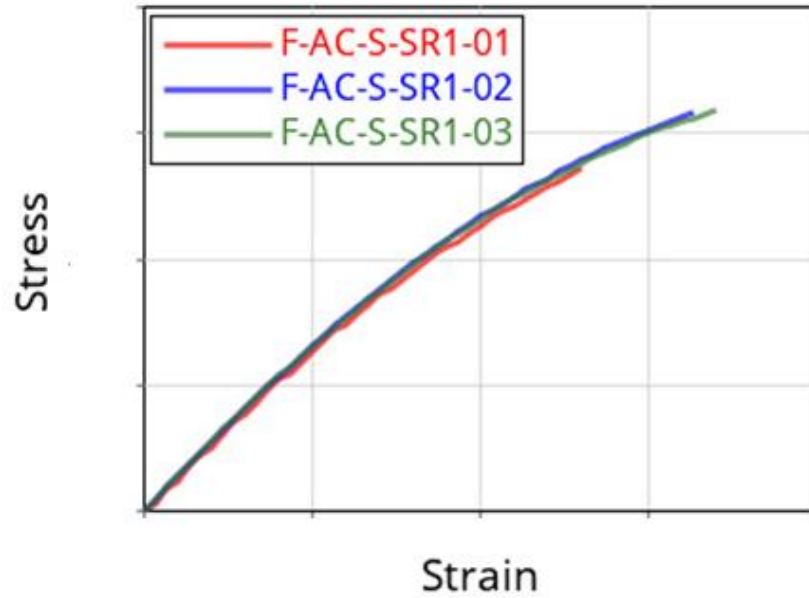
Figure 91. Shear test results for windshield.

After generating fundamental material properties for the windshield, a component-level impact test was performed on flat rectangular test specimens to validate the generated material card LS-DYNA MAT_187. The test article was clamped between two aluminum plates and attached to the test frame base using standoffs, as shown in Figure 92. A hemispherical impactor of 0.75" diameter was used to indent the test article at QS speeds. The indentation forces varied to introduce different damage levels, varying from no visible damage to the onset of penetration, as shown in Figure 93.
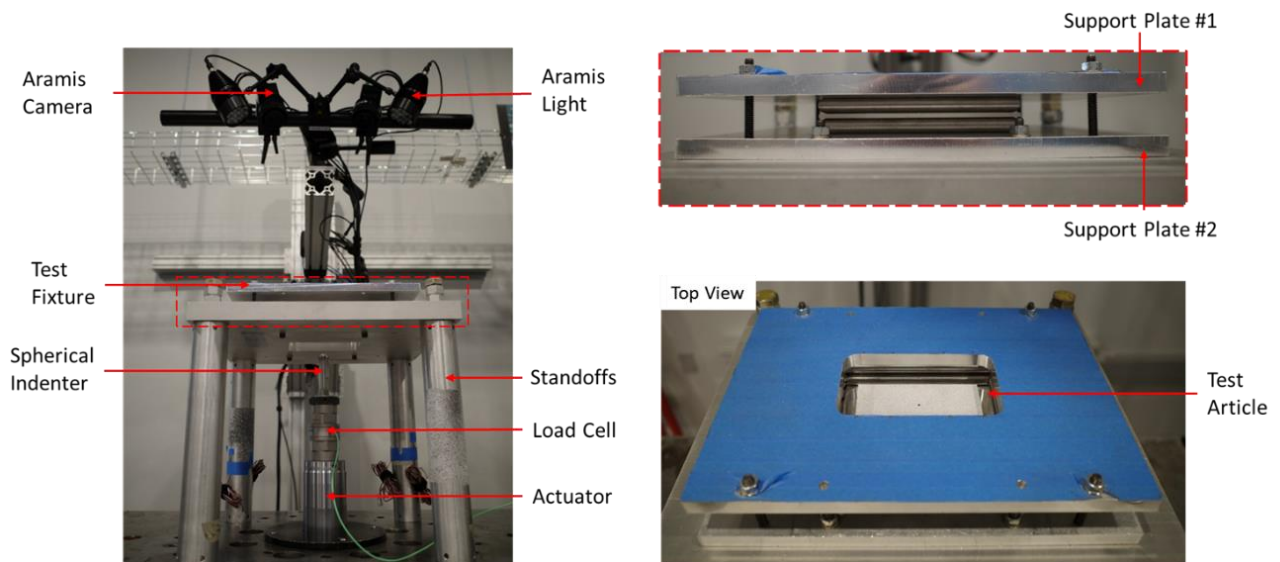
Figure 92. Impact test setup for windshield material model validation.
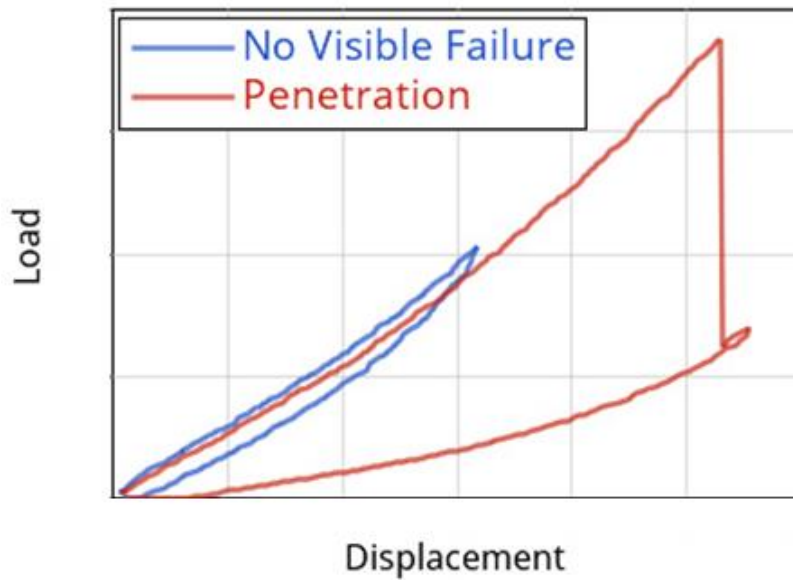
Figure 93. Indentation test results for the windshield.

A numerical model representing the impact test setup was developed to validate the material card (LS-DYNA MAT_187). Load and impactor displacement time history were compared between tests and analysis, as shown in Figure 95. This validated material model was then used for the full-scale analysis.
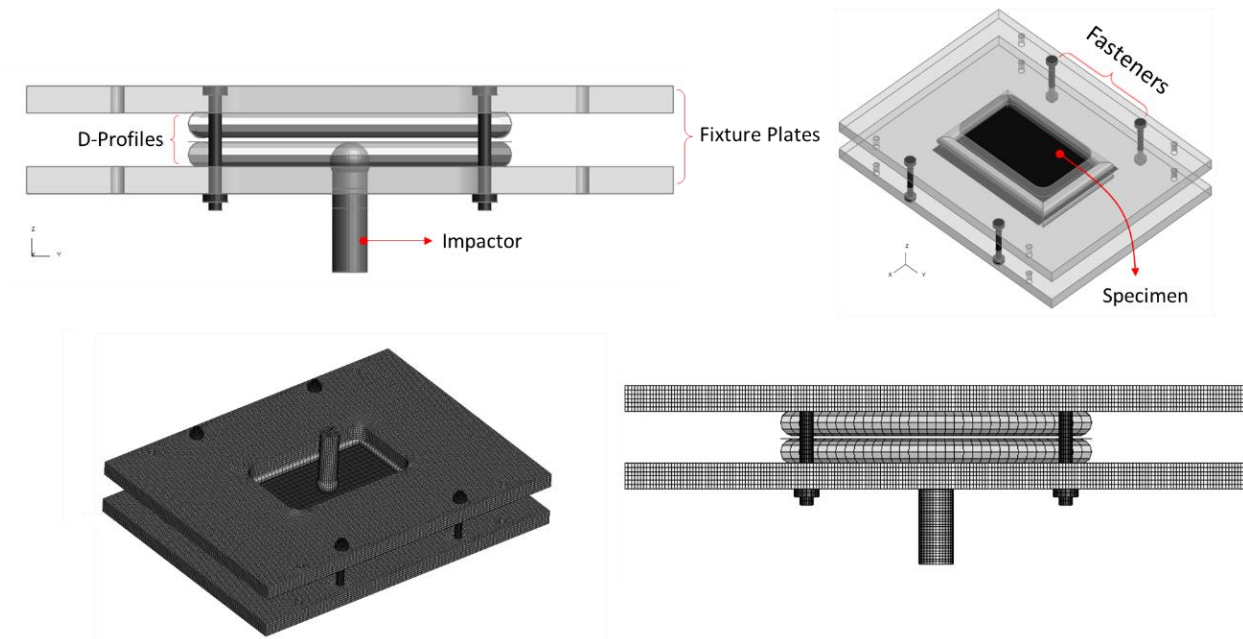
Figure 94. Indentation test results for windshield.
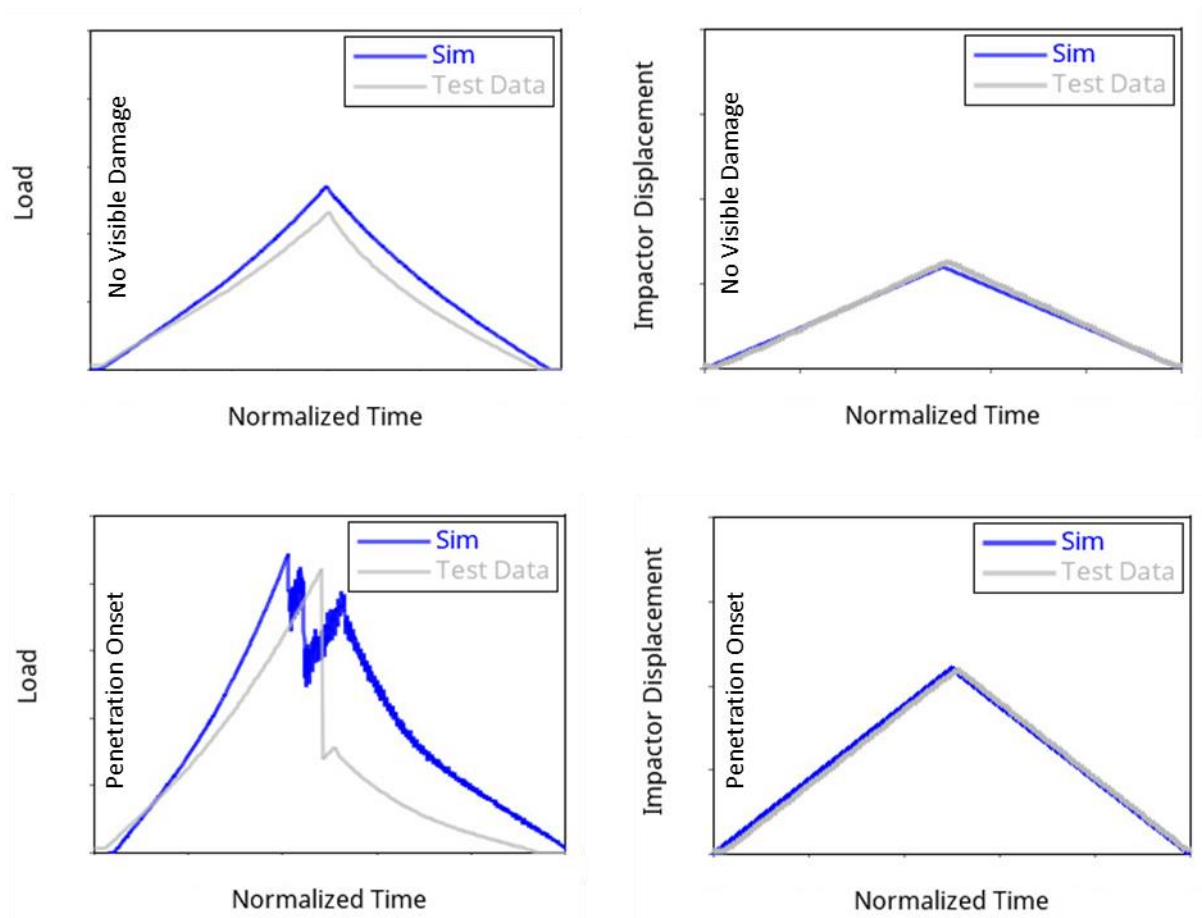
Figure 95. Indentation test-simulation comparison.

3.3   FINITE ELEMENT MODEL

This section explains the process followed to develop the FEM of the rotorcraft's components. The following procedure was carried out to create the FEM:

- − Obtain the CAD file of the component under consideration.
- − Geometry clean-up and preparation for meshing (extract mid-surface, defeature small fillets, etc.).
- − Select an element type for each part depending on geometry and element size constraints.
- − Discretize the geometry (meshing).
- − Check quality criteria.
- − Element properties definition: shell thickness and beam cross-section.
- − Assemble and connect discretized parts.
- − Check models for non-desired entities (penetrations, intersections, free nodes, free edges, mesh overlap, duplicate elements, non-aligned elements normal, etc.).
- − Assign material properties.

- Add non-structural mass to nodes wherever a part is not modeled (representing payload and fuel).
- Perform a mass and center of gravity check.
- Renumber model components to avoid clashes between the UAS and the target setup.

For meshing, LS-DYNA [40] offers a variety of element formulations for numerical modeling. These elements are categorized as scalar elements, one-dimensional (1D), two-dimensional (2D), and three-dimensional (3D). Additional details regarding the properties of the element types selected for the FEM are discussed in the A3 final report [22].

The accuracy of the FEM largely depends on correct input and a thorough understanding of the parameters selected in defining the models. Therefore, the same modeling techniques used to create the representative commercial transport and business jet aircraft models for Task A3 [22], the Part 29 rotorcraft and Part 23 general aviation aircraft in Task A16 [3, 6] were also used to develop the part 27 rotorcraft components presented in this report.

3.3.1 FE Quality Criteria

Table 32 and Table 33 contain the mesh quality criterion used to discretize the rotorcraft components. This quality criterion is based on recommended practices for crash analysis. Due to the size of the components and to reduce computational time, larger elements were used for areas not directly involved with the UAS impact. At the same time, the minimum element size was refined in a few specific areas to capture necessary details close to the impact regions. Also, small elements were needed to capture the tapering properly for complex geometries, like the honeycomb core boundary transitions. Finally, some simplifications were followed during the discretization process to improve the computational efficiency of the model while maintaining good mesh quality for crashworthiness analysis:

- Small fillets were defeatured.
- A minimum of two elements were kept on flanges to capture its stiffness better.
- All sheet metal parts meshed at the mid-surface with 2D elements (shells).
- The metal-fiberglass composite skins were modeled as a single layer and meshed at the mid-surface with 2D elements (shells).
- Honeycomb cores were modeled with 3D elements (solids).
- A near node-to-node mesh was used for the honeycomb and the multi-layer skin for the rotor blades. The adhesive interaction was captured using tiebreak-contacts (to model delamination) instead of the node-sharing method.
- Whenever possible, three through-thickness elements were used when meshing with 3D elements. A fully integrated formulation was used if it was not feasible due to the element size constraint.
- Solid parts in non-impact regions (like the engine) were modeled using tetrahedron elements with at least two layers per thickness.
- The total number of triangular elements was limited to less than 1%. In addition, triangular element clusters were avoided to reduce spurious stress concentrations.

Table 32. Mesh quality criterion for the rotorcraft FEMs – 2D elements.

Quality Parameter	Allowable Min.	Allowable Max.
Element Size	1 mm	15 mm
Aspect Ratio	-	5
Quad Angle	40	140
Tria Angle	20	120
Warp Angle	-	15 deg
Jacobian	0.7	-

Table 33. Mesh quality criterion for the rotorcraft FEMs – 3D elements.

Quality Parameter	Allowable Min.	Allowable Max.
Element Size	1 mm	15 mm
Aspect Ratio	-	5
Warp Angle	-	15 deg
Jacobian	0.6	-

3.3.2 Discretization

This section shows the results of the discretization process applied to the geometry of the horizontal stabilizer, vertical stabilizer, tail rotor, tail cone, fuselage, windshield, mast assembly, rotor blades, and engine of the rotorcraft's model. LS-DYNA offers a variety of element formulations for numerical modeling. These elements are categorized as scalar elements, 1D, 2D, and 3D. Some additional details regarding the properties of the element types selected for the FEM are discussed in the A3 Final Report [22].

Table 34 summarizes the number of elements on the rotorcraft model, and Table 36 presents the minimum element length of the target areas of the rotorcraft FEM. The assembled FEM of the rotorcraft is compared to the CAD model in Figure 96.

Figure 97 through Figure 105 provide detailed views of each major subassembly's discretization.

Some of the targets modeled in this study contain composite parts and sandwich structures. For this study, the metal-fiberglass composite skins were modeled as a single-layer laminate. In the case of sandwich structures, the reference meshing surface is generally the outer or inner surface, depending on its location with respect to the honeycomb core. The inner or outer surface is used as a reference meshing surface if the component does not contain a honeycomb core. In this study, the rotorcraft blade's honeycomb core and outer skins were modeled as separate parts. The multilayer skins were represented as a single layer with varying thickness along the length, and the adhesive was modeled using contacts.

Table 34. Rotorcraft FE quantity.

	2D elements	3D elements	1D elements
Rotorcraft	1,567,796	1,725,682	8,542

Table 35. Rotorcraft targets - minimum element size (mm).

		Min. Length (mm)
Rotorcraft	Horizontal Stabilizer	3
	Vertical Stabilizer	1.48
	Mast	1
	Nose	2.24
	Windshield	1
	Blades	0.6

CAD   MESH

Figure 96. Rotorcraft CAD vs. mesh.

Vertical Stabilizer   Horizontal Stabilizer

CAD   MESH   CAD   MESH
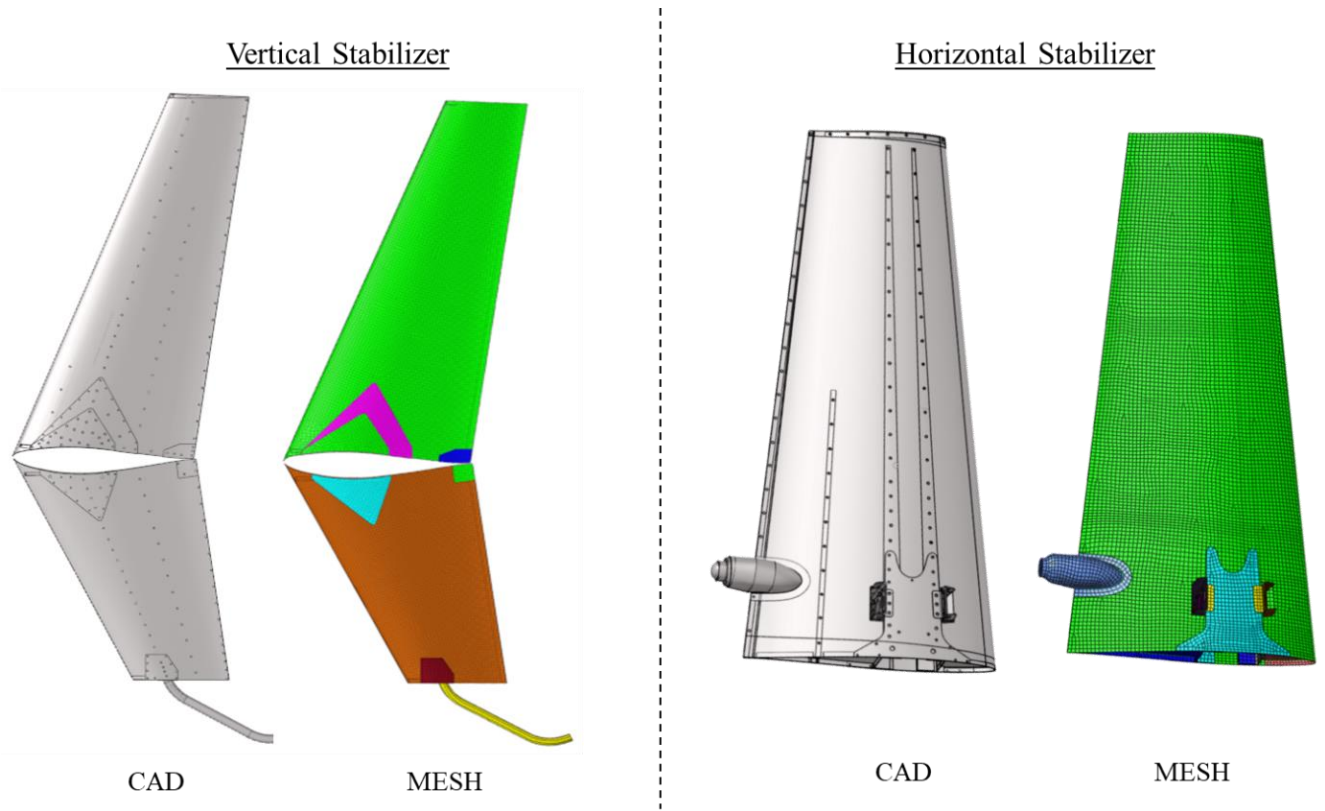
Figure 97. Rotorcraft stabilizers CAD vs. mesh.
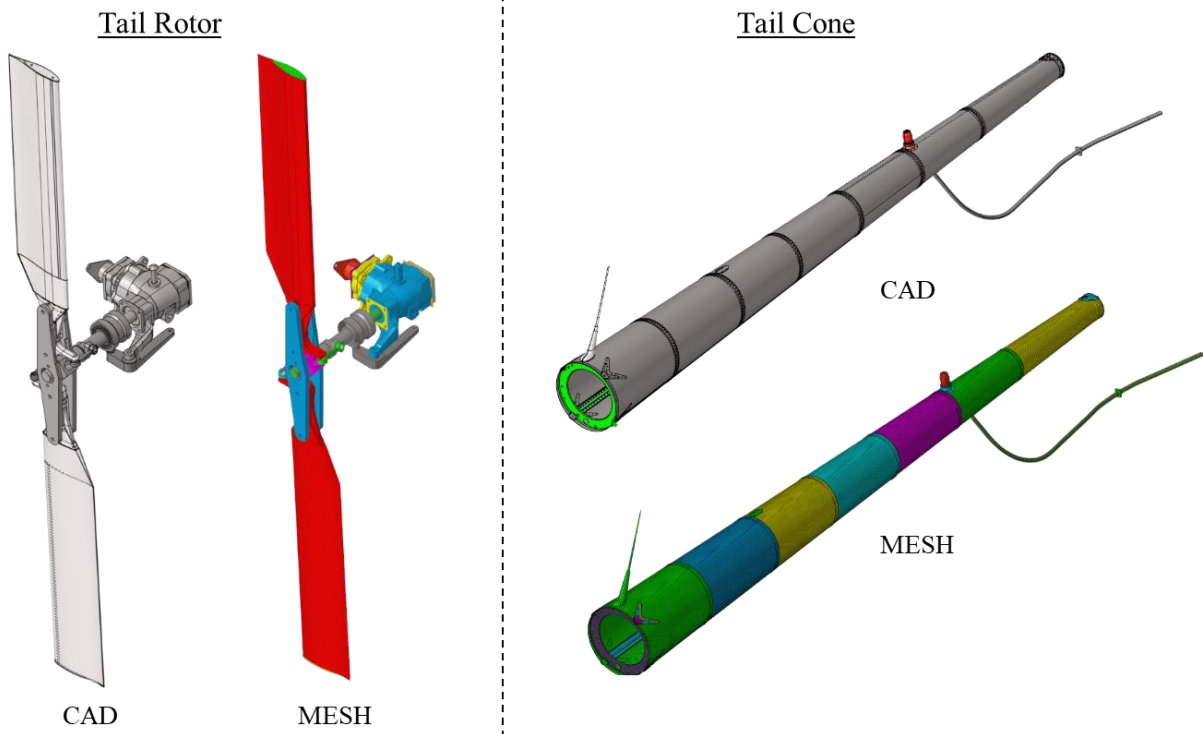
Figure 98. Rotorcraft tail rotor and tail cone CAD vs. mesh.
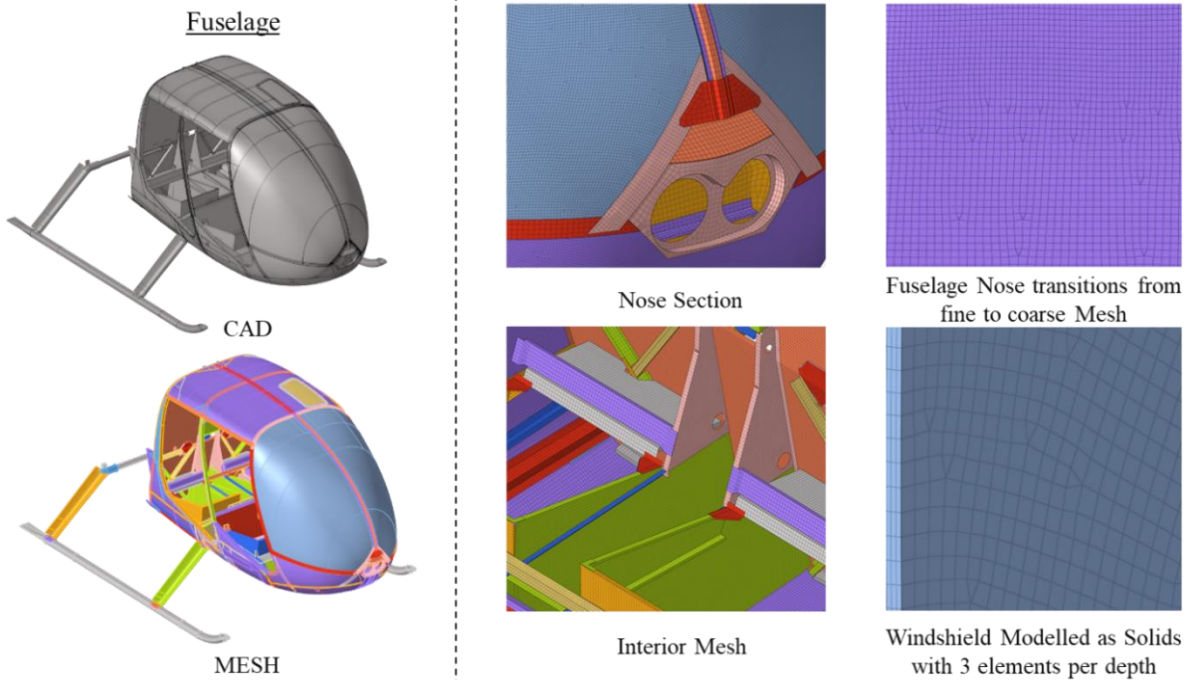
Figure 99. Rotorcraft front fuselage CAD vs. mesh details.

Fuselage

CAD

MESH

Front Section Mesh

Rear Section Mesh

Internal Skeleton Structure Mesh

These Solid Structures were modelled using Tetras
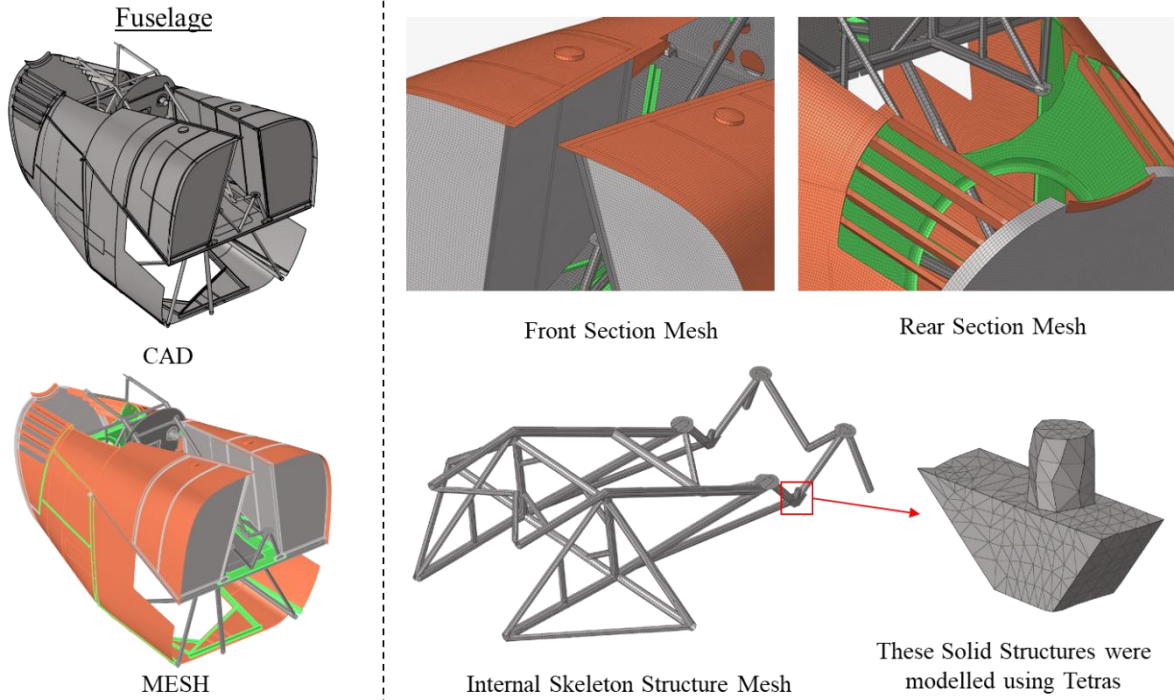
Figure 100. Rotorcraft rear fuselage CAD vs. mesh details.

Doors

CAD

MESH

Mesh near door fitting

Inner Stamped Skin Mesh

Transparent window modelled using shell elements

Door Handles modelled using solid elements
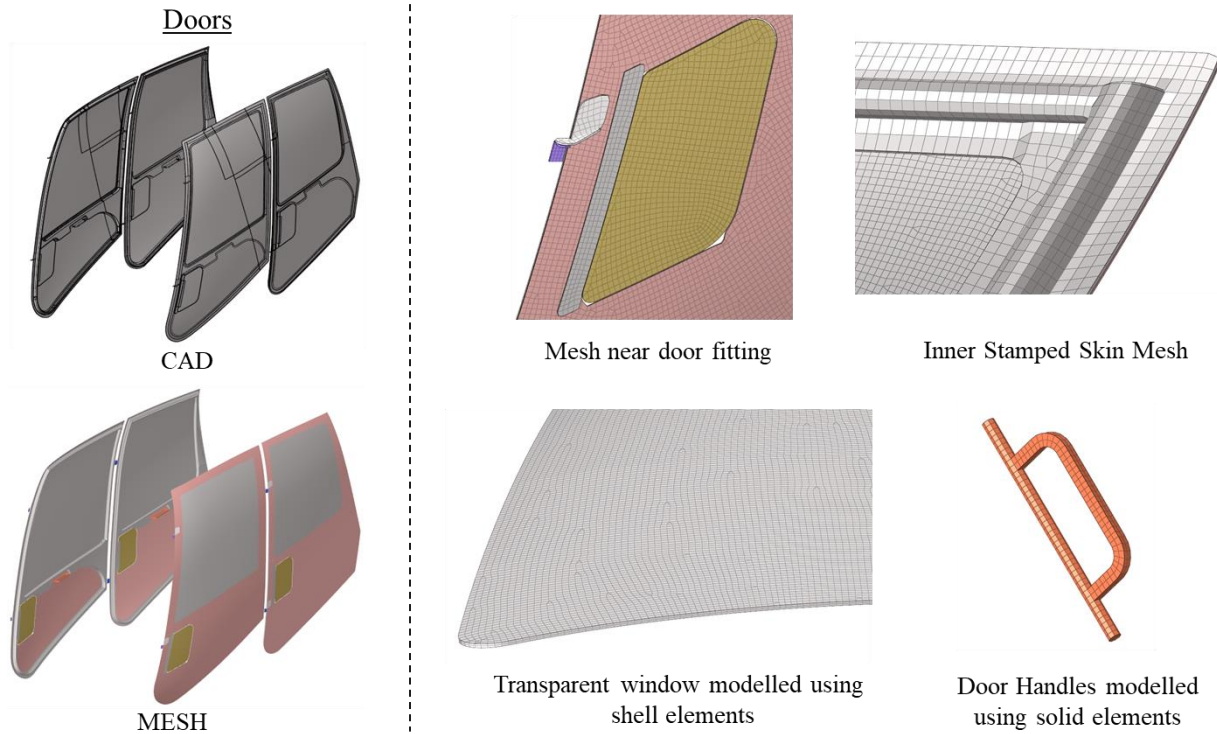
Figure 101. Rotorcraft doors CAD vs. mesh details.

Figure 102. Rotorcraft mast assembly CAD vs. mesh.

CAD

MESH

Engine Mast Assembly Mesh

Main Rotor Hub Mesh

Gear Box Mesh

Mast Fairing Ribs Mesh

Gear Box Closeup
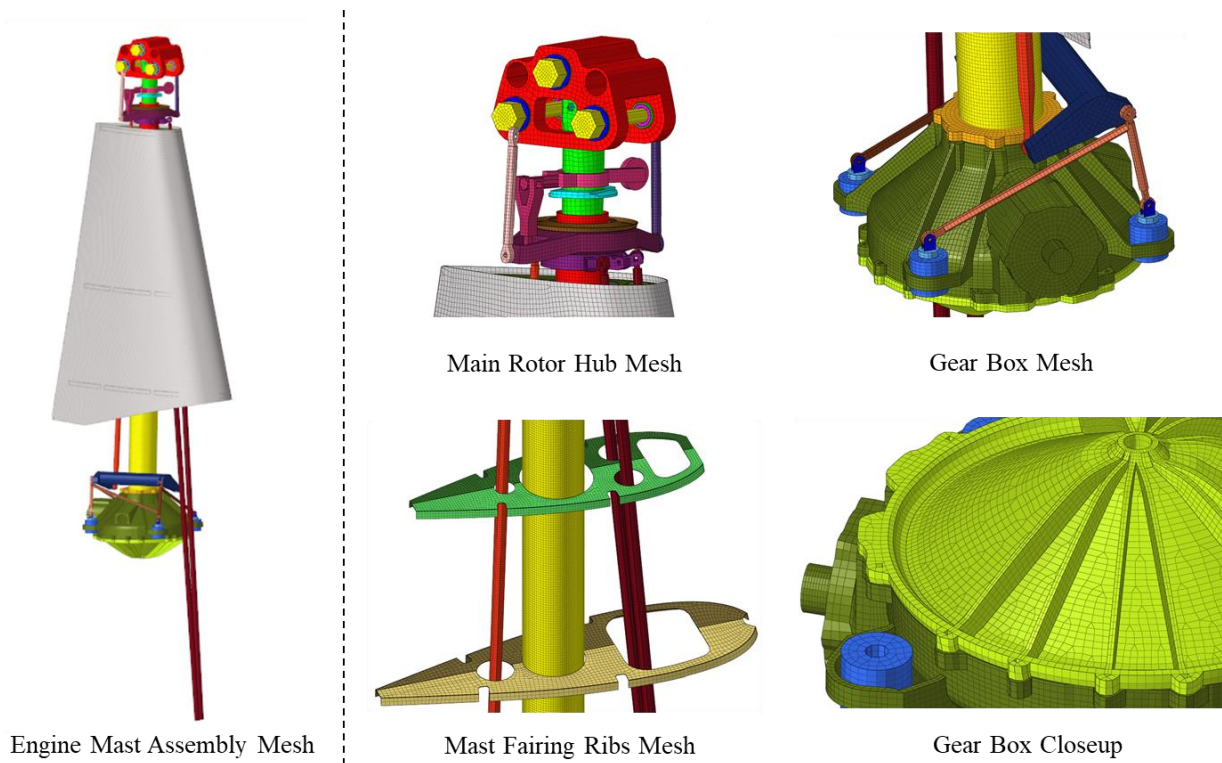
Figure 103. Rotorcraft mast assembly mesh details.

Main Rotor Blade Mesh

Blade Tip Section Mesh

Trailing Edge at Root

Trailing Edge at mid-section of the Blade

Root Section Mesh

Internal Structures at Blade Tip
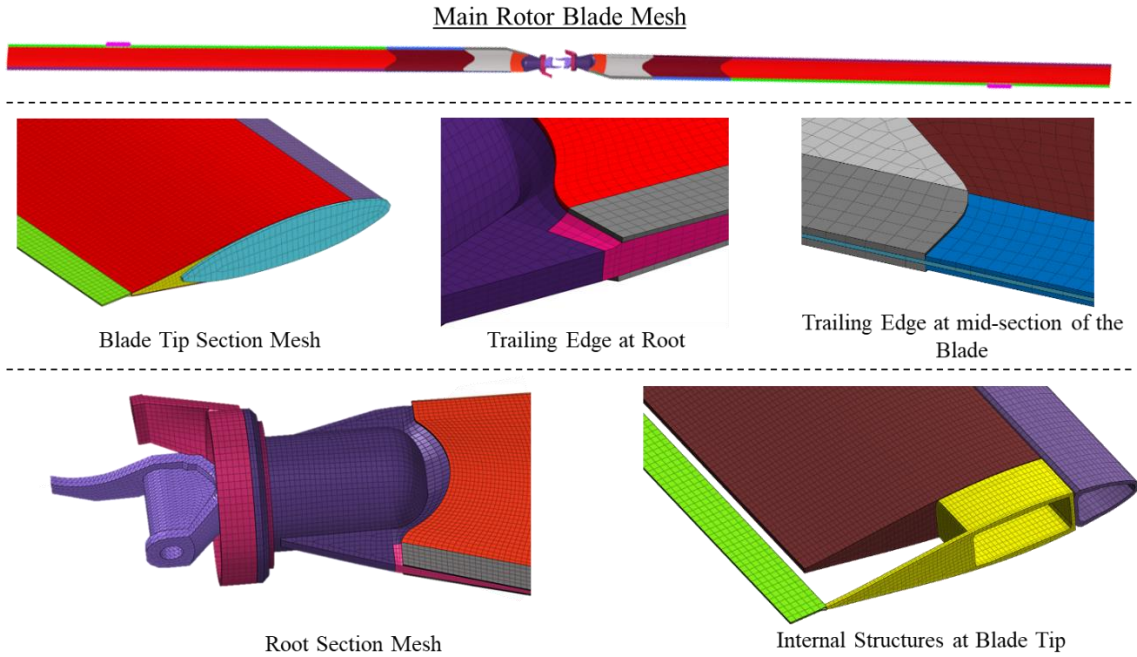
Figure.104. Rotorcraft blade mesh details.

Engine

CAD

Engine Front Cover 2D Mesh

Hoses 2D Mesh

MESH

Engine drive shaft modelled using solid elements

Engine core body modelled using Tetras
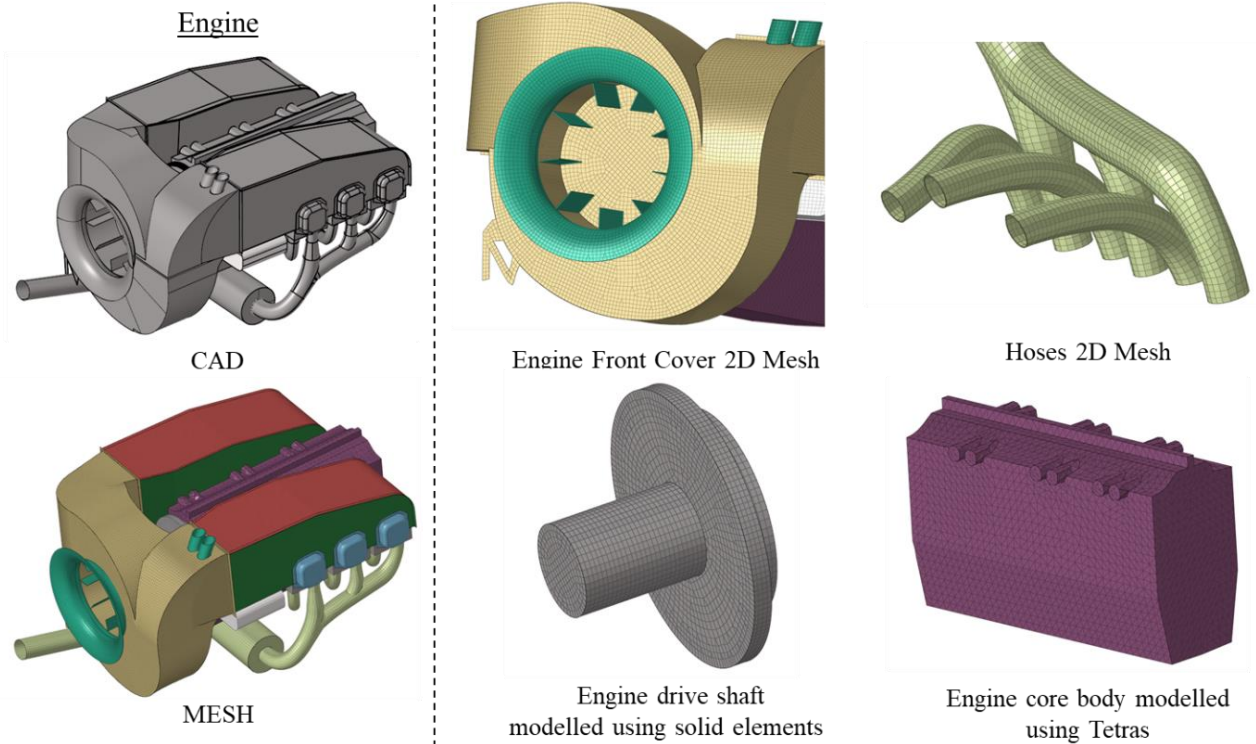
Figure 105. Rotorcraft engine CAD vs. mesh details.

3.3.3 *Connections*

The discretized model was connected using three types of connections:

- Mesh independent spot-weld beam elements: they are one of the several options to model fasteners in FEM. This connection method is practical for large models because the connection process can be automated.
- Nodal Rigid Body (NRB): the selected set of nodes are constrained rigidly, only allowing rigid body motion. Figure 106 shows an NRB around a hole.
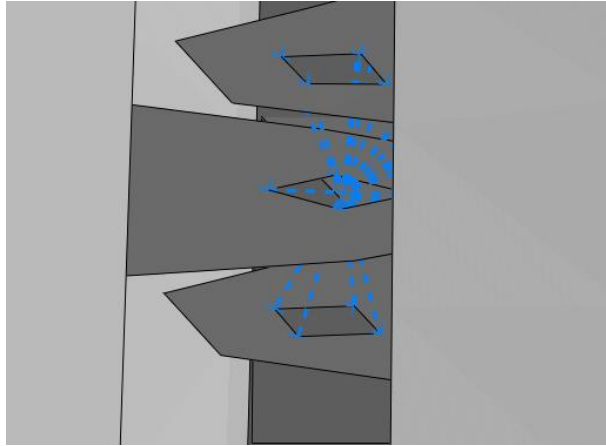
Figure 106. Nodal rigid body.

- Revolute Joint: This allows modeling joints that can rotate about an axis between two separate parts. For the rotorcraft model, the revolute joint was particularly useful to model rotation inside the gearbox for the tail rotor (as shown in Figure 109) and the main rotor blade.

The fastener locations of the rotorcraft were established using 3D scan data and hand measurements, as highlighted in Figure 107. The fastener head was measured, and the shank diameter was subsequently determined by correlating the head and shank diameters found in standard fasteners' specification sheets. Figure 108 shows the details of the connection of the tail cone sub-assembly. All rotorcraft connections are shown in Figure 110. Additionally, the total number of connections is presented in Table 36.

Table 36. Rotorcraft connections summary.

	Spot – weld beam	**NRB**	**Revolute Joint**
Rotorcraft	8,542	366	2
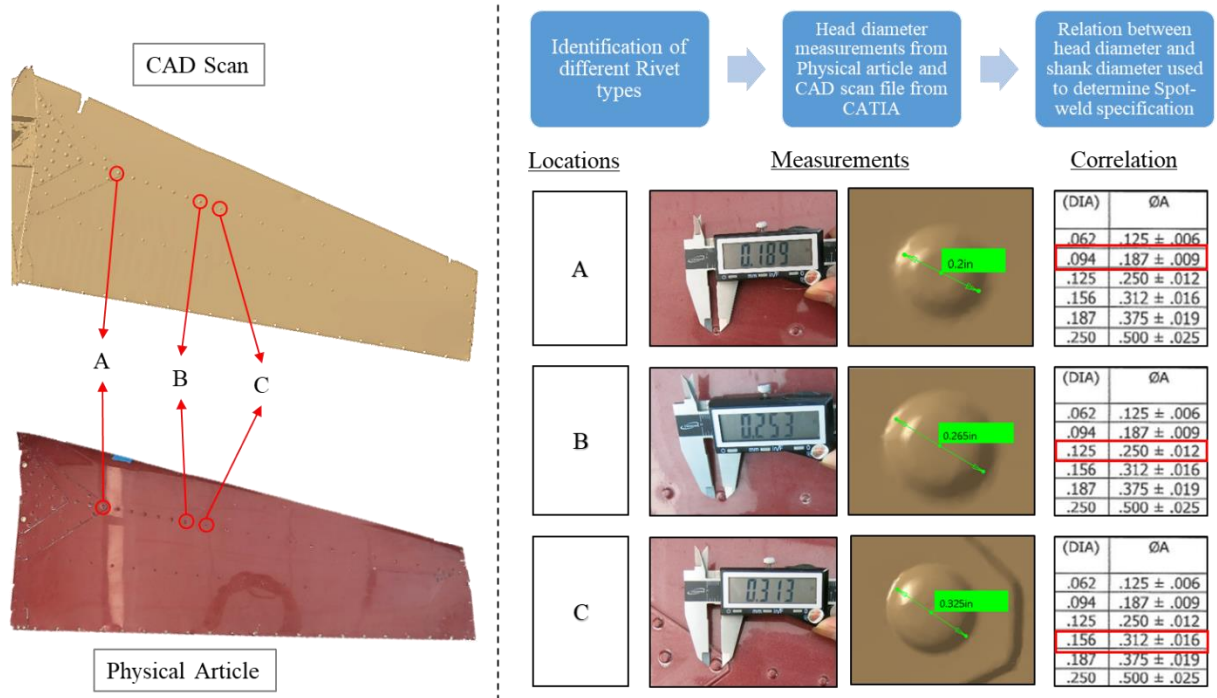
Figure 107. Fastener diameter identification process.

Connections	Identifier
1/8" Rivets	
5/32" Rivets	
1/4" Rivets	
3/8" Bolts	
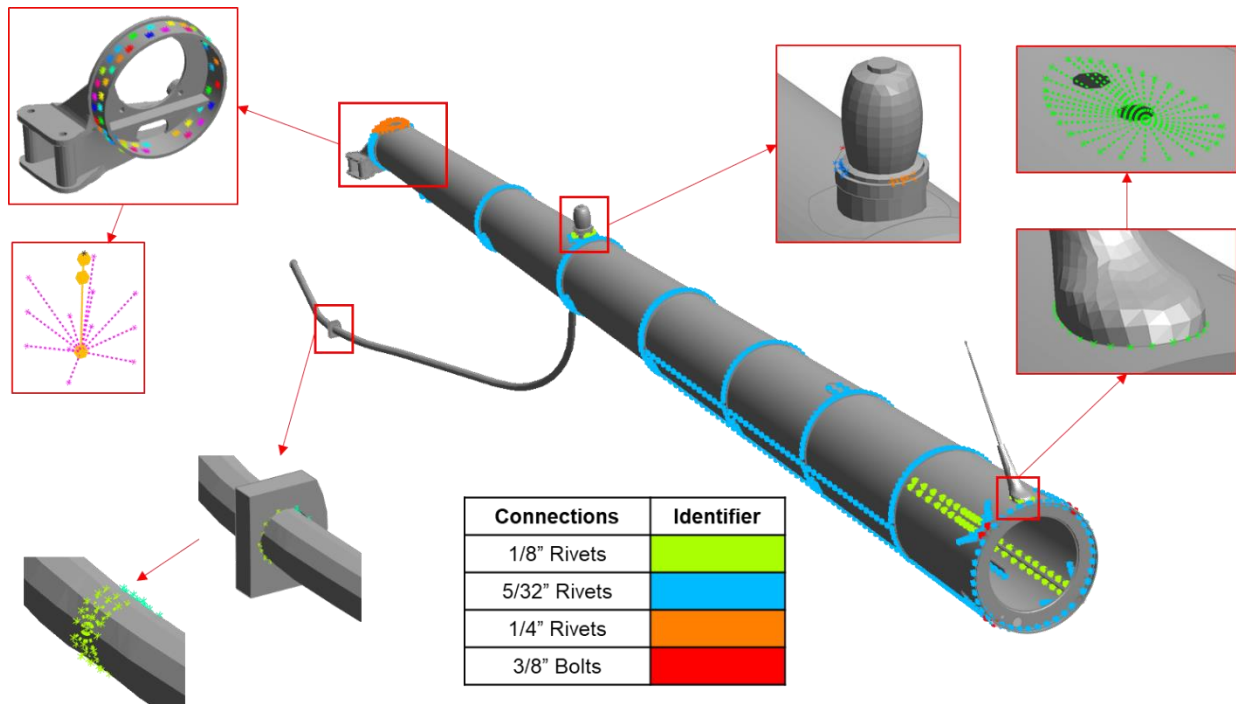
Figure 108. Tail cone connections.

Honeycomb connected to
main Structure using nrbs

1. Tied Contact used for constraining trailing edge of the airfoil
2. Tied contact used for honeycomb to skin interaction

L1

To allow the wings to
rotate a joint is modelled
at the Tail Rotor to Gear
Box intersection

Structure Missing on the back of
end rib, so end rib connected
using nrbs

All the bolt connections in this
section are modelled using nrbs

Figure 109. Tail rotor connections.

All connections

Fasteners only (beam spot-weld)

Connections	Identifier
3/32" Rivets (0.094")	
1/8" Rivets (0.125")	
5/32" Rivets (0.156")	
1/4" Rivets (0.25")	
1/4" Bolts (0.25")	
3/8" Bolts (0.375")	
3/16" Bolts (0.1875")	
Extra Nodes	
NRBs	
Revolute Joints	
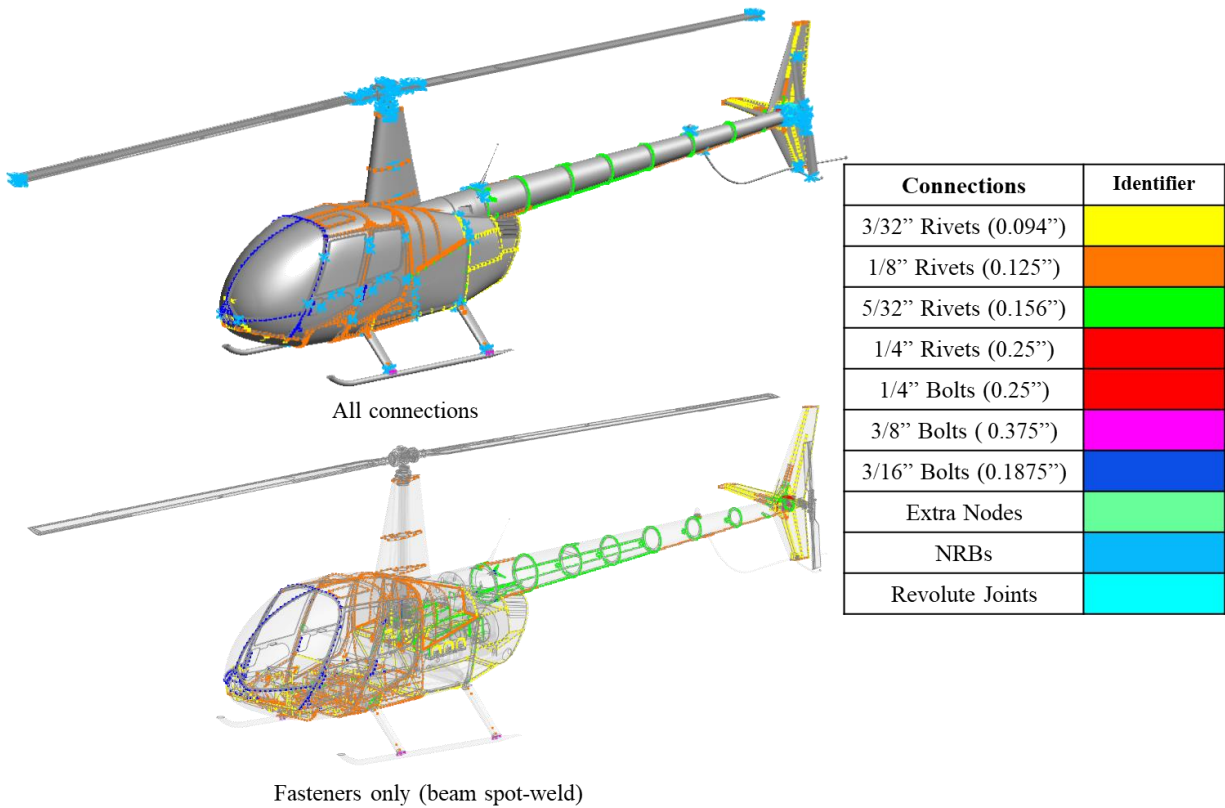
Figure 110. Rotorcraft connections.

93

3.3.4   Material definition

This section discusses the materials used in the rotorcraft FEM. Figure 111 highlights the materials applied for each rotorcraft component classified by Young's modulus. Additionally, Table 37 summarizes the materials used for different target components, as well as the LS-DYNA material card used. Material names such as RC-MRE-PXX-T-0X are materials defined from coupon-level tests. The name indicates the coupon specimens used to generate the material card. Further details for each material card are presented in Section 3.2.

Material Young's Modulus (E) Range - Mpa	Identifier
2-3k	
10-12k	
32-40k	
42-51k	
51-60k	
60-65k	
71-75k	
190-200k	
200-210k	
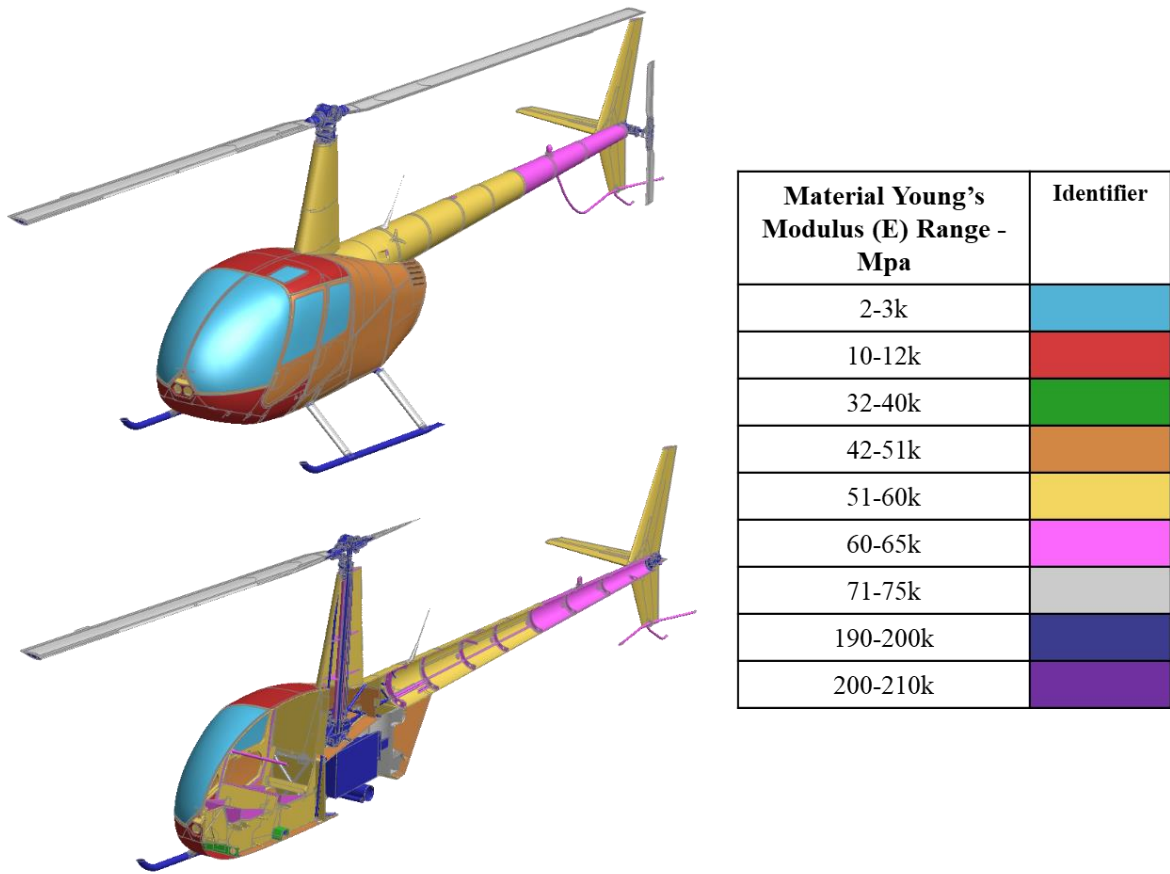
Figure 111. Materials applied to the rotorcraft FEM (grouped based on the range of Young's modulus value).

Table 37. Target area materials used on the rotorcraft FEM.

Part		Material	Ls-Dyna MAT card
Horizontal Stabilizer	Outer Skin	RC-MRE-P28-T-0X	Mat_024
	Internal Structures	RC-MRE-P23-T-0X	Mat_024
Vertical Stabilizer	Outer Skin	RC-MRE-P29-T-0X	Mat_024
	Internal Structures	RC-MRE-P24-T-0X	Mat_024
		RC-MRE-P26-T-0X	Mat_024
Fuselage	Composite Skins	Laminated Composite Fabric (RC-MRE-P03-T-L-0X)	Mat_058
	Metallic Skins	RC-MRE-P32-T-0X	Mat_024
	Rubber Seal	Elastic Rubber	Mat_001
	Landing Skids	STEEL_0.40C-300M_QuenchedTempered_AMS_6417_BarForgingTubing_t=<=5.0	Mat_024
	Internal Structures	STEEL_0.40C-300M_QuenchedTempered_AMS_6417_BarForgingTubing_t=<=5.0	Mat_024
		ALUMINUM_2024-T3_AMS_4037_Sheet_t=0.021-0.128	Mat_024
		RC-MRE-P20-T-0X	Mat_024
		RC-MRE-P17-T-0X	Mat_024
		RC-MRE-P34-T-0X	Mat_024
		RC-MRE-P32-T-0X	Mat_024
		RC-MRE-P05-T-0X	Mat_024
		RC-MRE-P06-T-0X	Mat_024
		RC-MRE-P19-T-0X	Mat_024
		RC-MRE-P33-T-0X	Mat_024
		RC-MRE-P07-T-0X - Longitudinal	Mat_024
		RC-MRE-P08-T-0X - Normal	Mat_024
		RC-MRE-P14-T-0X	Mat_024
		RC-MRE-P11-T-0X - Longitudinal	Mat_024
		RC-MRE-P15-T-0X	Mat_024
		RC-MRE-P10-T-0X	Mat_024
		RC-MRE-P16-T-0X	Mat_024
		RC-MRE-P09-T-0X	Mat_024
Windshield/Windows		SAMP-1	Mat_187
Mast	Outer Skin	RC-MRE-P20-T-0X	Mat_024
	Internal Structures	STEEL_0.40C-300M_QuenchedTempered_AMS_6417_BarForgingTubing_t=<=5.0	Mat_024
		Elastic STEEL	Mat_001
		RC-MRE-P26-T-0X	Mat_024
Rotor Blade	Honeycomb	Hexcel_Aluminum1/4-5052-0.0007-1.6-CR_PAA@CR_IIII	Mat_026
	Skins	ALUMINUM_7075-T6_AMS_4045_Sheet_t=0.012-0.039	Mat_024
	Front Spar/Hub	STEEL 15-5PH H1075	Mat_024

3.3.5 Contacts

For contact between all structural parts of the Rotorcraft FEM, AUTOMATIC_SINGLE_SURFACE contact was used. The windshield and windows were connected using TIED_SURFACE _TO_SURFACE contact. CONTACT_SPOTWELD was used to define the contact between the spot-weld beam elements and the rotorcraft parts. AUTOMATIC_SURFACE_TO_SURFACE_TIEBREAK was used to model the adhesive/resin of the main rotor blade and tail rotor.

3.3.6 Weight and Center of Gravity (CG)

The cabin interior, instruments, electrical system, auxiliary equipment, avionics, and special option packages were not modeled. The bare weight of the FEM, excluding these systems (only including engine mass), is 1380 lbs. The standard R44 rotorcraft empty weight is 1450-1500 lbs. [41]. As a result, 70-120 lbs. of weight is estimated for the components mentioned previously. The total fuel weight is 258 lbs. (31 US gal), and the total passenger payload limit is 748 lbs. [41]. These were modeled using non-structural mass elements. These mass elements were attached to various rotorcraft structural elements, as shown in Figure 112. The MTOW (gross) of the R44 rotorcraft is 2500 lb [41]. In comparison, the gross weight of the R44 rotorcraft FEM is approximately 2386 lbs. The FEM weights for an empty configuration and with payload are indicated in Figure 113
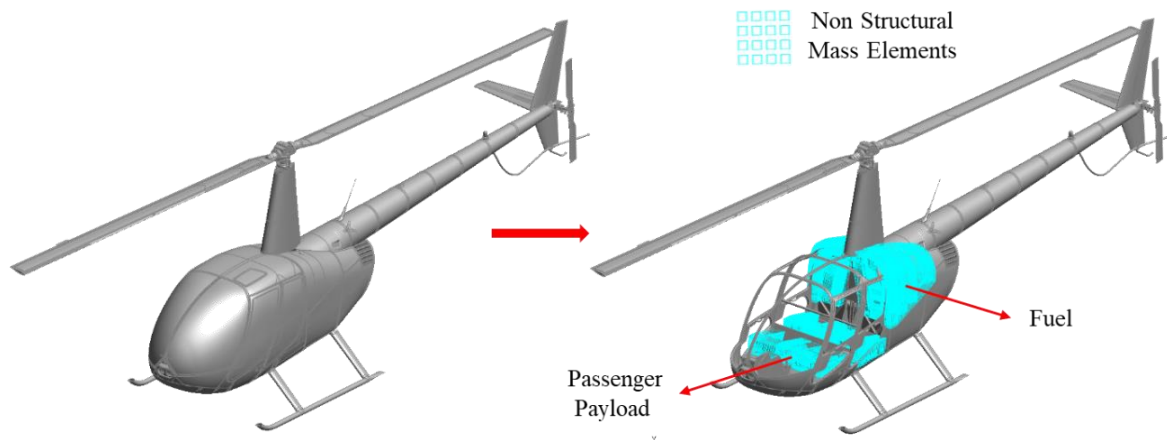
Figure 112. Mass elements applied to the rotorcraft FEM.

After applying the non-structural mass for the fuel and payload, the total weight of the rotorcraft FEM is approximately 2386 lbs., and the longitudinal axis CG is measured at 3.53 inches (89.7 mm) forward of the main rotor axis line as shown in Figure 114. Additionally, the lateral axis CG is measured at 0.129 inches (3.28 mm) from the symmetry line. The FEM CG is compared to the CG limit chart [41] in Figure 115, which indicates that the FEM CG is within the specified limits.
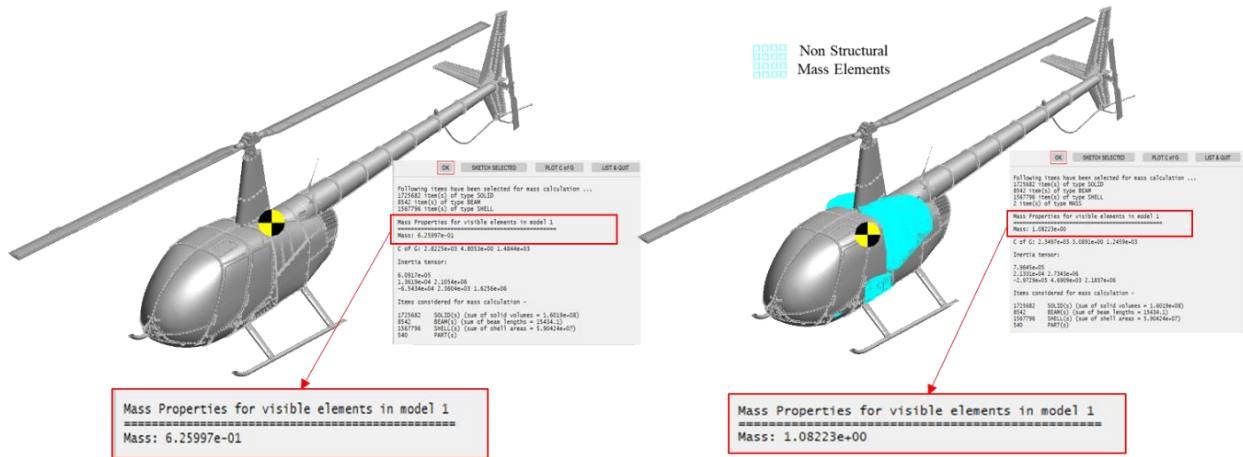
Figure 113. Rotorcraft FEM Weight – Empty (left) vs. with payload (right) mass in metric tons.
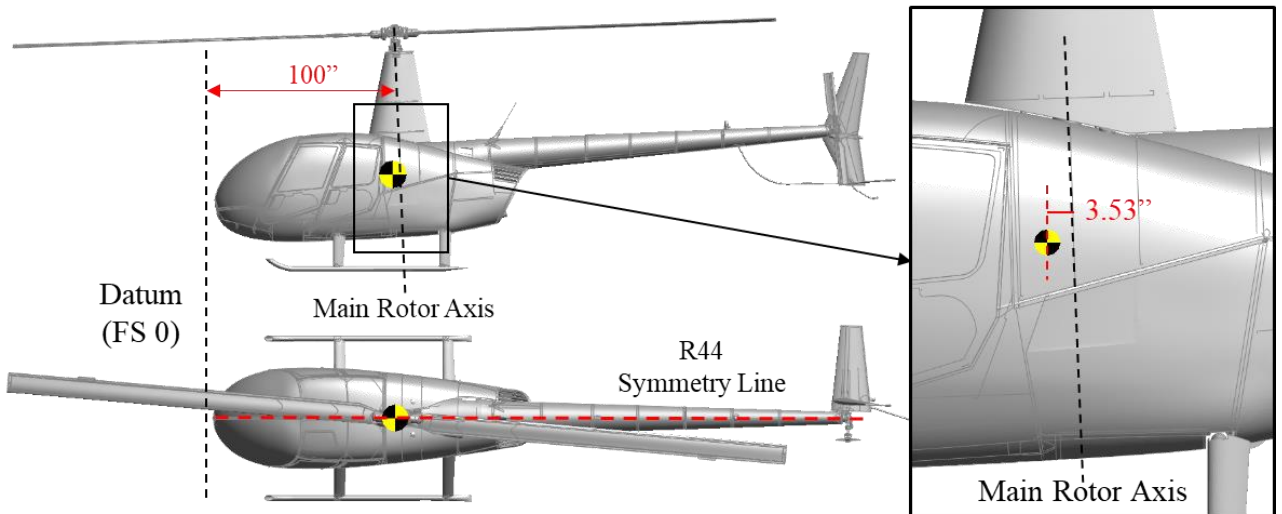
Figure 114. C.G. of the rotorcraft FEM (with payload).
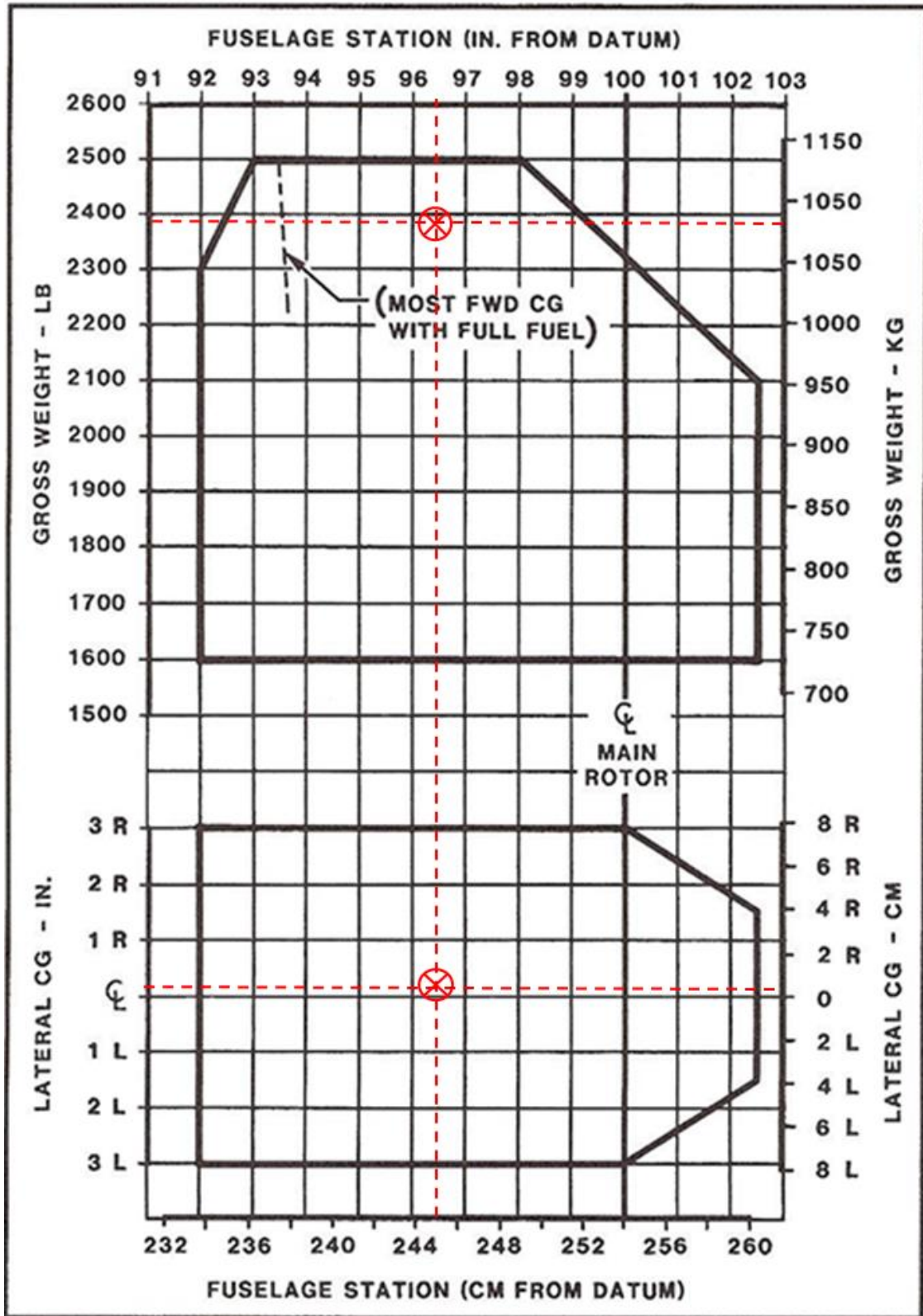
Figure 115. C.G. limit chart [41] with the rotorcraft FEM C.G. indicated in red.

4 MID-AIR COLLISION ANALYSIS

This section documents the conditions defined for analyzing collisions between sUAS and rotorcraft. Section 4.2 presents the criteria for assessing damage severity, which aligns with those specified in earlier airborne collision studies referenced in A3 [2] and A16 [3]. However, for the present research, the severity criterion pertaining to rotor blade damage has been refined and enhanced compared to the criteria outlined in A16 [3].

4.1 Impact Conditions Definitions

This research focuses on the collision between sUAS and typical rotorcraft airframes. Each impact structure was analyzed to determine the location likely to incur the most severe damage. The entire rotorcraft was modeled for each impact location, as the size disparity between the rotorcraft and UAS was minimal, ensuring consistent and unconstrained boundary conditions across all impact cases.

Collision analysis was performed by imparting initial velocity solely to the UAS model while maintaining the rotorcraft stationary. In instances of impacts on the vertical stabilizer, the tail rotor was simulated with rotational (angular) velocity and preload. Similarly, for impacts on the mast and rotor blade, the main rotor blade included rotational velocity and preload. The rotational velocity was defined based on the pilot's operation handbook information [41].

The preload refers to the loads generated by the rotational inertia of the blade. The analysis did not include the effect of aerodynamic loads or environmental factors (wind, temperature, etc.).

Various variables were considered for the current study:

- Aircraft Type: Rotorcraft
- UAS Configuration: Quadcopter and Fixed-Wing
- UAS Mass: 2.7, 4.0, 10, 12, 25, and 55lbs.
- Aircraft Velocity: 0, 55, and 110 knots
- sUAS Velocity: 39 knots
- Impact Relative Velocity: 39, 94, and 149 knots
- Tail rotor RPM: 2425.5 RPM (254 rad/s)
- Main rotor blade RPM: 408 RPM (42.73 rad/s)
- Impact Areas as shown in Figure 116

The following special considerations were accounted for in this study:

1. The same impact locations were maintained for all UAS models.
2. All impacts were considered for the worst-case scenario, with the UAS moving at a maximum speed of 39 knots.
3. Relative impact velocity was applied to the UAS.
4. For specific cases, tail rotor and main rotor blade rotations were included, respectively.
5. The aircraft target areas were modeled with the full aircraft, allowing for a realistic, unconstrained boundary condition.

Code	Location	Details
H1	Horizontal Stabilizer	Halfway from the Root
V1	Vertical Stabilizer	Upper: Half way from the Root
M1	Mast	Halfway from the Root
N1	Nose	Below the Headlights
W1	Windshield	Targeted at the Center
B1	Blade	Near Tip
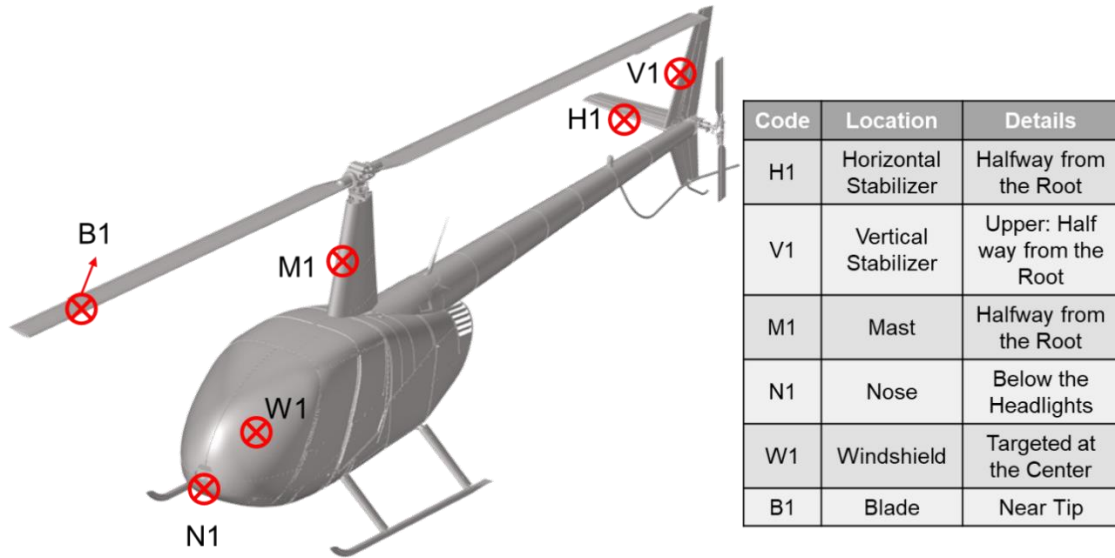
Figure 116. R44 rotorcraft impact areas.

4.1.1 Impact Velocity

The determination of rotorcraft velocity upon impact was defined based on the pilot's operation handbook [41]. Documentation within Section 4 of the pilot's operation handbook outlines the preparation for Part 27 rotorcraft cruise velocity, set at 110 knots. Additionally, two additional velocities were considered for analysis: a hover velocity of 0 knots and a moderate velocity of 55 knots. According to sUAS research conducted under Task A3 [2], the maximum velocity for a 2.7 lbs. sUAS is 39 knots. To ensure uniformity in comparing severity levels across different UAS architectures, the same velocity was applied to all other UAS.

In the simulation setup process, for each impact velocity case (hover, moderate, and cruise), the UAS was assigned the relative velocity of the impact at the start of the simulation. In impacts on the tail rotor and main rotor blade, the rotations of these components were modeled accordingly, and the UAS was assigned the relative velocity with respect to the center of gravity of the rotorcraft.

4.1.2 Impact Conditions

Where feasible, insights gleaned from the A3, A14, and A16 programs were leveraged to streamline the analysis conducted in this study. Consequently, the impact location and orientation sensitivity studies detailed in Volume II [22] are applicable to the current investigation.

As a result, the following guidelines were adhered to:

- In most instances, the UAS center of gravity was aligned with the initial point of impact to maximize damage to the target.
- In certain scenarios, the UAS was aligned to impact its battery, allowing for a comparison of damage severity across different alignments to ascertain the most critical impact scenario.

- Quadcopter models of the UAS were positioned to impact with their motors first, akin to methodologies employed in previous airborne collision investigations such as Task A3 [22] and Task A16 [3].
- When targeting leading edge structures, the UAS impacted between ribs to facilitate the potential for skin perforation and penetration into the airframe.

4.1.3 Load Case Name Convention

This research's broad spectrum of FE model combinations and parameters requires a code to identify the simulated impact conditions according to the UAS, aircraft type, target component, and local impact positions.

Impact conditions were coded using seven characters (ABij-CDE-F):

- A – Distinguishes aircraft; for this study, the Rotorcraft is denoted (R)
- Bij – Distinguishes between UAS Type and Size:
    - Quadcopter- (Q2.7, Q10, Q25, Q55)
    - Fixed Wing- (F4.0, F12, F25, F55)
- C – Distinguishes between impact areas:
    - Horizontal Stabilizer (H)
    - Vertical Stabilizer (V)
    - Mast (M)
    - Nose (N)
    - Windshield (W)
    - Blade (B)
- D – Impact location (1)
- E - Distinguishes between velocity categories associated with the rotorcraft:
    - Hover – 0 kts (H)
    - Medium – 55 kts (M)
    - Cruise – 110 kts (C)
- F – Downwash (D)

Example: RQ2.7-M1C-D

- Rotorcraft

- Quadcopter – 2.7 lbs.

- Mast

- Impact Location #1

- UAS Relative Velocity – 110 kts

- Downwash

4.1.4 Simulation Matrix
Table 38 describes all the simulation load cases analyzed in this study.

Table 38. Simulation matrix.

Case	Quadcopter 2.7 lbs.			Fixed-Wing 4 lbs.			Quadcopter 10 lbs.			Fixed-Wing 12 lbs.			Quadcopter 25 lbs.			Fixed-Wing 25 lbs.			Quadcopter 55 lbs.			Fixed-Wing 55 lbs.		
	RQ2.7-X1H	RQ2.7-X1M	RQ2.7-X1C	RF4-X1H	RF4-X1M	RF4-X1C	RQ10-X1H	RQ10-X1M	RQ10-X1C	RF12-X1H	RF12-X1M	RF12-X1C	RQ25-X1H	RQ25-X1M	RQ25-X1C	RF25-X1H	RF25-X1M	RF25-X1C	RQ55-X1H	RQ55-X1M	RQ55-X1C	RF55-X1H	RF55-X1M	RF55-X1C

Rotorcraft Impact Location (X) and all UAS

X is a placeholder for:

- H: Horizontal Stabilizer
- V: Vertical Stabilizer
- M: Mast
- N: Nose
- W: Windshield
- B: Blade

4.2 Damage Category Definition

A set of criteria was defined to categorize the damage level, as shown in Table 39. This criterion was developed under task A3 program [2] and applied to airframe structures.

Simulations with the least visible damage are categorized as Level 1, corresponding to minimal localized damage such as surface dents. Damage category Level 2 represents significant visible damage to the external surface of the aircraft with some internal component damage but no skin rupture. The third category, Level 3, describes impact events where the aircraft's outer surface is compromised in a way that could allow the ingress of foreign objects into the airframe, with some damage to the substructure. Finally, Level 4 indicates damage that includes all preceding aspects, extensive damage to internal components, and possibly compromising damage to the primary structure.

Table 40 describes the damage level categories that classify the damage caused to a rotorcraft blade by a UAS airborne collision in four levels.

Table 39. Damage level categories.
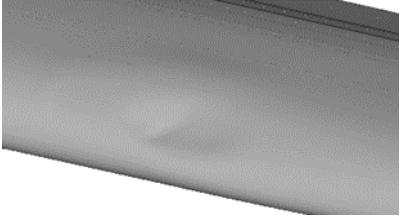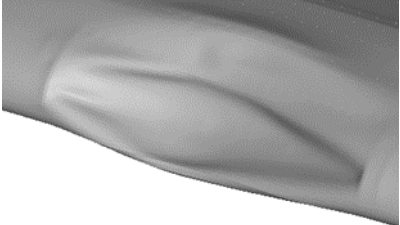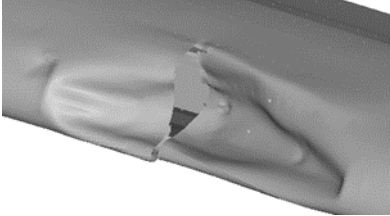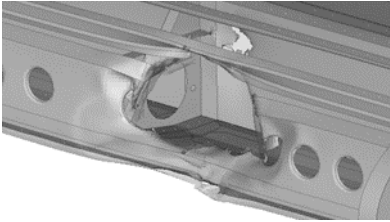
Severity	Description	Example
Level 1	• The airframe is undamaged. • Small deformations.	
Level 2	• Extensive permanent deformation on external surfaces. • Some deformation in internal structure. • No failure of the skin.	
Level 3	• Skin fracture. • Penetration of at least one component into the airframe.	
Level 4	• Penetration of UAS into airframe and failure of the primary structure.	
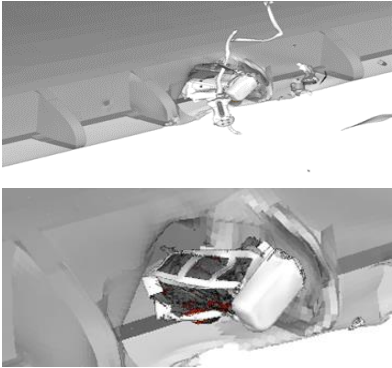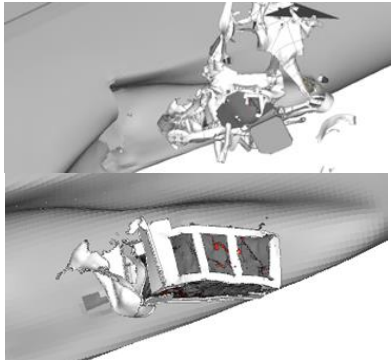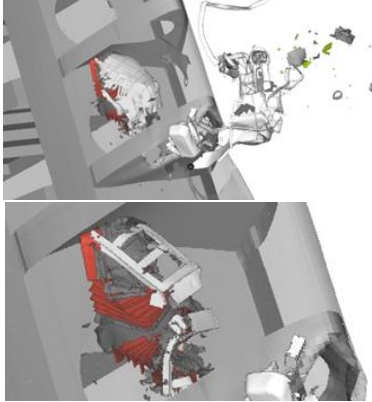
Table 40. Damage level categories for the rotorcraft blade.

Severity	Description
Level 1	• Blade undamaged • Scratches on a rotor blade
Level 2	• Dents on a rotor blade leading edge • Minor crack initiation • No debonding
Level 3	• Any debonding • Skin buckling • Major crack initiation
Level 4	• Any material loss leading to an imbalance on a single blade • Heavy blade twist and deflection leading to an imbalance on a single blade

4.3 Fire Risk

The risk of fire associated with damaged Lithium-ion Polymer (LiPo) type batteries is addressed for each simulation based on the trends observed during the component ballistic tests performed in the A3 research [2]. Note that the label "Fire Risk" indicates a potential outcome rather than an impending event due to the qualitative nature of the assessment. Further studies and physical testing into this phenomenon would be required to determine any additional severity. Table 41 explains the fire risk criterion.

Table 41. Risk of battery fire.

Fire Risk	Description	Example
Yes	• UAS (including the battery) penetrates the airframe. • The battery deforms but stays undamaged. • Physical tests showed that partly damaged batteries created heat and sparks.	
No	• The UAS does not penetrate the airframe.	
No	• UAS (including the battery) penetrates the airframe. • The battery sustains significant damage, destroying its cells. • Physical tests showed that completely damaged batteries did not create heat and sparks.	

5 MID-AIR COLLISION DAMAGE ASSESSMENT

5.1 Horizontal Stabilizer

This section presents the results of the airborne collision studies for all UAS and the rotorcraft's Horizontal Stabilizer. Figure 117 shows an example of the simulation setup for the Horizontal Stabilizer impact with a 55 lbs. quadcopter at cruise speed.
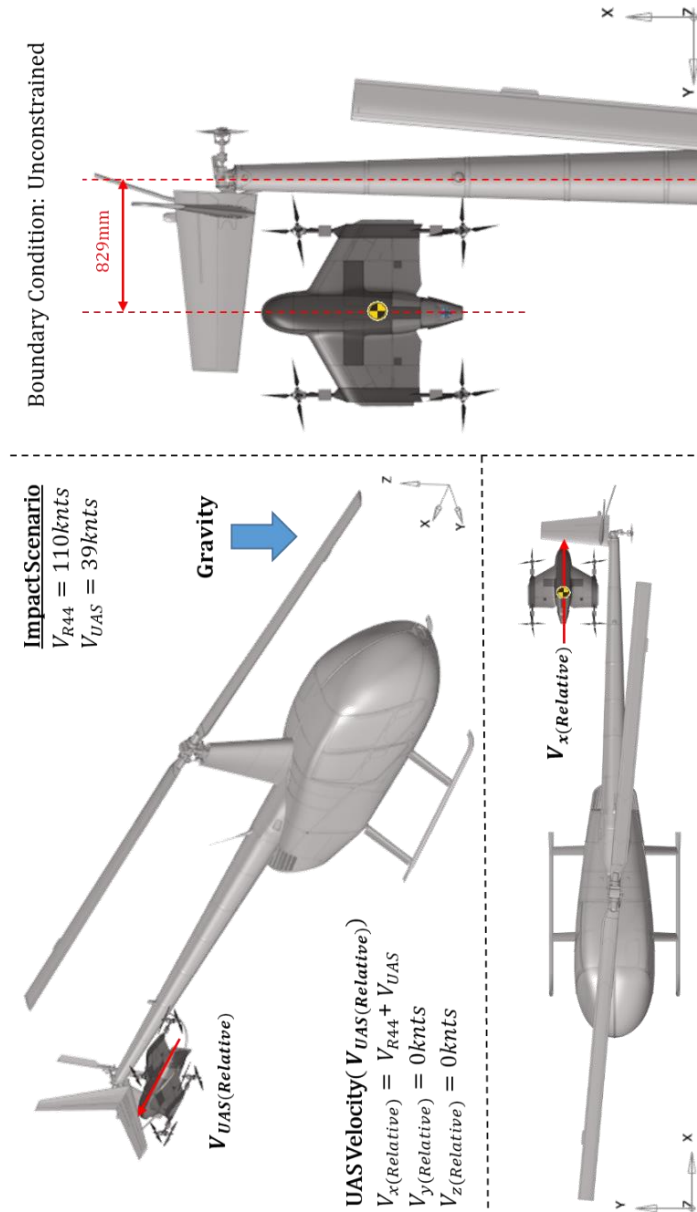
Figure 117. Simulation setup for impact between the horizontal stabilizer and 55 lbs. quadcopter at cruise velocity.

Table 42 summarizes the damage severity level evaluation and fire risk assessment for impact cases for all UAS with the Horizontal Stabilizer.

Table 42. Horizontal Stabilizer mid-air collision simulation assessment – damage severity level and fire risk.

		Case	Severity	Fire Risk
Mid-air collision Rotorcraft-Horizontal Stabilizer and all sUAS	Quadcopter 2.7 lbs.	RQ2.7-H1H	Level 1	No
		RQ2.7-H1M	Level 2	No
		RQ2.7-H1C	Level 3	No
	Fixed-Wing 4 lbs.	RF4-H1H	Level 2	No
		RF4-H1M	Level 2	No
		RF4-H1C	Level 3	No
	Quadcopter 10 lbs.	RQ10-H1H	Level 2	No
		RQ10-H1M	Level 3	No
		RQ10-H1C	Level 4	No
	Fixed-Wing 12 lbs.	RF12-H1H	-	-
		RF12-H1M	-	-
		RF12-H1C	-	-
	Quadcopter 25 lbs.	RQ25-H1H	Level 2	No
		RQ25-H1M	Level 4	No
		RQ25-H1C	Level 4	No
	Fixed-Wing 25 lbs.	RF25-H1H	-	-
		RF25-H1M	-	-
		RF25-H1C	-	-
	Quadcopter 55 lbs.	RQ55-H1H	Level 3	No
		RQ55-H1M	Level 4	No
		RQ55-H1C	Level 4	No
	Fixed-Wing 55 lbs.	RF55-H1H	-	-
		RF55-H1M	-	-
		RF55-H1C	-	-

5.1.1 UAS 2.7 lbs. Quadcopter

This section delineates the findings stemming from collisions involving 2.7 lbs. quadcopter and the rotorcraft's Horizontal Stabilizer at Hover, Medium, and Cruise velocities, as showcased in Figure 118, Figure 119, and Figure 120, respectively. These results unravel the temporal progression of the impact occurrences, spotlighting time intervals at 0.005s, 0.02s, and 0.05s. The upper trio of windows highlights the kinematic aspects of the impacts, while the lower trio shows the resultant effective plastic strain on the rotorcraft structures. Additionally, Figure 121 provides the energy balance plots for all three impact velocities.

Figure 118. RQ2.7-H1H kinematics (top) and effective plastic strain (bottom) frames.

Figure 119. RQ2.7-H1M kinematics (top) and effective plastic strain (bottom) frames.

Figure 120. RQ2.7-H1C kinematics (top) and effective plastic strain (bottom) frames.
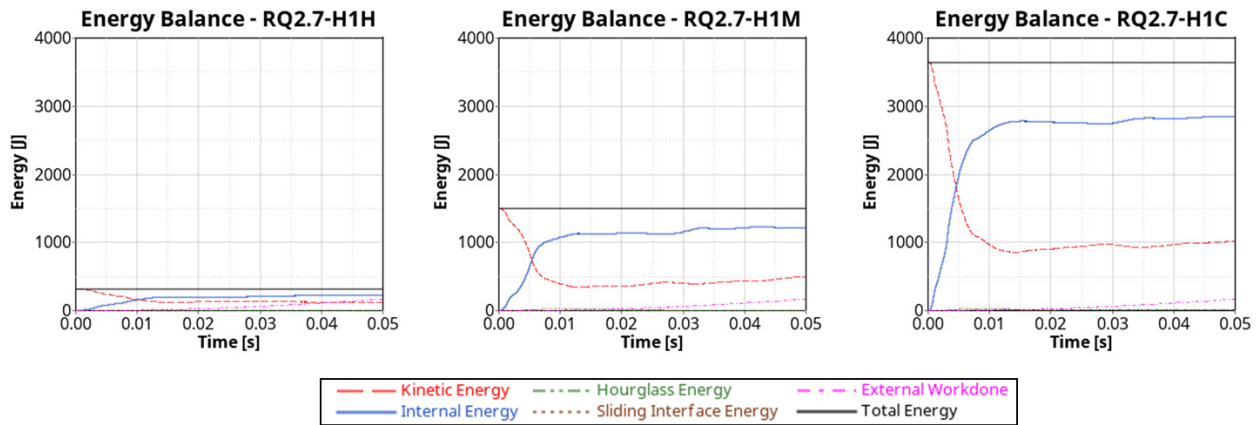
Figure 121. Horizontal stabilizer and 2.7 lbs. quadcopter impact energy balance.

At hover velocity, the collision between the 2.7 lbs. quadcopter and the horizontal stabilizer resulted in minor dents on the skin, indicative of a level 1 impact severity. Conversely, the horizontal stabilizer exhibited increased permanent deformation to the skin at medium impact velocity compared to the hover velocity, marking a level 2 impact severity. Subsequently, at cruise impact velocity, the horizontal stabilizer sustained substantially heightened damage in contrast to the hover velocity impact, characterized by major cracks and buckling of the skin, accompanied by minor damage to the primary spar, representing a level 3 impact severity.

5.1.2 *UAS 4 lbs. Fixed-Wing*

This section delineates the findings stemming from collisions involving 4 lbs. fixed-wing and the rotorcraft's Horizontal Stabilizer at Hover, Medium, and Cruise velocities, as showcased in Figure

122, Figure 123, and Figure 124, respectively. These results unravel the temporal progression of the impact occurrences, spotlighting time intervals at 0.005s, 0.02s, and 0.05s. The upper trio of windows highlights the kinematic aspects of the impacts, while the lower trio shows the resultant effective plastic strain on the rotorcraft structures. Additionally, Figure 125 provides the energy balance plots for all three impact velocities.

Figure 122. RF4-H1H kinematics (top) and effective plastic strain (bottom) frames.

Figure 123. RF4-H1M kinematics (top) and effective plastic strain (bottom) frames.
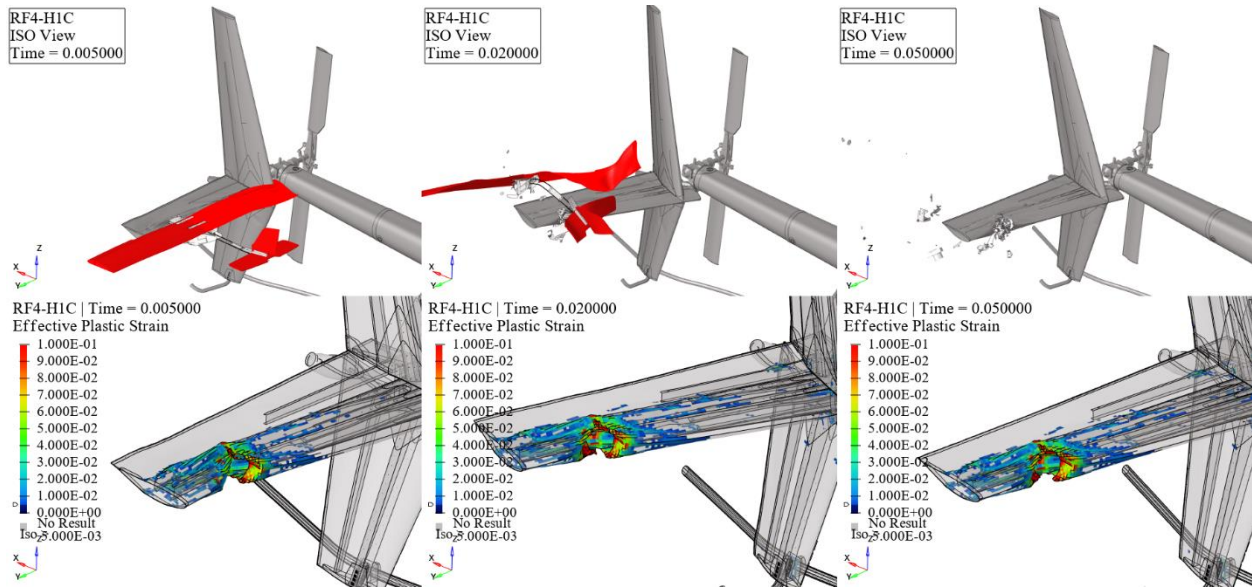
Figure 124. RF4-H1C kinematics (top) and effective plastic strain (bottom) frames.
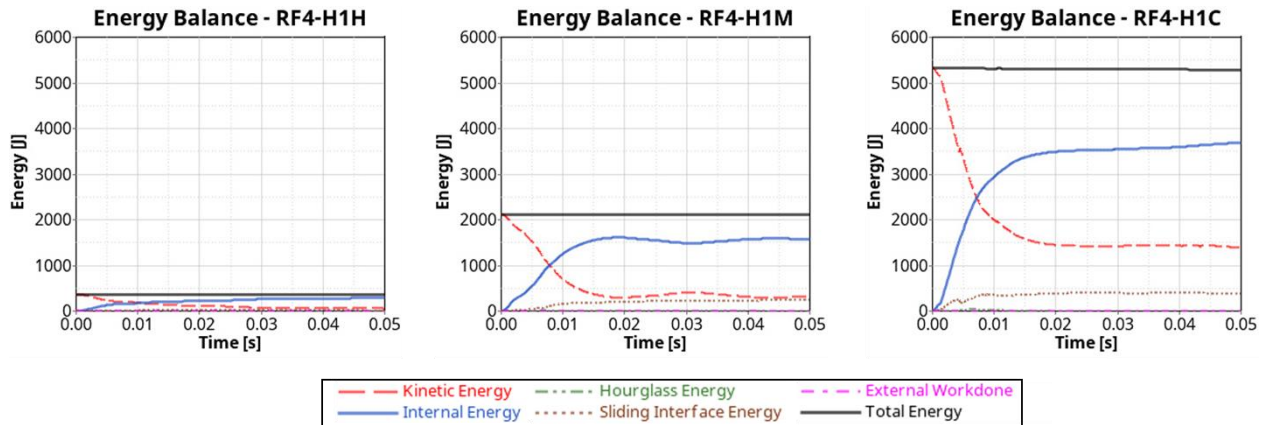
Figure 125. Horizontal stabilizer and 4 lbs. fixed-wing impact energy balance.

At hover velocity, the collision between the 4 lbs. fixed-wing and the horizontal stabilizer caused permanent deformation on the skin, indicating a level 2 impact severity. Similarly, the horizontal stabilizer showed increased permanent deformation at medium impact velocity compared to hover velocity, but the severity remained at level 2 without significant differences. However, the horizontal stabilizer sustained substantially greater damage at cruise impact velocity than at hover velocity impact. This included major skin cracks and minor damage to the primary spar, indicating a level 3 impact severity.

5.1.3 UAS 10 lbs. Quadcopter

This section delineates the findings stemming from collisions involving 10 lbs. quadcopter and the rotorcraft's Horizontal Stabilizer at Hover, Medium, and Cruise velocities, as showcased in Figure 126, Figure 127, and Figure 128, respectively. These results unravel the temporal progression of the impact occurrences, spotlighting time intervals at 0.005s, 0.02s, and 0.05s. The upper trio of

111

windows highlights the kinematic aspects of the impacts, while the lower trio shows the resultant effective plastic strain on the rotorcraft structures. Additionally, Figure 129 provides the energy balance plots for all three impact velocities.
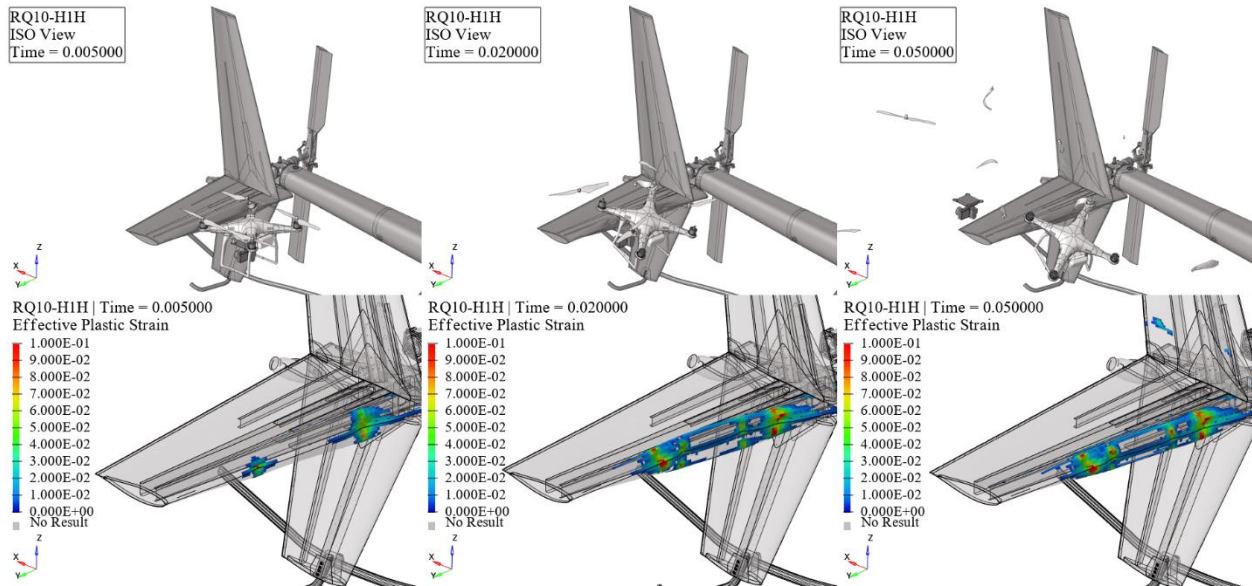
Figure 126. RQ10-H1H kinematics (top) and effective plastic strain (bottom) frames.
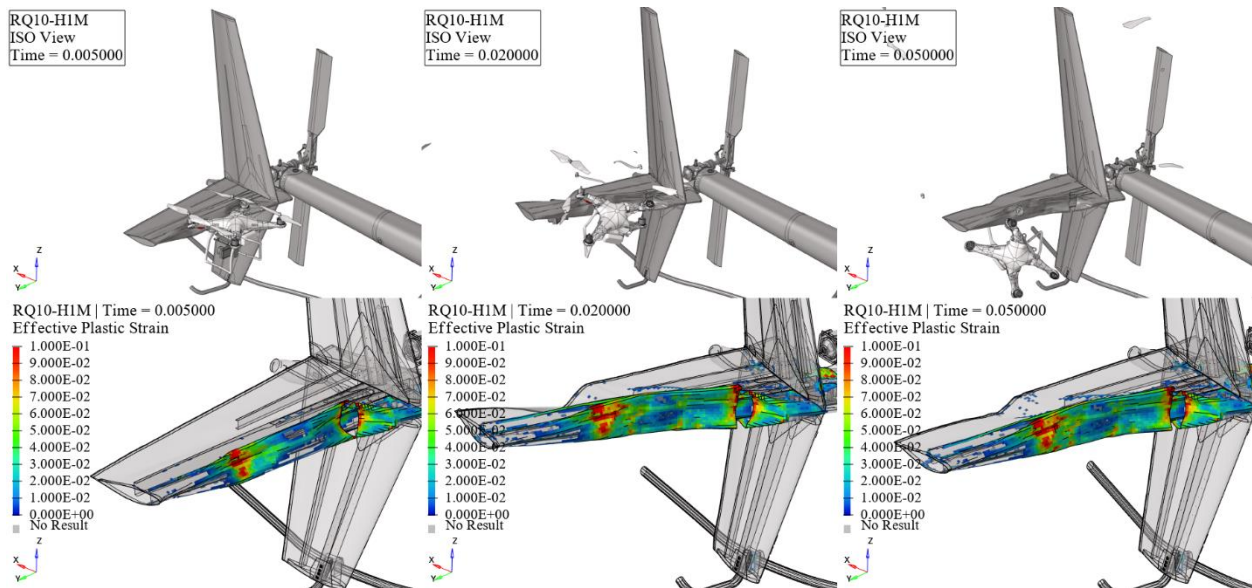
Figure 127. RQ10-H1M kinematics (top) and effective plastic strain (bottom) frames.
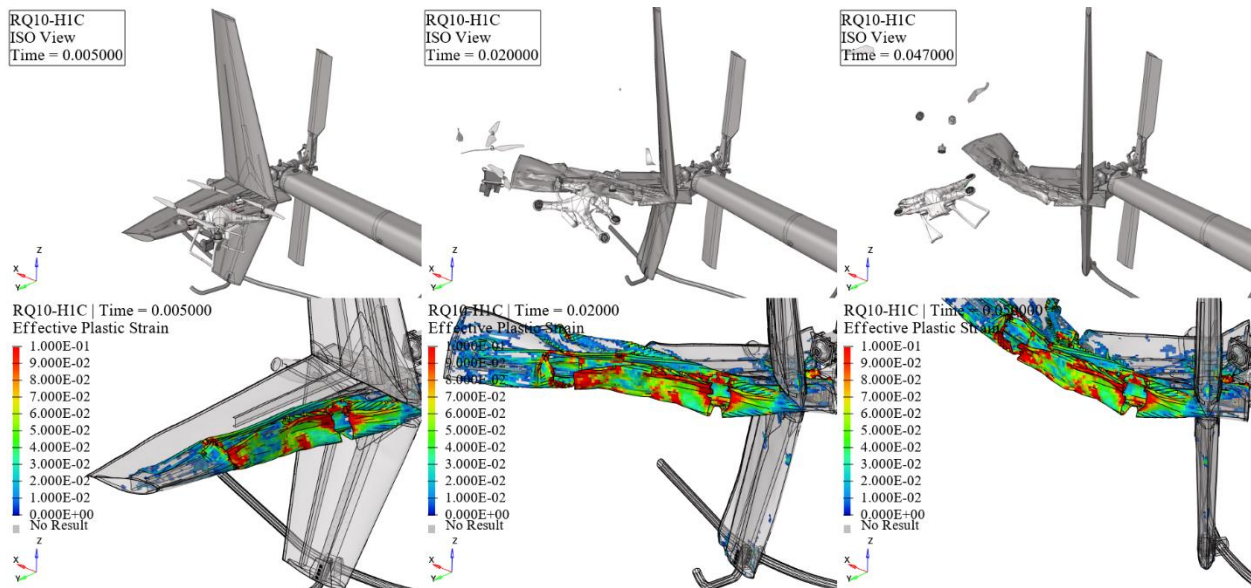
Figure 128. RQ10-H1C kinematics (top) and effective plastic strain (bottom) frames.
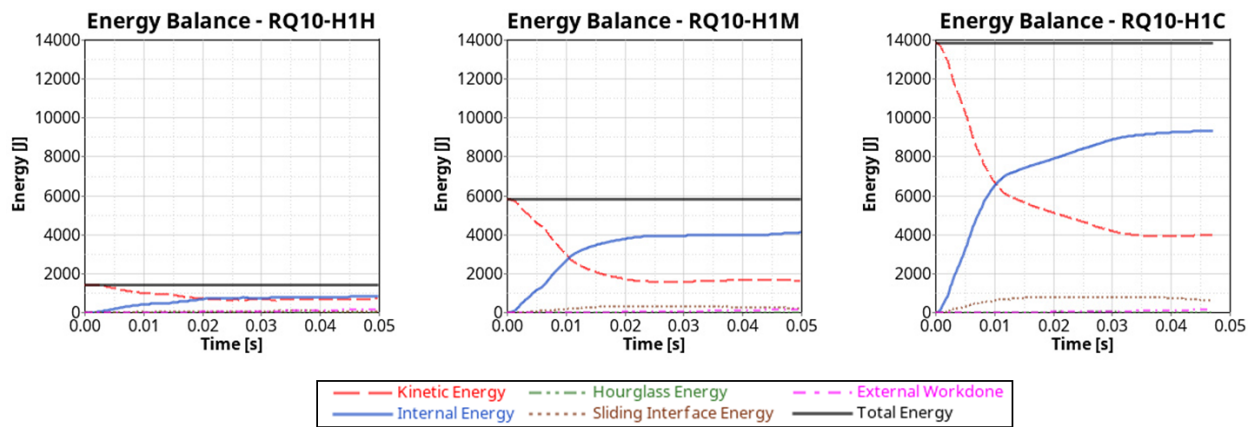
Figure 129. Horizontal stabilizer and 10 lbs. quadcopter impact energy balance.

At hover velocity, the collision between the 10 lbs. quadcopter and the horizontal stabilizer resulted in several instances of permanent deformation on the skin, signifying a level 2 impact severity. Conversely, at medium impact velocity, the horizontal stabilizer exhibited heightened permanent deformations and multiple cracks on the skin, indicating a level 3 impact severity. Finally, the horizontal stabilizer sustained severe damage at cruise impact velocity, reflecting a level 4 impact severity.

5.1.4 UAS 12 lbs. Fixed-Wing

The head-on collision between the 12 lbs. fixed-wing and the rotorcraft's Horizontal Stabilizer is not feasible due to the scale of the UAS. Potential collision scenarios that are feasible (not head-on) would not align with the scope of the current study and would likely result in lower impact severity, underestimating the potential damage to the aircraft structure compared to simulating the impact scenario with a much smaller UAS of similar mass to the NIAR's 12 lbs. fixed-wing.

113

5.1.5   UAS 25 lbs. Quadcopter

This section delineates the findings stemming from collisions involving 25 lbs. quadcopter and the rotorcraft's Horizontal Stabilizer at Hover, Medium, and Cruise velocities, as showcased in Figure 130, Figure 131, and Figure 132, respectively. These results unravel the temporal progression of the impact occurrences, spotlighting time intervals at 0.005s, 0.02s, and 0.05s. The upper trio of windows highlights the kinematic aspects of the impacts, while the lower trio shows the resultant effective plastic strain on the rotorcraft structures. Additionally, Figure 133 provides the energy balance plots for all three impact velocities.

Figure 130. RQ25-H1H kinematics (top) and effective plastic strain (bottom) frames.

Figure 131. RQ25-H1M kinematics (top) and effective plastic strain (bottom) frames.

Figure 132. RQ25-H1C kinematics (top) and effective plastic strain (bottom) frames.

Figure 133. Horizontal stabilizer and 25 lbs. quadcopter impact energy balance.

At hover velocity, the collision between the 25 lbs. quadcopter and the horizontal stabilizer caused several instances of permanent deformation on the skin, indicating a level 2 impact severity. However, at both medium and cruise velocities, the horizontal stabilizer sustained severe damage to the primary structure, as well as damage to the stabilizer connection point and the vertical stabilizer, indicating a level 4 impact severity.

5.1.6   UAS 25 lbs. Fixed-Wing

The head-on collision between the 25 lbs. fixed-wing and the rotorcraft's Horizontal Stabilizer is not feasible (not head-on) due to the scale of the UAS. Potential collision scenarios that are feasible would not align with the scope of the current study.

5.1.7   UAS 55 lbs. Quadcopter

This section delineates the findings stemming from collisions involving 55 lbs. quadcopter and the rotorcraft's Horizontal Stabilizer at Hover, Medium, and Cruise velocities, as showcased in Figure

134, Figure 135, and Figure 136, respectively. These results unravel the temporal progression of the impact occurrences, spotlighting time intervals at 0.005s, 0.02s, and 0.05s. The upper trio of windows highlights the kinematic aspects of the impacts, while the lower trio shows the resultant effective plastic strain on the rotorcraft structures. Additionally, Figure 137 provides the energy balance plots for all three impact velocities.
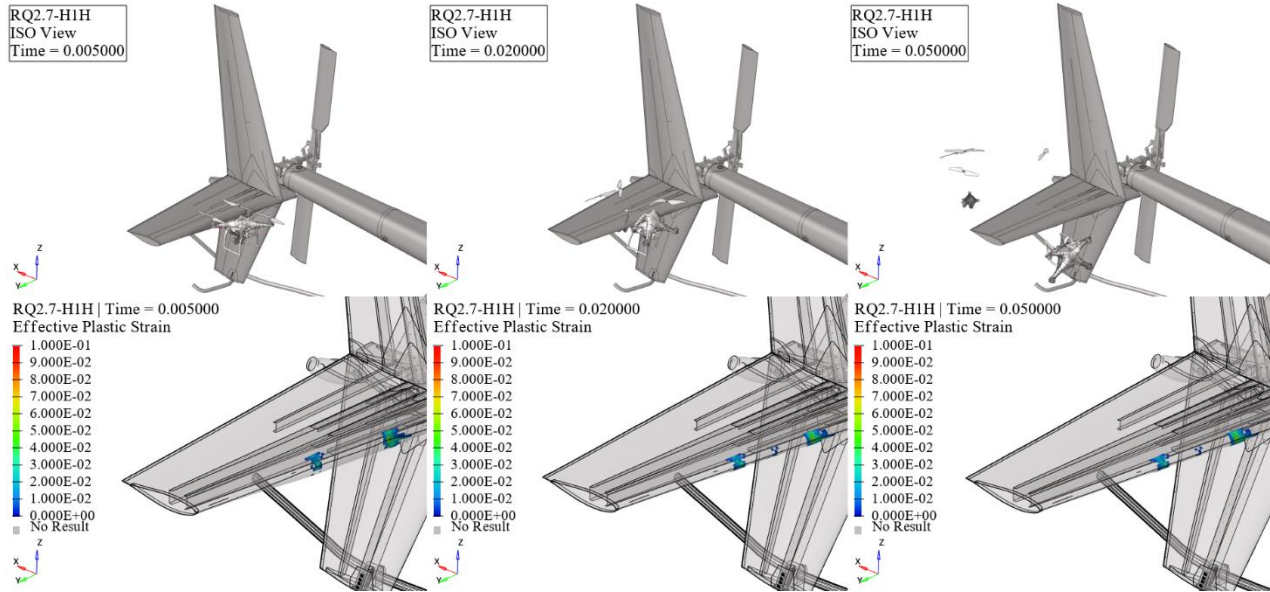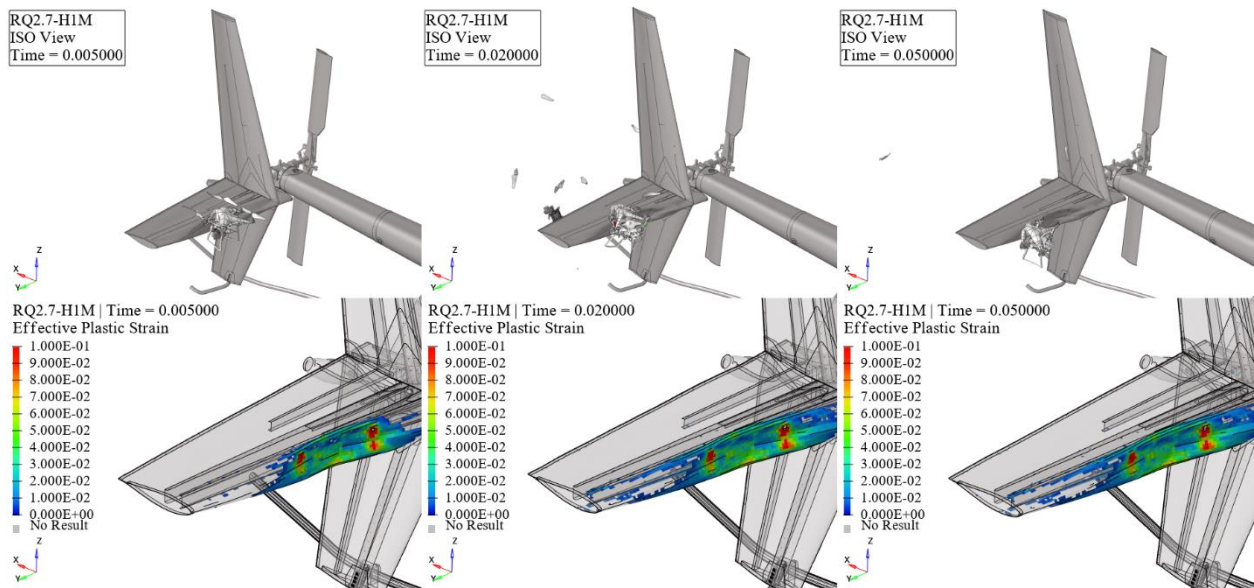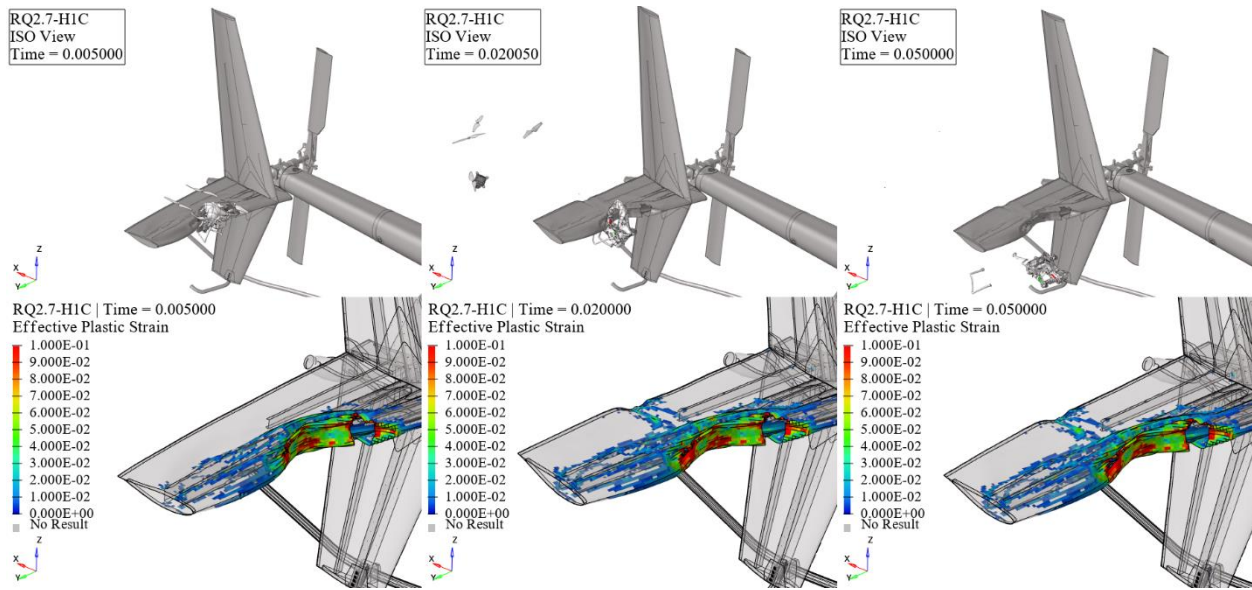

Figure 134. RQ55-H1H kinematics (top) and effective plastic strain (bottom) frames.

Figure 135. RQ55-H1M kinematics (top) and effective plastic strain (bottom) frames.

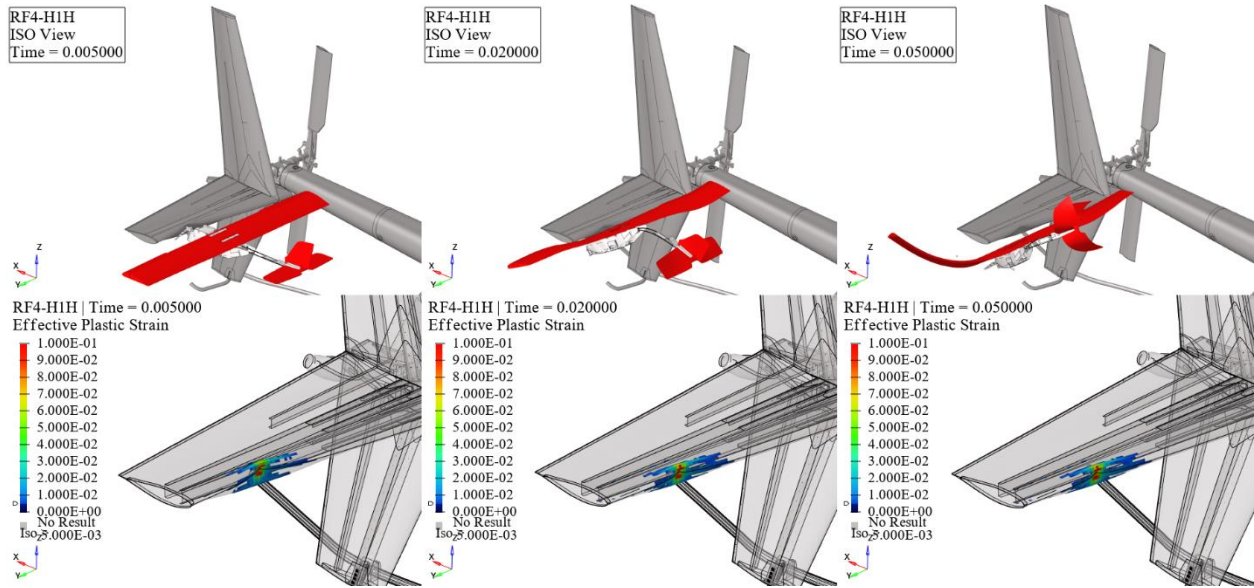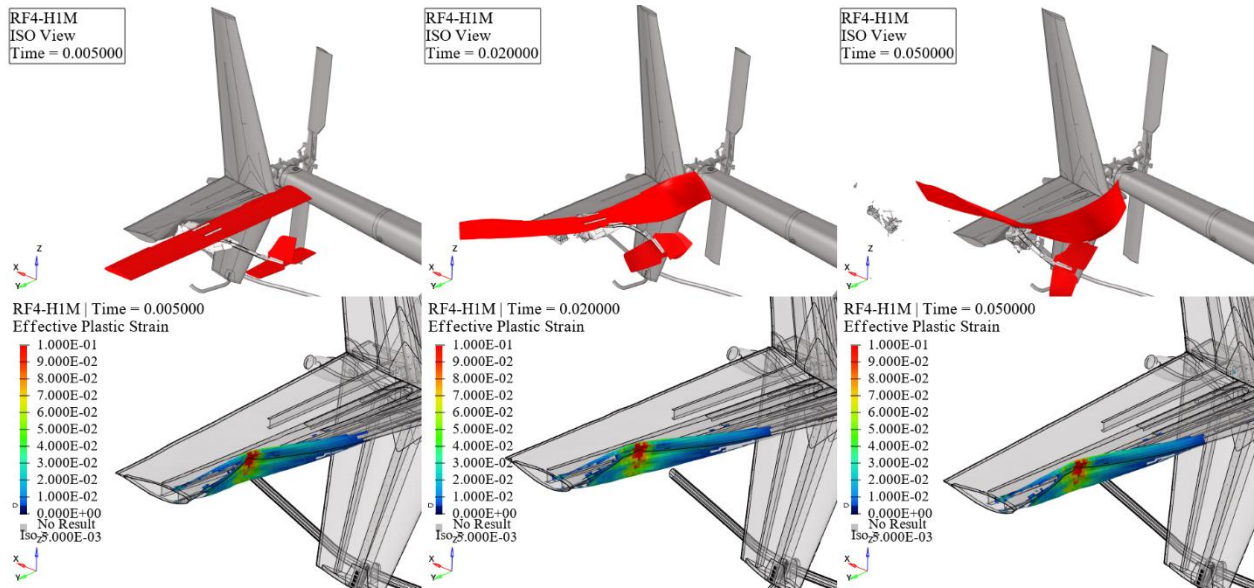Figure 136. RQ55-H1C kinematics (top) and effective plastic strain (bottom) frames.
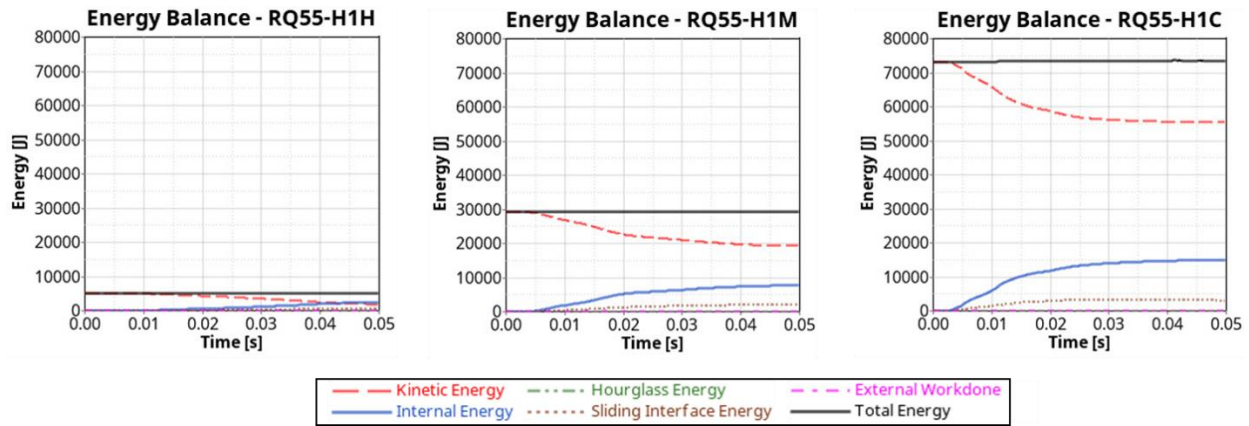
Figure 137. Horizontal stabilizer and 55 lbs. quadcopter impact energy balance.

At hover velocity, the collision between the 55 lbs. quadcopter and the horizontal stabilizer caused permanent deformation and fractures on the skin, indicating a level 3 impact severity. However, at both medium and cruise velocities, the horizontal stabilizer sustained severe damage to the primary structure, as well as damage to the stabilizer connection point and vertical stabilizer, indicating a level 4 impact severity.

5.1.8   UAS 55 lbs. Fixed Wing

The head-on collision between the 55 lbs. fixed-wing and the rotorcraft's Horizontal Stabilizer is not feasible due to the scale of the UAS. Potential collision scenarios that are feasible (not head-on) would not align with the scope of the current study.

5.2 Vertical Stabilizer

This section presents the results of the airborne collision studies for all UAS and the rotorcraft's Vertical Stabilizer. Figure 138 shows an example of the simulation setup for the Vertical Stabilizer impact with 55 lbs. quadcopter at cruise speed:
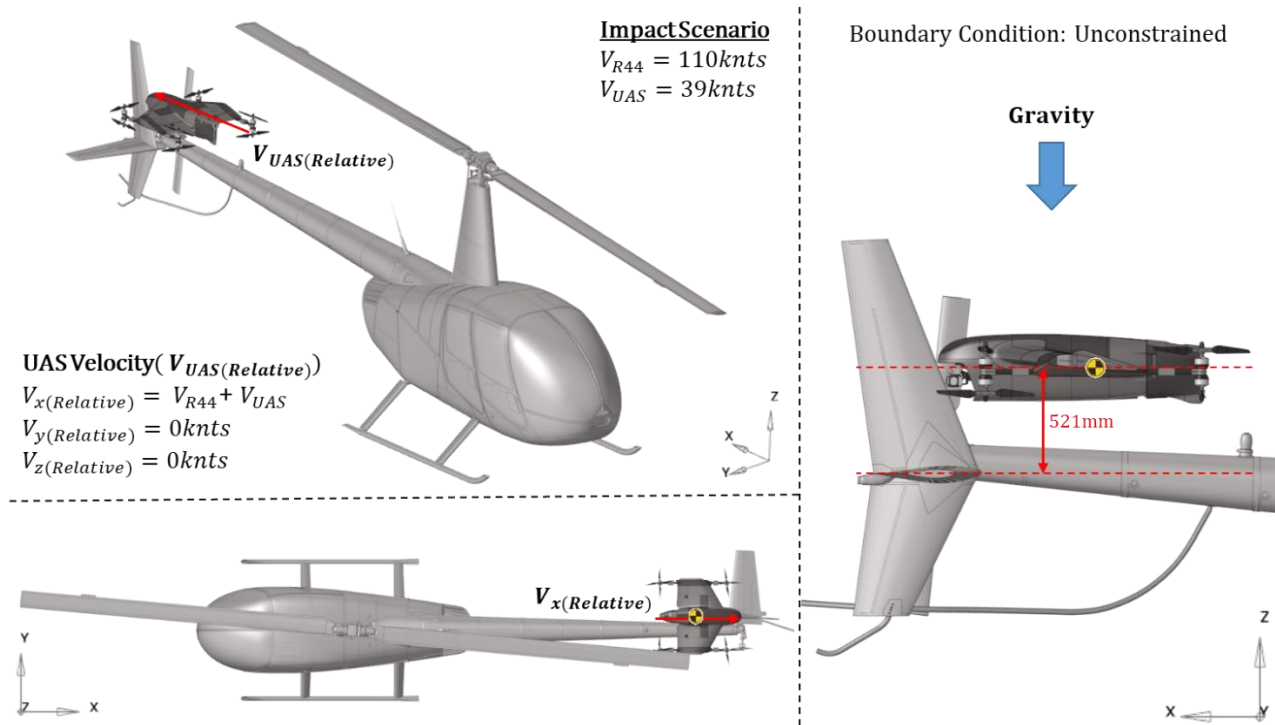
Figure 138. Simulation setup for impact between vertical stabilizer and 55 lbs. quadcopter at cruise velocity.

The rotation of the tail rotor was modeled for all vertical stabilizer to UAS impact scenarios. The tail rotor was preloaded using radial acceleration, which resulted from its constant rotational speed. This preload was simulated through explicit dynamic relaxation before the transient run, during which a rotational velocity of 254 rad/s (2425.5 RPM) was applied to simulate the rotor's rotation. Figure 139 illustrates the stable preload on the tail rotor, along with the load versus time data for the tail rotor hub cross-section during both the dynamic relaxation and transient rotation phases, demonstrating the stability of the preload.

Table 43 summarizes the damage severity level evaluation and fire risk assessment for impact cases for all UAS with the Vertical Stabilizer.
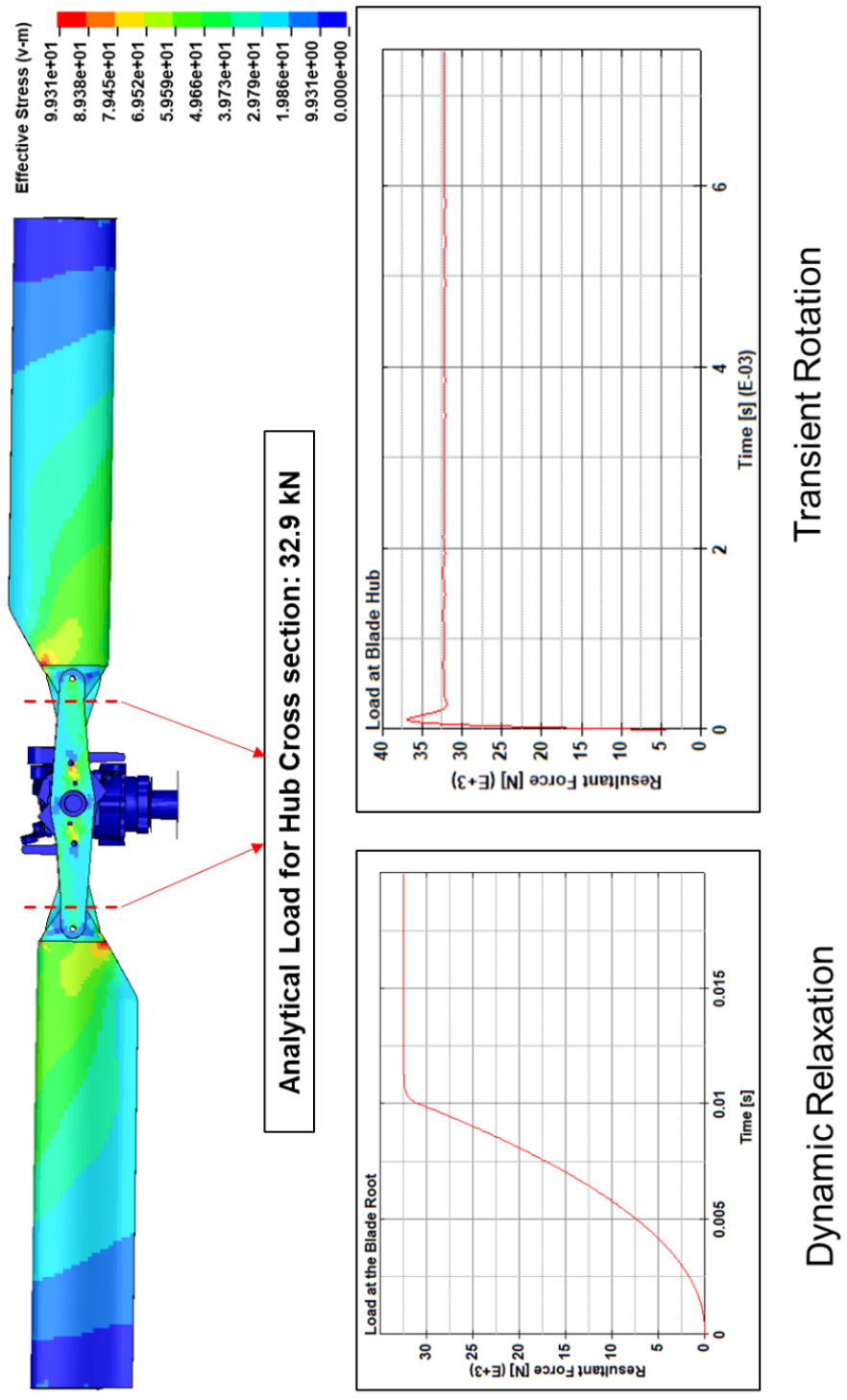
Figure 139. Tail rotor preload (Von Mises stress contour) and tail rotor hub cross section force comparison between dynamic relaxation and transient rotation.

Table 43. Vertical Stabilizer mid-air collision simulation assessment – damage severity level and fire risk.

		Case	Severity	Severity (considering tail rotor damage)	Fire Risk
Mid-air collision Rotorcraft-Vertical Stabilizer and all sUAS	Quadcopter 2.7 lbs.	RQ2.7-V1H	Level 1	Level 1	No
		RQ2.7-V1M	Level 2	Level 2	No
		RQ2.7-V1C	Level 3	Level 3	No
	Fixed-Wing 4 lbs.	RF4-V1H	Level 1	Level 4	No
		RF4-V1M	Level 3	Level 4	Yes
		RF4-V1C	Level 3	Level 4	Yes
	Quadcopter 10 lbs.	RQ10-V1H	Level 2	Level 2	No
		RQ10-V1M	Level 3	Level 3	No
		RQ10-V1C	Level 4	Level 4	No
	Fixed-Wing 12 lbs.	RF12-V1H	Level 2	Level 4	No
		RF12-V1M	Level 3	Level 4	Yes
		RF12-V1C	Level 4	Level 4	No
	Quadcopter 25 lbs.	RQ25-V1H	Level 2	Level 2	No
		RQ25-V1M	Level 3	Level 3	No
		RQ25-V1C	Level 4	Level 4	No
	Fixed-Wing 25 lbs.	RF25-V1H	Level 2	Level 4	No
		RF25-V1M	Level 4	Level 4	No
		RF25-V1C	Level 4	Level 4	No
	Quadcopter 55 lbs.	RQ55-V1H	Level 2	Level 4	No
		RQ55-V1M	Level 4	Level 4	No
		RQ55-V1C	Level 4	Level 4	No
	Fixed-Wing 55 lbs.	RF55-V1H	Level 2	Level 4	No
		RF55-V1M	Level 4	Level 4	No
		RF55-V1C	Level 4	Level 4	No

5.2.1 UAS 2.7 lbs. Quadcopter

This section delineates the findings stemming from collisions involving 2.7 lbs. quadcopter and the rotorcraft's Vertical Stabilizer at Hover, Medium, and Cruise velocities, as showcased in Figure 140, Figure 141, and Figure 142, respectively. These results unravel the temporal progression of the impact occurrences, spotlighting time intervals at 0.005s, 0.02s, and 0.05s. The upper trio of windows highlights the kinematic aspects of the impacts, while the lower trio shows the resultant effective plastic strain on the rotorcraft structures. Additionally, Figure 143 provides the energy balance plots for all three impact velocities.
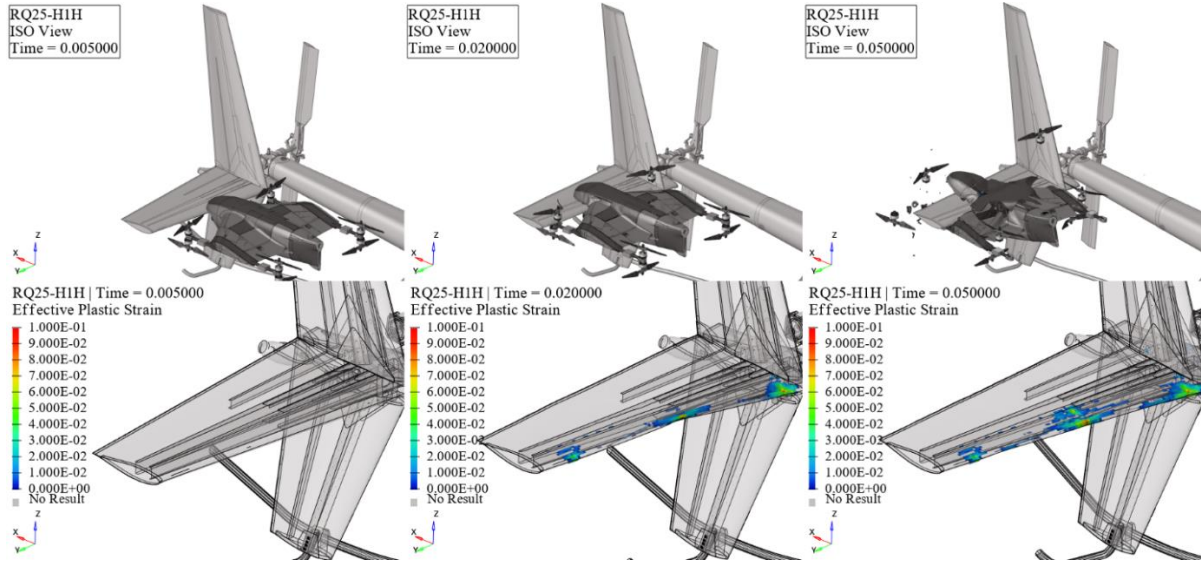

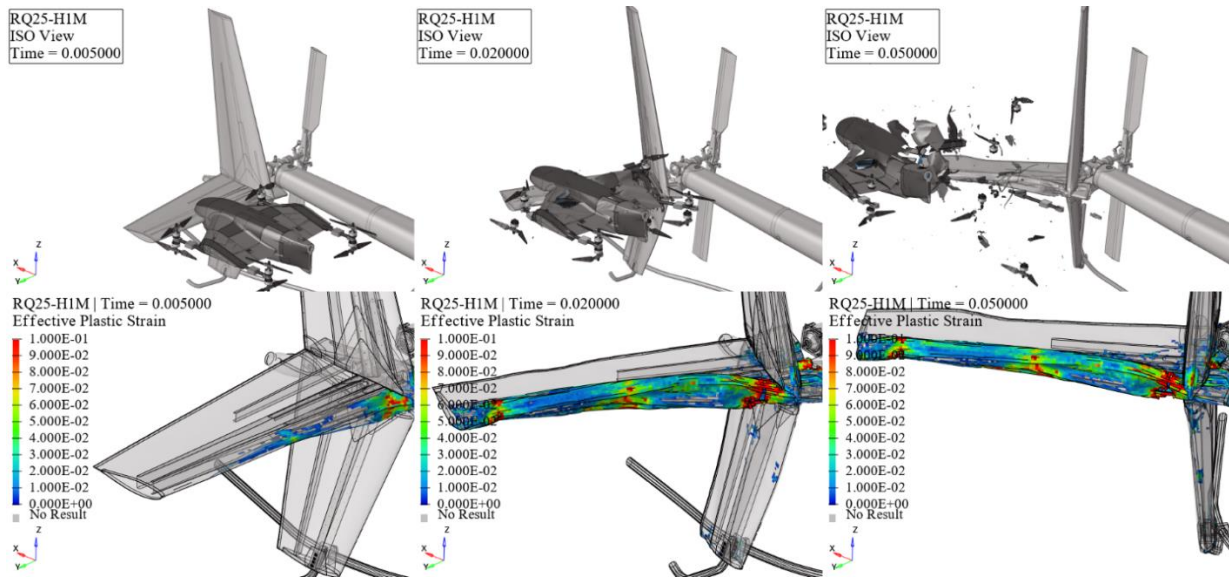Figure 140. RQ2.7-H1H kinematics (top) and effective plastic strain (bottom) frames.

Figure 141. RQ2.7-H1M kinematics (top) and effective plastic strain (bottom) frames.
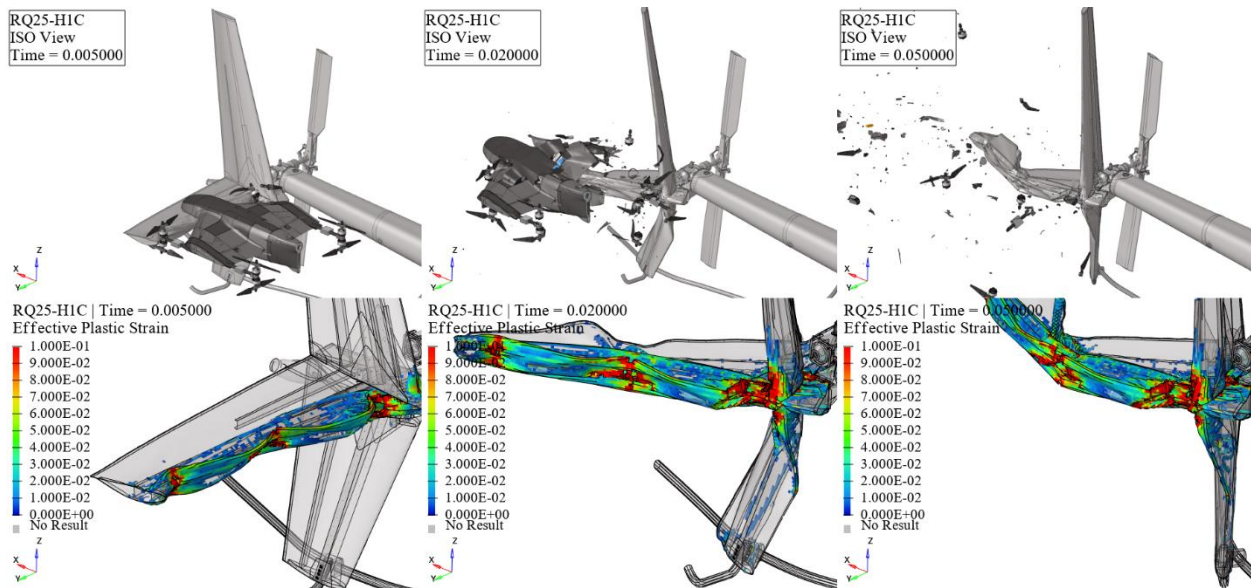
Figure 142. RQ2.7-H1C kinematics (top) and effective plastic strain (bottom) frames.
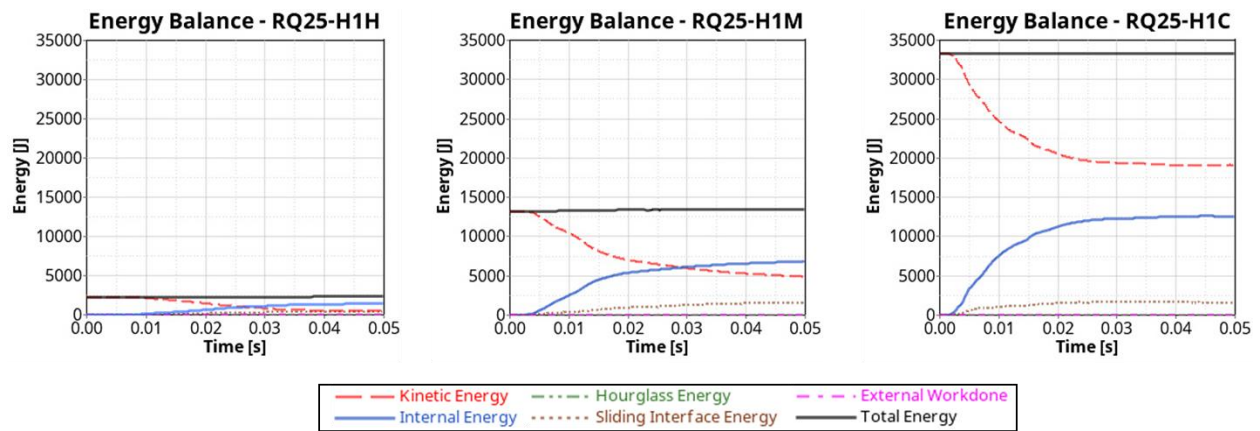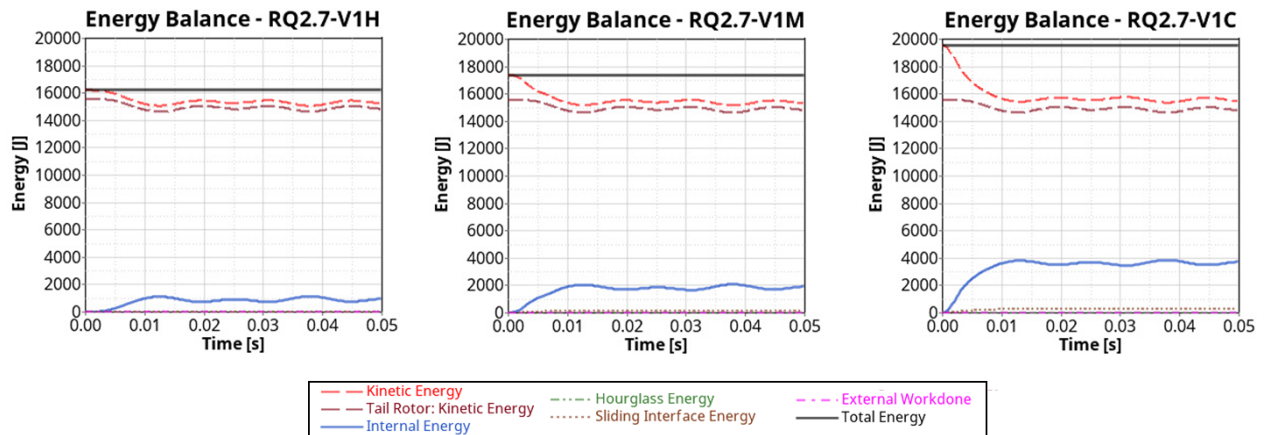

Figure 143. Vertical stabilizer and 2.7 lbs. quadcopter impact energy balance.

At hover velocity, the collision between the 2.7 lbs. quadcopter and the vertical stabilizer resulted in minor dents on the skin, indicating a level 1 impact severity. Conversely, the vertical stabilizer exhibited increased permanent deformation to the skin at medium impact velocity compared to the hover velocity, marking a level 2 impact severity. Subsequently, the vertical stabilizer sustained substantially heightened damage at cruise impact velocity compared to the hover and medium velocity impacts, characterized by major cracks and buckling of the skin, representing a level 3 impact severity. Additionally, no damage to the tail rotor was observed for all three impact velocities, so the combined impact severity for the vertical stabilizer and tail rotor remains unchanged.

5.2.2   UAS 4 lbs. Fixed-Wing

This section delineates the findings stemming from collisions involving 4 lbs. fixed-wing and the rotorcraft's Vertical Stabilizer at Hover, Medium, and Cruise velocities, as showcased in Figure 144, Figure 145, and Figure 146, respectively. These results unravel the temporal progression of

the impact occurrences, spotlighting time intervals at 0.005s, 0.02s, and 0.05s. The upper trio of windows highlights the kinematic aspects of the impacts, while the lower trio shows the resultant effective plastic strain on the rotorcraft structures. Additionally, Figure 147 provides the energy balance plots for all three impact velocities.
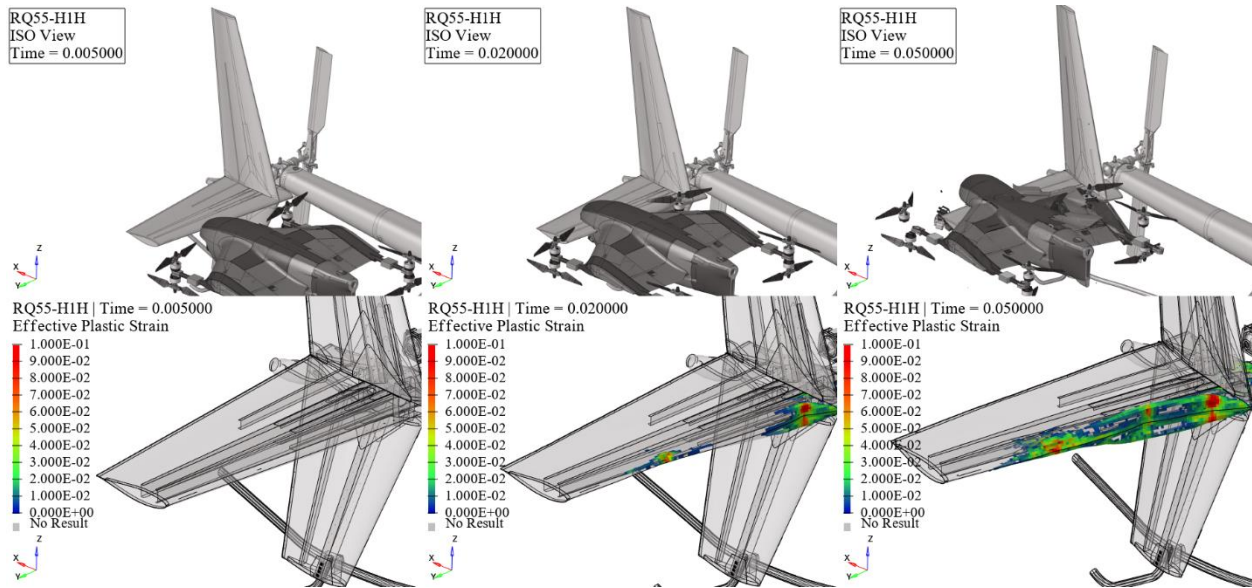

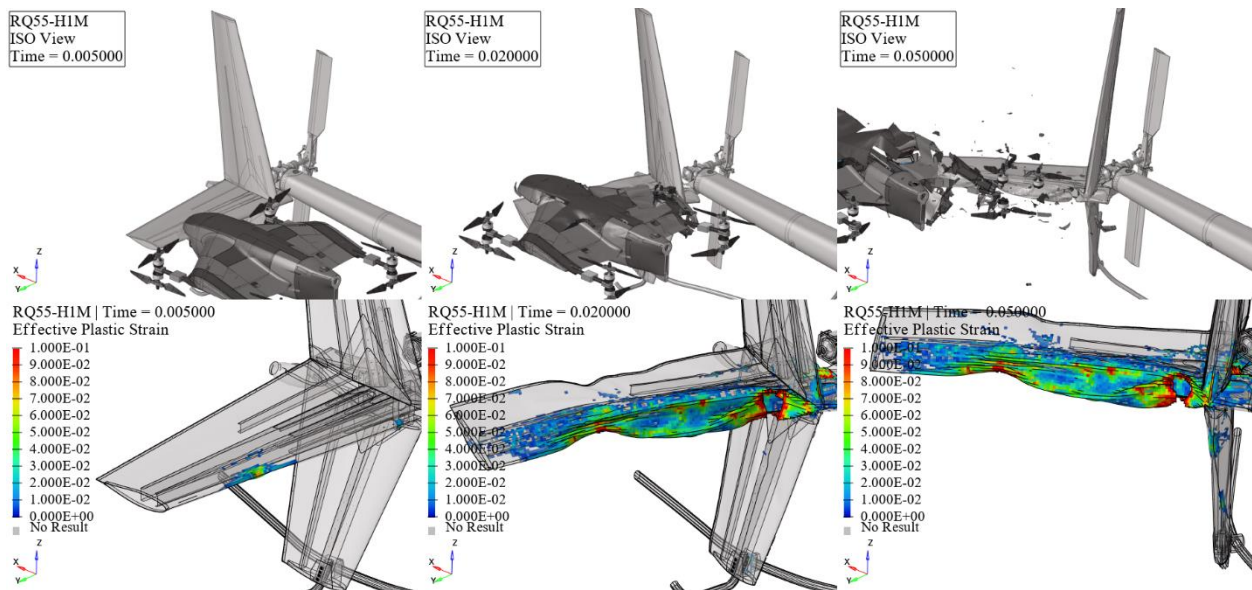Figure 144. RF4-V1H kinematics (top) and effective plastic strain (bottom) frames.

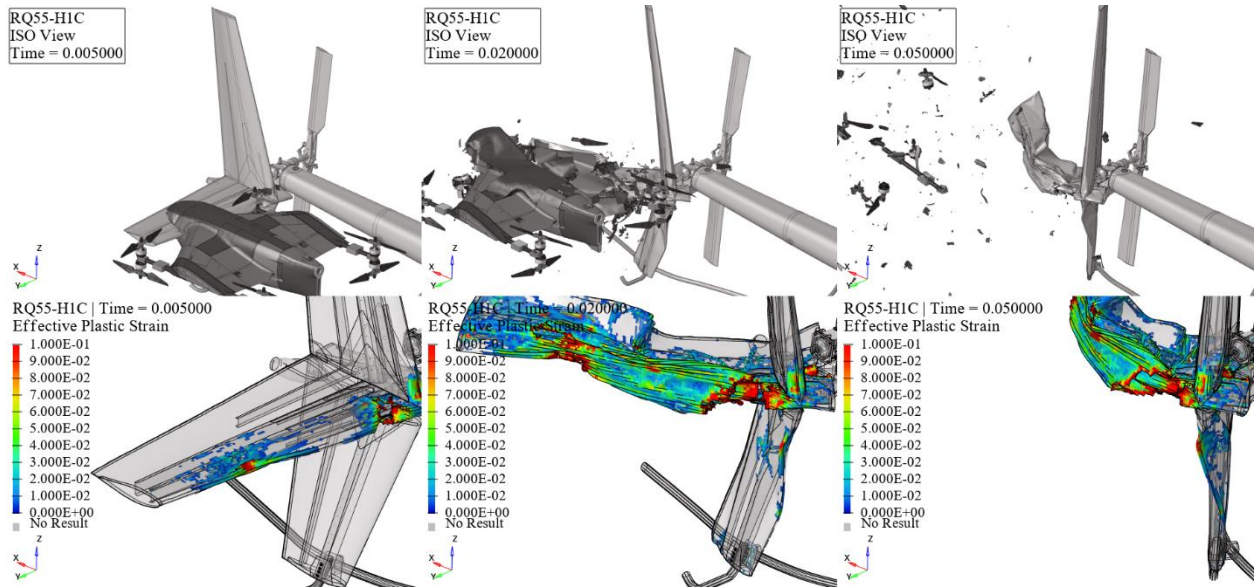Figure 145. RF4-V1M kinematics (top) and effective plastic strain (bottom) frames.

Figure 146. RF4-V1C kinematics (top) and effective plastic strain (bottom) frames.
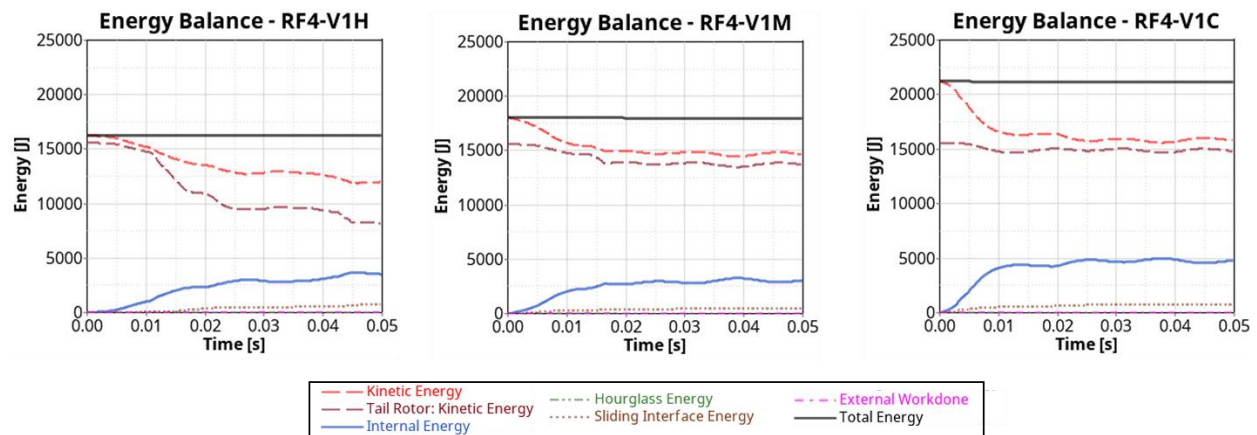
Figure 147. Vertical stabilizer and 4 lbs. fixed-wing impact energy balance.

At hover velocity, the collision between the 4 lbs. fixed-wing and the vertical stabilizer caused minor dents, indicating a level 1 impact severity for the vertical stabilizer. However, the tail rotor experienced trailing edge debonding, raising the combined impact severity for the vertical stabilizer and tail rotor to level 4 due to the adverse effect on flight stability. Conversely, the vertical stabilizer sustained significant skin fractures at medium impact velocity, indicating a level 3 impact severity. Although the tail rotor avoided contact with the UAS in this scenario, a similar impact could result in a combined severity level of 4 for both the vertical stabilizer and tail rotor. Subsequently, the vertical stabilizer suffered major skin cracks and minor primary spar damage at cruise impact velocity, resulting in a level 3 impact severity. Again, the tail rotor avoided the UAS in this scenario, but the combined severity could reach level 4 under different conditions.

5.2.3 UAS 10 lbs. Quadcopter

This section delineates the findings stemming from collisions involving 10 lbs. quadcopter and the rotorcraft's Vertical Stabilizer at Hover, Medium, and Cruise velocities, as showcased in Figure

124

148, Figure 149, and Figure 150, respectively. These results unravel the temporal progression of the impact occurrences, spotlighting time intervals at 0.005s, 0.02s, and 0.05s. The upper trio of windows highlights the kinematic aspects of the impacts, while the lower trio shows the resultant effective plastic strain on the rotorcraft structures. Additionally, Figure 151 provides the energy balance plots for all three impact velocities.

Figure 148. RQ10-V1H kinematics (top) and effective plastic strain (bottom) frames.

Figure 149. RQ10-V1M kinematics (top) and effective plastic strain (bottom) frames.

Figure 150. RQ10-V1C kinematics (top) and effective plastic strain (bottom) frames.

Figure 151. Vertical stabilizer and 10 lbs. quadcopter impact energy balance.

The collision between the 10 lbs. quadcopter and the vertical stabilizer at hover velocity caused permanent skin deformation, indicating a level 2 impact severity. The vertical stabilizer sustained significant skin fractures and buckling at medium impact velocity, resulting in a level 3 impact severity. The vertical stabilizer experienced severe damage at cruise impact velocity, leading to a level 4 impact severity. Across all three impact velocities, no tail rotor damage was observed, so the combined impact severity for the vertical stabilizer and tail rotor remains unchanged.

5.2.4 UAS 12 lbs. Fixed-Wing

This section delineates the findings stemming from collisions involving 12 lbs. fixed-wing and the rotorcraft's Vertical Stabilizer at Hover, Medium, and Cruise velocities, as showcased in Figure 152, Figure 153, and Figure 154, respectively. These results unravel the temporal progression of the impact occurrences, spotlighting time intervals at 0.005s, 0.02s, and 0.05s. The upper trio of windows highlights the kinematic aspects of the impacts, while the lower trio shows the resultant

126

effective plastic strain on the rotorcraft structures. Additionally, Figure 155 provides the energy balance plots for all three impact velocities.
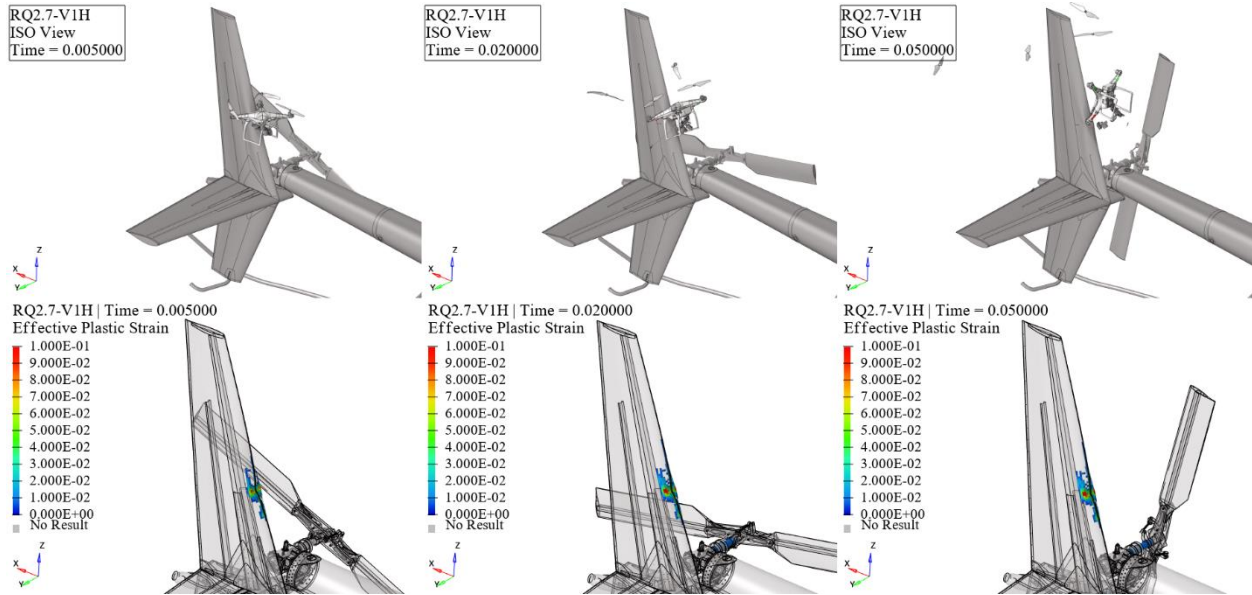

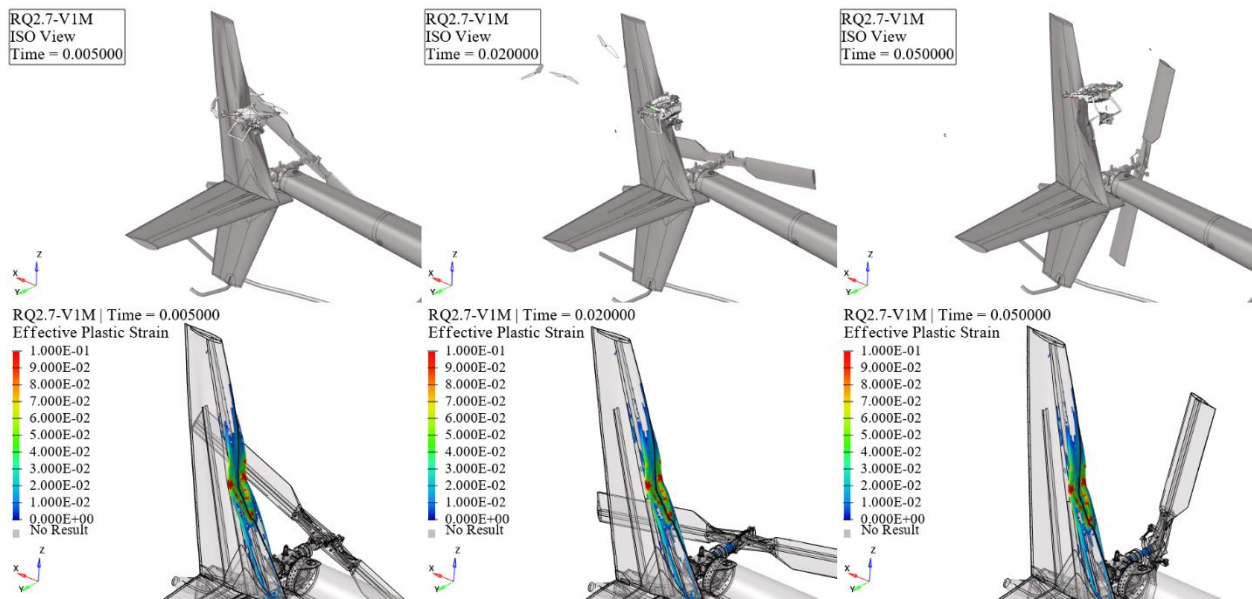Figure 152. RF12-V1H kinematics (top) and effective plastic strain (bottom) frames.

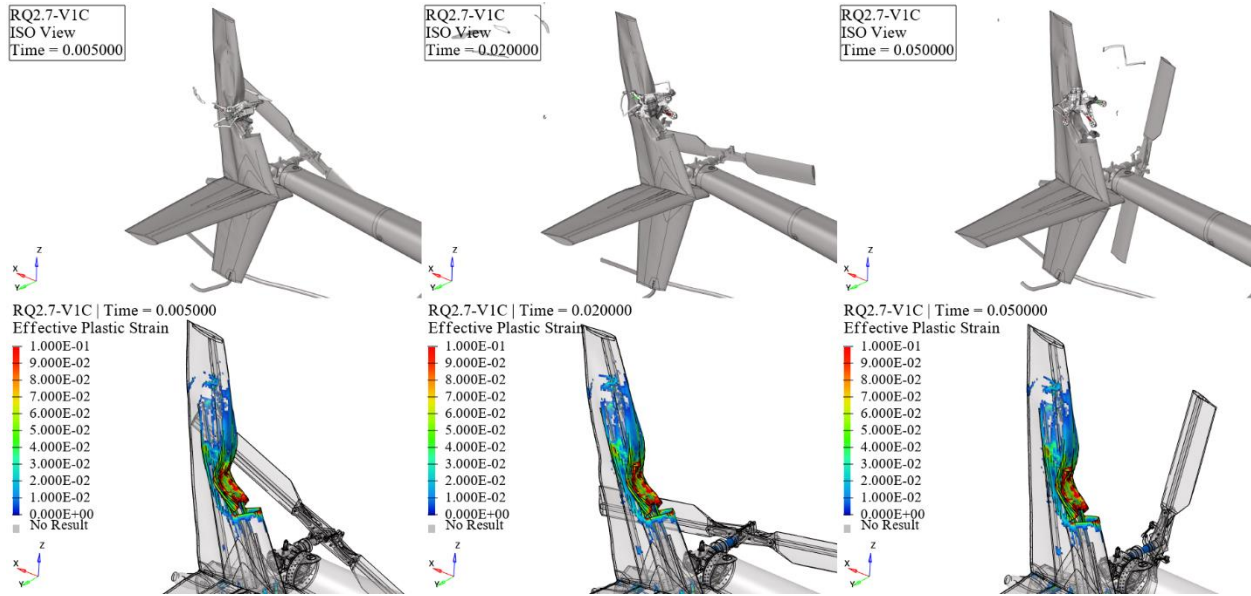Figure 153. RF12-V1M kinematics (top) and effective plastic strain (bottom) frames.

Figure 154. RF12-V1C kinematics (top) and effective plastic strain (bottom) frames.
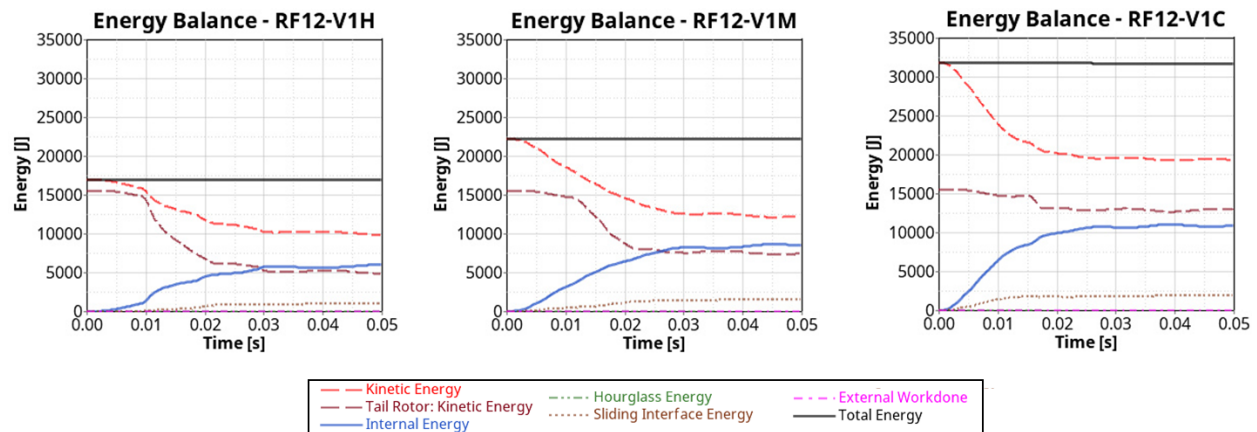
Figure 155. Vertical stabilizer and 12 lbs. fixed-wing impact energy balance.

At hover velocity, the collision between the 12 lbs. fixed wing and the vertical stabilizer caused permanent skin deformation and minor cracks but no penetration of UAS parts into the structure, indicating a level 2 impact severity. The vertical stabilizer exhibited significant skin fractures at medium impact velocity, indicating a level 3 impact severity. The vertical stabilizer sustained severe damage at cruise impact velocity, resulting in a level 4 impact severity. Additionally, all three impact velocities caused severe damage to the tail rotor, including trailing edge debonding, which would impair flight stability, resulting in a combined impact severity of level 4 for both the vertical stabilizer and tail rotor.

5.2.5 UAS 25 lbs. Quadcopter

This section delineates the findings stemming from collisions involving 25 lbs. quadcopter and the rotorcraft's Vertical Stabilizer at Hover, Medium, and Cruise velocities, as showcased in Figure 156, Figure 157, and Figure 158, respectively. These results unravel the temporal progression of the impact occurrences, spotlighting time intervals at 0.005s, 0.02s, and 0.05s. The upper trio of

windows highlights the kinematic aspects of the impacts, while the lower trio shows the resultant effective plastic strain on the rotorcraft structures. Additionally, Figure 159 provides the energy balance plots for all three impact velocities.
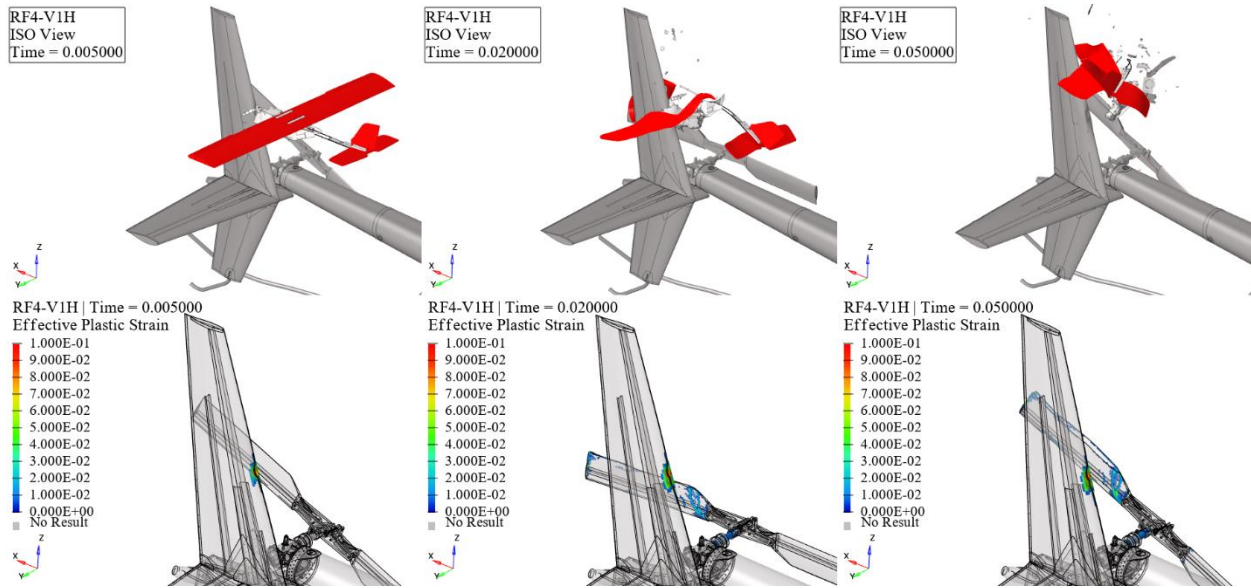

Figure 156. RQ25-V1H kinematics (top) and effective plastic strain (bottom) frames.
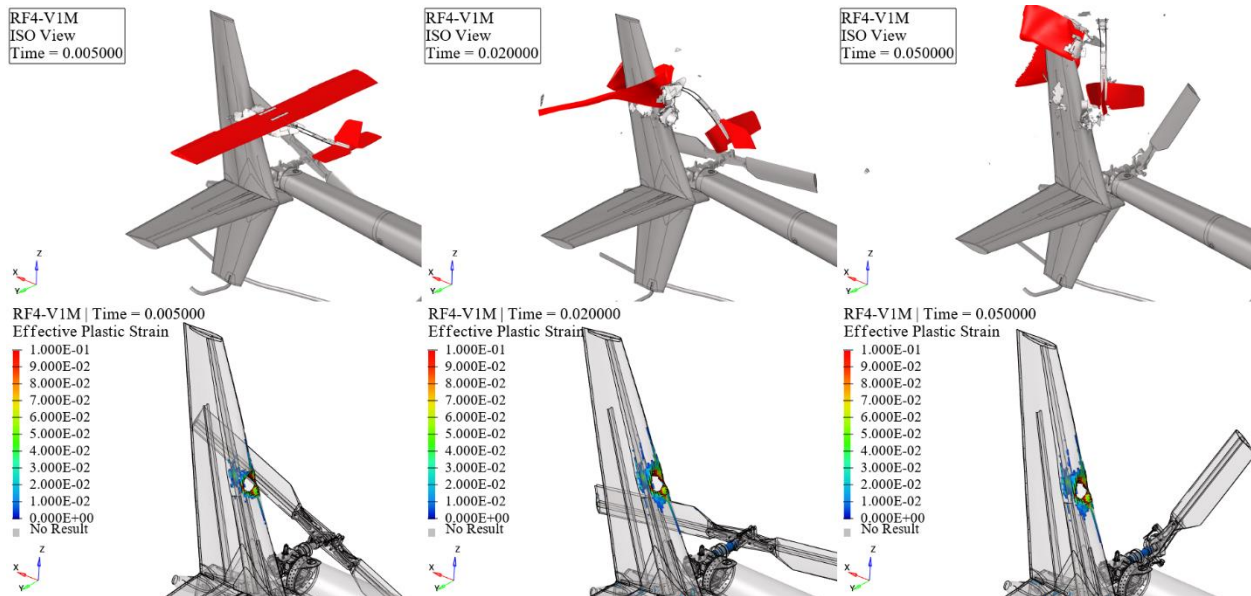

Figure 157. RQ25-V1M kinematics (top) and effective plastic strain (bottom) frames.
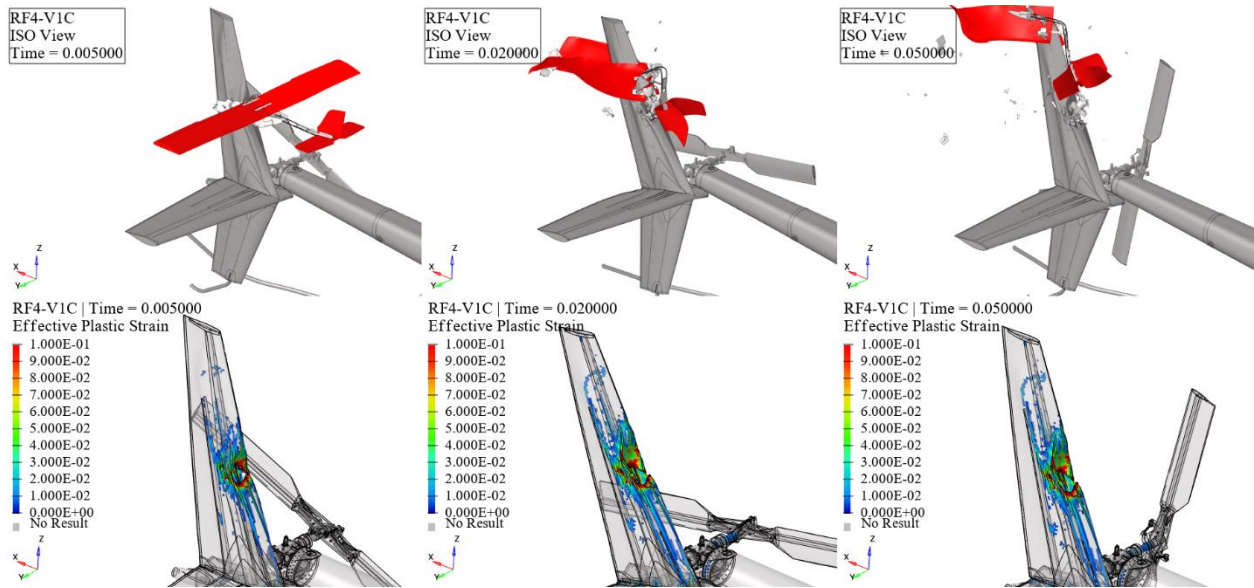
Figure 158. RQ25-V1C kinematics (top) and effective plastic strain (bottom) frames.


Figure 159. Vertical stabilizer and 25 lbs. quadcopter impact energy balance.

The collision between the 25 lbs. quadcopter and the vertical stabilizer at hover velocity caused permanent skin deformation, indicating a level 2 impact severity. The vertical stabilizer exhibited significant skin deformation, buckling, and damage at medium impact velocity, indicating a level 3 impact severity. The vertical stabilizer sustained severe damage at cruise impact velocity, resulting in a level 4 impact severity. Across all three impact velocities, negligible tail rotor damage was observed, so the combined impact severity for the vertical stabilizer and tail rotor remains unchanged.

5.2.6   UAS 25 lbs. Fixed-Wing

This section delineates the findings stemming from collisions involving 25 lbs. fixed-wing and the rotorcraft's Vertical Stabilizer at Hover, Medium, and Cruise velocities, as showcased in Figure 160, Figure 161, and Figure 162, respectively. These results unravel the temporal progression of the impact occurrences, spotlighting time intervals at 0.005s, 0.02s, and 0.05s. The upper trio of windows highlights the kinematic aspects of the impacts, while the lower trio shows the resultant

effective plastic strain on the rotorcraft structures. Additionally, Figure 163 provides the energy balance plots for all three impact velocities.
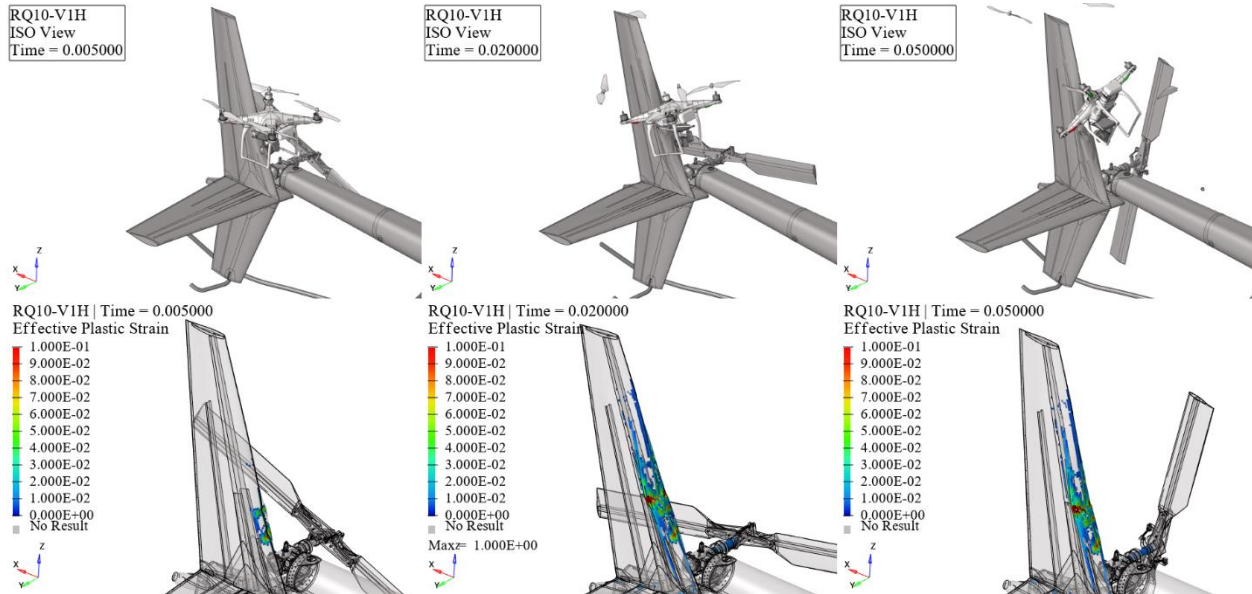

Figure 160. RF25-V1H kinematics (top) and effective plastic strain (bottom) frames.
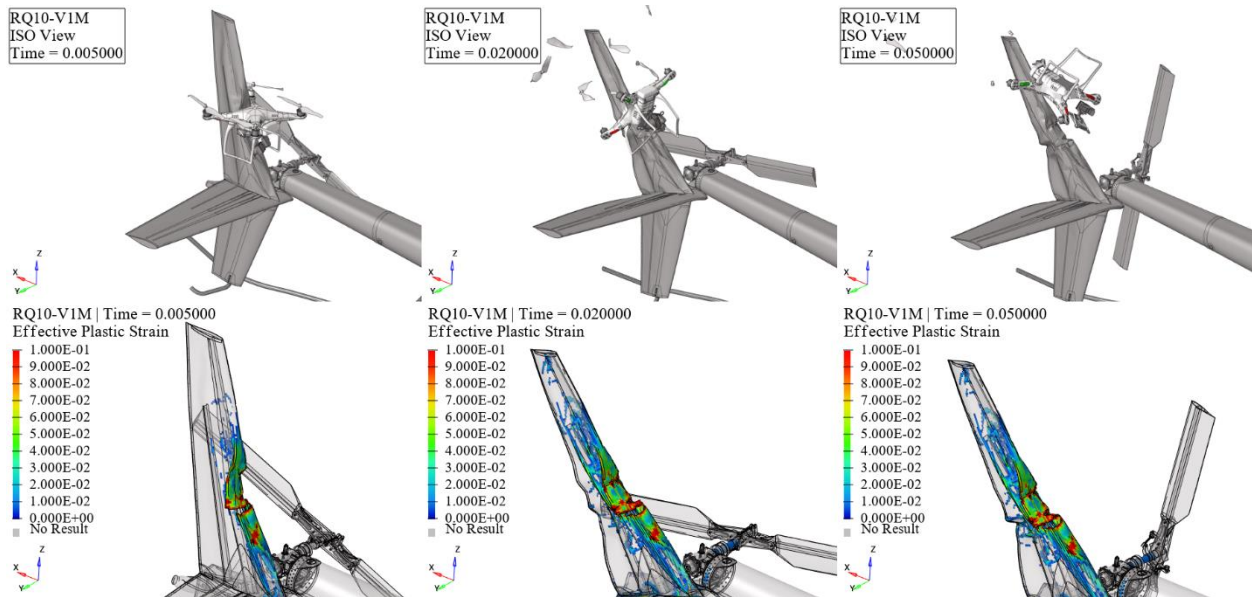

Figure 161. RF25-V1M kinematics (top) and effective plastic strain (bottom) frames.
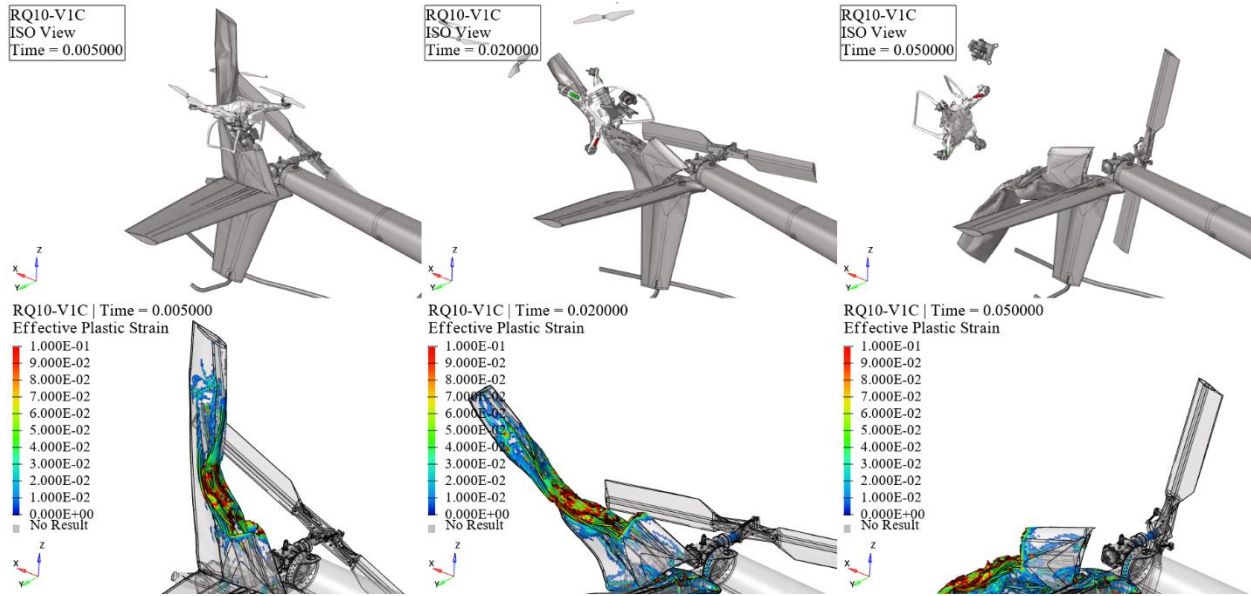
Figure 162. RF25-V1C kinematics (top) and effective plastic strain (bottom) frames.
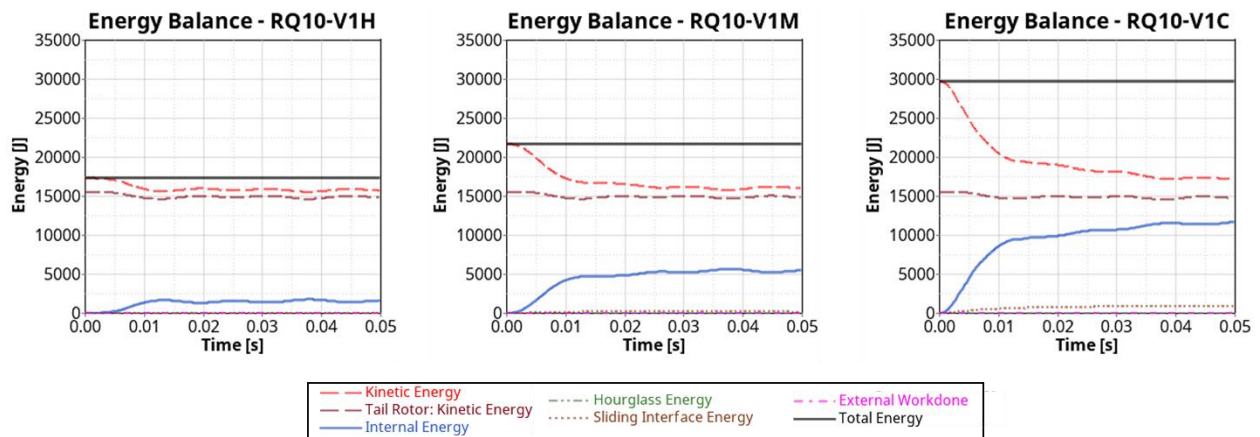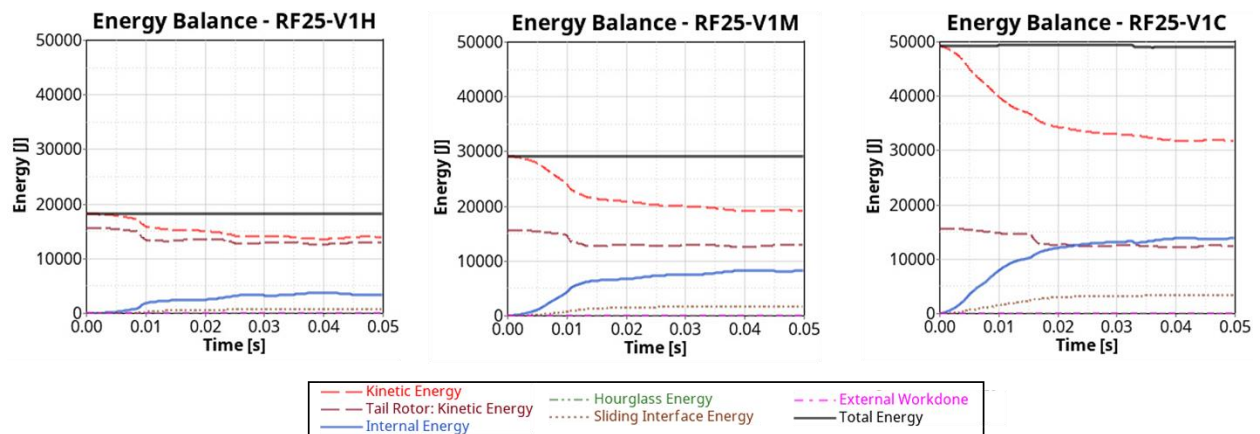

Figure 163. Vertical stabilizer and 25 lbs. fixed-wing impact energy balance.

At hover velocity, the collision between the 25 lbs. fixed-wing and the vertical stabilizer caused various permanent skin deformations, indicating a level 2 impact severity. In contrast, the vertical stabilizer sustained severe damage at medium and cruise impact velocities, resulting in a level 4 impact severity. Additionally, all three impact velocities caused considerable damage to the tail rotor, including trailing edge debonding, compromising flight stability, and resulting in a combined impact severity of level 4 for the vertical stabilizer and tail rotor.

5.2.7 UAS 55 lbs. Quadcopter

This section delineates the findings stemming from collisions involving 55 lbs. quadcopter and the rotorcraft's Vertical Stabilizer at Hover, Medium, and Cruise velocities, as showcased in Figure 164, Figure 165, and Figure 166, respectively. These results unravel the temporal progression of the impact occurrences, spotlighting time intervals at 0.005s, 0.02s, and 0.05s. The upper trio of windows highlights the kinematic aspects of the impacts, while the lower trio shows the resultant

132

effective plastic strain on the rotorcraft structures. Additionally, Figure 167 provides the energy balance plots for all three impact velocities.
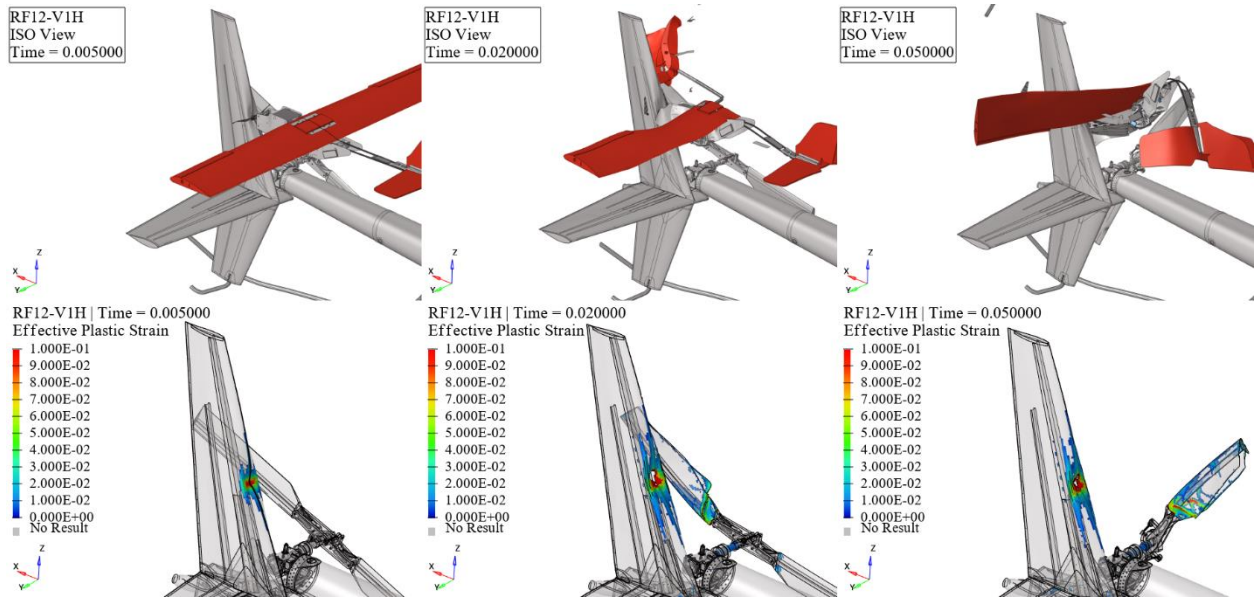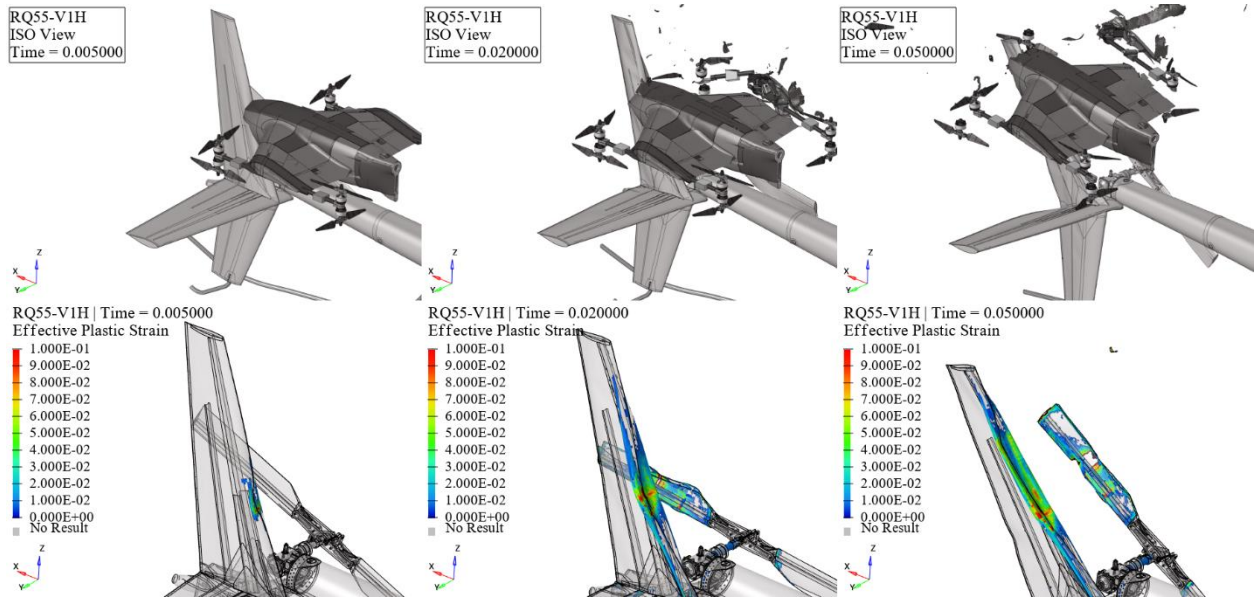

Figure 164. RQ55-V1H kinematics (top) and effective plastic strain (bottom) frames.
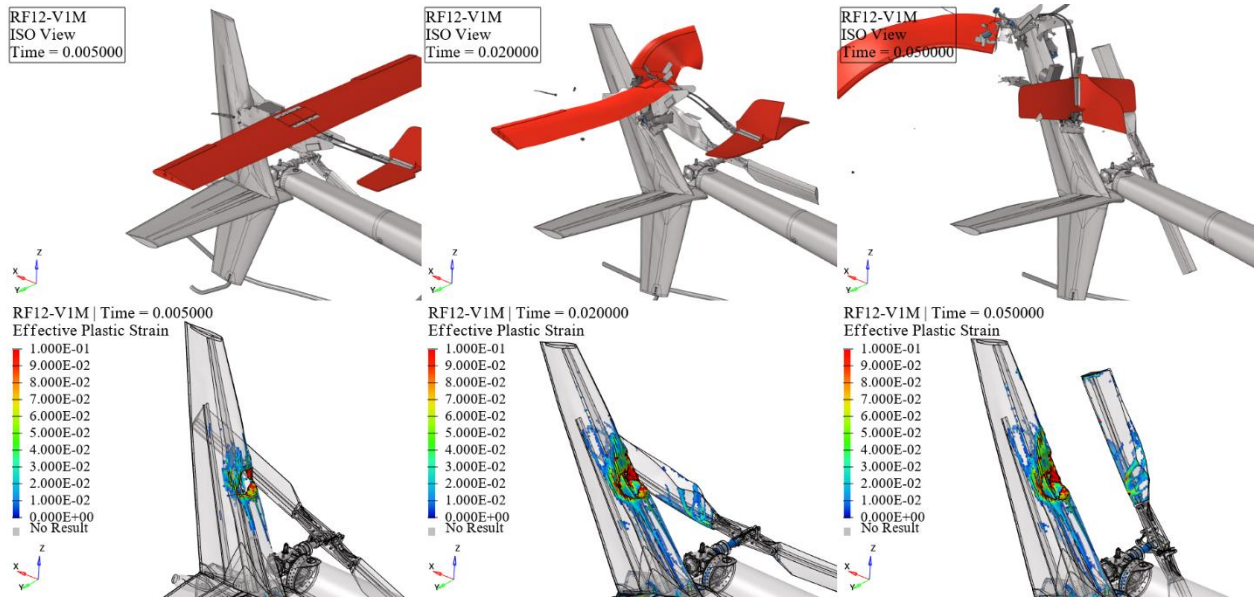

Figure 165. RQ55-V1M kinematics (top) and effective plastic strain (bottom) frames.
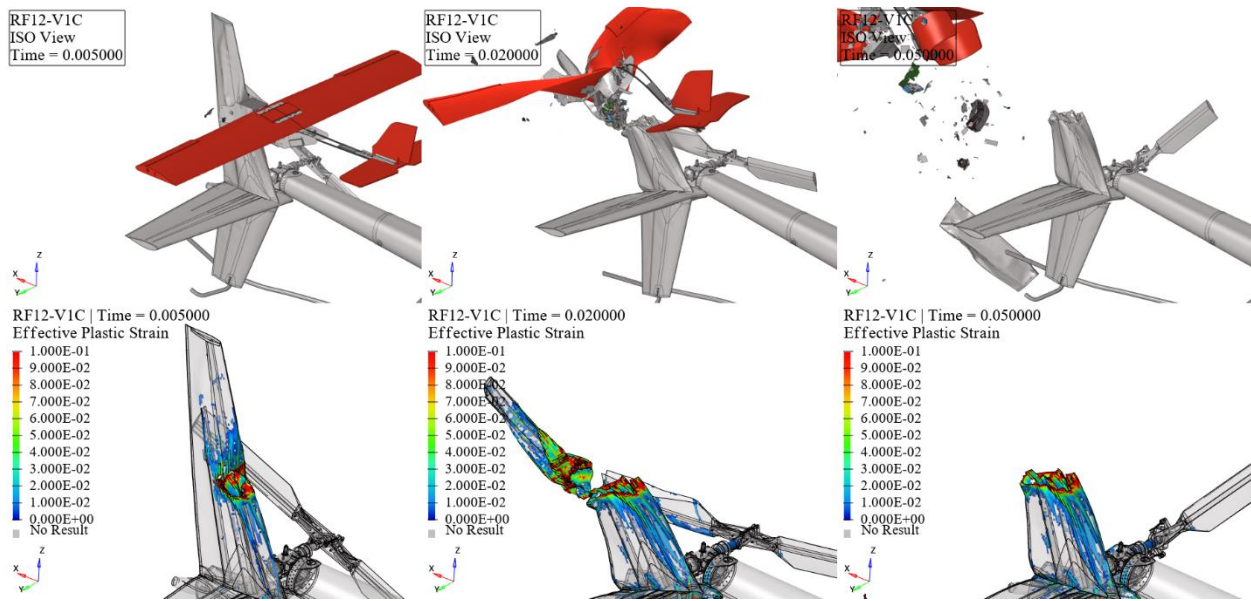
Figure 166. RQ55-V1C kinematics (top) and effective plastic strain (bottom) frames.


Figure 167. Vertical stabilizer and 55 lbs. quadcopter impact energy balance.

The collision between the 55 lbs. quadcopter and the vertical stabilizer at hover velocity caused various permanent skin deformations, indicating a level 2 impact severity. The vertical stabilizer sustained severe damage at medium and cruise impact velocities, resulting in a level 4 impact severity. Additionally, all three impact velocities caused severe damage to the tail rotor, including heavy deformation, material loss, and trailing edge debonding, significantly compromising flight stability, indicating a combined impact severity of level 4 for the vertical stabilizer and tail rotor.

5.2.8 UAS 55 lbs. Fixed-Wing

This section delineates the findings stemming from collisions involving 55 lbs. fixed-wing and the rotorcraft's Vertical Stabilizer at Hover, Medium, and Cruise velocities, as showcased in Figure 168, Figure 169, and Figure 170, respectively. These results unravel the temporal progression of the impact occurrences, spotlighting time intervals at 0.005s, 0.02s, and 0.05s. The upper trio of windows highlights the kinematic aspects of the impacts, while the lower trio shows the resultant

effective plastic strain on the rotorcraft structures. Additionally, Figure 171 provides the energy balance plots for all three impact velocities.
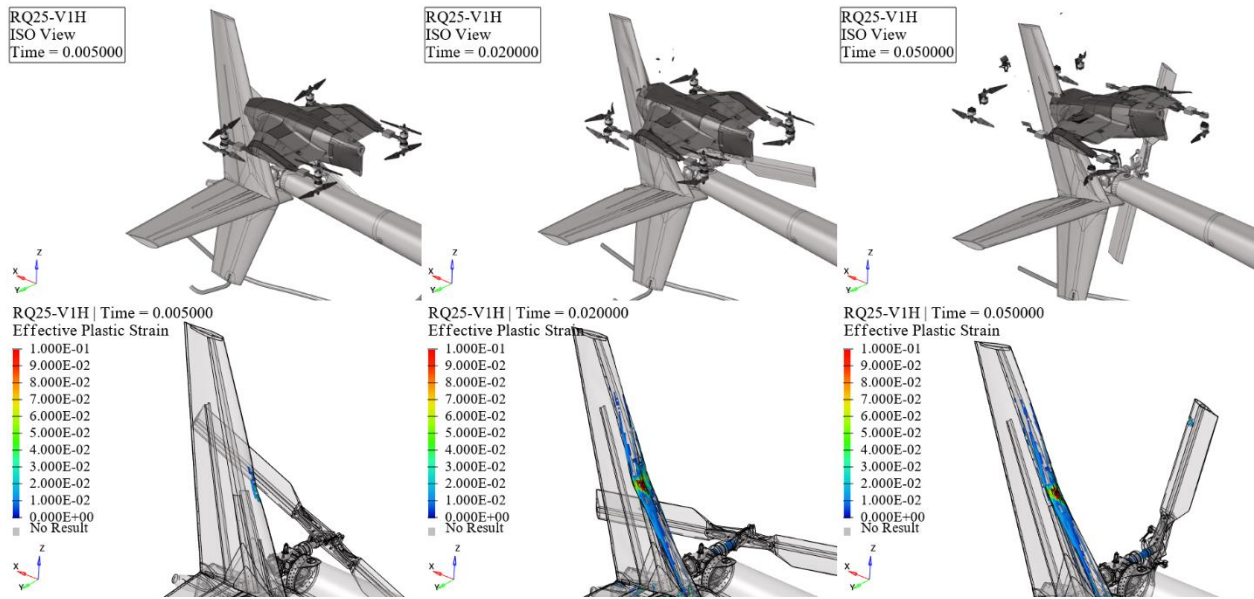

Figure 168. RF55-V1H kinematics (top) and effective plastic strain (bottom) frames.
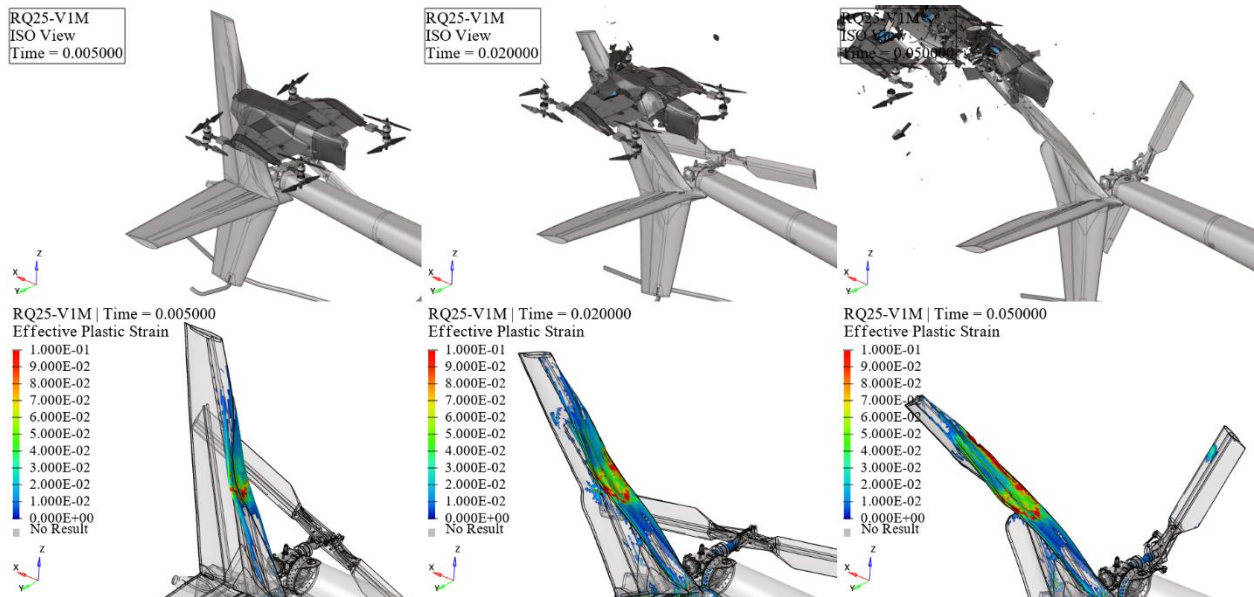

Figure 169. RF55-V1M kinematics (top) and effective plastic strain (bottom) frames.
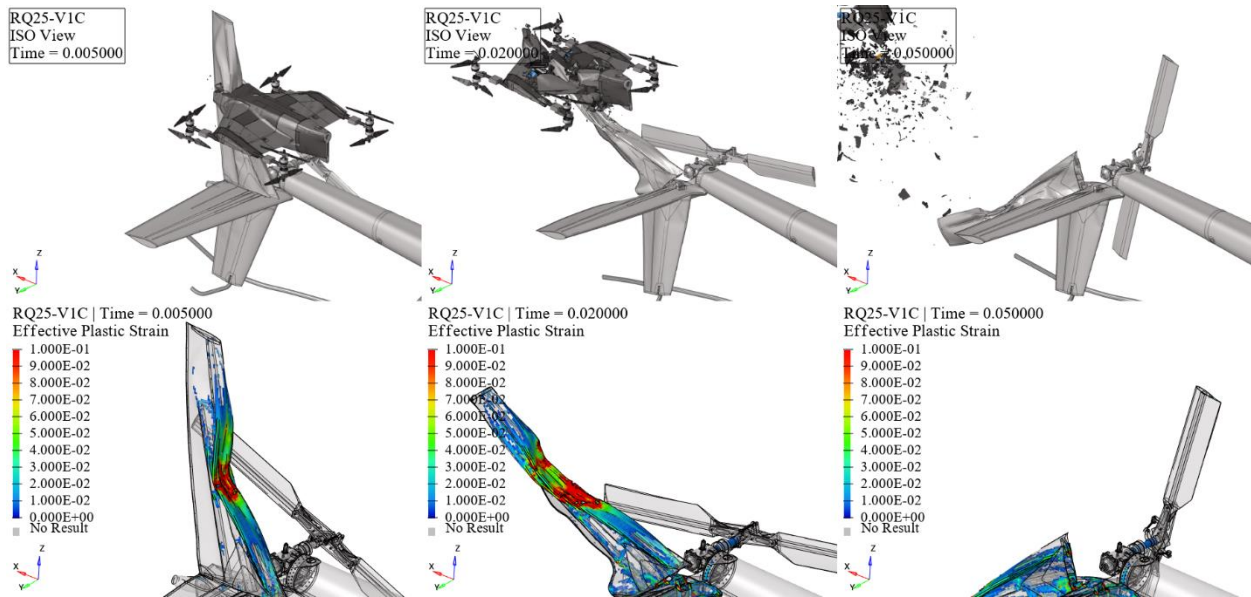
Figure 170. RF55-V1C kinematics (top) and effective plastic strain (bottom) frames.
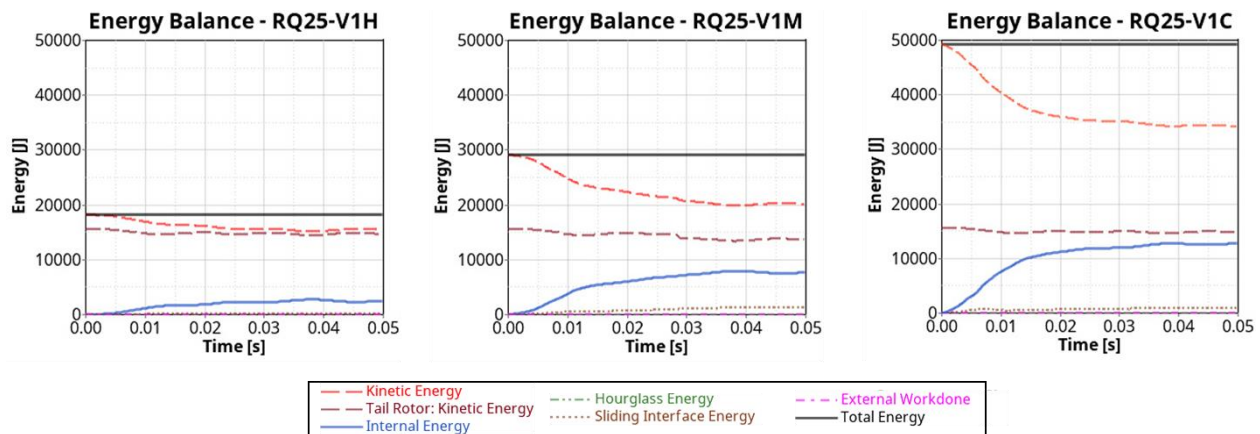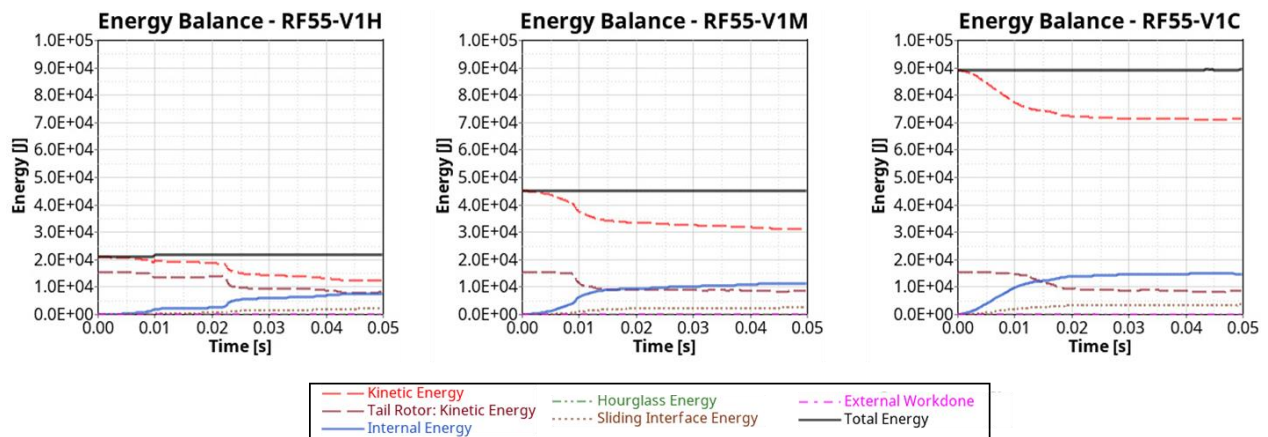

Figure 171. Vertical stabilizer and 55 lbs. fixed-wing impact energy balance.

At hover velocity, the collision between the 55 lbs. fixed-wing and the vertical stabilizer caused various permanent skin deformations, indicating a level 2 impact severity. The vertical stabilizer sustained severe damage at medium and cruise impact velocities, resulting in a level 4 impact severity. Additionally, all three impact velocities caused severe damage to the tail rotor, including heavy deformation, material loss, and trailing edge debonding, significantly compromising flight stability and resulting in a combined impact severity of level 4 for the vertical stabilizer and tail rotor.

5.3 Mast

This section presents the results of the airborne collision studies for all UAS and the rotorcraft's Mast. Figure 172 shows an example of the simulation setup for the Mast impact with 55 lbs. quadcopter at cruise speed.
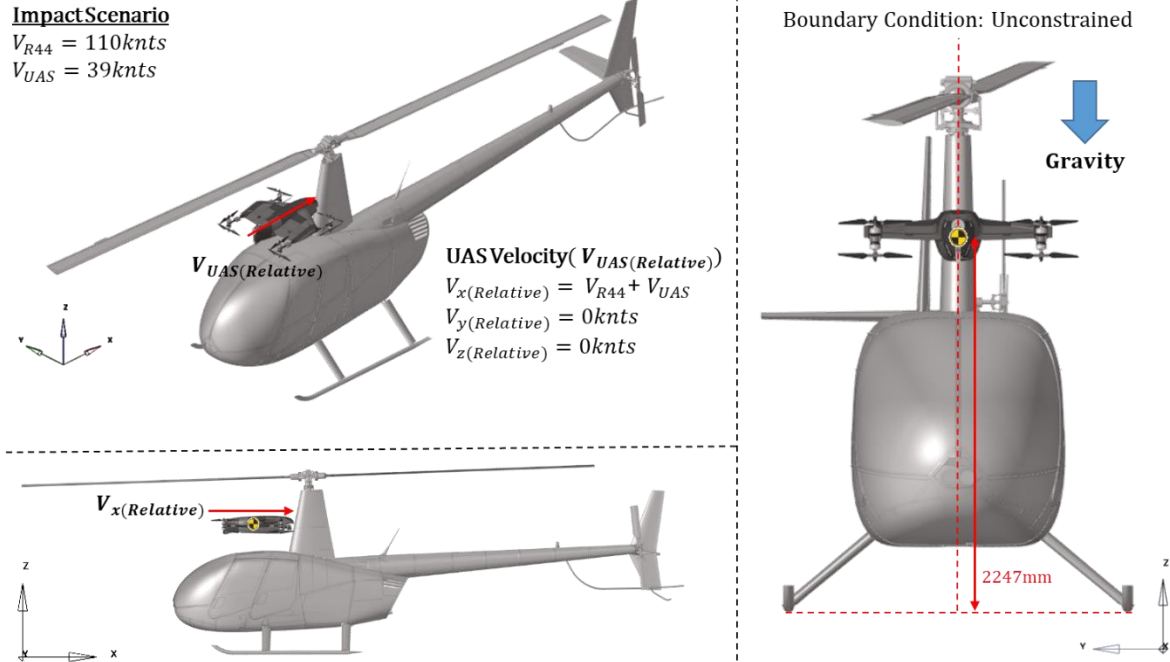
Figure 172. Simulation setup for impact between the mast and 55 lbs. quadcopter at cruise.

Within the mast, the skin shields crucial rotor blade components necessary for effective rotorcraft control. Consequently, any severe damage or deformation to these parts, such as the rotor blade links, could lead to a loss of rotorcraft control, potentially resulting in severe consequences. Figure 173 shows the difference between the damages of the internal components of the mast that result in a level 3 and level 4 impact severity, respectively.
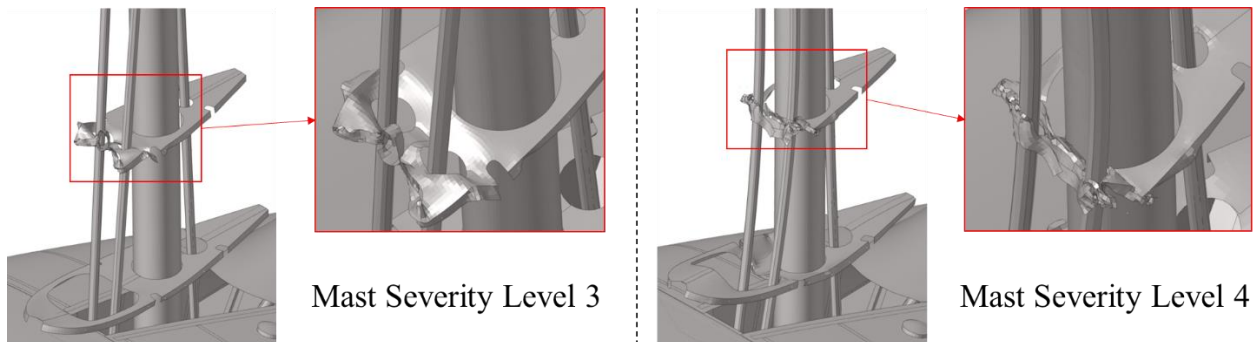
Figure 173. Mast severity level 3 and severity level 4 internal damage comparison.

Table 44 summarizes the damage severity level evaluation and fire risk assessment for impact cases for all UAS with the Mast.

Table 44. Mast mid-air collision simulation assessment – damage severity level and fire risk.

		Case	Severity	Fire Risk
Mid-air collision Rotorcraft-Mast and all sUAS	Quadcopter 2.7 lbs.	RQ2.7-M1H	Level 1	No
		RQ2.7-M1M	Level 2	No
		RQ2.7-M1C	Level 2	No
	Fixed-Wing 4 lbs.	RF4-M1H	Level 1	No
		RF4-M1M	Level 2	No
		RF4-M1C	Level 3	Yes
	Quadcopter 10 lbs.	RQ10-M1H	Level 2	No
		RQ10-M1M	Level 2	No
		RQ10-M1C	Level 3	No
	Fixed-Wing 12 lbs.	RF12-M1H	Level 2	No
		RF12-M1M	Level 2	No
		RF12-M1C	Level 3	No
	Quadcopter 25 lbs.	RQ25-M1H	Level 2	No
		RQ25-M1M	Level 3	No
		RQ25-M1C	Level 4	No
	Fixed-Wing 25 lbs.	RF25-M1H	Level 2	No
		RF25-M1M	Level 3	No
		RF25-M1C	Level 4	No
	Quadcopter 55 lbs.	RQ55-M1H	Level 3	No
		RQ55-M1M	Level 4	No
		RQ55-M1C	Level 4	No
	Fixed-Wing 55 lbs.	RF55-M1H	Level 4	No
		RF55-M1M	Level 4	No
		RF55-M1C	Level 4	No

5.3.1 UAS 2.7 lbs. Quadcopter

This section delineates the findings stemming from collisions involving 2.7 lbs. quadcopter and the rotorcraft's Mast at Hover, Medium, and Cruise velocities, as showcased in Figure 174, Figure 175, and Figure 176, respectively. These results unravel the temporal progression of the impact occurrences, spotlighting time intervals at 0.005s, 0.02s, and 0.05s. The upper trio of windows highlights the kinematic aspects of the impacts, while the lower trio shows the resultant effective

plastic strain on the rotorcraft structures. Additionally, Figure 177 provides the energy balance plots for all three impact velocities.
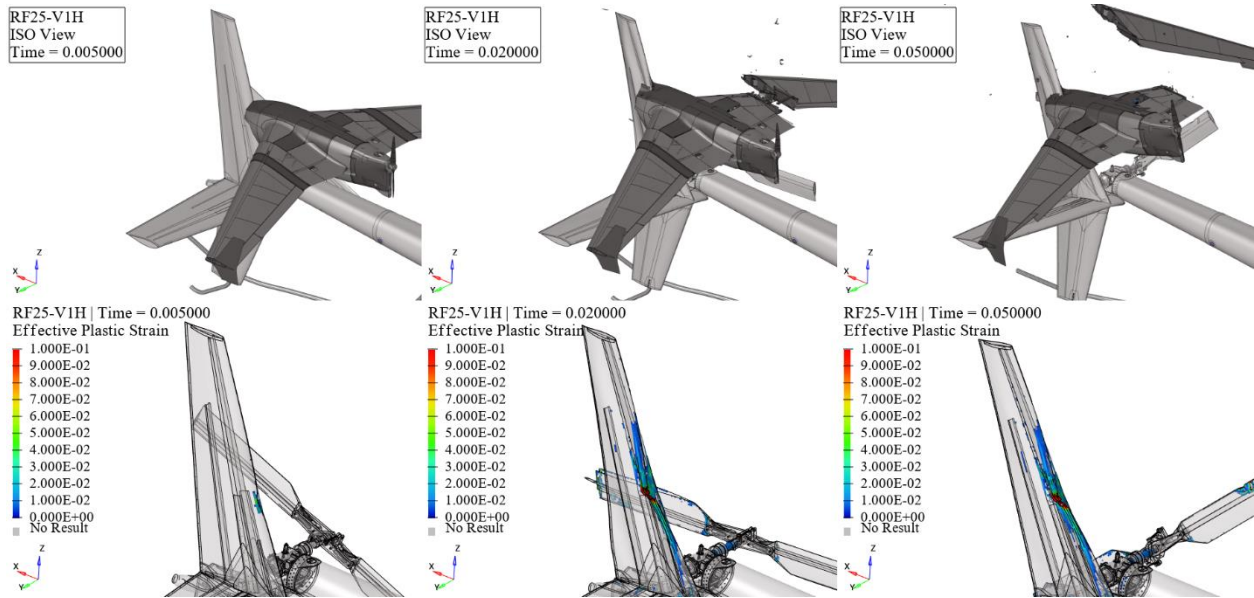

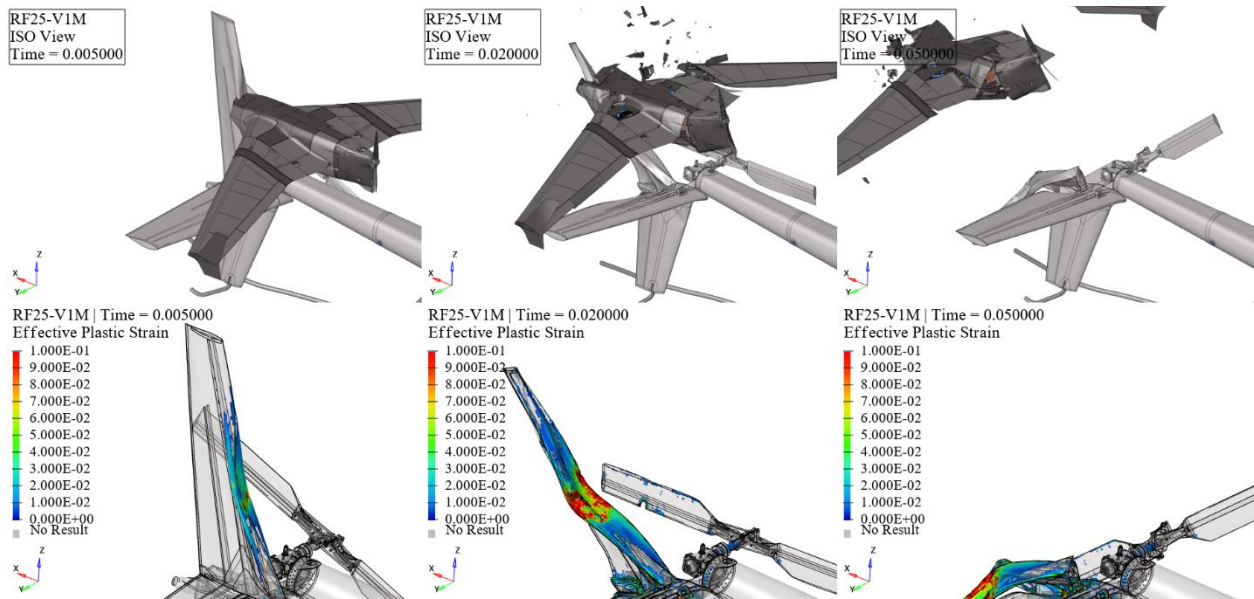Figure 174. RQ2.7-M1H kinematics (top) and effective plastic strain (bottom) frames.

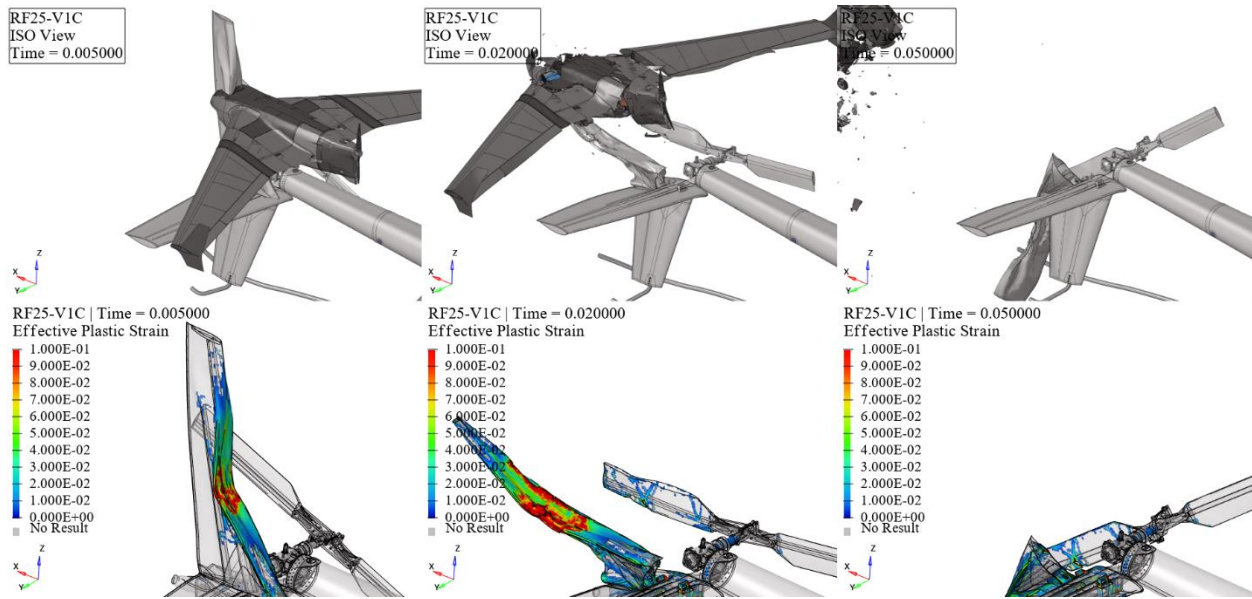Figure 175. RQ2.7-M1M kinematics (top) and effective plastic strain (bottom) frames.

Figure 176. RQ2.7-M1C kinematics (top) and effective plastic strain (bottom) frames.
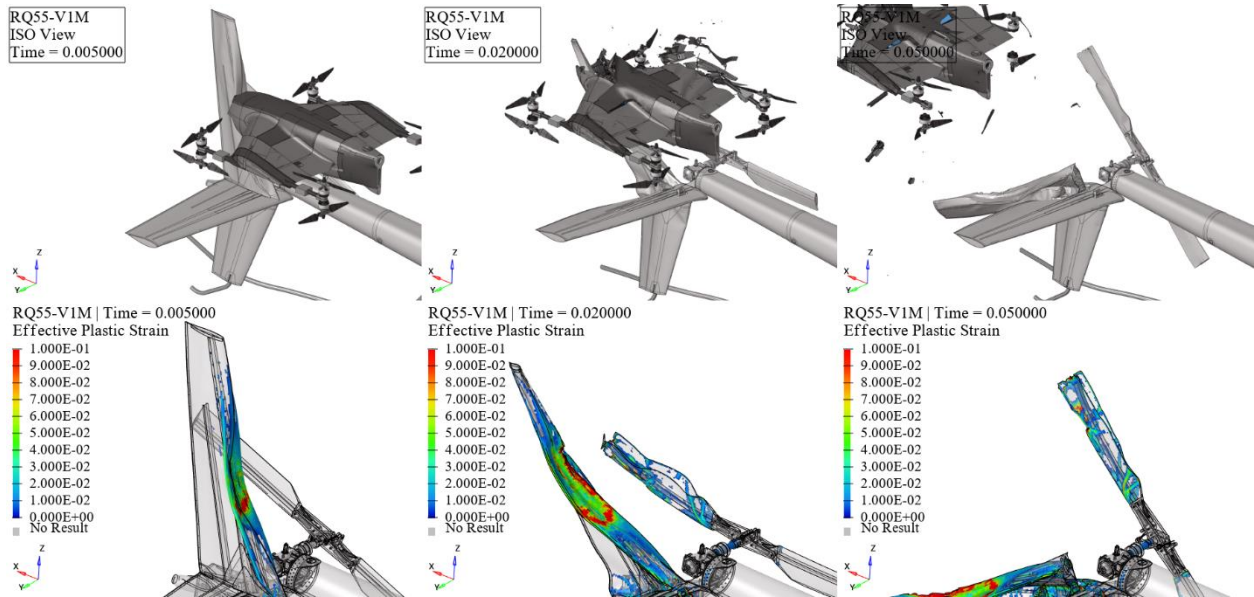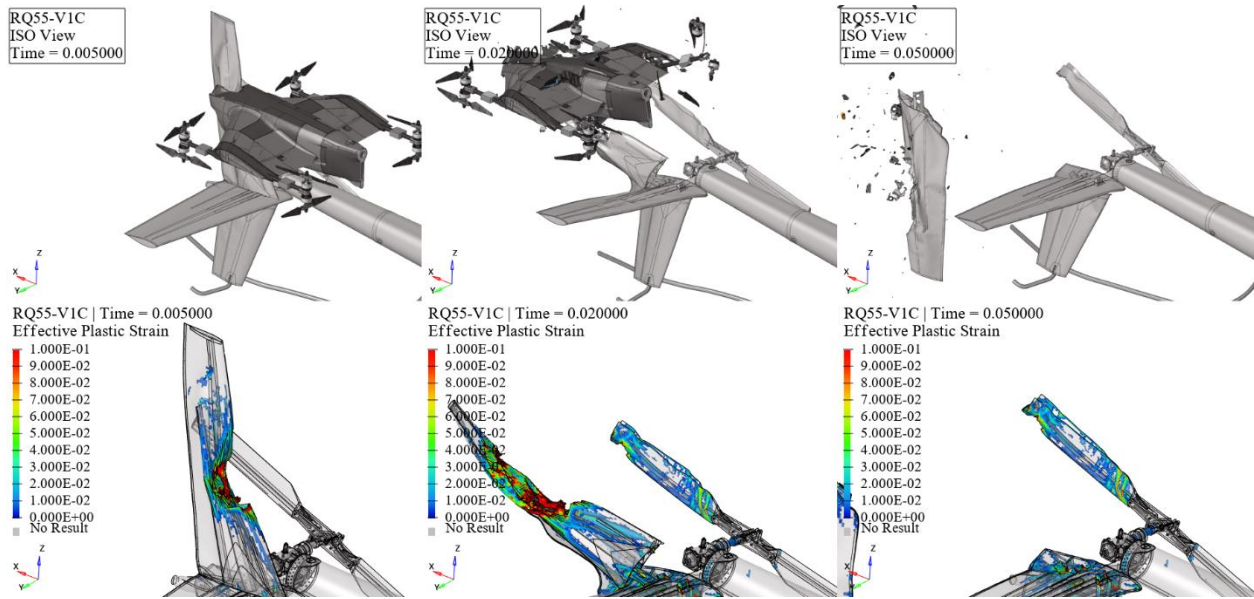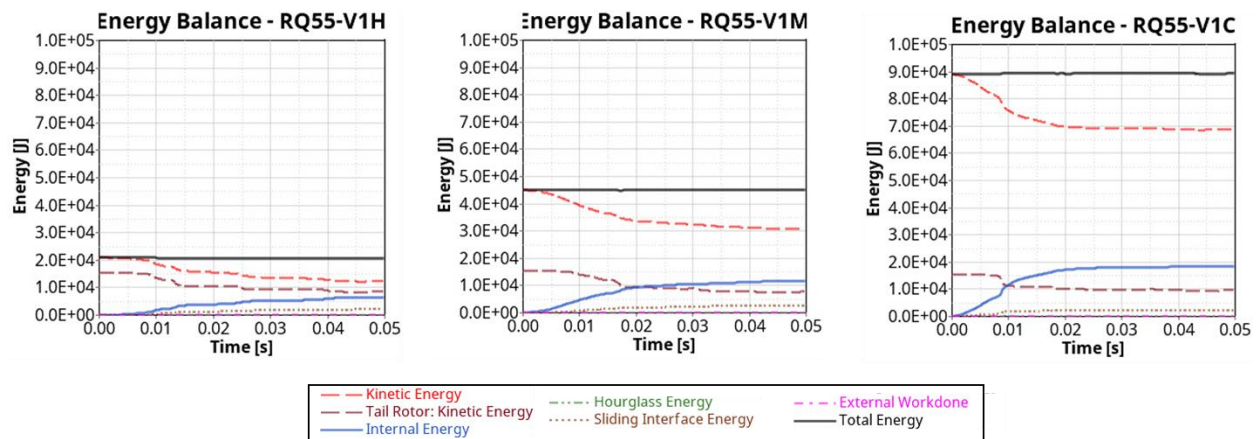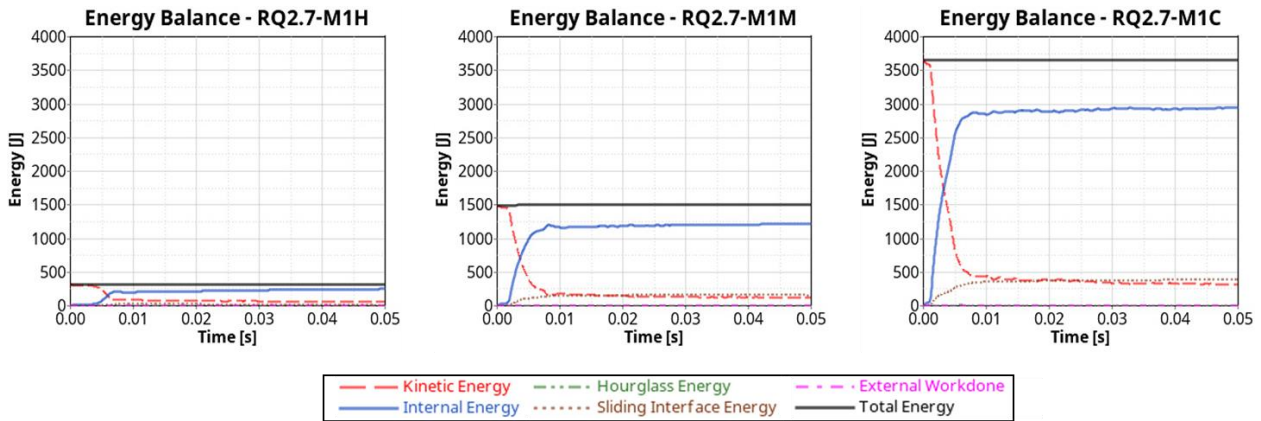

Figure 177. Mast and 2.7 lbs. quadcopter impact energy balance.

At hover velocity, the collision between the 2.7 lbs. quadcopter and the mast resulted in minor dents on the skin, indicative of a level 1 impact severity. Conversely, at medium and cruise impact velocities, the mast exhibited increased permanent deformation to the skin compared to the hover velocity but no skin fractures, resulting in a level 2 impact severity.

5.3.2 UAS 4 lbs. Fixed-Wing

This section delineates the findings stemming from collisions involving 4 lbs. fixed-wing and the rotorcraft's Mast at Hover, Medium, and Cruise velocities, as showcased in Figure 178, Figure 179, and Figure 180, respectively. These results unravel the temporal progression of the impact occurrences, spotlighting time intervals at 0.005s, 0.02s, and 0.05s. The upper trio of windows highlights the kinematic aspects of the impacts, while the lower trio shows the resultant effective plastic strain on the rotorcraft structures. Additionally, Figure 181 provides the energy balance plots for all three impact velocities.
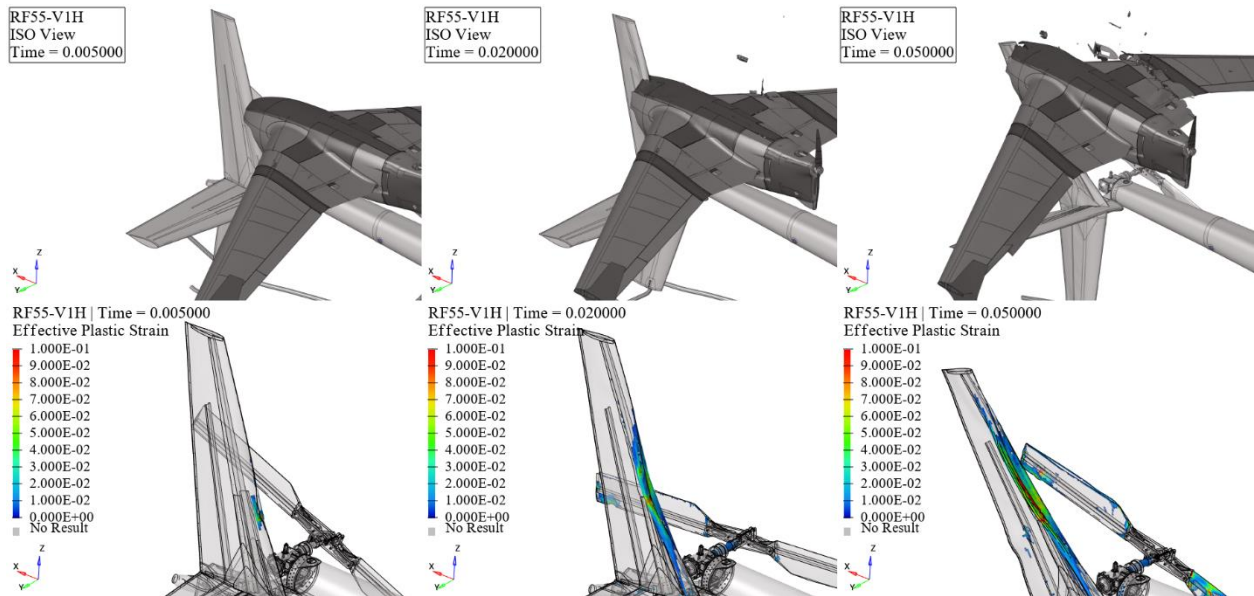
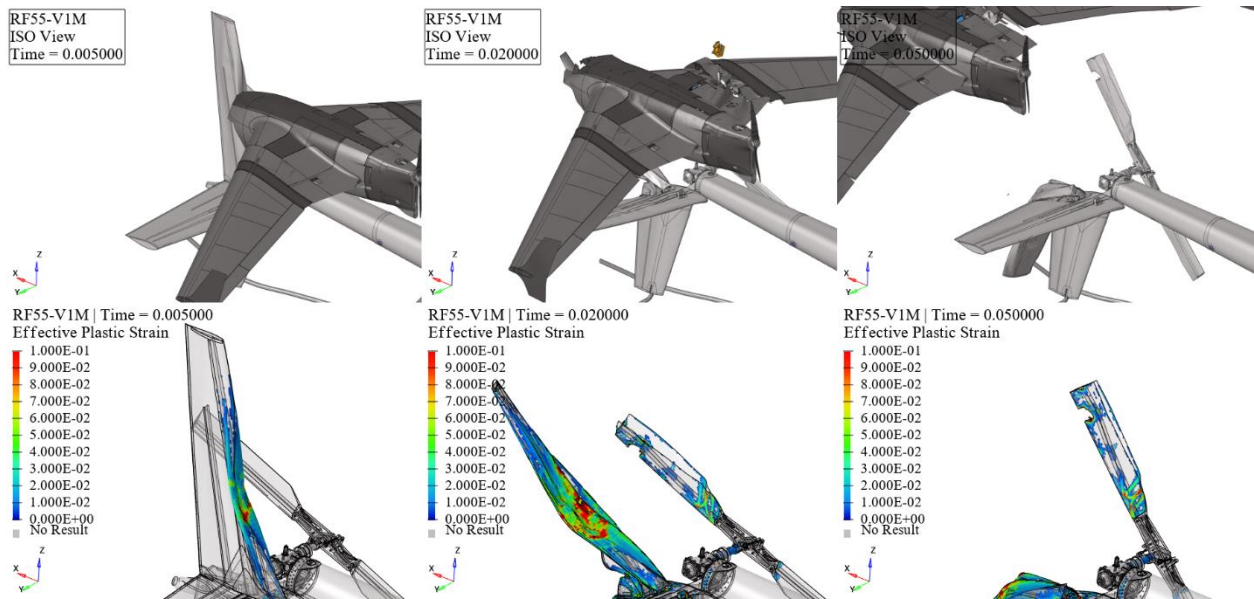Figure 178. RF4-M1H kinematics (top) and effective plastic strain (bottom) frames.

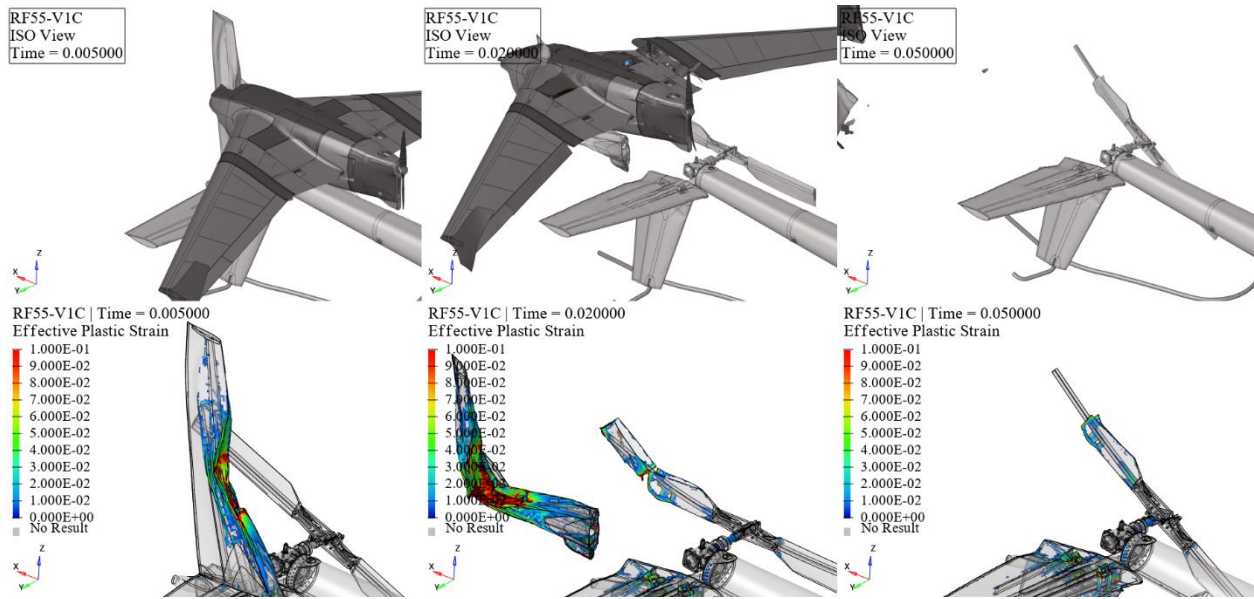Figure 179. RF4-M1M kinematics (top) and effective plastic strain (bottom) frames.

Figure 180. RF4-M1C kinematics (top) and effective plastic strain (bottom) frames.
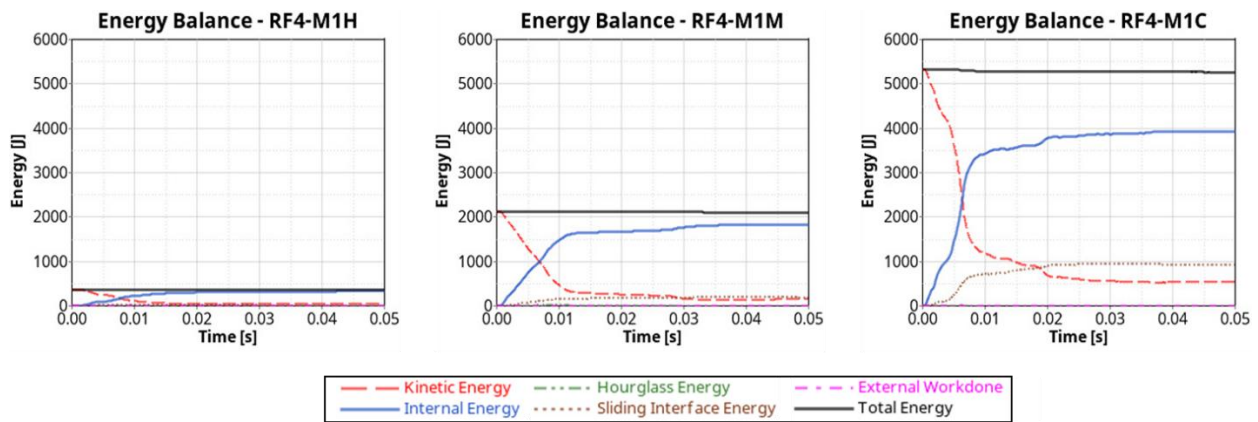
Figure 181. Mast and 4 lbs. fixed-wing impact energy balance.

At hover velocity, the collision between the 4 lbs. fixed-wing and the mast caused minor dents on the skin, reflecting a level 1 impact severity. Conversely, at medium impact velocity, the mast showed greater permanent deformation of the skin compared to the hover velocity, accompanied by minimal cracks, resulting in a level 2 impact severity. Subsequently, at cruise impact velocity, the mast incurred significantly heightened damage compared to the impacts at hover and medium velocities, characterized by major cracks on the skin, leading to a determined level 3 impact severity.

5.3.3   UAS 10 lbs. Quadcopter

This section delineates the findings stemming from collisions involving 10 lbs. quadcopter and the rotorcraft's Mast at Hover, Medium, and Cruise velocities, as showcased in Figure 182, Figure 183, and Figure 184, respectively. These results unravel the temporal progression of the impact occurrences, spotlighting time intervals at 0.005s, 0.02s, and 0.05s. The upper trio of windows highlights the kinematic aspects of the impacts, while the lower trio shows the resultant effective

142

plastic strain on the rotorcraft structures. Additionally, Figure 185 provides the energy balance plots for all three impact velocities.

Figure 182. RQ10-M1H kinematics (top) and effective plastic strain (bottom) frames.

Figure 183. RQ10-M1M kinematics (top) and effective plastic strain (bottom) frames.

Figure 184. RQ10-M1C kinematics (top) and effective plastic strain (bottom) frames.

Figure 185. Mast and 10 lbs. quadcopter impact energy balance.

At hover and medium velocities, the collision between the 10 lbs. quadcopter and the mast caused permanent skin deformation, resulting in a level 2 impact severity. Subsequently, at cruise impact velocity, the mast incurred significantly heightened damage compared to the impacts at hover and medium velocities, characterized by major cracks on the skin, leading to a determined level 3 impact severity.

5.3.4 UAS 12 lbs. Fixed-Wing

This section delineates the findings stemming from collisions involving 12 lbs. fixed-wing and the rotorcraft's Mast at Hover, Medium, and Cruise velocities, as showcased in Figure 186, Figure 187, and Figure 188, respectively. These results unravel the temporal progression of the impact occurrences, spotlighting time intervals at 0.005s, 0.02s, and 0.05s. The upper trio of windows highlights the kinematic aspects of the impacts, while the lower trio shows the resultant effective plastic strain on the rotorcraft structures. Additionally, Figure 189 provides the energy balance plots for all three impact velocities.
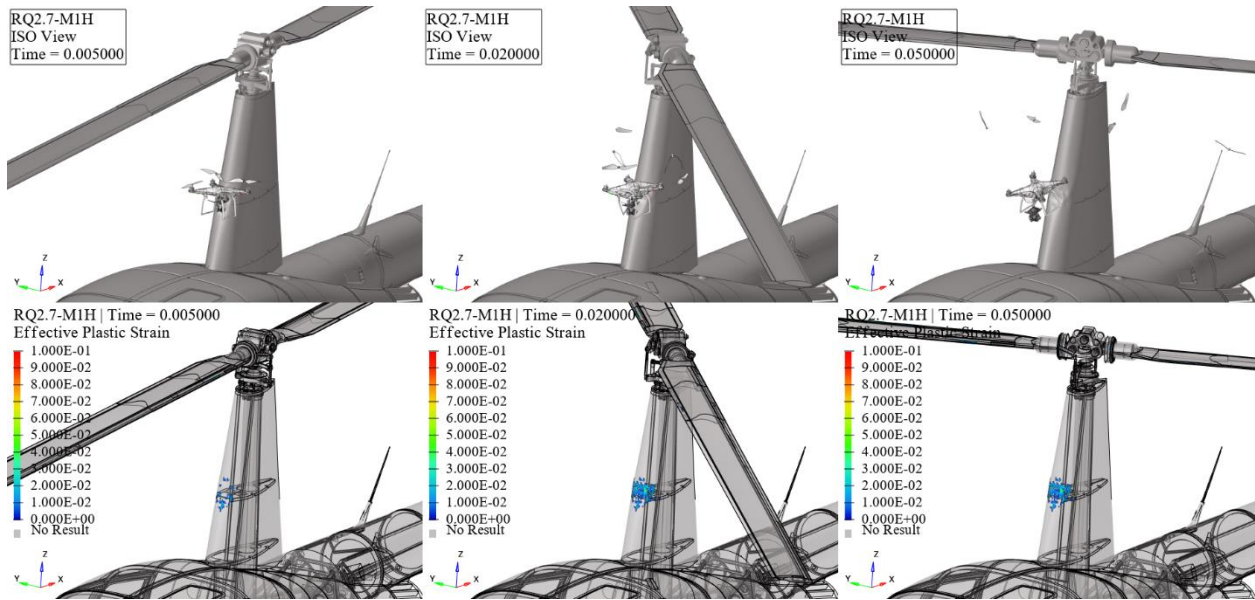
144
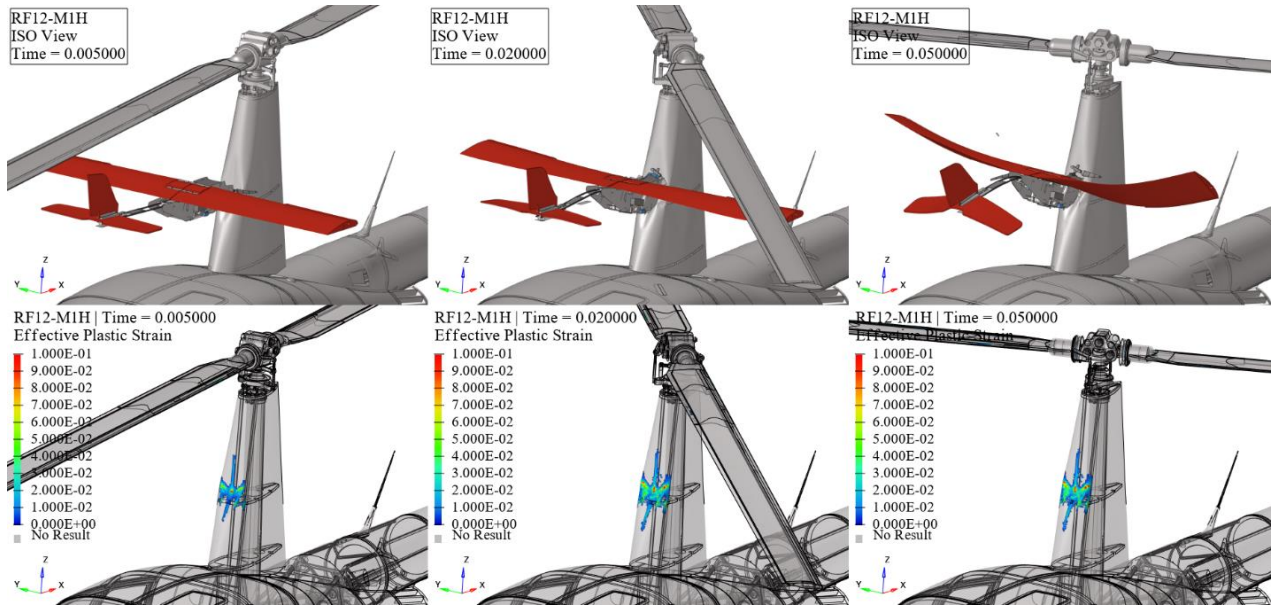
Figure 186. RF12-M1H kinematics (top) and effective plastic strain (bottom) frames.
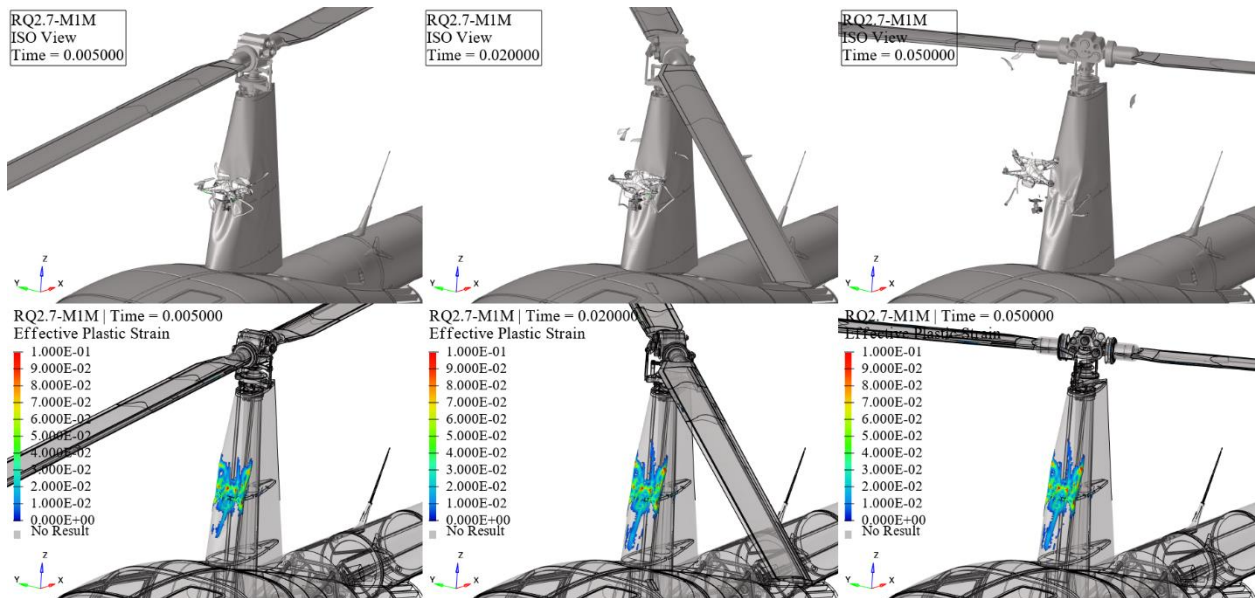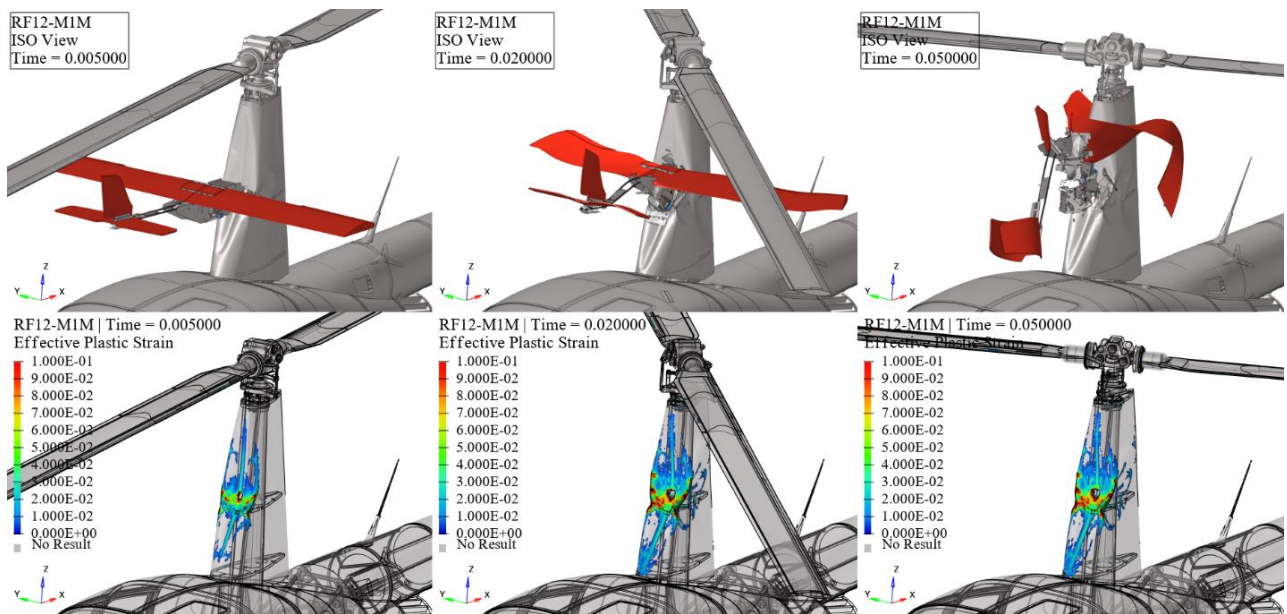

Figure 187. RF12-M1M kinematics (top) and effective plastic strain (bottom) frames.
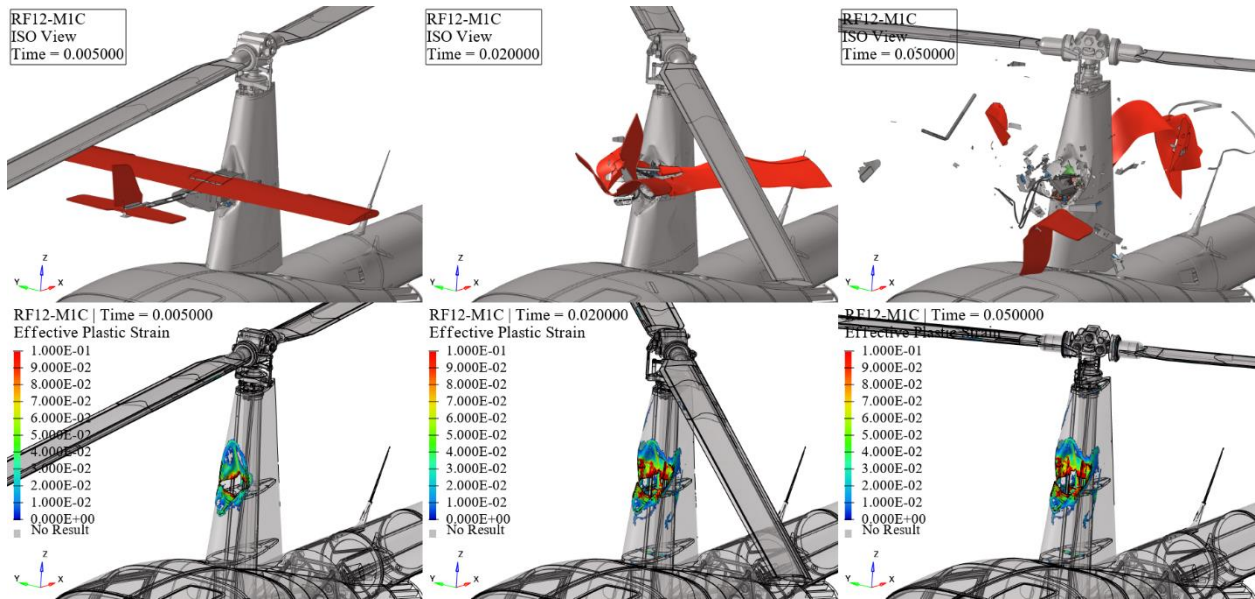
Figure 188. RF12-M1C kinematics (top) and effective plastic strain (bottom) frames.
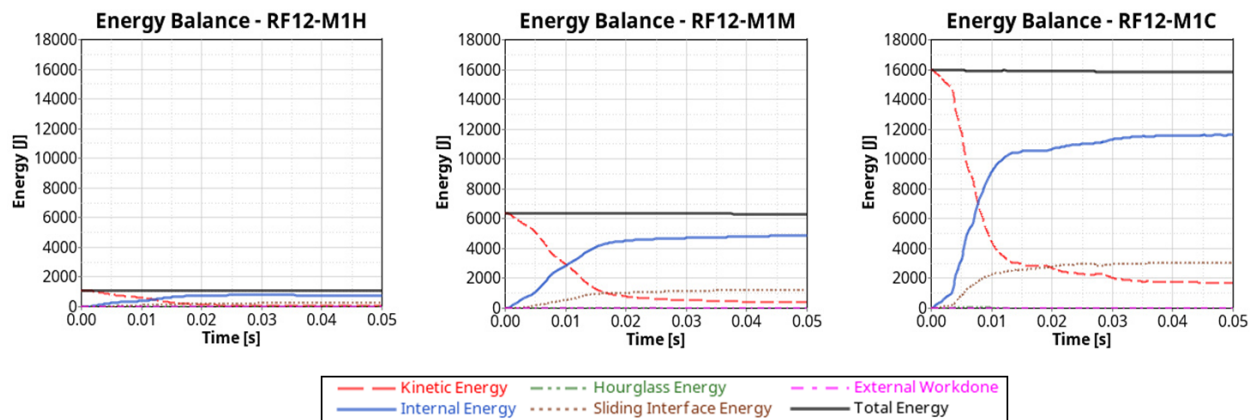
Figure 189. Mast and 12 lbs. fixed-wing impact energy balance.

At hover and medium velocities, the collision between the 12 lbs. fixed-wing and the mast caused permanent skin deformation, while medium velocity showed some minor cracks, resulting in a level 2 impact severity. Subsequently, at cruise impact velocity, the mast incurred significantly heightened damage compared to the impacts at hover and medium velocities, characterized by major cracks on the skin, leading to a level 3 impact severity.

5.3.5 UAS 25 lbs. Quadcopter

This section delineates the findings stemming from collisions involving 25 lbs. quadcopter and the rotorcraft's Mast at Hover, Medium, and Cruise velocities, as showcased in Figure 190, Figure 191, and Figure 192, respectively. These results unravel the temporal progression of the impact occurrences, spotlighting time intervals at 0.005s, 0.02s, and 0.05s. The upper trio of windows highlights the kinematic aspects of the impacts, while the lower trio shows the resultant effective plastic strain on the rotorcraft structures. Additionally, Figure 193 provides the energy balance plots for all three impact velocities.

Figure 190. RQ25-M1H kinematics (top) and effective plastic strain (bottom) frames.

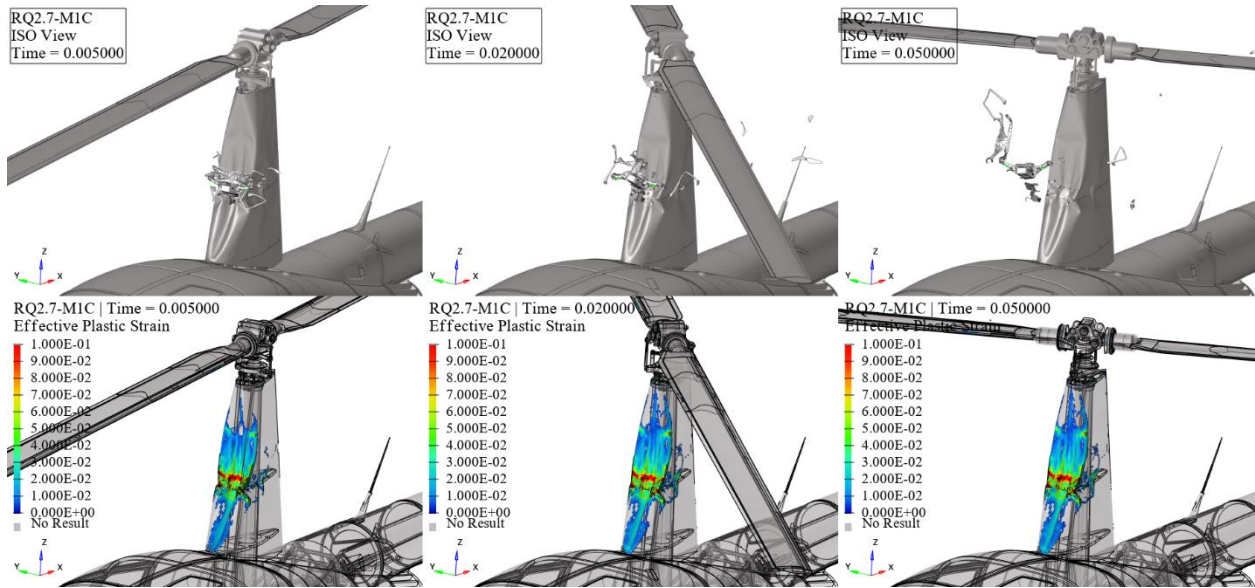Figure 191. RQ25-M1M kinematics (top) and effective plastic strain (bottom) frames.

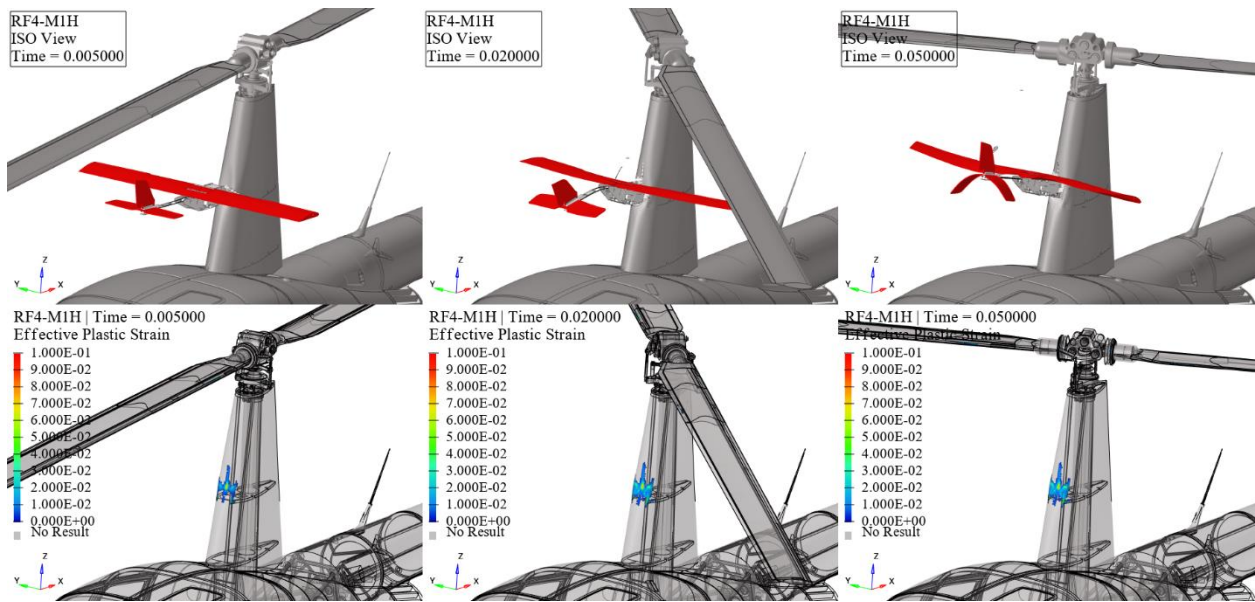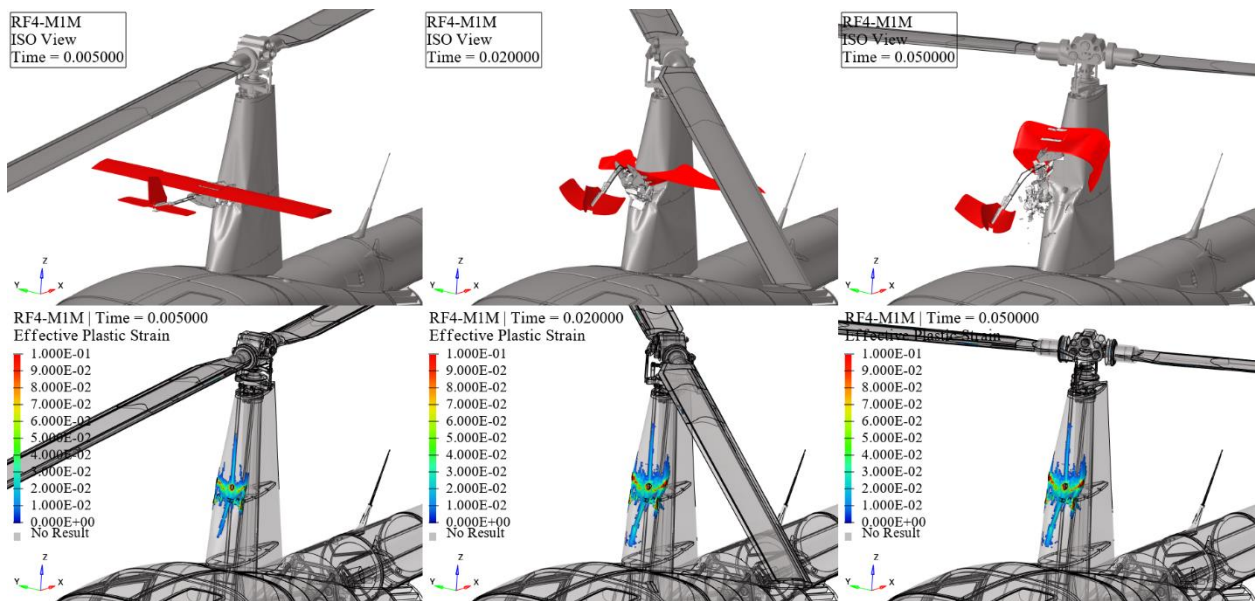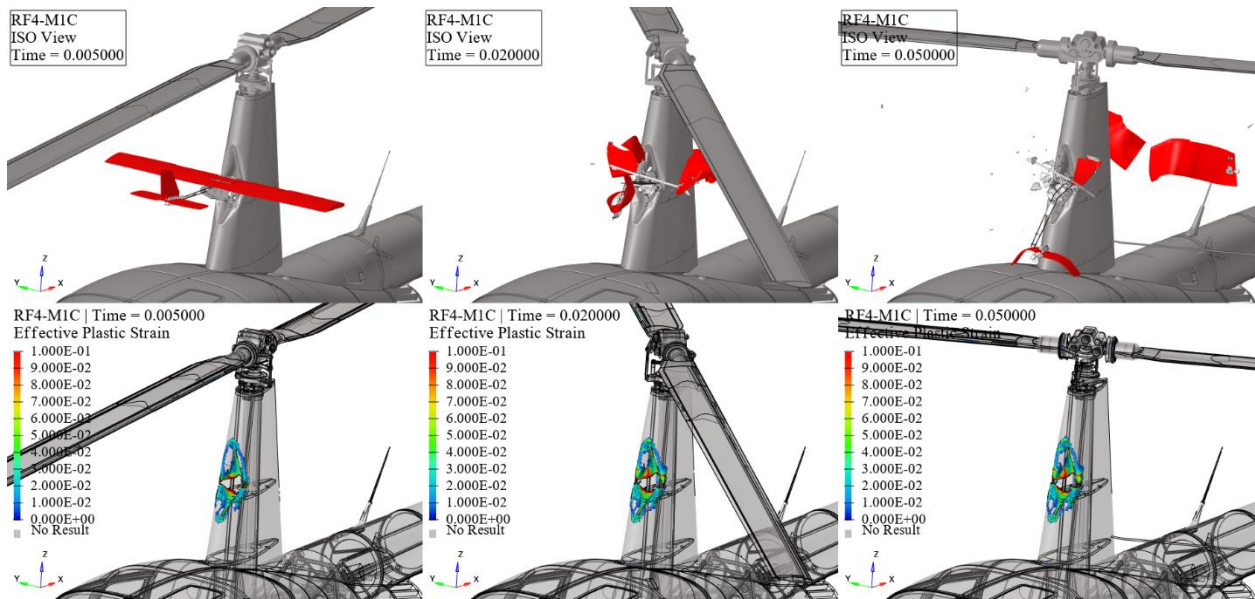Figure 192. RQ25-M1C kinematics (top) and effective plastic strain (bottom) frames.
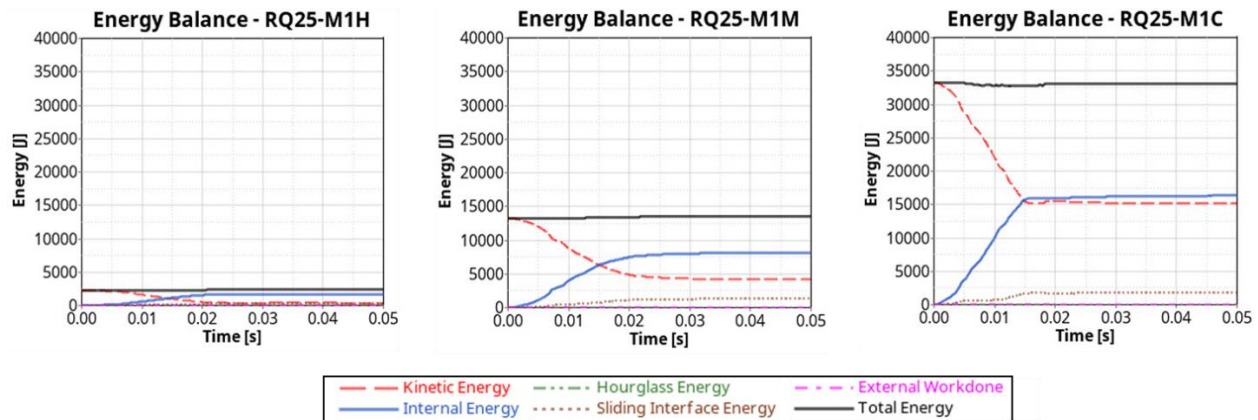
Figure 193. Mast and 25 lbs. quadcopter impact energy balance.

At hover velocity, the collision between the 25 lbs. quadcopter and the mast caused permanent skin deformation, resulting in a level 2 impact severity. Conversely, at medium impact velocity, the mast incurred significantly heightened damage compared to the impact at hover velocity, characterized by major cracks on the skin, leading to a level 3 impact severity. Subsequently, at cruise impact velocity, the mast sustained major skin fractures and deformation of the main blade links, rendering them non-functional. This would result in a loss of certain flight controls for the pilot, resulting in a level 4 impact severity.

5.3.6 UAS 25 lbs. Fixed-Wing

This section delineates the findings stemming from collisions involving 25 lbs. fixed-wing and the rotorcraft's Mast at Hover, Medium, and Cruise velocities, as showcased in Figure 194, Figure 195, and Figure 196, respectively. These results unravel the temporal progression of the impact occurrences, spotlighting time intervals at 0.005s, 0.02s, and 0.05s. The upper trio of windows highlights the kinematic aspects of the impacts, while the lower trio shows the resultant effective

148

plastic strain on the rotorcraft structures. Additionally, Figure 197 provides the energy balance plots for all three impact velocities.

Figure 194. RF25-M1H kinematics (top) and effective plastic strain (bottom) frames.

Figure 195. RF25-M1M kinematics (top) and effective plastic strain (bottom) frames.

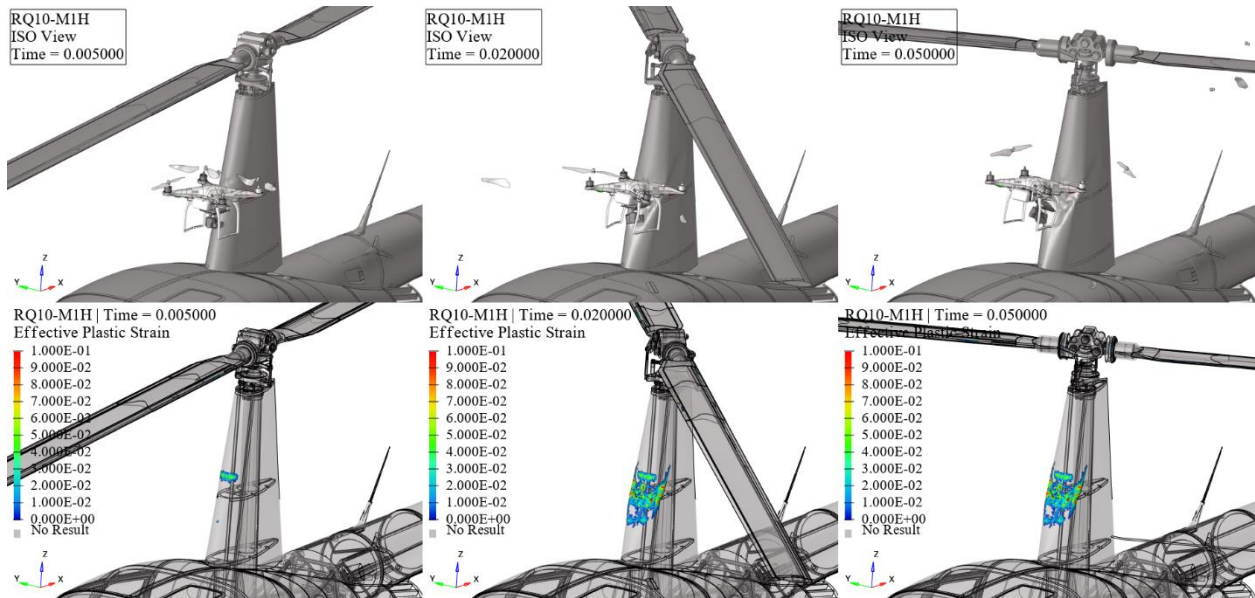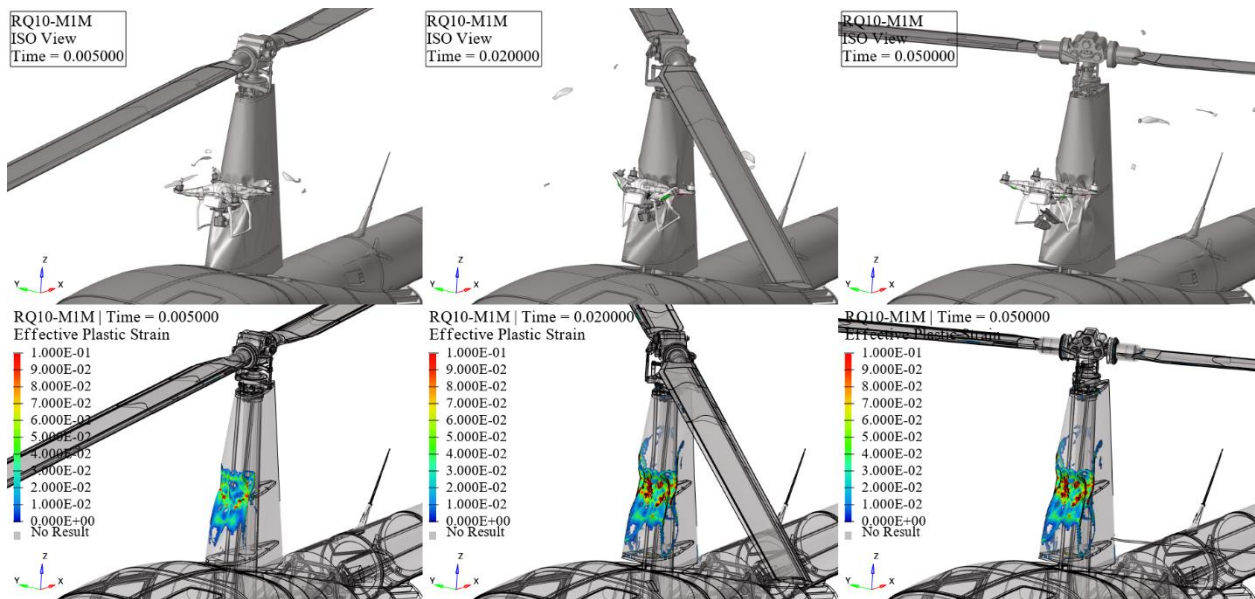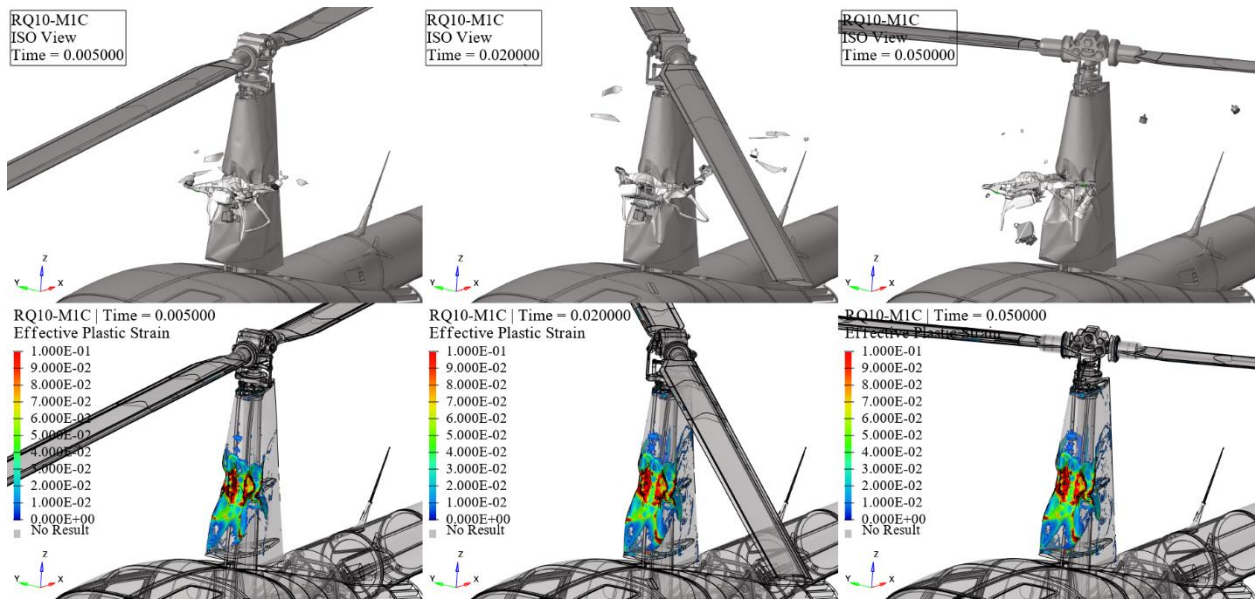Figure 196. RF25-M1C kinematics (top) and effective plastic strain (bottom) frames.
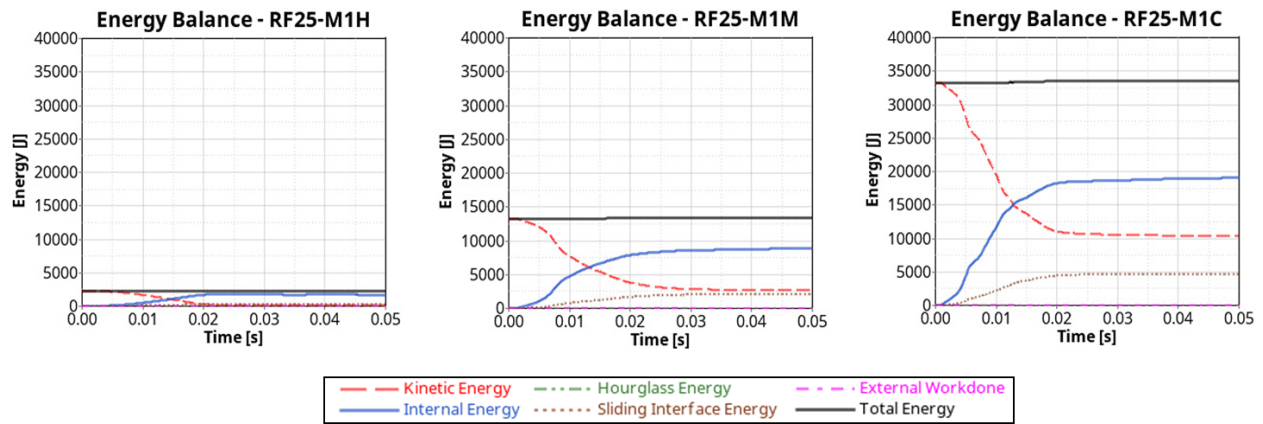
Figure 197. Mast and 25 lbs. fixed-wing impact energy balance.

At hover velocity, the collision between the 25 lbs. fixed-wing and the mast caused permanent skin deformation, resulting in a level 2 impact severity. Subsequently, at medium impact velocity, the mast incurred significantly heightened damage compared to the impact at hover velocity, characterized by major cracks on the skin, leading to a level 3 impact severity. Subsequently, at cruise impact velocity, the mast sustained major skin fractures and deformation of the main blade links, rendering them non-functional. This would result in a loss of certain flight controls for the pilot, resulting in a level 4 impact severity.

5.3.7 UAS 55 lbs. Quadcopter

This section delineates the findings stemming from collisions involving 55 lbs. quadcopter and the rotorcraft's Mast at Hover, Medium, and Cruise velocities, as showcased in Figure 198, Figure 199, and Figure 200, respectively. These results unravel the temporal progression of the impact occurrences, spotlighting time intervals at 0.005s, 0.02s, and 0.05s. The upper trio of windows highlights the kinematic aspects of the impacts, while the lower trio shows the resultant effective

150

plastic strain on the rotorcraft structures. Additionally, Figure 201 provides the energy balance plots for all three impact velocities.

Figure 198. RQ55-M1H kinematics (top) and effective plastic strain (bottom) frames.

Figure 199. RQ55-M1M kinematics (top) and effective plastic strain (bottom) frames.

Figure 200. RQ55-M1C kinematics (top) and effective plastic strain (bottom) frames.
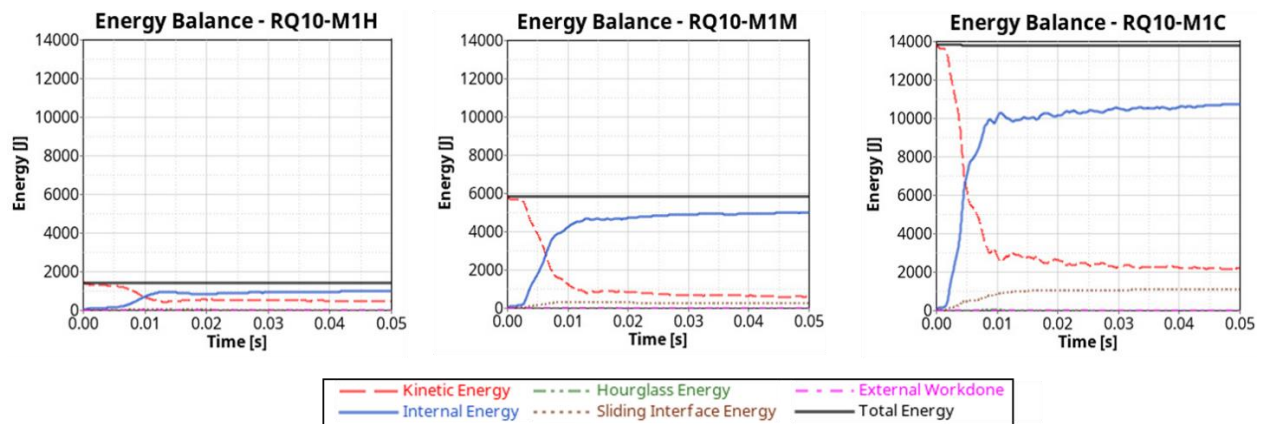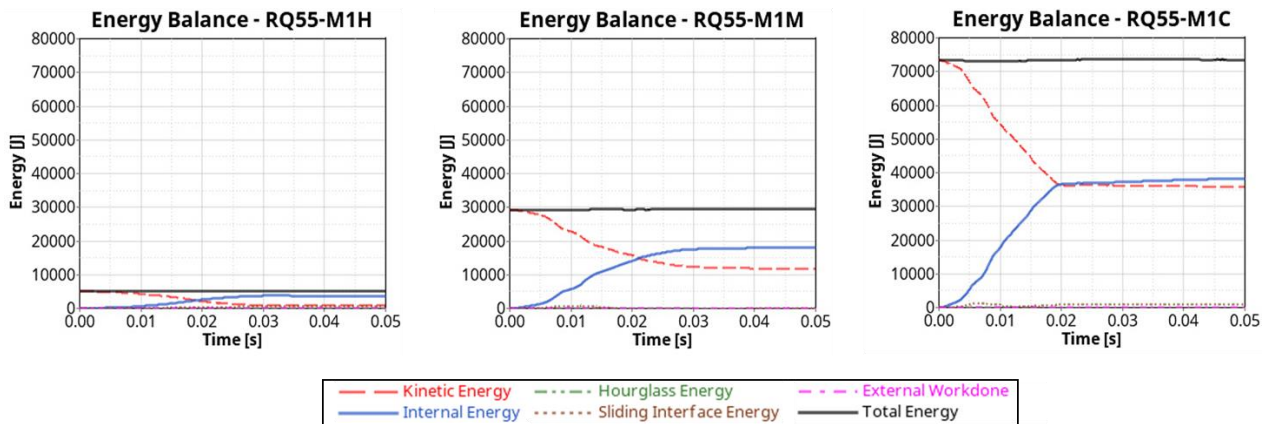

Figure 201. Mast and 55 lbs. quadcopter impact energy balance.

Due to the high stiffness of the mast's internal structures, all three impact velocities resulted in significant permanent deformation and major cracks on the skin without causing severe damage to the skin, indicating a level 3 impact severity. However, deformation of the main blade links behind the skin occurred at medium and cruise velocities, rendering them non-functional. This would lead to a loss of certain flight controls for the pilot, resulting in a level 4 impact severity.

5.3.8   UAS 55 lbs. Fixed-Wing

This section delineates the findings stemming from collisions involving 55 lbs. fixed-wing and the rotorcraft's Mast at Hover, Medium, and Cruise velocities, as showcased in Figure 202, Figure 203, and Figure 204, respectively. These results unravel the temporal progression of the impact occurrences, spotlighting time intervals at 0.005s, 0.02s, and 0.05s. The upper trio of windows highlights the kinematic aspects of the impacts, while the lower trio shows the resultant effective plastic strain on the rotorcraft structures. Additionally, Figure 205 provides the energy balance plots for all three impact velocities.
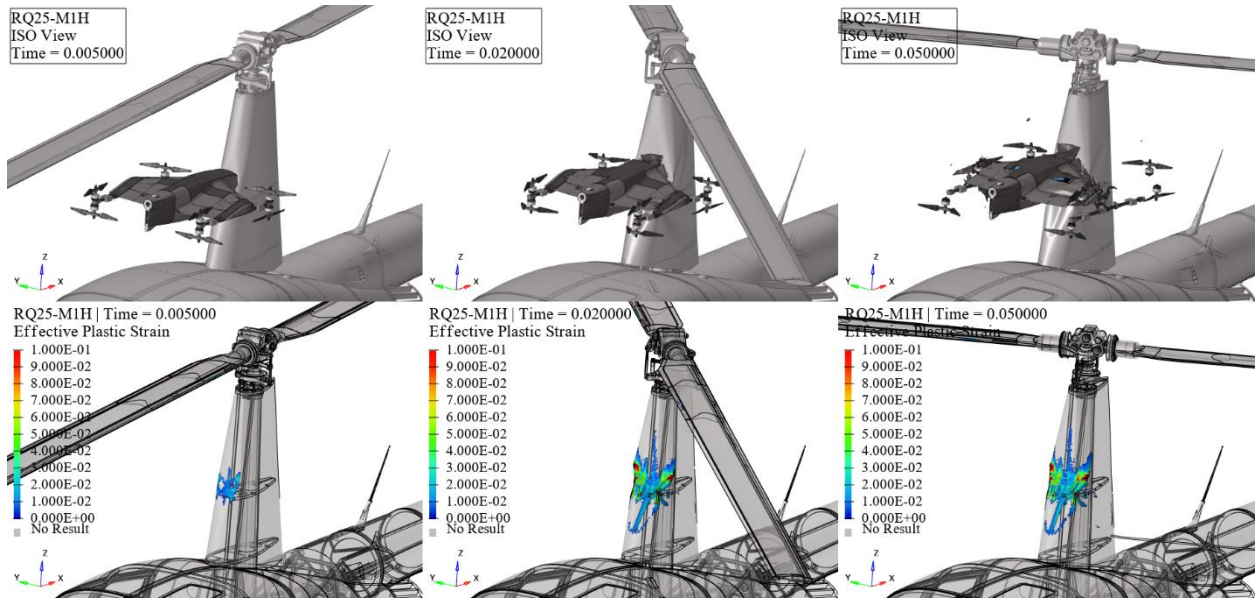
152

Figure 202. RF55-M1H kinematics (top) and effective plastic strain (bottom) frames.
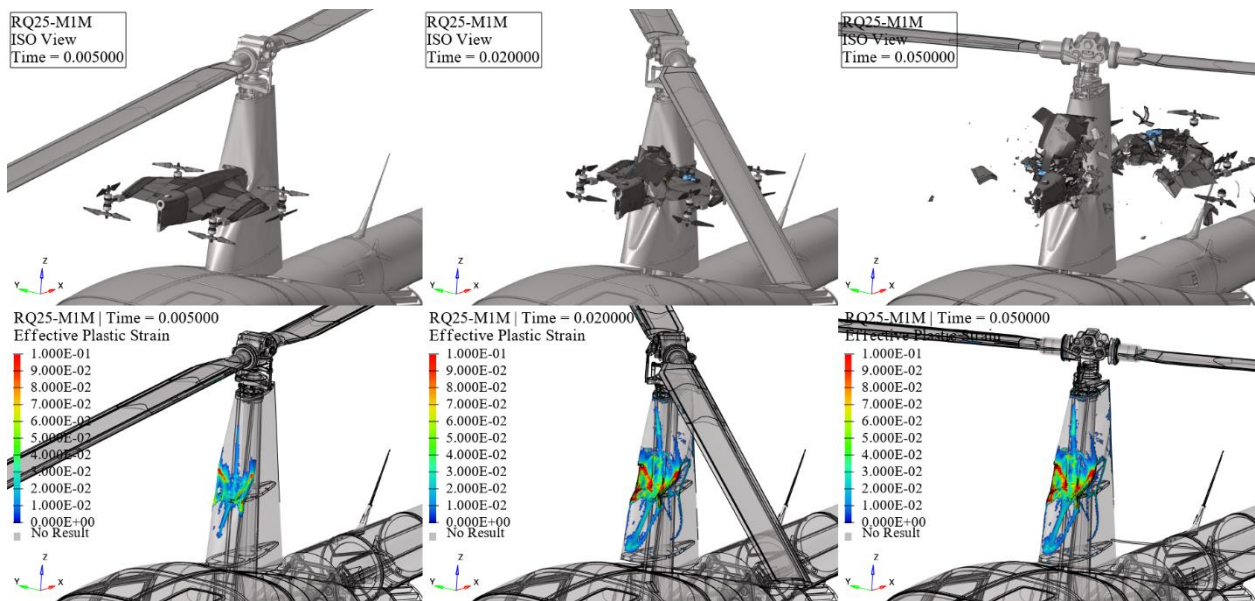

Figure 203. RF55-M1M kinematics (top) and effective plastic strain (bottom) frames.
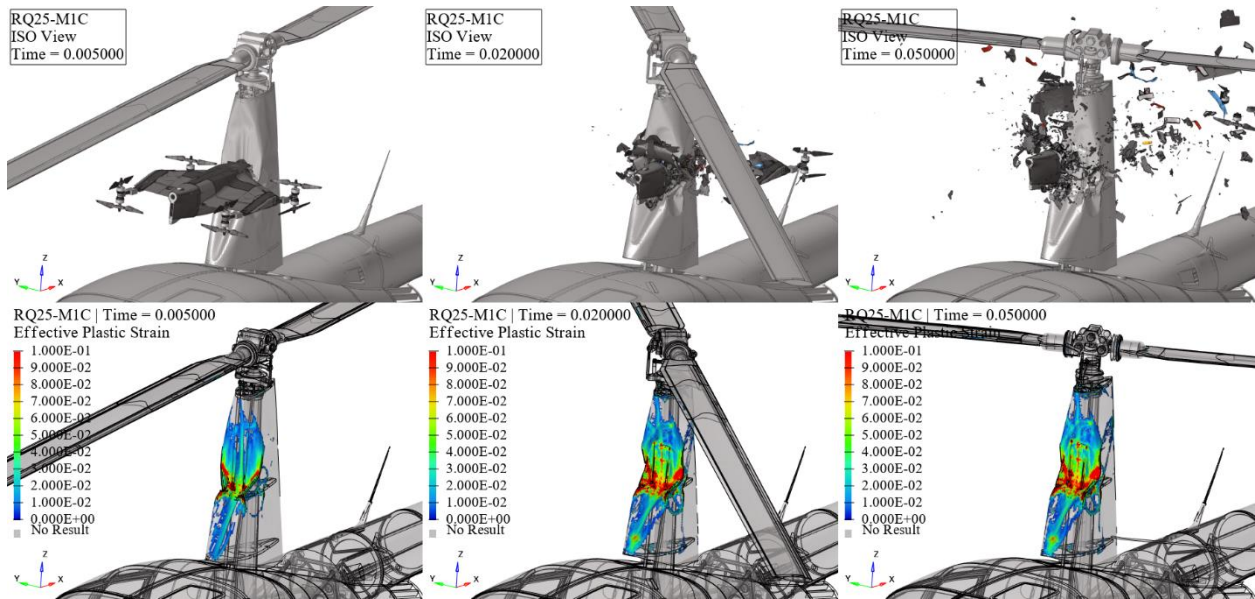
Figure 204. RF55-M1C kinematics (top) and effective plastic strain (bottom) frames.
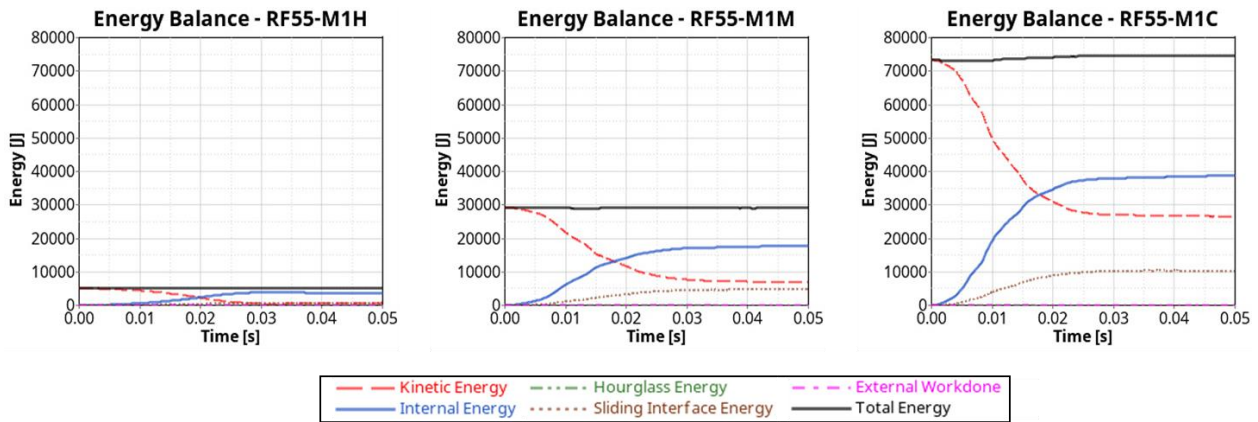
Figure 205. Mast and 55 lbs. fixed-wing impact energy balance.

Because of the high stiffness of the mast's internal structures, all three impact velocities resulted in significant permanent deformation and major cracks on the skin without causing severe damage, indicating a level 3 impact severity. However, deformation of the main blade links behind the skin occurred at all three impact velocities, rendering them non-functional. This would result in a loss of certain flight controls for the pilot, leading to a level 4 impact severity.

154

5.4 Nose

This section presents the results of the airborne collision studies for all UAS and the rotorcraft's Nose. Figure 206 shows an example of the simulation setup for the Nose impact with 55 lbs. quadcopter at cruise speed.
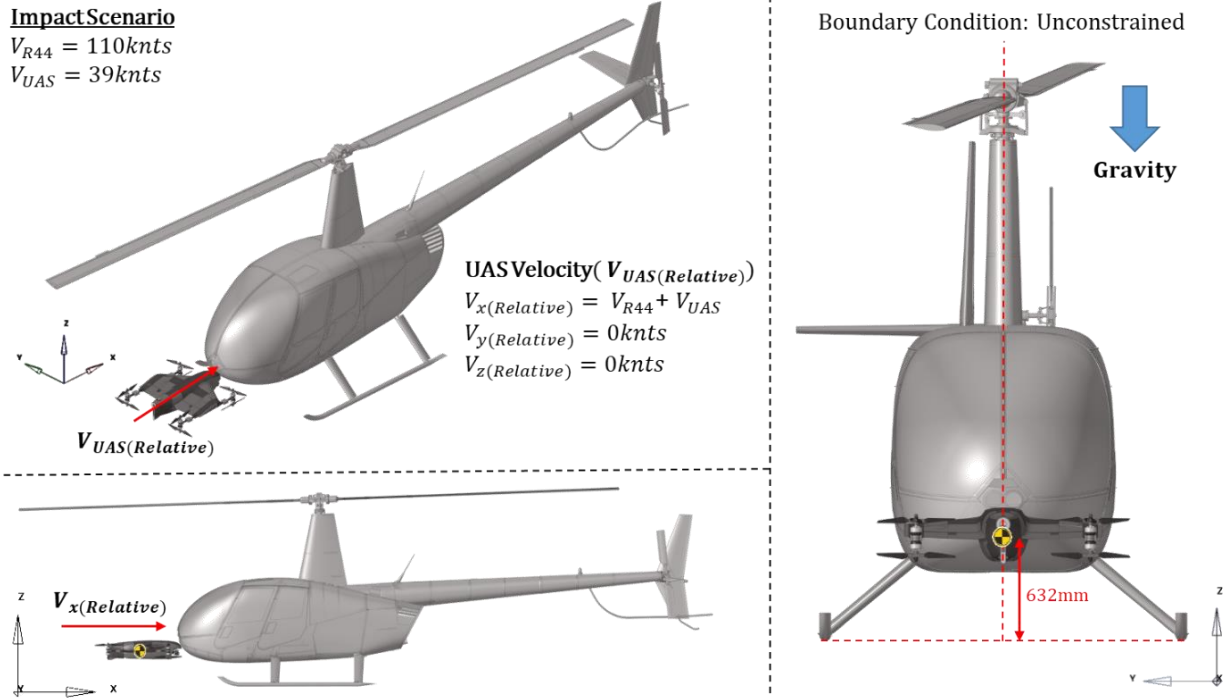
Figure 206. Simulation setup for impact between nose and 55 lbs. quadcopter at cruise velocity.

Table 45 summarizes the damage severity level evaluation and fire risk assessment for impact cases for all UAS with the Nose.

Table 45. Nose mid-air collision simulation assessment – damage severity level and fire risk.

		Case	Severity	Fire Risk
Mid-air collision Rotorcraft-Nose and all sUAS	Quadcopter 2.7 lbs.	RQ2.7-N1H	Level 2	No
		RQ2.7-N1M	Level 3	No
		RQ2.7-N1C	Level 3	No
	Fixed-Wing 4 lbs.	RF4-N1H	Level 2	No
		RF4-N1M	Level 3	No
		RF4-N1C	Level 3	No
	Quadcopter 10 lbs.	RQ10-N1H	Level 2	No
		RQ10-N1M	Level 3	No
		RQ10-N1C	Level 3	No
	Fixed-Wing 12 lbs.	RF12-N1H	Level 2	No
		RF12-N1M	Level 3	Yes
		RF12-N1C	Level 3	No
	Quadcopter 25 lbs.	RQ25-N1H	Level 2	No
		RQ25-N1M	Level 3	No
		RQ25-N1C	Level 4	No
	Fixed-Wing 25 lbs.	RF25-N1H	Level 2	No
		RF25-N1M	Level 3	No
		RF25-N1C	Level 4	No
	Quadcopter 55 lbs.	RQ55-N1H	Level 2	No
		RQ55-N1M	Level 4	Yes
		RQ55-N1C	Level 4	Yes
	Fixed-Wing 55 lbs.	RF55-N1H	Level 2	No
		RF55-N1M	Level 4	No
		RF55-N1C	Level 4	No

5.4.1   UAS 2.7 lbs. Quadcopter

This section delineates the findings stemming from collisions involving 2.7 lbs. quadcopter and the rotorcraft's Nose at Hover, Medium, and Cruise velocities, as showcased in Figure 207, Figure 208, and Figure 209, respectively. These results unravel the temporal progression of the impact

occurrences, spotlighting time intervals at 0.005s, 0.02s, and 0.05s. The upper trio of windows highlights the kinematic aspects of the impacts, while the lower trio shows the resultant effective plastic strain on the rotorcraft structures. Additionally, Figure 210 provides the energy balance plots for all three impact velocities.
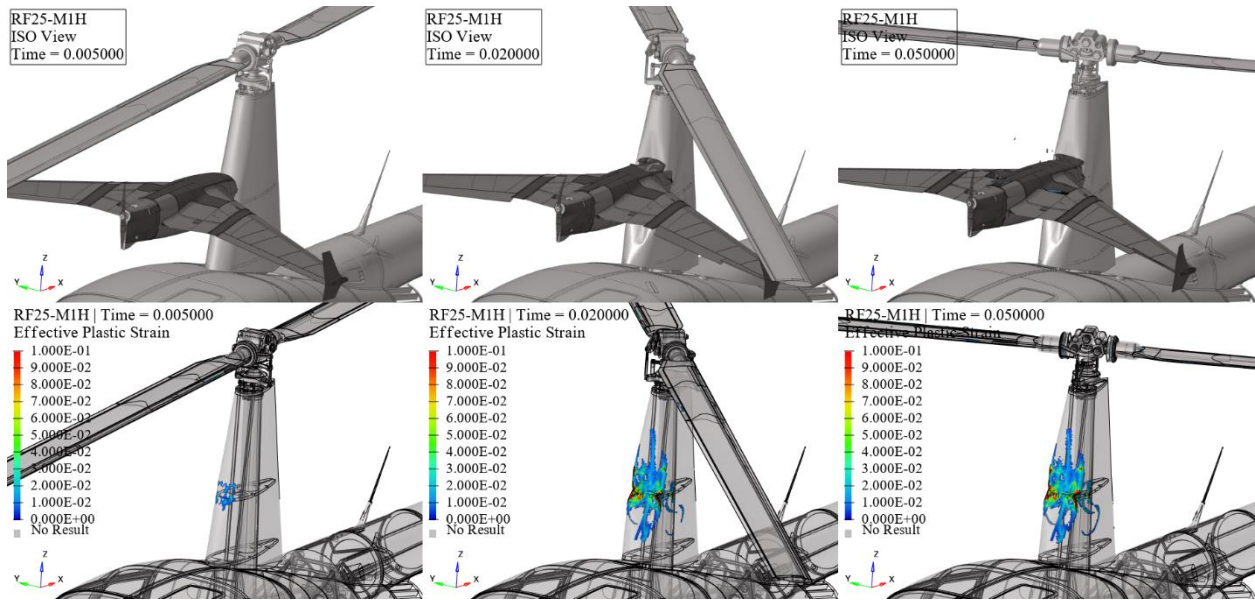

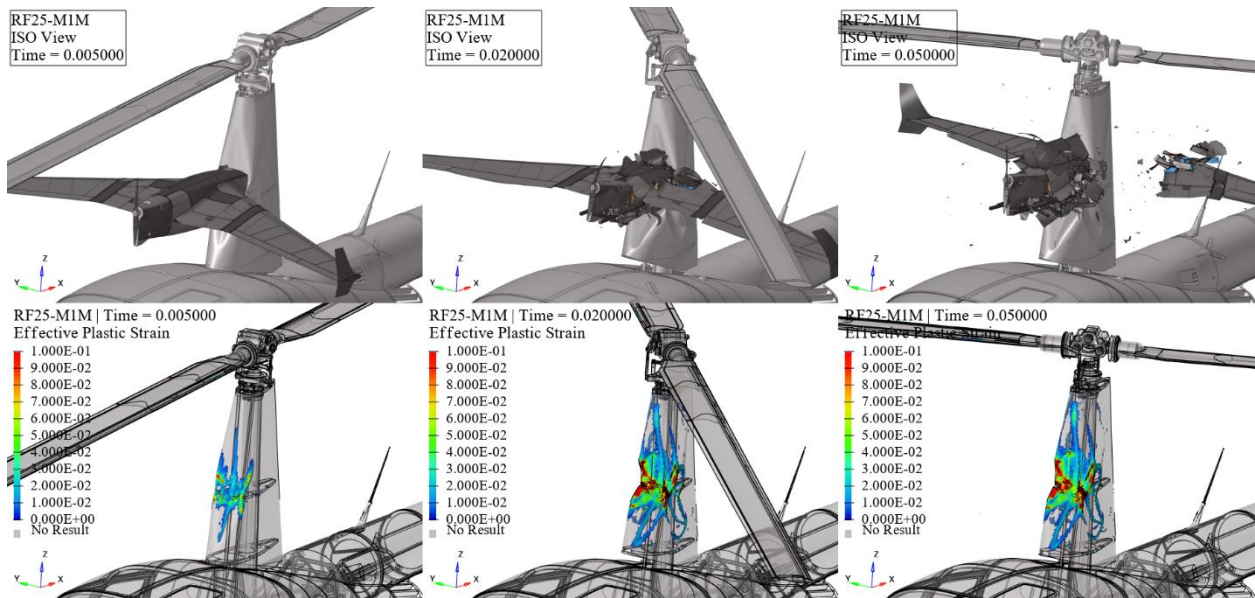Figure 207. RQ2.7-N1H kinematics (top) and effective plastic strain (bottom) frames.

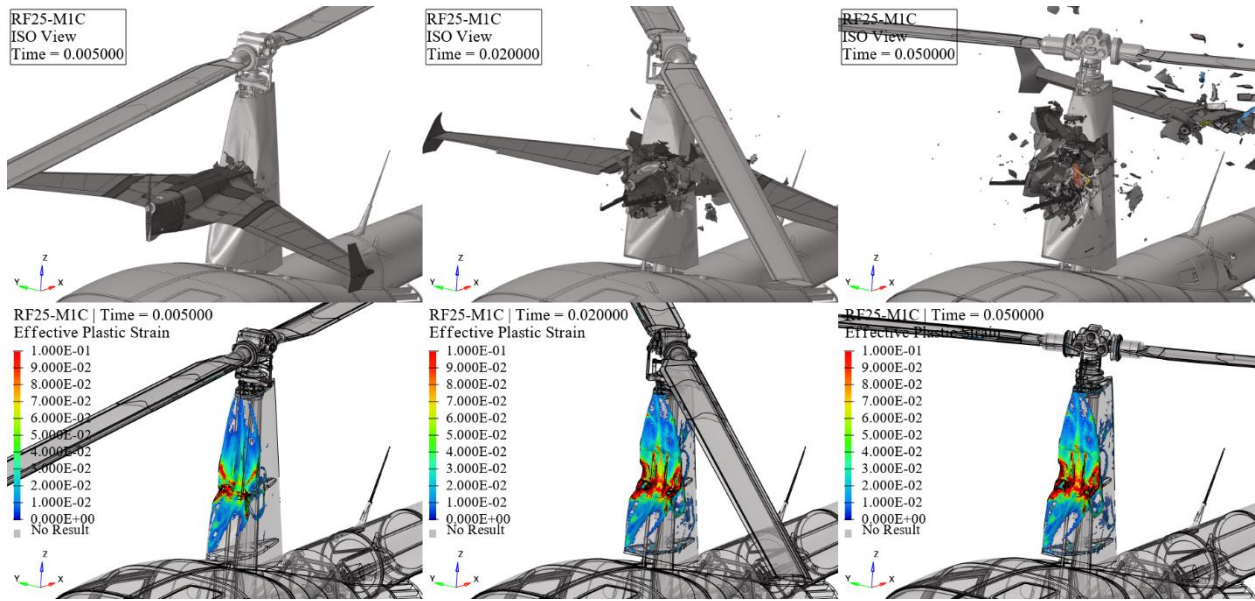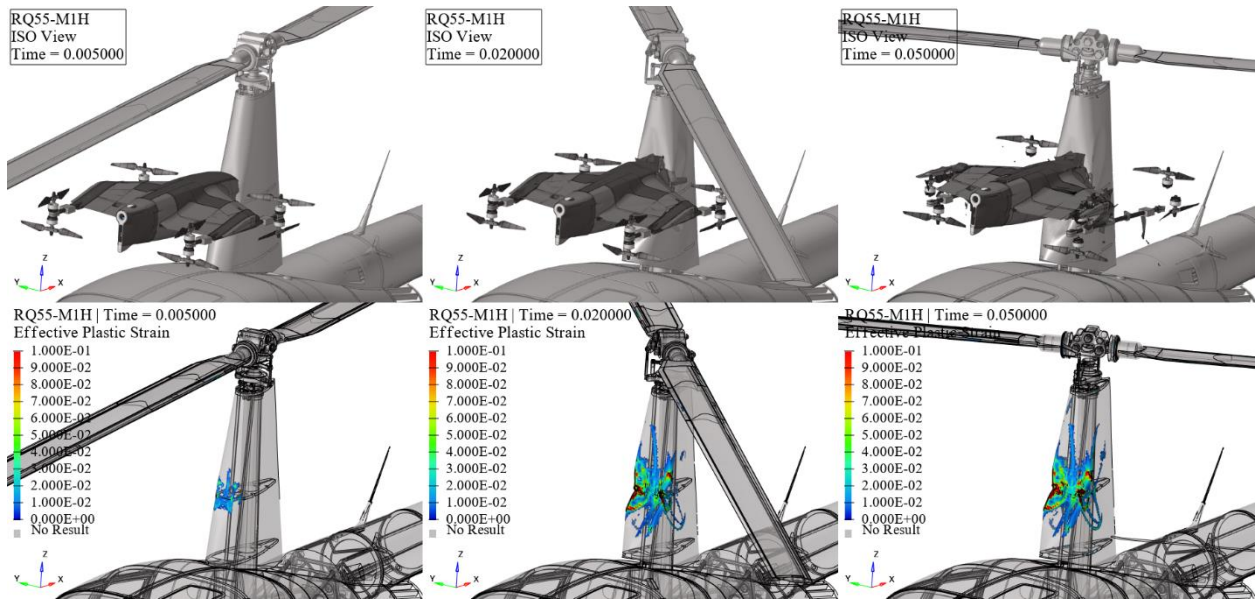Figure 208. RQ2.7-N1M kinematics (top) and effective plastic strain (bottom) frames.

Figure 209. RQ2.7-N1C kinematics (top) and effective plastic strain (bottom) frames.
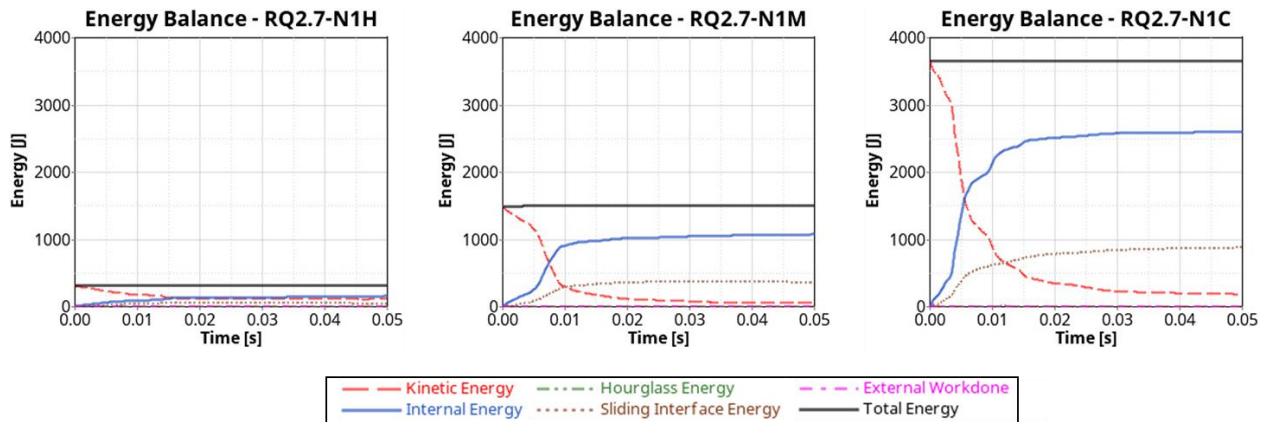
Figure 210. Nose and 2.7 lbs. quadcopter impact energy balance.

At hover velocity, the collision between the 2.7 lbs. quadcopter and the nose caused permanent skin deformation, resulting in a level 2 impact severity. At medium and cruise impact velocities, the nose sustained significantly greater damage compared to the hover velocity impact. This damage was characterized by major skin fractures and the penetration of several UAS components, leading to a level 3 impact severity.

5.4.2 UAS 4 lbs. Fixed-Wing

This section delineates the findings stemming from collisions involving 4 lbs. fixed-wing and the rotorcraft's Nose at Hover, Medium, and Cruise velocities, as showcased in Figure 211, Figure 212, and Figure 213, respectively. These results unravel the temporal progression of the impact occurrences, spotlighting time intervals at 0.005s, 0.02s, and 0.05s. The upper trio of windows highlights the kinematic aspects of the impacts, while the lower trio shows the resultant effective plastic strain on the rotorcraft structures. Additionally, Figure 214 provides the energy balance plots for all three impact velocities.

Figure 211. RF4-N1H kinematics (top) and effective plastic strain (bottom) frames.
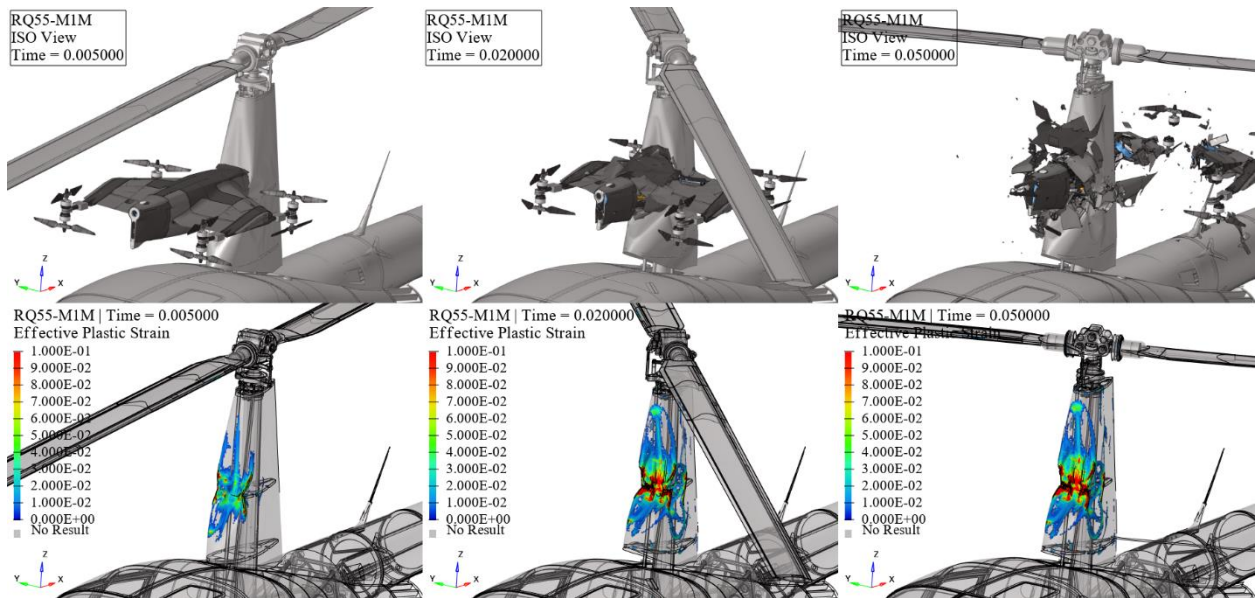

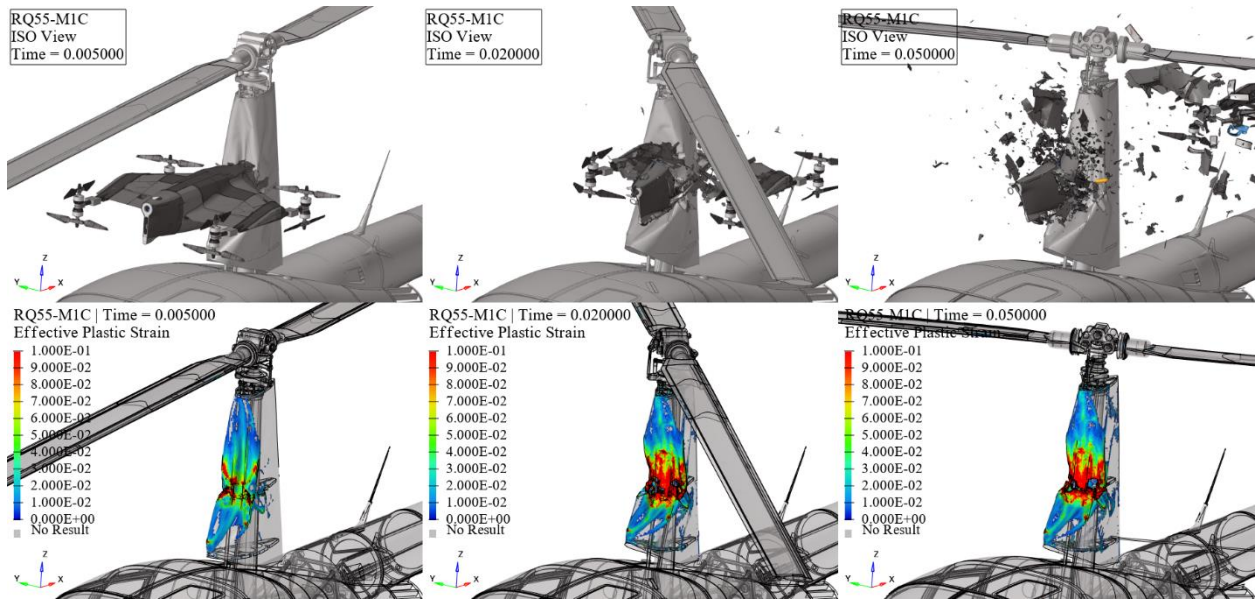Figure 212. RF4-N1M kinematics (top) and effective plastic strain (bottom) frames.

Figure 213. RF4-N1C kinematics (top) and effective plastic strain (bottom) frames.
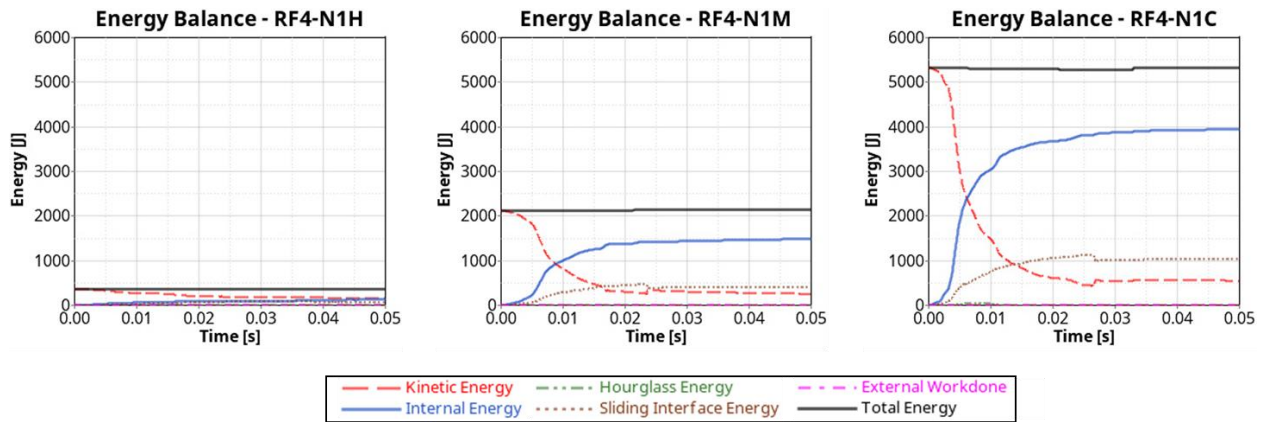
Figure 214. Nose and 4 lbs. fixed-wing impact energy balance.

At hover velocity, the collision between the 4 lbs. fixed-wing and the nose caused permanent skin deformation, resulting in a level 2 impact severity. At medium and cruise impact velocities, the nose sustained significantly greater damage compared to the hover velocity impact. This damage was characterized by major skin fractures and the penetration of a couple of UAS components, leading to a level 3 impact severity.

5.4.3   UAS 10 lbs. Quadcopter

This section delineates the findings stemming from collisions involving 10 lbs. quadcopter and the rotorcraft's Nose at Hover, Medium, and Cruise velocities, as showcased in Figure 215, Figure 216, and Figure 217, respectively. These results unravel the temporal progression of the impact occurrences, spotlighting time intervals at 0.005s, 0.02s, and 0.05s. The upper trio of windows highlights the kinematic aspects of the impacts, while the lower trio shows the resultant effective plastic strain on the rotorcraft structures. Additionally, Figure 218 provides the energy balance plots for all three impact velocities.
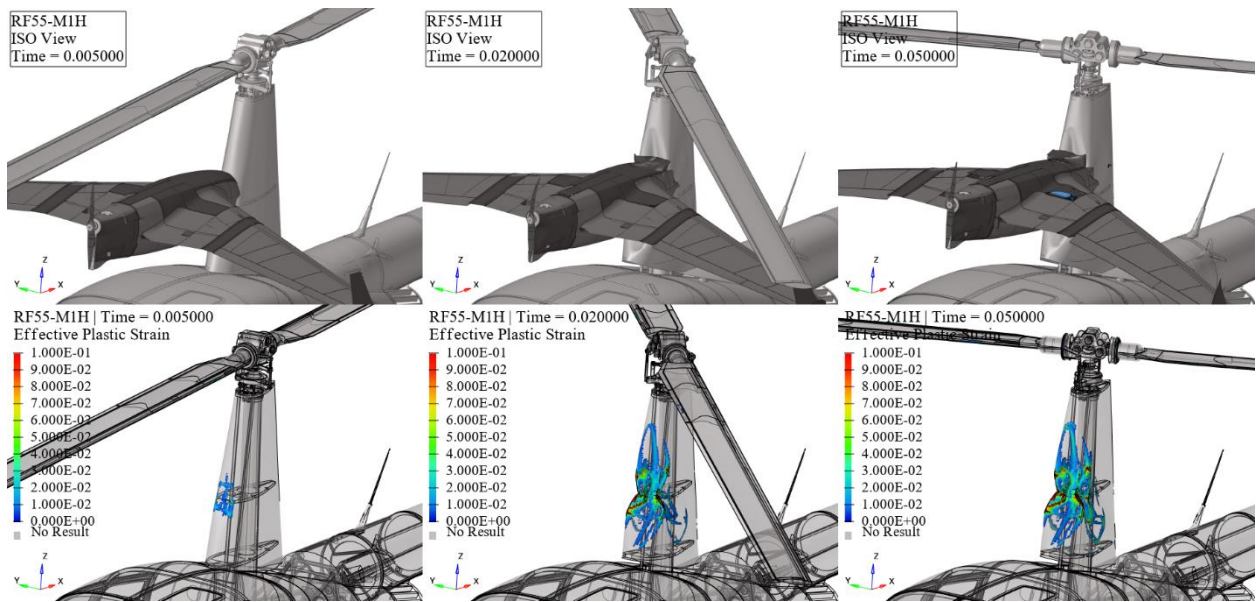
160

Figure 215. RQ10-N1H kinematics (top) and effective plastic strain (bottom) frames.
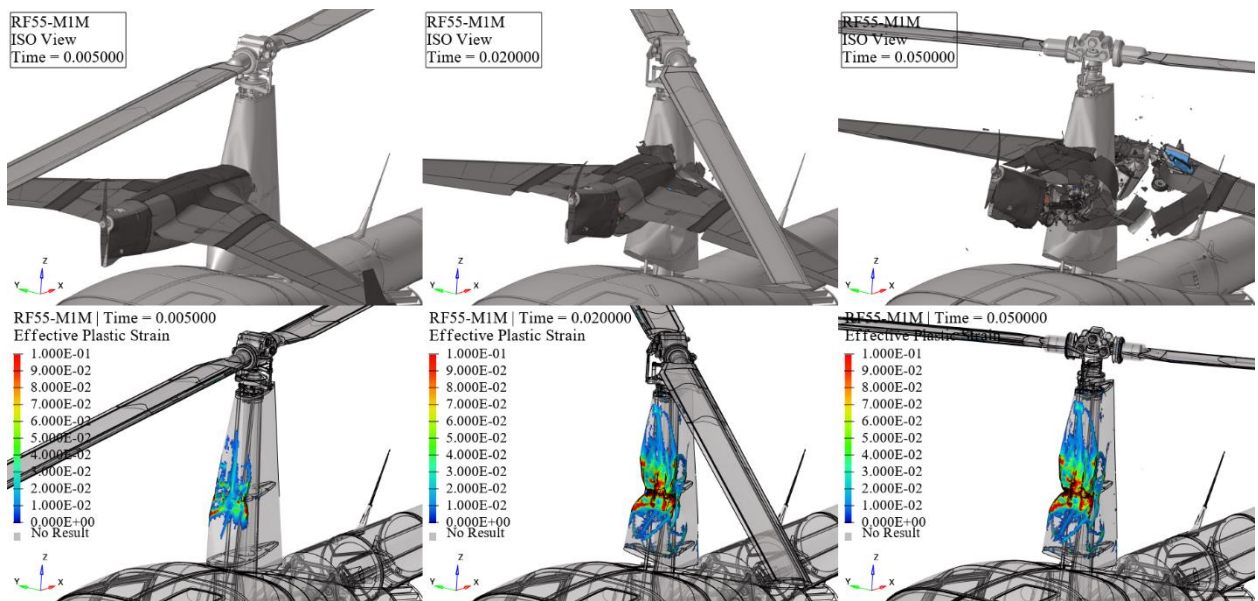

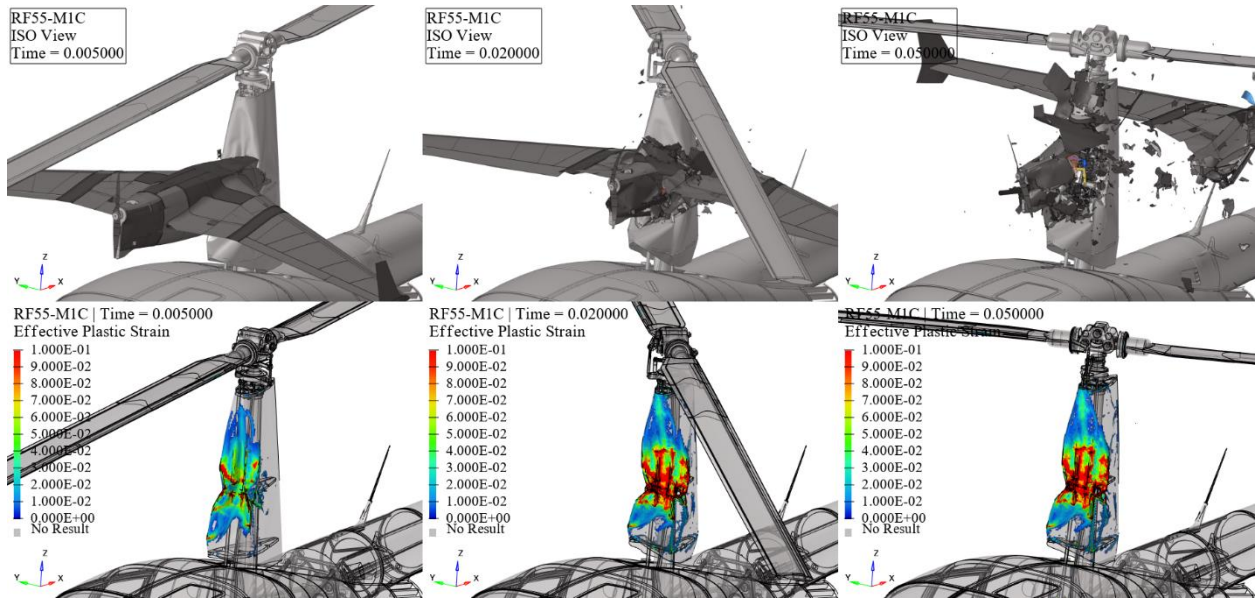Figure 216. RQ10-N1M kinematics (top) and effective plastic strain (bottom) frames.

161

Figure 217. RQ10-N1C kinematics (top) and effective plastic strain (bottom) frames.

Figure 218. Nose and 10 lbs. quadcopter impact energy balance.

At hover velocity, the collision between the 10 lbs. quadcopter and the nose caused permanent skin deformation, resulting in a level 2 impact severity. At medium and cruise impact velocities, the nose sustained significantly greater damage compared to the hover velocity impact. This damage was characterized by major skin fractures and the penetration of several UAS components, leading to a level 3 impact severity.

5.4.4   UAS 12 lbs. Fixed-Wing

This section delineates the findings stemming from collisions involving 12 lbs. fixed-wing and the rotorcraft's Nose at Hover, Medium, and Cruise velocities, as showcased in Figure 219, Figure 220, and Figure 221, respectively. These results unravel the temporal progression of the impact occurrences, spotlighting time intervals at 0.005s, 0.02s, and 0.05s. The upper trio of windows highlights the kinematic aspects of the impacts, while the lower trio shows the resultant effective plastic strain on the rotorcraft structures. Additionally, Figure 222 provides the energy balance plots for all three impact velocities.
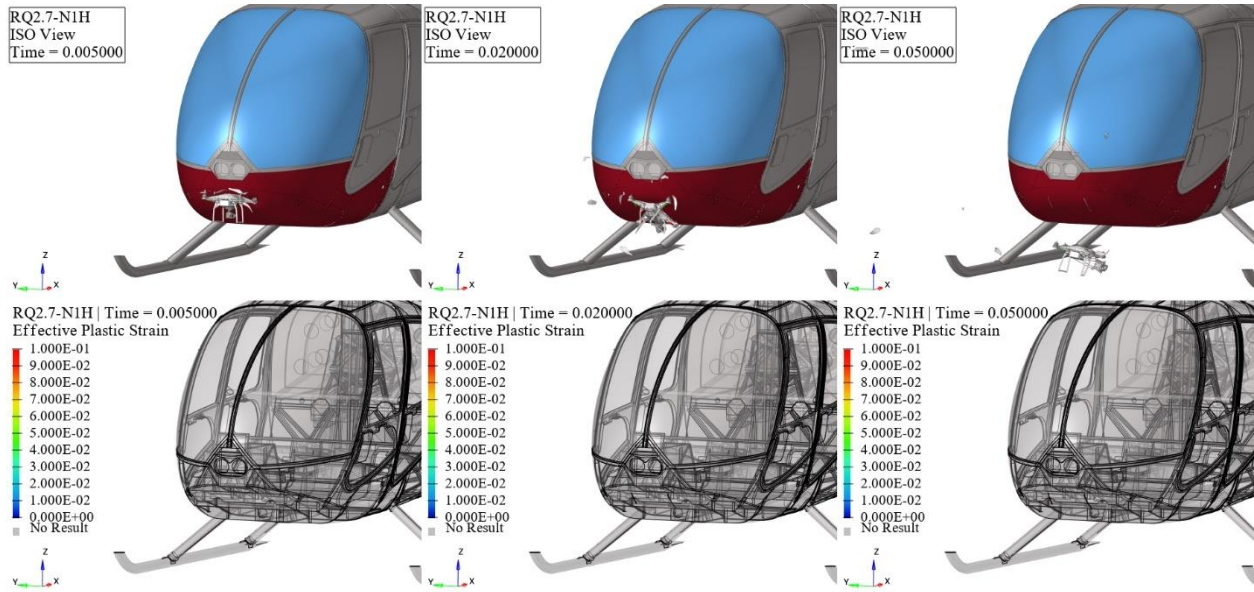
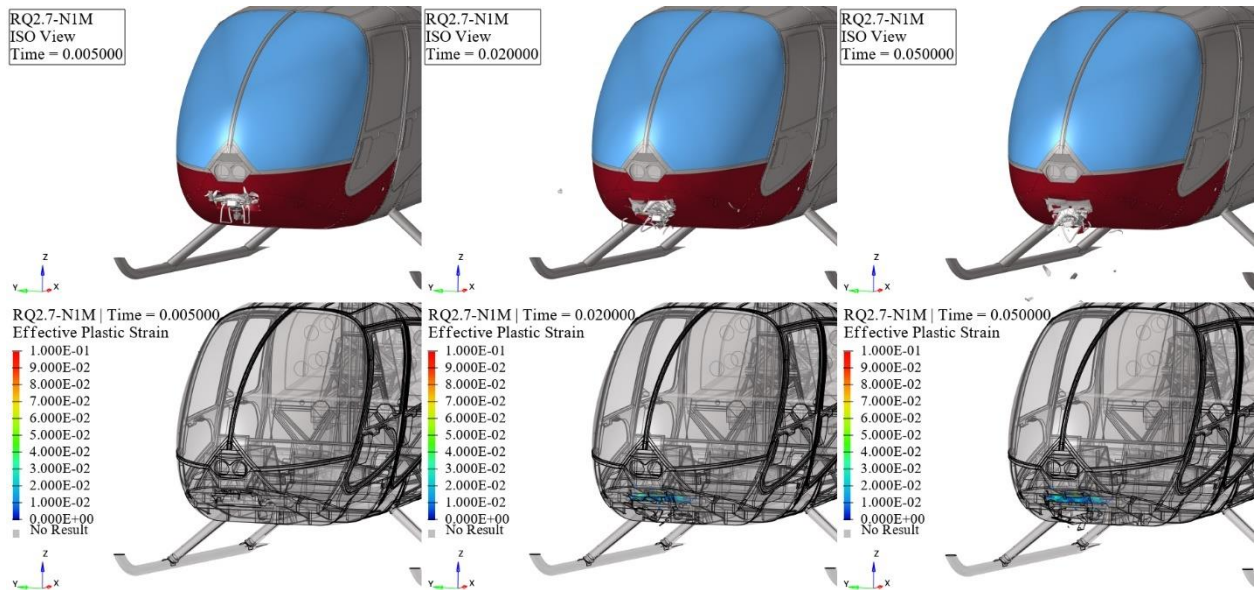Figure 219. RF12-N1H kinematics (top) and effective plastic strain (bottom) frames.

Figure 220. RF12-N1M kinematics (top) and effective plastic strain (bottom) frames.

Figure 221. RF12-N1C kinematics (top) and effective plastic strain (bottom) frames.

Figure 222. Nose and 12 lbs. fixed-wing impact energy balance.

At hover velocity, the collision between the 12 lbs. fixed-wing and the nose caused permanent skin deformation, resulting in a level 2 impact severity. At medium and cruise impact velocities, the nose sustained significantly greater damage compared to the hover velocity impact. This damage was characterized by major skin fractures and the penetration of several UAS components, leading to a level 3 impact severity.

5.4.5 UAS 25 lbs. Quadcopter

This section delineates the findings stemming from collisions involving 25 lbs. quadcopter and the rotorcraft's Nose at Hover, Medium, and Cruise velocities, as showcased in Figure 223, Figure 224, and Figure 225, respectively. These results unravel the temporal progression of the impact occurrences, spotlighting time intervals at 0.005s, 0.02s, and 0.05s. The upper trio of windows highlights the kinematic aspects of the impacts, while the lower trio shows the resultant effective plastic strain on the rotorcraft structures. Additionally, Figure 226 provides the energy balance plots for all three impact velocities.

164

Figure 223. RQ25-N1H kinematics (top) and effective plastic strain (bottom) frames.

Figure 224. RQ25-N1M kinematics (top) and effective plastic strain (bottom) frames.
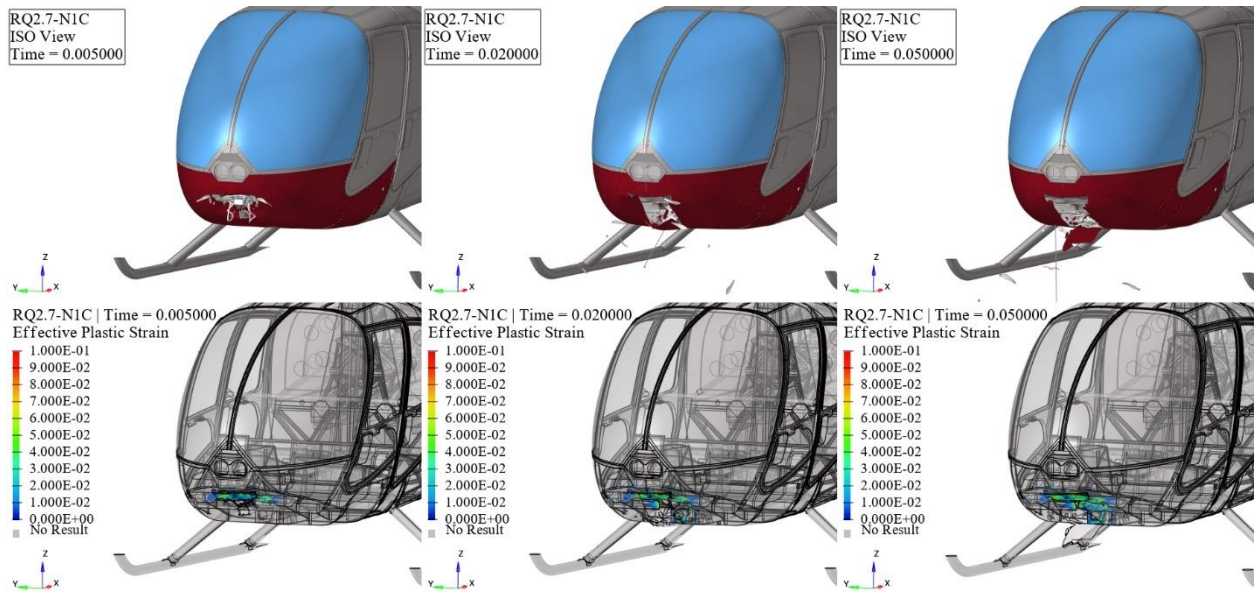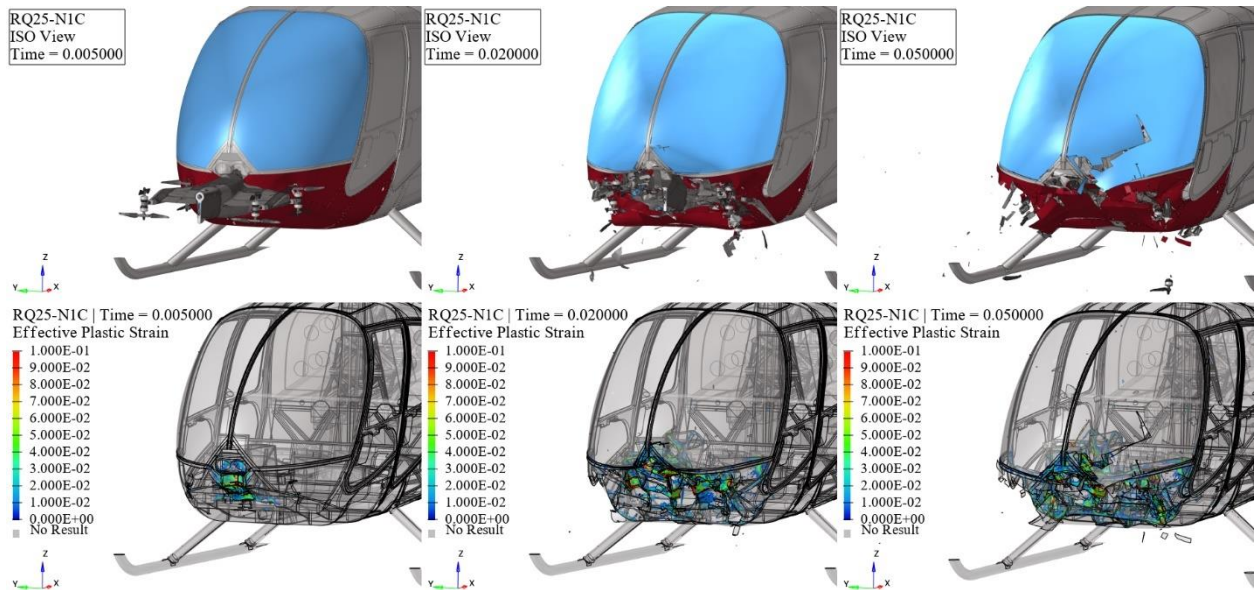
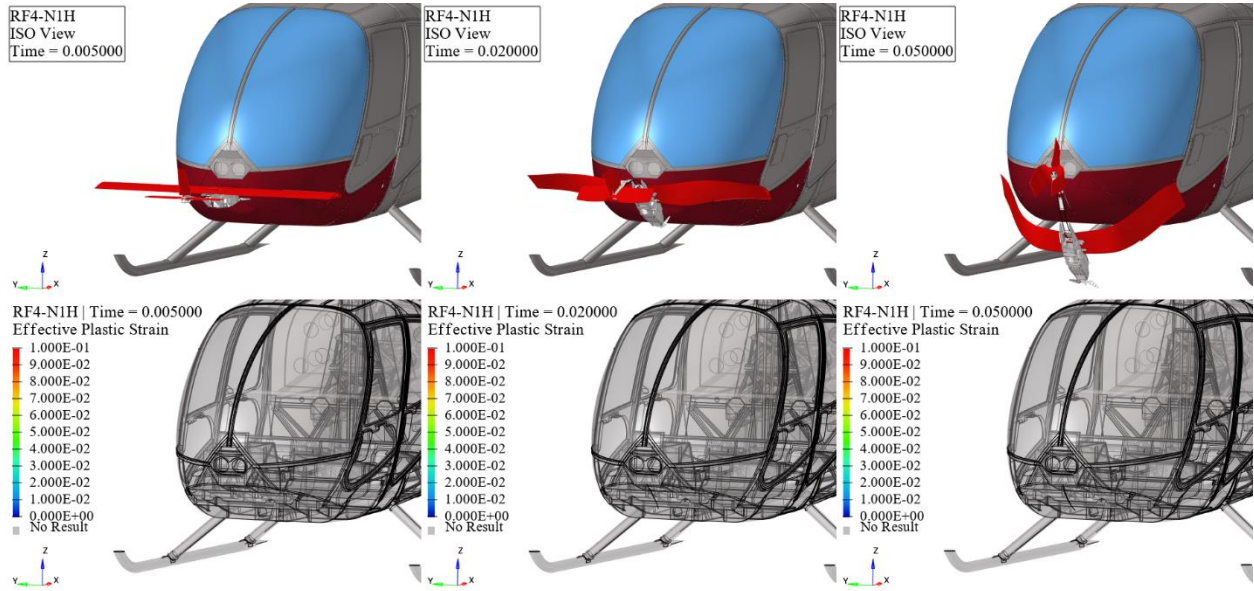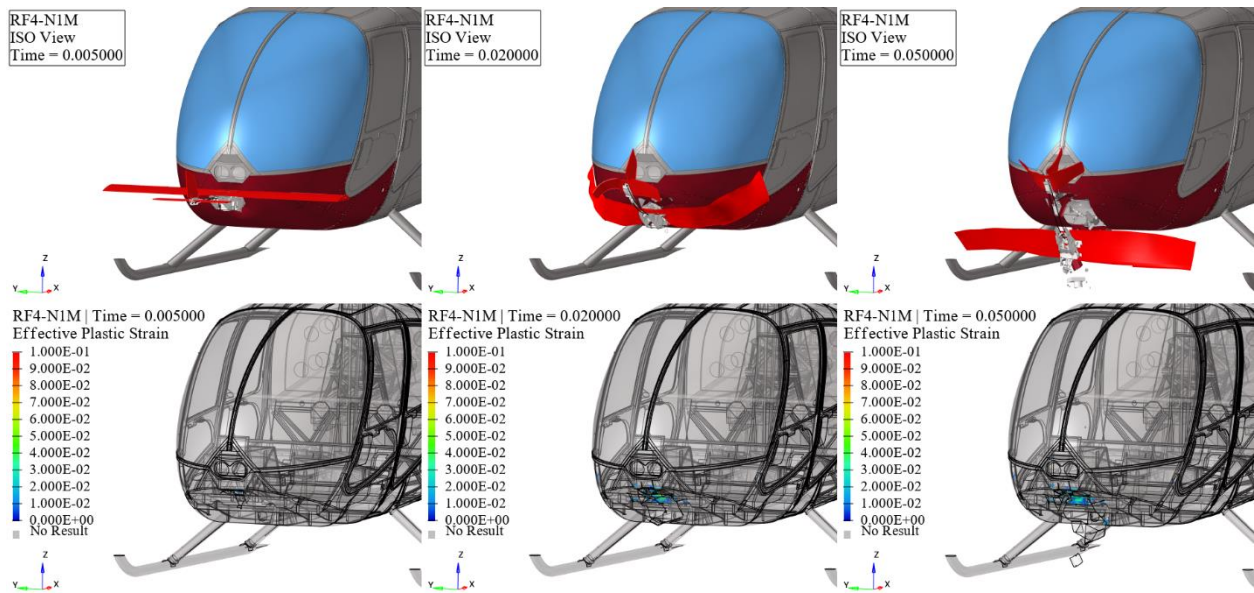Figure 225. RQ25-N1C kinematics (top) and effective plastic strain (bottom) frames.
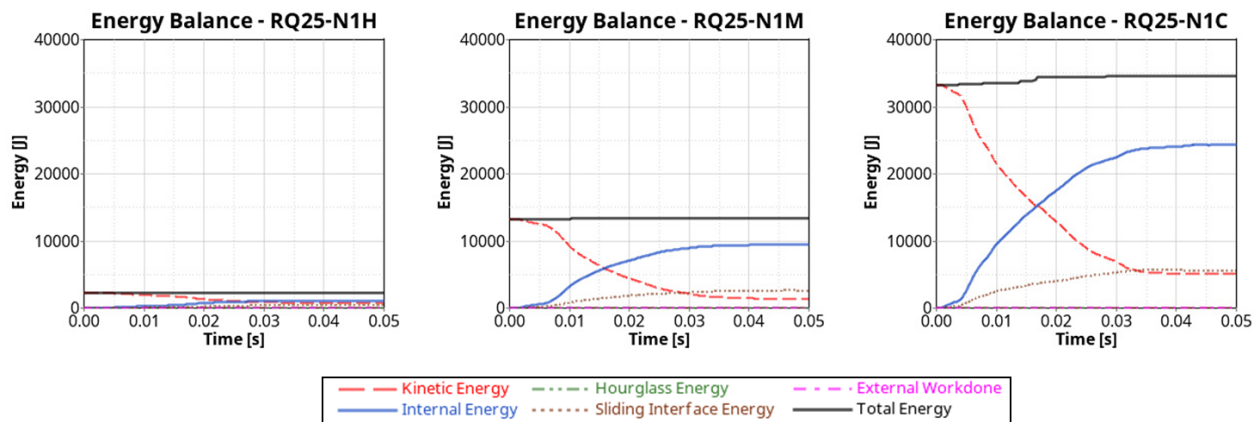
Figure 226. Nose and 25lbs. quadcopter impact energy balance.

At hover velocity, the collision between the 25lbs. quadcopter and the nose caused permanent skin deformation, resulting in a level 2 impact severity. At medium impact velocity, the nose sustained significantly greater damage compared to the hover velocity impact. This damage was characterized by major skin fractures and the penetration of several UAS components, leading to a level 3 impact severity. Subsequently, the rotorcraft's nose and windshield saw severe damage at cruise impact velocity, resulting in a level 4 impact severity.

5.4.6   UAS 25lbs. Fixed-Wing

This section delineates the findings stemming from collisions involving 25lbs. fixed-wing and the rotorcraft's Nose at Hover, Medium, and Cruise velocities, as showcased in Figure 227, Figure 228, and Figure 229, respectively. These results unravel the temporal progression of the impact occurrences, spotlighting time intervals at 0.005s, 0.02s, and 0.05s. The upper trio of windows highlights the kinematic aspects of the impacts, while the lower trio shows the resultant effective

166

plastic strain on the rotorcraft structures. Additionally, Figure 230 provides the energy balance plots for all three impact velocities.

Figure 227. RF25-N1H kinematics (top) and effective plastic strain (bottom) frames.

Figure 228. RF25-N1M kinematics (top) and effective plastic strain (bottom) frames.
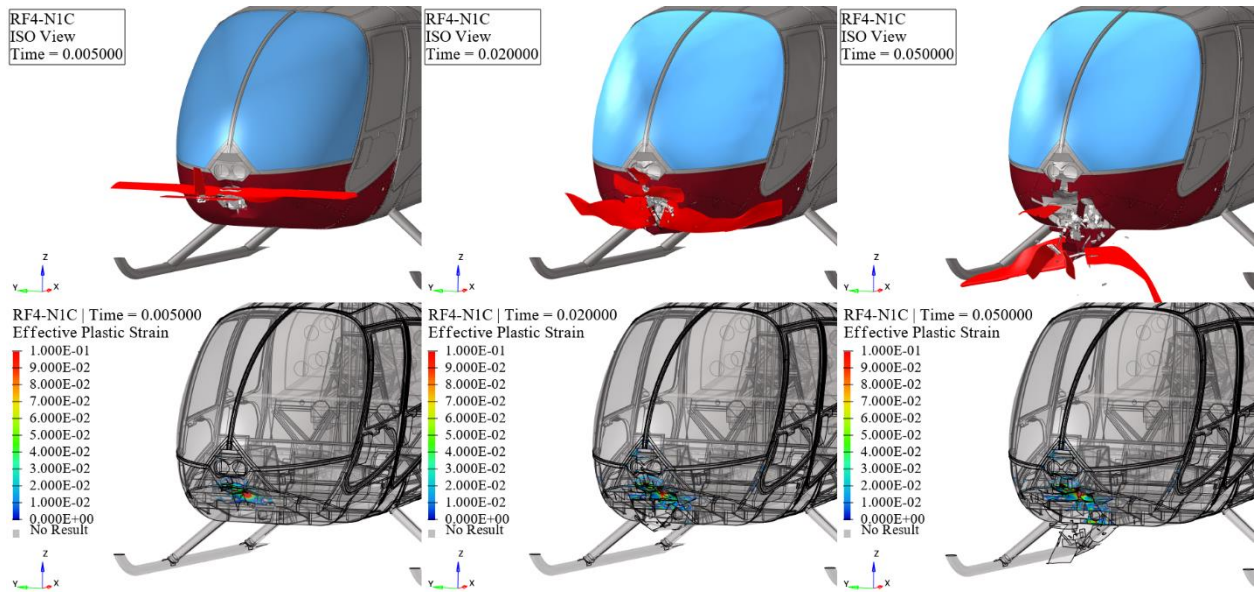
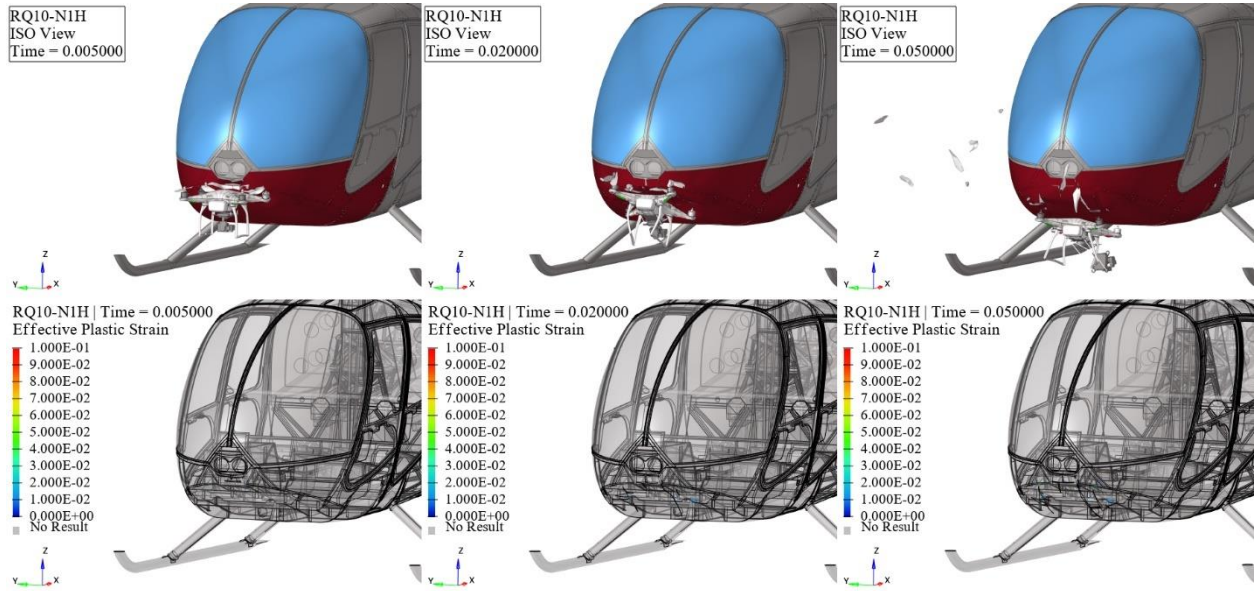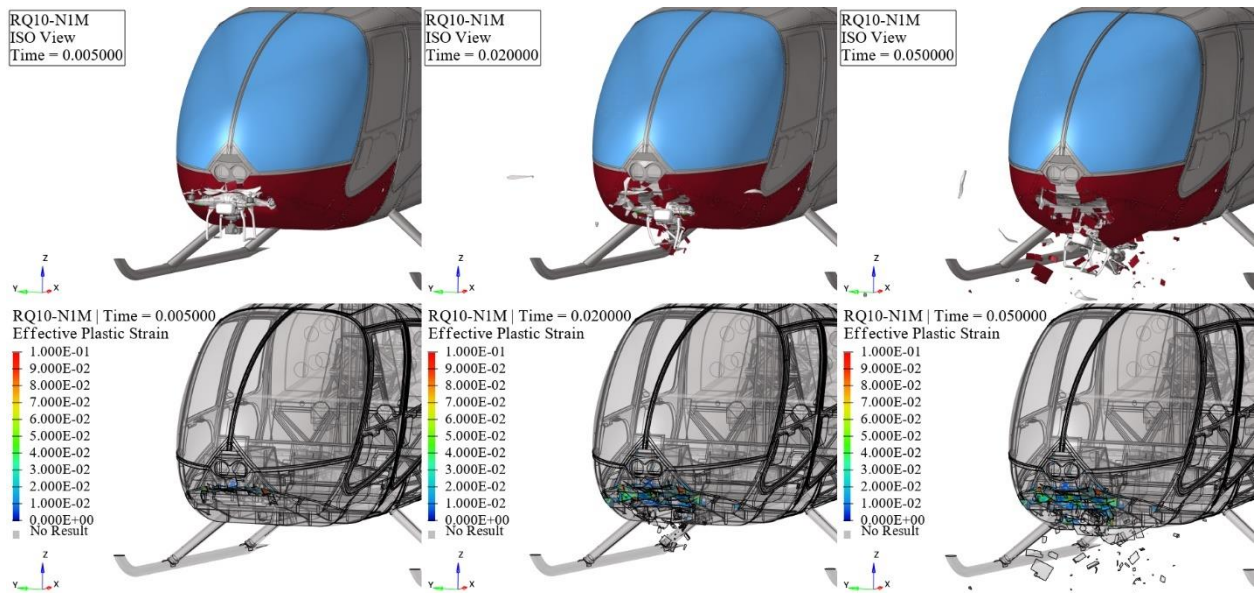Figure 229. RF25-N1C kinematics (top) and effective plastic strain (bottom) frames.
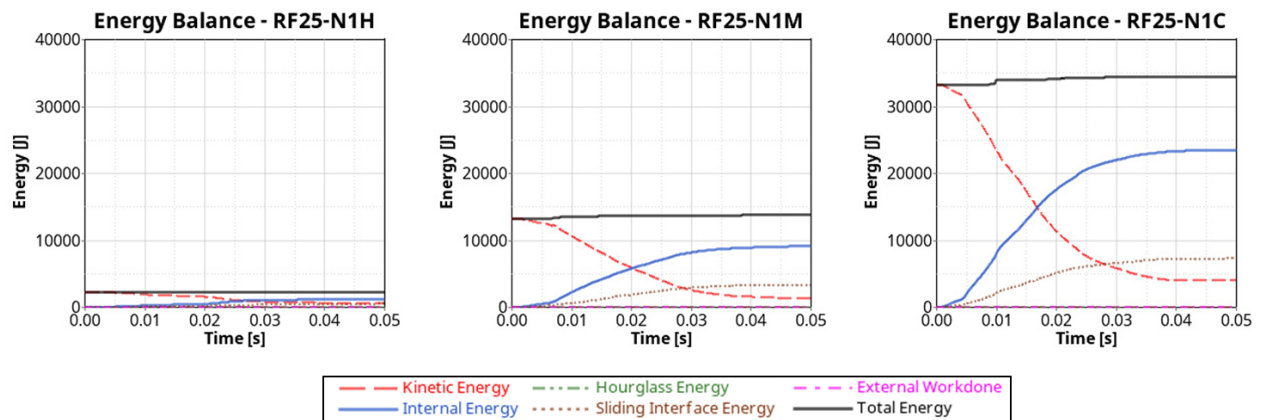
Figure 230. Nose and 25 lbs. fixed-wing impact energy balance.

At hover velocity, the collision between the 25 lbs. fixed-wing and the nose caused permanent skin deformation, resulting in a level 2 impact severity. At medium impact velocity, the nose sustained significantly greater damage compared to the hover velocity impact. This damage was characterized by major skin fractures and the penetration of several UAS components, leading to a level 3 impact severity. Subsequently, the rotorcraft's nose and windshield saw severe damage at cruise impact velocity, resulting in a level 4 impact severity.

5.4.7   UAS 55 lbs. Quadcopter

This section delineates the findings stemming from collisions involving 55 lbs. quadcopter and the rotorcraft's Nose at Hover, Medium, and Cruise velocities, as showcased in Figure 231, Figure 232, and Figure 233, respectively. These results unravel the temporal progression of the impact occurrences, spotlighting time intervals at 0.005s, 0.02s, and 0.05s. The upper trio of windows highlights the kinematic aspects of the impacts, while the lower trio shows the resultant effective

168

plastic strain on the rotorcraft structures. Additionally, Figure 234 provides the energy balance plots for all three impact velocities.

Figure 231. RQ55-N1H kinematics (top) and effective plastic strain (bottom) frames.

Figure 232. RQ55-N1M kinematics (top) and effective plastic strain (bottom) frames.
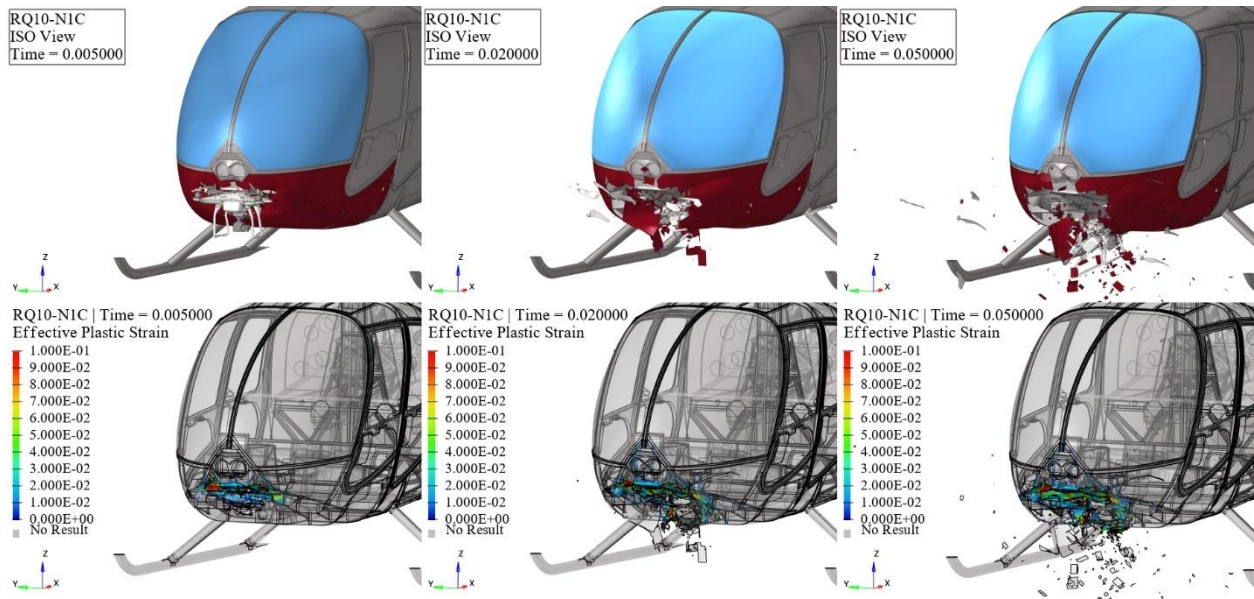
Figure 233. RQ55-N1C kinematics (top) and effective plastic strain (bottom) frames.
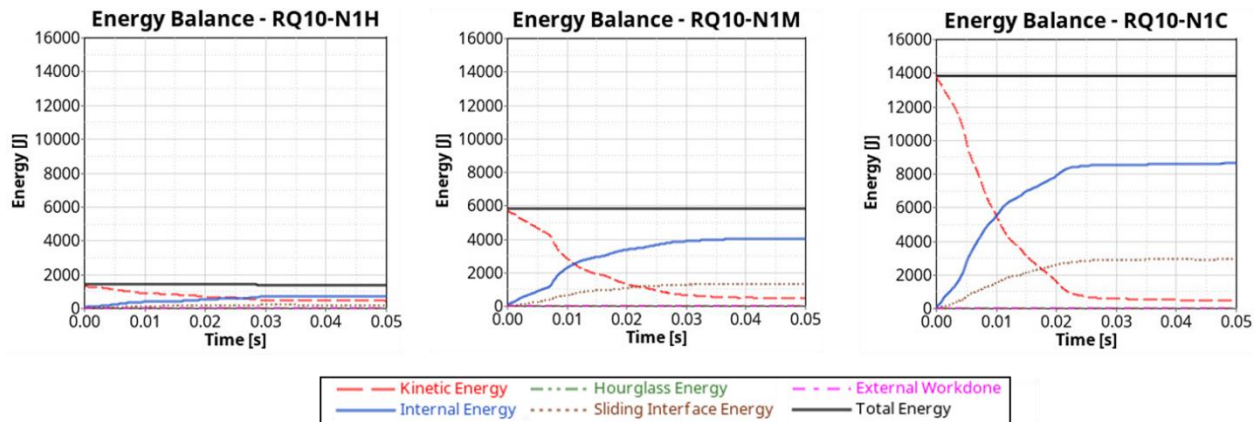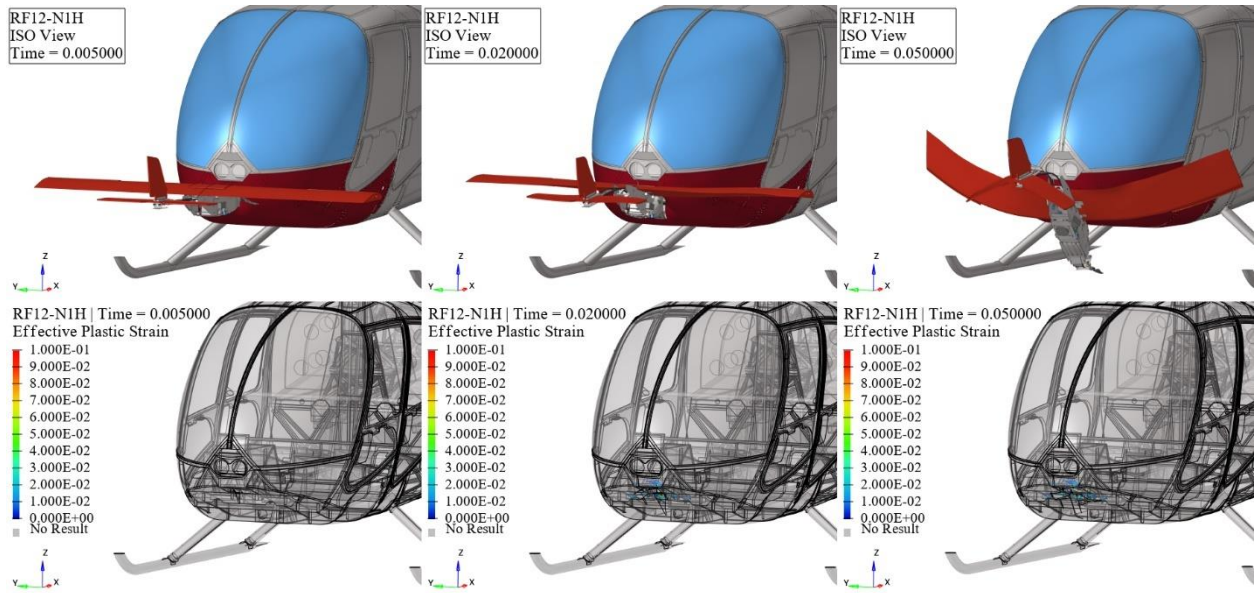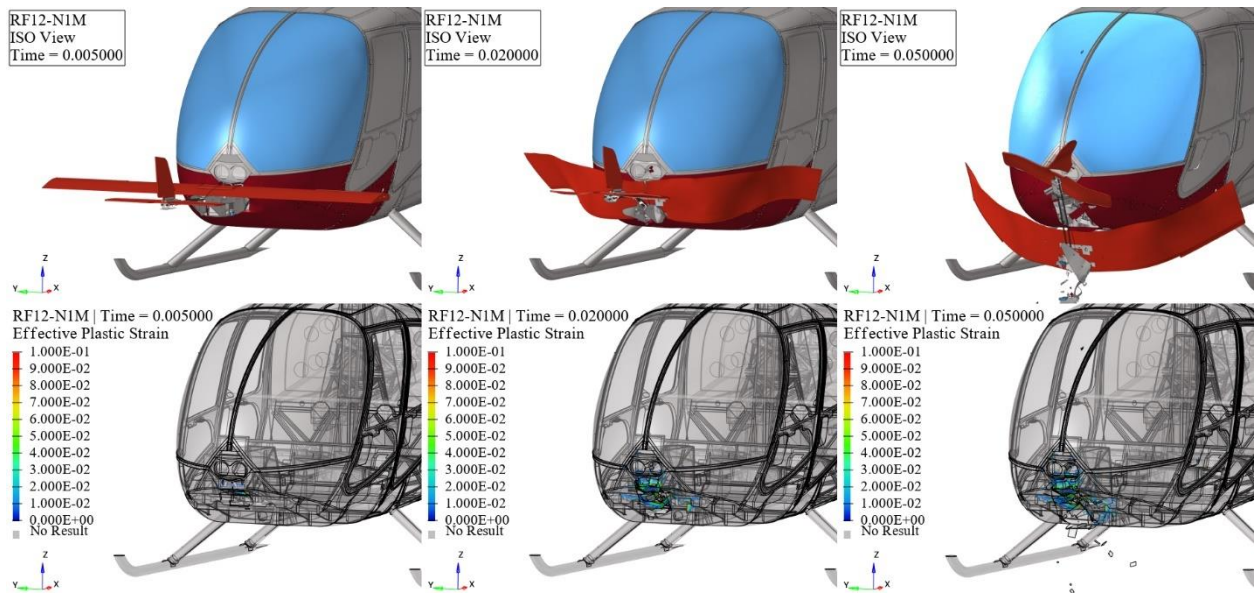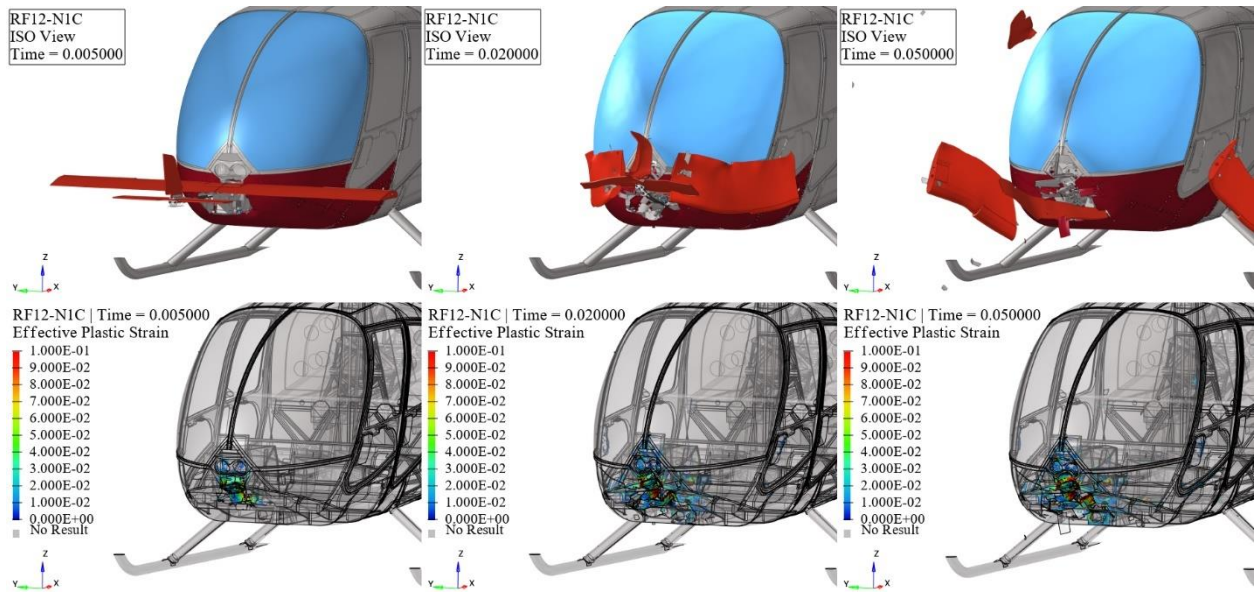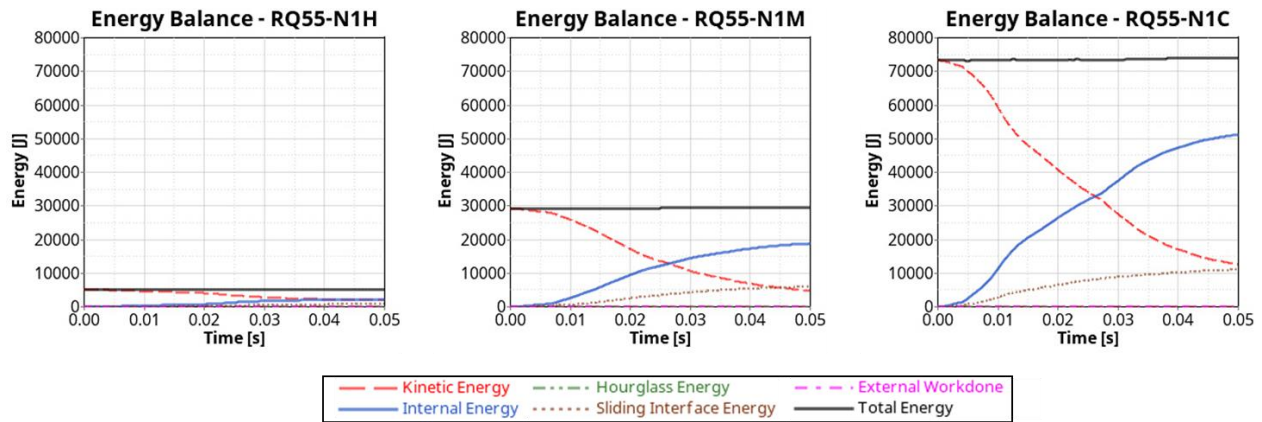

Figure 234. Nose and 55 lbs. quadcopter impact energy balance.

At hover velocity, the collision between the 55 lbs. quadcopter and the nose caused permanent skin deformation, resulting in a level 2 impact severity. At medium impact velocity, the nose sustained significantly greater damage compared to the hover velocity impact. This damage was characterized by complete skin fracture, damage to major internal structures, and full UAS penetration, leading to a level 4 impact severity. Subsequently, the rotorcraft's nose and windshield experienced severe damage at cruise impact velocity, resulting in a level 4 impact severity.

5.4.8   UAS 55 lbs. Fixed-Wing

This section delineates the findings stemming from collisions involving 55 lbs. fixed-wing and the rotorcraft's Nose at Hover, Medium, and Cruise velocities, as showcased in Figure 235, Figure 236, and Figure 237, respectively. These results unravel the temporal progression of the impact occurrences, spotlighting time intervals at 0.005s, 0.02s, and 0.05s. The upper trio of windows highlights the kinematic aspects of the impacts, while the lower trio shows the resultant effective

170

plastic strain on the rotorcraft structures. Additionally, Figure 238 provides the energy balance plots for all three impact velocities.

Figure 235. RF55-N1H kinematics (top) and effective plastic strain (bottom) frames.

Figure 236. RF55-N1M kinematics (top) and effective plastic strain (bottom) frames.

Figure 237. RF55-N1C kinematics (top) and effective plastic strain (bottom) frames.
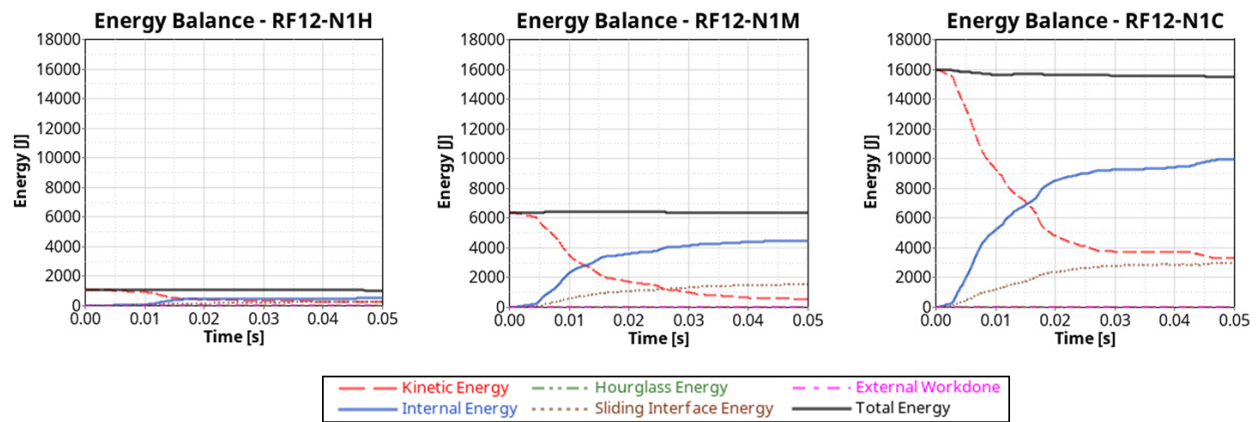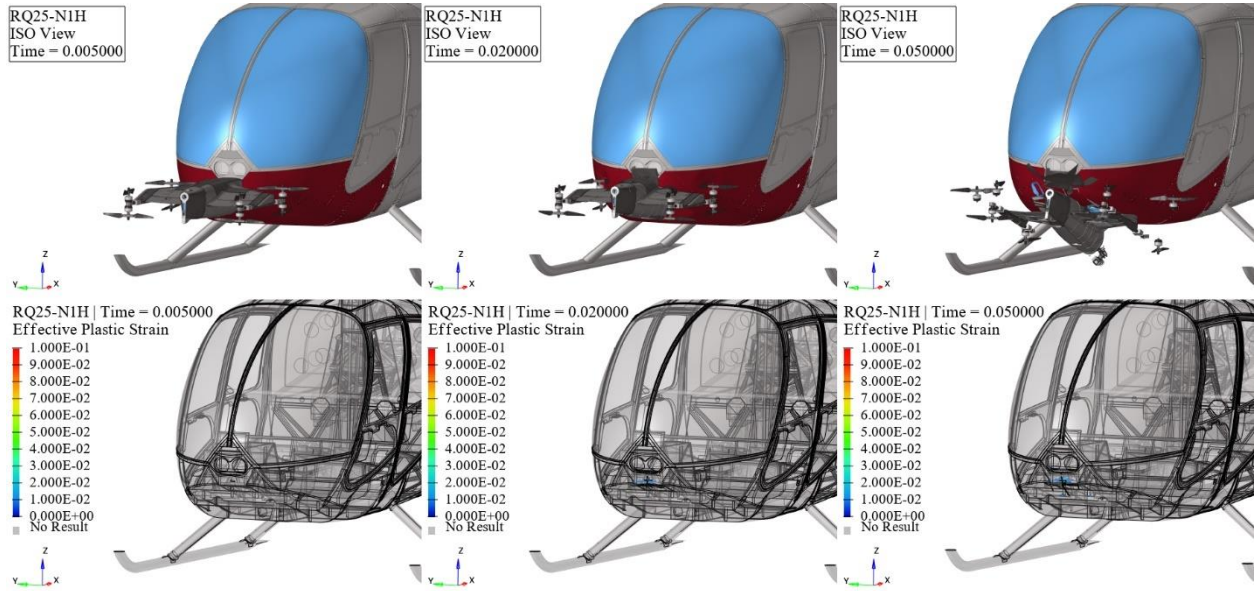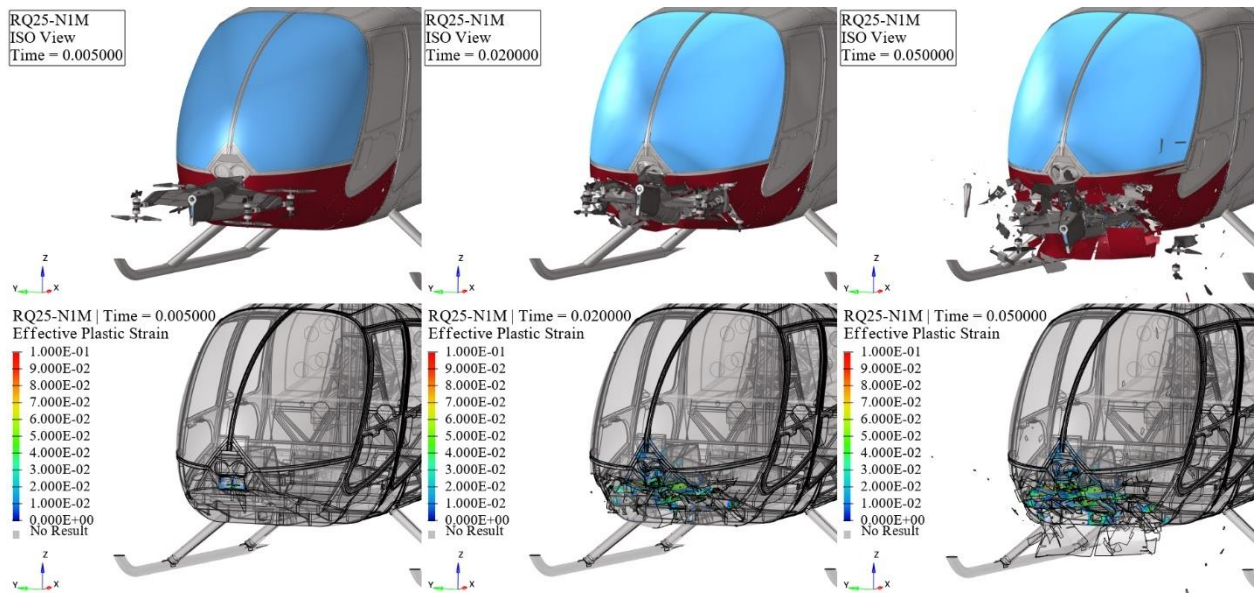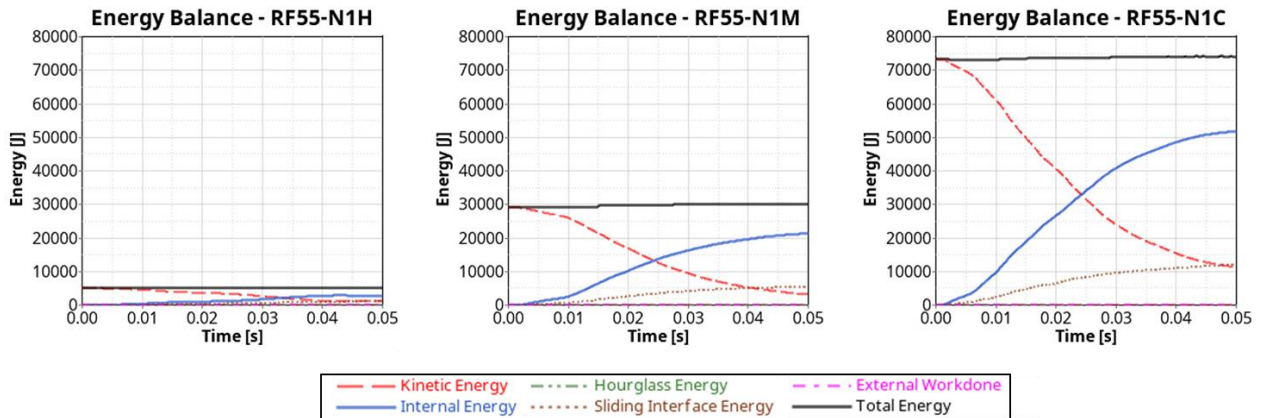

Figure 238. Nose and 55 lbs. fixed-wing impact energy balance.

At hover velocity, the collision between the 55 lbs. fixed-wing and the nose caused permanent skin deformation, resulting in a level 2 impact severity. At medium and cruise impact velocities, the rotorcraft's nose and windshield experienced severe damage, resulting in a level 4 impact severity.

5.5 Windshield

This section presents the results of the airborne collision studies for all UAS and the rotorcraft's Windshield. Figure 239 shows an example of the simulation setup for the Windshield impact with 55 lbs. quadcopter at cruise speed.
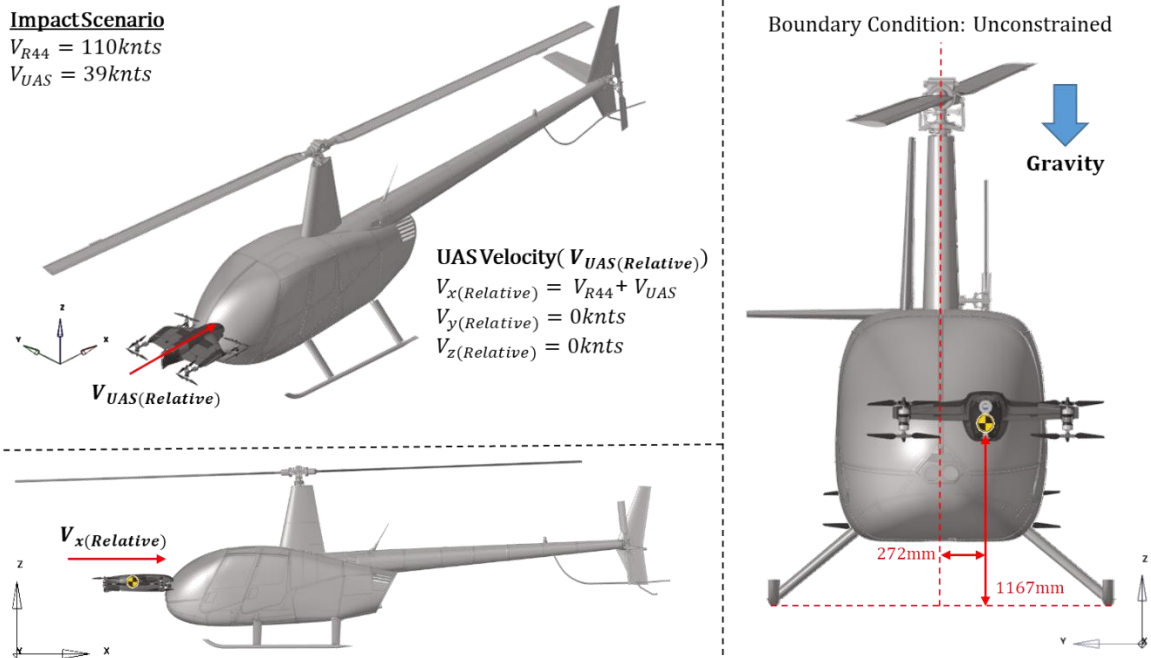
Figure 239. Simulation setup for impact between the windshield and 55 lbs. quadcopter at cruise velocity.

Table 46 summarizes the damage severity level evaluation and fire risk assessment for impact cases for all UAS with the Windshield.

Table 46. Windshield mid-air collision simulation assessment – damage severity level and fire risk.

		Case	Severity	Fire Risk
Mid-air collision Rotorcraft-Windshield and all sUAS	Quadcopter 2.7 lbs.	RQ2.7-W1H	Level 1	No
		RQ2.7-W1M	Level 4	No
		RQ2.7-W1C	Level 4	Yes
	Fixed-Wing 4 lbs.	RF4-W1H	Level 1	No
		RF4-W1M	Level 4	No
		RF4-W1C	Level 4	No
	Quadcopter 10 lbs.	RQ10-W1H	Level 4	No
		RQ10-W1M	Level 4	No
		RQ10-W1C	Level 4	No
	Fixed-Wing 12 lbs.	RF12-W1H	Level 2	No
		RF12-W1M	Level 4	Yes
		RF12-W1C	Level 4	No
	Quadcopter 25 lbs.	RQ25-W1H	Level 2	No
		RQ25-W1M	Level 4	Yes
		RQ25-W1C	Level 4	No
	Fixed-Wing 25 lbs.	RF25-W1H	Level 3	No
		RF25-W1M	Level 4	Yes
		RF25-W1C	Level 4	No
	Quadcopter 55 lbs.	RQ55-W1H	Level 4	No
		RQ55-W1M	Level 4	Yes
		RQ55-W1C	Level 4	No
	Fixed-Wing 55 lbs.	RF55-W1H	Level 4	No
		RF55-W1M	Level 4	Yes
		RF55-W1C	Level 4	No

5.5.1 UAS 2.7 lbs. Quadcopter

This section delineates the findings stemming from collisions involving 2.7 lbs. quadcopter and the rotorcraft's Windshield at Hover, Medium, and Cruise velocities, as showcased in Figure 240, Figure 241, and Figure 242, respectively. These results unravel the temporal progression of the impact occurrences, spotlighting time intervals at 0.005s, 0.02s, and 0.05s. The upper trio of

windows highlights the kinematic aspects of the impacts, while the lower trio shows the resultant effective plastic strain on the rotorcraft structures. Additionally, Figure 243 provides the energy balance plots for all three impact velocities.
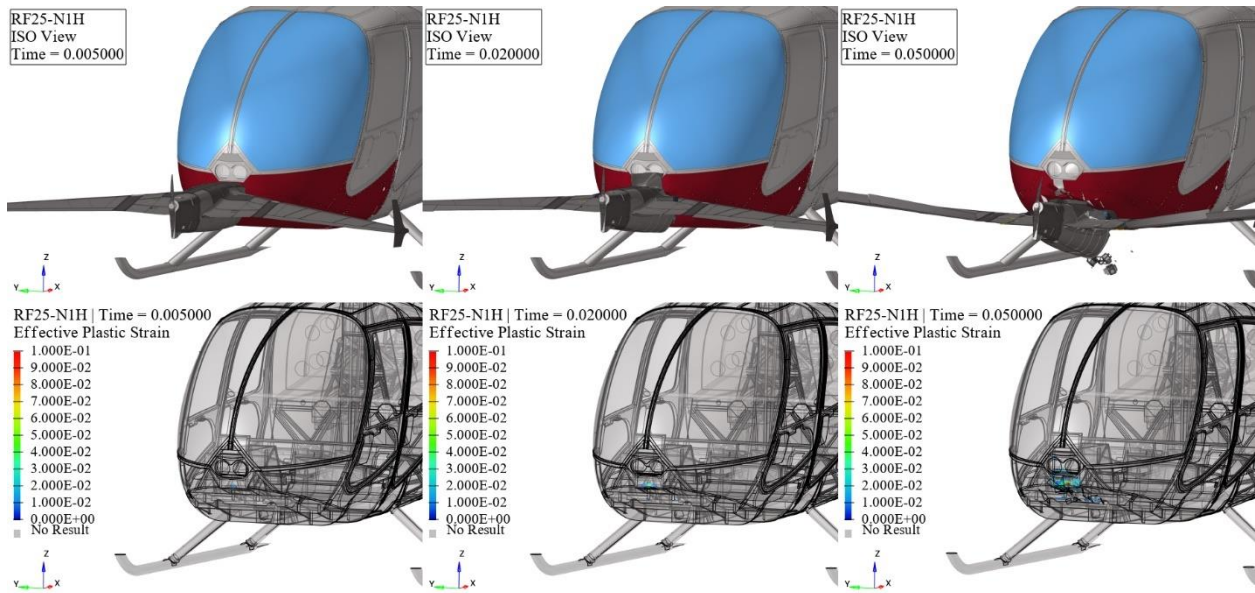

Figure 240. RQ2.7-W1H kinematics (top) and effective plastic strain (bottom) frames.
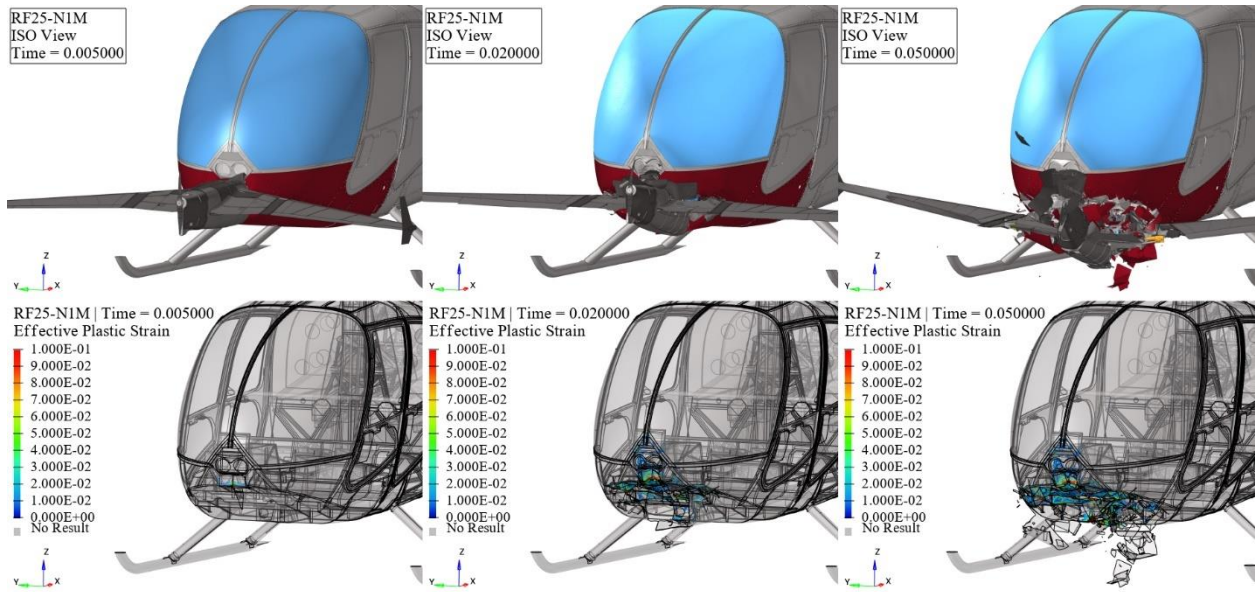

Figure 241. RQ2.7-W1M kinematics (top) and effective plastic strain (bottom) frames.
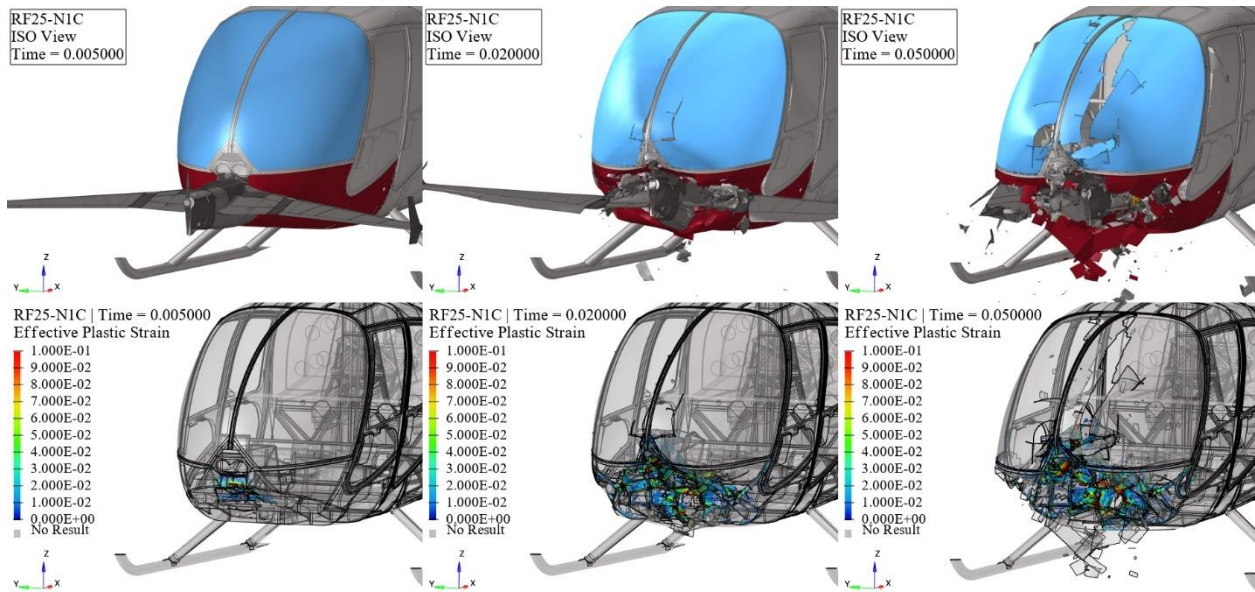
Figure 242. RQ2.7-W1C kinematics (top) and effective plastic strain (bottom) frames.
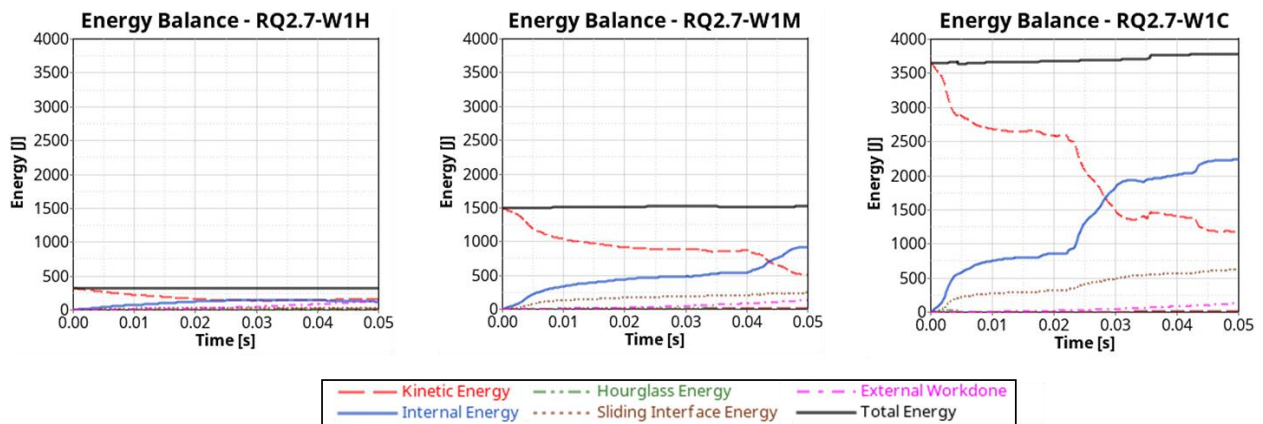
Figure 243. Windshield and 2.7 lbs. quadcopter impact energy balance.

At hover velocity, the collision between the 2.7 lbs. quadcopter and the windshield caused minor dents, resulting in a level 1 impact severity. The windshield fractured at medium, and cruise impact velocities, and the UAS penetrated the passenger cabin, resulting in a level 4 impact severity.

5.5.2   UAS 4 lbs. Fixed-Wing

This section delineates the findings stemming from collisions involving 4 lbs. fixed-wing and the rotorcraft's Windshield at Hover, Medium, and Cruise velocities, as showcased in Figure 244, Figure 245, and Figure 246, respectively. These results unravel the temporal progression of the impact occurrences, spotlighting time intervals at 0.005s, 0.02s, and 0.05s. The upper trio of windows highlights the kinematic aspects of the impacts, while the lower trio shows the resultant effective plastic strain on the rotorcraft structures. Additionally, Figure 247 provides the energy balance plots for all three impact velocities.
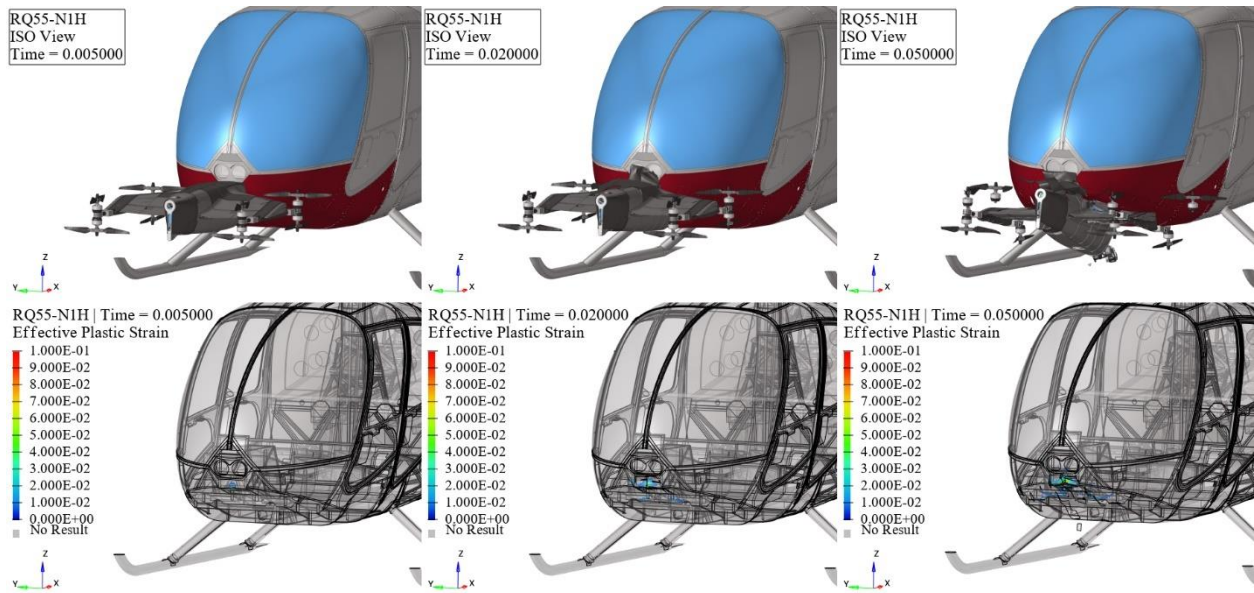
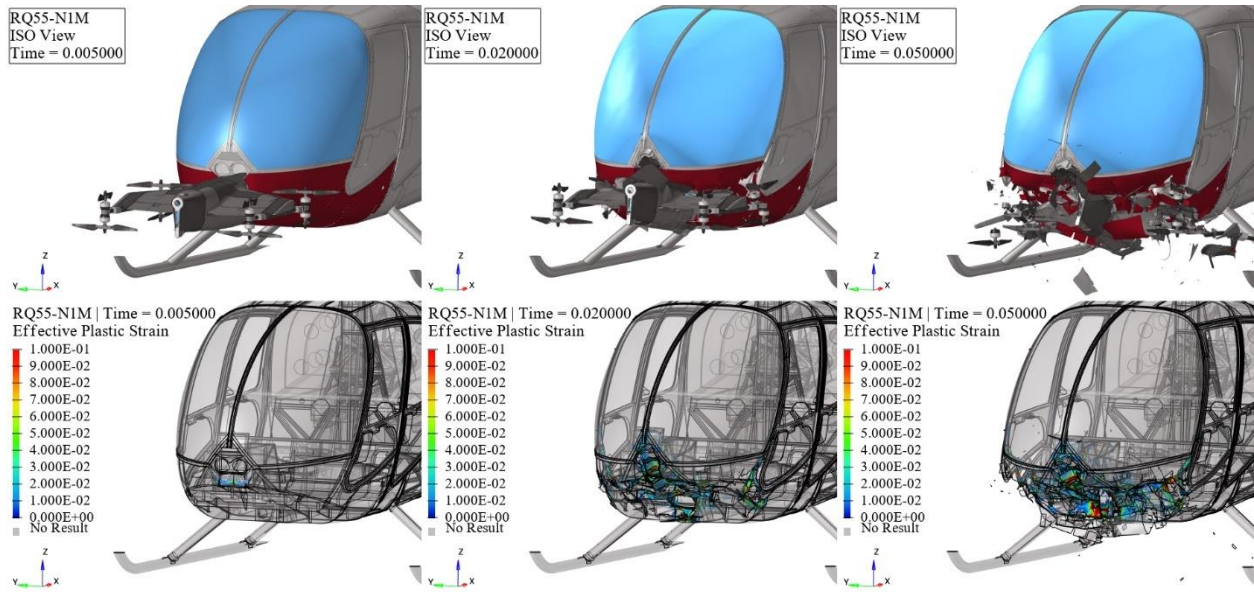Figure 244. RF4-W1H kinematics (top) and effective plastic strain (bottom) frames.

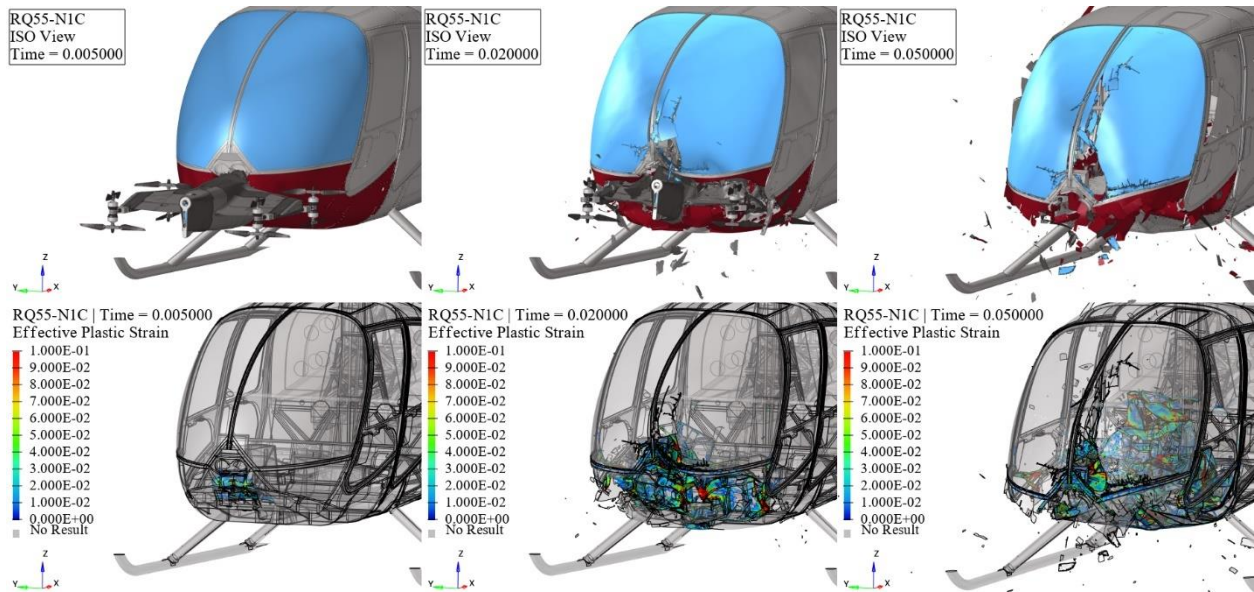Figure 245. RF4-W1M kinematics (top) and effective plastic strain (bottom) frames.

Figure 246. RF4-W1C kinematics (top) and effective plastic strain (bottom) frames.

Figure 247. Windshield and 4 lbs. fixed-wing impact energy balance.

At hover velocity, the collision between the 4 lbs. fixed-wing and the windshield caused minor dents, resulting in a level 1 impact severity. The windshield fractured at medium and cruise impact velocities, and the UAS penetrated the passenger cabin, resulting in a level 4 impact severity.

5.5.3   UAS 10 lbs. Quadcopter

This section delineates the findings stemming from collisions involving 10 lbs. quadcopter and the rotorcraft's Windshield at Hover, Medium, and Cruise velocities, as showcased in Figure 248, Figure 249, and Figure 250, respectively. These results unravel the temporal progression of the impact occurrences, spotlighting time intervals at 0.005s, 0.02s, and 0.05s. The upper trio of windows highlights the kinematic aspects of the impacts, while the lower trio shows the resultant effective plastic strain on the rotorcraft structures. Additionally, Figure 251 provides the energy balance plots for all three impact velocities.
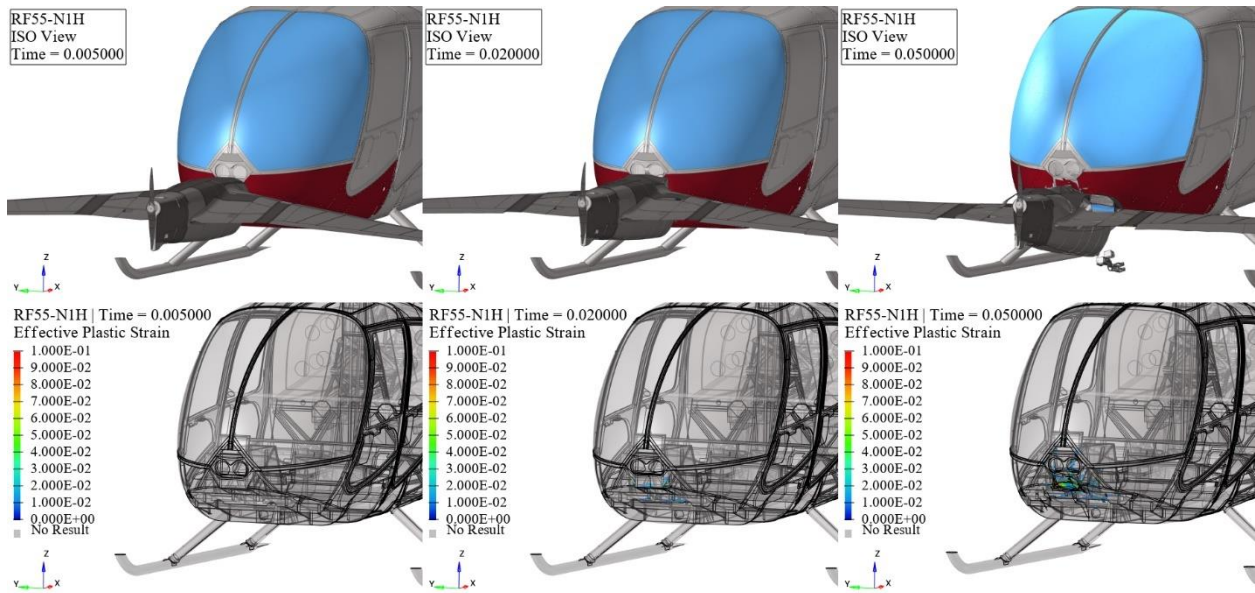
Figure 248. RQ10-W1H kinematics (top) and effective plastic strain (bottom) frames.
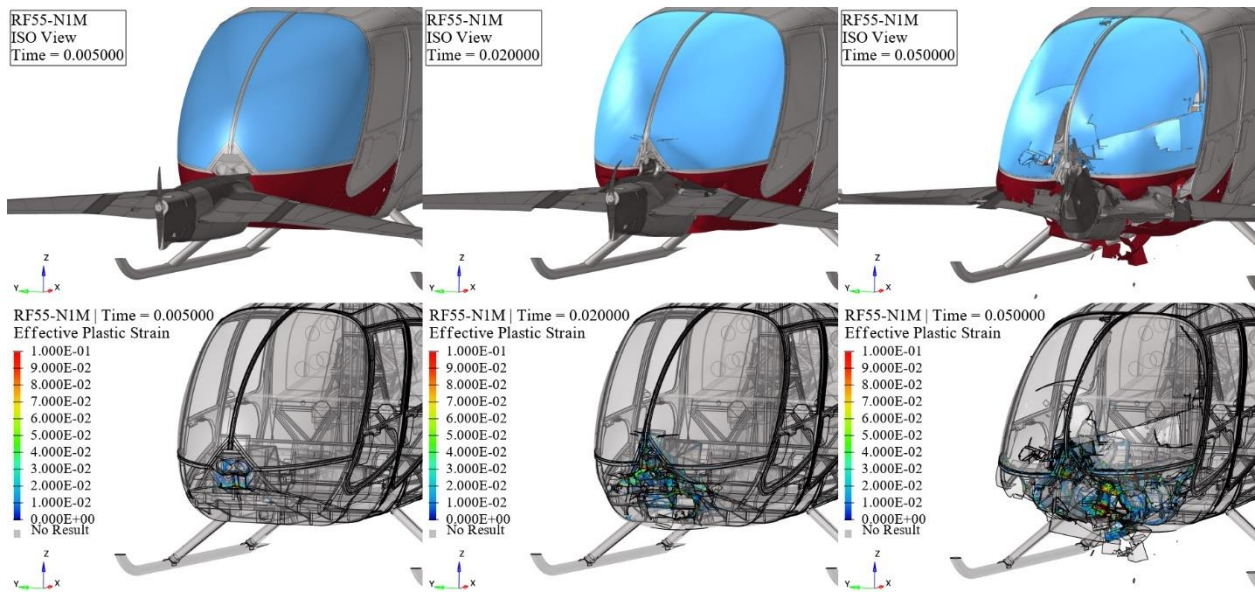

Figure 249. RQ10-W1M kinematics (top) and effective plastic strain (bottom) frames.
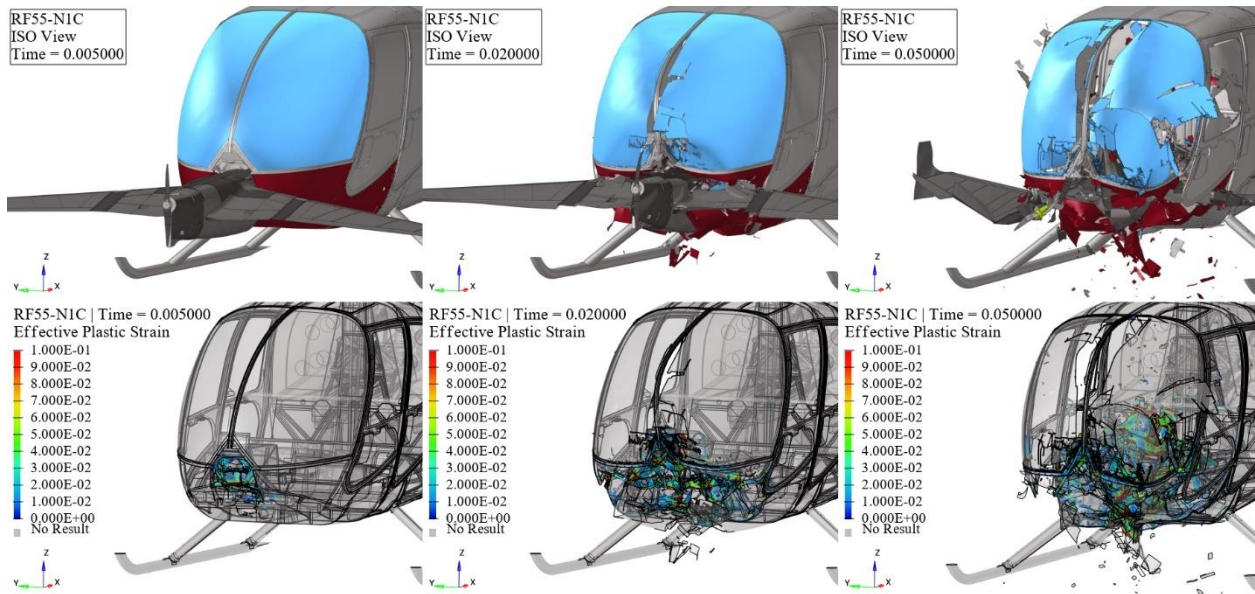
Figure 250. RQ10-W1C kinematics (top) and effective plastic strain (bottom) frames.
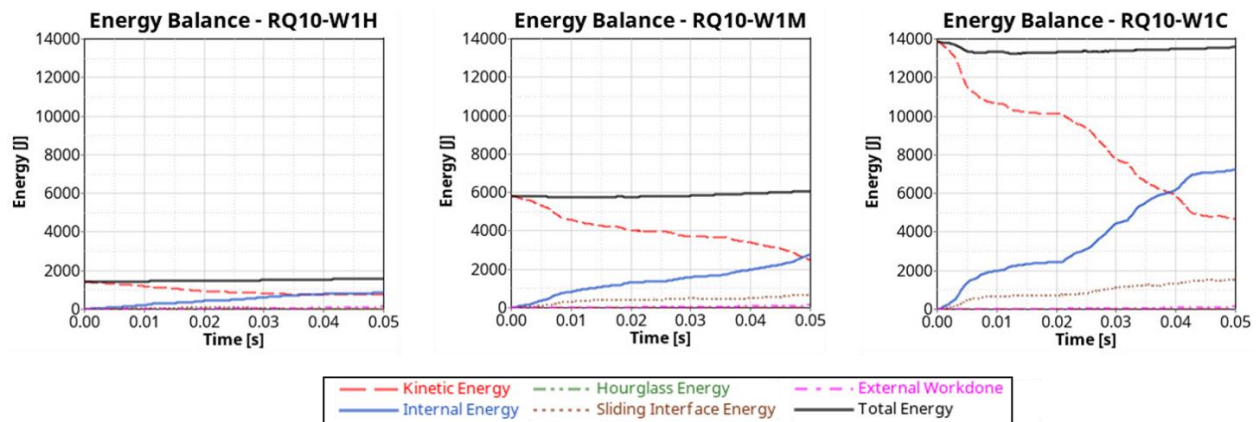
Figure 251. Windshield and 10 lbs. quadcopter impact energy balance.

At all three impact velocities (hover, medium, and cruise), the windshield fractured, and the UAS penetrated the passenger cabin, resulting in a level 4 impact severity.

5.5.4   UAS 12 lbs. Fixed-Wing

This section delineates the findings stemming from collisions involving 12 lbs. fixed-wing and the rotorcraft's Windshield at Hover, Medium, and Cruise velocities, as showcased in Figure 252, Figure 253, and Figure 254, respectively. These results unravel the temporal progression of the impact occurrences, spotlighting time intervals at 0.005s, 0.05s, and 0.15s for hover and 0.005s, 0.02s, and 0.05s for medium and cruise. The upper trio of windows highlights the kinematic aspects of the impacts, while the lower trio shows the resultant effective plastic strain on the rotorcraft structures. Additionally, Figure 255 provides the energy balance plots for all three impact velocities.

Figure 252. RF12-W1H kinematics (top) and effective plastic strain (bottom) frames.

Figure 253. RF12-W1M kinematics (top) and effective plastic strain (bottom) frames.

Figure 254. RF12-W1C kinematics (top) and effective plastic strain (bottom) frames.
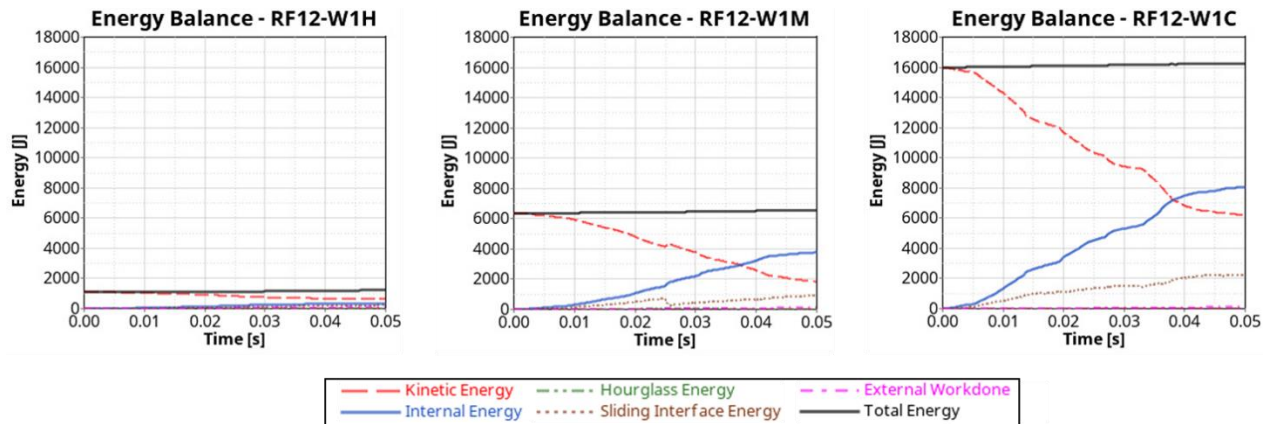
Figure 255. Windshield and 12 lbs. fixed-wing impact energy balance.

At hover velocity, the collision between the 12 lbs. fixed-wing and the windshield caused some dents and minor cracks with no UAS component penetration, resulting in a level 2 impact severity. A longer run time was used for this case to judge the severity of the impact properly. The results for this impact scenario can vary based on the location and orientation of the UAS. The windshield fractured at medium and cruise impact velocities, and the UAS penetrated the passenger cabin, resulting in a level 4 impact severity.

5.5.5 UAS 25 lbs. Quadcopter

This section delineates the findings stemming from collisions involving 25 lbs. quadcopter and the rotorcraft's Windshield at Hover, Medium, and Cruise velocities, as showcased in Figure 256, Figure 257, and Figure 258, respectively. These results unravel the temporal progression of the impact occurrences, spotlighting time intervals at 0.005s, 0.05s, and 0.15s for hover and 0.005s, 0.02s, and 0.05s for medium and cruise. The upper trio of windows highlights the kinematic aspects of the impacts, while the lower trio shows the resultant effective plastic strain on the

rotorcraft structures. Additionally, Figure 259 provides the energy balance plots for all three impact velocities.
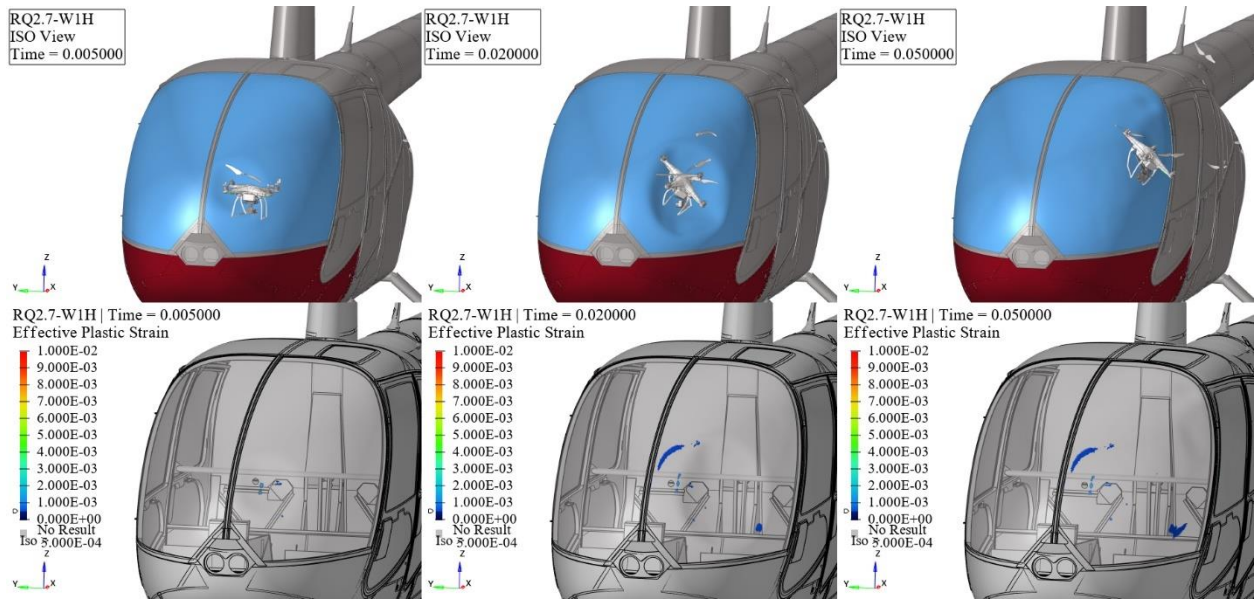

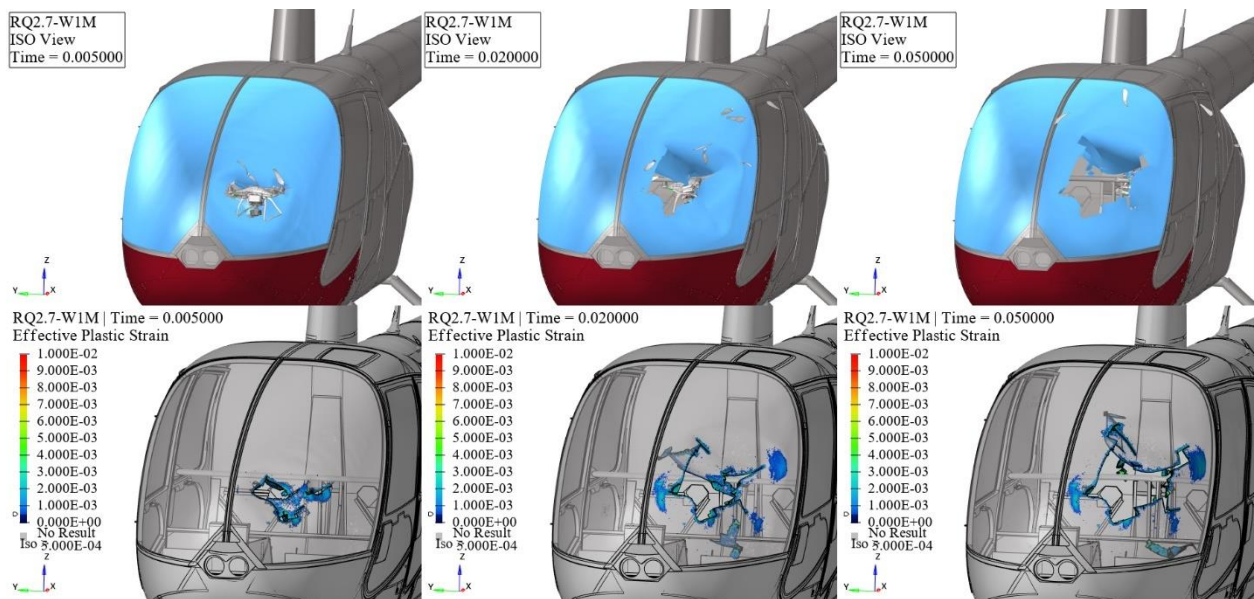Figure 256. RQ25-W1H kinematics (top) and effective plastic strain (bottom) frames.

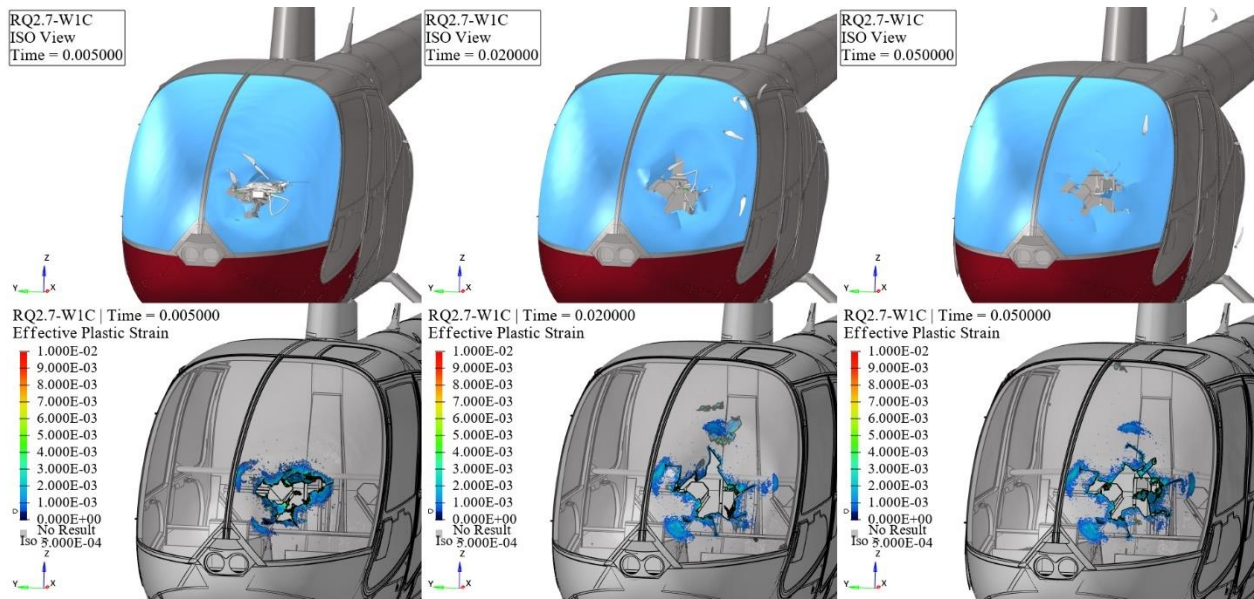Figure 257. RQ25-W1M kinematics (top) and effective plastic strain (bottom) frames.

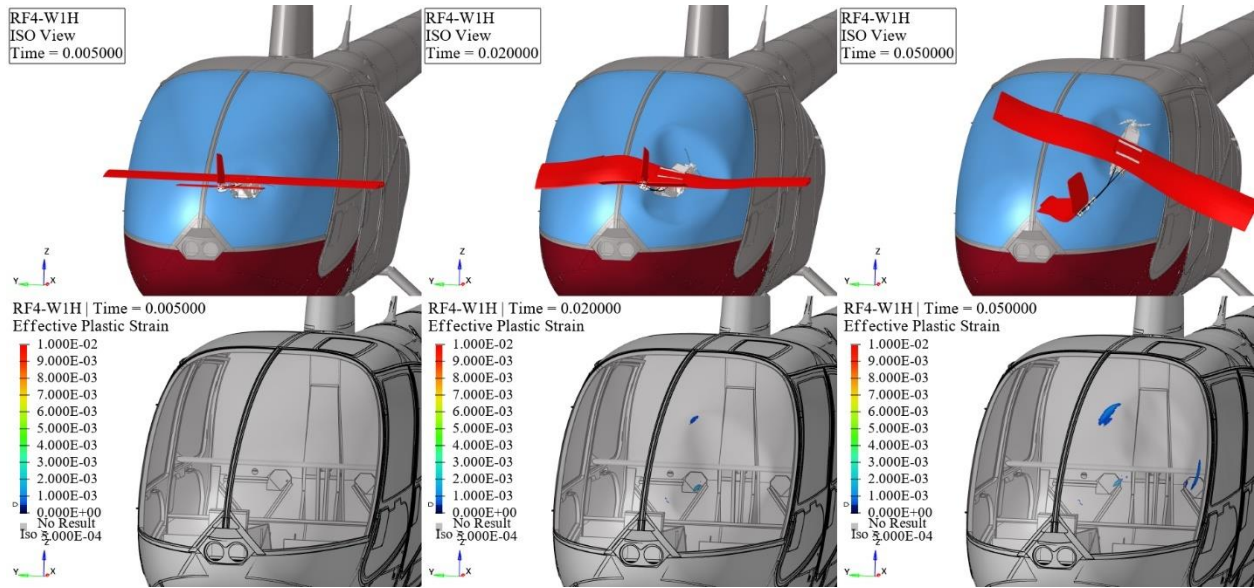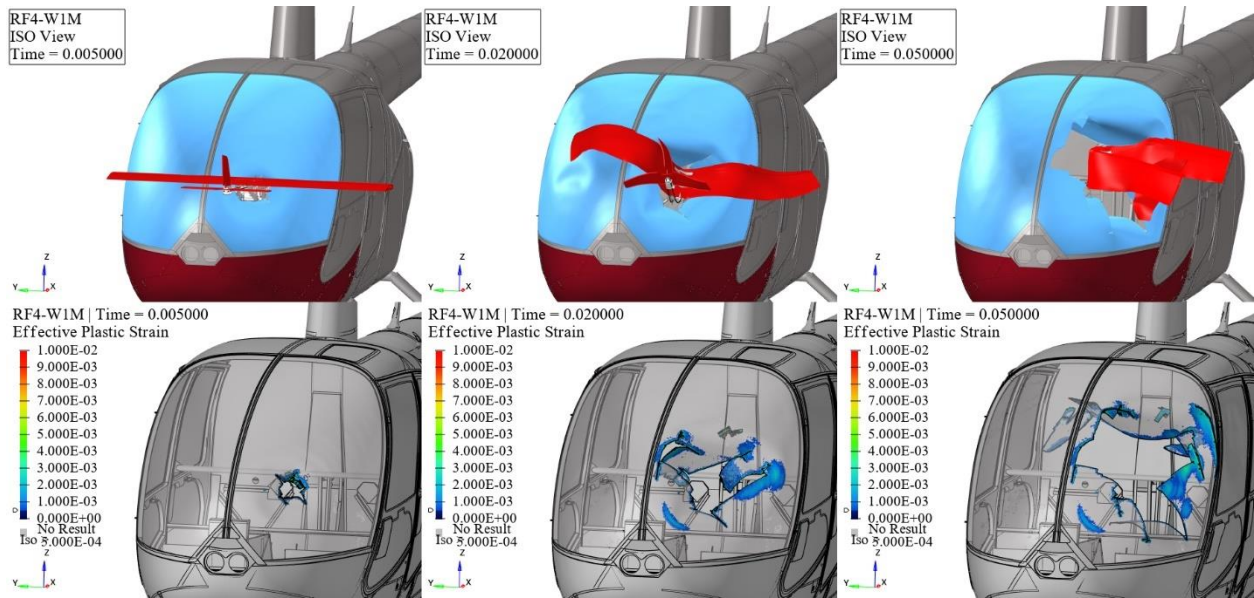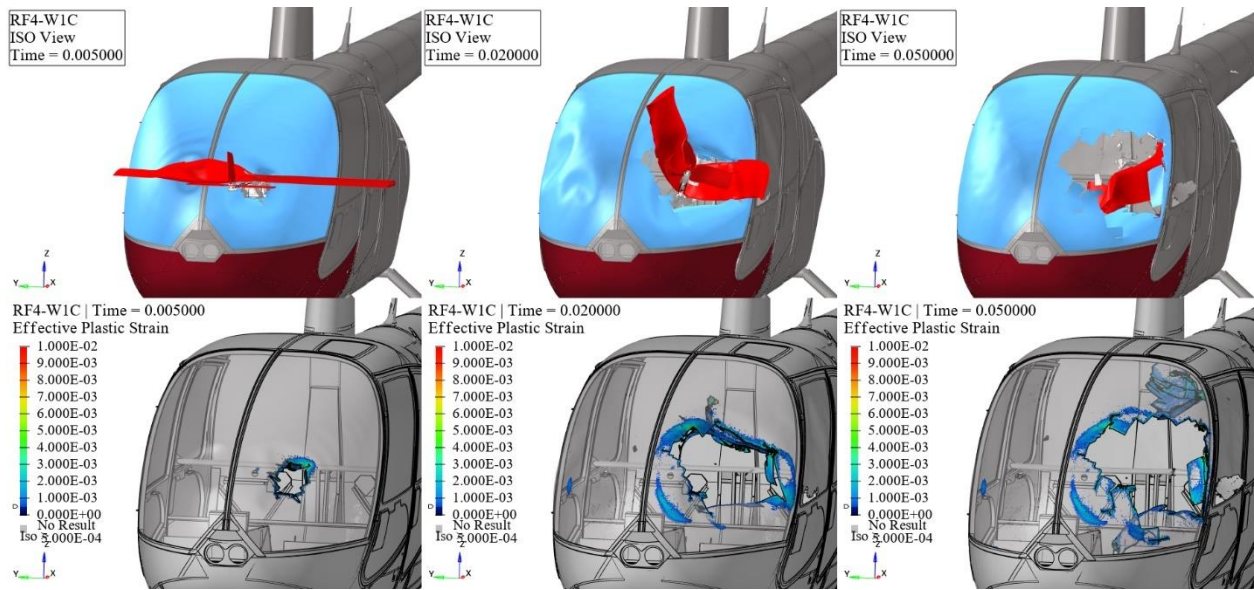Figure 258. RQ25-W1C kinematics (top) and effective plastic strain (bottom) frames.
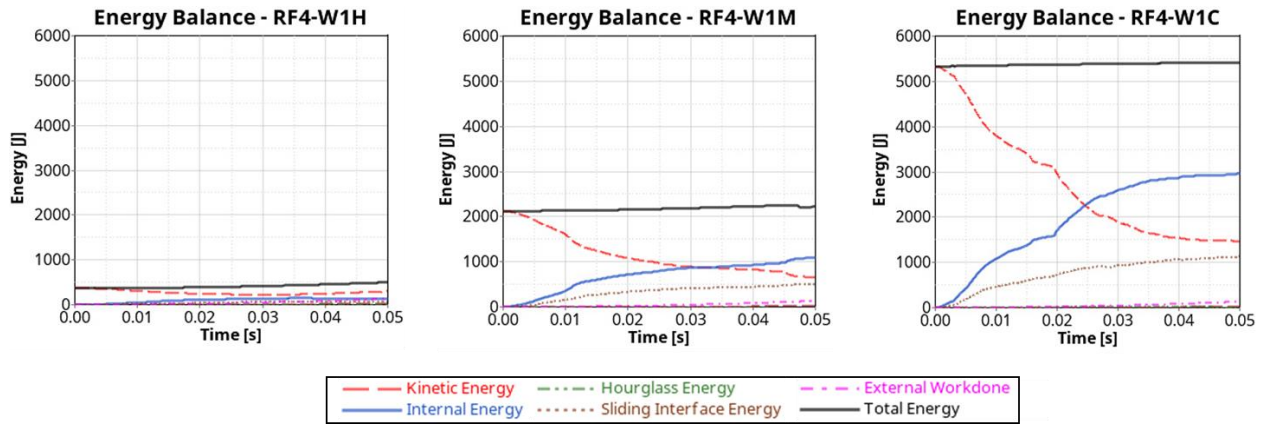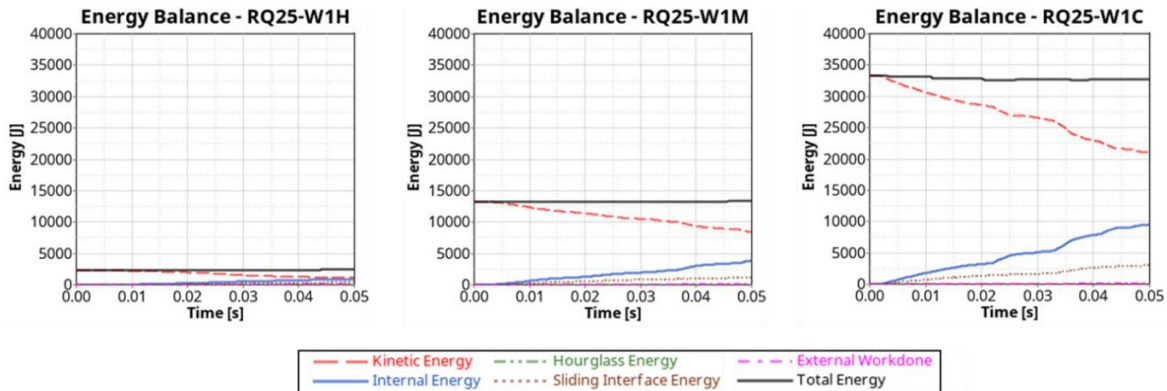

Figure 259. Windshield and 25 lbs. quadcopter impact energy balance.

At hover velocity, the collision between the 25 lbs. quadcopter and the windshield caused some permanent deformation with minor cracks but no UAS penetration, resulting in a level 2 impact severity. A longer run time was used for this case to judge the severity of the impact properly. The results for this impact scenario can vary based on the location and orientation of the UAS. At medium and cruise impact velocities, the windshield fractured, and the UAS penetrated the passenger cabin, resulting in a level 4 impact severity.

Usually, heavier sUAS of the same architecture result in equal or higher severity at the same speed. However, the Q25 hover case severity results in less severity (no penetration) compared to the Q10 case (penetration). This can be explained by the geometric differences between the sUAS. The Q10 impact is concentrated on one side of the windshield, while the Q25 spans both sides of the windshield, which helps distribute the impact loads across a larger surface area. Similarly, the Q10 first impacts with its motors without being deflected by the windshield. On the other hand, the Q25 first impacts with its larger composite body, which causes the sUAS to be deflected upward. Although, it is likely that a change in orientation in the Q10 case could also lead to the sUAS being deflected.

184

5.5.6 UAS 25 lbs. Fixed-Wing

This section delineates the findings stemming from collisions involving 25 lbs. fixed-wing and the rotorcraft's Windshield at Hover, Medium, and Cruise velocities, as showcased in Figure 260, Figure 261, and Figure 262, respectively. These results unravel the temporal progression of the impact occurrences, spotlighting time intervals at 0.005s, 0.02s, and 0.05s. The upper trio of windows highlights the kinematic aspects of the impacts, while the lower trio shows the resultant effective plastic strain on the rotorcraft structures. Additionally, Figure 263 provides the energy balance plots for all three impact velocities.
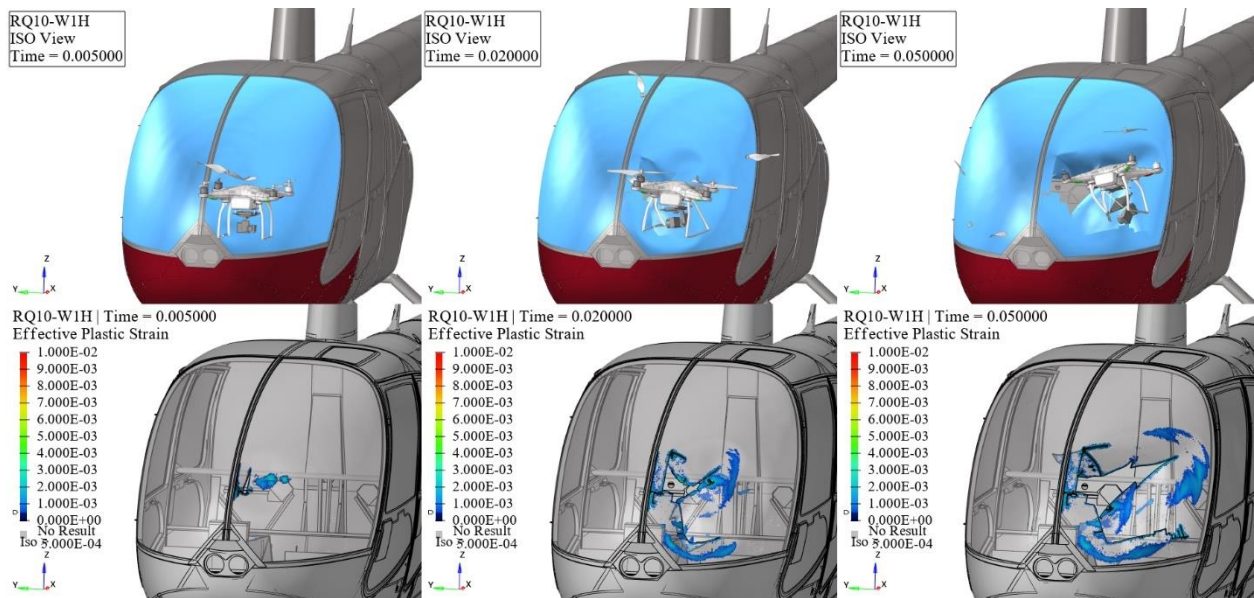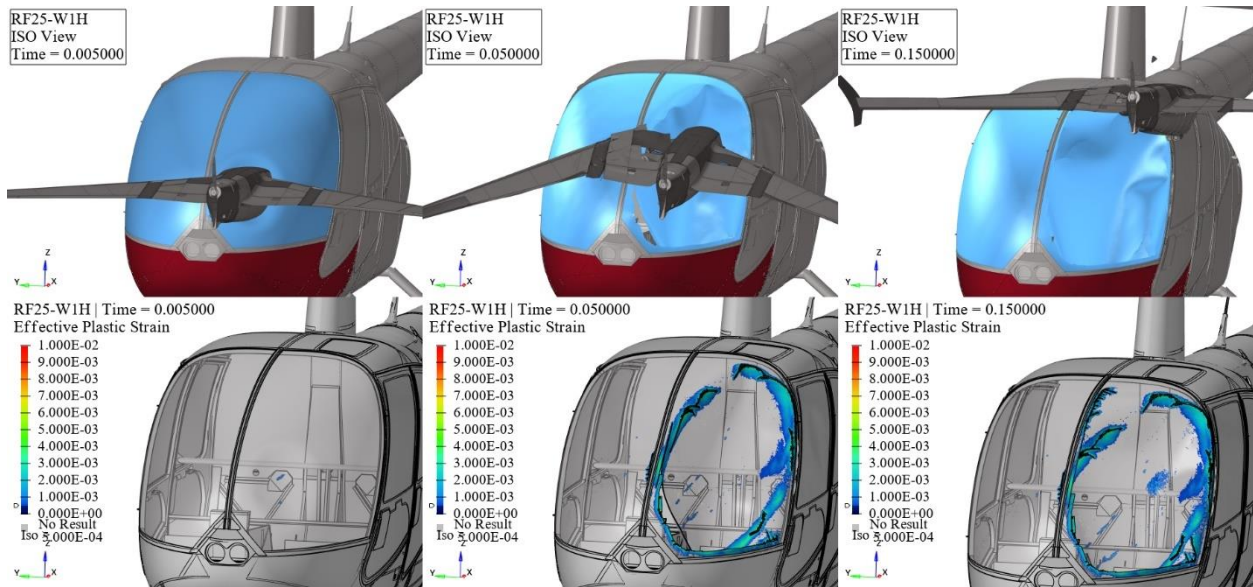

Figure 260. RF25-W1H kinematics (top) and effective plastic strain (bottom) frames.
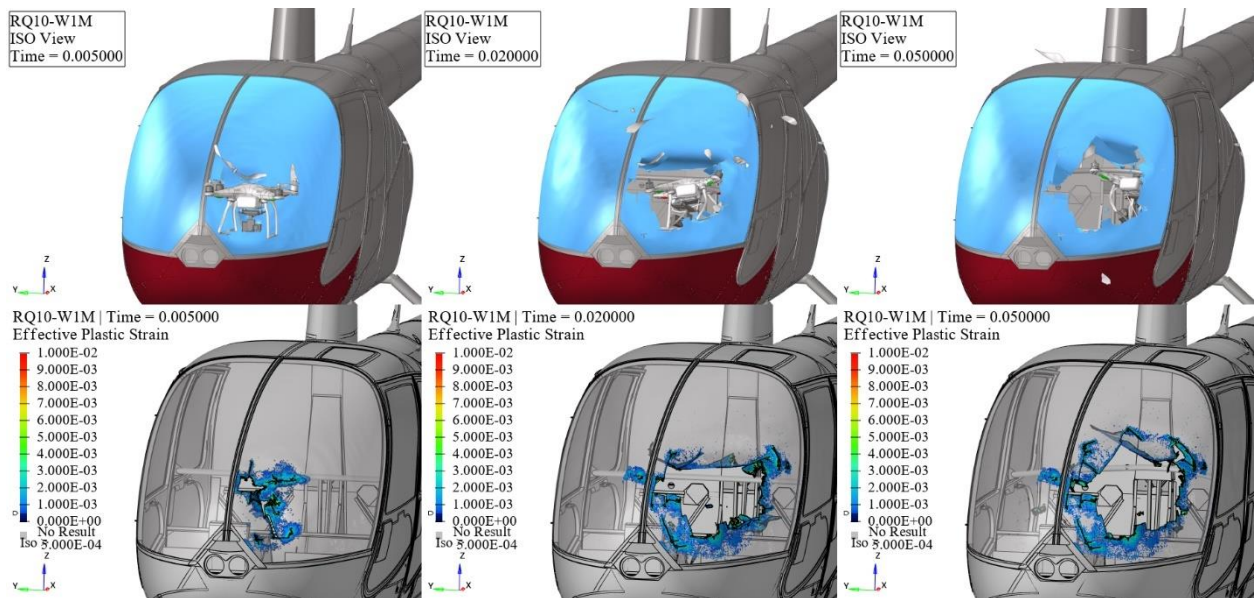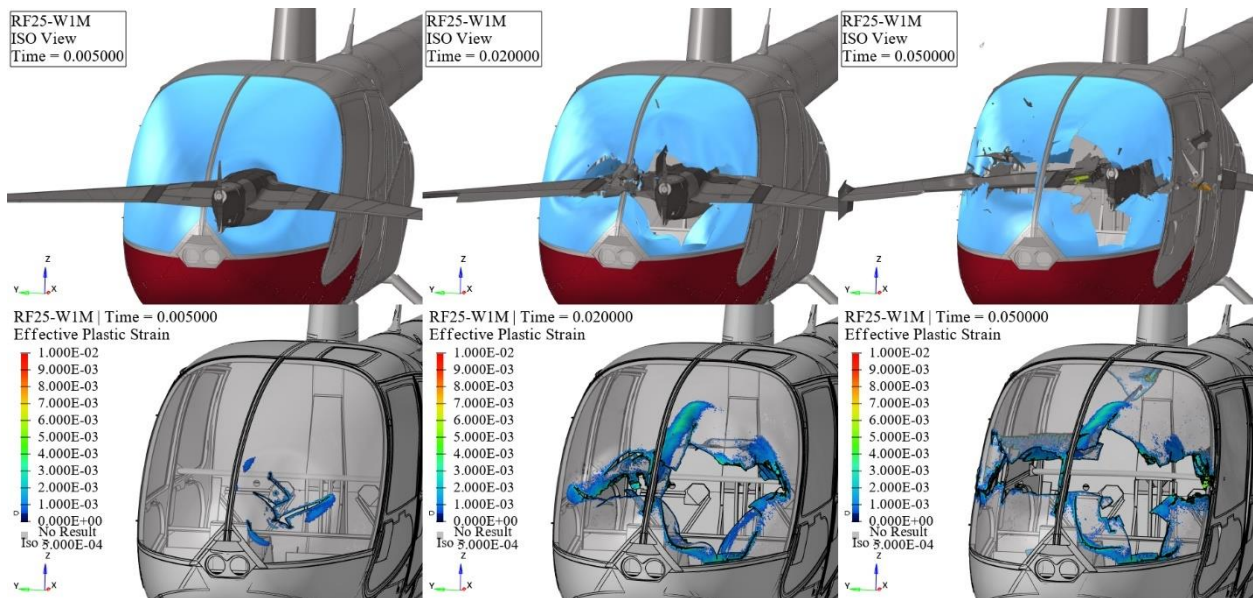

Figure 261. RF25-W1M kinematics (top) and effective plastic strain (bottom) frames.
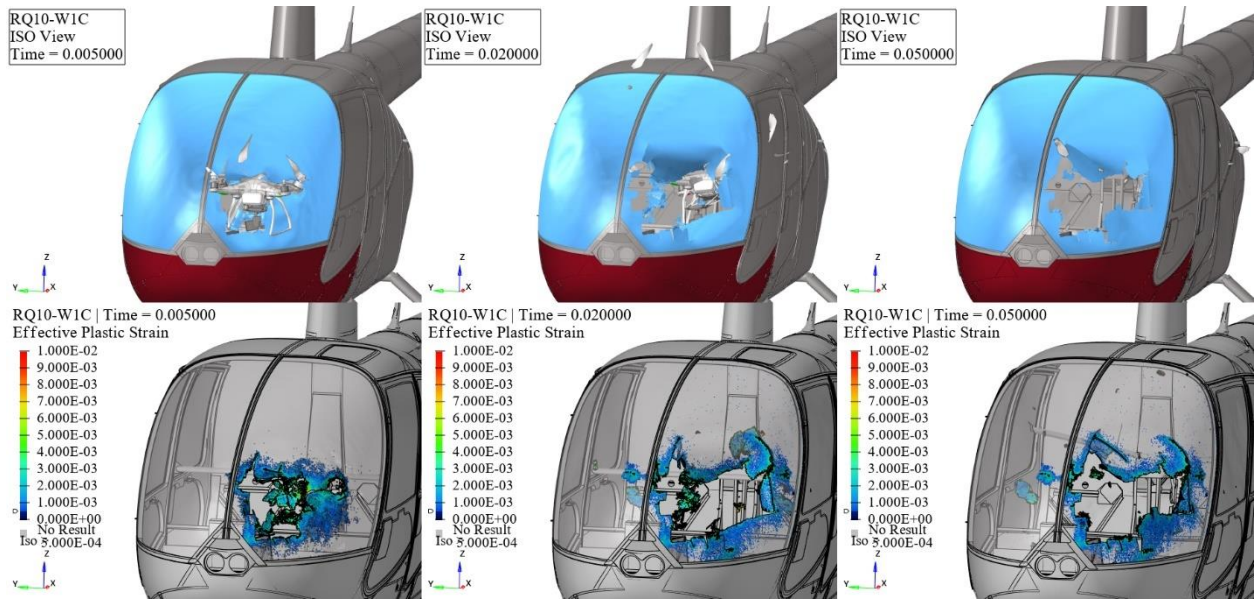
185
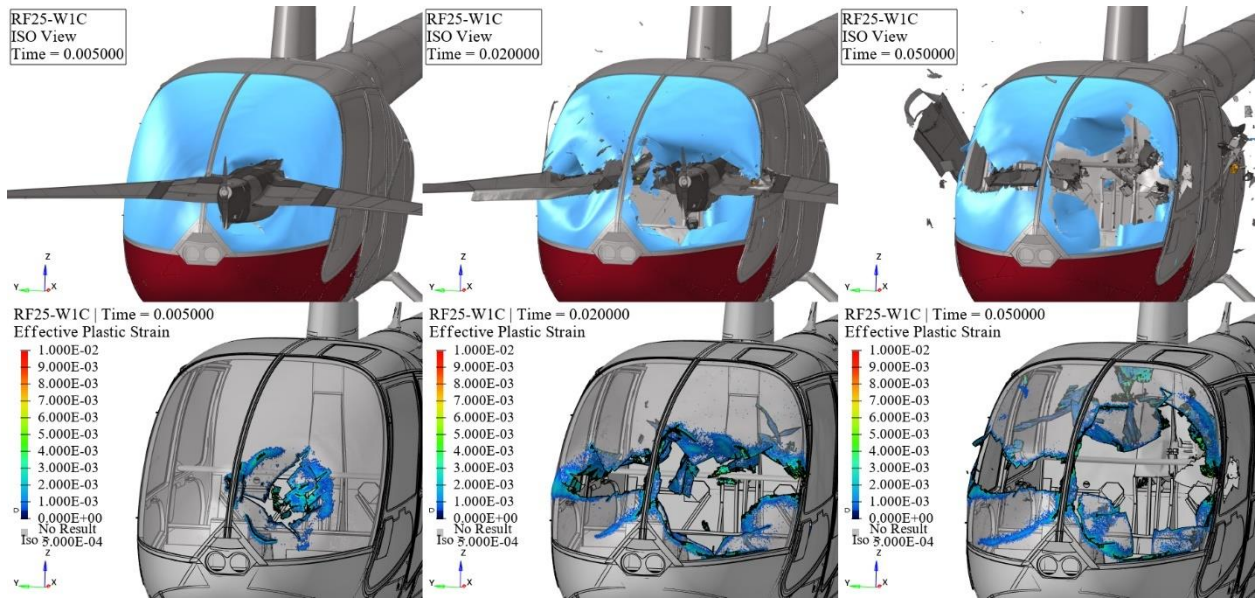
Figure 262. RF25-W1C kinematics (top) and effective plastic strain (bottom) frames.
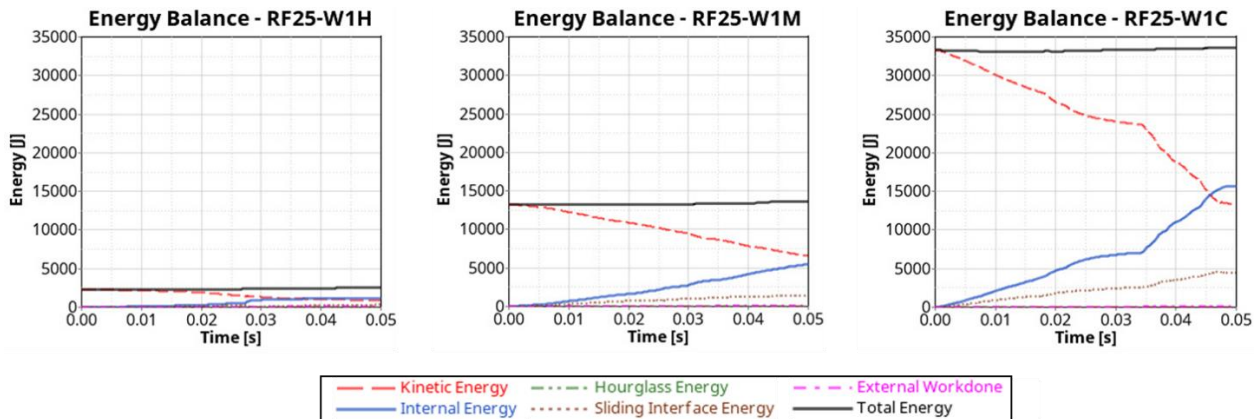
Figure 263. Windshield and 25 lbs. fixed-wing impact energy balance.

At hover velocity, the collision between the 25 lbs. fixed-wing and the windshield caused some fractures while some UAS components penetrated the passenger cabin, resulting in a level 3 impact severity. A longer run time was used for this case to judge the severity of the impact properly. The results for this impact scenario can vary based on the location and orientation of the UAS. At medium and cruise impact velocities, the windshield fractured, and the UAS penetrated the passenger cabin, resulting in a level 4 impact severity.

5.5.7 UAS 55 lbs. Quadcopter

This section delineates the findings stemming from collisions involving 55 lbs. quadcopter and the rotorcraft's Windshield at Hover, Medium, and Cruise velocities, as showcased in Figure 264, Figure 265, and Figure 266, respectively. These results unravel the temporal progression of the impact occurrences, spotlighting time intervals at 0.005s, 0.02s, and 0.05s. The upper trio of

windows highlights the kinematic aspects of the impacts, while the lower trio shows the resultant effective plastic strain on the rotorcraft structures. Additionally, Figure 267 provides the energy balance plots for all three impact velocities.
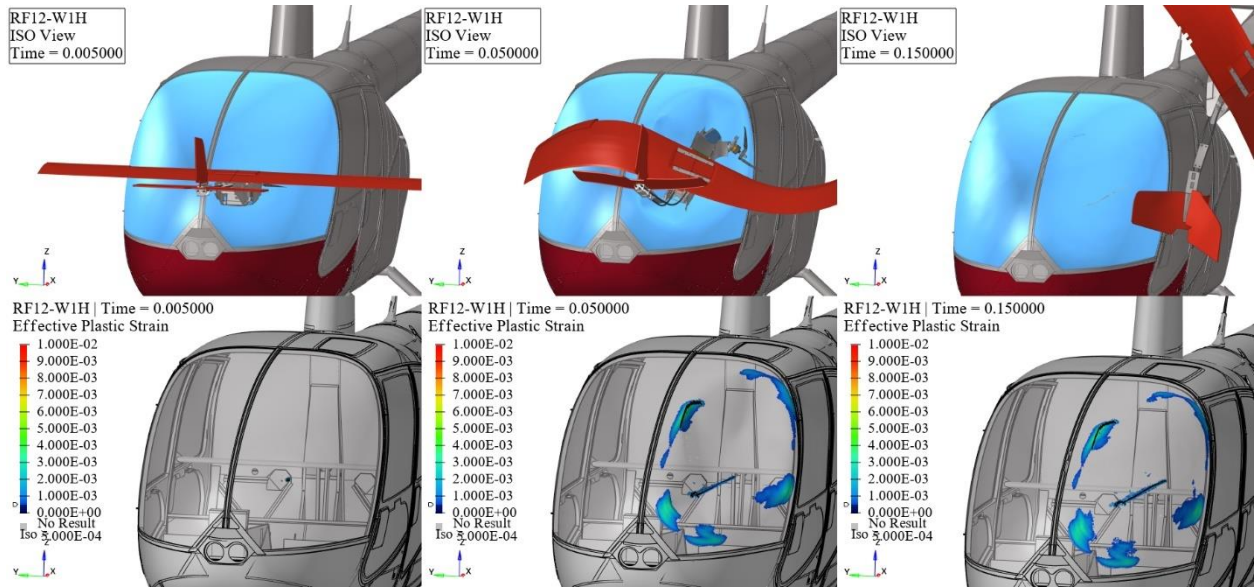

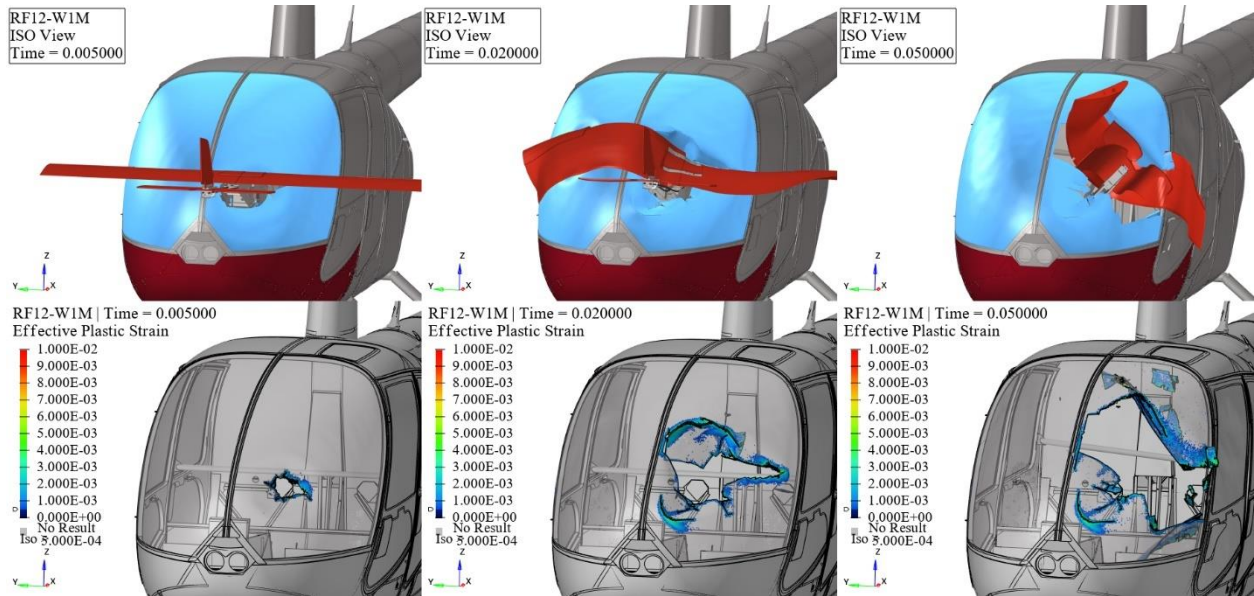Figure 264. RQ55-W1H kinematics (top) and effective plastic strain (bottom) frames.

Figure 265. RQ55-W1M kinematics (top) and effective plastic strain (bottom) frames.
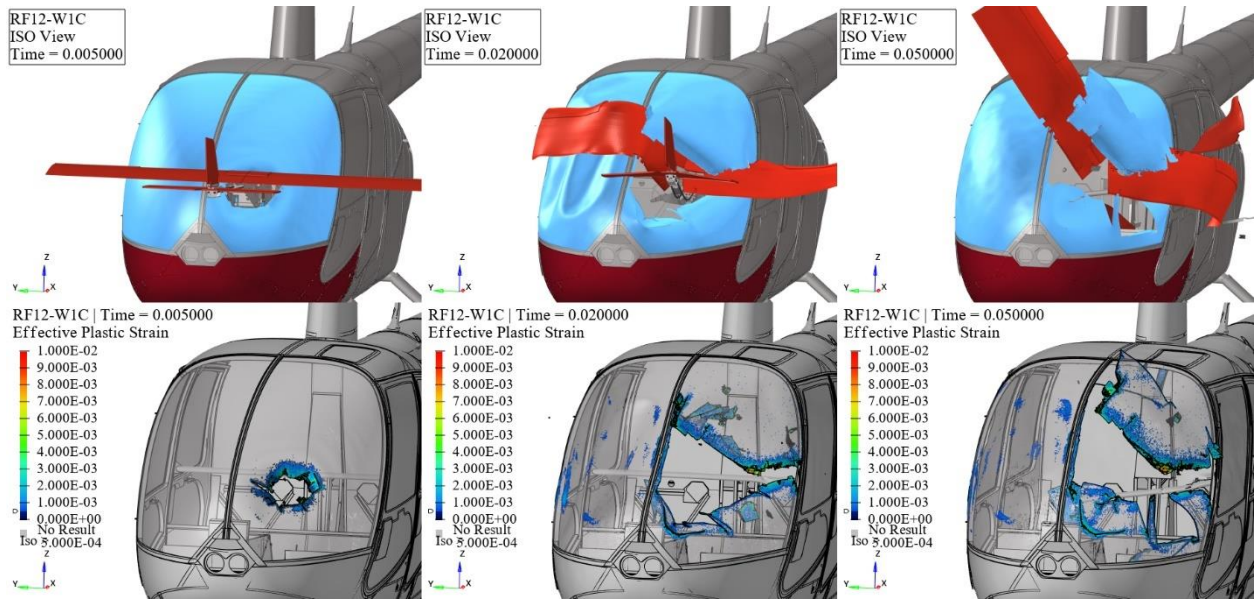
187

Figure 266. RQ55-W1C kinematics (top) and effective plastic strain (bottom) frames.
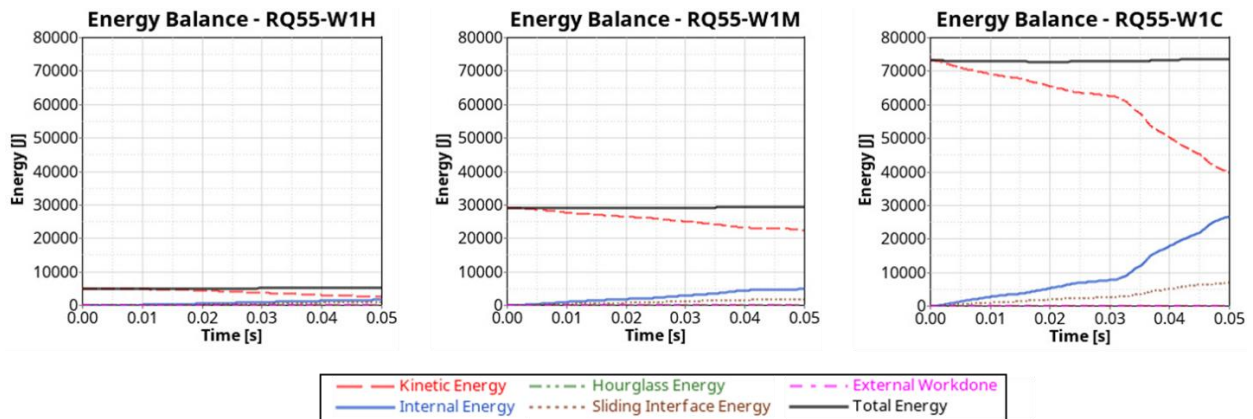
Figure 267. Windshield and 55 lbs. quadcopter impact energy balance.

At hover velocity, the collision between the 55 lbs. quadcopter and the windshield caused some fractures, and no UAS components penetrated the passenger cabin until time frame 0.05s; however, after running the simulation till 0.15s, it could be observed that the fracture propagates and major UAS parts penetrate the passenger cabin, resulting in a level 4 impact severity. Similarly, at medium and cruise impact velocities, the windshield fractured, and the UAS penetrated the passenger cabin, resulting in a level 4 impact severity.

5.5.8 UAS 55 lbs. Fixed-Wing

This section delineates the findings stemming from collisions involving 55 lbs. fixed-wing and the rotorcraft's Windshield at Hover, Medium, and Cruise velocities, as showcased in Figure 268, Figure 269, and Figure 270, respectively. These results unravel the temporal progression of the impact occurrences, spotlighting time intervals at 0.005s, 0.02s, and 0.05s. The upper trio of windows highlights the kinematic aspects of the impacts, while the lower trio shows the resultant

188

effective plastic strain on the rotorcraft structures. Additionally, Figure 271 provides the energy balance plots for all three impact velocities.
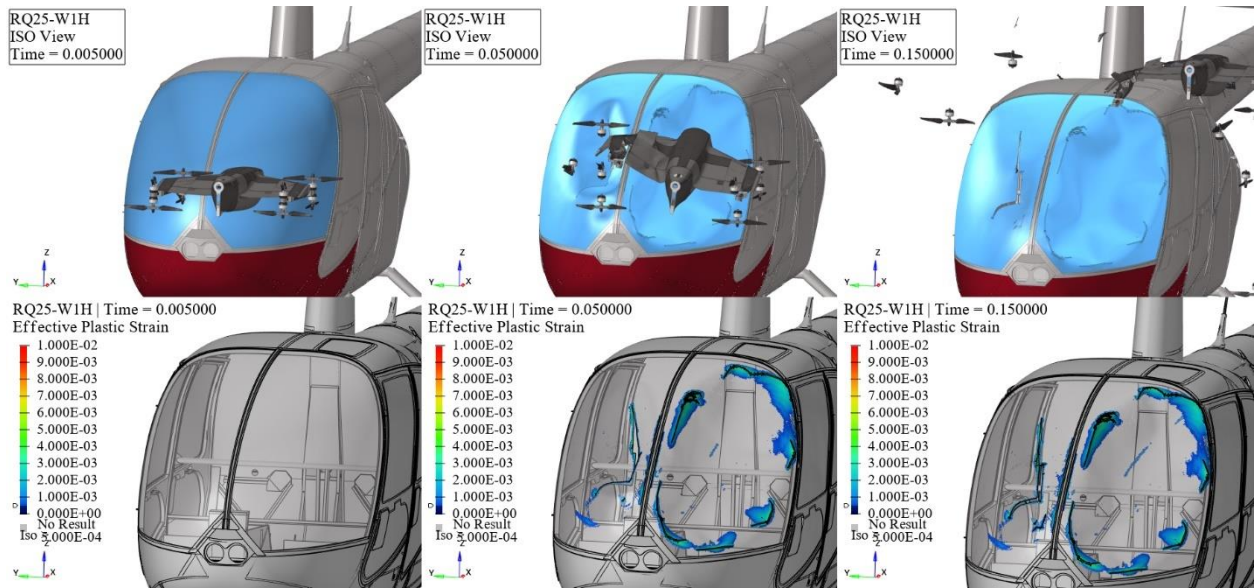

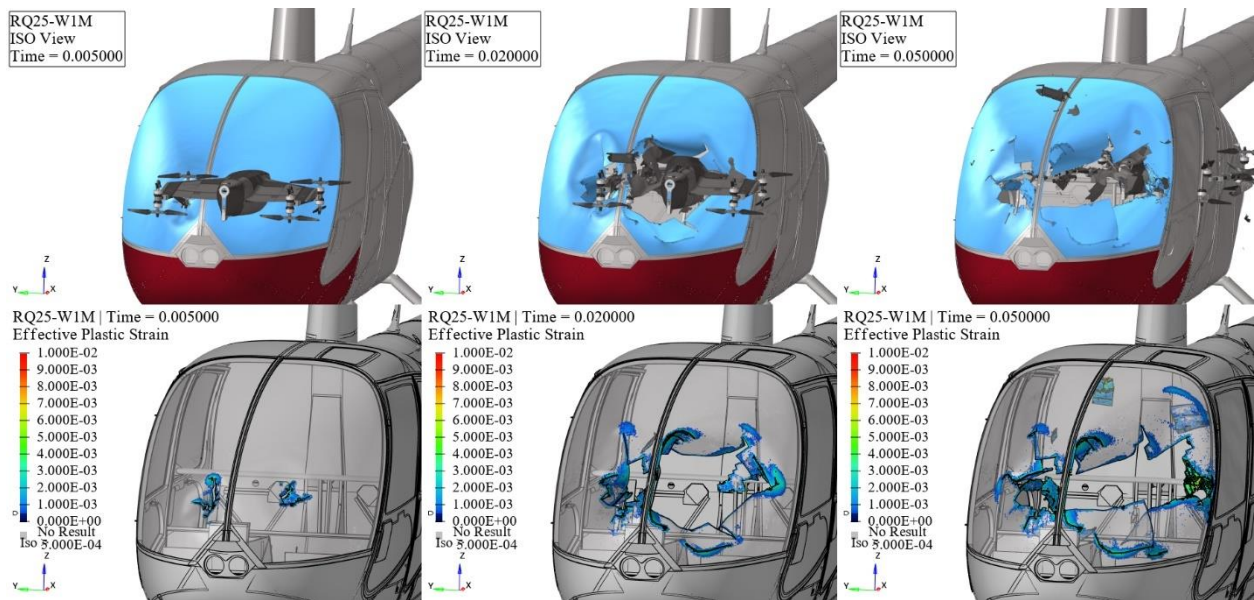Figure 268. RF55-W1H kinematics (top) and effective plastic strain (bottom) frames.

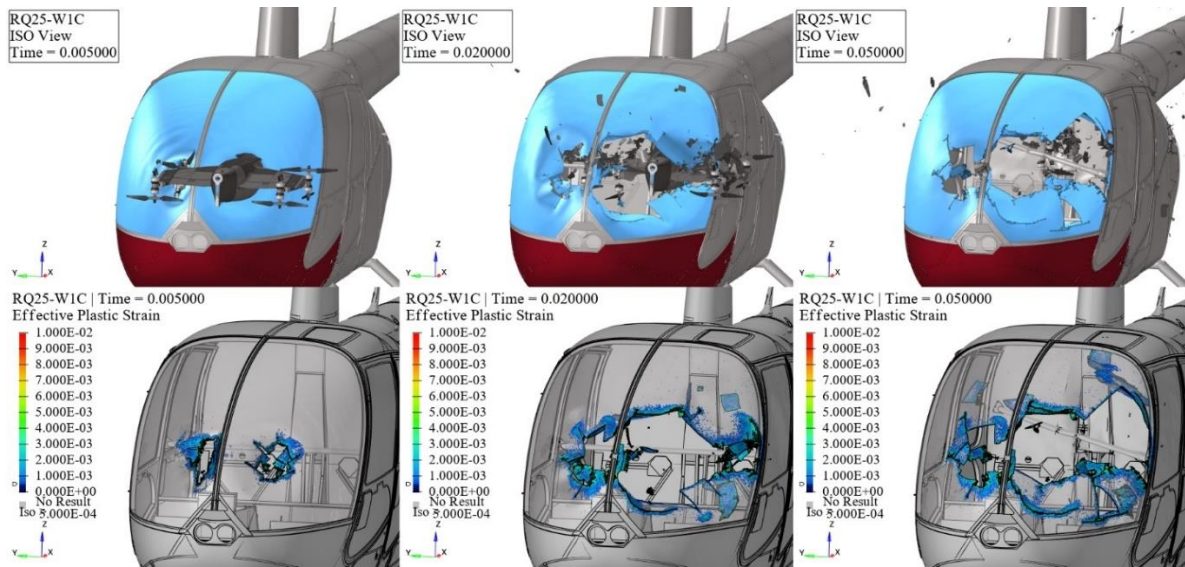Figure 269. RF55-W1M kinematics (top) and effective plastic strain (bottom) frames.

Figure 270. RF55-W1C kinematics (top) and effective plastic strain (bottom) frames.
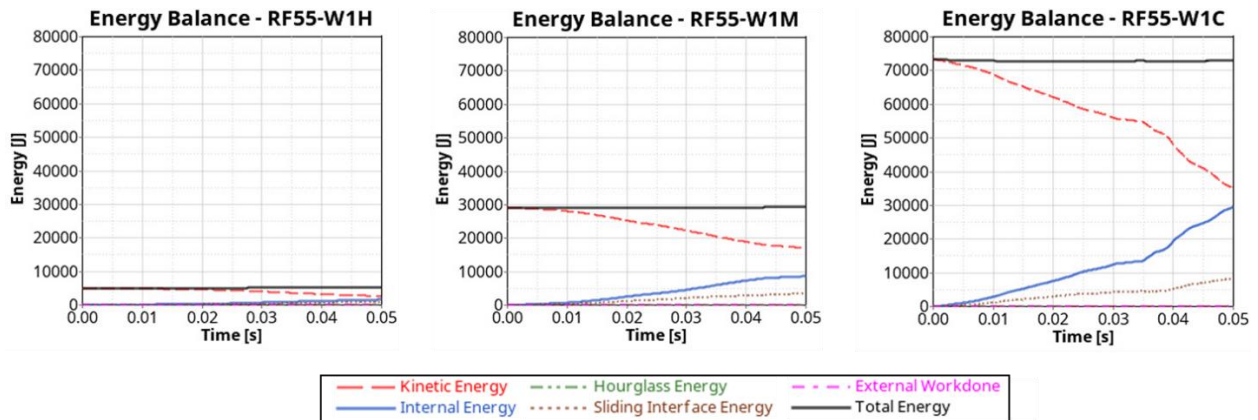
Figure 271. Windshield and 55 lbs. fixed-wing impact energy balance.

At hover velocity, the collision between the 55 lbs. fixed-wing and the windshield caused some fractures, and no UAS components penetrated the passenger cabin until time frame 0.05s; however, after running the simulation till 0.15s, it could be observed that the fracture propagates, and the windshield pieces and couple UAS components penetrates the passenger cabin, resulting in a level 4 impact severity. Similarly, at medium and cruise impact velocities, the windshield fractured, and the UAS penetrated the passenger cabin, resulting in a level 4 impact severity.

5.6 Blade

This section presents the results of the airborne collision studies for all UAS and the rotorcraft's main rotor blade. Figure 272 shows an example of the simulation setup for the main rotor blade impact with 55 lbs. quadcopter at cruise speed.
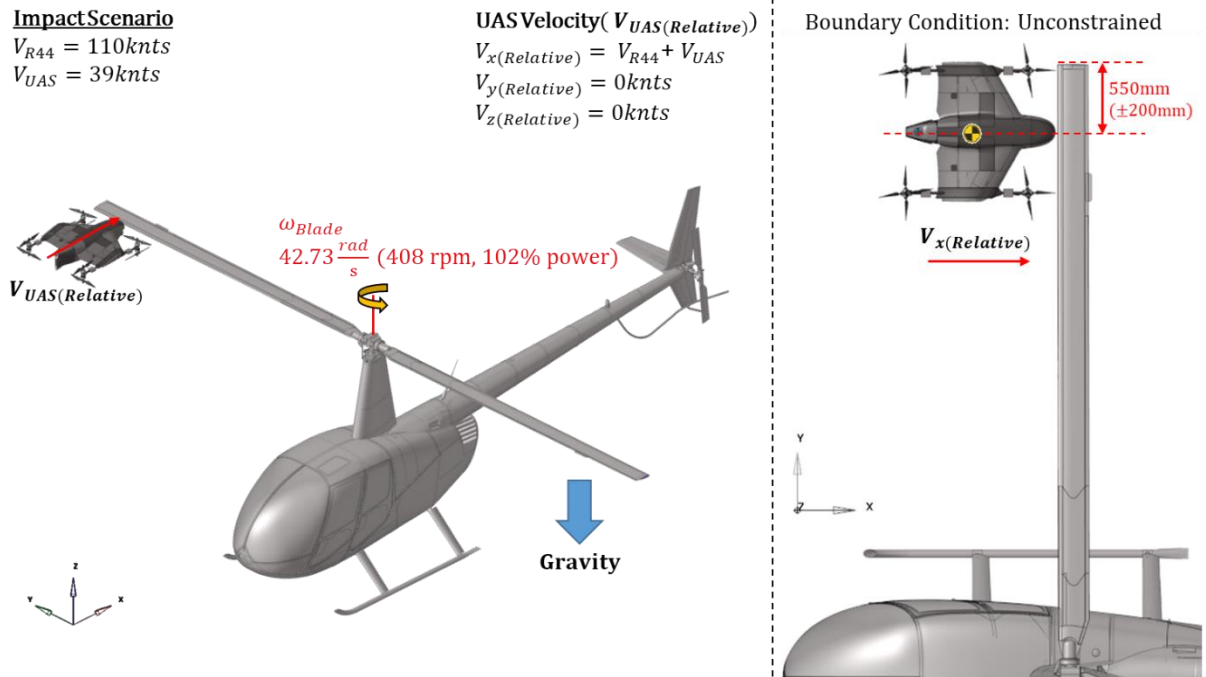
Figure 272. Simulation setup for impact between blade and 55 lbs. quadcopter at cruise velocity.

The rotation of the main rotor blade was modeled for all blade to UAS impact scenarios. The blade was preloaded using radial acceleration, resulting from the constant rotational speed of the blade. This preload was simulated through explicit dynamic relaxation. Upon completion of the preload simulation, the blade's element stresses and strains were incorporated into the final model to simulate the impact of the main rotor blade with the UAS. To maintain constant stresses on the blade, a brief dynamic relaxation was performed before the transient run, during which a rotational velocity of 42.73 rad/s (408 RPM) was applied to the blade to simulate its rotation. Figure 273 illustrates the stable preload on the main rotor blade, while Figure 274 compares the forces on two different cross-sections of the blade between the dynamic relaxation and transient rotation phases, demonstrating the stability of the preload.
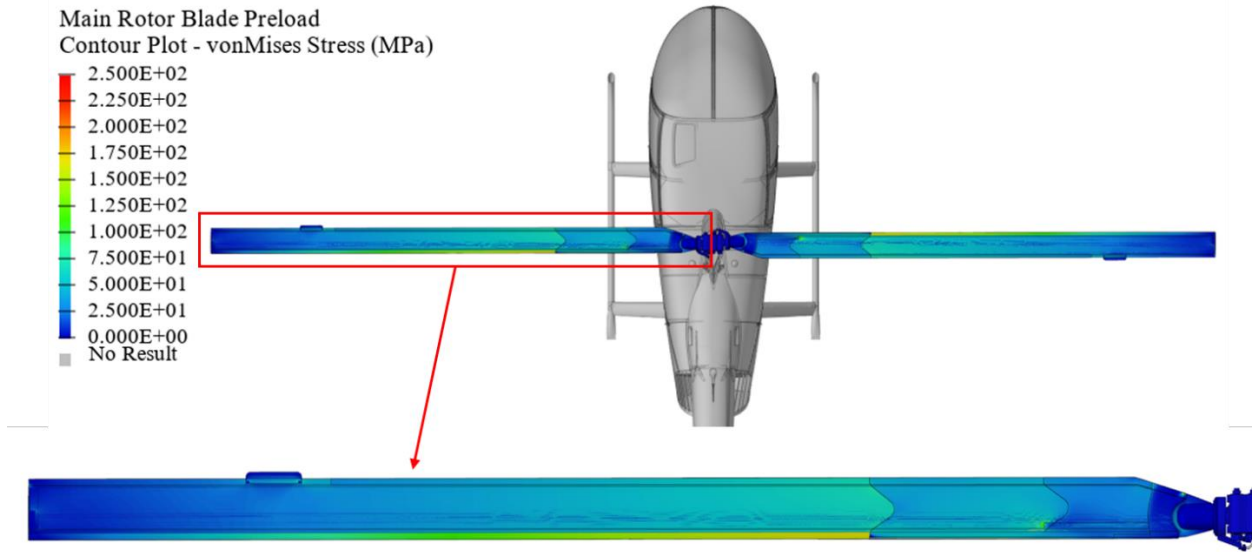
Figure 273. Main rotor blade preload (Von Mises stress contour).
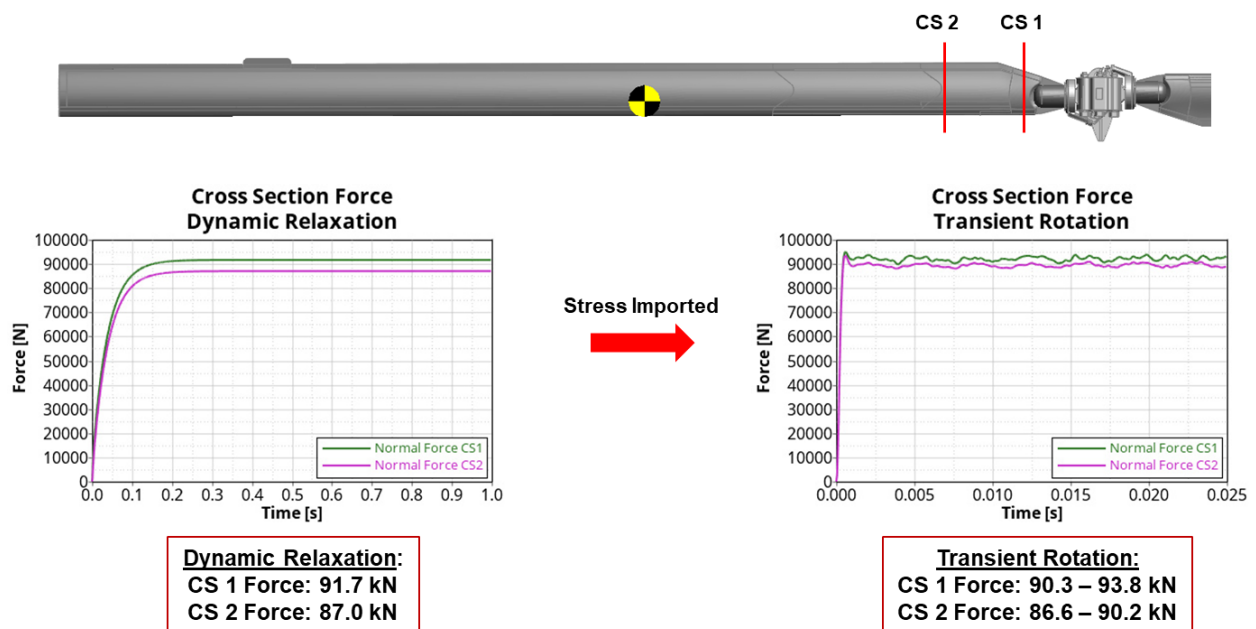
Figure 274. Dynamic relaxation vs. transient rotation cross-section forces.

Table 47 summarizes the damage severity level evaluation and fire risk assessment for impact cases for all UAS with the main rotor blade.

Table 47. Blade mid-air collision simulation assessment – damage severity level and fire risk.

		Case	Severity	Fire Risk
Mid-air collision Rotorcraft-Blade and all sUAS	Quadcopter 2.7 lbs.	RQ2.7-B1H	2	No
		RQ2.7-B1M	2	No
		RQ2.7-B1C	2	No
	Fixed-Wing 4 lbs.	RF4-B1H	3	No
		RF4-B1M	3	No
		RF4-B1C	3	No
	Quadcopter 10 lbs.	RQ10-B1H	3	No
		RQ10-B1M	3	No
		RQ10-B1C	3	No
	Fixed-Wing 12 lbs.	RF12-B1H	4	No
		RF12-B1M	4	No
		RF12-B1C	4	No
	Quadcopter 25 lbs.	RQ25-B1H	4	No
		RQ25-B1M	4	No
		RQ25-B1C	4	No
	Fixed-Wing 25 lbs.	RF25-B1H	4	No
		RF25-B1M	4	No
		RF25-B1C	4	No
	Quadcopter 55 lbs.	RQ55-B1H	4	No
		RQ55-B1M	4	No
		RQ55-B1C	4	No
	Fixed-Wing 55 lbs.	RF55-B1H	4	No
		RF55-B1M	4	No
		RF55-B1C	4	No

5.6.1   UAS 2.7 lbs. Quadcopter

This section delineates the findings stemming from collisions involving 2.7 lbs. quadcopter and the rotorcraft's Main Blade at Hover, Medium, and Cruise velocities, as showcased in Figure 275, Figure 276, and Figure 277, respectively. These results unravel the temporal progression of the impact occurrences, spotlighting time intervals at 0.0005s, 0.005s, and 0.0125s. The upper trio of

windows highlights the kinematic aspects of the impacts, while the lower trio shows the resultant effective plastic strain on the rotorcraft structures. Additionally, Figure 278 illustrates the close-up damage summary, and Figure 279 provides the energy balance plots for all three impact velocities.
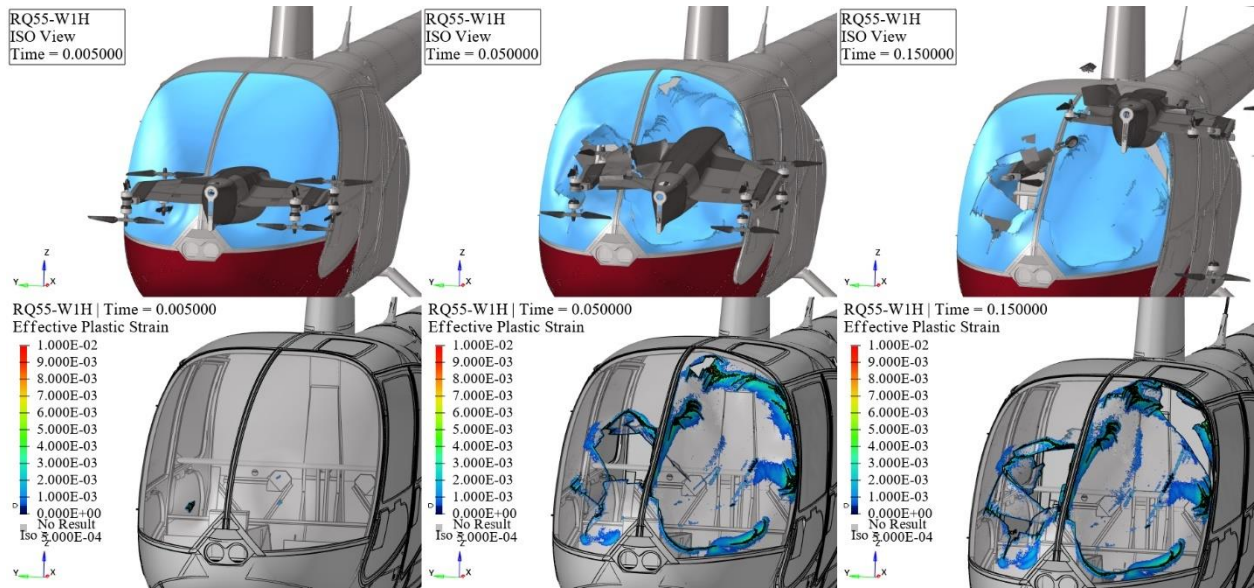

Figure 275. RQ2.7-B1H kinematics (top) and effective plastic strain (bottom) frames.
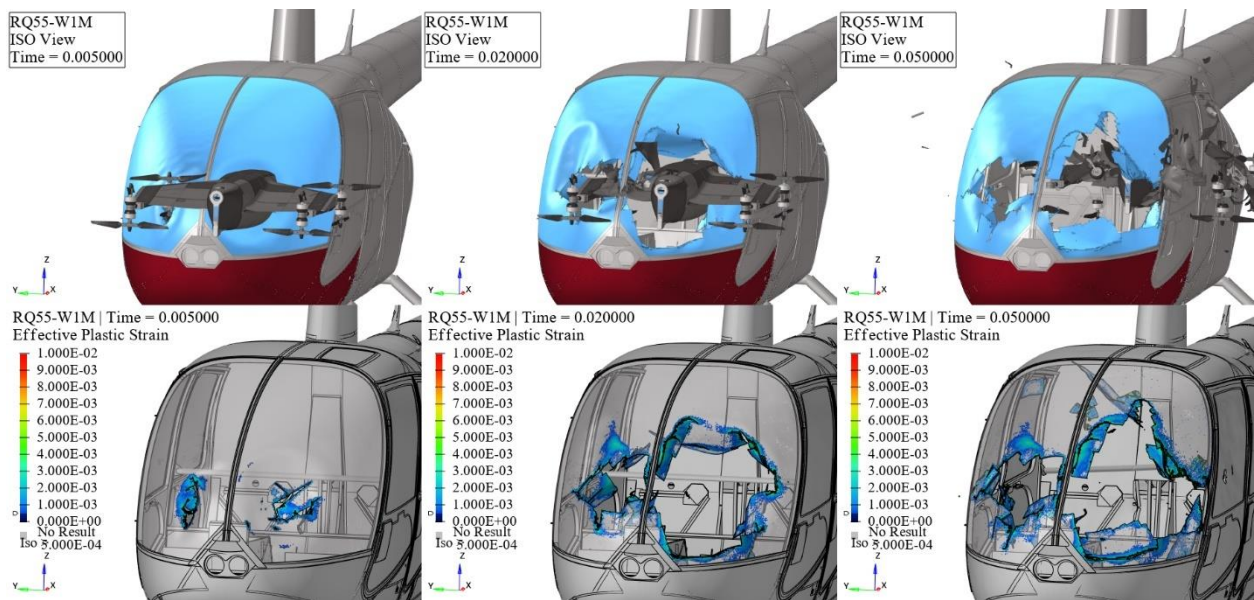

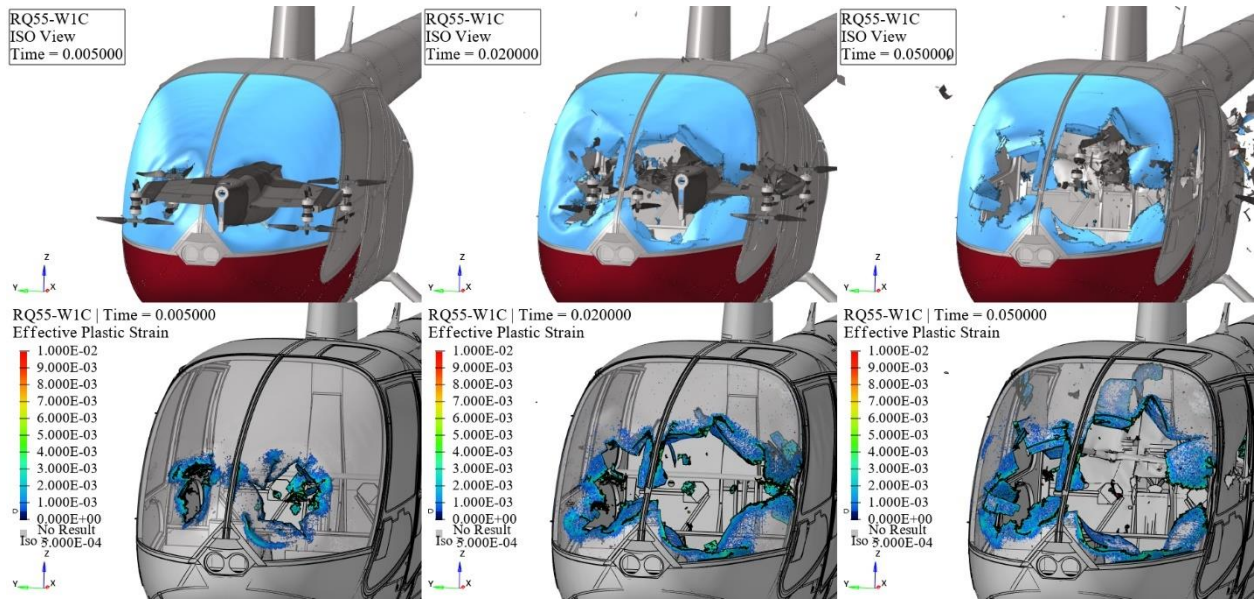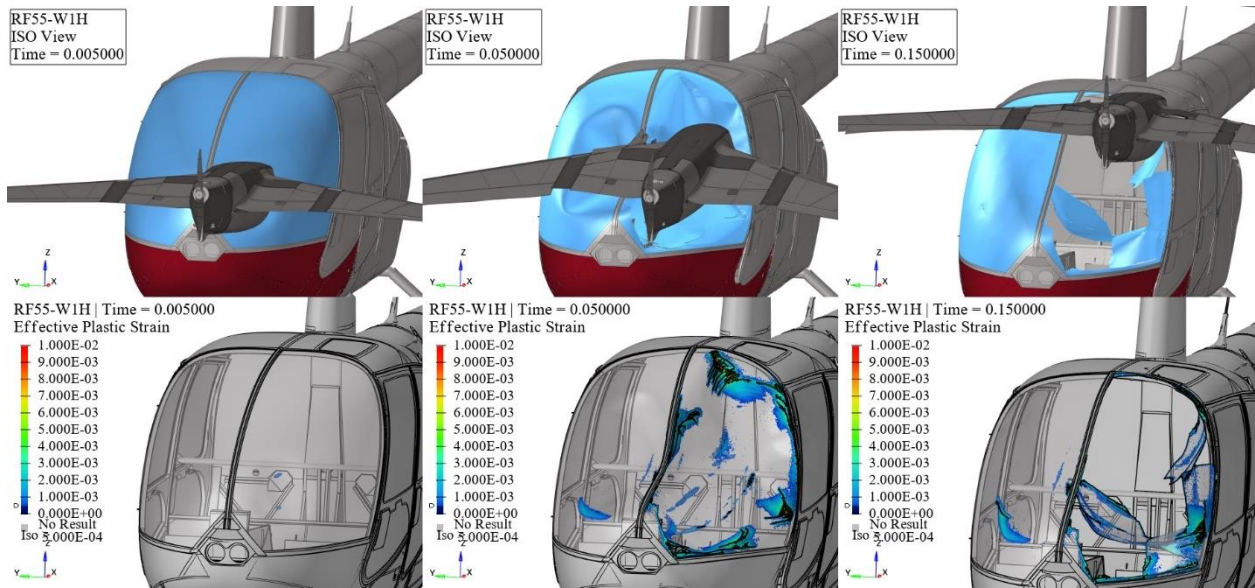Figure 276. RQ2.7-B1M kinematics (top) and effective plastic strain (bottom) frames.

194

Figure 277. RQ2.7-B1C kinematics (top) and effective plastic strain (bottom) frames.
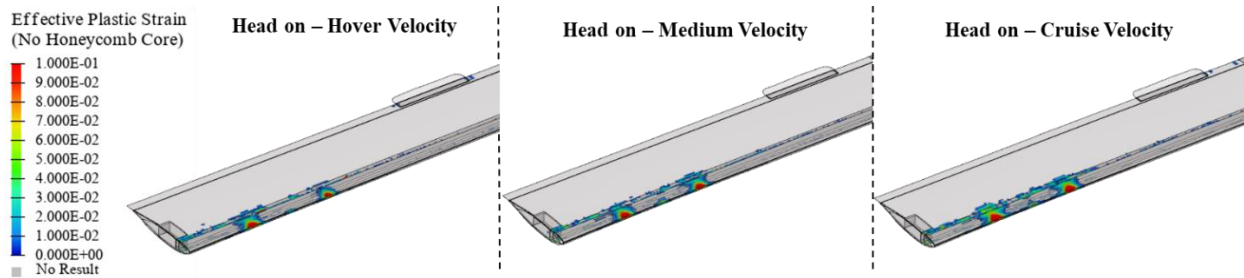
Figure 278. Main rotor blade and 2.7 lbs. quadcopter damage summary.

Figure 279. Main rotor blade and 2.7 lbs. quadcopter impact energy balance.

At all three impact velocities (hover, medium, and cruise), the collision between the 2.7 lbs. quadcopter and the main rotor blade resulted in minor dents and scuffs on the leading edge of the rotor blade, with no cracks or significant damage observed, indicating a level 2 impact severity.

195

5.6.2 UAS 4 lbs. Fixed-Wing

This section delineates the findings stemming from collisions involving 4 lbs. fixed-wing and the rotorcraft's Main Blade at Hover, Medium, and Cruise velocities, as showcased in Figure 280, Figure 281, and Figure 282, respectively. These results unravel the temporal progression of the impact occurrences, spotlighting time intervals at 0.0005s, 0.005s, and 0.0125s. The upper trio of windows highlights the kinematic aspects of the impacts, while the lower trio shows the resultant effective plastic strain on the rotorcraft structures. Additionally, Figure 283 illustrates the close-up damage summary, and Figure 284 provides the energy balance plots for all three impact velocities.

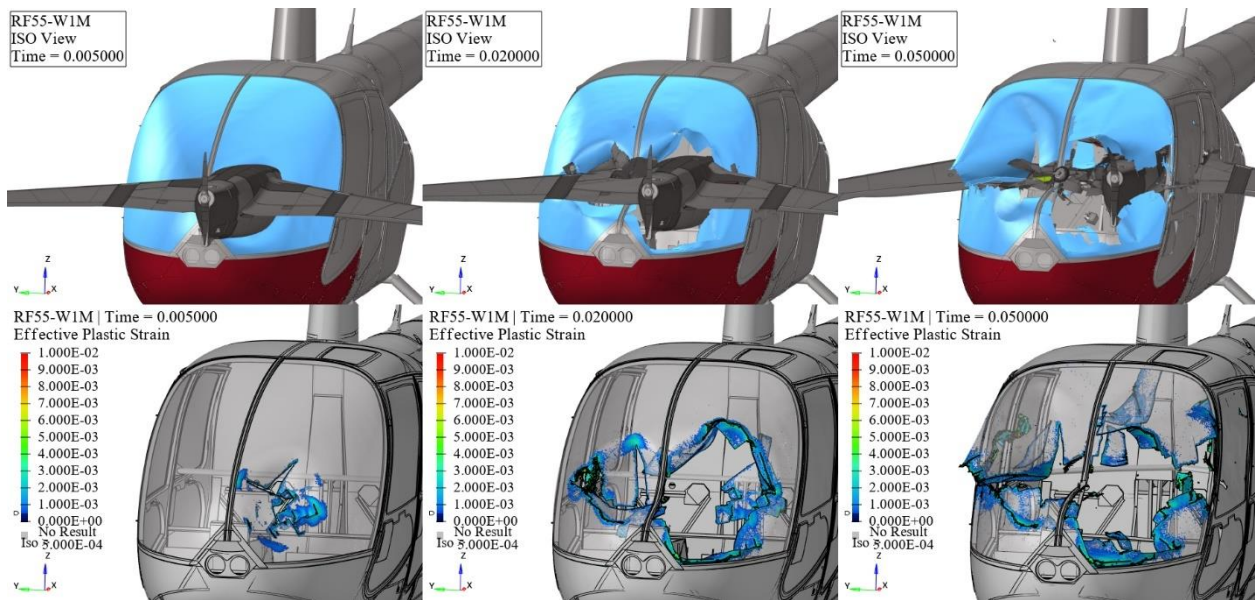Figure 280. RF4-B1H kinematics (top) and effective plastic strain (bottom) frames.

Figure 281. RF4-B1M kinematics (top) and effective plastic strain (bottom) frames.
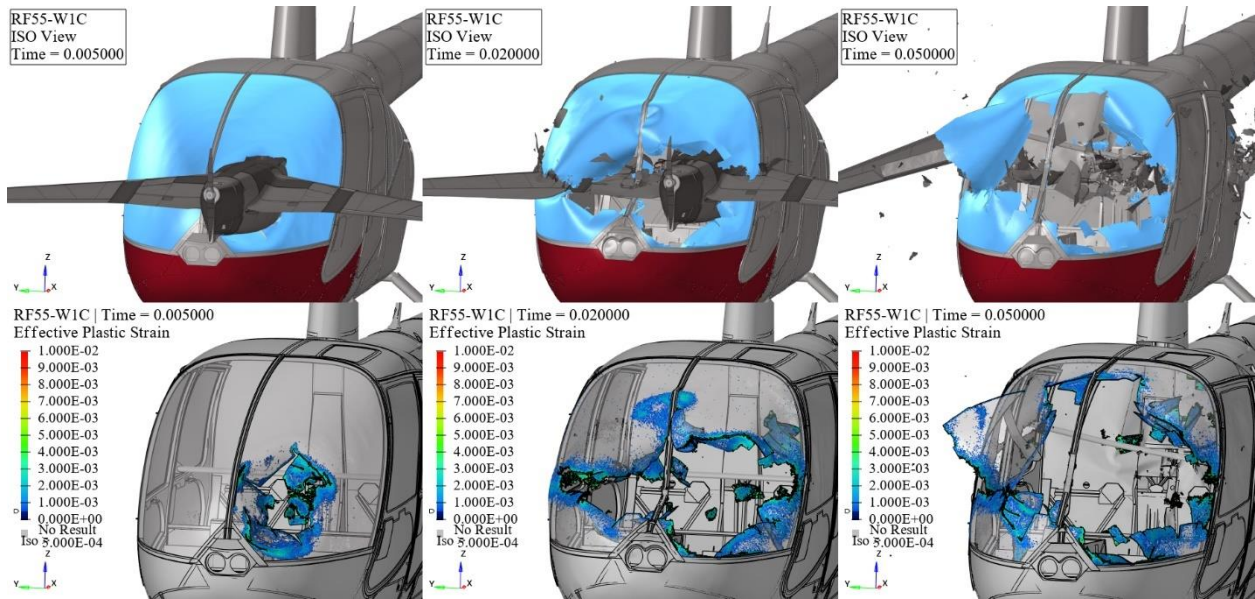
Figure 282. RF4-B1C kinematics (top) and effective plastic strain (bottom) frames.

Figure 283. Main rotor blade and 4 lbs. fixed-wing damage summary.

Figure 284. Main rotor blade and 4 lbs. fixed-wing impact energy balance.

At all three impact velocities (hover, medium, and cruise), the collision between the 4 lbs. fixed-wing and the main rotor blade resulted in permanent deformation of the leading edge of the rotor blade, characterized by multiple crack initiation and skin buckling, indicating a level 3 impact severity.

197

5.6.3   UAS 10 lbs. Quadcopter

This section delineates the findings stemming from collisions involving 10 lbs. quadcopter and the rotorcraft's Main Blade at Hover, Medium, and Cruise velocities, as showcased in Figure 285, Figure 286, and Figure 287, respectively. These results unravel the temporal progression of the impact occurrences, spotlighting time intervals at 0.0005s, 0.005s, and 0.0125s. The upper trio of windows highlights the kinematic aspects of the impacts, while the lower trio shows the resultant effective plastic strain on the rotorcraft structures. Additionally, Figure 288 illustrates the close-up damage summary, and Figure 289 provides the energy balance plots for all three impact velocities.

Figure 285. RQ10-B1H kinematics (top) and effective plastic strain (bottom) frames.

Figure 286. RQ10-B1M kinematics (top) and effective plastic strain (bottom) frames.

198

Figure 287. RQ10-B1C kinematics (top) and effective plastic strain (bottom) frames.

Figure 288. Main rotor blade and 10 lbs. quadcopter damage summary.

Figure 289. Main rotor blade and 10 lbs. quadcopter impact energy balance.

At all three impact velocities (hover, medium, and cruise), the collision between the 10 lbs. quadcopter and the main rotor blade resulted in permanent deformation of the leading edge of the rotor blade, characterized by multiple crack initiation and skin buckling, indicating a level 3 impact severity.

5.6.4 UAS 12 lbs. Fixed-Wing

This section delineates the findings stemming from collisions involving 12 lbs. fixed-wing and the rotorcraft's Main Blade at Hover, Medium, and Cruise velocities, as showcased in Figure 290, Figure 291, and Figure 292, respectively. These results unravel the temporal progression of the impact occurrences, spotlighting time intervals at 0.0005s, 0.005s, and 0.0125s for hover, 0.0005s, 0.005s, and 0.0095s for medium, and 0.0005s, 0.005s, and 0.0085s for cruise. The upper trio of windows highlights the kinematic aspects of the impacts, while the lower trio shows the resultant effective plastic strain on the rotorcraft structures. Additionally, Figure 293 illustrates the close-up damage summary, and Figure 294 provides the energy balance plots for all three impact velocities.
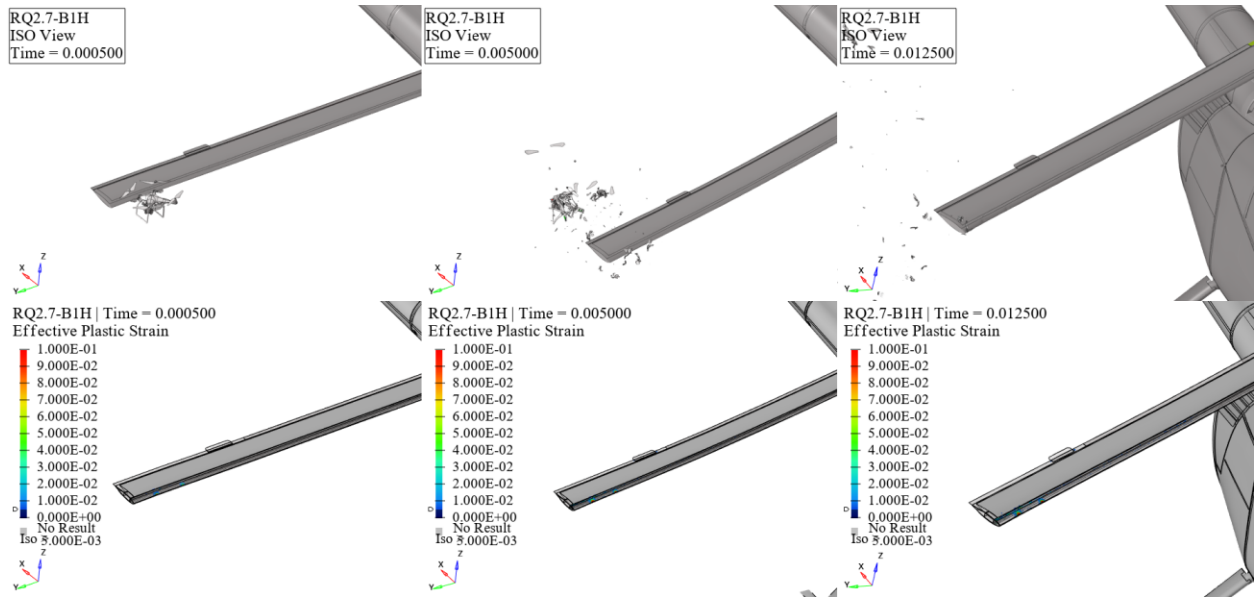

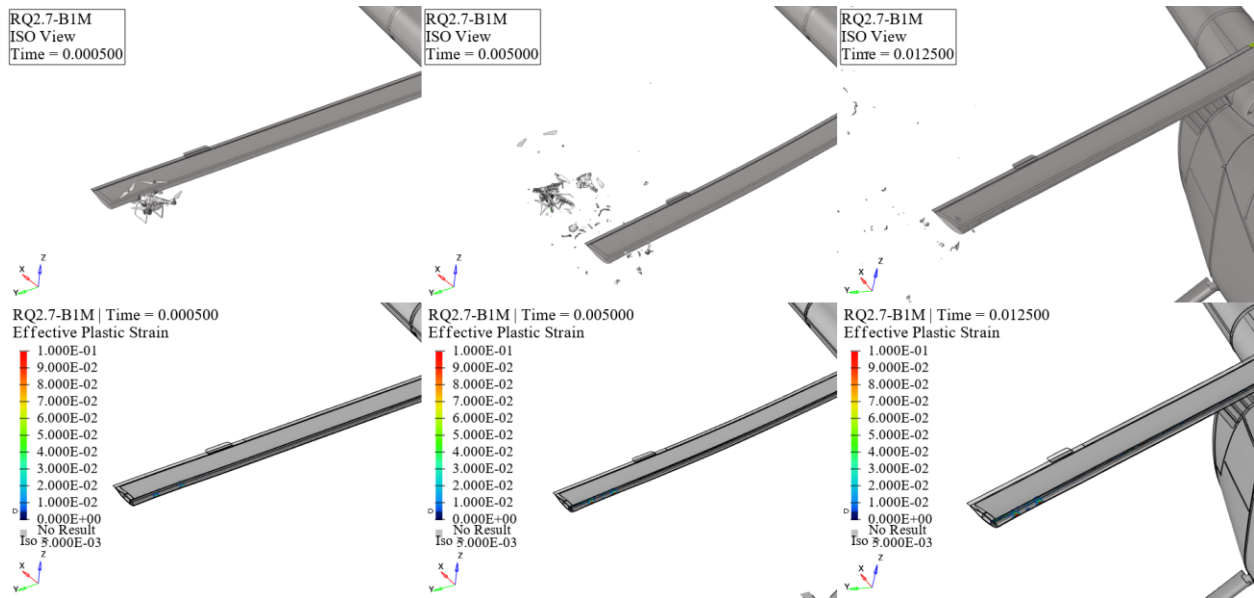Figure 290. RF12-B1H kinematics (top) and effective plastic strain (bottom) frames.

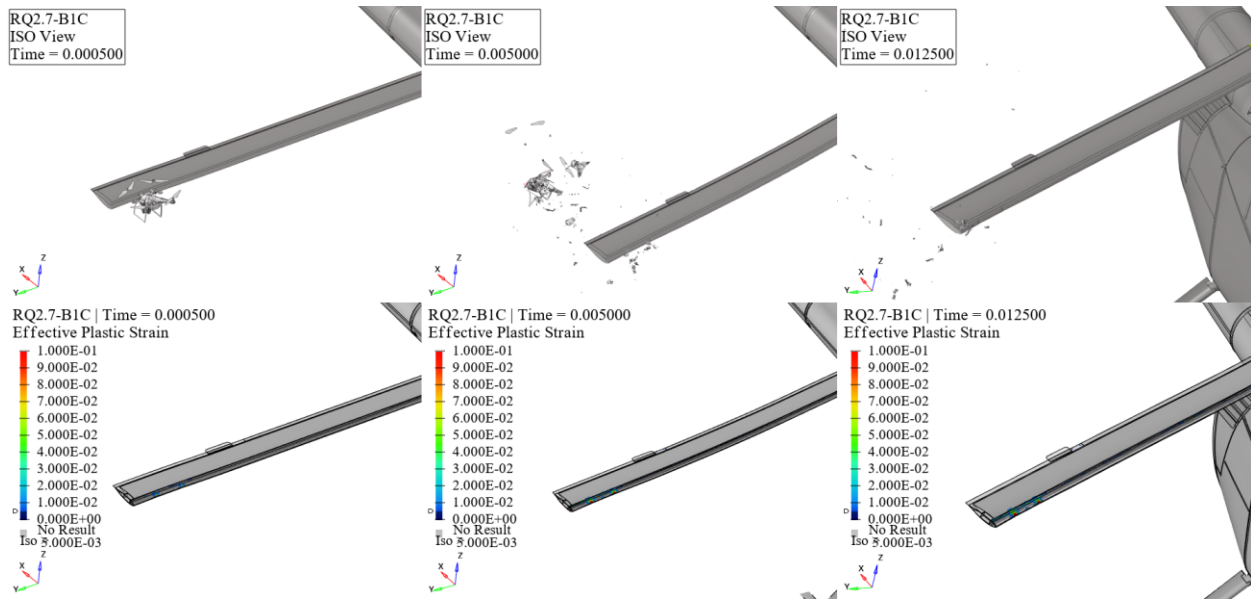Figure 291. RF12-B1M kinematics (top) and effective plastic strain (bottom) frames.

200

Figure 292. RF12-B1C kinematics (top) and effective plastic strain (bottom) frames.
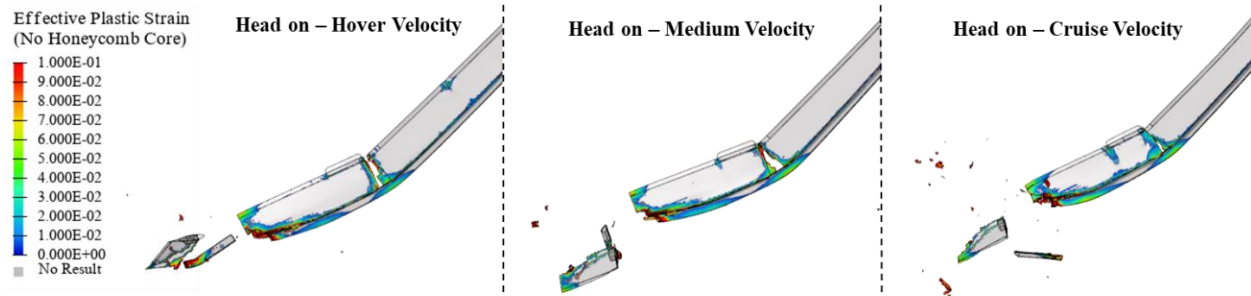
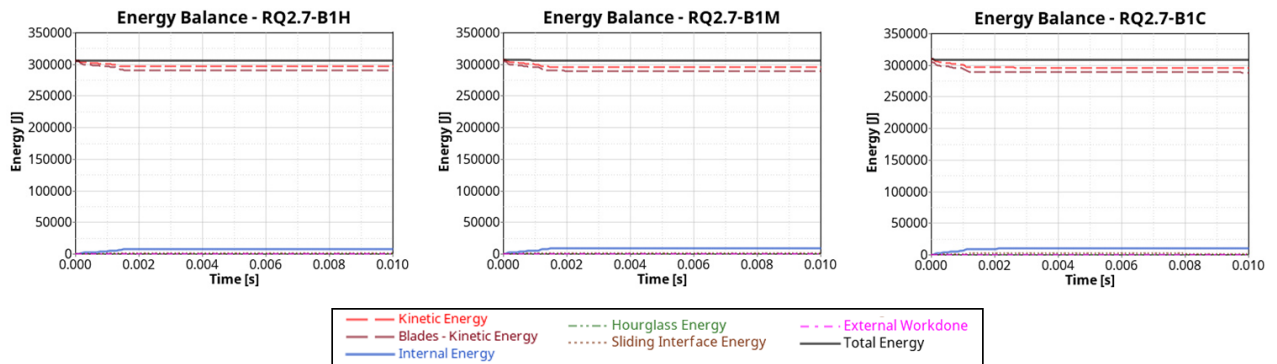Figure 293. Main rotor blade and 12 lbs. fixed-wing damage summary.
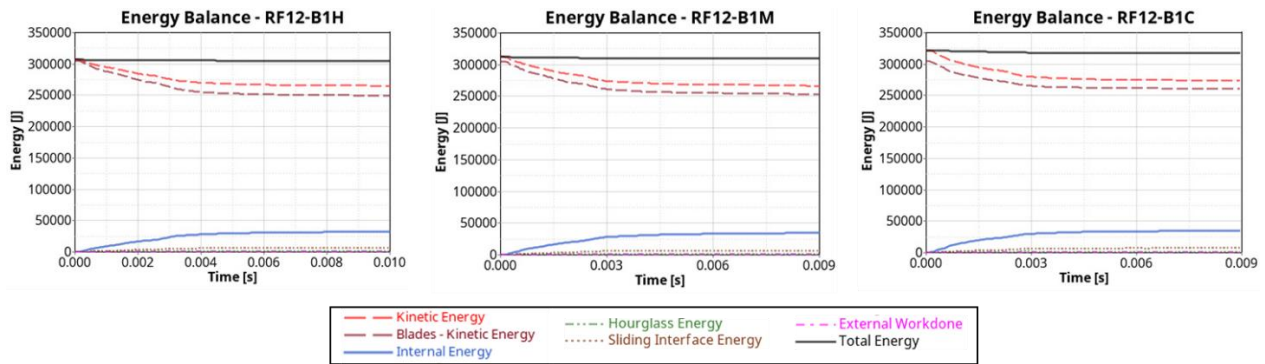
Figure 294. Main rotor blade and 12 lbs. fixed-wing impact energy balance.

At all three impact velocities (hover, medium, and cruise), the collision between the 12 lbs. fixed-wing and the main rotor blade resulted in significant loss of rotor blade, leading to rotorcraft instability and ultimately severe consequences, indicating a level 4 impact severity.

5.6.5 UAS 25 lbs. Quadcopter

This section delineates the findings stemming from collisions involving 25 lbs. quadcopter and the rotorcraft's Main Blade at Hover, Medium, and Cruise velocities, as showcased in Figure 295, Figure 296, and Figure 297, respectively. These results unravel the temporal progression of the impact occurrences, spotlighting time intervals at 0.0005s, 0.005s, and 0.0125s. The upper trio of windows highlights the kinematic aspects of the impacts, while the lower trio shows the resultant effective plastic strain on the rotorcraft structures. Additionally, Figure 298 illustrates the close-up damage summary, and Figure 299 provides the energy balance plots for all three impact velocities.
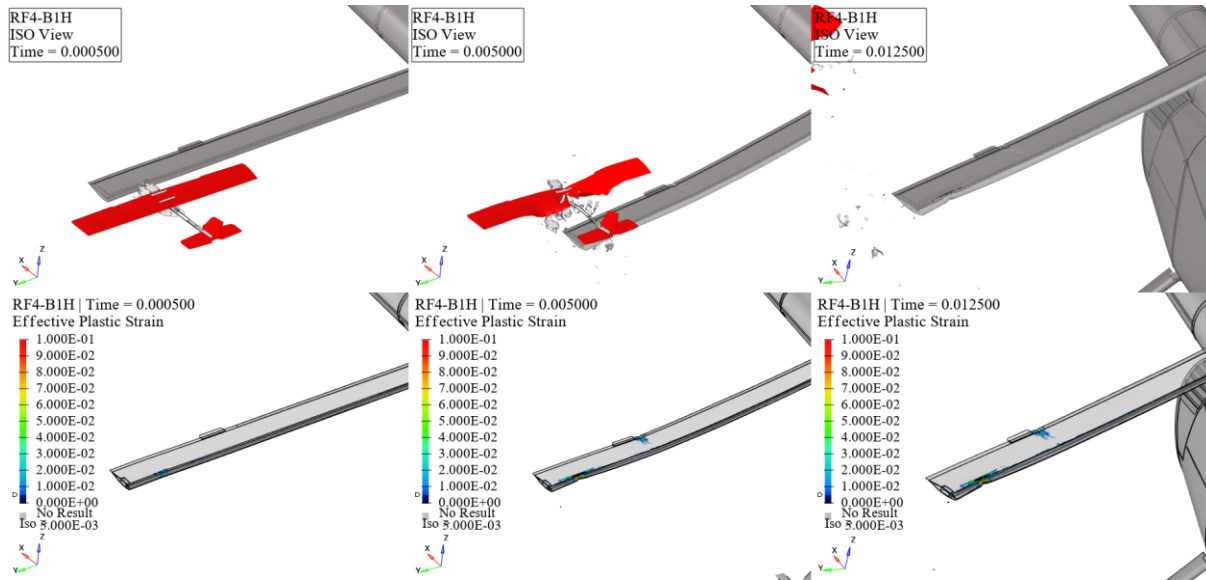

Figure 295. RQ25-B1H kinematics (top) and effective plastic strain (bottom) frames.
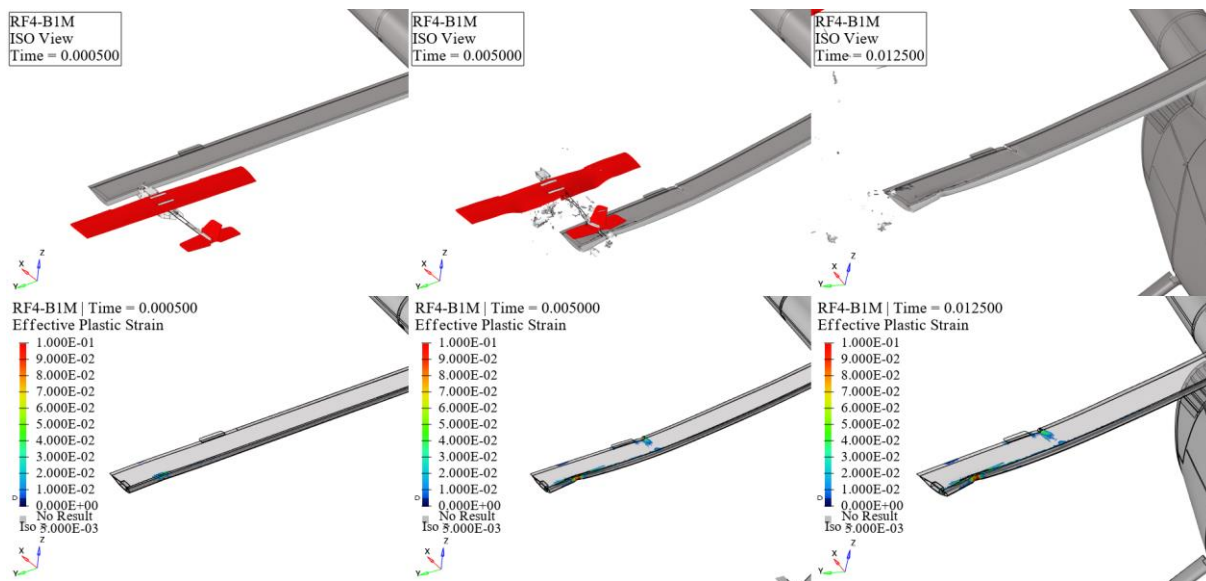

Figure 296. RQ25-B1M kinematics (top) and effective plastic strain (bottom) frames.
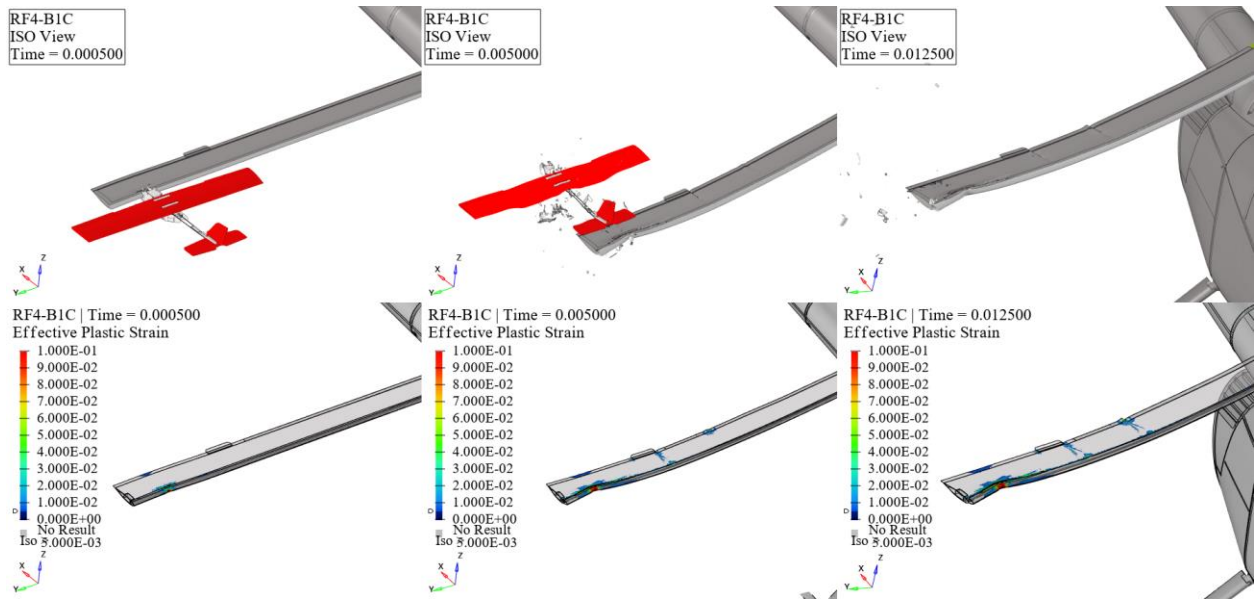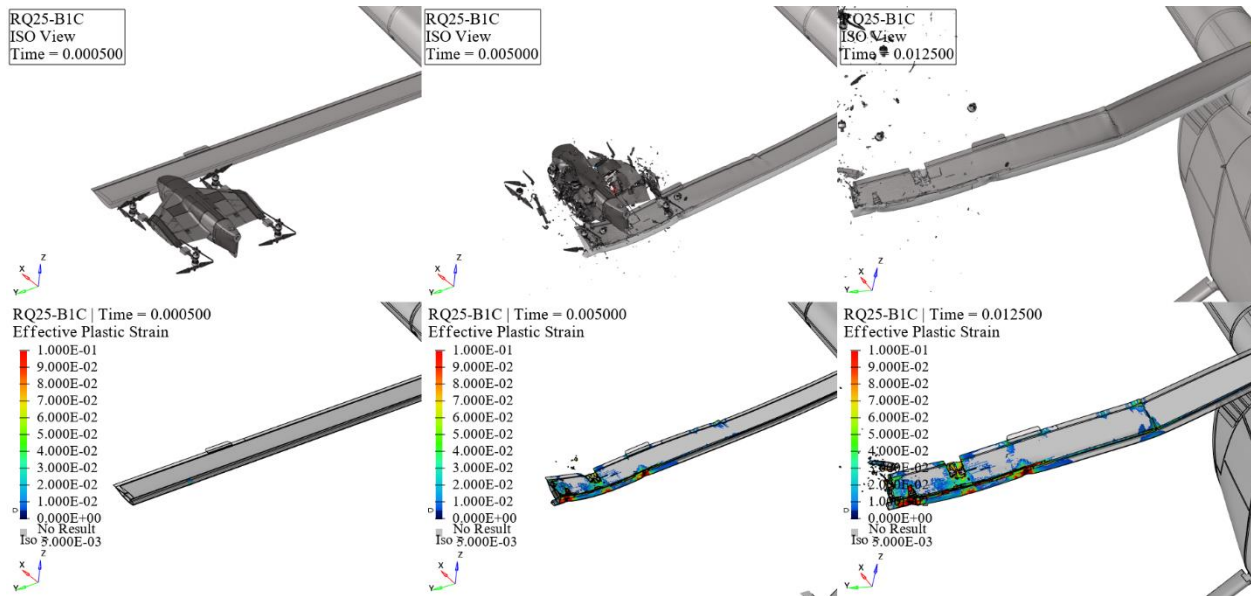
Figure 297. RQ25-B1C kinematics (top) and effective plastic strain (bottom) frames.
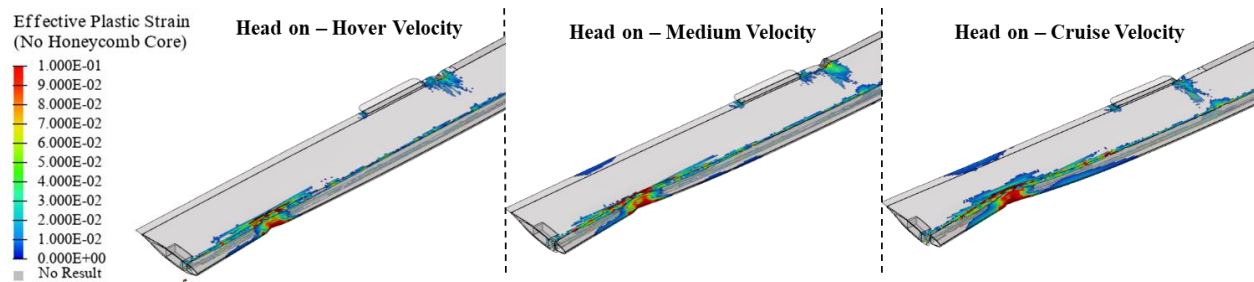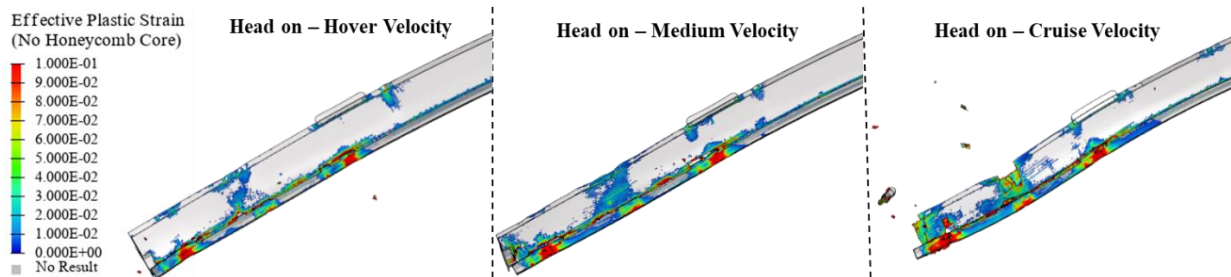

Figure 298. Main rotor blade and 25 lbs. quadcopter damage summary.
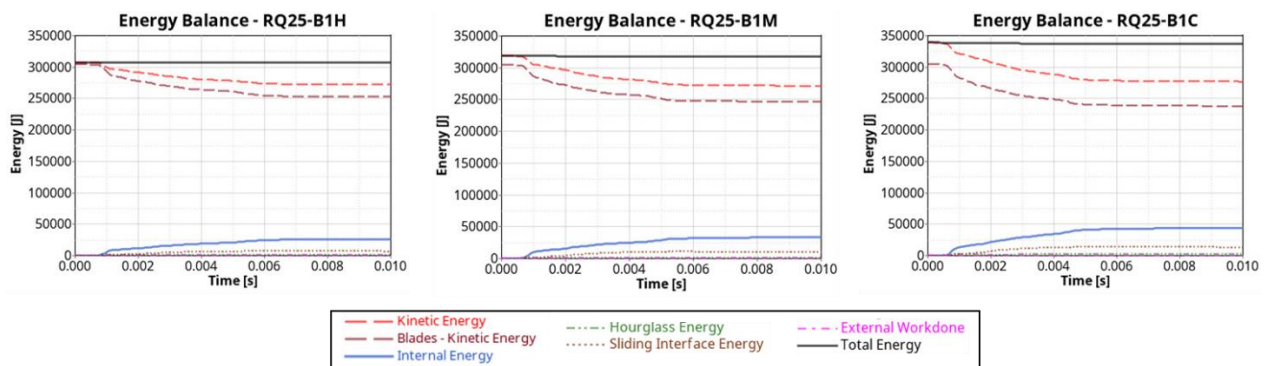
Figure 299. Main Rotor Blade and 25 lbs. quadcopter impact energy balance.

At all three impact velocities (hover, medium, and cruise), the collision between the 25 lbs. quadcopter and the main rotor blade resulted in significant damage, including major cracks, dents, debonding, buckling, and heavy blade twist and deflection. This extensive damage collectively leads to a loss of rotorcraft control and stability, indicating a level 4 impact severity.

5.6.6   UAS 25 lbs. Fixed-Wing

This section delineates the findings stemming from collisions involving 25 lbs. fixed-wing and the rotorcraft's Main Blade at Hover, Medium, and Cruise velocities, as showcased in Figure 300, Figure 301, and Figure 302, respectively. These results unravel the temporal progression of the impact occurrences, spotlighting time intervals at 0.0005s, 0.005s, and 0.0125s. The upper trio of windows highlights the kinematic aspects of the impacts, while the lower trio shows the resultant effective plastic strain on the rotorcraft structures. Additionally, Figure 303 illustrates the close-up damage summary and Figure 304 provides the energy balance plots for all three impact velocities.
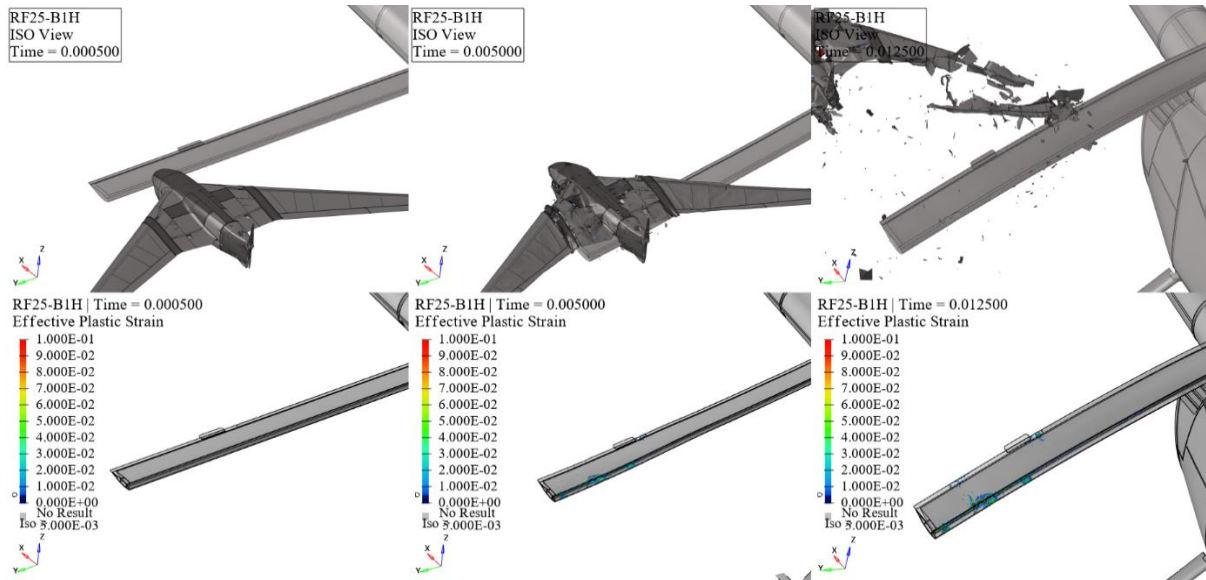
Figure 300. RF25-B1H kinematics (top) and effective plastic strain (bottom) frames.
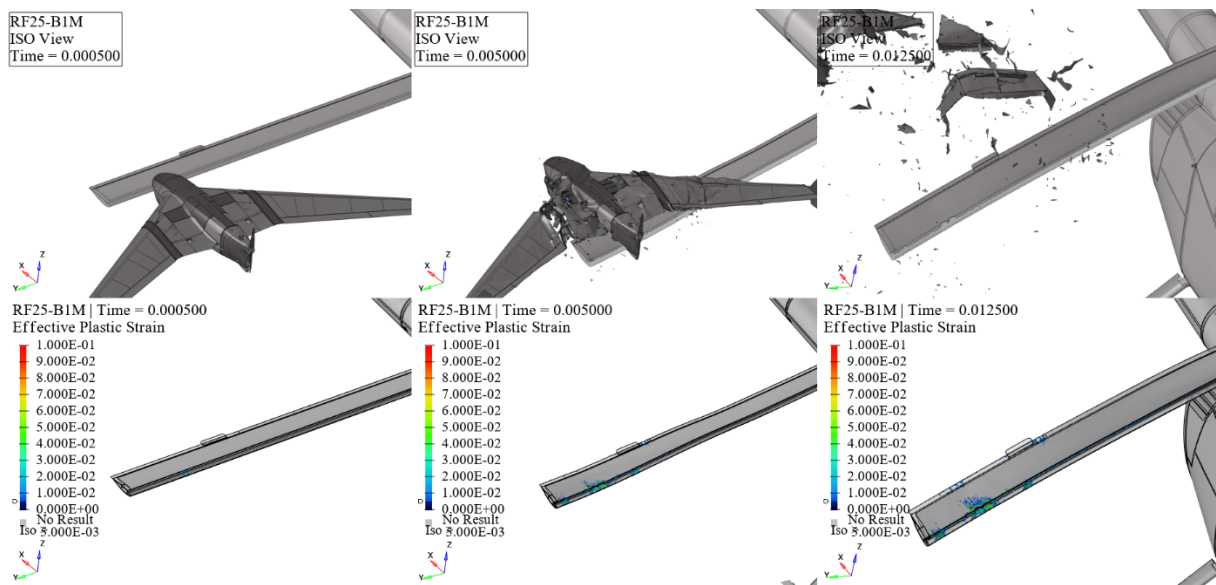
Figure 301. RF25-B1M kinematics (top) and effective plastic strain (bottom) frames.
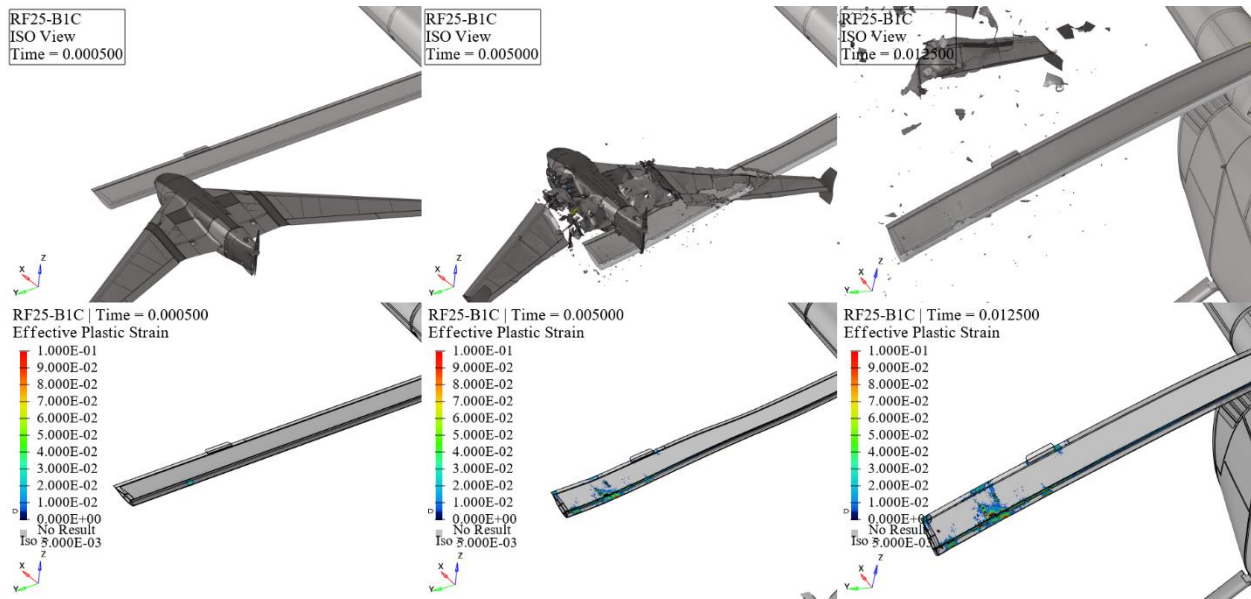
Figure 302. RF25-B1C kinematics (top) and effective plastic strain (bottom) frames.
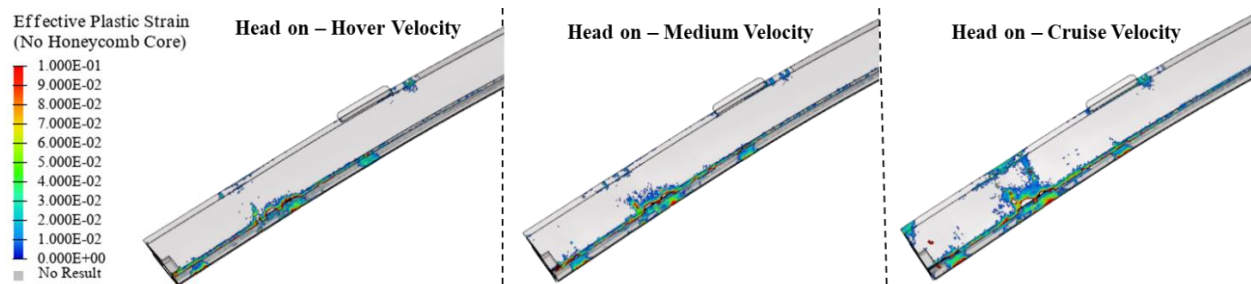
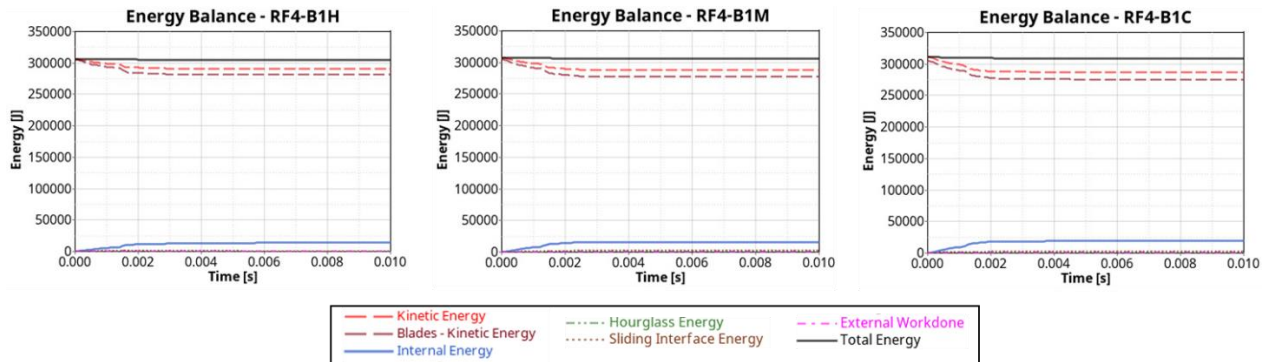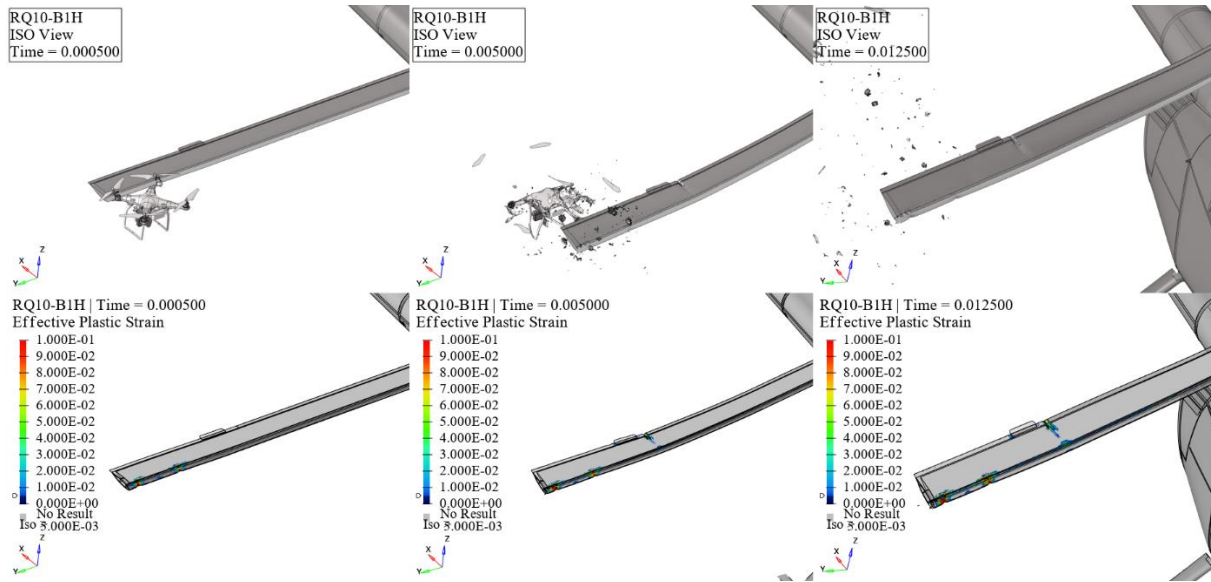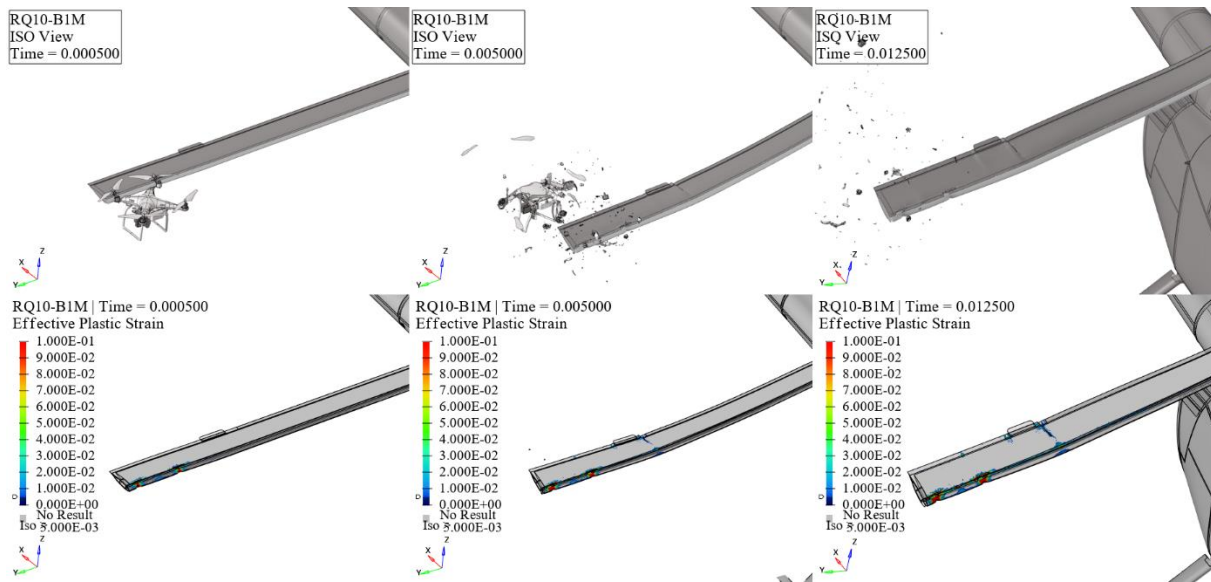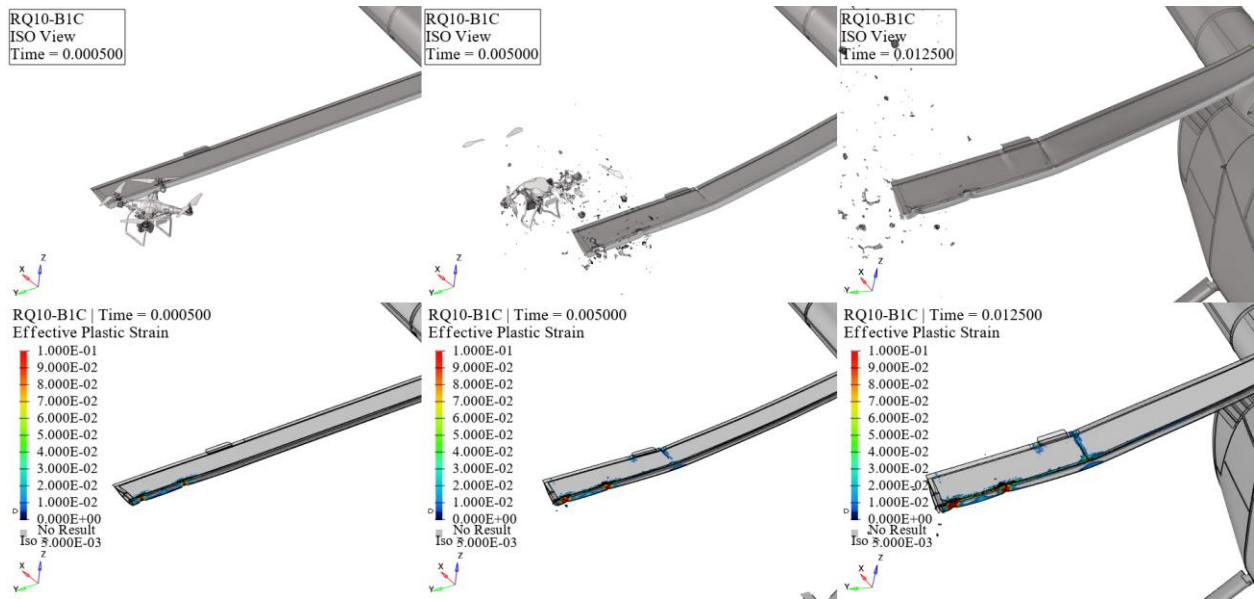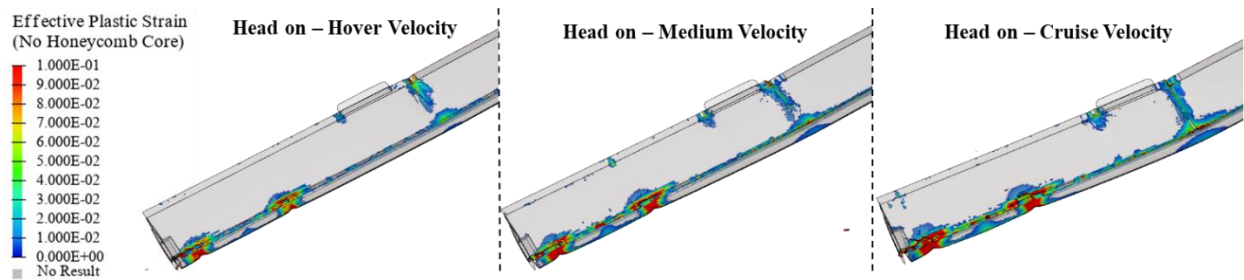Figure 303. Main rotor blade and 25 lbs. fixed-wing damage summary.
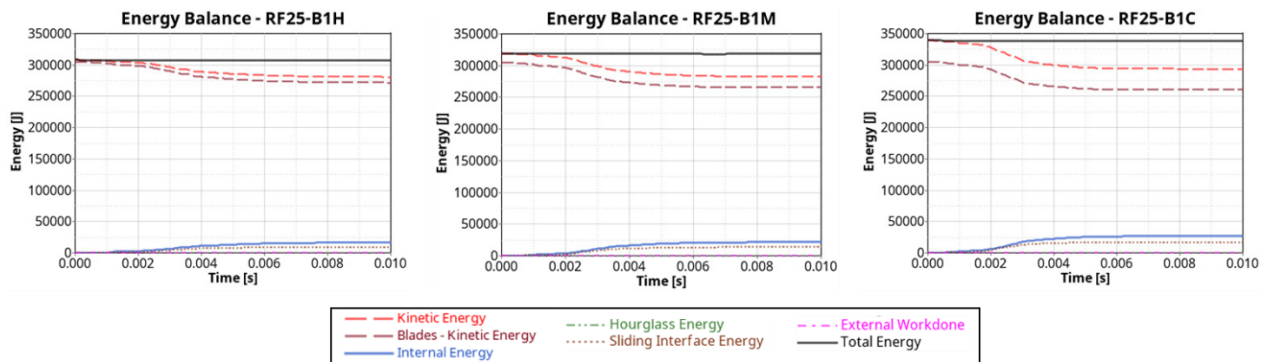
Figure 304. Main rotor blade and 25 lbs. fixed-wing impact energy balance.

At all three impact velocities (hover, medium, and cruise), the collision between the 25 lbs. quadcopter and the main rotor blade resulted in moderate damage, with no buckling or severe debonding, categorizing it as a level 2 impact severity purely based on structural damage. However, due to the blade's heavy backward deflection and twist, the rotor blade's flight performance is compromised, leading to instability and, ultimately, loss of rotorcraft control, resulting in a level 4 impact severity.

5.6.7 UAS 55 lbs. Quadcopter

This section delineates the findings stemming from collisions involving 55 lbs. quadcopter and the rotorcraft's Main Blade at Hover, Medium, and Cruise velocities, as showcased in Figure 305, Figure 306, and Figure 307, respectively. These results unravel the temporal progression of the impact occurrences, spotlighting time intervals at 0.0005s, 0.005s, and 0.0125s. The upper trio of windows highlights the kinematic aspects of the impacts, while the lower trio shows the resultant effective plastic strain on the rotorcraft structures. Additionally, Figure 308 illustrates the close-up damage summary, and Figure 309 provides the energy balance plots for all three impact velocities.

Figure 305. RQ55-B1H kinematics (top) and effective plastic strain (bottom) frames.

Figure 306. RQ55-B1M kinematics (top) and effective plastic strain (bottom) frames.
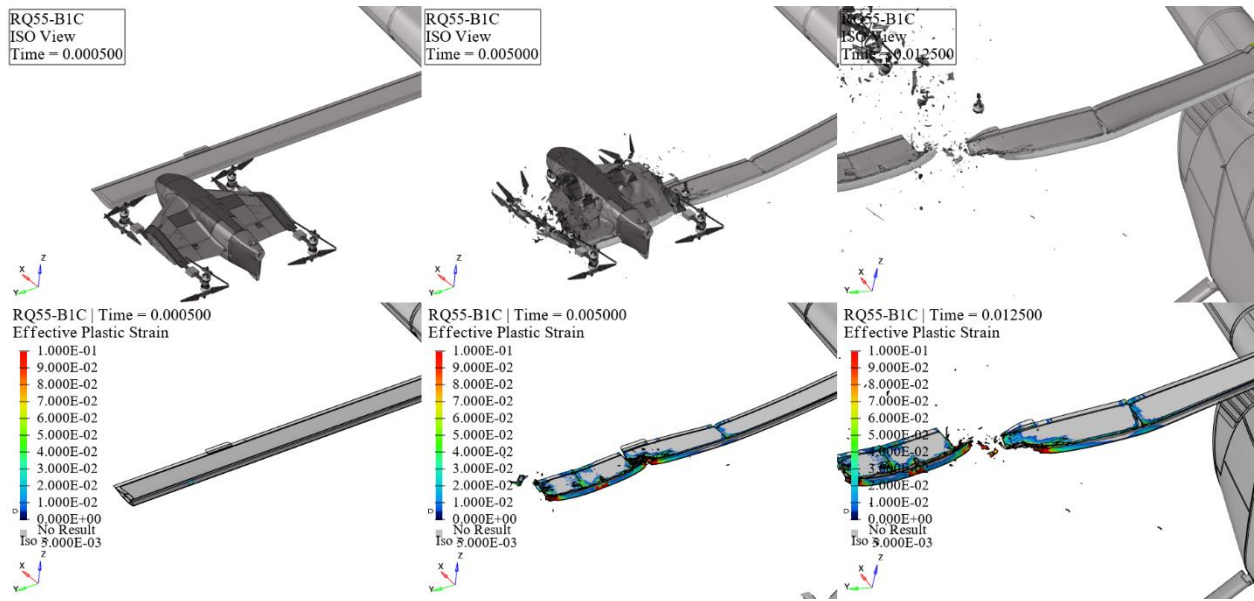
Figure 307. RQ55-B1C kinematics (top) and effective plastic strain (bottom) frames.
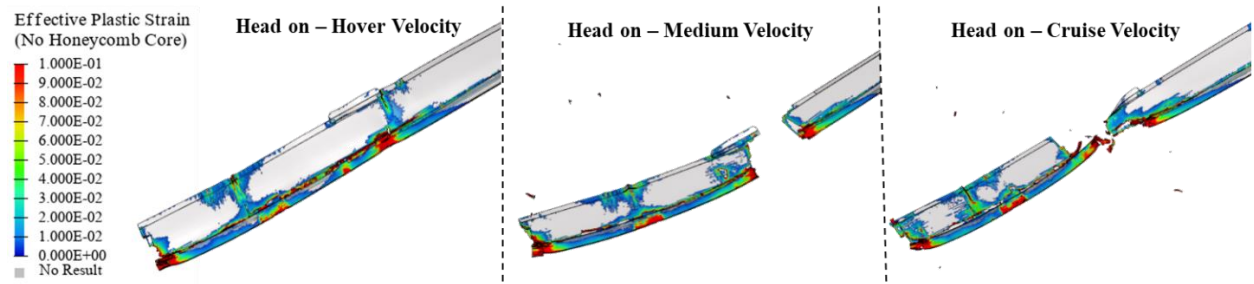
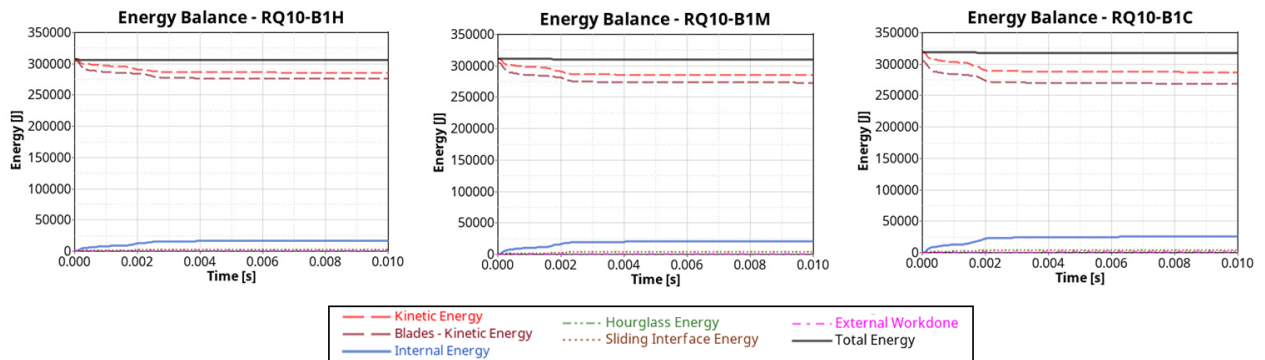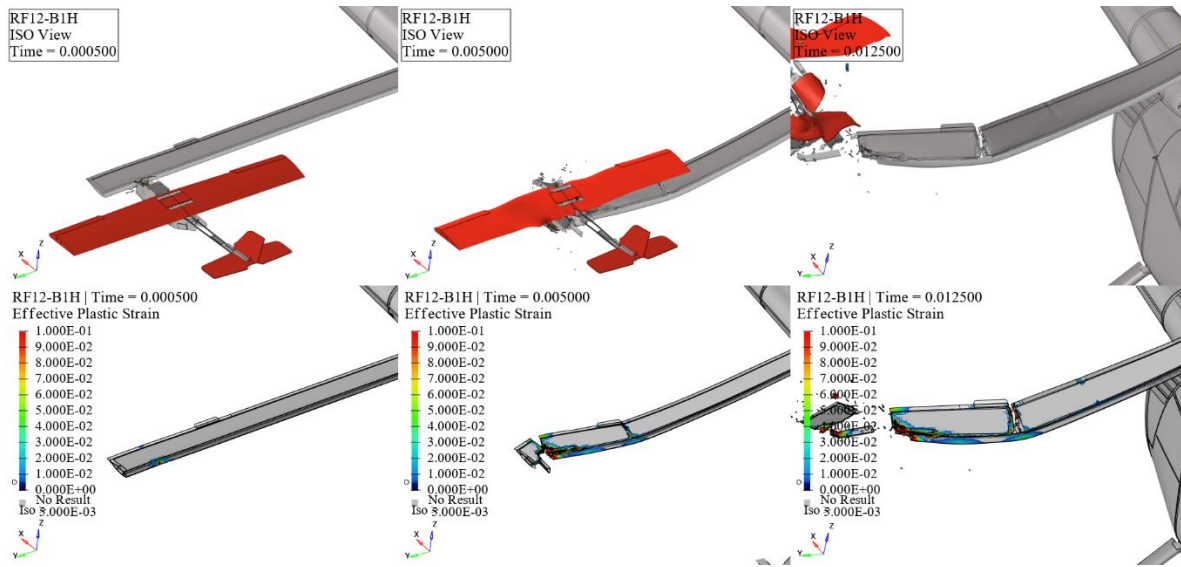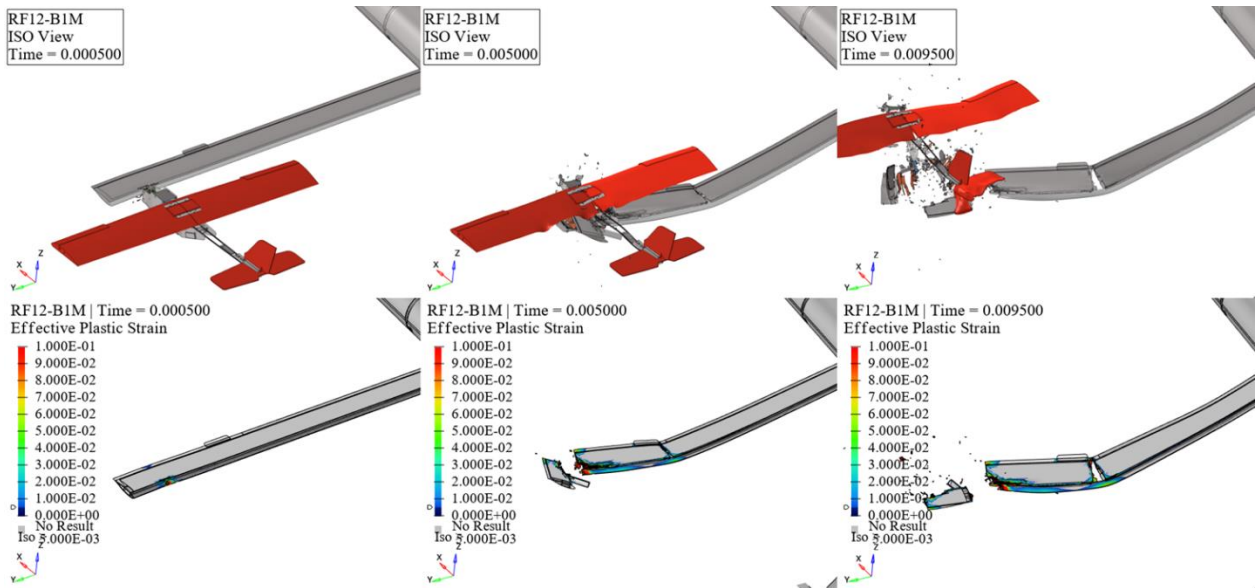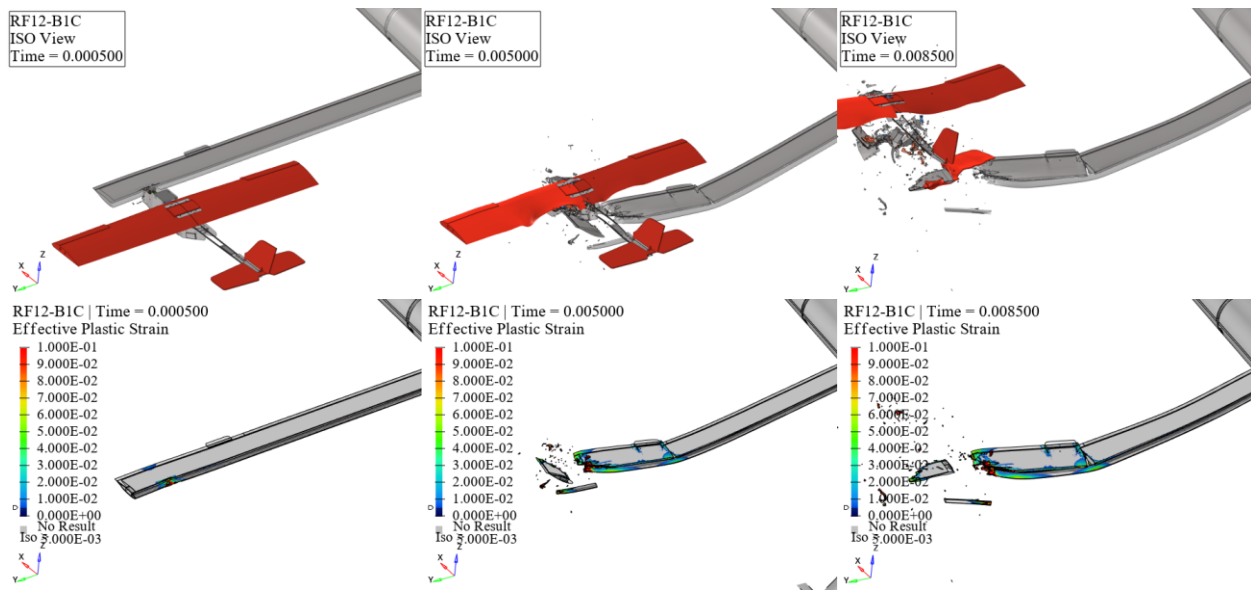Figure 308. Main rotor blade and 55 lbs. quadcopter damage summary.
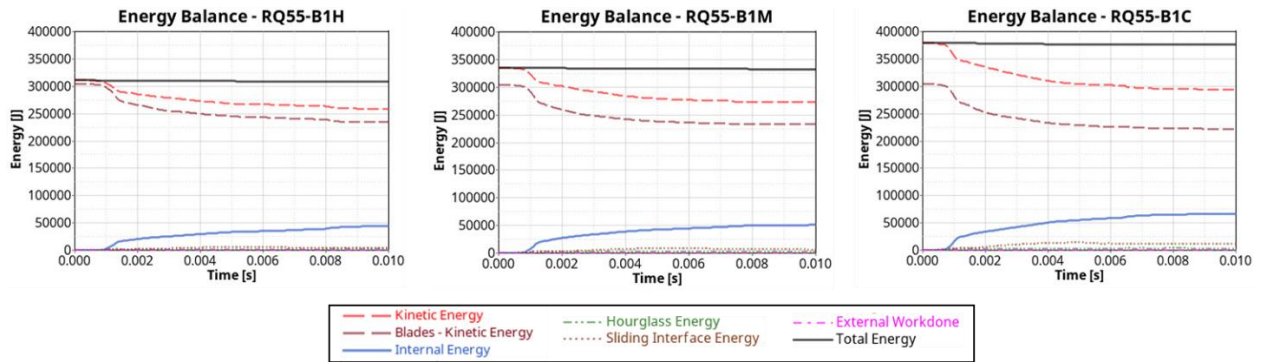
Figure 309. Main rotor blade and 55 lbs. quadcopter impact energy balance.

At all three impact velocities (hover, medium, and cruise), the collision between the 55 lbs. quadcopter and the main rotor blade resulted in significant rotor blade damage and considerable material loss, leading to rotorcraft instability and ultimately severe consequences, indicating a level 4 impact severity.

5.6.8 UAS 55 lbs. Fixed-Wing

This section delineates the findings stemming from collisions involving 55 lbs. fixed-wing and the rotorcraft's Main Blade at Hover, Medium, and Cruise velocities, as showcased in Figure 310, Figure 311, and Figure 312, respectively. These results unravel the temporal progression of the impact occurrences, spotlighting time intervals at 0.0005s, 0.005s, and 0.0125s. The upper trio of windows highlights the kinematic aspects of the impacts, while the lower trio shows the resultant effective plastic strain on the rotorcraft structures. Additionally, Figure 313 illustrates the close-up damage summary, and Figure 313 provides the energy balance plots for all three impact velocities.
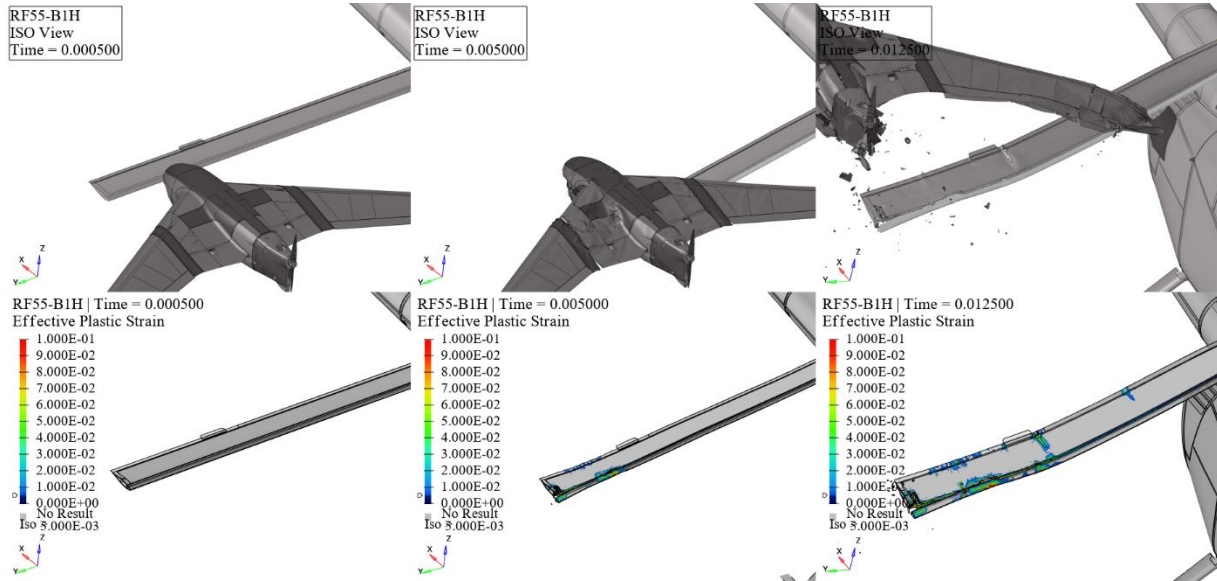
Figure 310. RF55-B1H kinematics (top) and effective plastic strain (bottom) frames.
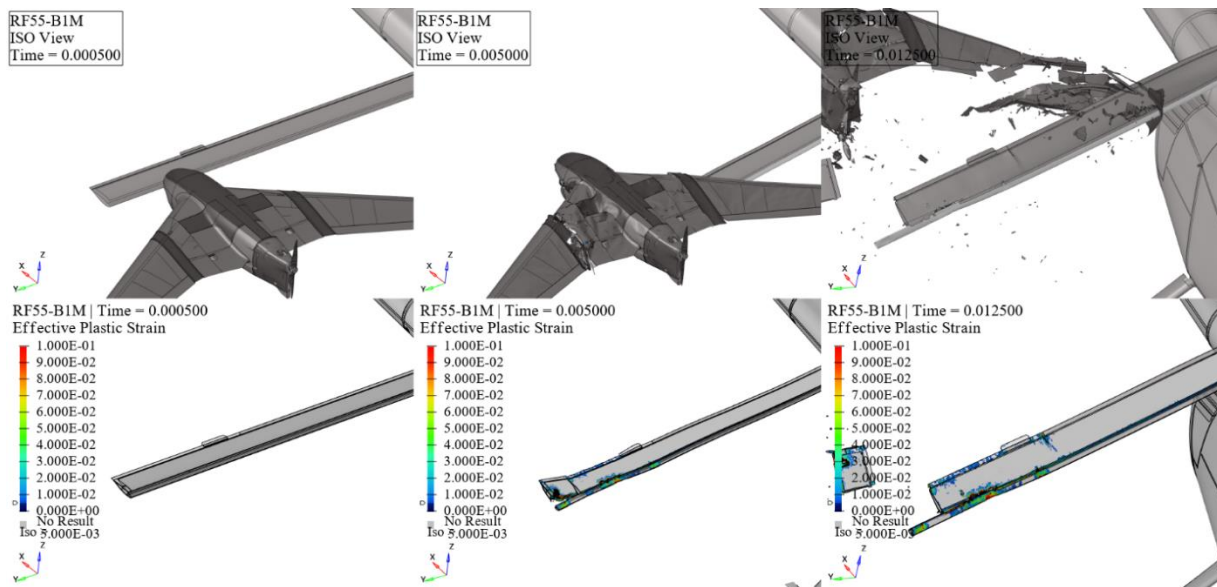
Figure 311. RF55-B1M kinematics (top) and effective plastic strain (bottom) frames.
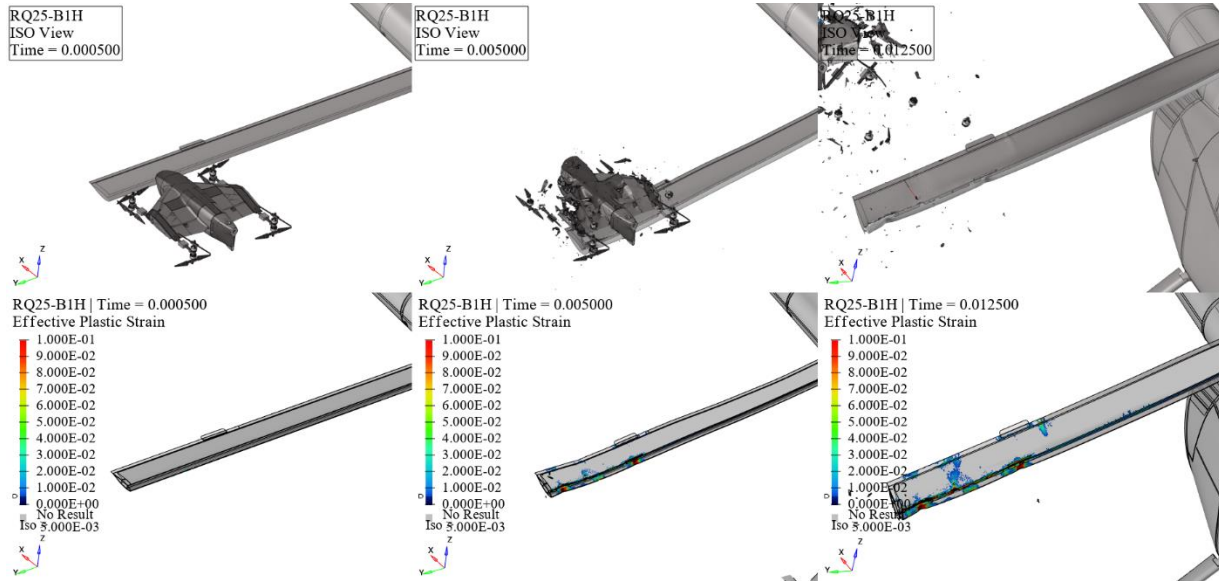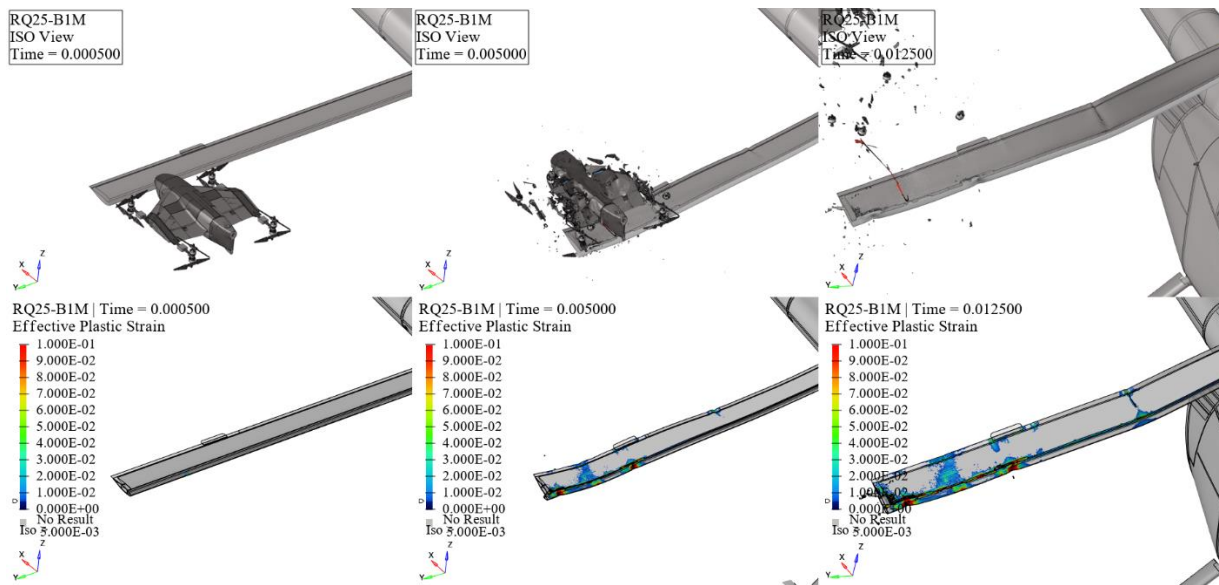
208
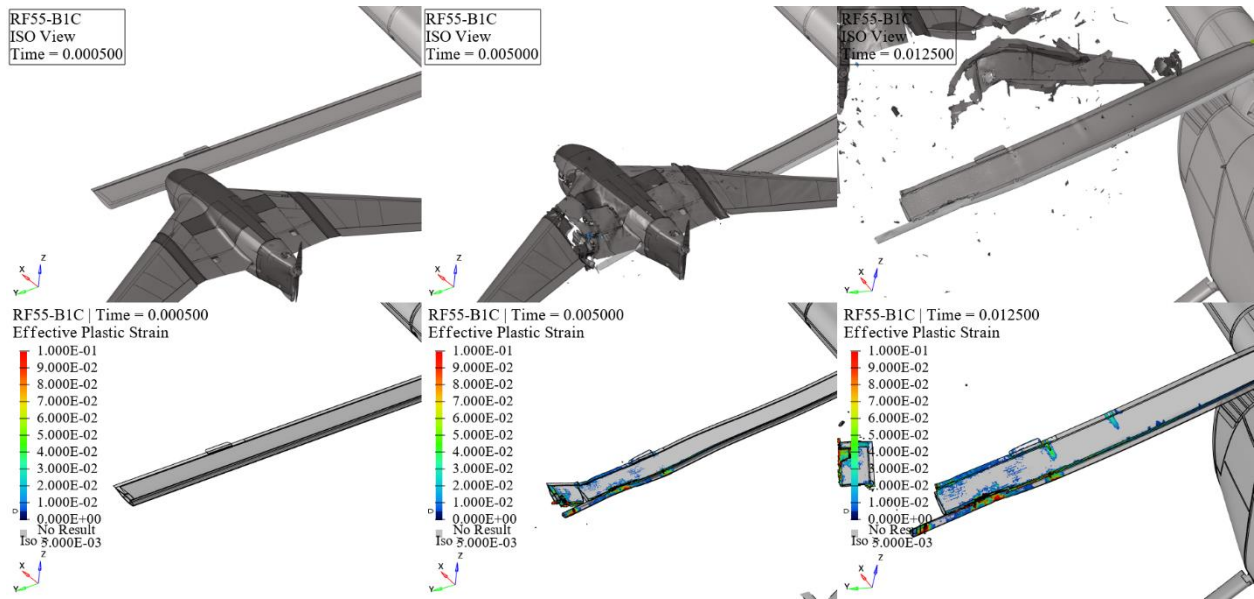
Figure 312. RF55-B1C kinematics (top) and effective plastic strain (bottom) frames.
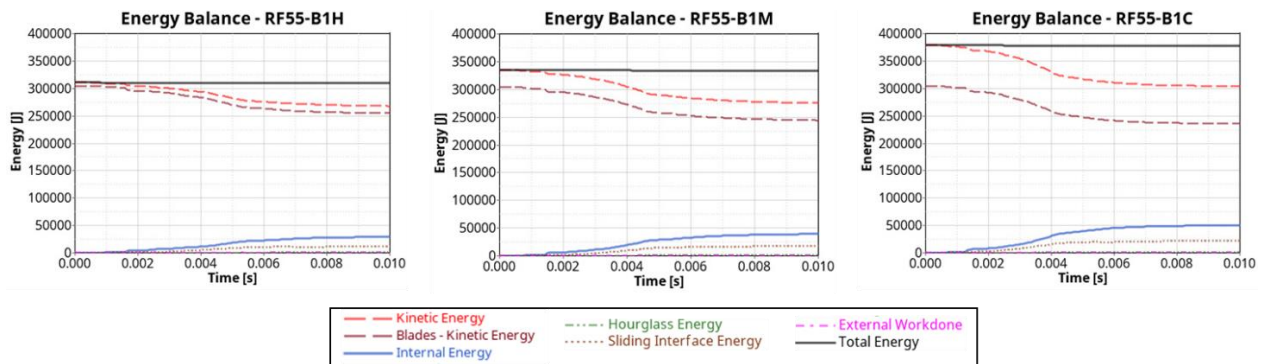
Figure 313. Main rotor blade and 55 lbs. fixed-wing impact energy balance.
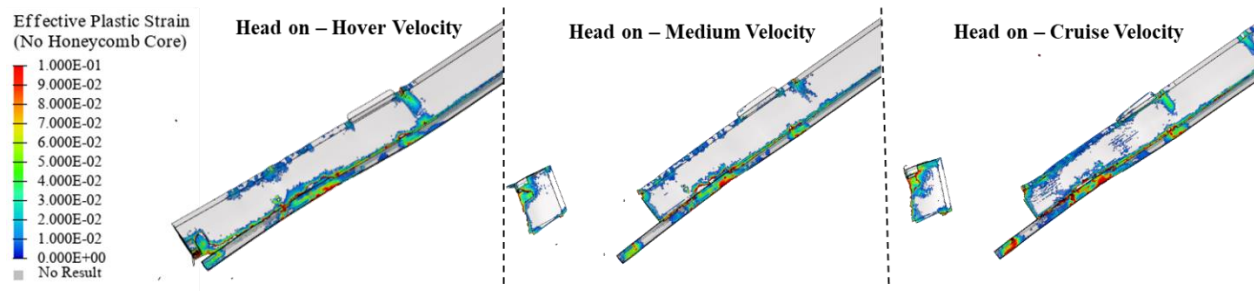
Figure 314. Main rotor blade and 55 lbs. fixed-wing damage summary.

At all three impact velocities (hover, medium, and cruise), the collision between the 55 lbs. fixed-wing and the main rotor blade resulted in significant rotor blade damage and considerable material loss, leading to rotorcraft instability and ultimately severe consequences, indicating a level 4 impact severity.

5.7   2.7 lbs. Quadcopter downwash mid-air collision analysis and damage assessment.

As mentioned, the results presented in previous sections did not consider any aerodynamic loads. As it is well known, one of the major aerodynamic effects of rotorcraft is the downwash effect generated by the main rotor blade due to its rotation. Previous work conducted by NIAR showed that significant changes in the sUAS trajectories are possible for some specific flying conditions [42]. Due to its small size and weight, the 2.7 lb quadcopter experienced the most severe downwash effects among all UAS architectures evaluated in this research. Consequently, the 2.7 lbs. quadcopter was selected for the downwash mid-air collision study for this Part 27 rotorcraft.

Downwash conditions were initially predicted using Computational Fluid Dynamics (CFD) analyses from previous studies [42]. However, these analyses did not precisely replicate the impact conditions presented in earlier sections of this report. Therefore, an approximation approach was employed to determine the impact conditions, incorporating downwash effects. The location of the UAS impact was kept consistent with those detailed in Section 4.1 to allow for a direct comparison between head-on and deflected impacts. The orientation and velocity of the UAS were derived from the CFD analysis, which most closely matched the head-on impact condition. Figure 315 illustrates the process used to define the impact conditions for this study.
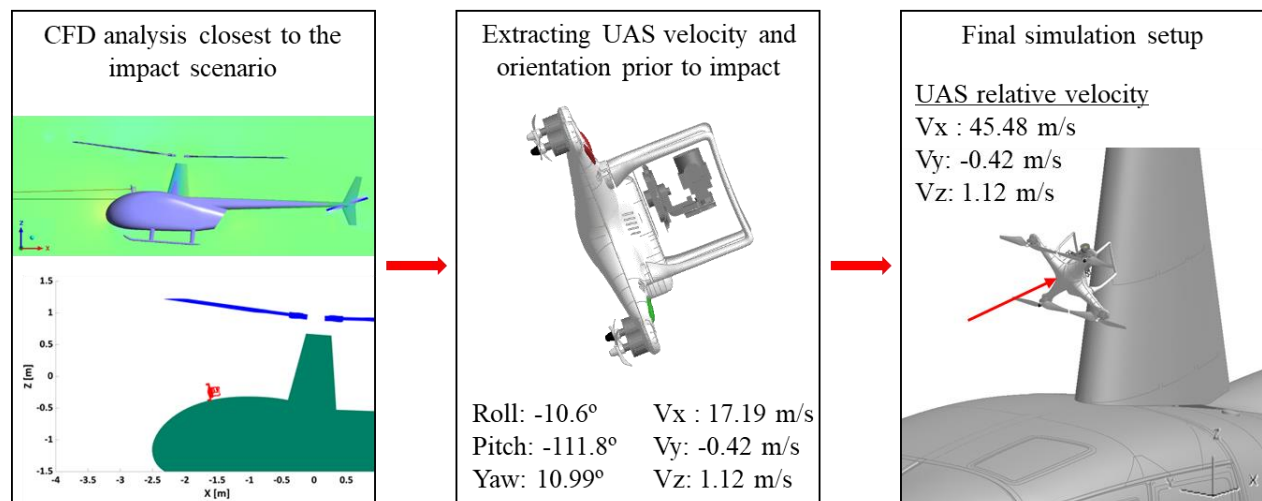
Figure 315. Impact conditions definition process.

This study examines the impact of a 2.7 lbs. quadcopter with a rotorcraft's mast, windshield, and rotor blade at two rotorcraft flight speeds: medium (55 knots) and cruise (110 knots). The UAS's initial velocity, prior to encountering the downwash effect, was set at 39 knots. For the simulation, the relative velocity was applied to the UAS while the rotorcraft remained stationary, and rotor blade rotation was simulated for all impact conditions. This section presents the simulation results, mid-air collision damage assessment, fire risk assessment, and a comparison of impact severity with the equivalent head-on impact for each simulation.

5.7.1   Mast

This section provides the findings stemming from collisions involving 2.7 lbs. quadcopter and the rotorcraft's mast, including downwash effects at medium and cruise velocities, as showcased in

Figure 316 and Figure 317, respectively. These results unravel the temporal progression of the impact occurrences, spotlighting time intervals at 0.005s, 0.02s, and 0.04s. The upper trio of windows highlights the kinematic aspects of the impacts, while the lower trio shows the resultant effective plastic strain on the rotorcraft structure. Additionally, Figure 318 provides the energy balance plots for both impact velocities.
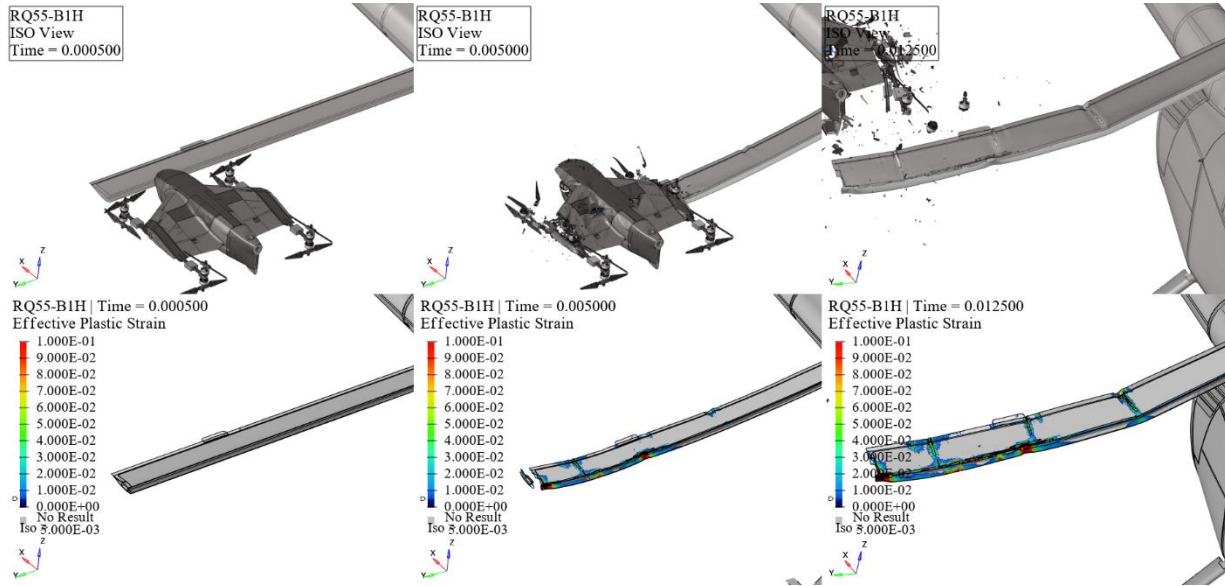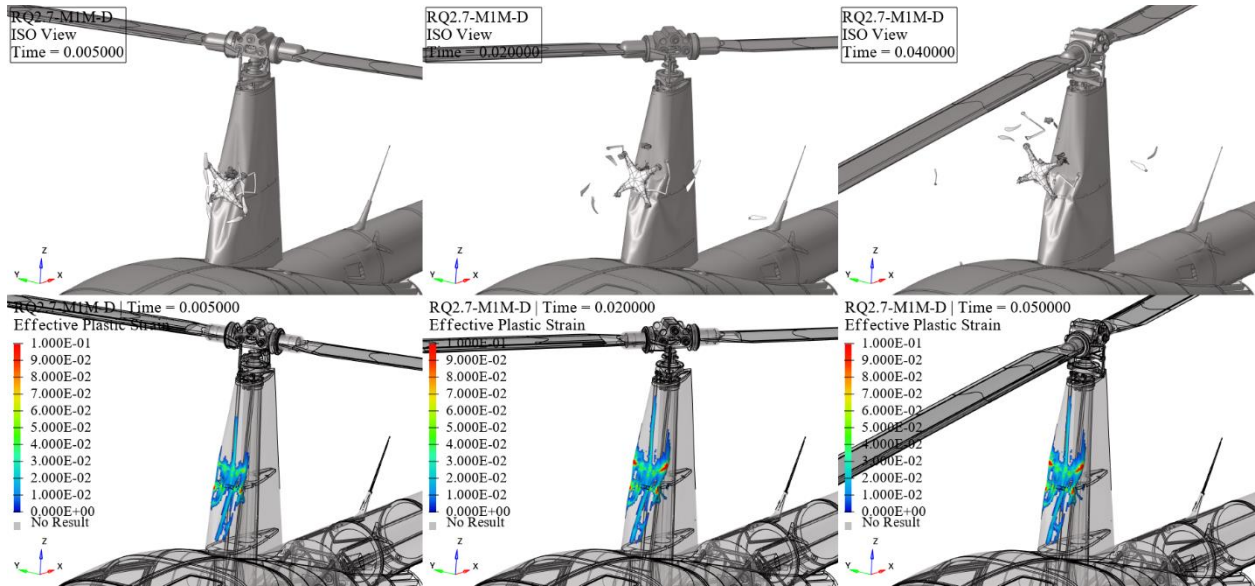

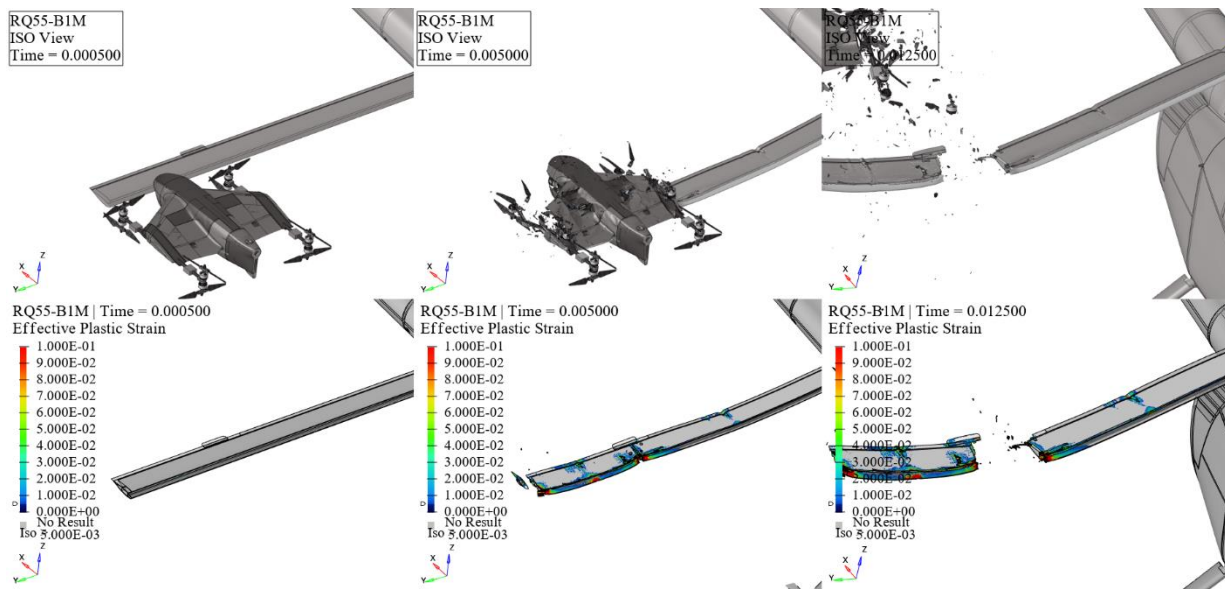Figure 316. RQ2.7-M1M-D kinematics (top) and effective plastic strain (bottom) frames.
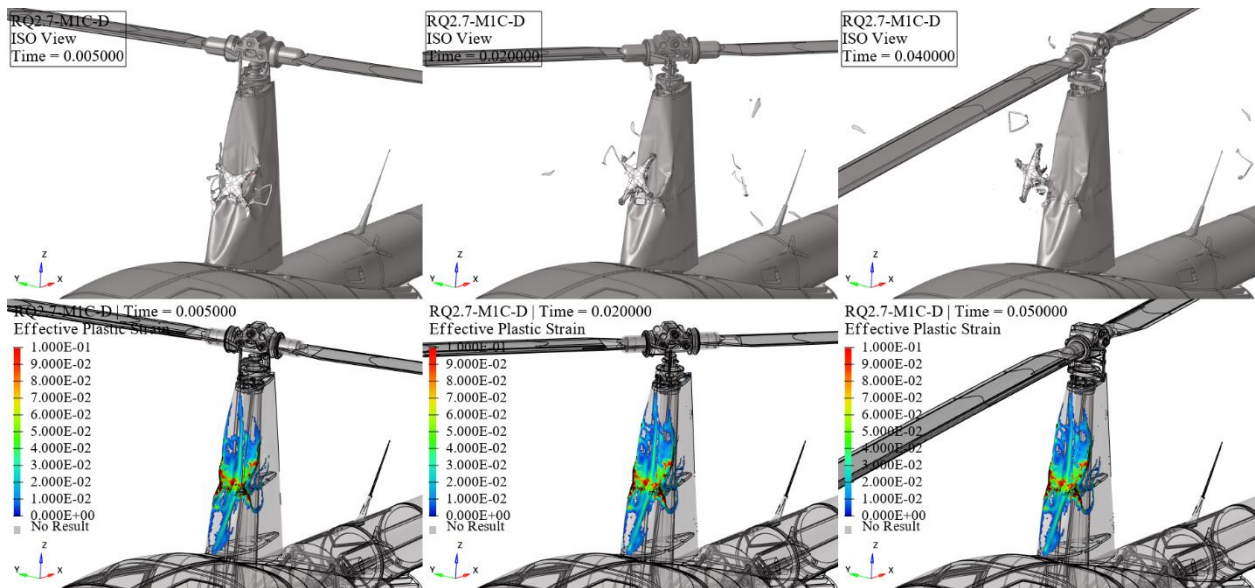
Figure 317. RQ2.7-M1C-D kinematics (top) and effective plastic strain (bottom) frames.
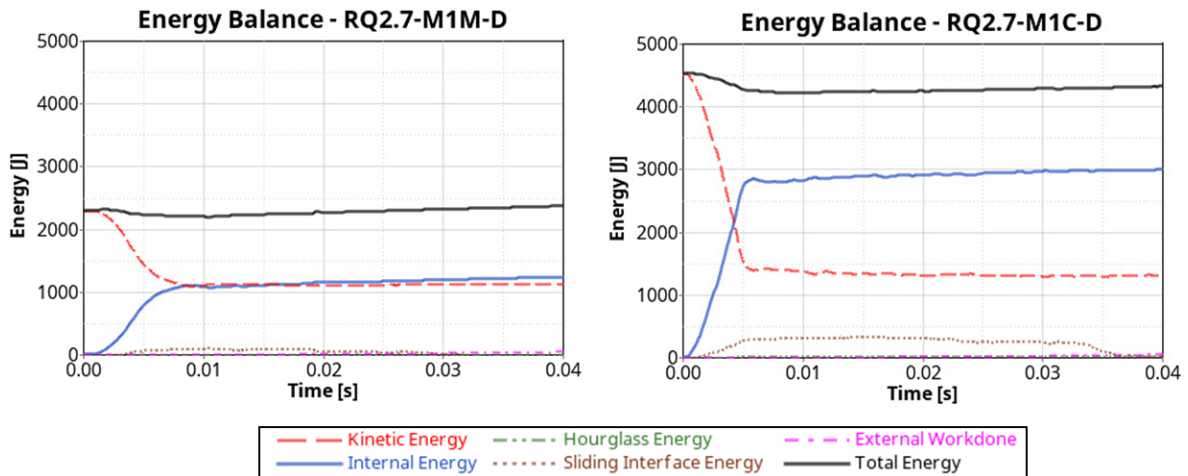
Figure 318. Mast and 2.7 lbs. quadcopter downwash impact energy balance.

At both medium and cruise impact velocities, the mast exhibited permanent skin deformation but no skin fracture, resulting in a level 2 impact severity. The severity remained the same for both head-on and deflected impact between the 2.7 lb quadcopter and the mast, and there was not much difference in the area affected by the impact, as shown in Figure 319. Table 49 summarizes the findings.
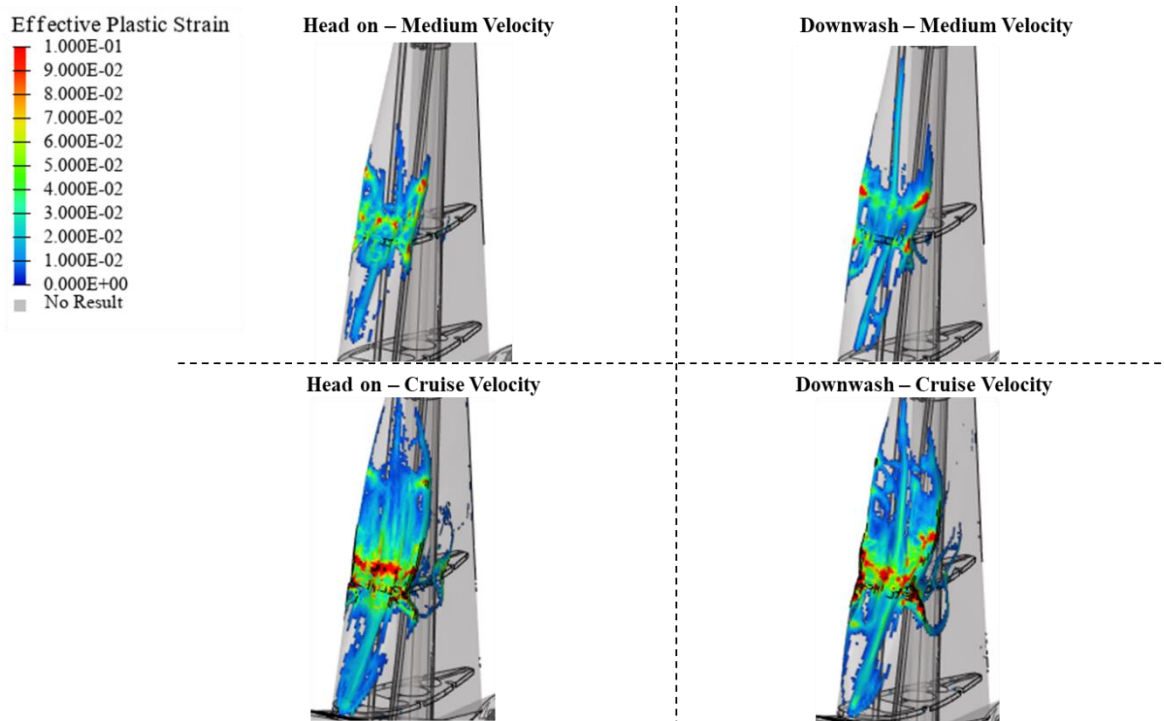
Figure 319. RQ2.7-M1 and RQ2.7-M1-D damage comparison.

Table 48. Mast mid-air collision simulation assessment – damage severity level, fire risk, and comparison.

Mid air collision: 2.7 lbs. quadcopter and mast	Case	Direct impact (head-on)		Deflected impact (downwash)	
		Severity	Fire Risk	Severity	Fire Risk
	RQ2.7-M1M	Level 2	No	Level 2	No
	RQ2.7-M1C	Level 2	No	Level 2	No

5.7.2 *Windshield*

This section provides the findings stemming from collisions involving 2.7 lbs. quadcopter and the rotorcraft's Windshield, including downwash effects at medium and cruise velocities, as showcased in Figure 320 and Figure 321, respectively. These results unravel the temporal progression of the impact occurrences, spotlighting time intervals at 0.005s, 0.02s, and 0.03s. The upper trio of windows highlights the kinematic aspects of the impacts, while the lower trio shows the resultant effective plastic strain on the rotorcraft structure. Additionally, Figure 322 provides the energy balance plots for both impact velocities.
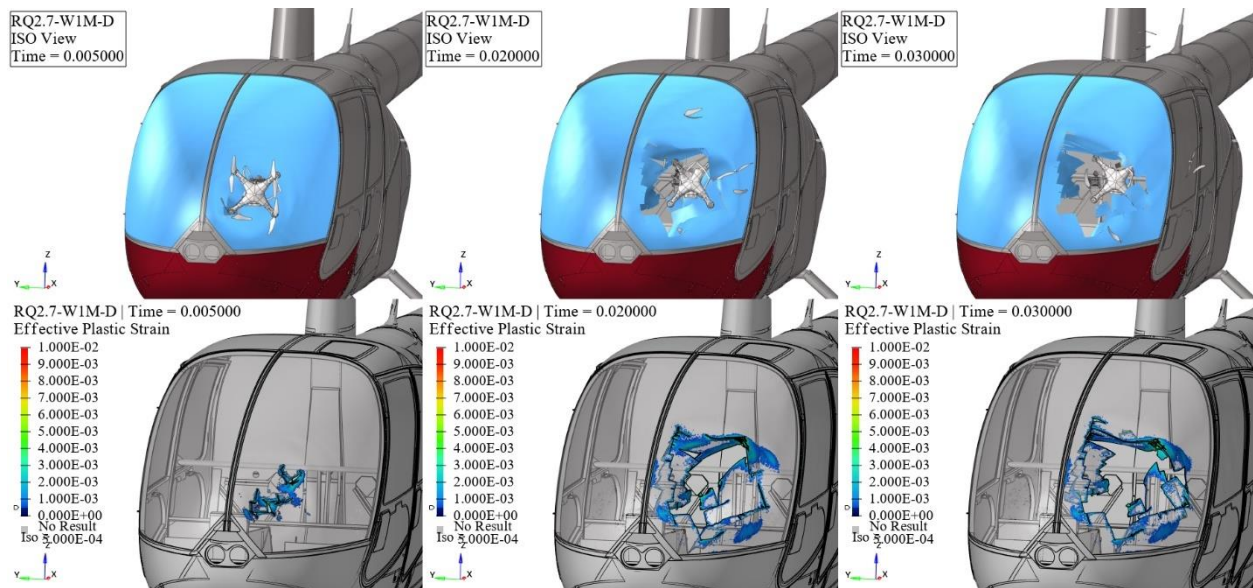
Figure 320. RQ2.7-W1M-D kinematics (top) and effective plastic strain (bottom) frames.
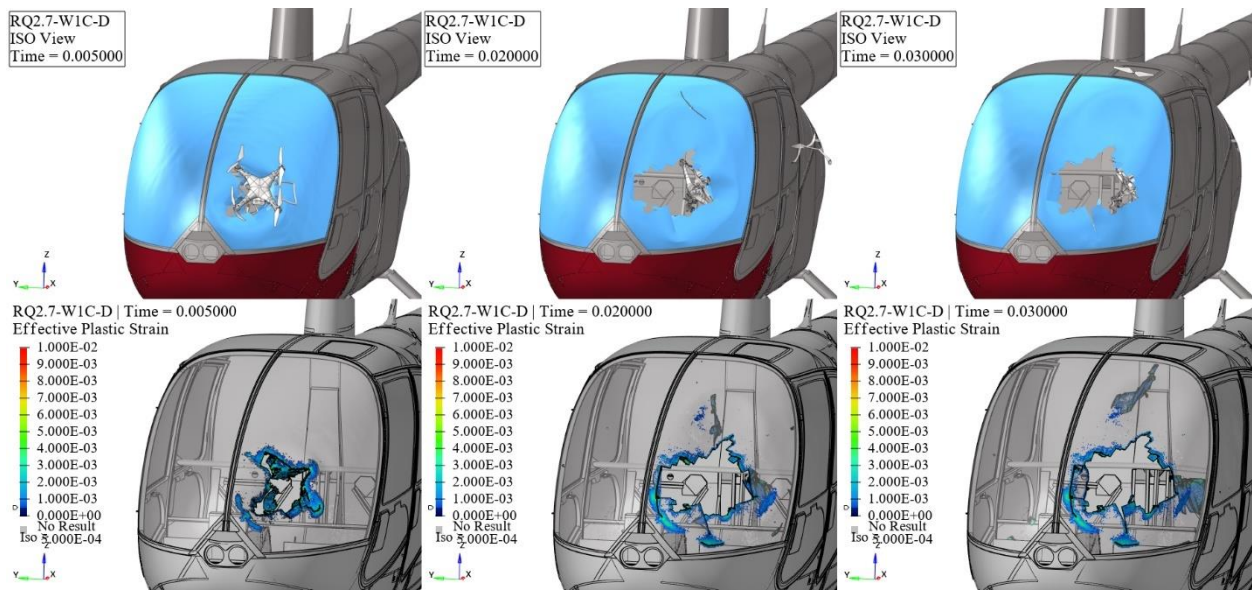
Figure 321. RQ2.7-W1C-D kinematics (top) and effective plastic strain (bottom) frames.
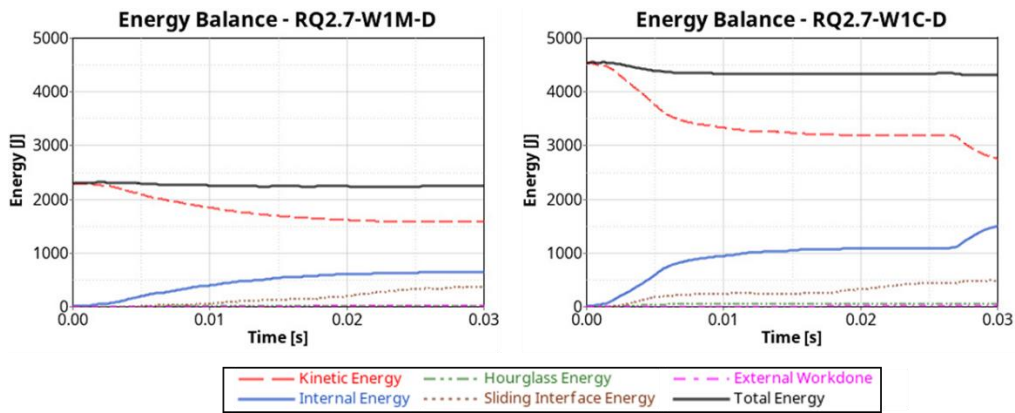

Figure 322. Windshield and 2.7 lbs. quadcopter downwash impact energy balance.

At both medium and cruise impact velocities, the windshield fractured, and the UAS penetrated the passenger cabin, resulting in a level 4 impact severity. The severity remained the same for both head-on and deflected impacts between the 2.7 lbs. quadcopter and the windshield. The only differences were that the area of the fractured windshield was bigger for the deflected impacts than the head-on impacts for both impact velocities, as shown in Figure 323. The fire risk was less prominent for the downwash medium impact velocity while fire risk became more prominent for the downwash cruise impact velocity as can be seen in Figure 324. Table 49 summarizes the findings.

214
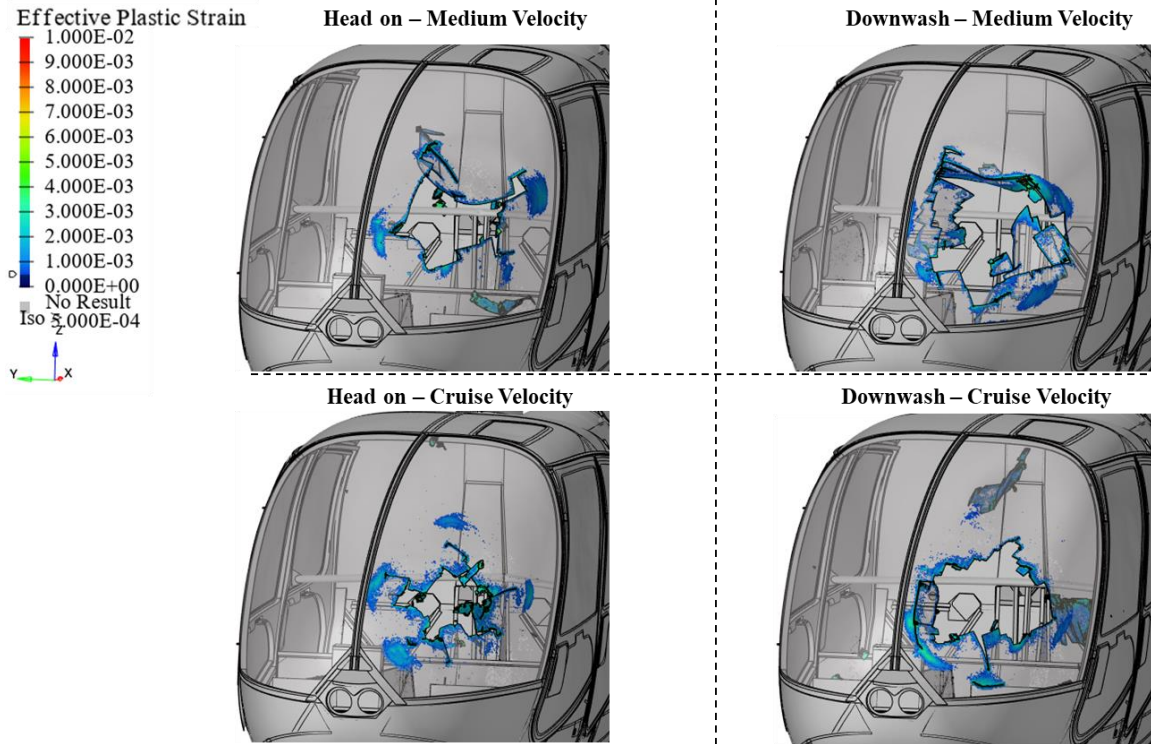
Figure 323. RQ2.7-W1 and RQ2.7-W1-D damage comparison.
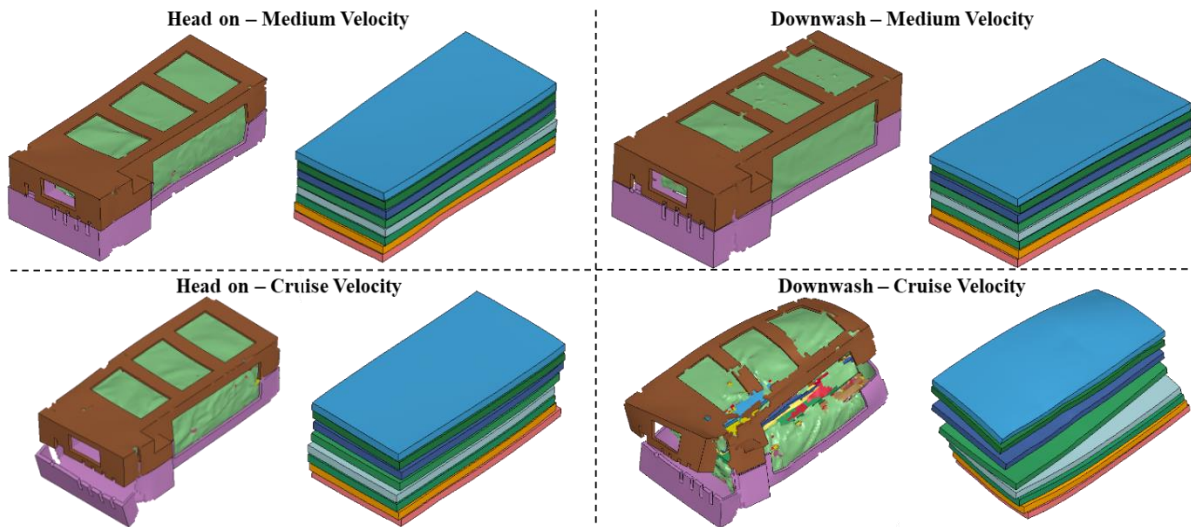
Figure 324. RQ2.7-W1 and RQ2.7-W1-D battery damage comparison.

Table 49. Windshield mid-air collision simulation assessment – damage severity level, fire risk, and comparison.

Mid air collision: 2.7 lbs. quadcopter and windshield	Case	Direct impact (head-on)		Deflected impact (downwash)	
		Severity	Fire Risk	Severity	Fire Risk
	RQ2.7-W1M	Level 4	No	Level 4	No
	RQ2.7-W1C	Level 4	Yes	Level 4	Yes

5.7.3 Blade

This section provides the findings stemming from collisions involving a 2.7 lbs. quadcopter and the rotorcraft's main rotor blade, including downwash effects at medium and cruise velocities, as showcased in Figure 325 and Figure 326, respectively. These results unravel the temporal progression of the impact occurrences, spotlighting time intervals at 0.0005s, 0.005s, and 0.0125s. The upper trio of windows highlights the kinematic aspects of the impacts, while the lower trio shows the resultant effective plastic strain on the rotorcraft structure. Additionally, Figure 327 provides the energy balance plots for both impact velocities.
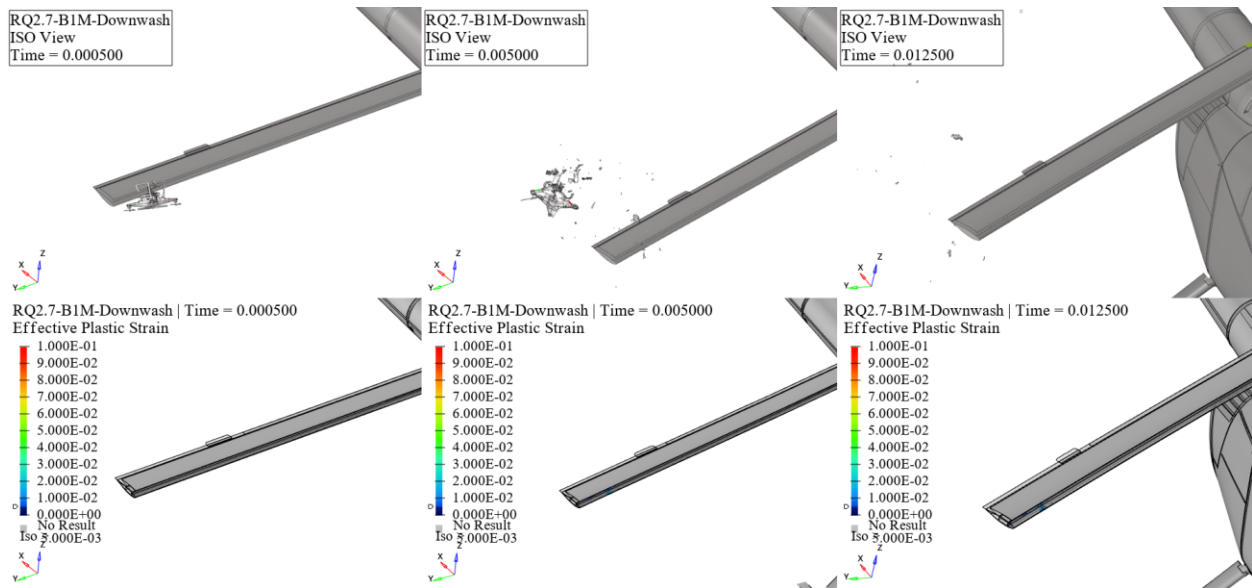
Figure 325. RQ2.7-B1M-D kinematics (top) and effective plastic strain (bottom) frames.
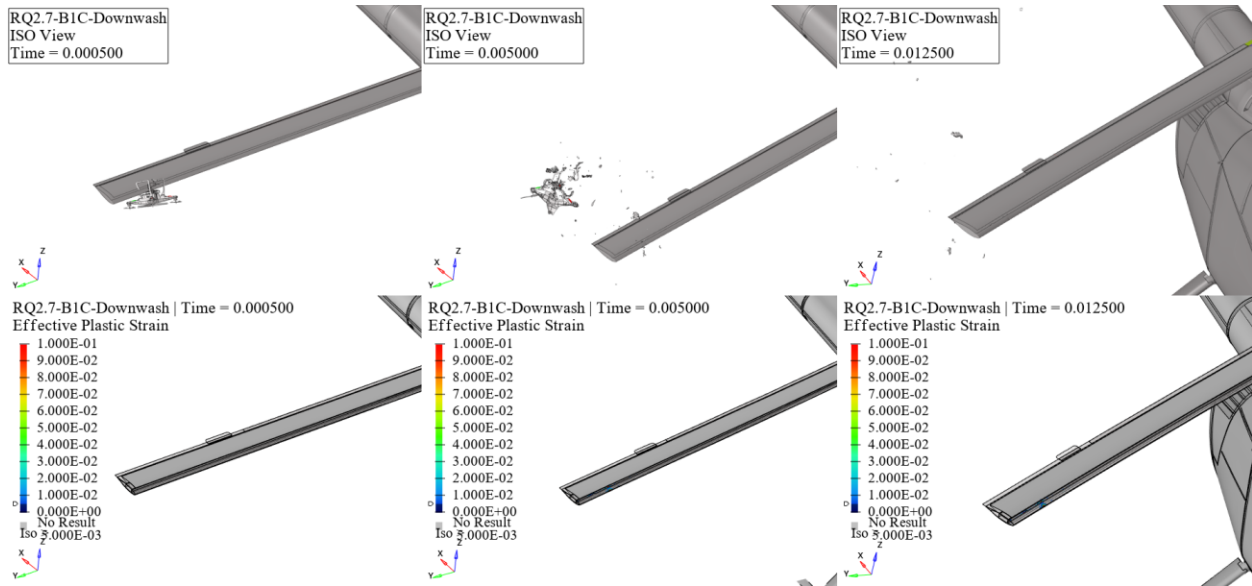
Figure 326. RQ2.7-B1C-D kinematics (top) and effective plastic strain (bottom) frames.
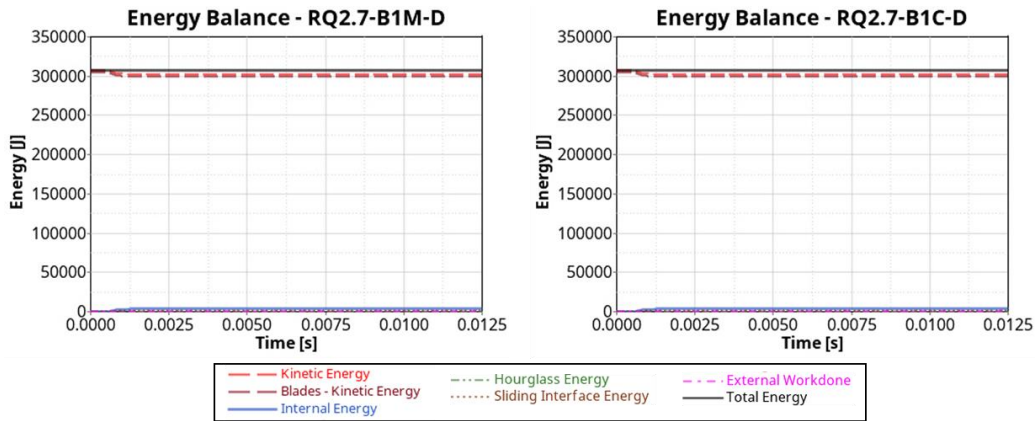
Figure 327. Main rotor blade and 2.7 lbs. quadcopter downwash impact energy balance.

At both medium and cruise impact velocities, the collision between the 2.7 lb quadcopter and the main rotor blade resulted in minor dents and scuffs on the leading edge of the rotor blade, with no cracks or significant damage observed, indicating a Level 2 impact severity. The severity remained consistent for both head-on and deflected impacts. The only difference was that the blade area affected by the impact was smaller for the deflected impact than the head-on impact, as shown in Figure 328, due to the UAS motors being away from the line of direct impact. Table 50 summarizes the findings.
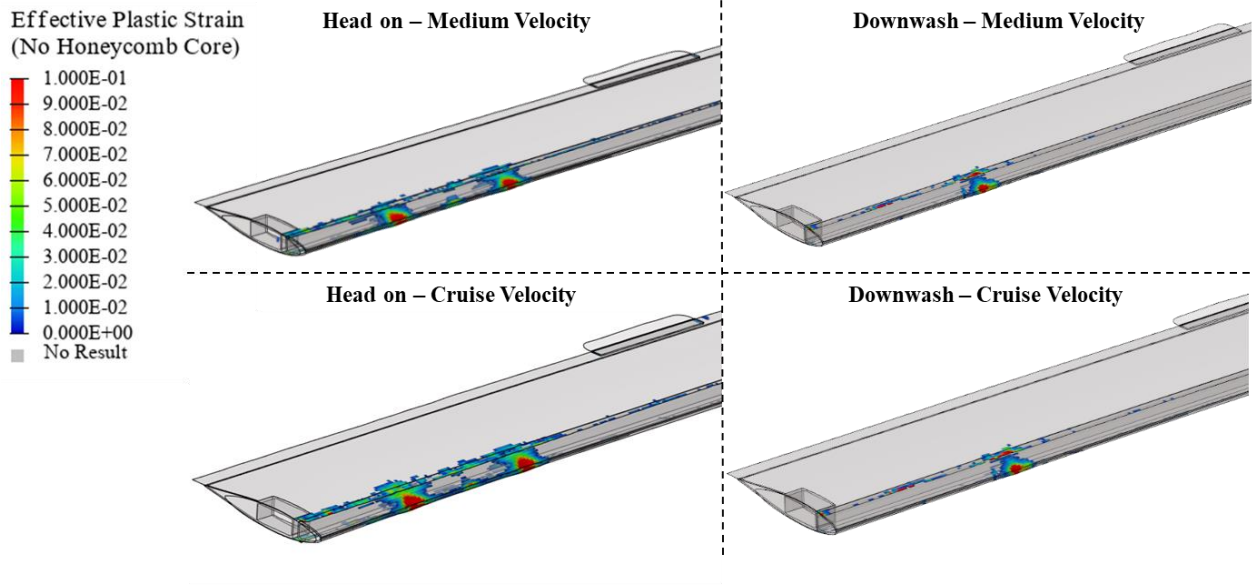
Figure 328. RQ2.7-B1 and RQ2.7-B1-D damage comparison.

Table 50. Blade mid-air collision simulation assessment – damage severity level, fire risk, and comparison.

	Case	Direct impact (head-on)		Deflected impact (downwash)	
		Severity	Fire Risk	Severity	Fire Risk
Mid air collision: 2.7 lbs. quadcopter and blade	RQ2.7-B1M	Level 2	No	Level 2	No
	RQ2.7-B1C	Level 2	No	Level 2	No

5.8   Comparison to Actual Mid-Air Collision Events

5.8.1   *Windshield*

On January 23rd, 2021, a Bell UH-57B had a mid-air collision with a DJI Mavic Air 2. The incident occurred in Santo Domingo, Chile. The sUAS pierced the helicopter's windshield and injured the pilot [43]. The Bell UH-57B is a military version of the Bell 206B. The windshield of this aircraft is of similar construction to the R44 presented in this report. The DJI Mavic Air 2 is a quadcopter sUAS weighing approximately 1.26 lbs. The exact flight conditions at the time of the incident are unknown. The damage was compared with the RQ2.7-W1C case, as shown in Figure 329.

Bell UH-57B. Different helicopter but similar
windshield construction (plexiglass).
sUAS was a DJI Mavic Air 2, 0.57kg (1.26lbs)
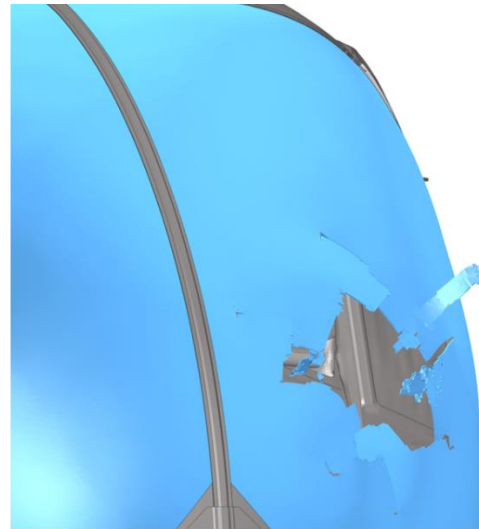
RQ2.7-W1C
sUAS penetrates in this impact condition

Figure 329. Comparison of windshield impact – Bell UH-57B vs. RQ2.7-W1C. Image adapted from [43].

In a different incident, a Robinson R22 helicopter was struck by an unknown object on its windscreen. The helicopter was flying at about 70 knots [44]. The incident is listed as a bird strike on the FAA's incident and notification system. However, the pilot suggested there was no evidence of a bird strike [44]. This incident was compared to the RF4-W1M case, shown in Figure 330. This is the medium velocity case (94 knots). In the analysis, the sUAS penetrated the cabin, while in the actual event, there was no trace of a sUAS or bird.

R22 possible sUAS impact.
No sUAS found inside of cabin
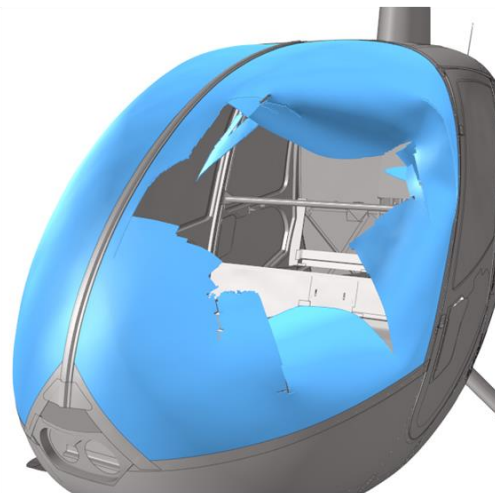
RF4-W1M
sUAS penetrates in this impact condition

Figure 330. Comparison of windshield impact – R22 possible sUAS impact vs. RF4-W1M. Image adapted from [44].

219

5.8.2 Blade

On December 30th, 2023, a Robinson R44 helicopter struck a DJI Mavic 2 Pro in Daytona Beach [45]. The DJI Mavic 2 Pro weighs about 2 lbs. [46]. The helicopter blade sustained damage to its leading edge, causing damage of $60,000 [45]. This event was compared to RQ2.7-W1M-D, which is a main blade impact with a 2.7 lbs. quadcopter at medium speed (94 knots) with a downwash effect. The analysis shows the blade sustained a dent to the blade's leading edge without skin debonding. This damage compares well to the damage observed in the actual event, as shown in Figure 331.
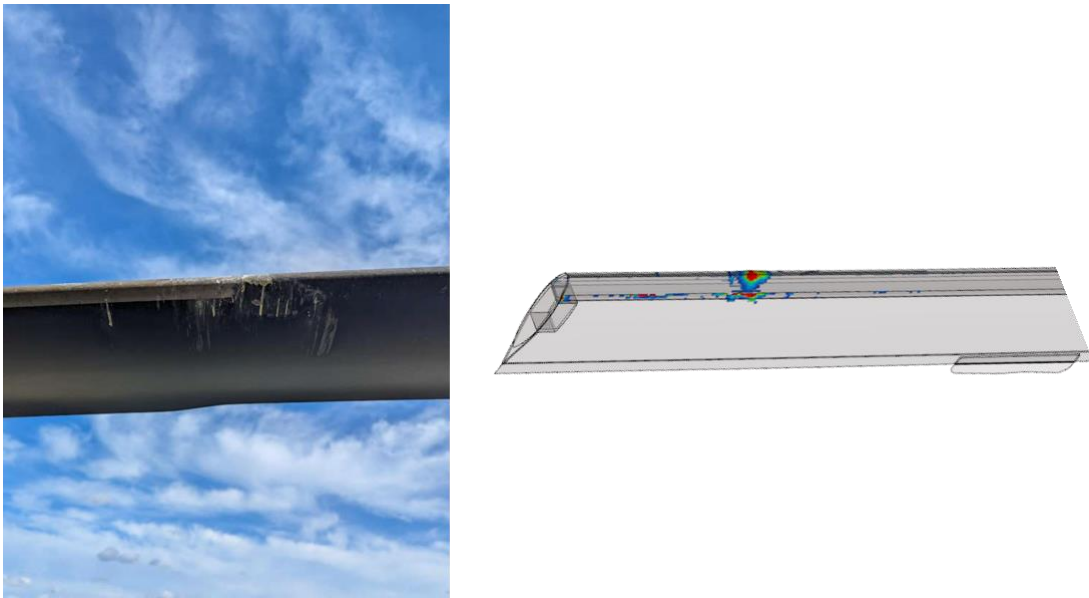
Figure 331. Comparison of main rotor blade impact – R44 at Daytona Beach vs. RQ2.7-W1M-D. Image adapted from [45].

6 CONCLUSIONS

The effect of an airborne collision between an sUAS and a crewed aircraft is a concern to the public and government officials at all levels. The ASSURE group has performed and has ongoing research to assess the damage of sUAS airborne collisions to aircraft using FE advanced virtual models. These are some of the completed research programs concerning this subject:

- Airborne Collision Phase I (Task A3) [2]: sUAS (mass range: 2.7 to 8 lbs. architectures: Quadcopter and Fixed Wing) impacts on Narrow Body Commercial Aircraft and Business Jets operating under FAR 25 requirements [13]
- Airborne Collision Phase I research extension (Task A30) [26]: Large sUAS (mass range: 10 to 55 lbs. architectures: Quadcopter and Fixed Wing) impacts on Narrow Body Commercial Aircraft and Business Jets operating under FAR 25 requirements [13]
- Airborne Collision Phase II research extension [6][47]: sUAS (mass range: 2.7 to 55 lbs. architectures: Quadcopter and Fixed Wing) impacts on General Aviation aircraft operating under FAR 23 requirements [7]
- Airborne Collision Severity Evaluation Volume VI (Task A16) [3]: sUAS (2.7 lbs. quadcopter and 4 lbs. fixed wing) impacts on Part 29 rotorcraft

This report focuses on the collision between sUAS (2.7 lbs to 55 lbs) and a Part 27 rotorcraft. NIAR has developed and validated advanced virtual models of representative rotorcraft structures that could be subjected to mid-air collision and are critical for flight safety. The structures under consideration are the horizontal stabilizer, vertical stabilizer, windshield, nose, mast, and main rotor blade. A Robinson R44 was reverse-engineered to include all structural elements and develop a numerical model representative of a Part 27 rotorcraft utilizing the building block approach. Creating advanced virtual models facilitates analyzing and evaluating several impact conditions without conducting full-scale physical testing. The UAS models selected for this work were developed during Task A3 [2]: 2.7 lbs. quadcopter [22] and 4.0 lbs. fixed-wing [24]. Additional component-level test experiments were performed in Task A16 [3] to extend the validation of the sUAS FEM for mid-air airborne collisions up to 500 knots. The previous work accelerated the timeframe needed to complete a large analysis matrix. An analysis matrix of 135 impact cases was defined to evaluate the damage severity of airborne collisions between sUAS and a Part 27 rotorcraft.

The severity evaluation criterion follows the guidelines of the ASSURE Airborne Collision Phase I program [2]. The lowest damage category, Level 1, generally corresponds to minimal localized damage. The next category, Level 2, represents significant visible damage to the external surface of the aircraft, with some internal component damage but with no appreciable skin rupture. The third category, Level 3, describes impact events where the aircraft's outer surface is compromised in a way that could allow the ingress of foreign objects into the airframe, with some damage to the substructure. Finally, Level 4 indicates extensive damage to internal components and possibly compromising part of the primary structure. A separate severity category was devised for the main rotor impacts based on industry and pilot feedback. The severity categories are listed in Table 51. The risk of fire associated with damaged LiPo-type batteries was addressed for each simulation based on the trends observed during component-level ballistic testing and the particular kinematics of a given impact scenario. Note that the label "Fire Risk" indicates a potential outcome rather

than an impending event due to the qualitative nature of the assessment. Further studies and physical testing into this phenomenon would be required to determine any additional severity.

It should be noted that the orientation of the sUAS with respect to the targets' impact area was selected using a conservative approach, aligning the center of gravity of the sUAS normal to the aircraft impact area or the hard contact points (e.g., Metallic motors) depending on the impact condition. The head-on impacts are considered worst-case conditions for the mid-air collisions. The models generated in this program should be used in the future to assess the effect of the sUAS impact area offset and orientation on the severity classification of the impact event. Previous efforts have demonstrated that likely mid-air collisions have an overall lower severity than when considering only head-on collisions [48].

Table 51. Damage severity evaluation criteria.

Severity	Airframe Damage Description	Blade Damage Description
Level 1	The airframe is undamaged. Small deformations.	Blade undamaged. Scratches or small dents on a rotor blade. No crack initiation.
Level 2	Extensive permanent deformation on external surfaces. Some deformation in internal structure. No Skin Failure.	Dents on a rotor blade leading edge. Minor crack initiation. No debonding.
Level 3	Skin fracture. Penetration of at least one component into the airframe.	Any debonding. Skin buckling. Major crack initiation.
Level 4	Penetration of UAS into airframe and failure of the primary structure.	Any material loss leading to a blade imbalance. Heavy blade twist and deflection leading to an imbalance on a single blade.

The results of the 135 impact scenarios, corresponding to the quadcopter and fixed-wing sUAS architectures from 2.7 lbs. to 55 lbs., are summarized in Table 52. A summary of all cases, including fire risk, is documented in APPENDIX B. In addition, Figure 332 through Figure 337 illustrate the highest severity level observed on each target's impact location for the eight sUAS analyzed. The following parameters affect the severity classification of the impact events:

1. There is a clear trend with the increase of sUAS mass and impact velocity on the severity outcome. Less severity for smaller mass sUAS and lower impact velocities.
2. Nonetheless, it should be noted that the architecture and construction of the sUAS also influence the severity levels significantly:
   a. Direct impact with stiff components (i.e., the motors) increases stress concentration and larger damage to the impacted structure.
3. From a severity level point of view, the most critical impact location is the windshield. All sUAS impacts result in severity level 4 when the speed is greater than 39 knots (hover). Some sUAS (F12, Q55, and F55) produced a level 4 severity at hover speed. This could be related to the fact that conventional Part 27 rotorcraft windshields are not bird-strike resistant.
4. The main source of severity for main rotor blade impacts is the weight and size of sUAS. This is due to the blade rotational speed being the largest component of the relative impact velocity.

a. Larger sUAS impacts do not result in direct damage to the blade, as opposed to small-size UAS with their stiff components (i.e., motors). However, they create excessive blade bending and twisting, which could lead to unrecoverable loss of control.

5. Any impact on the tail rotor will likely result in the tail rotor skin debonding, leading to loss of control. This occurred even on secondary impacts with the foam wings of the 4 lbs. fixed-wing sUAS.
   a. This correlates with the tail rotor test observations in Task A16 [3] for larger Part 29 rotorcraft.

6. Impact with the nose at hover speed (39 knots) is the least severe. All sUAS were deflected at hover speed, which resulted in minimal damage to the rotorcraft skin.
   a. However, impacts at higher speeds (149 knots) with the larger sUAS (25 and 55 lbs.) result in loss of structural integrity in the forward fuselage.

7. Impacts with the mast do not result in sUAS penetration or severe structural damage. However, A level 4 severity was assigned to cases where the swash plate links are pinched or compressed, which could interfere with pilot control of the aircraft.
   a. Impacts with the rotor blade links or swash plate were not considered in this research. Nevertheless, the rotor downwash effect is expected to change the trajectory of the smaller sUAS (less than 4 lbs.) [42] shielding this area. In comparison, the impacts with larger sUAS (greater than 4 lbs.) are expected to result in similar severity levels to the mast analysis presented in the present report. However, additional analyses are necessary to determine the likelihood of impacts with the blade hub links or swash plate.

Impact cases on the windshield and the main rotor blade were compared to actual sUAS mid-air collision, as discussed in Section 5.8. The observed damage in the analysis correlates well with the actual event observations, as highlighted in Figure 329 through Figure 331. These events are used as additional validation data points and add confidence to the analysis results.

Overall, the small size and type of construction utilized in the Part 27 rotorcraft results in severe damage when there is a mid-air collision with larger sUAS (25 and 55 lbs.). Conversely, impacts with sUAS less than 10 lbs. are less severe, even at higher speeds (149 knots). The findings from this research may be used to conservatively define airborne hazard severity thresholds for collisions between sUAS of several sizes and weights and a Part 27 [4] rotorcraft.

Table 52. Simulation Severity Matrix – Summary.

UAS\Impact Area	Horizontal Stabilizer			Vertical Stabilizer			Mast			Nose			Windshield			Blade		
	Hover	Medium	Cruise	Hover	Medium	Cruise	Hover	Medium	Cruise	Hover	Medium	Cruise	Hover	Medium	Cruise	Hover	Medium	Cruise
Q2.7	1	2	3	1	2	3	1	2	2	2	3	3	1	4	4	2	2	2
F4	2	2	3	4	4	4	1	2	3	2	3	3	1	4	4	3	3	3
Q10	2	3	4	2	3	4	2	2	3	2	3	3	4	4	4	3	3	3
F12	-	-	-	4	4	4	2	2	3	2	3	3	2	4	4	4	4	4
Q25	2	4	4	2	3	4	2	3	4	2	3	4	2	4	4	4	4	4
F25	-	-	-	4	4	4	2	3	4	2	3	4	3	4	4	4	4	4
Q55	3	4	4	4	4	4	3	4	4	2	4	4	4	4	4	4	4	4
F55	-	-	-	4	4	4	4	4	4	2	4	4	4	4	4	4	4	4

Figure 332. Summary of impact severity levels – Rotorcraft targets and 2.7 lbs. quadcopter sUAS.

Figure 333. Summary of impact severity levels – Rotorcraft targets and 4 lbs. fixed-wing sUAS.

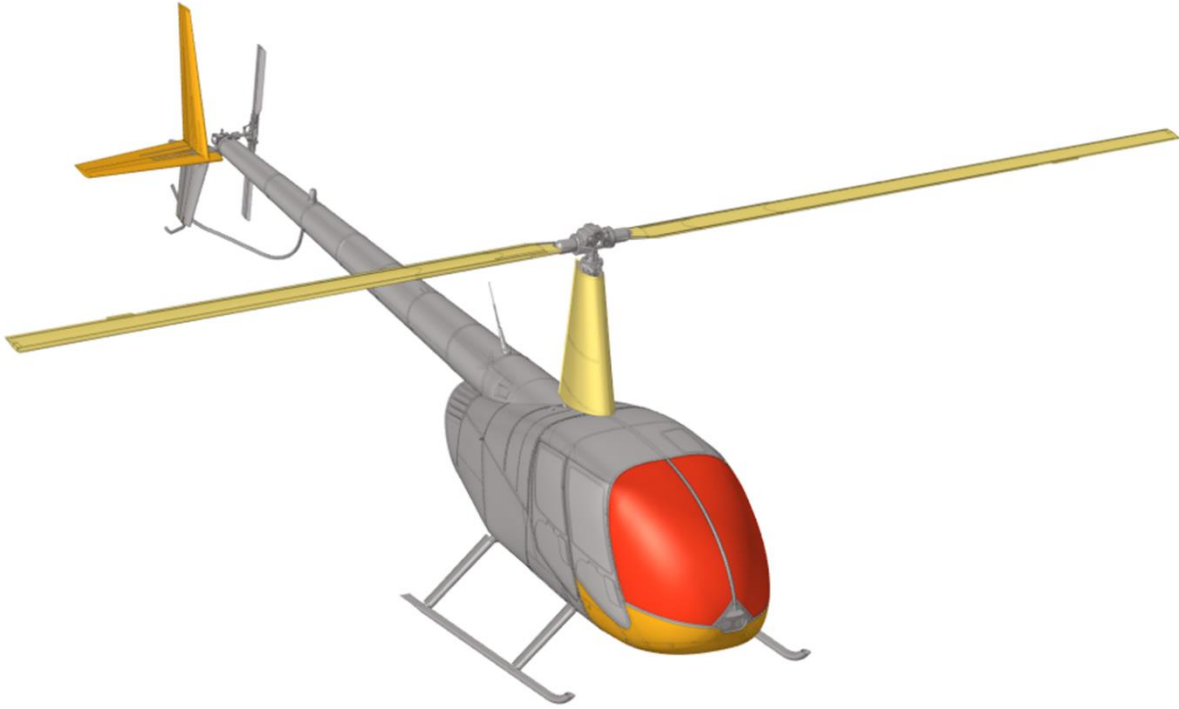Figure 334. Summary of impact severity levels – Rotorcraft targets and 10 lbs. quadcopter sUAS.
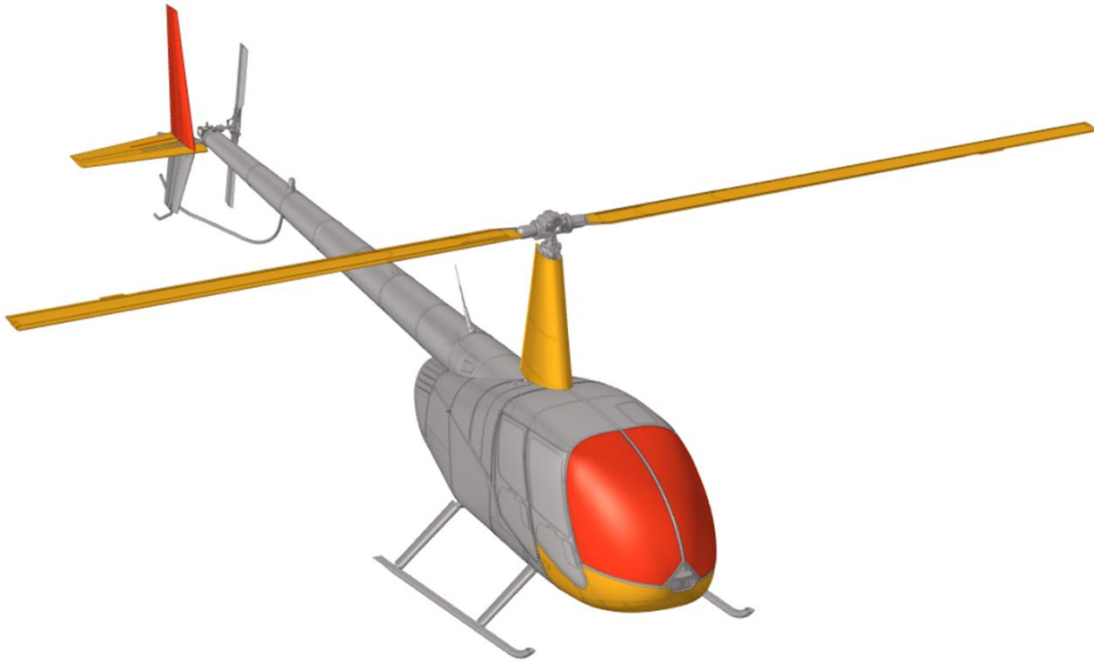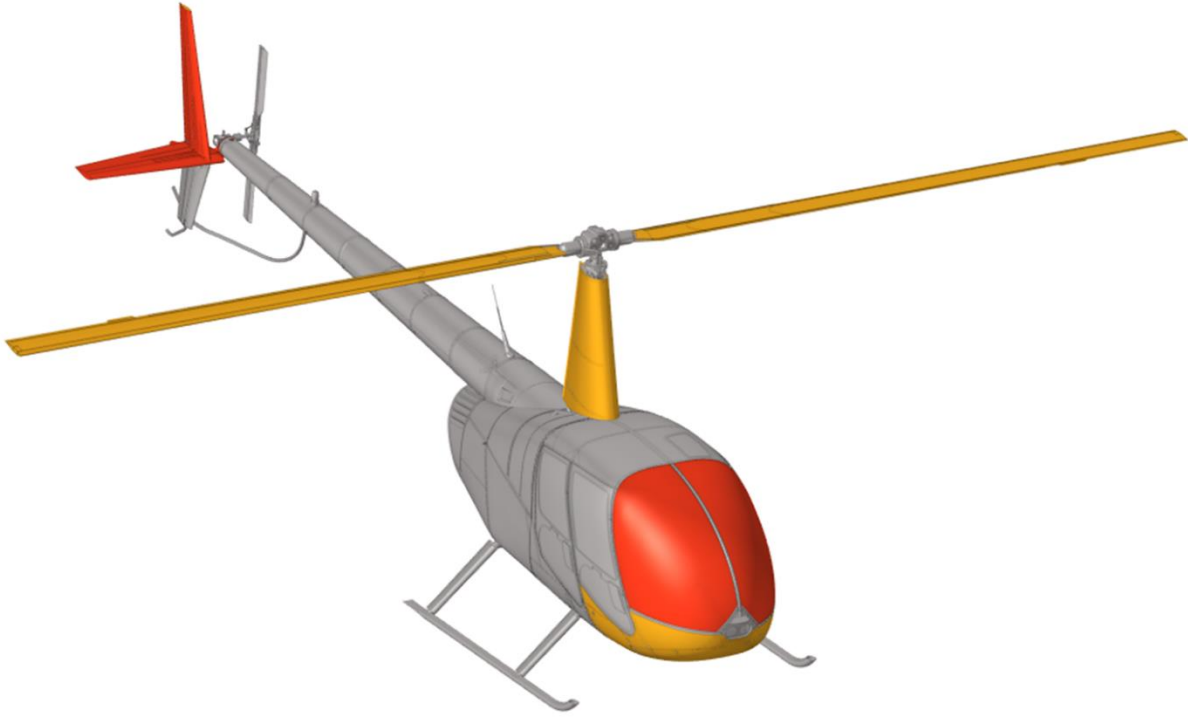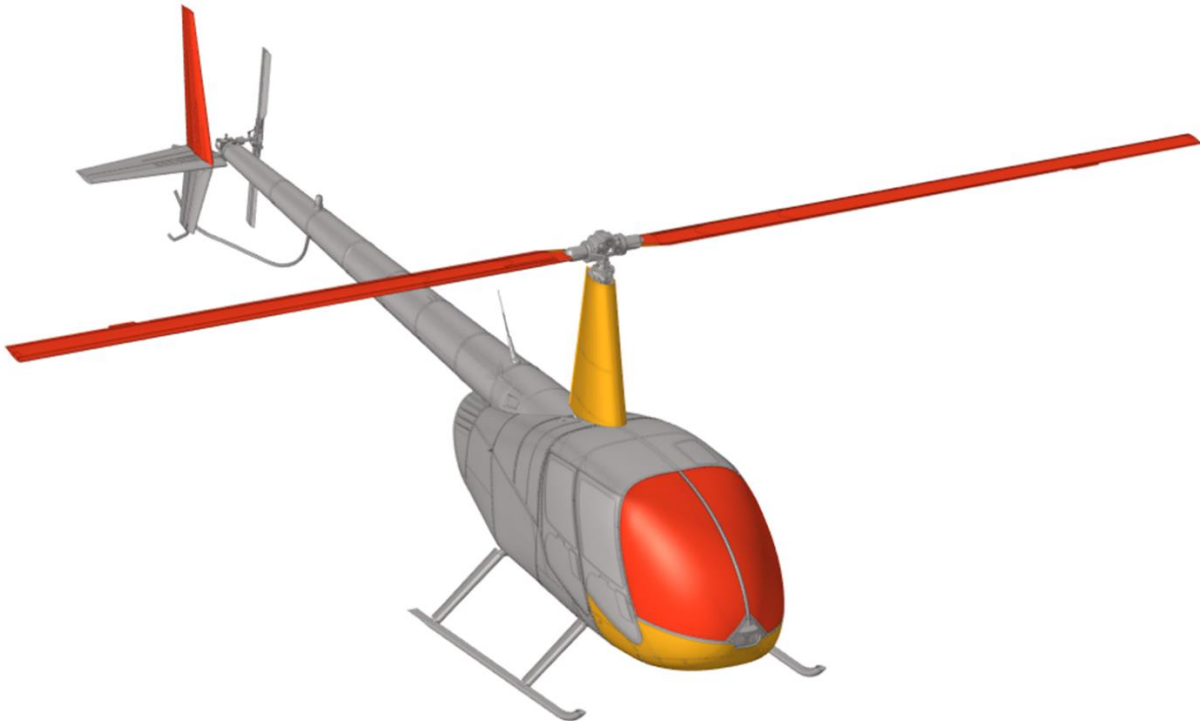

Figure 335. Summary of impact severity levels – Rotorcraft targets and 12 lbs. fixed-wing sUAS.
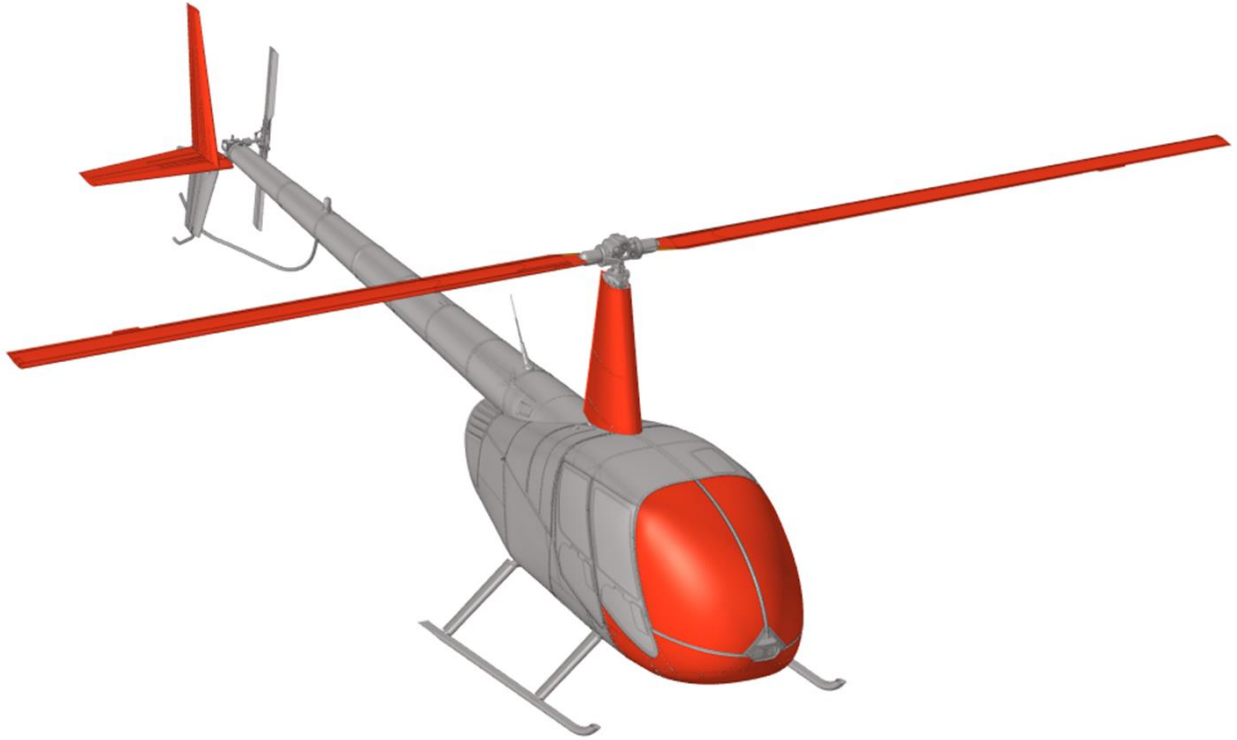
Figure 336. Summary of impact severity levels – Rotorcraft targets and 25 lbs./55 lbs. quadcopter sUAS.

Figure 337. Summary of impact severity levels – Rotorcraft targets and 25 lbs./55 lbs. fixed-wing sUAS.

6.1 Future Work

Based on the findings from this work, the researchers believe that the following topics should be addressed in future airborne collision studies:

1) Complete an extensive sensitivity analysis to impact location and sUAS orientation. All the work conducted thus far focuses on worst-case conditions where the sUAS impacts the highest level of energy and with the stiffer components in the structure under consideration. Previous work indicates that this could result in significantly higher severity levels than expected in real-impact scenarios, where this worst-impact condition won't happen that often.

2) Link all the severity evaluation work to the estimation of the probability of a mid-air collision between sUAS and manned aircraft. Once the probability of an airborne collision is determined, the severity level results can be combined with the probabilistic collision models to define an appropriate Equivalent Level of Safety criteria.

3) Study the influence of the main rotor downwash over the sUAS impact trajectory. This analysis should include a likelihood analysis of impact locations when considering the effect of downwash.

4) "Fire Risk" indicates a potential outcome rather than an impending event due to the qualitative nature of the assessment. Further studies and physical testing into this phenomenon would be required to determine any additional severity criteria.

5) Study the influence of aerodynamic loads on the severity of the blade collision analysis.

6) Perform additional analysis with refined blade hub links, rods, joints, and swash plate to include the blade flapping effect in the FEM.
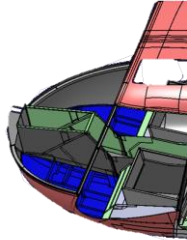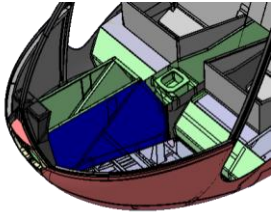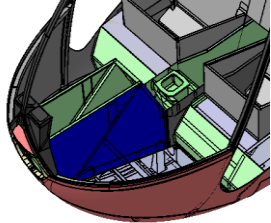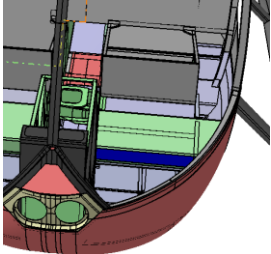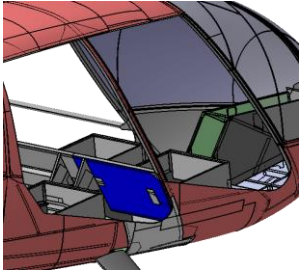
7 REFERENCES

[1] Federal Aviation Administration, "FAA Aerospace Forecast Fiscal Years 2023-2043," 2023. [Online]. Available: https://www.faa.gov/dataresearch/aviation/aerospaceforecasts/faa-aerospace-forecast-fy-2023-2043

[2] G. Olivares *et al.*, "UAS Airborne Collision Severity Evaluation. Executive Summary – Structural Evaluation," Assure Report 2017. [Online]. Available: https://assureuas.com/wp-content/uploads/2021/06/A3-Volume-1.pdf

[3] G. Olivares *et al.*, "Volume VI – UAS Airborne Collision Severity Evaluation – 14 CFR Part 29 Rotorcraft," Assure Report 2022. [Online]. Available: https://assureuas.com/wp-content/uploads/2021/06/Volume-VI-Airborne-Collision-Severity-Evaluation-14-CFR-Part-29-Rotorcraft.pdf

[4] *Airworthiness standards: normal category rotorcraft*, U.S. Code of Federal Regulations, Title 14, Part 27, U.S. Government Publishing Office, Washington, DC, 2016.

[5] AUVSI, "The Economic Impact of Unmanned Aircraft Systems Integration in the United States," 2013. [Online]. Available: https://www.auvsi.org/our-impact/economic-report

[6] G. Olivares, L. Gomez, and R. Marco, "Volume VII – UAS Airborne Collision Severity Evaluation – 14 CFR Part 23 General Aviation," Assure Report 2022. [Online]. Available: https://assureuas.com/wp-content/uploads/2021/06/Volume-VII-Airborne-Collision-Severity-Evaluation-14-CFR-Part-23-General-Aviation.pdf

[7] *Airworthiness standards: normal category airplanes*, U.S. Code of Federal Regulations, Title 14, Part 23, U.S. Government Publishing Office, Washington, DC, 2016.

[8] *Airworthiness standards: transport category rotorcraft*, U.S. Code of Federal Regulations, Title 14, Part 29, U.S. Government Publishing Office, Washington, DC, 2016.

[9] Federal Aviation Administration, "Rotorcraft Bird Strike Working Group Recommendations to the Aviation Rulemaking Advisory Committee (ARAC)," ARAC Rotorcraft Bird Strike Working Group, Rev B 2019.

[10] Public Law 112-95, Section 331(8).

[11] *Small Unmanned Aircraft Systems*, U.S. Code of Federal Regulations, Title 14, Part 107, U.S. Government Publishing Office, Washington, DC, 2016.

[12] Micro Unmanned Aircraft Systems Aviation Rulemaking Committee, "ARC Recommendations Final Report," 2016.

[13] *Airworthiness standards: transport category airplanes*, U.S. Code of Federal Regulations, Title 14, Part 25, U.S. Government Publishing Office, Washington, DC, 2016.

[14] R. C. C. Range Safety Group, "Range Safety Criteria for Unmanned Air Vehicles," Document 323-99 2001.

[15] C. W. Lum and B. Waggoner, "A Risk Based Paradigm and Model for Unmanned Aerial Systems in the National Airspace," in *Infotech@Aerospace Conferences*, St. Louis, MO, 2011: AIAA, pp. 2011-1424.

[16] K. Dalamagkidis, K. Valavanis, and L. A. Piegl, *On Integrating Unmanned Aircraft Systems into the National Airspace System*, 2nd ed. Springer Netherlands,, 2012.

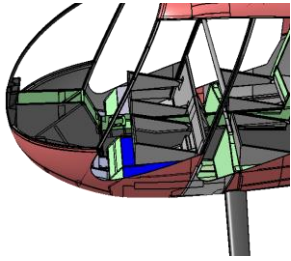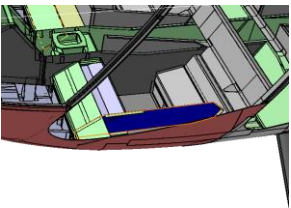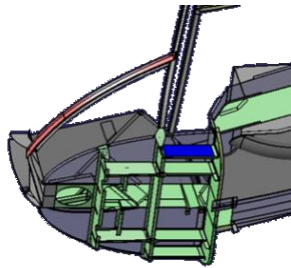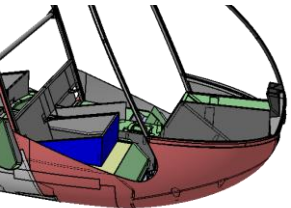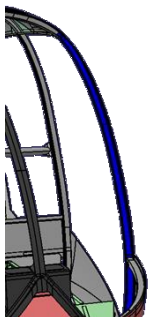[17] T. McGeer, "Aerosonde Hazard Estimation," The Insitu Group 1994.

[18]   Civil Aviation Safety Authority, "Potential Damage Assessment of a Mid-Air Collision with a Small UAV," Technical Report 2013.

[19]   C. S. R. Fraser and D. Donnithorne-Tait, "An Approach to the Classification of Unmanned Aircraft," in *26th International Conference on Unmanned Air Vehicle Systems*, Bristol, UK, 2011, pp. 157-211.

[20]   H. Jimenez, D. Mavris, D. Hoffman, J. Mines, and S. O'Sullivan, "A Survey of Evaluation Methods for Unmanned Aircraft Risk and Safety to Third Parties," Report, Federal Aviation Administration, 2015.

[21]   M. M. Marshall, E. E. Anderson, and D. E. Tighe, "A Literature Review in Support of TCRG 14-05: UAS Systems Safety Criteria," Draft Report, FAA Award 14-G-007, 2015.

[22]   G. Olivares, L. Gomez, J. Espinosa de los Monteros, R. Baldridge, C. Zinzuwadia, and T. Aldag, "UAS Airborne Collision Severity Evaluation – Volume II – Quadcopter," ASSURE Report 2017. [Online]. Available: https://assureuas.com/wp-content/uploads/2021/06/A3-Volume-2.pdf

[23]   G. Olivares, L. Gomez, J. Espinosa de los Monteros, R. Baldridge, and R. Marco, "Annex B NIAR Final Report Task A14: UAS Ground Collision Severity Evaluation 2017-2018," Assure Report 2019. [Online]. Available: https://assureuas.com/wp-content/uploads/2021/06/A14-Annex-B.pdf

[24]   G. Olivares *et al.*, "UAS Airborne Collision Severity Evaluation – Volume III – Fixed Wing," Assure Report 2017. [Online]. Available: https://assureuas.com/wp-content/uploads/2021/06/A3-Volume-3.pdf

[25]   G. Olivares, L. Gomez, J. Espinosa de los Monteros, R. Baldridge, and C. Zinzuwadia, "NIAR Internal Report UAS-0001 Search and Rescue Drone," 2019.

[26]   G. Olivares, L. Gomez, R. J. Baldridge, R. Marco, and H. Ly, "Large sUAS Airborne Collision Severity Evaluation with 14 CFR 25 Aircraft -ATO Office of Safety," Federal Aviation Administration, Report DOT/FAA/AR-XX/XX 2020.

[27]   MMPDS-09, *Metallic Material Properties Development and Standardization (MMPDS)*, 7 ed. Battelle Memorial Institute, 2014.

[28]   A. Dadouche *et al.*, "Drone Impact Assessment on Aircraft Structure: Flat Plate Testing and Analysis," National Research Council Canada, Report CR-GTL-2020-0053 2020.

[29]   G. Olivares, L. Gomez, H. Ly, and R. Marco, "Task A17: UAS Engine Ingestion Severity Evaluation," ASSURE Report 2022. [Online]. Available: https://www.assureuas.org/wp-content/uploads/2021/06/Task_A17_Cover_Report_Final.pdf

[30]   K. Christensen. "Danger spins from the sky: The Robinson R44, the world's best-selling civilian helicopter, has a long history of deadly crashes." www.latimes.com. https://www.latimes.com/projects/la-me-robinson-helicopters/ (accessed Apr. 10, 2024).

[31]   Robinson Helicopter Company. "Robinson Helicopter Company Timeline - Robinson Helicopter Company." https://shop.robinsonheli.com/robinson-helicopter-company-timeline (accessed Apr. 10, 2024).

[32]   Robinson Helicopter Company, "R44 Illustrated Parts Catalog RTR 460 Volume II," 2024.

[33]   Transport Safety Board of Canada. "Air transportation safety investigation report A19Q0109 - Transportation Safety Board of Canada." https://www.bst-tsb.gc.ca/eng/rapports-reports/aviation/2019/a19q0109/a19q0109.html (accessed Apr. 10.
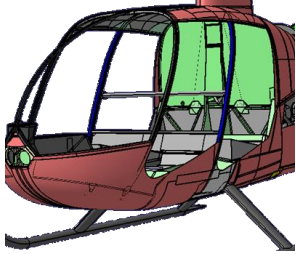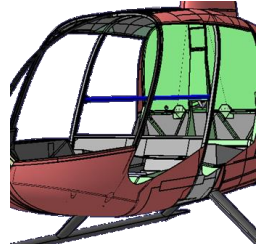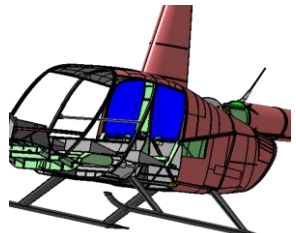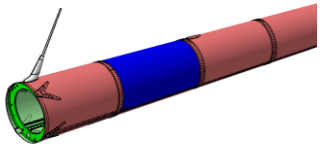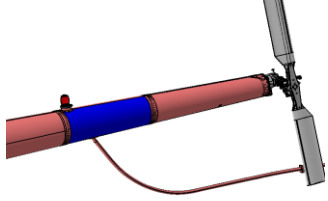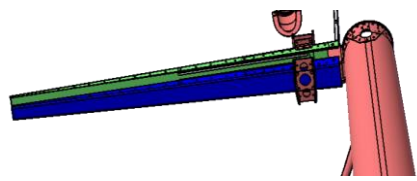
[34]   *Standard Test Methods for Tension Testing of Metallic Materials*, ASTM E8/E8M – 16a, ASTM International, 100 Barr Harbor Drive, POB Box C700, West Conshohocken, PA 19428-2959, United States, 2017.

[35]   *Standard Test Method for Tensile Properties of Polymer Matrix Composite Materials*, ASTM D3039/3039M – 17, ASTM International, 100 Barr Harbor Drive, POB Box C700, West Conshohocken, PA 19428-2959, United States, 2020.

[36]   *Standard Test Method for Compressive Properties of Polymer Matrix Composite Materials Using a Combined Loading Compression (CLC) Test Fixture*, ASTM D6641/D6641M– 16, ASTM International, 100 Barr Harbor Drive, POB Box C700, West Conshohocken, PA 19428-2959, United States, 2016.

[37]   *Standard Test Method for Shear Properties of Composites Materials by V-Notched Rail Shear Method*, ASTM D7078/D7078M– 12, ASTM International, 100 Barr Harbor Drive, POB Box C700, West Conshohocken, PA 19428-2959, United States, 2019.

[38]   *Standard Test Method for Tensile Properties of Plastics*, ASTM D638-14, ASTM International, 100 Barr Harbor Drive, POB Box C700, West Conshohocken, PA 19428-2959, United States, 2022.

[39]   *Standard Test Method for Compressive Properties of Rigid Plastics*, ASTM D695-23, ASTM International, 100 Barr Harbor Drive, POB Box C700, West Conshohocken, PA 19428-2959, United States, 2023.

[40]   Livermore Software Technology Corporation, *LS-DYNA Theory Manual* (LS-DYNA R8.0 User Manual). 2015.

[41]   Robinson Helicopter Company, *R44 II Pilot's Operating Handbook and Rotorcraft Flight Manual RTR 462*. 2021.

[42]   N. Sathyanarayana, H. Shah, J. Calderon Del Rey, G. Olivares, and L. Gomez, "Rotorcraft Airborne Collision Severity Evaluation – Assessment of sUAS deflections due to aerodynamic interaction with a 14 CFR Part 27 Rotorcraft," Assure report 2023.

[43]   S. Georgilidakis. "INCIDENT: Drone – Helicopter Collision, Occupant Injury." https://mentourpilot.com/incident-drone-helicopter-collision-occupant-injury/ (accessed May 20th, 2024).

[44]   Vertical Mag. "Possible drone collides with helicopter in Los Angeles." https://verticalmag.com/news/possibledronecollideswithhelicopterinlosangeles/ (accessed May 20th 2024).

[45]   sUAS News. "Mavic 2 hits R44 helicopter." https://www.suasnews.com/2023/12/mavic-2-hits-r44/ (accessed June 20th, 2024).

[46]   DJI. "MAVIC 2 Specs." https://www.dji.com/mavic-2/info (accessed June 20th, 2024).

[47]   G. Olivares, L. Gomez, C. Zinzuwadia, S. S. Kadiyala, and R. Marco, "Analysis of Collision Severity Between Small Unmanned Aircraft Systems and Fixed Wing General Aviation Aircraft," Federal Aviation Administration, Report DOT/FAA/AR-XX/XX 2021.

[48]   A. De Abreu *et al.*, "sUAS Mid Air Collision Likelihood - Final Report," Assure Report 2023. [Online]. Available: https://www.assureuas.org/wp-content/uploads/2021/06/A47_Final-Report.pdf
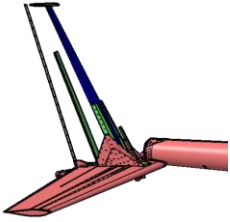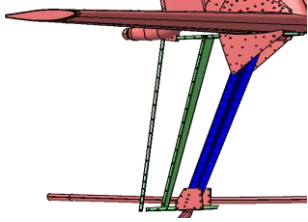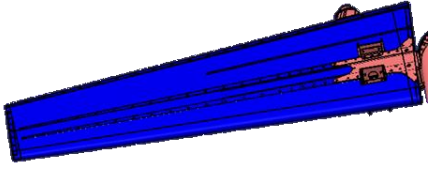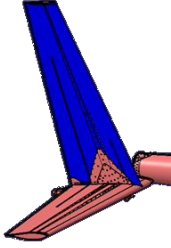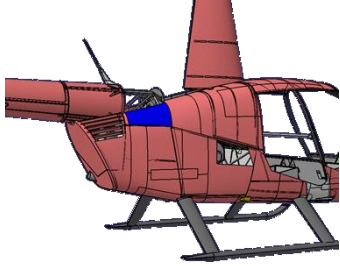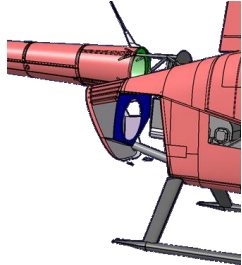
APPENDIX A. <u>METALLIC MATERIALS REVERSE ENGINEERING DOCUMENTATION</u>

Table 53. Reference location of metallic extractions for destructive testing.

Test ID	Part Description	Reference Part Image
RC-MRE-P05-T-0X	Front Floor Panel 1	
RC-MRE-P07-T-0X	Control Panel Support (Longitudinal Direction)	
RC-MRE-P08-T-0X	Control Panel Support (Normal Direction)	
RC-MRE-P09-T-0X	Front Floor Panel 3	
RC-MRE-P10-T-0X	Panel Between Seats	

RC-MRE-P11-T-0X	Front Floor Panel 4	
RC-MRE-P13-T-0X	Pilot Seat Lateral Panel	
RC-MRE-P14-T-0X	Floor Panel Stringer	
RC-MRE-P15-T-0X	Pilot Seat Base	
RC-MRE-P16-T-0X	Windshield Frame	

RC-MRE-P17-T-0X	Lateral Frame of the Fuselage	
RC-MRE-P18-NDT-0X	Frame Cross Tube	
RC-MRE-P19-T-0X	Bulkhead	
RC-MRE-P20-T-0X	Tail Cone Skin 2	
RC-MRE-P21-T-0X	Tail Cone Skin 6	
RC-MRE-P23-T-0X	Horizontal Stabilizer Leading Edge Stringer	

RC-MRE-P24-T-0X	Vertical Stabilizer Leading Edge Stringer	
RC-MRE-P26-T-0X	Lower Vertical Stabilizer Leading Edge Stringer	
RC-MRE-P28-T-0X	Horizontal Stabilizer Skin	
RC-MRE-P29-T-0X	Upper Vertical Stabilizer Skin	
RC-MRE-P32-T-0X-	Engine Bay Skin Door	
RC-MRE-P33-T-0X	Engine Bay Frame	
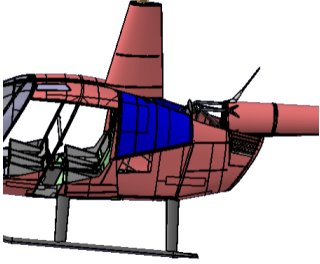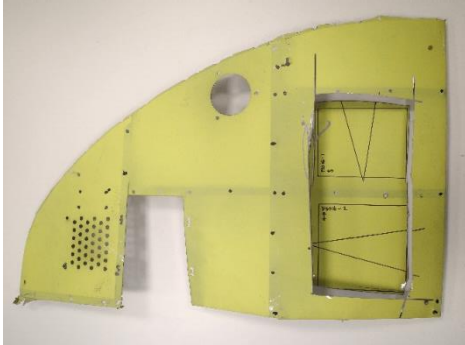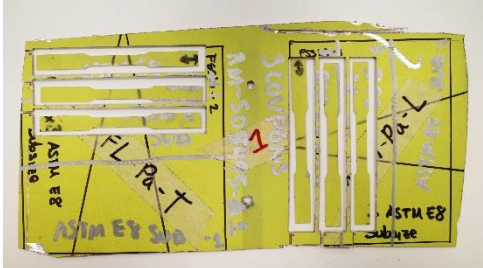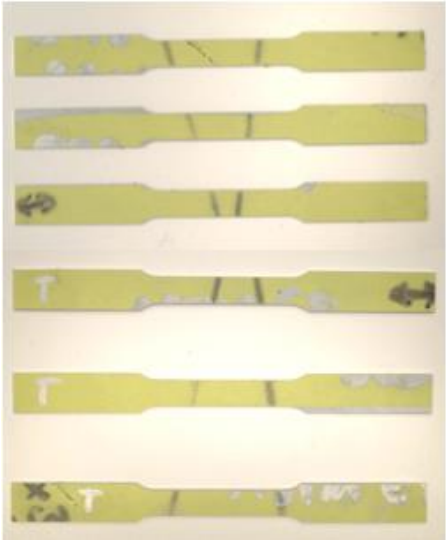
RC-MRE-P34-T-0X	Fuel Tank Skin	
Honeycomb	Honeycomb inside the blades	

Table 54. Metallic extractions.

Extracted Part for RC-MRE-P05-T-0X
Test Specimen Extraction for RC-MRE-P05-T-0X

Extracted Part for RC-MRE-P07-T-0X
Machined Specimens for RC-MRE-P07-T-0X
Extracted Part for RC-MRE-P08-T-0X
Machined Specimens for RC-MRE-P08-T-0X
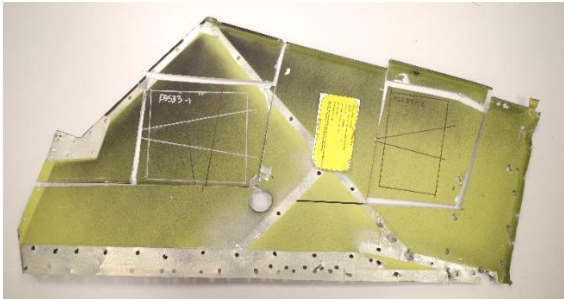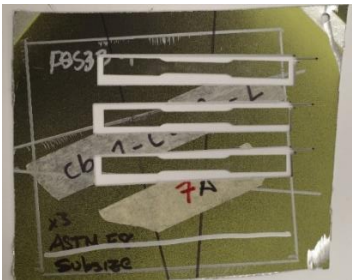
Extracted Part for RC-MRE-P09-T-0X
Machined Specimens for RC-MRE-P09-T-0X
Extracted Part for RC-MRE-P10-T-0X
Machined Specimens for RC-MRE-P10-T-0X
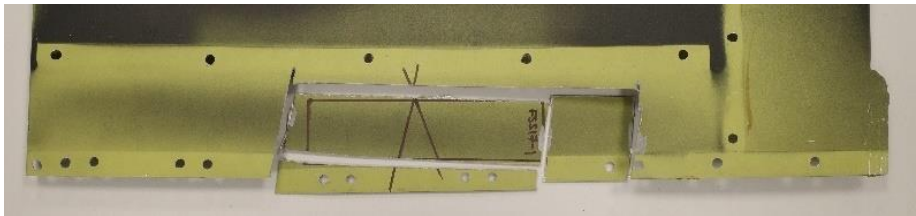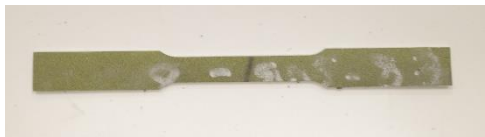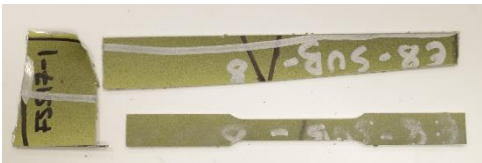
Extracted Part for RC-MRE-P11-T-0X
Machined Specimens for RC-MRE-P11-T-0X
Extracted Part for RC-MRE-P13-T-0X
Machined Specimens for RC-MRE-P13-T-0X
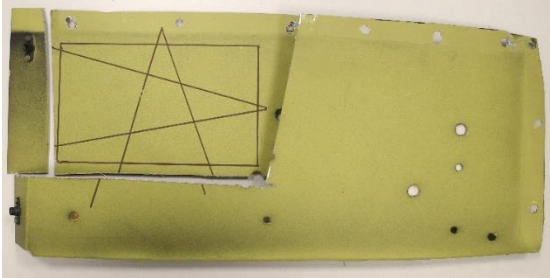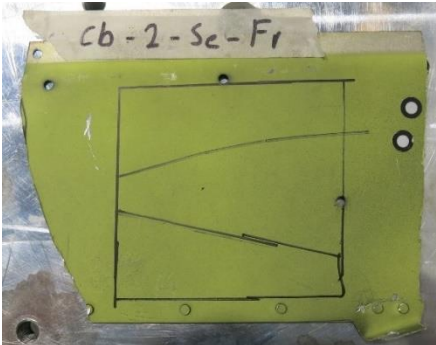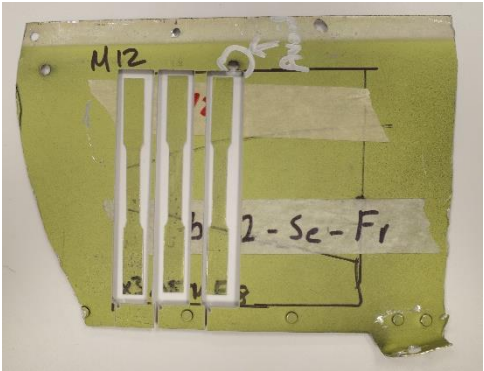
Extracted Part for RC-MRE-P14-T-0X
Machined Specimens for RC-MRE-P14-T-0X
Extracted Part for RC-MRE-P15-T-0X
Machined Specimens for RC-MRE-P15-T-0X
Extracted Part for RC-MRE-P16-T-0X
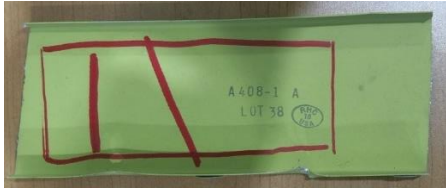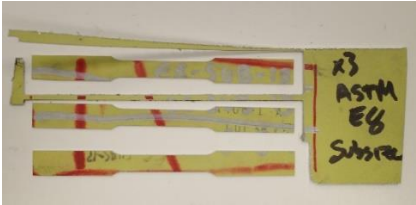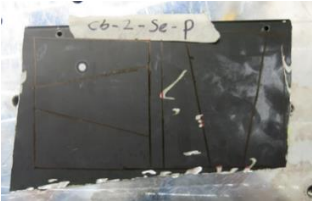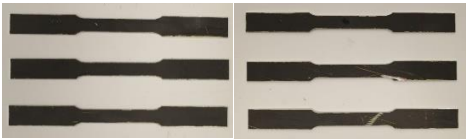
Machined Specimens for RC-MRE-P16-T-0X
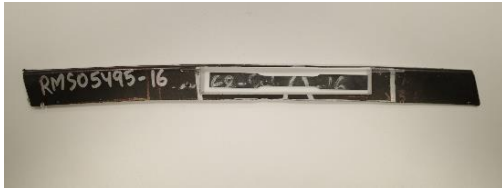
Extracted Part for RC-MRE-P17-T-0X

Machined Specimens for RC-MRE-P17-T-0X

Extracted Part for RC-MRE-P19-T-0X
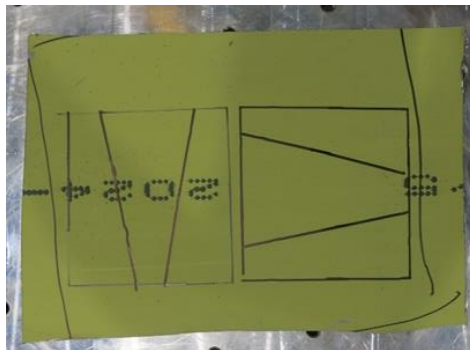
Machined Specimens for RC-MRE-P19-T-0X
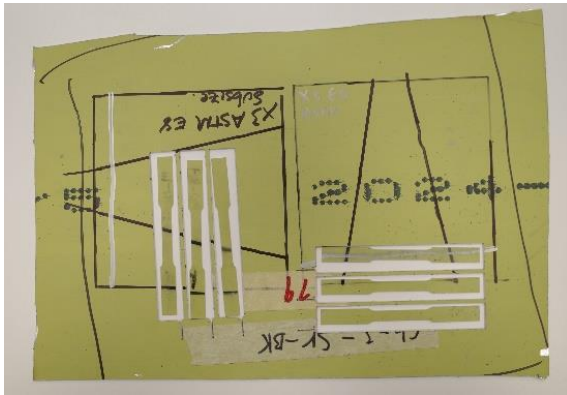
Extracted Part for RC-MRE-P20-T-0X
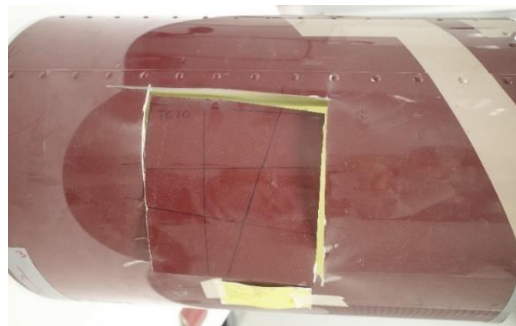
Machined Specimens for RC-MRE-P20-T-0X
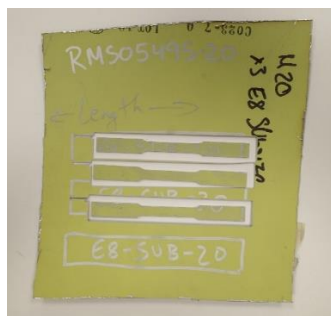
Extracted Part for RC-MRE-P21-T-0X
Machined Specimens for RC-MRE-P21-T-0X
Extracted Part for RC-MRE-P23-T-0X
Machined Specimens for RC-MRE-P23-T-0X
Extracted Part for RC-MRE-P24-T-0X
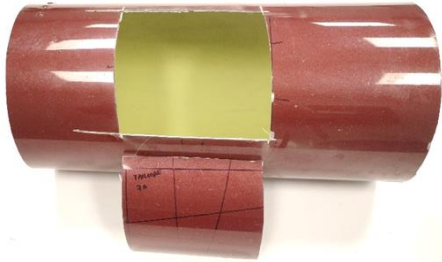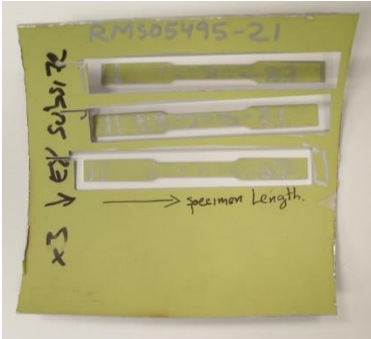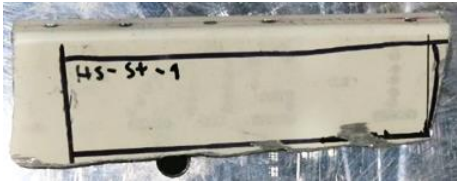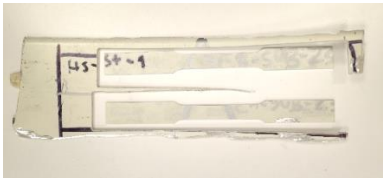
Machined Specimens for RC-MRE-P24-T-0X	
Extracted Part for RC-MRE-P26-T-0X	
Machined Specimens for RC-MRE-P26-T-0X	
Extracted Part for RC-MRE-P28-T-0X	
Machined Specimens for RC-MRE-P28-T-0X	

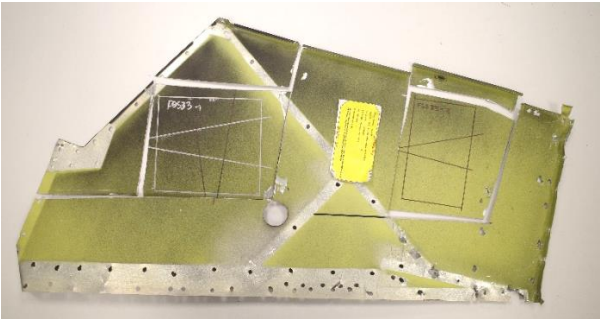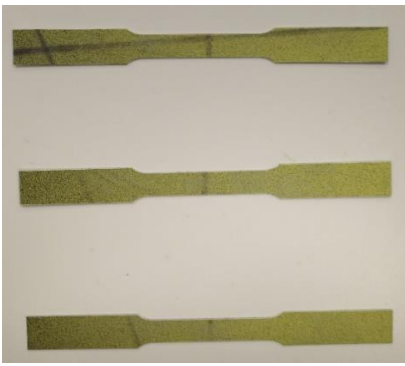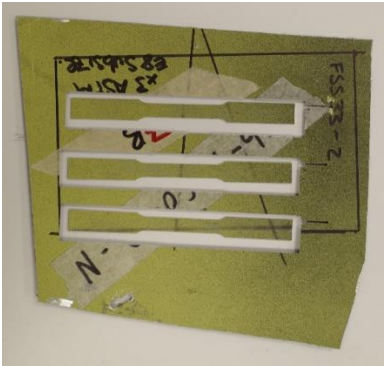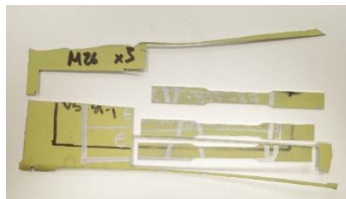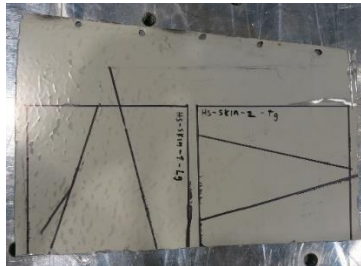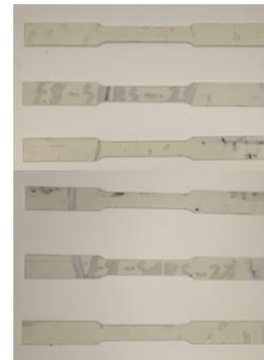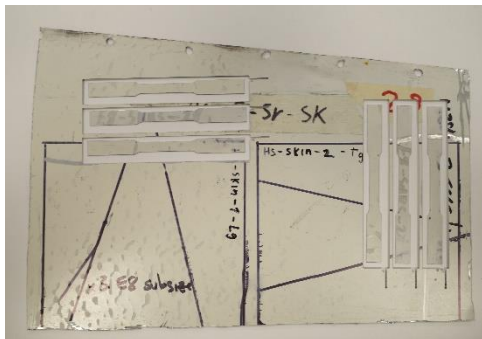| Extracted Part for RC-MRE-P29-T-0X |
|---|
| |
| Machined Specimens for RC-MRE-P29-T-0X |
| |
| Extracted Part for RC-MRE-P32-T-0X |
| |
| Machined Specimens for RC-MRE-P32-T-0X |
| |
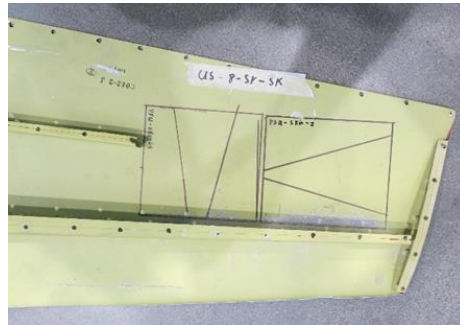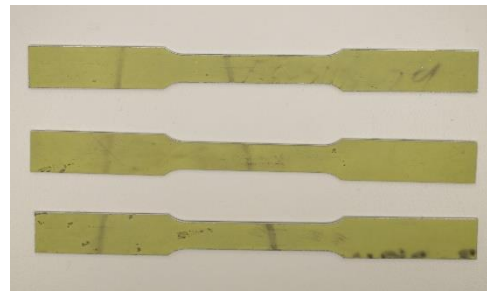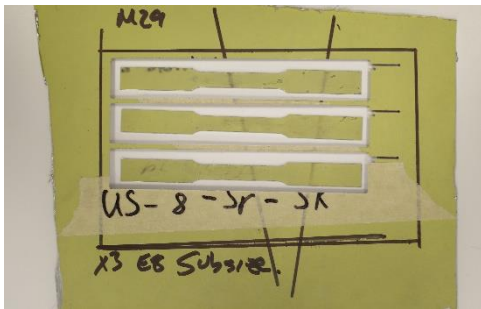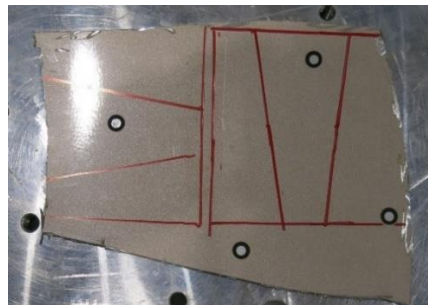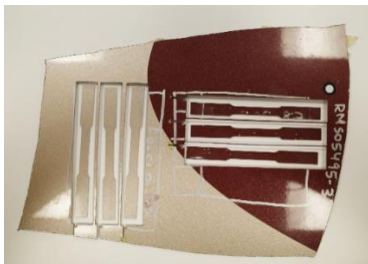
Extracted Part for RC-MRE-P33-T-0X
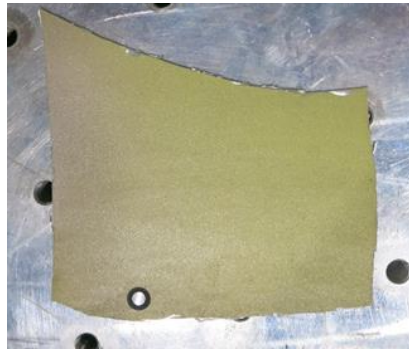
Machined Specimens for RC-MRE-P33-T-0X	
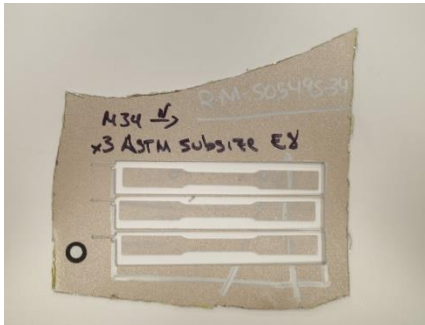
Extracted Part for RC-MRE-P34-T-0X
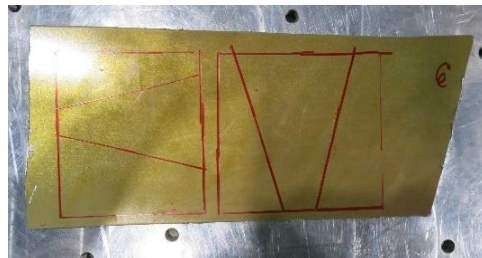
Machined Specimens for RC-MRE-P34-T-0X
Extracted Part for the Honeycomb
Machined Specimens for the Honeycomb
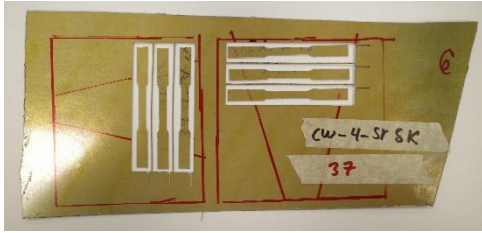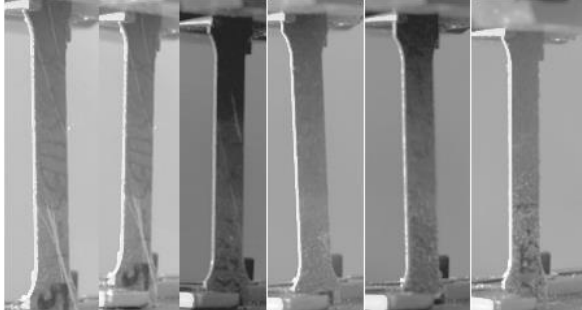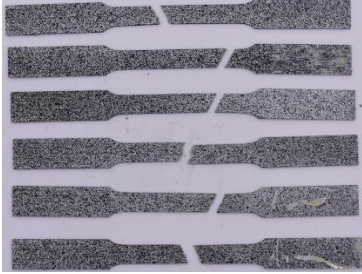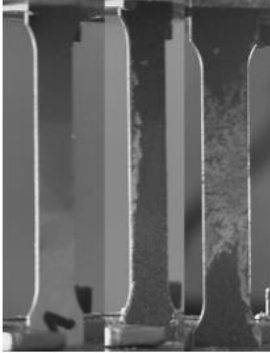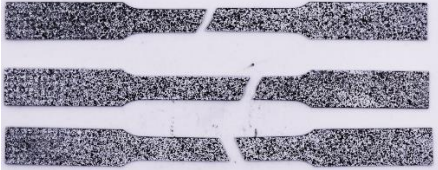
Table 55. Test setup and post-test photographs of all destructive testing.

Specimen Type	Sheet Type- Subsize
Test Setup for RC-MRE-P05-T-0X	
Post Test Picture for RC-MRE-P05-T-0X	
Test Setup for RC-MRE-P07-T-0X	
Post Test Picture for RC-MRE-P07-T-0X	

Test Setup for RC-MRE-P08-T-0X
Post Test Picture for RC-MRE-P08-T-0X
Test Setup for RC-MRE-P09-T-0X
Post Test Picture for RC-MRE-P09-T-0X
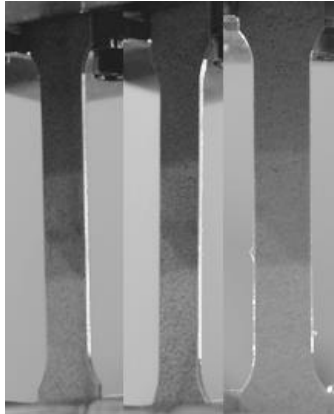
Test Setup RC-MRE-P10-T-0X
Post Test Picture RC-MRE-P10-T-0X
Test Setup RC-MRE-P11-T-0X
Post Test Picture RC-MRE-P11-T-0X
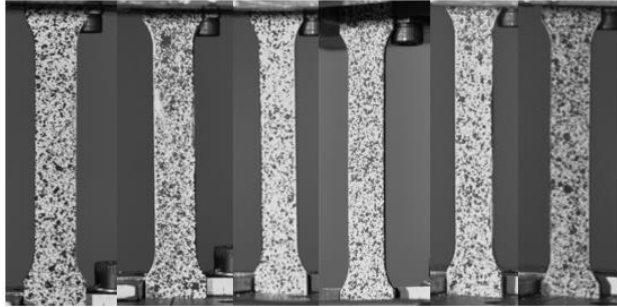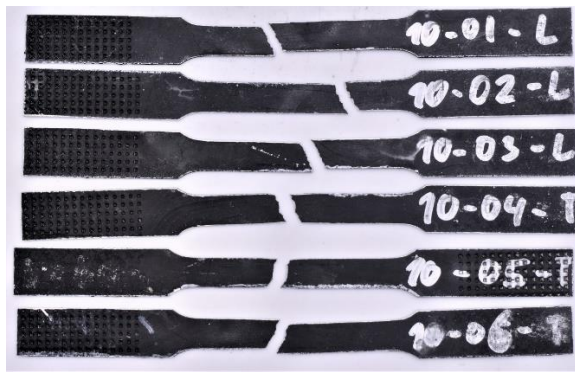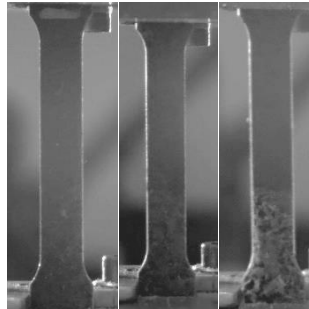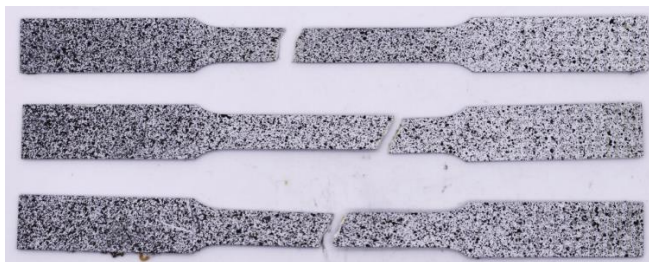
Test Setup for RC-MRE-P13-T-0X
Post Test Picture for RC-MRE-P13-T-0X
Test Setup for RC-MRE-P14-T-0X
Post Test Picture for RC-MRE-P14-T-0X
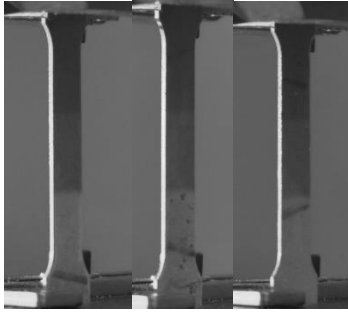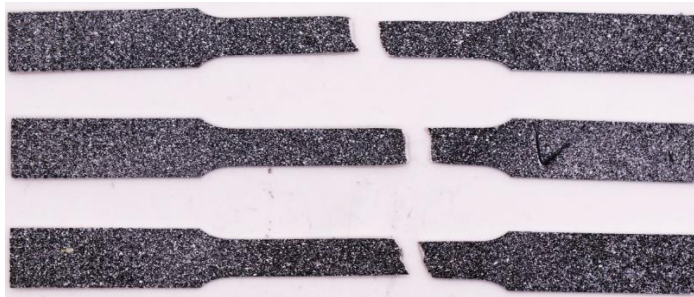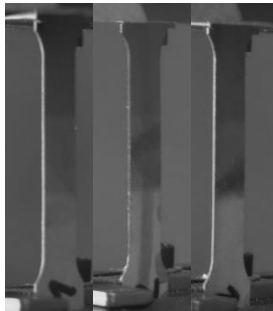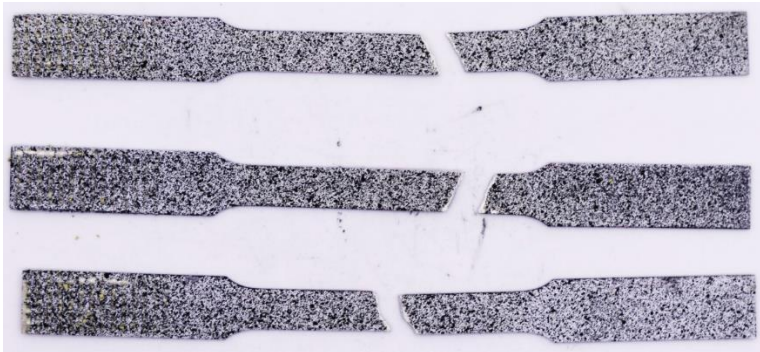
Test Setup for RC-MRE-P15-T-0X
Post Test Picture for RC-MRE-P15-T-0X
Test Setup for RC-MRE-P16-T-0X
Post Test Picture for RC-MRE-P16-T-0X
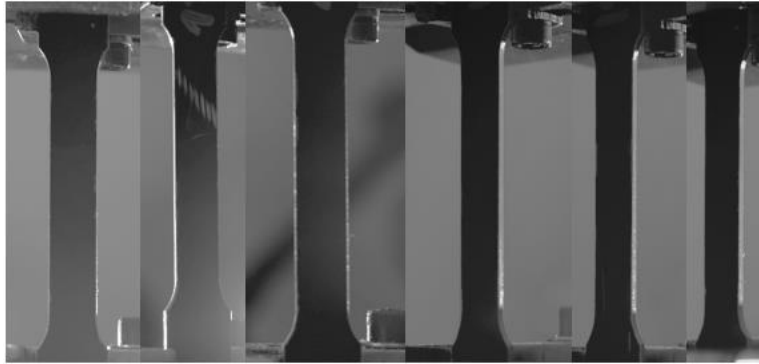
Test Setup RC-MRE-P17-T-0X
Post Test Picture for RC-MRE-P17-T-0X
Test Setup for RC-MRE-P19-T-0X
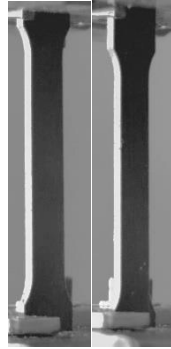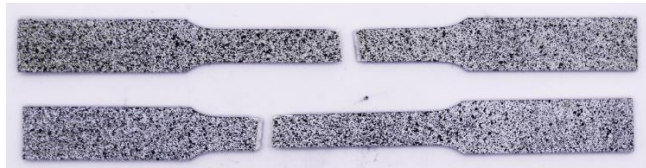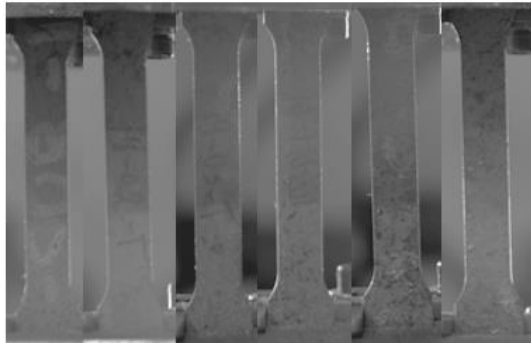
Post Test Picture for RC-MRE-P19-T-0X
Test Setup for RC-MRE-P20-T-0X
Post Test Picture for RC-MRE-P20-T-0X
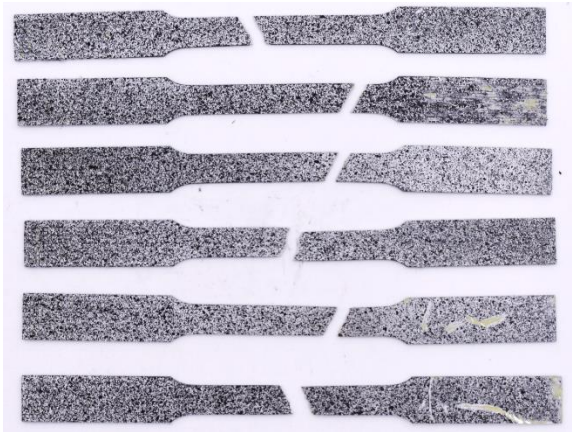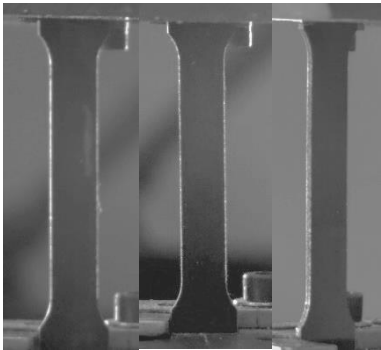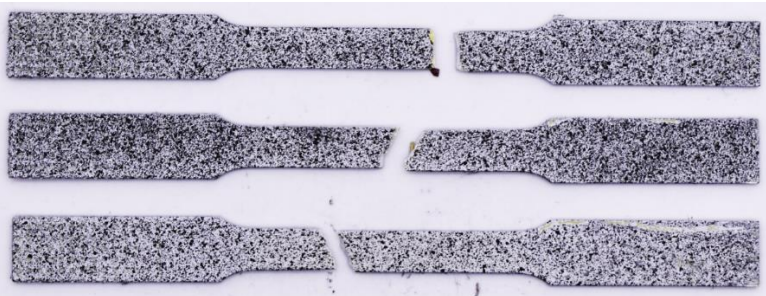
Test Setup for RC-MRE-P21-T-0X
Post Test Picture for RC-MRE-P21-T-0X
Test Setup for RC-MRE-P23-T-0X
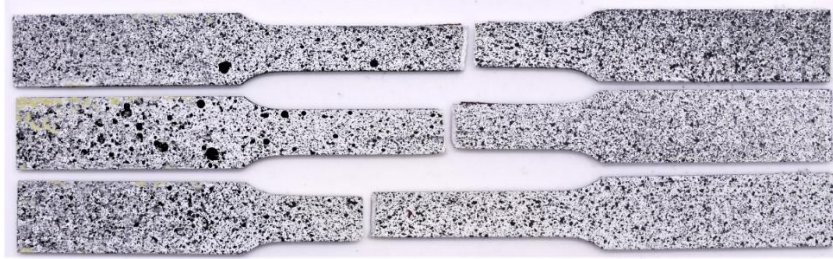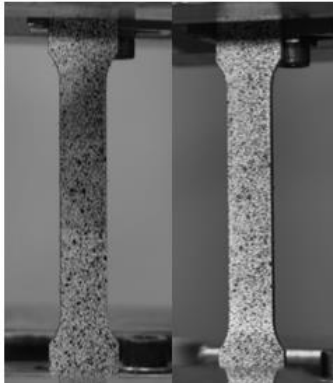
Post Test Picture for RC-MRE-P23-T-0X
Test Setup for RC-MRE-P24-T-0X
Post Test Picture for RC-MRE-P24-T-0X
Test Setup for RC-MRE-P26-T-0X
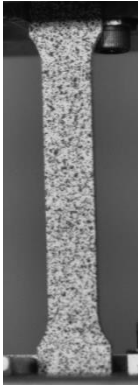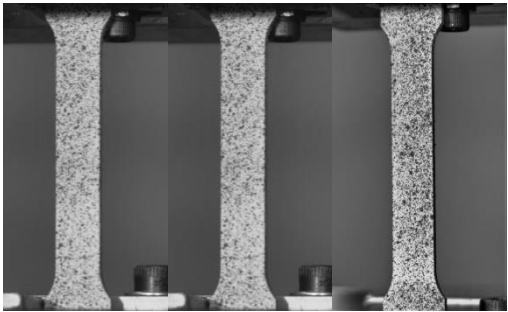
Post Test Picture for RC-MRE-P26-T-0X
Test Setup for RC-MRE-P28-T-0X
Post Test Picture for RC-MRE-P28-T-0X
Test Setup for RC-MRE-P29-T-0X
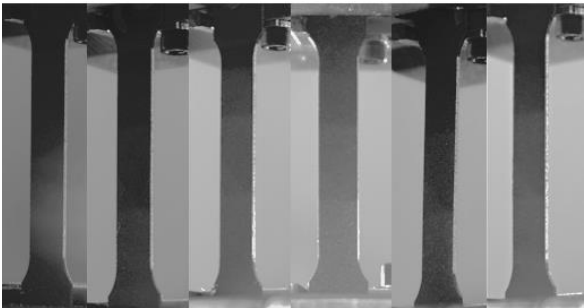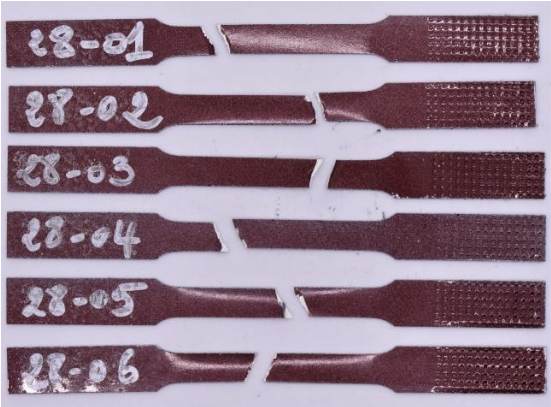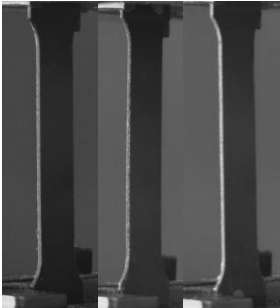
Post Test Picture for RC-MRE-P29-T-0X
Test Setup for RC-MRE-P32-T-0X
Post Test Picture for **RC-MRE-P32-T-0X**
Test Setup for RC-MRE-P33-T-0X
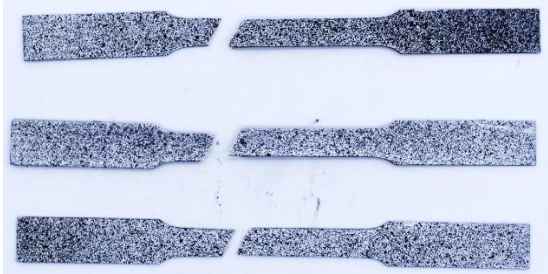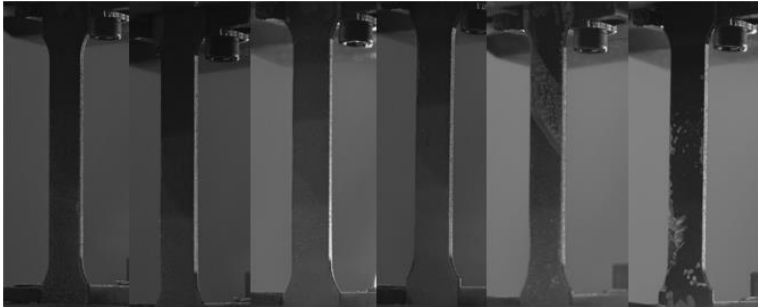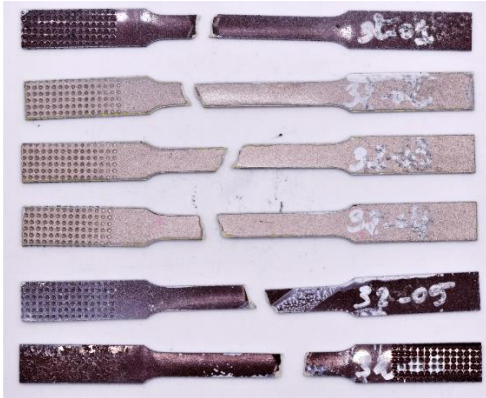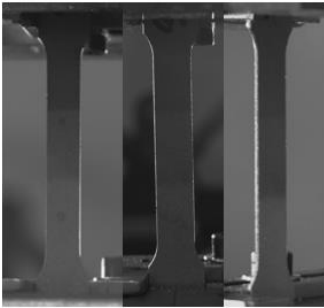
Post Test Picture for RC-MRE-P33-T-0X
Test Setup
Post Test Picture
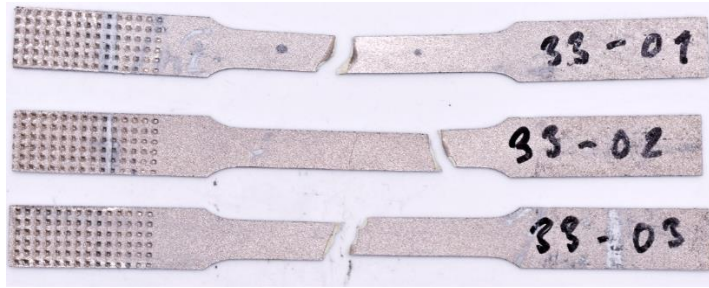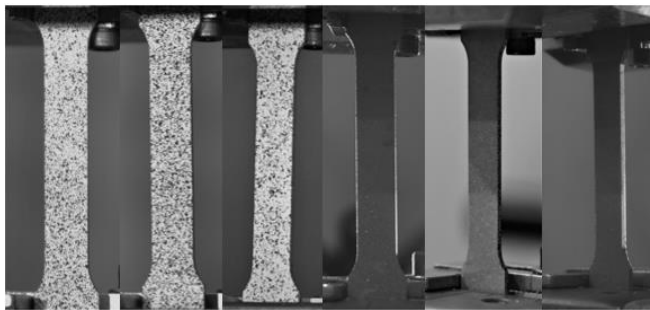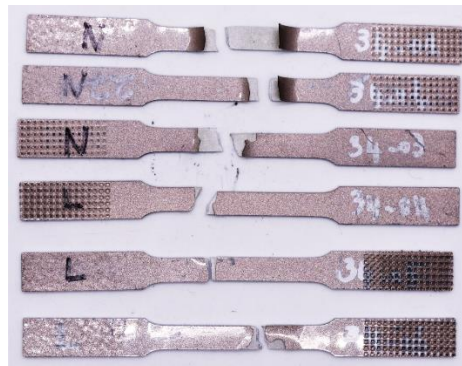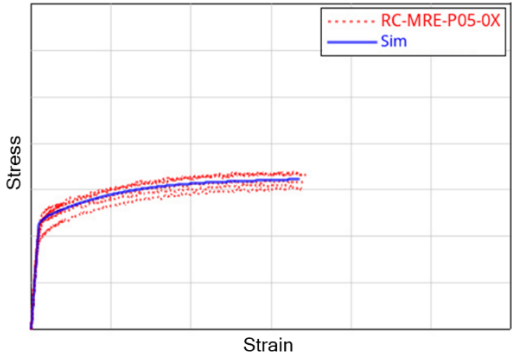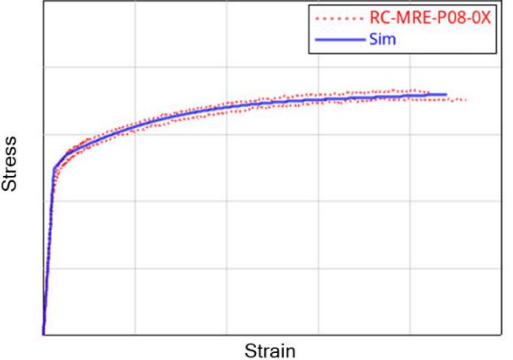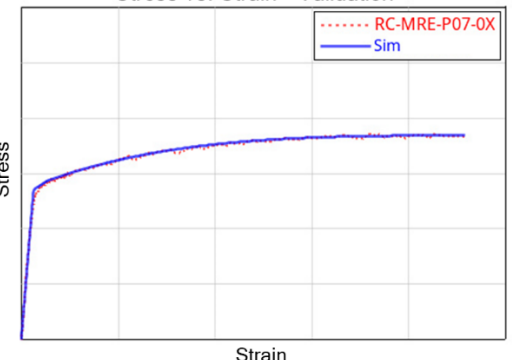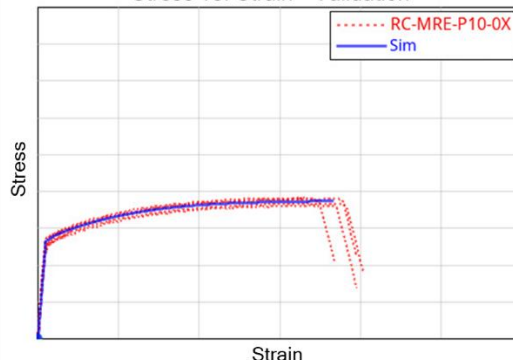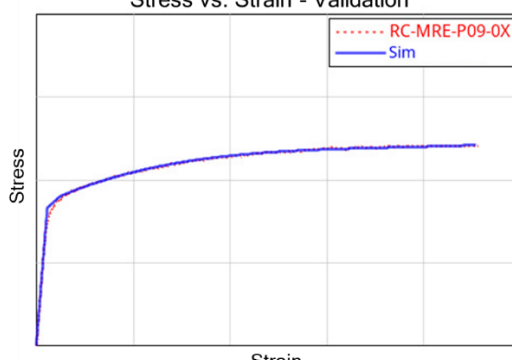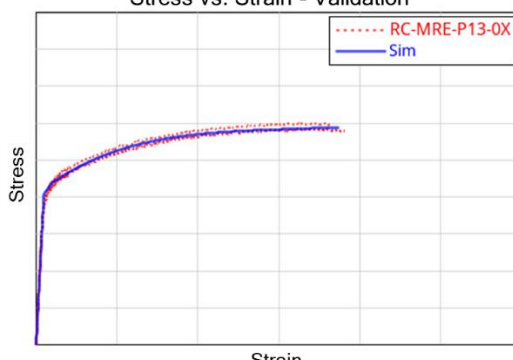
Table 56. Material card validation for all specimens.

Validation for RC-MRE-P05-T-0X	Validation for RC-MRE-P08-T-0X
Validation for RC-MRE-P07-T-0X	Validation for RC-MRE-P10-T-0X
Validation for RC-MRE-P09-T-0X	Validation for RC-MRE-P13-T-0X

Validation for RC-MRE-P11-T-0X	Validation for RC-MRE-P15-T-0X
Validation for RC-MRE-P14-T-0X	Validation for RC-MRE-P17-T-0X
Validation for RC-MRE-P16-T-0X	Validation for RC-MRE-P20-T-0X

Validation for RC-MRE-P19-T-0X	Validation for RC-MRE-P23-T-0X
Validation for RC-MRE-P21-T-0X	Validation for RC-MRE-P26-T-0X
Validation for RC-MRE-P24-T-0X	Validation for RC-MRE-P29-T-0X

Validation for RC-MRE-P28-T-0X	Validation for RC-MRE-P33-T-0X
Validation for RC-MRE-P32-T-0X	Validation for RC-MRE-P34-T-0X
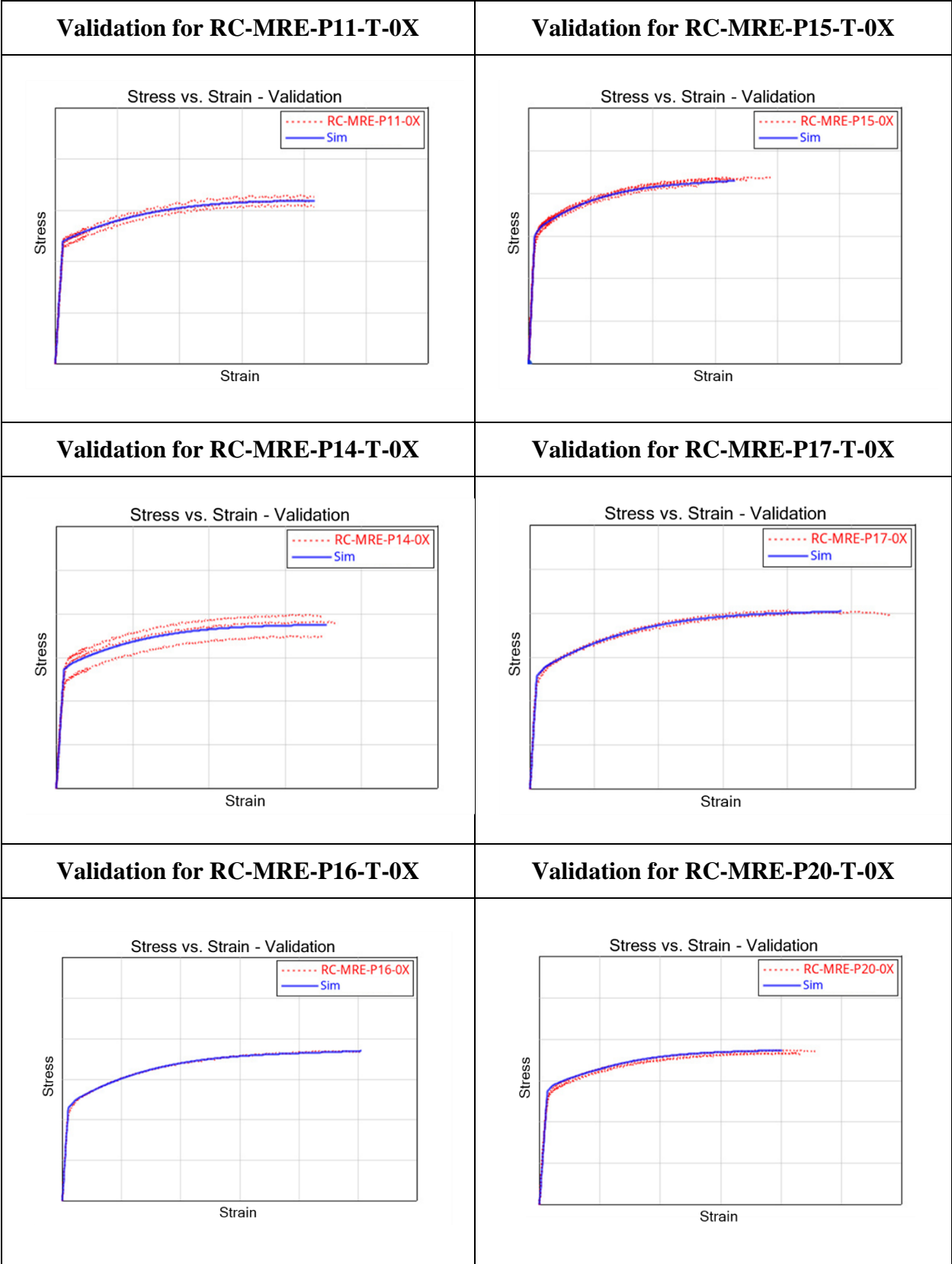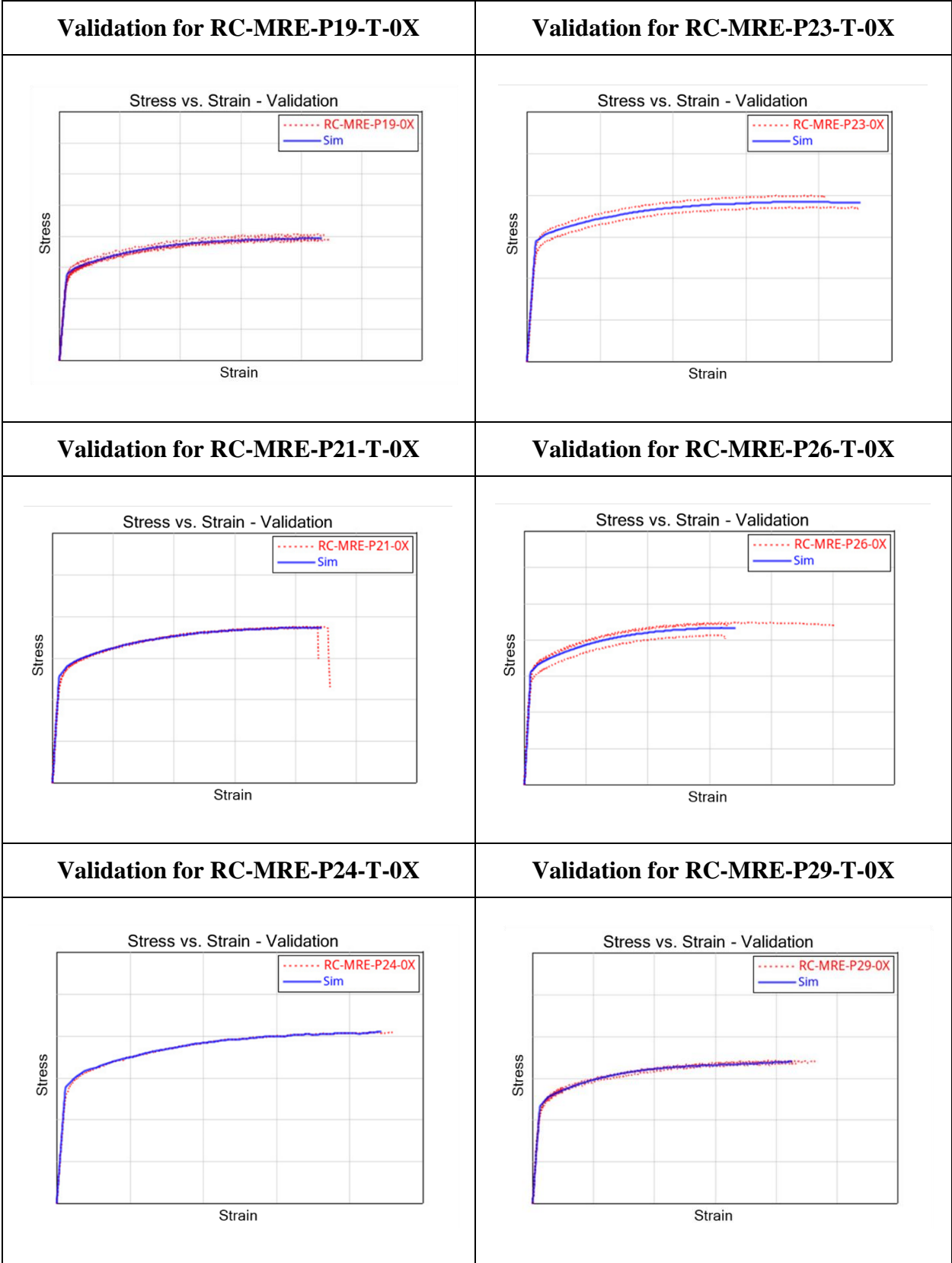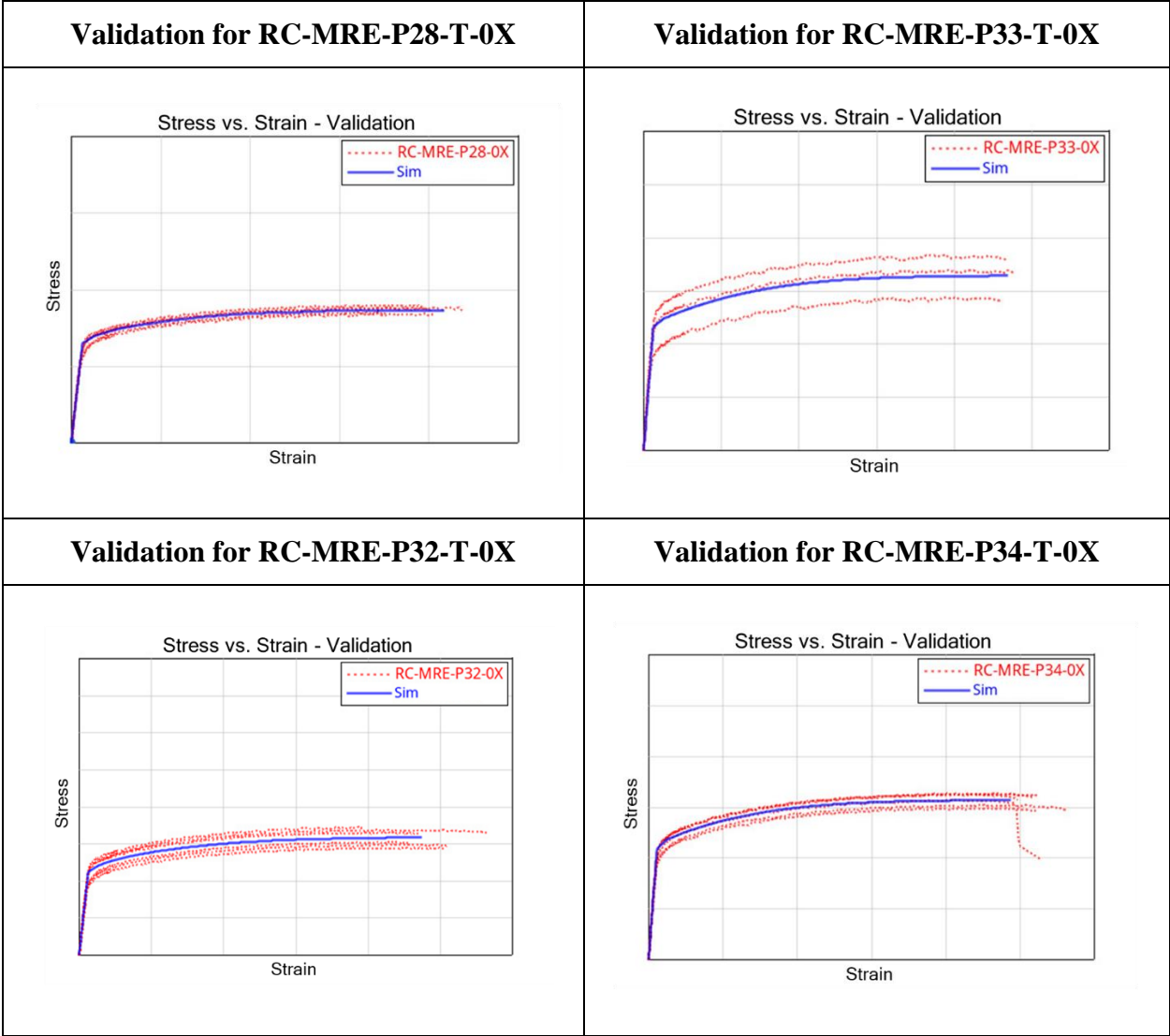
APPENDIX B. <u>MID-AIR COLLISION SEVERITY ASSESSMENT TABLE</u>
Table 57. Severity and Fire Risk Summary – Analysis Matrix.

Aircraft	Impact Area	Projectile	UAS Mass [kg]	Aircraft Mass [kg]	Impact Velocity	UAS [m/s]	Aircraft [m/s]	Impact Velocity [m/s]	Total Impact Energy [J]	Case ID	Severity Level	Risk of Fire (Battery)
Rotorcraft	Horizontal Stabilizer	Quadcopter - 2.7lb	1.22	1,082.27	Hover [H]	20.06	0.00	20.06	246.49	RQ2.7-H1H	Level 1	No
Rotorcraft	Horizontal Stabilizer	Quadcopter - 2.7lb	1.22	1,082.27	Medium [M]	20.06	28.29	48.36	1431.94	RQ2.7-H1M	Level 2	No
Rotorcraft	Horizontal Stabilizer	Quadcopter - 2.7lb	1.22	1,082.27	Cruise [C]	20.06	56.59	76.65	3597.83	RQ2.7-H1C	Level 3	No
Rotorcraft	Horizontal Stabilizer	Fixed-Wing - 4.0lb	1.81	1,082.27	Hover [H]	20.06	0.00	20.06	365.17	RF4.0-H1H	Level 2	No
Rotorcraft	Horizontal Stabilizer	Fixed-Wing - 4.0lb	1.81	1,082.27	Medium [M]	20.06	28.29	48.36	2121.39	RF4.0-H1M	Level 2	No
Rotorcraft	Horizontal Stabilizer	Fixed-Wing - 4.0lb	1.81	1,082.27	Cruise [C]	20.06	56.59	76.65	5330.12	RF4.0-H1C	Level 3	No
Rotorcraft	Horizontal Stabilizer	Quadcopter - 10lb	4.54	1,082.27	Hover [H]	20.06	0.00	20.06	912.92	RQ 10-H1H	Level 2	No
Rotorcraft	Horizontal Stabilizer	Quadcopter - 10lb	4.54	1,082.27	Medium [M]	20.06	28.29	48.36	5303.48	RQ 10-H1M	Level 3	No
Rotorcraft	Horizontal Stabilizer	Quadcopter - 10lb	4.54	1,082.27	Cruise [C]	20.06	56.59	76.65	13325.31	RQ 10-H1C	Level 4	No
Rotorcraft	Horizontal Stabilizer	Fixed-Wing - 12lb	5.44	1,082.27	Hover [H]	20.06	0.00	20.06	1095.51	RF 12-H1H	-	-
Rotorcraft	Horizontal Stabilizer	Fixed-Wing - 12lb	5.44	1,082.27	Medium [M]	20.06	28.29	48.36	6364.17	RF 12-H1M	-	-
Rotorcraft	Horizontal Stabilizer	Fixed-Wing - 12lb	5.44	1,082.27	Cruise [C]	20.06	56.59	76.65	15990.37	RF 12-H1C	-	-
Rotorcraft	Horizontal Stabilizer	Quadcopter - 25lb	11.34	1,082.27	Hover [H]	20.06	0.00	20.06	2282.31	RQ 25-H1H	Level 2	No
Rotorcraft	Horizontal Stabilizer	Quadcopter - 25lb	11.34	1,082.27	Medium [M]	20.06	28.29	48.36	13258.69	RQ 25-H1M	Level 4	No
Rotorcraft	Horizontal Stabilizer	Quadcopter - 25lb	11.34	1,082.27	Cruise [C]	20.06	56.59	76.65	33313.28	RQ 25-H1C	Level 4	No
Rotorcraft	Horizontal Stabilizer	Fixed-Wing - 25lb	11.34	1,082.27	Hover [H]	20.06	0.00	20.06	2282.31	RF 25-H1H	-	-
Rotorcraft	Horizontal Stabilizer	Fixed-Wing - 25lb	11.34	1,082.27	Medium [M]	20.06	28.29	48.36	13258.69	RF 25-H1M	-	-
Rotorcraft	Horizontal Stabilizer	Fixed-Wing - 25lb	11.34	1,082.27	Cruise [C]	20.06	56.59	76.65	33313.28	RF 25-H1C	-	-
Rotorcraft	Horizontal Stabilizer	Quadcopter - 55lb	24.95	1,082.27	Hover [H]	20.06	0.00	20.06	5021.08	RQ 55-H1H	Level 3	No
Rotorcraft	Horizontal Stabilizer	Quadcopter - 55lb	24.95	1,082.27	Medium [M]	20.06	28.29	48.36	29169.11	RQ 55-H1M	Level 4	No
Rotorcraft	Horizontal Stabilizer	Quadcopter - 55lb	24.95	1,082.27	Cruise [C]	20.06	56.59	76.65	73289.22	RQ 55-H1C	Level 4	No
Rotorcraft	Horizontal Stabilizer	Fixed-Wing - 55lb	24.95	1,082.27	Hover [H]	20.06	0.00	20.06	5021.08	RF 55-H1H	-	-
Rotorcraft	Horizontal Stabilizer	Fixed-Wing - 55lb	24.95	1,082.27	Medium [M]	20.06	28.29	48.36	29169.11	RF 55-H1M	-	-
Rotorcraft	Horizontal Stabilizer	Fixed-Wing - 55lb	24.95	1,082.27	Cruise [C]	20.06	56.59	76.65	73289.22	RF 55-H1C	-	-
Rotorcraft	Vertical Stabilizer	Quadcopter - 2.7lb	1.22	1,082.27	Hover [H]	20.06	0.00	20.06	246.49	RQ2.7-V1H	Level 1	No
Rotorcraft	Vertical Stabilizer	Quadcopter - 2.7lb	1.22	1,082.27	Medium [M]	20.06	28.29	48.36	1431.94	RQ2.7-V1M	Level 2	No
Rotorcraft	Vertical Stabilizer	Quadcopter - 2.7lb	1.22	1,082.27	Cruise [C]	20.06	56.59	76.65	3597.83	RQ2.7-V1C	Level 3	No
Rotorcraft	Vertical Stabilizer	Fixed-Wing - 4.0lb	1.81	1,082.27	Hover [H]	20.06	0.00	20.06	365.17	RF4.0-V1H	Level 4	No
Rotorcraft	Vertical Stabilizer	Fixed-Wing - 4.0lb	1.81	1,082.27	Medium [M]	20.06	28.29	48.36	2121.39	RF4.0-V1M	Level 4	Yes
Rotorcraft	Vertical Stabilizer	Fixed-Wing - 4.0lb	1.81	1,082.27	Cruise [C]	20.06	56.59	76.65	5330.12	RF4.0-V1C	Level 4	Yes
Rotorcraft	Vertical Stabilizer	Quadcopter - 10lb	4.54	1,082.27	Hover [H]	20.06	0.00	20.06	912.92	RQ 10-V1H	Level 2	No
Rotorcraft	Vertical Stabilizer	Quadcopter - 10lb	4.54	1,082.27	Medium [M]	20.06	28.29	48.36	5303.48	RQ 10-V1M	Level 3	No
Rotorcraft	Vertical Stabilizer	Quadcopter - 10lb	4.54	1,082.27	Cruise [C]	20.06	56.59	76.65	13325.31	RQ 10-V1C	Level 4	No
Rotorcraft	Vertical Stabilizer	Fixed-Wing - 12lb	5.44	1,082.27	Hover [H]	20.06	0.00	20.06	1095.51	RF 12-V1H	Level 4	No
Rotorcraft	Vertical Stabilizer	Fixed-Wing - 12lb	5.44	1,082.27	Medium [M]	20.06	28.29	48.36	6364.17	RF 12-V1M	Level 4	Yes
Rotorcraft	Vertical Stabilizer	Fixed-Wing - 12lb	5.44	1,082.27	Cruise [C]	20.06	56.59	76.65	15990.37	RF 12-V1C	Level 4	No
Rotorcraft	Vertical Stabilizer	Quadcopter - 25lb	11.34	1,082.27	Hover [H]	20.06	0.00	20.06	2282.31	RQ 25-V1H	Level 2	No
Rotorcraft	Vertical Stabilizer	Quadcopter - 25lb	11.34	1,082.27	Medium [M]	20.06	28.29	48.36	13258.69	RQ 25-V1M	Level 3	No
Rotorcraft	Vertical Stabilizer	Quadcopter - 25lb	11.34	1,082.27	Cruise [C]	20.06	56.59	76.65	33313.28	RQ 25-V1C	Level 4	No
Rotorcraft	Vertical Stabilizer	Fixed-Wing - 25lb	11.34	1,082.27	Hover [H]	20.06	0.00	20.06	2282.31	RF 25-V1H	Level 4	No
Rotorcraft	Vertical Stabilizer	Fixed-Wing - 25lb	11.34	1,082.27	Medium [M]	20.06	28.29	48.36	13258.69	RF 25-V1M	Level 4	No
Rotorcraft	Vertical Stabilizer	Fixed-Wing - 25lb	11.34	1,082.27	Cruise [C]	20.06	56.59	76.65	33313.28	RF 25-V1C	Level 4	No
Rotorcraft	Vertical Stabilizer	Quadcopter - 55lb	24.95	1,082.27	Hover [H]	20.06	0.00	20.06	5021.08	RQ 55-V1H	Level 4	No
Rotorcraft	Vertical Stabilizer	Quadcopter - 55lb	24.95	1,082.27	Medium [M]	20.06	28.29	48.36	29169.11	RQ 55-V1M	Level 4	No
Rotorcraft	Vertical Stabilizer	Quadcopter - 55lb	24.95	1,082.27	Cruise [C]	20.06	56.59	76.65	73289.22	RQ 55-V1C	Level 4	No
Rotorcraft	Vertical Stabilizer	Fixed-Wing - 55lb	24.95	1,082.27	Hover [H]	20.06	0.00	20.06	5021.08	RF 55-V1H	Level 4	No
Rotorcraft	Vertical Stabilizer	Fixed-Wing - 55lb	24.95	1,082.27	Medium [M]	20.06	28.29	48.36	29169.11	RF 55-V1M	Level 4	No
Rotorcraft	Vertical Stabilizer	Fixed-Wing - 55lb	24.95	1,082.27	Cruise [C]	20.06	56.59	76.65	73289.22	RF 55-V1C	Level 4	No
Rotorcraft	Mast	Quadcopter - 2.7lb	1.22	1,082.27	Hover [H]	20.06	0.00	20.06	246.49	RQ2.7-M1H	Level 1	No
Rotorcraft	Mast	Quadcopter - 2.7lb	1.22	1,082.27	Medium [M]	20.06	28.29	48.36	1431.94	RQ2.7-M1M	Level 2	No
Rotorcraft	Mast	Quadcopter - 2.7lb	1.22	1,082.27	Cruise [C]	20.06	56.59	76.65	3597.83	RQ2.7-M1C	Level 2	No
Rotorcraft	Mast	Fixed-Wing - 4.0lb	1.81	1,082.27	Hover [H]	20.06	0.00	20.06	365.17	RF4.0-M1H	Level 1	No
Rotorcraft	Mast	Fixed-Wing - 4.0lb	1.81	1,082.27	Medium [M]	20.06	28.29	48.36	2121.39	RF4.0-M1M	Level 2	No
Rotorcraft	Mast	Fixed-Wing - 4.0lb	1.81	1,082.27	Cruise [C]	20.06	56.59	76.65	5330.12	RF4.0-M1C	Level 3	Yes
Rotorcraft	Mast	Quadcopter - 10lb	4.54	1,082.27	Hover [H]	20.06	0.00	20.06	912.92	RQ 10-M1H	Level 2	No
Rotorcraft	Mast	Quadcopter - 10lb	4.54	1,082.27	Medium [M]	20.06	28.29	48.36	5303.48	RQ 10-M1M	Level 2	No
Rotorcraft	Mast	Quadcopter - 10lb	4.54	1,082.27	Cruise [C]	20.06	56.59	76.65	13325.31	RQ 10-M1C	Level 3	No
Rotorcraft	Mast	Fixed-Wing - 12lb	5.44	1,082.27	Hover [H]	20.06	0.00	20.06	1095.51	RF 12-M1H	Level 2	No
Rotorcraft	Mast	Fixed-Wing - 12lb	5.44	1,082.27	Medium [M]	20.06	28.29	48.36	6364.17	RF 12-M1M	Level 2	No
Rotorcraft	Mast	Fixed-Wing - 12lb	5.44	1,082.27	Cruise [C]	20.06	56.59	76.65	15990.37	RF 12-M1C	Level 3	No
Rotorcraft	Mast	Quadcopter - 25lb	11.34	1,082.27	Hover [H]	20.06	0.00	20.06	2282.31	RQ 25-M1H	Level 2	No
Rotorcraft	Mast	Quadcopter - 25lb	11.34	1,082.27	Medium [M]	20.06	28.29	48.36	13258.69	RQ 25-M1M	Level 3	No
Rotorcraft	Mast	Quadcopter - 25lb	11.34	1,082.27	Cruise [C]	20.06	56.59	76.65	33313.28	RQ 25-M1C	Level 4	No
Rotorcraft	Mast	Fixed-Wing - 25lb	11.34	1,082.27	Hover [H]	20.06	0.00	20.06	2282.31	RF 25-M1H	Level 2	No
Rotorcraft	Mast	Fixed-Wing - 25lb	11.34	1,082.27	Medium [M]	20.06	28.29	48.36	13258.69	RF 25-M1M	Level 3	No
Rotorcraft	Mast	Fixed-Wing - 25lb	11.34	1,082.27	Cruise [C]	20.06	56.59	76.65	33313.28	RF 25-M1C	Level 4	No
Rotorcraft	Mast	Quadcopter - 55lb	24.95	1,082.27	Hover [H]	20.06	0.00	20.06	5021.08	RQ 55-M1H	Level 3	No
Rotorcraft	Mast	Quadcopter - 55lb	24.95	1,082.27	Medium [M]	20.06	28.29	48.36	29169.11	RQ 55-M1M	Level 4	No
Rotorcraft	Mast	Quadcopter - 55lb	24.95	1,082.27	Cruise [C]	20.06	56.59	76.65	73289.22	RQ 55-M1C	Level 4	No
Rotorcraft	Mast	Fixed-Wing - 55lb	24.95	1,082.27	Hover [H]	20.06	0.00	20.06	5021.08	RF 55-M1H	Level 4	No
Rotorcraft	Mast	Fixed-Wing - 55lb	24.95	1,082.27	Medium [M]	20.06	28.29	48.36	29169.11	RF 55-M1M	Level 4	No
Rotorcraft	Mast	Fixed-Wing - 55lb	24.95	1,082.27	Cruise [C]	20.06	56.59	76.65	73289.22	RF 55-M1C	Level 4	No

Table 57. Severity and Fire Risk Summary – Analysis Matrix (Continued)

Rotorcraft	Nose	Quadcopter - 2.7lb	1.22	1,082.27	Hover [H]	20.06	0.00	20.06	246.49	RQ2.7-N1H	Level 2	No
Rotorcraft	Nose	Quadcopter - 2.7lb	1.22	1,082.27	Medium [M]	20.06	28.29	48.36	1431.94	RQ2.7-N1M	Level 3	No
Rotorcraft	Nose	Quadcopter - 2.7lb	1.22	1,082.27	Cruise [C]	20.06	56.59	76.65	3597.83	RQ2.7-N1C	Level 3	No
Rotorcraft	Nose	Fixed-Wing - 4.0lb	1.81	1,082.27	Hover [H]	20.06	0.00	20.06	365.17	RF4.0-N1H	Level 2	No
Rotorcraft	Nose	Fixed-Wing - 4.0lb	1.81	1,082.27	Medium [M]	20.06	28.29	48.36	2121.39	RF4.0-N1M	Level 3	No
Rotorcraft	Nose	Fixed-Wing - 4.0lb	1.81	1,082.27	Cruise [C]	20.06	56.59	76.65	5330.12	RF4.0-N1C	Level 3	No
Rotorcraft	Nose	Quadcopter - 10lb	4.54	1,082.27	Hover [H]	20.06	0.00	20.06	912.92	RQ 10-N1H	Level 2	No
Rotorcraft	Nose	Quadcopter - 10lb	4.54	1,082.27	Medium [M]	20.06	28.29	48.36	5303.48	RQ 10-N1M	Level 3	No
Rotorcraft	Nose	Quadcopter - 10lb	4.54	1,082.27	Cruise [C]	20.06	56.59	76.65	13325.31	RQ 10-N1C	Level 3	No
Rotorcraft	Nose	Fixed-Wing - 12lb	5.44	1,082.27	Hover [H]	20.06	0.00	20.06	1095.51	RF 12-N1H	Level 2	No
Rotorcraft	Nose	Fixed-Wing - 12lb	5.44	1,082.27	Medium [M]	20.06	28.29	48.36	6364.17	RF 12-N1M	Level 3	Yes
Rotorcraft	Nose	Fixed-Wing - 12lb	5.44	1,082.27	Cruise [C]	20.06	56.59	76.65	15990.37	RF 12-N1C	Level 3	No
Rotorcraft	Nose	Quadcopter - 25lb	11.34	1,082.27	Hover [H]	20.06	0.00	20.06	2282.31	RQ 25-N1H	Level 2	No
Rotorcraft	Nose	Quadcopter - 25lb	11.34	1,082.27	Medium [M]	20.06	28.29	48.36	13258.69	RQ 25-N1M	Level 3	No
Rotorcraft	Nose	Quadcopter - 25lb	11.34	1,082.27	Cruise [C]	20.06	56.59	76.65	33313.28	RQ 25-N1C	Level 4	No
Rotorcraft	Nose	Fixed-Wing - 25lb	11.34	1,082.27	Hover [H]	20.06	0.00	20.06	2282.31	RF 25-N1H	Level 2	No
Rotorcraft	Nose	Fixed-Wing - 25lb	11.34	1,082.27	Medium [M]	20.06	28.29	48.36	13258.69	RF 25-N1M	Level 3	No
Rotorcraft	Nose	Fixed-Wing - 25lb	11.34	1,082.27	Cruise [C]	20.06	56.59	76.65	33313.28	RF 25-N1C	Level 4	No
Rotorcraft	Nose	Quadcopter - 55lb	24.95	1,082.27	Hover [H]	20.06	0.00	20.06	5021.08	RQ 55-N1H	Level 2	No
Rotorcraft	Nose	Quadcopter - 55lb	24.95	1,082.27	Medium [M]	20.06	28.29	48.36	29169.11	RQ 55-N1M	Level 4	Yes
Rotorcraft	Nose	Quadcopter - 55lb	24.95	1,082.27	Cruise [C]	20.06	56.59	76.65	73289.22	RQ 55-N1C	Level 4	Yes
Rotorcraft	Nose	Fixed-Wing - 55lb	24.95	1,082.27	Hover [H]	20.06	0.00	20.06	5021.08	RF 55-N1H	Level 2	No
Rotorcraft	Nose	Fixed-Wing - 55lb	24.95	1,082.27	Medium [M]	20.06	28.29	48.36	29169.11	RF 55-N1M	Level 4	No
Rotorcraft	Nose	Fixed-Wing - 55lb	24.95	1,082.27	Cruise [C]	20.06	56.59	76.65	73289.22	RF 55-N1C	Level 4	No
Rotorcraft	Windshield	Quadcopter - 2.7lb	1.22	1,082.27	Hover [H]	20.06	0.00	20.06	246.49	RQ2.7-W1H	Level 1	No
Rotorcraft	Windshield	Quadcopter - 2.7lb	1.22	1,082.27	Medium [M]	20.06	28.29	48.36	1431.94	RQ2.7-W1M	Level 4	No
Rotorcraft	Windshield	Quadcopter - 2.7lb	1.22	1,082.27	Cruise [C]	20.06	56.59	76.65	3597.83	RQ2.7-W1C	Level 4	Yes
Rotorcraft	Windshield	Fixed-Wing - 4.0lb	1.81	1,082.27	Hover [H]	20.06	0.00	20.06	365.17	RF4.0-W1H	Level 1	No
Rotorcraft	Windshield	Fixed-Wing - 4.0lb	1.81	1,082.27	Medium [M]	20.06	28.29	48.36	2121.39	RF4.0-W1M	Level 4	No
Rotorcraft	Windshield	Fixed-Wing - 4.0lb	1.81	1,082.27	Cruise [C]	20.06	56.59	76.65	5330.12	RF4.0-W1C	Level 4	No
Rotorcraft	Windshield	Quadcopter - 10lb	4.54	1,082.27	Hover [H]	20.06	0.00	20.06	912.92	RQ 10-W1H	Level 4	No
Rotorcraft	Windshield	Quadcopter - 10lb	4.54	1,082.27	Medium [M]	20.06	28.29	48.36	5303.48	RQ 10-W1M	Level 4	No
Rotorcraft	Windshield	Quadcopter - 10lb	4.54	1,082.27	Cruise [C]	20.06	56.59	76.65	13325.31	RQ 10-W1C	Level 4	No
Rotorcraft	Windshield	Fixed-Wing - 12lb	5.44	1,082.27	Hover [H]	20.06	0.00	20.06	1095.51	RF 12-W1H	Level 2	No
Rotorcraft	Windshield	Fixed-Wing - 12lb	5.44	1,082.27	Medium [M]	20.06	28.29	48.36	6364.17	RF 12-W1M	Level 4	Yes
Rotorcraft	Windshield	Fixed-Wing - 12lb	5.44	1,082.27	Cruise [C]	20.06	56.59	76.65	15990.37	RF 12-W1C	Level 4	No
Rotorcraft	Windshield	Quadcopter - 25lb	11.34	1,082.27	Hover [H]	20.06	0.00	20.06	2282.31	RQ 25-W1H	Level 2	No
Rotorcraft	Windshield	Quadcopter - 25lb	11.34	1,082.27	Medium [M]	20.06	28.29	48.36	13258.69	RQ 25-W1M	Level 4	Yes
Rotorcraft	Windshield	Quadcopter - 25lb	11.34	1,082.27	Cruise [C]	20.06	56.59	76.65	33313.28	RQ 25-W1C	Level 4	No
Rotorcraft	Windshield	Fixed-Wing - 25lb	11.34	1,082.27	Hover [H]	20.06	0.00	20.06	2282.31	RF 25-W1H	Level 3	No
Rotorcraft	Windshield	Fixed-Wing - 25lb	11.34	1,082.27	Medium [M]	20.06	28.29	48.36	13258.69	RF 25-W1M	Level 4	Yes
Rotorcraft	Windshield	Fixed-Wing - 25lb	11.34	1,082.27	Cruise [C]	20.06	56.59	76.65	33313.28	RF 25-W1C	Level 4	No
Rotorcraft	Windshield	Quadcopter - 55lb	24.95	1,082.27	Hover [H]	20.06	0.00	20.06	5021.08	RQ 55-W1H	Level 4	No
Rotorcraft	Windshield	Quadcopter - 55lb	24.95	1,082.27	Medium [M]	20.06	28.29	48.36	29169.11	RQ 55-W1M	Level 4	Yes
Rotorcraft	Windshield	Quadcopter - 55lb	24.95	1,082.27	Cruise [C]	20.06	56.59	76.65	73289.22	RQ 55-W1C	Level 4	No
Rotorcraft	Windshield	Fixed-Wing - 55lb	24.95	1,082.27	Hover [H]	20.06	0.00	20.06	5021.08	RF 55-W1H	Level 4	No
Rotorcraft	Windshield	Fixed-Wing - 55lb	24.95	1,082.27	Medium [M]	20.06	28.29	48.36	29169.11	RF 55-W1M	Level 4	Yes
Rotorcraft	Windshield	Fixed-Wing - 55lb	24.95	1,082.27	Cruise [C]	20.06	56.59	76.65	73289.22	RF 55-W1C	Level 4	No
Rotorcraft	Blade	Quadcopter - 2.7lb	1.22	1,082.27	Hover [H]	20.06	0.00	20.06	246.49	RQ2.7-B1H	Level 2	No
Rotorcraft	Blade	Quadcopter - 2.7lb	1.22	1,082.27	Medium [M]	20.06	28.29	48.36	1431.94	RQ2.7-B1M	Level 2	No
Rotorcraft	Blade	Quadcopter - 2.7lb	1.22	1,082.27	Cruise [C]	20.06	56.59	76.65	3597.83	RQ2.7-B1C	Level 2	No
Rotorcraft	Blade	Fixed-Wing - 4.0lb	1.81	1,082.27	Hover [H]	20.06	0.00	20.06	365.17	RF4.0-B1H	Level 3	No
Rotorcraft	Blade	Fixed-Wing - 4.0lb	1.81	1,082.27	Medium [M]	20.06	28.29	48.36	2121.39	RF4.0-B1M	Level 3	No
Rotorcraft	Blade	Fixed-Wing - 4.0lb	1.81	1,082.27	Cruise [C]	20.06	56.59	76.65	5330.12	RF4.0-B1C	Level 3	No
Rotorcraft	Blade	Quadcopter - 10lb	4.54	1,082.27	Hover [H]	20.06	0.00	20.06	912.92	RQ 10-B1H	Level 3	No
Rotorcraft	Blade	Quadcopter - 10lb	4.54	1,082.27	Medium [M]	20.06	28.29	48.36	5303.48	RQ 10-B1M	Level 3	No
Rotorcraft	Blade	Quadcopter - 10lb	4.54	1,082.27	Cruise [C]	20.06	56.59	76.65	13325.31	RQ 10-B1C	Level 3	No
Rotorcraft	Blade	Fixed-Wing - 12lb	5.44	1,082.27	Hover [H]	20.06	0.00	20.06	1095.51	RF 12-B1H	Level 4	No
Rotorcraft	Blade	Fixed-Wing - 12lb	5.44	1,082.27	Medium [M]	20.06	28.29	48.36	6364.17	RF 12-B1M	Level 4	No
Rotorcraft	Blade	Fixed-Wing - 12lb	5.44	1,082.27	Cruise [C]	20.06	56.59	76.65	15990.37	RF 12-B1C	Level 4	No
Rotorcraft	Blade	Quadcopter - 25lb	11.34	1,082.27	Hover [H]	20.06	0.00	20.06	2282.31	RQ 25-B1H	Level 4	No
Rotorcraft	Blade	Quadcopter - 25lb	11.34	1,082.27	Medium [M]	20.06	28.29	48.36	13258.69	RQ 25-B1M	Level 4	No
Rotorcraft	Blade	Quadcopter - 25lb	11.34	1,082.27	Cruise [C]	20.06	56.59	76.65	33313.28	RQ 25-B1C	Level 4	No
Rotorcraft	Blade	Fixed-Wing - 25lb	11.34	1,082.27	Hover [H]	20.06	0.00	20.06	2282.31	RF 25-B1H	Level 4	No
Rotorcraft	Blade	Fixed-Wing - 25lb	11.34	1,082.27	Medium [M]	20.06	28.29	48.36	13258.69	RF 25-B1M	Level 4	No
Rotorcraft	Blade	Fixed-Wing - 25lb	11.34	1,082.27	Cruise [C]	20.06	56.59	76.65	33313.28	RF 25-B1C	Level 4	No
Rotorcraft	Blade	Quadcopter - 55lb	24.95	1,082.27	Hover [H]	20.06	0.00	20.06	5021.08	RQ 55-B1H	Level 4	No
Rotorcraft	Blade	Quadcopter - 55lb	24.95	1,082.27	Medium [M]	20.06	28.29	48.36	29169.11	RQ 55-B1M	Level 4	No
Rotorcraft	Blade	Quadcopter - 55lb	24.95	1,082.27	Cruise [C]	20.06	56.59	76.65	73289.22	RQ 55-B1C	Level 4	No
Rotorcraft	Blade	Fixed-Wing - 55lb	24.95	1,082.27	Hover [H]	20.06	0.00	20.06	5021.08	RF 55-B1H	Level 4	No
Rotorcraft	Blade	Fixed-Wing - 55lb	24.95	1,082.27	Medium [M]	20.06	28.29	48.36	29169.11	RF 55-B1M	Level 4	No
Rotorcraft	Blade	Fixed-Wing - 55lb	24.95	1,082.27	Cruise [C]	20.06	56.59	76.65	73289.22	RF 55-B1C	Level 4	No

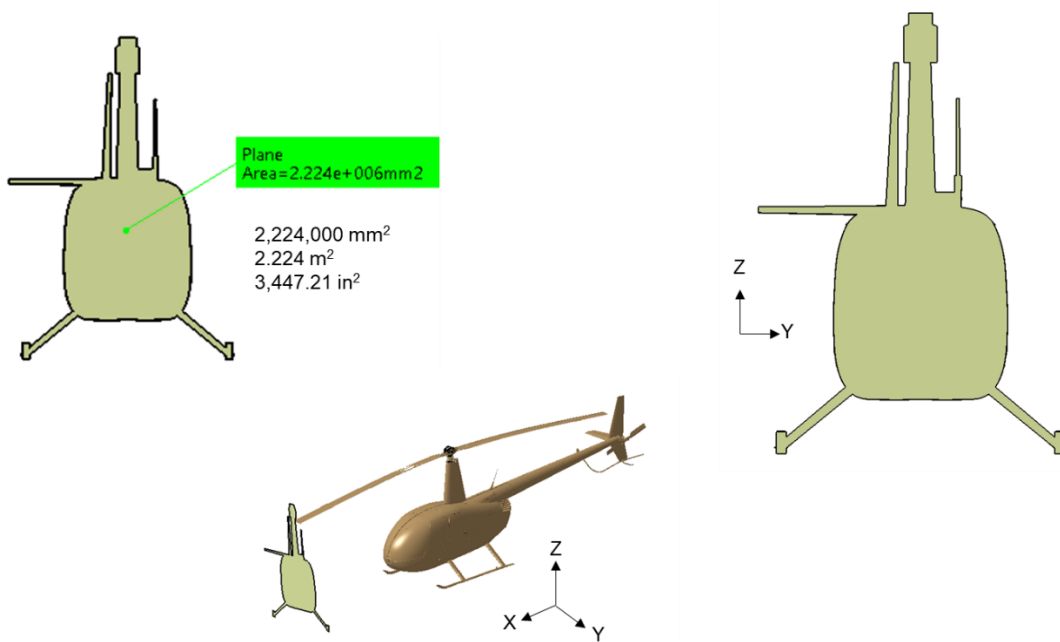# APPENDIX C. <u>APPROXIMATE TARGET EXPOSED SURFACE</u>

Figure 338. Approximate exposed surface for the R44 Rotorcraft – Parallel Blades.
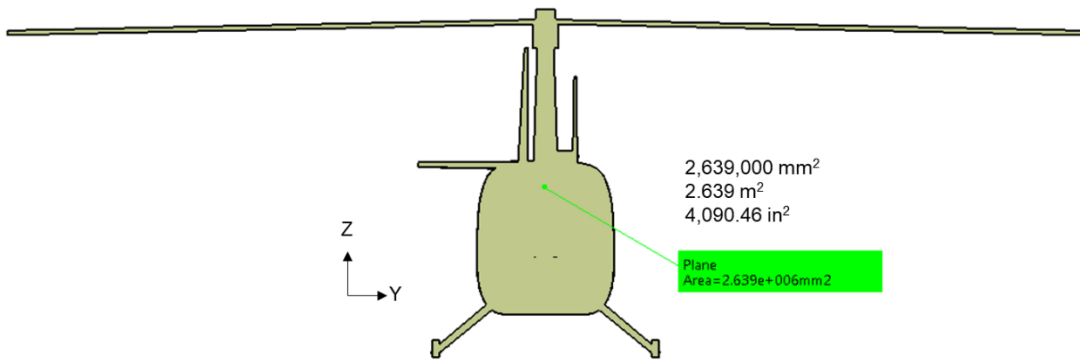

Figure 339. Approximate exposed surface for the R44 Rotorcraft – Perpendicular Blades.